



Application of Molybdenum Carbide Catalysts for the CO₂-assisted Oxidative Dehydrogenation of Ethane

by

Wijnand Marquart

MSc. Chemical Engineering, University of Cape Town

BSc. Chemical Engineering, University of Applied Sciences Utrecht

Thesis presented to the University of Cape Town in the
fulfilment of the requirements for the degree of

DOCTOR OF PHILOSOPHY

DSI-NRF Centre of Excellence in Catalysis c*change

Catalysis Institute

in the Department of Chemical Engineering

UNIVERSITY OF CAPE TOWN

Cape Town

August 2022

The copyright of this thesis vests in the author. No quotation from it or information derived from it is to be published without full acknowledgement of the source. The thesis is to be used for private study or non-commercial research purposes only.

Published by the University of Cape Town (UCT) in terms of the non-exclusive license granted to UCT by the author.

Dedicated to my parents

Declaration

I, **Mr Wijnand Marquart**, declare that the content of this unique thesis submission is my own unaided work, except for the information acquired from literature sources and my prescribed supervisors. All formal sources of information from literature have been adequately acknowledged and referenced in honour of the efforts of all the authors and their work. I have not received assistance from any other source in completing this work. This thesis has also not been, is not being and is not to be submitted for another degree at the University of Cape Town or any other university. I consent the University of Cape Town to reproduce either the whole or any part of the contents of this work in any manner whatsoever for the purpose of research.

Date: 17 August 2022

Acknowledgments

The work presented in this thesis was completed from July 2018 to August 2022 at the Catalysis Institute in the Department of Chemical Engineering at the University of Cape Town (UCT), South Africa.

Firstly, I would like to extend my sincere thanks to my supervisors, Assoc. Prof. Nico Fischer and Prof. Michael Claeys, for giving me the opportunity to conduct this work in their laboratories, for their continuous patience, support, and advice throughout the project. I would like to express my deepest appreciation to Assoc. Prof. Nico Fischer for his extraordinary guidance throughout the years, both MSc and PhD, by making available endless amounts of time for scientific discussions, manuscript and thesis corrections, advancing my laboratory skills and trusting me to direct my own research pathway. Due to his open door policy, he created an environment for me to feel free to approach him with any questions, suggestions or challenges I faced. No topics were off bounds.

I would like to thank the DSI-NRF Centre of Excellence in Catalysis c*change for their financial support throughout the thesis, the National Research Foundation (NRF) for the student extension support and the Catalysis Society of South Africa (CATSA) for the Student International Travel Grant to attend the 27th Meeting of the North American Catalysis Society in New York, USA.

A special thanks goes out to the external researchers I have had the pleasure to collaborate with: Prof. Jan-Dierk Grunwaldt, Dr. Anna Zimina and Dr Bidyut Bikash Sarma (Karlsruhe Institute of Technology, KIT) for their contribution to conduct *in situ* XAS experiments, and the extensive data analysis thereof, at the KIT Synchrotron in Karlsruhe, Germany; Dr. Gonzalo Prieto (Insituto de Tecnología Química, ITQ) for his contribution to conduct *in situ* Raman experiments, and the Diamond Light Source for time on B18 as part of the Block Allocation Group beamtime of the UK Catalysis Hub in December 2018.

Many thanks to everyone in the Catalysis Institute, the Analytical Laboratory, the Electron Microscope Unit and in particular my research group for their support and assistance in and outside the laboratories and for creating a fruitful atmosphere that makes one excited to go to the labs every day. In particular, I would like to mention Shaine Raseale, Dominic de Oliveira, and Dr. Mohamed Fadlalla, for always making themselves available when I reached out for their assistance.

Words cannot express my gratitude to all my friends and family, in the Netherlands and in South Africa, specifically my housemates Regardt Hennop and Rutger Marquart, as they all contributed to turning my PhD journey into the best time of my life. Finally, I am deeply grateful to my parents, for their unconditional love and support.

Synopsis

The rising demand for light olefins is at present mainly met *via* catalytic/thermal dehydrogenation of alkanes at temperatures of up to 900 °C. Under these severe process conditions, competing side reactions and catalyst deactivation *via* coking are the major challenges. Co-feeding an oxidant significantly decreases the reaction temperature. The oxidative dehydrogenation of ethane to ethylene, using CO₂ as the oxidant (CO₂-ODH), has earned a lot of interest in the past decade. The use of CO₂, a soft oxidant in comparison to O₂, prevents the overoxidation reaction of the paraffin to CO₂ and allows for improved heat control. Besides that, the coking effect, which is believed to be the main catalyst deactivation pathway during these high temperature processes, could be significantly lowered due to the reverse Boudouard reaction. The most common catalytic materials reported are reducible metal oxides (MO_x) due to their redox properties; a key concept to activate the C-H bond of the alkane and subsequently activate CO₂. Besides metal oxides, transition metal carbides have also shown to be active for the CO₂-ODH, reaching high yields of ethylene. Specifically, molybdenum carbide (Mo_xC_y) has shown to be a highly efficient catalyst for CO₂ activation and alkane dehydrogenation, demonstrating its ability to cleave C-H bonds. These characteristics are important in making a Mo_xC_y-based catalyst a serious candidate for the CO₂-ODH of light alkanes.

This work entails the design of novel Mo_xC_y-based catalysts for application in the CO₂-ODH of C₂H₆. Previous work on Mo_xC_y-based catalysts found that the bulk material has limited activity and selectivity towards producing C₂H₄ but is significantly improved once dispersed on a support material. The type of support material dictates whether the CO₂-ODH reaction takes place, or if one of the major side reactions, the dry-reforming of C₂H₆ to synthesis gas, is preferred. In this study, Mo_xC_y nanoparticles were prepared *via* various (novel) synthesis techniques, dispersed on a variety of MO_x support materials as well as modified with various promoters. Besides the exploratory nature of this study, gaining knowledge on the activity of the various formulations of Mo_xC_y-based catalysts, the preparation conditions of the carbide materials were investigated. To prepare Mo_xC_y, the precursor samples (in the molybdate or oxide phase) are exposed to a temperature programmed treatment (carburization) in the presence of a carbonaceous and reductive gas mixture. The carbide formation, in terms of crystallite structure, surface composition as well as potential fouling mechanisms is highly dependent on the heating rate, gas mixture, final temperature and precursor composition. Various experiments utilizing *in situ* characterization techniques, such as *in situ* X-ray diffraction, X-ray adsorption and Raman spectroscopy as well as online product analysis techniques were employed to gain knowledge on the carburization process, the structural and chemical

properties and their effect on the activity of the various prepared catalysts in the CO₂-ODH as well as the reverse water-gas-shift reaction.

The use of Mo_xC_y-based catalysts in the CO₂-ODH reaction has not been thoroughly investigated in literature before and is still a very new topic to the scientific community. The presented research can contribute on various aspects of the use and viability of Mo_xC_y-based catalysts in CO₂ utilizing reactions and can be extended to dry-reforming or CO₂ hydrogenation to fuels. In terms of catalyst synthesis, the extensive characterization exposing the various possible crystal structures of Mo_xC_y nanoparticles and application of surface sensitive techniques, allowed for a better understanding of the possible active phases responsible for CO₂ and alkane activation. Besides the identification of the active phase, the deactivation mechanism for Mo_xC_y-based catalysts in the CO₂-ODH reaction is studied in more detail by focusing on the crystal structure and the presence of carbon on the catalyst surface. By varying catalyst compositions as well as reaction conditions, including the use of various co-feeding experiments, an increase in catalytic stability, while maintaining high yields of the desired product from CO₂-ODH (ethylene), was achieved.

Table of Contents

Table of Contents	i
List of Tables	vi
List of Figures.....	viii
Nomenclature	xxi
1 Introduction	1
References	4
2 Literature Review.....	5
2.1 Carbon capture, storage and utilization.....	6
2.2 Light olefins, the world's chemical building block.....	9
2.3 CO ₂ -assisted oxidative dehydrogenation of light alkanes.....	11
2.3.1. <i>Metal oxide catalysts</i>	13
2.3.2. <i>(Bi)metallic catalysts</i>	17
2.3.3. <i>Molybdenum carbide based catalysts</i>	18
2.4 Molybdenum carbide catalyst	22
2.4.1. <i>Synthesis methods of (supported) Mo_xC_y catalysts</i>	22
2.4.2. <i>Promoter addition and effect on Mo_xC_y catalysts</i>	26
References	28
3 Scope of the thesis.....	36
References	39
4 Experimental Methodology	40
4.1 Synthesis of supported molybdenum carbide nanoparticles	40
4.1.1. <i>Slurry (wet) impregnation method</i>	40
4.1.2. <i>Sol-Gel method</i>	40
4.1.3. <i>Hybrid nanocrystal method</i>	41

4.1.4.	<i>Carburization method</i>	41
4.2	Characterization of supported molybdenum carbide nanoparticles	42
4.2.1.	<i>Powder X-Ray diffraction (XRD)</i>	42
4.2.2.	<i>Raman spectroscopy</i>	43
4.2.3.	<i>Transmission electron microscopy (TEM)</i>	43
4.2.4.	<i>Scanning electron microscopy (SEM)</i>	43
4.2.5.	<i>X-ray absorption spectroscopy (XAS)</i>	44
4.2.6.	<i>Inductively Coupled Plasma-Optical Emission Spectroscopy (ICP-OES)</i>	44
4.2.7.	<i>Surface area and pore volume measurements</i>	45
4.2.8.	<i>CO₂ temperature-programmed desorption (CO₂-TPD)</i>	45
4.2.9.	<i>NH₃ temperature-programmed desorption (NH₃-TPD)</i>	45
4.2.10.	<i>Temperature-programmed reaction of CO₂ (TP-CO₂)</i>	45
4.2.11.	<i>Thermogravimetric analysis (TGA)</i>	46
4.2.12.	<i>In situ powder X-ray diffraction</i>	46
4.2.13.	<i>In situ Raman spectroscopy</i>	46
4.2.14.	<i>In situ X-ray absorption spectroscopy</i>	47
4.3	Catalytic performance evaluation in CO ₂ -ODH and RWGS	48
4.3.1.	<i>Test unit and reactor set-up</i>	48
4.3.2.	<i>Experimental procedure for CO₂-ODH experiments</i>	50
4.3.3.	<i>Experimental procedure for RWGS experiments</i>	54
4.3.4.	<i>Product analysis</i>	55
	References	59

5	<i>In situ carburization and CO₂-ODH performance of SiO₂ supported Mo_xC_y nanoparticles</i>	60
5.1	Thermodynamic analysis of the CO ₂ -ODH reaction	60
5.2	<i>In situ</i> characterization of the carburization process	67
5.3	CO ₂ -ODH catalytic performance	73

5.4	Concluding remarks	80
	References	82
6	Supported Mo_xC_y via different synthesis techniques	84
6.1	Thermodynamic analysis of the RWGS reaction.....	84
6.2	Catalyst characterizatop: effect of synthesis techniques	86
6.2.1.	<i>Hybrid nano-crystal technique</i>	86
6.2.2.	<i>Sol-Gel technique</i>	88
6.2.3.	<i>Characterization of activated catalysts: effect of synthesis techniques</i>	89
6.3	CO ₂ activation: effect of synthesis technique	93
6.4	RWGS performance: effect of synthesis technique	100
6.5	CO ₂ -ODH performance: effect of synthesis technique	104
6.6	Concluding remarks	107
	References	109
7	Mo_xC_y supported on various metal oxides	111
7.1	Thermodynamic analysis of the CO ₂ -ODH reaction: effect of H ₂ or H ₂ O co-feeding.....	111
7.2	Catalyst characterization: effect of MO _x support.....	114
7.3	Acid-base properties: effect of MO _x support	118
7.4	CO ₂ activation: effect of MO _x support.....	123
7.5	CO ₂ -ODH performance: effect of MO _x support	125
7.5.1.	<i>Effect of support</i>	125
7.5.2.	<i>Effect of feed composition</i>	128
7.6	Concluding remarks	135
	References	137
8	Promoter addition to SiO₂ supported Mo_xC_y	138
8.1	Catalyst characterization: effect of promotion	138
8.1.1.	<i>Fe promotion</i>	140

8.1.2.	<i>Pt promotion</i>	143
8.1.3.	<i>Ni promotion</i>	145
8.1.4.	<i>K promotion</i>	147
8.1.5.	<i>Characterization of activated catalysts: effect of promotion</i>	149
8.2	Acid-base properties: effect of promotion	151
8.3	CO ₂ activation: effect of promotion	154
8.4	RWGS performance: effect of promotion.....	155
8.5	CO ₂ -ODH performance: effect of promotion.....	158
8.5.1.	<i>Use of different gas supply on Mo_xC_y/SiO₂</i>	158
8.5.2.	<i>Effect of promotion</i>	161
8.5.3.	<i>Effect of feed composition</i>	169
8.6	Concluding remarks	173
	References	175
9	Conclusions and Summary	176
	References	180
10	Recommendations and Future Work	181
	Appendix	183
A	Thermodynamic analysis of CO ₂ -ODH	183
B	CO ₂ -ODH testing results of selected samples.....	185
C	TGA measurements of selected samples.....	192
D	XRD and Rietveld refined patterns of selected samples	193
E	Raman spectra of selected samples	196
F	CO ₂ -TPD results of selected samples	197
G	XANES linear combination fits and EXAFS radial distribution fits	198
H	Reactor heating block design and reactor packing.....	201
I	GC-TCD configuration and calibration details	203

J	MS configuration and calibration details	205
K	Supplementary tables	207
L	Curriculum vitae	220

List of Tables

Table 2.1. Crystallographic information of common molybdenum carbide phases. Table is adapted from De Zanet and Kondrat ¹¹⁸	25
Table 4.1. Overview of reference patterns used in this work obtained from the PDF-4+ (2019/20) in the ICDD database.....	42
Table 4.2. Raman bands observed in literature of their respective metal oxide materials.	43
Table 4.3. Overview of CO ₂ -ODH experiments discussed in Chapter 5.	50
Table 4.4. Overview of CO ₂ -ODH experiments discussed in Chapter 6.	51
Table 4.5. Overview of CO ₂ -ODH experiments discussed in Chapter 7.	51
Table 4.6. Overview of CO ₂ -ODH experiments discussed in Chapter 8.	53
Table 4.7. Overview of RWGS experiments discussed in Chapter 6.	54
Table 4.8. Overview of RWGS experiments discussed in Chapter 8.	55
Table 4.9. The effect of reaction pathway on the conversion ratio (at a 1:1 and 5:1 CO ₂ to C ₂ H ₆ feed), the product ratios, and the C ₂ H ₄ and CO selectivity.	58
Table 5.1. Overview of possible side reactions considered in the CO ₂ -ODH. Sorted in order from endothermic to exothermic at 25 °C and 1 bar pressure: Non-selective reaction (NSR), carbon formation (CF), dry-reforming of ethane (DR), CO ₂ -oxidative dehydrogenation of ethane (ODH), direct dehydrogenation of ethane (DH), ethane decomposition (EAD), methane decomposition (MD), reverse water-gas-shift (RWGS), ethylene decomposition (EED), ethane hydrogenolysis (EH), CO reduction (COR), methanation of CO ₂ (MCO ₂), Boudouard reaction (BR) and methanation of CO (MCO).	62
Table 5.2. Phase composition <i>via</i> XANES linear combination fitting and XRD Rietveld analysis, including crystallite sizes, on bulk β-Mo ₂ C carburized at different temperatures and exposed to air with (P) and without (NP) passivation treatment.....	72
Table 5.3. Phase composition obtained <i>via</i> XANES linear combination fitting of a freshly carburized Mo _x C _y /SiO ₂ at 700 °C, and exposed to CO ₂ -ODH conditions at 550 °C, 650 °C and 750 °C.	80
Table 6.1. Phase composition and crystallite sizes determined <i>via</i> XRD Rietveld analysis of the freshly carburized catalysts.....	90
Table 6.2. Overview of phase quantification of the XANES spectra <i>via</i> linear combination fitting, measured at room temperature after carburization and after TP-CO ₂ activation.....	100
Table 7.1. Phase composition and crystallite sizes determined <i>via</i> XRD Rietveld analysis of the freshly carburized Mo _x C _y catalysts supported on SiO ₂ , Al ₂ O ₃ , ZrO ₂ , Ga ₂ O ₃ , TiO ₂ or CeO ₂	115

Table 8.1. Overview of phase quantification and crystallite sizes determined <i>via</i> Rietveld analysis of the synthesized catalysts.....	149
Table I.1. GC-TCD configuration.....	204
Table I.2. TCD calibration of CO ₂ -ODH mixture and standard gas mixture,.....	204
Table J.1. MS configuration details.....	206
Table J.2. Compound specific cracking patterns and library RSF values.....	206
Table K.1. Sample nomenclature and physiochemical properties of all synthesized samples.....	207
Table K.2. Overview of phase quantification and crystallite size determined <i>via</i> XRD Rietveld analysis of the spent CO ₂ -ODH catalysts.	209
Table K.3. Overview of phase quantification and crystallite size determined <i>via</i> Rietveld refinement of the spent TP-CO ₂ activation catalysts.	213
Table K.4. Overview of phase quantification and crystallite size determined <i>via</i> Rietveld refinement of the spent CO ₂ -TPD catalysts.	214
Table K.5. Overview of phase quantification and crystallite size determined <i>via</i> Rietveld refinement of the spent NH ₃ -TPD catalysts.....	215
Table K.6. Overview of phase quantification and crystallite size determined <i>via</i> Rietveld refinement of the spent RWGS catalysts.	216
Table K.7. Fit parameter corresponding to the radial distribution fits in Figure G.4. For Mo foil, crystal structure with ICSD code 76147 was used. S ₀ ² is amplitude reduction factor, CN is coordination number, E ₀ is energy shift, R is radial distance, DW is Debye-Waller factor and r is quality of fit.....	217
Table K.8. Surface area to volume ratio normalized to Mo content of fresh and spent samples.....	217
Table K.9. Overview of peak positions, peak width (FWHM) and the goodness of fit (R ²), obtained through curve fitting CO ₂ desorption spectra.....	219

List of Figures

Figure 2.1. [A] Change in global surface temperature relative to 1951-1980 average temperatures. [B] Concentration of atmospheric CO ₂ over the past 800,000 years. Insert: CO ₂ concentration since 1960 until today. Figure reproduced from Shaftel <i>et al.</i> ²	5
Figure 2.2. Share of the world's CO ₂ emissions by fuel combustion only, per region and by fuel source, recorded in 2019. ¹⁵	7
Figure 2.3. CO ₂ emissions from different technologies producing light olefins (or aromatics) per tonne of high-value chemicals (HVC). Figure is adapted from Amghizar <i>et al.</i> ³¹ . Red bars indicate CO ₂ emitted from energy generation; grey bars indicate CO ₂ emitted from chemical reactions. Annotations indicate the carbon source (naphtha, ethane, methane, biomass or coal) and the process application (steam cracking (SC), Fischer-Tropsch (FT) synthesis, oxidative coupling of methane (OCM) and methanol to olefin (MTO).	11
Figure 2.4. Gibbs free energy calculations as a function of temperature on the possible individual reactions to occur during CO ₂ -ODH of ethane.....	12
Figure 2.5. Graphical representation of a reducible metal oxide catalyst proceeding <i>via</i> a Mars-van-Krevelen type mechanism in the CO ₂ -ODH of ethane.	13
Figure 2.6. Graphical representation of the dehydrogenation of ethylbenzene to styrene and H ₂ over an Al ₂ O ₃ catalyst. Figure adapted from Sato <i>et al.</i> ⁹¹	14
Figure 2.7. Graphical representation of the CO ₂ assisted dehydrogenation of ethylbenzene to styrene, CO and water over a Na ₂ O/Al ₂ O ₃ catalyst. Figure adapted from Sato <i>et al.</i> ⁹¹	14
Figure 2.8. Metal oxides in the CO ₂ oxidative dehydrogenation of C ₂ H ₆ . Process conditions: T = 650 °C, CO ₂ to C ₂ H ₆ ratio = 5:1, SV = 9 L h ⁻¹ ·g _{cat} ⁻¹ . Figure adapted from Nakagawa <i>et al.</i> ⁹²	15
Figure 2.9. Catalytic performance of the unpromoted and promoted Cr ₂ O ₃ /ZrO ₂ catalysts. Process conditions: CO ₂ to C ₂ H ₆ ratio = 3:1, SV = 4.5 L·h ⁻¹ ·g ⁻¹ . Figure is reproduced with data obtained from Deng <i>et al.</i> ⁹⁷	16
Figure 2.10. Graphical representation of the proposed ODH mechanism over transition metal carbide catalysts. A successful catalyst is required to support CO ₂ activation to form oxygen surface species or MoO _x C _y . Subsequently, by means of the oxygen sites, ethane is activated by C-H bond scission, forming water and ethylene.	18
Figure 2.11. DFT-calculated energy profile of reforming and oxidative dehydrogenation of ethane over [A] Mo ₂ C(001) and [B] Pt(111) and CeO ₂ /Pt(111) surface. Figure reproduced from Porosoff <i>et al.</i> ⁵⁵	20
Figure 2.12: Temperature-programmed reaction of MoO ₃ with 20 vol.-% CH ₄ in H ₂ reaction mixture while heating to 730 °C with 1 °C min ⁻¹ . Conditions: 0.5 g MoO ₃ , GHSV = 11 L h ⁻¹ g _{cat} ⁻¹ . Figure is adapted from Lee <i>et al.</i> ¹¹⁵	23

Figure 4.1. XRD patterns of the XAS reference materials.	44
Figure 4.2. Process flow diagram of the rig set-up used for carburization and testing of the catalysts. Red lines are heated lines.....	49
Figure 5.1. Thermodynamic equilibrium conversions as a function of temperature at 1 bar pressure of the non-selective reaction (NSR), carbon formation (CF), dry-reforming of ethane (DR), CO ₂ -oxidative dehydrogenation of ethane (ODH), direct dehydrogenation of ethane (DH), ethane decomposition (EAD), methane decomposition (MD), reverse water-gas-shift (RWGS), ethylene decomposition (EED), ethane hydrogenolysis (EH), CO reduction (COR), methanation of CO ₂ (MCO ₂), Boudouard reaction (BR) and methanation of CO (MCO). Red shaded area indicates temperature range of interest for CO ₂ -ODH. Compound specific thermodynamic data from Knacke <i>et al.</i> ¹⁰	63
Figure 5.2. Thermodynamic equilibrium conversion for ODH and DH as a function of CO ₂ to C ₂ H ₆ feed ratio and dilution at 600 °C and 1 bar pressure. Compound specific thermodynamic data from Knacke <i>et al.</i> ¹⁰	64
Figure 5.3. Product equilibrium of the CO ₂ -ODH system as a function of temperature. [A] All compounds considered, [B] carbon formation neglected, [C] methane formation neglected and [D] carbon and methane formation neglected. Red shaded area indicates temperature range of interest for CO ₂ -ODH. Compound specific thermodynamic data from Knacke <i>et al.</i> ¹⁰	66
Figure 5.4. Product equilibrium of the system as a function of temperature including Mo-phases. [A] and [B] all compounds considered, [C] and [D] methane formation neglected. Red shaded area indicates temperature range of interest for CO ₂ -ODH. Compound specific thermodynamic data from Knacke <i>et al.</i> ¹⁰	67
Figure 5.5. Carburization process of Mo _x C _y /SiO ₂ as function of temperature, with [A] top view of <i>in situ</i> XRD patterns, [B] corresponding Rietveld refinement analysis with phase composition and [D] particle size and [C] TGA analysis with TG curve (red dashed line) and differential thermal analysis (DTA) signal (grey solid line). Conditions: T _{final} = 600 °C, P = 1 atm, heating rate = 1 °C min ⁻¹ , holding time = 5 hours.	68
Figure 5.6. <i>In situ</i> Raman spectra collected for [A] the carburization and [B] the calcination of Mo _x C _y /SiO ₂ . Conditions: T = 600 °C, P = 1 atm, heating rate = 3 °C min ⁻¹ . For the carburization a 10 vol.-% CH ₄ , 40 vol.-% H ₂ , balance He mixture was used at 60 L h ⁻¹ g _{cat} ⁻¹	70
Figure 5.7. <i>In situ</i> Raman spectra collected at room temperature for Mo _x C _y /SiO ₂ with [A] after passivation treatment, [B] after reactivation treatment of passivated sample, and [C, D] after exposure of the passivated-reactivated-passivated sample to air at room temperature overnight, recorded in [C] helium and [D] air atmosphere.	70
Figure 5.8. [A] Mo K-edge XANES region, shifted to 20,000 eV and [B] XRD patterns of bulk β-Mo ₂ C samples carburized at different temperatures, exposed to air with (P) and without (NP) passivation treatment. The XAS references, MoO ₃ , MoO ₂ and β-Mo ₂ C, used for linear combination fitting are indicated in black.	71

Figure 5.9. Schematic representation of bulk Mo ₂ C particles with a residual oxide core and different possible surface states and their effect on reactivity: [A] Bare carbide surface is partially re-oxidized, causing (and subsequently accelerated by) localized temperature spikes when exposed to high concentrations of oxygen such as in air. [B] O ₂ is dissociated on a bare carbide surface at low partial pressures of the oxidant, forming a passivating layer around the carbide particle. [C] Thick layer of carbon deposits around the carbide particle at higher carburization temperatures, protecting the carbide surface from reoxidation in air (compare case [A]).	73
Figure 5.10. XRD patterns of freshly carburized samples at 600 °C and 700 °C.	74
Figure 5.11. C ₂ H ₆ conversion, C ₂ H ₄ selectivity and C ₂ H ₄ yield, of Mo _x C _y /SiO ₂ and Mo _x C _y /SiO ₂ -O ₂ . Conditions: T = 550 °C (0-12 hours TOS), 600 °C (12-24 hours TOS), 650 °C (24-36 hours TOS), 700 °C (36-48 hours TOS), 750 °C (48-60 hours TOS) and 650 °C (60-66 hours TOS). P = 1 atm, SV = 9.4 L h ⁻¹ g _{cat} ⁻¹ , C ₂ H ₆ :CO ₂ :Ar = 1:1:2. Theoretical maximum C ₂ H ₄ selectivity for CO ₂ -ODH indicated by solid black line.	75
Figure 5.12. CO ₂ conversion, CO selectivity, C ₂ H ₆ to CO ₂ conversion ratio, C ₂ H ₄ to CO product ratio, H ₂ to CO product ratio and C ₂ H ₄ to H ₂ product ratio, of Mo _x C _y /SiO ₂ and Mo _x C _y /SiO ₂ -O ₂ . Conditions: T = 550 °C (0-12 hours TOS), 600 °C (12-24 hours TOS), 650 °C (24-36 hours TOS), 700 °C (36-48 hours TOS), 750 °C (48-60 hours TOS) and 650 °C (60-66 hours TOS). P = 1 atm, SV = 9.4 L h ⁻¹ g _{cat} ⁻¹ , C ₂ H ₆ :CO ₂ :Ar = 1:1:2. Theoretical maximum CO selectivity for CO ₂ -ODH indicated by solid black line.	76
Figure 5.13. XRD patterns of the spent catalysts Mo _x C _y /SiO ₂ and Mo _x C _y /SiO ₂ -O ₂ , after exposure to CO ₂ -ODH conditions over a range of reaction temperatures.	77
Figure 5.14. Raman spectra of the spent catalysts, Mo _x C _y /SiO ₂ and Mo _x C _y /SiO ₂ -O ₂ , after exposure to CO ₂ -ODH conditions over a range of reaction temperatures.	78
Figure 5.15. C ₂ H ₆ conversion, C ₂ H ₄ selectivity and C ₂ H ₄ yield, of Mo _x C _y /SiO ₂ . Conditions: T = 550 °C, 650 °C or 700 °C, P = 1 atm, SV = 9.4 L h ⁻¹ g _{cat} ⁻¹ , C ₂ H ₆ :CO ₂ :Ar = 1:1:2. Theoretical maximum C ₂ H ₄ selectivity for CO ₂ -ODH indicated by solid black line.	79
Figure 5.16. XRD patterns of the spent catalysts after exposure to CO ₂ -ODH conditions at 550 °C, 650 °C and 750 °C.	79
Figure 5.17. Raman spectra of the spent Mo _x C _y /SiO ₂ after exposure to CO ₂ -ODH conditions at 550, 650 and 750 °C.	80
Figure 6.1. Effect of feed ratio (H ₂ to CO ₂) and temperature on the equilibrium conversion of the reverse water-gas-shift (RWGS) reaction and the methanation of CO ₂ (MCO ₂), at 1 bar pressure. Thermodynamic parameters are from Knacke <i>et al.</i> ¹	84
Figure 6.2. Product equilibrium of the RWGS system as a function of temperature at a H ₂ to CO ₂ feed ratio of 1 [A, B], 2.5 [C], or 5.0 [D], with [A, C, D] all compounds considered, and [B] carbon formation neglected. Compound specific thermodynamic data from Knacke <i>et al.</i> ¹	85

Figure 6.3. TEM micrographs of [A, B] freshly prepared hybrid nano-crystals and [C, D] MoO ₃ supported on SBA-15 prepared <i>via</i> HNC synthesis route.....	86
Figure 6.4. Carburization process of Mo _x C _y /SBA-15-HNC as function of temperature, with [A] top view of <i>in situ</i> XRD patterns, [B] corresponding Rietveld refinement analysis with phase composition and [D] particle size and [C] TGA analysis with TG curve (red dashed line) and differential thermal analysis (DTA) signal (grey solid line). Conditions: T _{final} = 600 °C, P = 1 atm, heating rate = 1 °C min ⁻¹ , holding time = 5 hours.....	87
Figure 6.5. TEM micrographs of MoO ₃ supported on SiO ₂ prepared <i>via</i> the sol-gel method.	88
Figure 6.6. Carburization process of Mo _x C _y /SiO ₂ -SG as function of temperature, with [A] top view of <i>in situ</i> XRD patterns [B] XRD patterns obtained at 50 °C, 550 °C and 600 °C.....	89
Figure 6.7. XRD patterns of the freshly carburized samples at 600 °C.....	89
Figure 6.8. TEM micrographs of the freshly carburized samples at 600 °C. No micrographs available for Mo _x C _y /SiO ₂ -HNC.	91
Figure 6.9. SEM-EDS micrographs and elemental mapping of the freshly carburized samples at 600 °C. No micrographs available for Mo _x C _y /SBA-15-WI.	92
Figure 6.10. Raman spectra of freshly carburized samples at 600 °C.	93
Figure 6.11. Temperature programmed CO ₂ activation, with [A] CO yield normalized to mass of Mo content in the catalyst and [B] TP-CO ₂ activation over bulk β-Mo ₂ C. Conditions: heating rate from RT to 700 °C at 1 °C min ⁻¹ in 1 vol.-% CO ₂ /N ₂ with a SV of 60 L h ⁻¹ g _{cat} ⁻¹ at a pressure of 1 atm.	94
Figure 6.12. XRD patterns of the spent TP-CO ₂ activation catalysts.	95
Figure 6.13. <i>In situ</i> XANES spectra on Mo _x C _y /SiO ₂ -WI with [A] carburization treatment and [B] TP-CO ₂ activation and their corresponding LCF results in [C] and [D], respectively. For detailed experimental conditions, see section 4.2.14.	96
Figure 6.14. Normalized <i>in situ</i> XANES spectra of the Mo K edge, of Mo _x C _y /SiO ₂ -WI during carburization from 390 to 470 °C.	96
Figure 6.15. <i>In situ</i> XANES spectra on Mo _x C _y /SBA-15-HNC with [A] carburization treatment and [B] TP-CO ₂ activation and their corresponding LCF results in [C] and [D], respectively. For detailed experimental conditions, see section 4.2.14.....	97
Figure 6.16. <i>In situ</i> XANES spectra on Mo _x C _y /SiO ₂ -SG with [A] carburization treatment and [B] TP-CO ₂ activation and their corresponding LCF results in [C] and [D], respectively. For detailed experimental conditions, see section 4.2.14.	98
Figure 6.17. k ³ -weighed Mo K edge EXAFS spectra of Mo _x C _y /SiO ₂ -WI, Mo _x C _y /SBA-15-HNC, Mo _x C _y /SiO ₂ -WI, β-Mo ₂ C-reference and α-MoC _{1-x} -reference in [A] k-space and [B] R-space.	99

Figure 6.18. [A, B] CO ₂ conversion, [C, D] H ₂ conversion and [E, F] CO and CH ₄ selectivity, of [A, C, E] Mo _x C _y /SiO ₂ -WI* and Mo _x C _y /SBA-15-WI and Mo _x C _y /SBA-15-HNC, with T = 400 °C (0-12 hours TOS), T = 500 °C (12-24 hours TOS), T = 600 °C (24-36 hours TOS) and 400 °C (36-42 hours TOS). For Mo _x C _y /SBA-15-HNC, T = 400 °C (0-24 hours TOS). H ₂ /CO ₂ ratio = 1, SV (CO ₂ + H ₂) = 60 L h ⁻¹ g _{cat} ⁻¹ . [B, D, F] Mo _x C _y /SiO ₂ -WI** and Mo _x C _y /SiO ₂ -SG: T = 400 °C, H ₂ /CO ₂ ratio of 1.0, 3.5 or 7.0. SV = 120 L h ⁻¹ g _{cat} ⁻¹ . Thermodynamic equilibrium conversions for CO ₂ and H ₂ are displayed by X _{eq} .	102
Figure 6.19. XRD patterns of the spent catalysts after exposure to various RWGS conditions.	103
Figure 6.20. Accumulative formation of CO as a function of time under RWGS conditions normalized to the Mo content in the catalysts. Mo _x C _y /SiO ₂ -WI** (red) and Mo _x C _y /SiO ₂ -SG (purple): T = 400 °C for 24 hours at H ₂ /CO ₂ ratio of 1.0, 3.5 or 7.0. SV = 120 L h ⁻¹ g _{cat} ⁻¹ .	103
Figure 6.21. C ₂ H ₆ conversion, C ₂ H ₄ selectivity and C ₂ H ₄ yield, of Mo _x C _y /SiO ₂ -WI, Mo _x C _y /SBA-15-HNC, Mo _x C _y /SiO ₂ -HNC and Mo _x C _y /SiO ₂ -SG evaluated under the following CO ₂ -ODH conditions: T = 600 °C, P = 1 atm, SV = 15 L h ⁻¹ g _{cat} ⁻¹ , CO ₂ :C ₂ H ₆ :Ar = 1:1:2. Theoretical maximum C ₂ H ₄ selectivity for CO ₂ -ODH indicated by solid black line.	105
Figure 6.22. XRD patterns of the spent CO ₂ -ODH catalysts.	106
Figure 6.23. Optical inspection of Mo _x C _y /SiO ₂ -WI post CO ₂ -ODH reaction in the quartz reactor.	107
Figure 6.24. Raman spectra of the spent CO ₂ -ODH catalysts. No data available for Mo _x C _y /SBA-15-HNC.	107
Figure 7.1. Product equilibrium of the CO ₂ -ODH system as a function of temperature and H ₂ co-feeding at a stoichiometric feed of CO ₂ to C ₂ H ₆ (1:1) and 1 bar pressure, with all compounds considered [A] including the four different Mo phases [B].	112
Figure 7.2. Product equilibrium of the CO ₂ -ODH system as a function of temperature and H ₂ O co-feeding at a stoichiometric feed of CO ₂ to C ₂ H ₆ (1:1) and 1 bar pressure, with all compounds considered [A] including the four different Mo phases [B].	113
Figure 7.3. XRD patterns of the freshly carburized Mo _x C _y catalysts supported on SiO ₂ , Al ₂ O ₃ , ZrO ₂ , Ga ₂ O ₃ , TiO ₂ or CeO ₂ .	114
Figure 7.4. Raman spectra of the freshly carburized Mo _x C _y catalysts supported on SiO ₂ , Al ₂ O ₃ , ZrO ₂ , Ga ₂ O ₃ , TiO ₂ or CeO ₂ .	116
Figure 7.5. SEM-EDS micrographs and elemental mapping of the freshly carburized Mo _x C _y supported on SiO ₂ , Al ₂ O ₃ , ZrO ₂ , Ga ₂ O ₃ , TiO ₂ or CeO ₂ .	117
Figure 7.6. CO ₂ temperature programmed desorption profiles of Mo _x C _y catalysts supported on SiO ₂ , Al ₂ O ₃ , ZrO ₂ , Ga ₂ O ₃ or TiO ₂ , with one experiment supported on SiO ₂ , recorded omitting a CO ₂ adsorption step. Temperature heated up to 800 °C at 10 °C min ⁻¹ , in an Ar atmosphere. Area plots: CO ₂ , with deconvoluted peaks in white, dashed lines: CO.	119

Figure 7.7. Overview of CO ₂ desorbed (normalized to mmol per m ² surface area) as a function of temperature recorded during CO ₂ desorption of Mo _x C _y catalysts supported on SiO ₂ , Al ₂ O ₃ , ZrO ₂ , Ga ₂ O ₃ or TiO ₂	119
Figure 7.8. XRD patterns of the spent CO ₂ -TPD Mo _x C _y catalysts supported on SiO ₂ , Al ₂ O ₃ , ZrO ₂ , Ga ₂ O ₃ or TiO ₂	120
Figure 7.9. NH ₃ temperature programmed desorption profiles normalized to surface area of Mo _x C _y catalysts supported on SiO ₂ , Al ₂ O ₃ , ZrO ₂ , Ga ₂ O ₃ or TiO ₂ , with one experiment, supported on SiO ₂ , recorded omitting a NH ₃ adsorption step. The grey background signals (--) show the original data, prior to normalization. Temperature heated up to 800 °C at 10 °C min ⁻¹ , in an He atmosphere.	121
Figure 7.10. XRD patterns of spent NH ₃ -TPD Mo _x C _y catalysts supported on SiO ₂ , Al ₂ O ₃ , ZrO ₂ , Ga ₂ O ₃ or TiO ₂ . ..	122
Figure 7.11. CO yield observed as a function of temperature, normalized to the mass fraction of Mo in the Mo _x C _y catalysts supported on SiO ₂ , Al ₂ O ₃ , ZrO ₂ , Ga ₂ O ₃ or TiO ₂ . Temperature increased to 700 °C at 5 °C min ⁻¹ , holding for 10 minutes at maximum temperature at atmospheric pressure in 1 vol.-% CO ₂ in Ar at a space velocity of 60 L h ⁻¹ g _{cat} ⁻¹	124
Figure 7.12. XRD patterns of the spent TP-CO ₂ activation Mo _x C _y catalysts supported on SiO ₂ , Al ₂ O ₃ , ZrO ₂ , Ga ₂ O ₃ or TiO ₂	124
Figure 7.13. C ₂ H ₆ conversion, C ₂ H ₄ selectivity and C ₂ H ₄ yield, of Mo _x C _y catalysts supported on SiO ₂ , Al ₂ O ₃ , ZrO ₂ , Ga ₂ O ₃ , TiO ₂ and CeO ₂ . CO ₂ -ODH conditions: T = 600 °C, P = 1 atm, SV = 15 L h ⁻¹ g _{cat} ⁻¹ , CO ₂ :C ₂ H ₆ :Ar = 1:1:2. Theoretical maximum C ₂ H ₄ selectivity for CO ₂ -ODH indicated by solid black line.....	126
Figure 7.14. XRD patterns of the spent CO ₂ -ODH Mo _x C _y catalysts supported on SiO ₂ , Al ₂ O ₃ , ZrO ₂ , Ga ₂ O ₃ , TiO ₂ or CeO ₂	127
Figure 7.15. Raman spectra of the spent CO ₂ -ODH Mo _x C _y catalysts supported on SiO ₂ , Al ₂ O ₃ , ZrO ₂ , Ga ₂ O ₃ , TiO ₂ or CeO ₂	128
Figure 7.16. C ₂ H ₆ conversion, C ₂ H ₄ selectivity and C ₂ H ₄ yield, of Mo _x C _y catalysts supported on Al ₂ O ₃ , ZrO ₂ and Ga ₂ O ₃ . CO ₂ -ODH conditions: T = 600 °C, P = 1 atm, SV = 15 L h ⁻¹ g _{cat} ⁻¹ , CO ₂ :C ₂ H ₆ :Ar = 5:1:6. Theoretical maximum C ₂ H ₄ selectivity for CO ₂ -ODH indicated by solid black line.....	129
Figure 7.17. Absolute amount of ethane converted and loss of ethane conversion with time on stream of Mo _x C _y catalysts supported on Al ₂ O ₃ , ZrO ₂ and Ga ₂ O ₃ evaluated in a 1:1 and 5:1 CO ₂ to C ₂ H ₆ feed ratio.	129
Figure 7.18. XRD patterns of the spent CO ₂ -ODH (5:1) Mo _x C _y catalysts supported on Al ₂ O ₃ , ZrO ₂ or Ga ₂ O ₃	130
Figure 7.19. C ₂ H ₆ conversion, C ₂ H ₄ selectivity and C ₂ H ₄ yield, of Mo _x C _y catalysts supported on SiO ₂ . H ₂ /CO ₂ -ODH conditions: T = 600 °C, P = 1 atm, SV = 18.2 L h ⁻¹ g _{cat} ⁻¹ , CO ₂ :C ₂ H ₆ :Ar = 1:1:2, with H ₂ co-feeding at 0, 5, 10 and 17 vol.-%. Theoretical maximum C ₂ H ₄ selectivity for CO ₂ -ODH indicated by solid black line.	131
Figure 7.20. C ₂ H ₆ conversion, C ₂ H ₄ selectivity and C ₂ H ₄ yield, of Mo _x C _y catalysts supported on ZrO ₂ evaluated under the following H ₂ /CO ₂ -ODH conditions: T = 600 °C, P = 1 atm, SV = 18.2 L h ⁻¹ g _{cat} ⁻¹ , CO ₂ :C ₂ H ₆ :Ar =	

1:1:2, with and without co-feeding of H ₂ at 0, 5 and 17 vol.-%. Theoretical maximum C ₂ H ₄ selectivity for CO ₂ -ODH indicated by solid black line.....	132
Figure 7.21. XRD patterns of the spent H ₂ /CO ₂ -ODH Mo _x C _y catalysts supported on SiO ₂ or ZrO ₂	133
Figure 7.22. Raman spectra of the spent H ₂ /CO ₂ -ODH Mo _x C _y catalysts supported on SiO ₂ or ZrO ₂	134
Figure 7.23. C ₂ H ₆ conversion, C ₂ H ₄ selectivity and C ₂ H ₄ yield, of Mo _x C _y catalysts supported on Ga ₂ O ₃ . H ₂ /CO ₂ -ODH conditions: T = 600 °C, P = 1 atm, SV = 18.2 L h ⁻¹ g _{cat} ⁻¹ , CO ₂ :C ₂ H ₆ :Ar = 1:1:2, with co-feeding of H ₂ at 5 or 10 vol.-%. Theoretical maximum C ₂ H ₄ selectivity for CO ₂ -ODH indicated by solid black line..	135
Figure 7.24. XRD patterns of the spent H ₂ /CO ₂ -ODH Mo _x C _y catalysts supported on Ga ₂ O ₃	135
Figure 8.1 [left] Top view of <i>in situ</i> XRD patterns following the calcination process of MoO ₃ /SiO ₂ as a function of temperature and [right] the individual patterns at 50, 220 and 400 °C (right). Conditions: T _{final} = 400 °C, P = 1 atm, heating rate = 1 °C min ⁻¹ , holding time = 5 hours.....	139
Figure 8.2: Carburization of [A] AHM/SiO ₂ and [B] MoO ₃ /SiO ₂ to Mo _x C _y , monitored by mass spectrometry <i>via</i> the formation of H ₂ O, CO and CO ₂ . Conditions: T _{final} = 600 °C, P = 1 atm, heating rate = 1 °C min ⁻¹ , holding time = 5 hours.	140
Figure 8.3. XRD patterns of Mo _x C _y /SiO ₂ after direct carburization of AHM/SiO ₂ and after calcination at 400 °C to MoO ₃ /SiO ₂	140
Figure 8.4. Carburization process of Fe-Mo _x C _y /SiO ₂ (Co-Imp) as function of temperature, with [A] top view of <i>in situ</i> XRD patterns [B] individual patterns obtained at 50, 300, 450 and 600 °C and [C] mass spectrometry signal monitoring the formation of H ₂ O, CO and CO ₂ . Conditions: T _{final} = 600 °C, P = 1 atm, heating rate = 1 °C min ⁻¹ , holding time = 5 hours.....	141
Figure 8.5. Carburization process of Fe-Mo _x C _y /SiO ₂ (Calc-Imp) as function of temperature followed by <i>in situ</i> XRD (left) and the individual patterns at 50, 525 and 600 °C (right). Conditions: T _{final} = 600 °C, P = 1 atm, heating rate = 1 °C min ⁻¹ , holding time = 5 hours.....	142
Figure 8.6. XRD patterns of the freshly carburized Mo _x C _y on SiO ₂ promoted with Fe <i>via</i> co-impregnation (Co-Imp), after calcination (Calc-Imp) or sequential impregnation (Seq-Imp).	142
Figure 8.7. Carburization process of Pt-Mo _x C _y /SiO ₂ (Co-Imp) as function of temperature, with [A] top view of <i>in situ</i> XRD patterns [B] individual patterns at 50, 230, 300, 460 and 600 °C and [C] mass spectrometry signal monitoring the formation of H ₂ O, CO and CO ₂ . Conditions: T _{final} = 600 °C, P = 1 atm, heating rate = 1 °C min ⁻¹ , holding time = 5 hours.....	143
Figure 8.8. [A, B] Calcination process of Pt-MoO ₃ /SiO ₂ and [C, D] carburization process of Pt-Mo _x C _y /SiO ₂ (Co-Imp-Calc) as function of temperature, with [A, C] top view of <i>in situ</i> XRD patterns, [B, D] individual patterns at selected temperatures. Conditions: T _{final} = 600 °C, P = 1 atm, heating rate = 1 °C min ⁻¹ , holding time = 5 hours.	144

Figure 8.9. [A] XRD patterns of Pt-MoO₃/SiO₂ in (a) air atmosphere, (b) upon short term exposure to 20 vol.-% CH₄/H₂, followed by (c) overnight exposure to air and finally (d) long term exposure to 20 vol.-% CH₄/H₂. [B] XRD patterns of the freshly carburized Pt-Mo_xC_y/SiO₂ prepared *via* Co-Imp and Co-Imp-Calc, including patterns of the precursors Pt-MoO₃/SiO₂ and Pt-AHM/SiO₂. 145

Figure 8.10. Carburization process of Ni-Mo_xC_y/SiO₂ as function of temperature, with [A] top view of *in situ* XRD patterns, [B] individual patterns at 50, 300, 550 and 600 °C, [C] mass spectrometry signal monitoring the formation of H₂O, CO and CO₂ and [D] XRD pattern of the freshly carburized sample Ni-Mo_xC_y/SiO₂. Conditions: T_{final} = 600 °C, P = 1 atm, heating rate = 1 °C min⁻¹, holding time = 5 hours. 146

Figure 8.11. Carburization process of K-Mo_xC_y/SiO₂ as function of temperature, with [A] top view of *in situ* XRD patterns [B] individual patterns at 50, 300, 550 and 600 °C, [C] mass spectrometry signal monitoring the formation of H₂O, CO and CO₂ and [D] XRD pattern of the freshly carburized K-Mo_xC_y/SiO₂. Conditions: T_{final} = 600 °C, P = 1 atm, heating rate = 1 °C min⁻¹, holding time = 5 hours. 147

Figure 8.12. Carburization of Mo_xC_y/SiO₂ with a diluted carburization mixture, monitored by mass spectrometry *via* the formation of H₂O, CO and CO₂. Conditions: T_{final} = 600 °C, P = 1 atm, heating rate = 1 °C min⁻¹, holding time = 5 hours. 148

Figure 8.13. Raman spectra of the freshly carburized Fe-Mo_xC_y/SiO₂, Pt-Mo_xC_y/SiO₂, Ni-Mo_xC_y/SiO₂ and K-Mo_xC_y/SiO₂, prepared *via* co-impregnation. 149

Figure 8.14. TEM micrographs of the freshly carburized Fe-Mo_xC_y/SiO₂, Pt-Mo_xC_y/SiO₂, Ni-Mo_xC_y/SiO₂ and K-Mo_xC_y/SiO₂, prepared *via* co-impregnation. 150

Figure 8.15. SEM-EDS micrographs and elemental mapping of the freshly carburized Fe-Mo_xC_y/SiO₂, Pt-Mo_xC_y/SiO₂, Ni-Mo_xC_y/SiO₂ and K-Mo_xC_y/SiO₂, prepared *via* co-impregnation. 151

Figure 8.16. CO₂ temperature programmed desorption of Fe-Mo_xC_y/SiO₂, Pt-Mo_xC_y/SiO₂, Ni-Mo_xC_y/SiO₂ and K-Mo_xC_y/SiO₂. Temperature heated up to 800 °C at 10 °C min⁻¹ in an Ar atmosphere. Area plots: CO₂, with deconvoluted peaks in white, dashed lines: CO. The unpromoted sample is shown in the background of each plot by the grey area and black line plot. 152

Figure 8.17. NH₃ temperature programmed desorption of Fe-Mo_xC_y/SiO₂, Pt-Mo_xC_y/SiO₂, Ni-Mo_xC_y/SiO₂ and K-Mo_xC_y/SiO₂. Temperature heated up to 800 °C at 10 °C min⁻¹, in an He atmosphere. The unpromoted sample is presented in the background of each plot by the grey area plot. 153

Figure 8.18. XRD patterns of the spent samples after CO₂- and NH₃-TPD experiments of Fe-Mo_xC_y/SiO₂, Pt-Mo_xC_y/SiO₂, Ni-Mo_xC_y/SiO₂ and K-Mo_xC_y/SiO₂. 154

Figure 8.19. [left] CO yield observed as a function of temperature of Fe-Mo_xC_y/SiO₂, Pt-Mo_xC_y/SiO₂, Ni-Mo_xC_y/SiO₂ and K-Mo_xC_y/SiO₂, normalized to the mass fraction of Mo in the catalysts. Temperature increased to 700 °C at 5 °C min⁻¹, holding for 10 min at maximum temperature at atmospheric pressure in 1

vol.-% CO ₂ in Ar at a space velocity of 60 L h ⁻¹ g _{cat} ⁻¹ . [right] XRD patterns of the spent TP-CO ₂ activation experiments.....	155
Figure 8.20. [A] CO ₂ conversion, [B] H ₂ conversion, [C] CO selectivity (solid markers) and CH ₄ selectivity (open markers) of Mo _x C _y /SiO ₂ , Fe-Mo _x C _y /SiO ₂ , Pt-Mo _x C _y /SiO ₂ , Ni-Mo _x C _y /SiO ₂ and K-Mo _x C _y /SiO ₂ and [D] XRD patterns of the spent RWGS catalysts. Conditions: T = 600 °C for 36 h TOS at H ₂ /CO ₂ ratio of 2.5. SV = 60 L h ⁻¹ g _{cat} ⁻¹	156
Figure 8.21. [A] CO ₂ conversion, [B] H ₂ conversion, [C] CO selectivity (solid markers) and CH ₄ selectivity (open markers) of Mo _x C _y /SiO ₂ , Fe-Mo _x C _y /SiO ₂ , Pt-Mo _x C _y /SiO ₂ and Ni-Mo _x C _y /SiO ₂ and [D] XRD patterns of the spent RWGS catalysts. Conditions: T = 600 °C for 36 h TOS at H ₂ /CO ₂ ratio of 2.5. SV = 120 L h ⁻¹ g _{cat} ⁻¹	157
Figure 8.22. C ₂ H ₆ conversion, C ₂ H ₄ selectivity and C ₂ H ₄ yield, of Mo _x C _y supported on SiO ₂ , with the feed gas sourced from individual gas cylinders (IND) or single cylinder pre-mix (MIX). CO ₂ -ODH conditions: T = 600 °C, P = 1 atm, SV = 15 L h ⁻¹ g _{cat} ⁻¹ , CO ₂ :C ₂ H ₆ :Ar = 1:1:2. Theoretical maximum C ₂ H ₄ selectivity for CO ₂ -ODH indicated by solid black line.....	159
Figure 8.23. XRD patterns of spent CO ₂ -ODH experiments of Mo _x C _y supported on SiO ₂ with [A] the spent samples exposed to different gas supplies (Mo _x C _y /SiO ₂ (MIX)* is presented in Figure 8.26) and [B] the repeatedly tested Mo _x C _y /SiO ₂ (IND), terminated at 1, 3 and 12 h TOS. The fresh and the 24 h TOS (same as Mo _x C _y /SiO ₂ (IND)**) samples are presented again for comparison.	160
Figure 8.24. Schematic representation of C ₂ H ₆ to CO ₂ conversion ratio, C ₂ H ₄ to CO product ratio, H ₂ to CO product ratio and C ₂ H ₄ to H ₂ product ratio, of Mo _x C _y supported on SiO ₂ , with the feed gas sourced from individual gas cylinders (IND) or single cylinder pre-mix (MIX). CO ₂ -ODH conditions: T = 600 °C, P = 1 atm, SV = 15 L h ⁻¹ g _{cat} ⁻¹ , CO ₂ :C ₂ H ₆ :Ar = 1:1:2.....	161
Figure 8.25. C ₂ H ₆ conversion (relative to unpromoted sample), C ₂ H ₄ selectivity and C ₂ H ₄ yield (relative to unpromoted sample), of Mo _x C _y supported on SiO ₂ , promoted with iron, platinum, nickel or potassium. CO ₂ -ODH conditions: T = 600 °C, P = 1 atm, SV = 15 L h ⁻¹ g _{cat} ⁻¹ , CO ₂ :C ₂ H ₆ :Ar = 1:1:2. Theoretical maximum C ₂ H ₄ selectivity for CO ₂ -ODH indicated by solid black line.	162
Figure 8.26. XRD patterns of the spent CO ₂ -ODH catalysts of Mo _x C _y supported on SiO ₂ , promoted with iron, platinum, nickel or potassium.	163
Figure 8.27. Raman spectra of the spent CO ₂ -ODH catalysts of Mo _x C _y supported on SiO ₂ , promoted with iron, platinum, nickel or potassium.	164
Figure 8.28. Schematic representation of C ₂ H ₆ to CO ₂ conversion ratio, C ₂ H ₄ to CO product ratio, H ₂ to CO product ratio and C ₂ H ₄ to H ₂ product ratio, of Mo _x C _y supported on SiO ₂ , promoted with iron, platinum, nickel or potassium. CO ₂ -ODH conditions: T = 600 °C, P = 1 atm, SV = 15 L h ⁻¹ g _{cat} ⁻¹ , CO ₂ :C ₂ H ₆ :Ar = 1:1:2.	165
Figure 8.29. Raman spectrum of the spent Pt-Mo _x C _y /SiO ₂	166

Figure 8.30 C ₂ H ₆ conversion (relative to unpromoted sample), C ₂ H ₄ selectivity and C ₂ H ₄ yield (relative to unpromoted sample), of Fe-Mo _x C _y /SiO ₂ , promoted <i>via</i> co-impregnation, sequential impregnation or after calcination. CO ₂ -ODH conditions: T = 600 °C, P = 1 atm, SV = 15 L h ⁻¹ g _{cat} ⁻¹ , CO ₂ :C ₂ H ₆ :Ar = 1:1:2. Theoretical maximum C ₂ H ₄ selectivity for CO ₂ -ODH indicated by solid black line.....	166
Figure 8.31. C ₂ H ₆ conversion, C ₂ H ₄ selectivity and C ₂ H ₄ yield, of Mo _x C _y /SiO ₂ carburized with and without prior calcination. CO ₂ -ODH conditions: T = 600 °C, P = 1 atm, SV = 15 L h ⁻¹ g _{cat} ⁻¹ , CO ₂ :C ₂ H ₆ :Ar = 1:1:2. Theoretical maximum C ₂ H ₄ selectivity for CO ₂ -ODH indicated by solid black line.....	167
Figure 8.32. C ₂ H ₆ conversion, C ₂ H ₄ selectivity and C ₂ H ₄ yield, of Pt-Mo _x C _y /SiO ₂ , promoted <i>via</i> co-impregnation and carburized with and without prior calcination. CO ₂ -ODH conditions: T = 600 °C, P = 1 atm, SV = 15 L h ⁻¹ g _{cat} ⁻¹ , CO ₂ :C ₂ H ₆ :Ar = 1:1:2. Theoretical maximum C ₂ H ₄ selectivity for CO ₂ -ODH indicated by solid black line.	168
Figure 8.33. XRD patterns of the spent CO ₂ -ODH of [A] Mo _x C _y /SiO ₂ carburized with and without prior calcination and [B] -Mo _x C _y /SiO ₂ , promoted <i>via</i> co-impregnation, sequential impregnation or after calcination and Pt-Mo _x C _y /SiO ₂ , promoted <i>via</i> co-impregnation and carburized with and without prior calcination.	169
Figure 8.34. C ₂ H ₆ conversion, C ₂ H ₄ selectivity and C ₂ H ₄ yield, of the following samples exposed to varying feed compositions: water co-feeding for Mo _x C _y /SiO ₂ , co-feeding of 5 vol.-% H ₂ for Fe-Mo _x C _y /SiO ₂ , a 5:1 CO ₂ to C ₂ H ₆ feed ratio for Pt-Mo _x C _y /SiO ₂ and Ni-Mo _x C _y /SiO ₂ . CO ₂ -ODH conditions, see section 4.3.2 for more details. Theoretical maximum C ₂ H ₄ selectivity for CO ₂ -ODH indicated by solid black line.	170
Figure 8.35. Schematic representation of C ₂ H ₆ to CO ₂ conversion ratio, C ₂ H ₄ to CO product ratio, H ₂ to CO product ratio and C ₂ H ₄ to H ₂ product ratio, of Pt-Mo _x C _y /SiO ₂ and Ni Pt-Mo _x C _y /SiO ₂ . CO ₂ -ODH conditions: T = 600 °C, P = 1 atm, SV = 15 L h ⁻¹ g _{cat} ⁻¹ , CO ₂ :C ₂ H ₆ :Ar = 5:1:6.	171
Figure 8.36. Schematic representation of C ₂ H ₆ to CO ₂ conversion ratio, C ₂ H ₄ to CO product ratio, H ₂ to CO product ratio and C ₂ H ₄ to H ₂ product ratio, of Mo _x C _y /SiO ₂ . H ₂ O/CO ₂ -ODH conditions: T = 600 °C, P = 1 atm, SV = 15 L h ⁻¹ g _{cat} ⁻¹ , CO ₂ :C ₂ H ₆ :Ar = 1:1:2, with H ₂ O co-feeding of about 4-5 vol.-%.....	172
Figure 8.37. [A] XRD patterns and [B] Raman spectra of the spent CO ₂ -ODH catalysts exposed to varying feed compositions: water co-feeding for Mo _x C _y /SiO ₂ , co-feeding of 5 vol.-% H ₂ for Fe-Mo _x C _y /SiO ₂ , a 5:1 CO ₂ to C ₂ H ₆ feed ratio for Pt-Mo _x C _y /SiO ₂ and Ni-Mo _x C _y /SiO ₂	173
Figure A.1. Product equilibrium of the Mo system in the presence of CO ₂ , as a function of temperature, with all CO ₂ -ODH compounds considered [A] including the four different Mo phases [B]. Red shaded area indicates temperature range of interest for CO ₂ -ODH. Compound specific thermodynamic data from Knacke <i>et al.</i> ¹ ...	183
Figure A.2. Product equilibrium of the CO ₂ -ODH system as a function of temperature and H ₂ co-feeding at a stoichiometric feed of CO ₂ to C ₂ H ₆ (1:1) and 1 bar pressure, with all compounds considered.	183

Figure A.3. Product equilibrium of the CO ₂ -ODH system as a function of temperature and H ₂ O co-feeding at a stoichiometric feed of CO ₂ to C ₂ H ₆ (1:1) and 1 bar pressure, with all compounds considered.	184
Figure A.4. Product equilibrium of the CO ₂ -ODH system as a function of temperature and inert co-feeding at a stoichiometric feed of CO ₂ to C ₂ H ₆ (1:1) and 1 bar pressure, with all compounds considered [A] including the four different Mo phases [B].....	184
Figure B.1. CO ₂ conversion, CO selectivity and C ₂ H ₆ to CO ₂ conversion ratio, C ₂ H ₄ to CO product ratio, H ₂ to CO product ratio and C ₂ H ₄ to H ₂ product ratio, of Mo _x C _y /SiO ₂ , evaluated within a range of reaction temperatures. Conditions: T = 550 °C, 650 °C or 700 °C, P = 1 atm, SV = 9.4 L h ⁻¹ g _{cat} ⁻¹ , C ₂ H ₆ :CO ₂ :Ar = 1:1:2. Theoretical maximum CO selectivity for CO ₂ -ODH indicated by solid black line.	185
Figure B.2. CO ₂ conversion, CO selectivity and C ₂ H ₆ to CO ₂ conversion ratio of Mo _x C _y /SiO ₂ -WI, Mo _x C _y /SBA-15-HNC, Mo _x C _y /SiO ₂ -HNC and Mo _x C _y /SiO ₂ -SG. Conditions: T = 600 °C, P = 1 atm, SV = 15 L h ⁻¹ g _{cat} ⁻¹ , CO ₂ :C ₂ H ₆ :Ar = 1:1:2. Theoretical maximum CO selectivity for CO ₂ -ODH indicated by solid black line.....	185
Figure B.3. C ₂ H ₆ conversion, C ₂ H ₄ selectivity and CO ₂ conversion, of bulk metal oxide supports, SiO ₂ , ZrO ₂ , Ga ₂ O ₃ and TiO ₂ . CO ₂ -ODH conditions: T = 600 °C, P = 1 atm, SV = 21.4 L h ⁻¹ g _{cat} ⁻¹ , CO ₂ :C ₂ H ₆ :Ar = 1:1:2. Theoretical maximum C ₂ H ₄ selectivity for CO ₂ -ODH indicated by solid black line.....	186
Figure B.4. CO ₂ conversion, CO selectivity and C ₂ H ₄ formation rate of Mo _x C _y supported on SiO ₂ , Al ₂ O ₃ , ZrO ₂ , Ga ₂ O ₃ , TiO ₂ and CeO ₂ . CO ₂ -ODH conditions: T = 600 °C, P = 1 atm, SV = 15 L h ⁻¹ g _{cat} ⁻¹ , CO ₂ :C ₂ H ₆ :Ar = 1:1:2. Theoretical maximum CO selectivity for CO ₂ -ODH indicated by solid black line.	186
Figure B.5. CO ₂ conversion, CO selectivity and C ₂ H ₄ formation rate of Mo _x C _y supported on Al ₂ O ₃ , ZrO ₂ and Ga ₂ O ₃ . CO ₂ -ODH conditions: T = 600 °C, P = 1 atm, SV = 15 L h ⁻¹ g _{cat} ⁻¹ , CO ₂ :C ₂ H ₆ :Ar = 5:1:6. Theoretical maximum CO selectivity for CO ₂ -ODH indicated by solid black line.....	187
Figure B.6. CO ₂ conversion, CO selectivity and C ₂ H ₄ formation rate of Mo _x C _y supported on SiO ₂ . H ₂ /CO ₂ -ODH conditions: T = 600 °C, P = 1 atm, SV = 15 L h ⁻¹ g _{cat} ⁻¹ , CO ₂ :C ₂ H ₆ :Ar = 1:1:2, with H ₂ co-feeding at 0, 5, 10 and 17 vol.-%. Theoretical maximum CO selectivity for CO ₂ -ODH indicated by solid black line.....	187
Figure B.7. CO ₂ conversion, CO selectivity and C ₂ H ₄ formation rate of Mo _x C _y supported on ZrO ₂ . H ₂ /CO ₂ -ODH conditions: T = 600 °C, P = 1 atm, SV = 15 L h ⁻¹ g _{cat} ⁻¹ , CO ₂ :C ₂ H ₆ :Ar = 1:1:2, with H ₂ co-feeding at 0, 5 and 17 vol.-%. Theoretical maximum CO selectivity for CO ₂ -ODH indicated by solid black line.....	188
Figure B.8. CO ₂ conversion, CO selectivity and C ₂ H ₄ formation rate of Mo _x C _y supported on Ga ₂ O ₃ . H ₂ /CO ₂ -ODH conditions: T = 600 °C, P = 1 atm, SV = 15 L h ⁻¹ g _{cat} ⁻¹ , CO ₂ :C ₂ H ₆ :Ar = 1:1:2, with H ₂ co-feeding at 5 and 17 vol.-%. Theoretical maximum CO selectivity for CO ₂ -ODH indicated by solid black line.....	188
Figure B-9. CO ₂ conversion, CO selectivity and C ₂ H ₄ formation rate, of Mo _x C _y supported on SiO ₂ , with the feed gas sourced from individual gas cylinders (IND) or single cylinder pre-mix (MIX). CO ₂ -ODH conditions: T = 600	

°C, P = 1 atm, SV = 15 L h ⁻¹ g _{cat} ⁻¹ , CO ₂ :C ₂ H ₆ :Ar = 1:1:2. Theoretical maximum CO selectivity for CO ₂ -ODH indicated by solid black line.....	189
Figure B-10. CO ₂ conversion (relative to unpromoted sample), CO selectivity and C ₂ H ₄ formation rate, of Mo _x C _y supported on SiO ₂ , promoted with iron, platinum, nickel or potassium. CO ₂ -ODH conditions: T = 600 °C, P = 1 atm, SV = 15 L h ⁻¹ g _{cat} ⁻¹ , CO ₂ :C ₂ H ₆ :Ar = 1:1:2. Theoretical maximum CO selectivity for CO ₂ -ODH indicated by solid black line.	189
Figure B-11. CO ₂ conversion (relative to unpromoted sample), CO selectivity and C ₂ H ₄ formation rate, of Fe-Mo _x C _y /SiO ₂ , promoted <i>via</i> co-impregnation, sequential impregnation or after calcination. CO ₂ -ODH conditions: T = 600 °C, P = 1 atm, SV = 15 L h ⁻¹ g _{cat} ⁻¹ , CO ₂ :C ₂ H ₆ :Ar = 1:1:2. Theoretical maximum CO selectivity for CO ₂ -ODH indicated by solid black line.	190
Figure B-12. CO ₂ conversion, CO selectivity and C ₂ H ₄ formation rate, of Mo _x C _y /SiO ₂ carburized with and without prior calcination. CO ₂ -ODH conditions: T = 600 °C, P = 1 atm, SV = 15 L h ⁻¹ g _{cat} ⁻¹ , CO ₂ :C ₂ H ₆ :Ar = 1:1:2. Theoretical maximum CO selectivity for CO ₂ -ODH indicated by solid black line.	190
Figure B-13. CO ₂ conversion, CO selectivity and C ₂ H ₄ formation rate, of Pt-Mo _x C _y /SiO ₂ , promoted <i>via</i> co-impregnation and carburized with and without prior calcination. CO ₂ -ODH conditions: T = 600 °C, P = 1 atm, SV = 15 L h ⁻¹ g _{cat} ⁻¹ , CO ₂ :C ₂ H ₆ :Ar = 1:1:2. Theoretical maximum CO selectivity for CO ₂ -ODH indicated by solid black line.	191
Figure B-14. CO ₂ conversion, CO selectivity and C ₂ H ₄ formation rate, of the following samples exposed to varying feed compositions: water co-feeding for Mo _x C _y /SiO ₂ , co-feeding of 5 vol.-% H ₂ for Fe-Mo _x C _y /SiO ₂ , a 5:1 CO ₂ to C ₂ H ₆ feed ratio for Pt-Mo _x C _y /SiO ₂ and Ni-Mo _x C _y /SiO ₂ . CO ₂ -ODH conditions, see section 4.3.2 for more details. Theoretical maximum CO selectivity for CO ₂ -ODH indicated by solid black line.	191
Figure C.1. TGA analysis of the carburization process of bulk ammonium heptamolybdate with TG curve (red dashed line) and differential thermal analysis (DTA) signal (grey solid line). Conditions: T = 650 °C, P = 1 atm, heating rate = 1 °C min ⁻¹ and holding time = 5 hours.	192
Figure C.2. TGA analysis of carburization process of bulk MoO ₃ with TG curve (red dashed line) and differential thermal analysis (DTA) signal (grey solid line). Conditions: T = 650 °C, P = 1 atm, heating rate = 1 °C min ⁻¹ and holding time = 5 hours.	192
Figure D.1. XRD patterns of MoO ₃ /SBA-15-HNC, calcined at 400 °C, and MoO ₃ /SiO ₂ -SG, calcined at 500 °C. ..	193
Figure D.2. XRD pattern of Mo _x C _y /SiO ₂ after being exposed to a thermal treatment up until 600 °C, to confirm thermal stability of the catalyst prior to reaction.....	193
Figure D.3. Rietveld refined patterns displaying the raw, calculated, difference, crystal phases, background, and amorphous phase (representing SiO ₂ or SBA-15) data of the freshly carburized samples at 600 °C.	194

Figure D.4. Rietveld refined patterns displaying the raw, calculated, difference, crystal phases, background, and amorphous phase (representing SiO ₂ or SBA-15) data of Mo _x C _y /SBA-15-HNC carburized at 650 °C and Mo _x C _y /SiO ₂ -SG carburized at 700 °C.	195
Figure D.5. XRD patterns of the spent CO ₂ -ODH catalysts, of bulk metal oxide supports, SiO ₂ , ZrO ₂ , Ga ₂ O ₃ and TiO ₂ . Conditions: T = 600 °C, P = 1 atm, SV = 21.4 L h ⁻¹ g _{cat} ⁻¹ , CO ₂ :C ₂ H ₆ :Ar = 1:1:2.	195
Figure E.1. Raman spectra of the spent CO ₂ -ODH catalysts, of bulk metal oxide supports, SiO ₂ , ZrO ₂ , Ga ₂ O ₃ and TiO ₂ . Conditions: T = 600 °C, P = 1 atm, SV = 21.4 L h ⁻¹ g _{cat} ⁻¹ , CO ₂ :C ₂ H ₆ :Ar = 1:1:2.	196
Figure F.1. CO ₂ temperature programmed desorption profiles of Mo _x C _y supported on SiO ₂ , Al ₂ O ₃ , ZrO ₂ , Ga ₂ O ₃ and TiO ₂ . CO ₂ and CO signals normalized to Mo content in the sample.	197
Figure F-2. Overview of CO ₂ desorbed (normalized to mmol per gram of molybdenum) as a function of temperature recorded during CO ₂ desorption of Fe-Mo _x C _y /SiO ₂ , Pt-Mo _x C _y /SiO ₂ , Ni-Mo _x C _y /SiO ₂ and K-Mo _x C _y /SiO ₂	197
Figure G.1. Linear combination fits on the first derivative of the normalized absorption, corresponding to Table 5.2, of bulk Mo ₂ C samples carburized at different temperatures, with and without passivation.	198
Figure G.2. Linear combination fits on the first derivative of the normalized absorption, corresponding to Table 5.3, of a freshly carburized Mo _x C _y /SiO ₂ at 700 °C, and exposed to CO ₂ -ODH conditions at 550 °C, 650 °C and 750 °C.	199
Figure G.3. LCF of Mo K XANES spectra (Mo K-edge at 20,000 eV shifted to 0 eV), corresponding to	199
Figure G.4. Radial distribution fits to a β-Mo ₂ C crystallographic data set with ICSD code 39461 (k ³ -weighted FT EXAFS data).	200
Figure H.1. Schematic overview of heating block equipped with heating cartridges.	201
Figure H.2. Schematic overview of reactor packing and calibration of isothermal zone.	202

Nomenclature

Abbreviations

2WNV	2-way needle valve
2WV	2-way valve
3WV	3-way valve
A3WV	Automated 3-way valve
AHM	Ammonium heptamolybdate
BR	Boudouard reaction
CAPEX	Capital expenditure
CCS	Carbon capture and storage
CCU	Carbon capture and utilization
CF	Carbon formation
CN	Coordination number
CNT	Carbon nanotubes
COR	Carbon monoxide reduction
D	Diameter
DFT	Density functional theory
DH	Dehydrogenation
DR	Dry-reforming
DTA	Differential thermal analysis
DW	Debye-Waller
EAD	Ethane decomposition
EDS	Energy dispersive spectroscopy
EED	Ethylene decomposition
EH	Ethane hydrogenolysis
EXAFS	Extended X-ray adsorption fine structure
FCC	Fluid catalytic cracking

fcc	Face centered cubic
FIC	Flow indicator and controller
FT(S)	Fischer-Tropsch (synthesis)
FWHM	Full width at half maximum
GC	Gas chromatography
hcp	Hexagonal closed packed
HNC	Hybrid nanocrystal
HVC	High-value chemical
ICDD	The International Centre for Diffraction Data
ICP-OES	Inductively Coupled Plasma-Optical Emission Spectroscopy
ICSD	Inorganic Crystal Structure Database
ID	Inner diameter
L	Length
LCF	Linear combination fitting
MCO	Methanation of carbon monoxide
MCO ₂	Methanation of carbon dioxide
MD	Methane decomposition
MFC	Mass flow controller
MO _x	Metal oxides
MS	Mass spectrometry
MTBE	Methyl tertiary-butyl ether
MTO	Methanol to olefin
N	Normalized
NSR	Non-selective reaction
OCM	Oxidative coupling of methane
OD	Outer diameter
ODH	Oxidative dehydrogenation
PI	Pressure indicator

PIC	Pressure indicator and controller
PONKCS	Partial or not known crystal structure
ppm	Parts per million
PR	Pressure regulator
rpm	Revolutions per minute
RSF	Relative sensitivity factor
RWGS	Reverse water-gas-shift
S	Wall thickness
SC	Steam cracking
SDV	Shut down valve
SEM	Scanning electron microscopy
TCD	Thermo conductivity detector
TEM	Transmission electron microscopy
TGA	Thermogravimetric analysis
TOS	Time on stream
TP	Temperature programmed
TPD	Temperature programmed desorption
TPR	Temperature programmed reduction
TPRe	Temperature programmed reaction
UV-vis	Ultraviolet-visible spectroscopy
V	Volt
W	Watt
WI	Wet-impregnation
XANES	X-ray adsorption near edge structure
XAS	X-ray adsorption spectroscopy
XPS	X-ray photoelectron spectroscopy
XRD	X-ray diffraction

Chemical formulas

$(\text{NH}_4)_2\text{Mo}_4\text{O}_{13}$	Ammonium tetramolybdate
$(\text{NH}_4)_6\text{Mo}_7\text{O}_{24} \cdot 4\text{H}_2\text{O}$	Ammonium heptamolybdate nonahydrate
$(\text{NH}_4)_8\text{Mo}_{10}\text{O}_{34}$	Ammonium decamolybdate
Al_2O_3	Aluminum oxide
Ar	Argon
C	Carbon
C_2	Hydrocarbon with a carbon number of 2
C_2H_4	Ethylene
C_2H_6	Ethane
C_4	Hydrocarbon with a carbon number of 4
CeO_2	Cerium oxide
CH_3COOK	Potassium acetate
CH_4	Methane
Co	Cobalt
CO	Carbon monoxide
CO_2	Carbon dioxide
CoO_x	Cobalt oxide
Cr_2O_3	Chromium oxide
CTAB	Cetyl trimethyl ammonium bromide
Cu	Copper
Fe	Iron
Ga_2O_3	Gallium oxide
H_2	Hydrogen
H_2O	Water
H_2SO_4	Sulfuric acid
H_3BO_3	Boric acid
HCl	Hydrochloric chloride

HCOOCH ₃	Methyl formate
HCOOH	Formic acid
HF	Hydrofluoric acid
HMT	Hexamethylenetetramine
HNO ₃	Nitric acid
<i>hP</i> -MoO ₃	Hexagonal molybdenum trioxide
H _x MoO ₃	Molybdenum bronze
H-Y	Zeolite
H-ZSM-5	Zeolite
K	Potassium
K ₂ CO ₃	Potassium carbonate
K ₂ SO ₄	Potassium sulphate
KCl	Potassium chloride
KOH	Potassium hydroxide
La ₂ O ₃	Lanthanum oxide
MgO	Magnesium oxide
Mn	Manganese
Mo	Molybdenum
Mo(CO) ₆	Molybdenum carbonyl
Mo ₂ N	Molybdenum nitride
Mo ₃ O ₁₀ (C ₆ H ₈ N) ₂ ·2H ₂ O	Organic-inorganic hybrid precursor
MoO ₂	Molybdenum dioxide
MoO ₃	Molybdenum trioxide
Mo _x C _y / Mo ₂ C	Molybdenum carbide
N ₂	Nitrogen
N ₂ O	Nitrous oxide
Na ₂ MoO ₄ ·2H ₂ O	Sodium molybdate dihydrate
Na ₂ O	Sodium oxide

NH ₃	Ammonia
NH ₄ OH	Ammonium hydroxide
Ni	Nickel
O ₂	Oxygen
<i>oP</i> -MoO ₃	Orthorhombic molybdenum trioxide
Pt	Platinum
SiO ₂	Silicon dioxide
Sn	Tin
TEOS	Tetraethyl orthosilicate
TiO ₂	Titanium oxide
V ₂ O ₅	Vanadium oxide
ZnO	Zinc oxide
ZrO ₂	Zirconia oxide
η	Eta

Notations

\dot{n}	Molar flowrate	mmol min ⁻¹
nC_p	Number of carbons in product p	-
μ_i	Chemical potential of compound <i>i</i>	kJ mol ⁻¹
ΔG	Gibbs free energy	kJ mol ⁻¹
ΔH	Entropy	kJ mol ⁻¹
m/z	Mass over charge ratio	-
S_g	Surface area	m ² g ⁻¹
SV	Space velocity	L h ⁻¹ g _{cat} ⁻¹
<i>S</i>	Selectivity	C-%
<i>X</i>	Conversion	%
<i>Y</i>	Yield	%
<i>y</i>	Molar fraction of compound x	-

1 Introduction

Climate change and global warming are currently the most critical and highlighted environmental issues the world is facing. A global temperature rise, warmer oceans, decreasing ice sheets, loss of glaciers and an accelerating rise of sea levels are only a few of the many disastrous effects climate change can have. It is believed that 95 % of the observed climate change is a direct result of human activities.¹ A significant increase in the concentration of greenhouse gases in the atmosphere, since the industrial revolution, has without a doubt the most impact on the warming of the earth. CO₂ is a minor component of the world's atmosphere (~419 ppm) but it represents over three quarters of the total greenhouse gases emitted from natural processes and human activities, mostly *via* the burning of fossil fuels.² CO₂ in the atmosphere acts as heat-trap and thus limits the loss of heat *via* reflection through the earth's atmosphere.¹ Therefore it is of high importance to invest in research attempting to find efficient ways to decrease CO₂ concentrations in the atmosphere or at least reduce CO₂ emissions. Possible ways to do so is to capture CO₂ before it is emitted or even capture it directly from air.³ The captured CO₂ can be stored or utilized directly in industrial applications. These are for example CO₂ injection for increased oil recovery⁴ or as a supercritical solvent in the caffeine extraction.⁵ The disadvantage of CO₂ sequestration is that the world's confirmed suitable storage space is relatively small and will run out. In addition, every mol of CO₂ stored excludes one carbon atom from the carbon economy.⁶

Catalytic conversion of the captured CO₂ into useful chemical products is potentially much more efficient and can play a role in decreasing the atmospheric CO₂ levels. It has to be noted that utilizing captured CO₂ does not reduce the eventual CO₂ concentration in the atmosphere directly but rather avoids the emission of new fossil-based carbon. The largest commercial processes making use of captured CO₂ are the production of urea (150 million tonnes annually) and methanol (100 million tonnes annually).⁷ Urea synthesis is also the most efficient in utilizing CO₂ with an annual consumption of 112 million tonnes, in comparison to methanol consuming only 2 million tonnes annually.⁷ Other processes such as the direct CO₂ hydrogenation to fuels and CO₂ dry-reforming of hydrocarbons (usually methane) into synthesis gas have received a lot of interest in the past decades.^{6, 8, 9} Especially the latter is currently being commercialized on industrial scale by BASF SE. Research towards the formation of fine chemicals from CO₂ is being conducted in order to add value to the products, however their market size is not substantial enough and thus their impact to reduce the CO₂ concentration in the atmosphere is minor.⁷ A more specific reaction focusing on large scale chemicals will be dealt with in the here presented study: the oxidative dehydrogenation (ODH) of light alkanes, specifically ethane. The ODH of light alkanes is useful as it can accommodate the rising demand for light olefins. Light olefins, i.e., ethylene and

propylene, are a major building block in the chemical industry to produce polymers, oxygenates and chemical intermediates such as ethylbenzene and propionaldehyde.^{10, 11}

Ethane is the second largest component of natural gas (5-15 wt.-%) and is at present mainly converted *via* steam cracking and thermal dehydrogenation at elevated temperatures of up to 900 °C. At these high temperatures, the process has several disadvantages, such as an uncontrollable degree of side reactions and catalyst deactivation *via* coking.^{12, 13} Other possible pathways producing light olefins that are investigated intensively are; the conversion of methanol into olefins¹⁴⁻¹⁶, the Fischer-Tropsch synthesis and the oxidative coupling of methane.¹⁷ However, these processes are high in investment costs, indirect pathways, produce large amounts of CO₂ or are not efficient enough to be economically viable compared to steam cracking. Oxidative dehydrogenation utilizing O₂ as the oxidant significantly reduces reaction temperature compared to direct thermal dehydrogenation, however heat removal and limiting the over oxidation of the alkane to CO₂ is challenging. The use of CO₂ as a soft oxidant has been shown to prevent over oxidation and yet reduces reaction temperatures and increases the production towards olefins.⁶

The ODH of light alkanes utilizing CO₂ is a promising pathway to produce light olefins while in parallel activating carbon dioxide. The resulting CO can be used in conjunction with green hydrogen for established synthesis gas conversion processes such as methanol formation or the FTS. Thermodynamically, the process is heavily challenged by the dry-reforming reaction of CO₂ into synthesis gas and the direct dehydrogenation of light alkanes as all three reactions are possible at the elevated reaction temperatures applied. Therefore, for the reaction to be successful the catalyst designed needs to be able to kinetically favour the ODH reaction. To do this, the catalysts must activate and dissociate CO₂ on the catalytic surface, forming oxygen surface species while activating the hydrocarbon and cleaving the C-H bond, retaining the C-C bond. CO₂ is thermodynamically more stable than CO and activation of CO₂ is therefore difficult, but crucial for the ODH reaction and it could aid in removing pre-adsorbed carbon. Catalysts bearing redox properties could enhance the activation of ethane. The redox properties must be strong enough to activate the ethane, but not too strong to suppress over-oxidation of the hydrocarbon towards CO or CO₂.

In this study, novel Mo_xC_y-based catalysts are designed and synthesized for the application in the CO₂-ODH of C₂H₆. Previous work on Mo_xC_y-based catalysts found that the bulk material has limited activity and selectivity towards producing C₂H₄ but is significantly improved once dispersed on a support material. The type of support material dictates whether the CO₂-ODH reaction proceeds, or if one of the major side reactions, the dry-reforming of C₂H₆ to synthesis gas is preferred. Mo_xC_y nanoparticles are prepared *via* various synthesis techniques, dispersed on MO_x support materials (SiO₂, Al₂O₃, ZrO₂, Ga₂O₃, TiO₂ and CeO₂) and modified with promoters (Fe, Pt, Ni and K). Besides the exploratory nature of

this study, gaining knowledge on the activity of the various combinations of Mo_xC_y -based catalysts, the preparation conditions of the carbide materials were also investigated. Mo_xC_y is prepared *via* the exposure of the precursor sample to a temperature programmed treatment in the presence of a carbonaceous and reductive gas mixture (i.e., carburization). The carbide formation, in terms of crystallite structure, surface composition as well as potential fouling mechanisms are highly dependent on the heating rate, gas mixture, final temperature and precursor composition. Various experiments utilizing *in situ* characterization techniques, such as *in situ* XRD, XAS and Raman spectroscopy as well as online product analysis techniques were conducted to gain knowledge on the carburization process, the structural and chemical properties and their effect on the activity of the various prepared catalysts in the CO_2 -ODH of ethane.

References

1. H. Shaftel, R. Jackson, S. Callery and D. Bailey, The Causes of Climate Change, <https://climate.nasa.gov/>, (accessed October 28, 2019, 2019).
2. V. G. Azevedo, S. Sartori and L. M. S. Campos, CO₂ emissions: A quantitative analysis among the BRICS nations, *Renewable and Sustainable Energy Reviews*, 2018, **81**, 107-115.
3. D. W. Keith, G. Holmes, D. St. Angelo and K. Heidel, A Process for Capturing CO₂ from the Atmosphere, *Joule*, 2018, **2**, 1573-1594.
4. Z. Dai, R. Middleton, H. Viswanathan, J. Fessenden-Rahn, J. Bauman, R. Pawar, S.-Y. Lee and B. McPherson, An Integrated Framework for Optimizing CO₂ Sequestration and Enhanced Oil Recovery, *Environmental Science & Technology Letters*, 2013, **1**, 49-54.
5. W. Leitner, Designed to dissolve, *Nature*, 2000, **405**, 129-130.
6. S. Kawi and Y. Kathiraser, CO₂ as an Oxidant for High-Temperature Reactions, *Frontiers in Energy Research*, 2015, **3**, 1-17.
7. E. Alper and O. Yuksel Orhan, CO₂ utilization: Developments in conversion processes, *Petroleum*, 2017, **3**, 109-126.
8. Y. Chen, S. Choi and L. T. Thompson, Low temperature CO₂ hydrogenation to alcohols and hydrocarbons over Mo₂C supported metal catalysts, *Journal of Catalysis*, 2016, **343**, 147-156.
9. B. Zhao, B. Yan, Z. Jiang, S. Yao, Z. Liu, Q. Wu, R. Ran, S. D. Senanayake, D. Weng and J. G. Chen, High selectivity of CO₂ hydrogenation to CO by controlling the valence state of nickel using perovskite, *Chem Commun (Camb)*, 2018, **54**, 7354-7357.
10. H. Zimmermann and R. Walzl, in *Ullmann's Encyclopedia of Industrial Chemistry*, 2009, DOI: 10.1002/14356007.a10_045.pub3.
11. J. J. Sattler, J. Ruiz-Martinez, E. Santillan-Jimenez and B. M. Weckhuysen, Catalytic dehydrogenation of light alkanes on metals and metal oxides, *Chem Rev*, 2014, **114**, 10613-10653.
12. S. Yao, B. Yan, Z. Jiang, Z. Liu, Q. Wu, J. H. Lee and J. G. Chen, Combining CO₂ Reduction with Ethane Oxidative Dehydrogenation by Oxygen-Modification of Molybdenum Carbide, *ACS Catalysis*, 2018, **8**, 5374-5381.
13. K. Nakagawa, C. Kajita, K. Okumura, N.-o. Ikenaga, M. Nishitani-Gamo, T. Ando, T. Kobayashi and T. Suzuki, Role of Carbon Dioxide in the Dehydrogenation of Ethane over Gallium-Loaded Catalysts, *Journal of Catalysis*, 2001, **203**, 87-93.
14. M. J. G. Janssen and J. A. Zboray, *United States Patent No.* 6,121,503, 2000, Exxon Chemical Patents Inc.
15. J. A. Montalbano, *United States Patent No.* US 2011/0144404 A1, 2011, UOP LLC.
16. L. W. Miller, *United States Patent No.* 6,166,282, 2000, UOP LLC.
17. G. E. Keller and M. M. Bhasin, Synthesis of Ethylene via Oxidative Coupling of Methane, *Journal of Catalysis*, 1982, **73**, 9-19.

2 Literature Review

At the time of writing, the average global temperature has risen by 1.18 °C since 1880. Studying paleoclimate archives allows researchers to reconstruct the average global temperature and the concentration of atmospheric greenhouse gases (GHGs) of the past.¹ The increase in GHGs in the atmosphere, unequivocally caused by human activities, is the main cause for the warming of the global surface temperature (see Figure 2.1-A). The concentration of carbon dioxide (CO₂) in the atmosphere has risen to 419 ppm as of 2022, equal to a 49 % increase since the start of the industrial revolution (1850) (see Figure 2.1-B).²

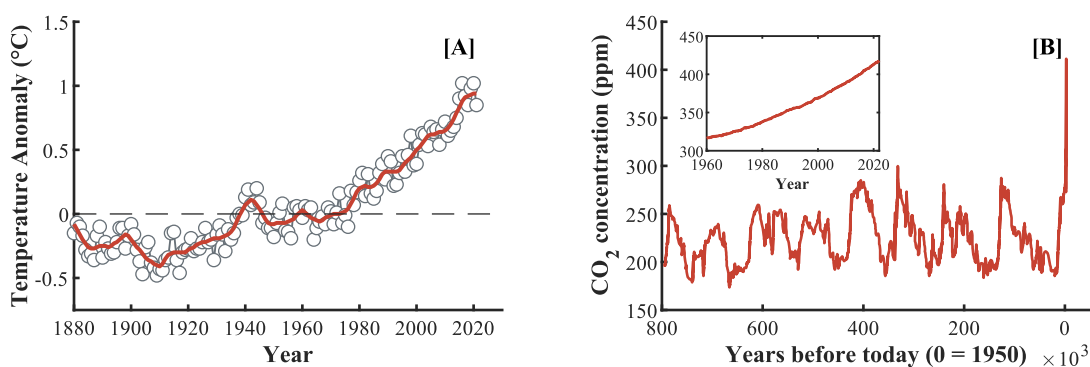


Figure 2.1. [A] Change in global surface temperature relative to 1951-1980 average temperatures. [B] Concentration of atmospheric CO₂ over the past 800,000 years. Insert: CO₂ concentration since 1960 until today. Figure reproduced from Shaftel *et al.*².

While CO₂ remains a minor component in the earth's atmosphere, it represents over three quarters of the total greenhouse gases emitted from natural processes and human activities, mostly *via* the burning of fossil fuels, such as natural gas, crude oil and coal.³⁻⁵ The release of CO₂ into the atmosphere by combustion has a significant impact on the global carbon cycle; a natural process of carbon flow between the oceans, atmosphere, plants, soil, and fossil fuels.⁶ The global carbon cycle plays a key role in stabilizing the average surface temperature on the earth, often referred to as the world's thermostat. CO₂ in the atmosphere acts as heat-trap and thus limits the loss of heat *via* reflection through the earth's atmosphere. Due to rising concentrations of CO₂ in the earth's atmosphere, the global surface temperature increases, and more water is evaporated into the atmosphere. In addition, the oceans get warmer resulting in decreasing ice sheets and the loss of glaciers. This is subsequently followed by rising sea levels with frequent flooding as result. Extreme weather events cause more frequently occurring natural disasters such as droughts, bush fires and acidic rainfall. The acidity of the ocean increases due to the high levels of CO₂ adsorbed by and converted to carbonic acid. This ocean acidification causes large scale damages to

the marine environment. These are only a few of the many disastrous effects of global warming. It is thus of utmost importance to limit the rise of the global surface temperature to a maximum of 2 °C, preferably to 1.5 °C, as agreed upon in the Paris Agreement by the United Nations in 2015. To combat global warming and climate change, the rising concentration of CO₂ in the atmosphere must be halted by reducing CO₂ emissions from human activities and capturing already emitted CO₂.

2.1 Carbon capture, storage and utilization

Our current and constantly improving standard of life is mostly based on carbon-based fuels and materials resulting in a substantial amount of CO₂ emitted. Globally a total of 33.4 gigatonnes (Gt) of energy-related CO₂ was emitted into the atmosphere in 2019.⁷ Due to the Covid-19 pandemic, the global CO₂ emissions decreased to 31.5 Gt, which is the largest ever decline recorded, 5.8 %. However, in 2021, it quickly recovered to 33.0 Gt CO₂. The only possible way of limiting CO₂ concentrations in the atmosphere requires the capturing of CO₂ before it is emitted at point sources such as fossil or biomass fuelled power stations, or directly from the atmosphere.^{8,9} Commercially, the capture of CO₂ can be split into three groups: 1) post-combustion, 2) pre-combustion and 3) direct air capture. Post-combustion capture technologies (capturing CO₂ after burning of fuel with air for electricity or heat generation) are the most efficient methods to reduce emissions in the short term as they can simply be added to existing power plants.¹⁰ Generally, the methods applied for post-combustion capture are based on the use of biological (by means of photosynthesis, algae or bacteria), physical (using physical adsorption, cryogenic condensation or membrane separation) and chemical (adsorption, absorption or chemical looping combustion) methods. The most effective commercial post-combustion capturing process is the absorption in amine solvents or cold methanol.¹⁰ The separation of CO₂, which is formed as a co-product of an existing process such as the production of synthesis gas *via* natural gas reforming or coal gasification, is called the pre-combustion capture method, i.e., capturing CO₂ directly from the produced synthesis gas prior to combustion of fuel for electricity or heat generation.¹¹ During natural gas reforming, CO₂ is formed *via* the water-gas-shift reaction. Subsequently, the produced CO₂ can be separated by means of adsorption, absorption, membrane or cryogenic processes directly in the process rather than from the off gas. At low partial pressures of CO₂, the use of chemical adsorption is more efficient than physical adsorption, however this is inverted at higher partial pressures.¹² The main advantage of pre-combustion over post-combustion capture is the higher concentration of CO₂ in the mixture (15-50 % vs 5-15 %).

Although the concentration of CO₂ in atmospheric air is relatively low (419 ppm), the process to capture CO₂ directly from air was already commercialised in the 1950s and is used as a pre-treatment for

cryogenic air separation. In the 1990s this process was upscaled to capture previously emitted CO₂ directly from air. Large variations in the cost estimations, due to a lack of information provided in literature so far, resulted in uncertainties regarding the feasibility of the process. In 2018, Keith *et al.* published a detailed description of a technology promoted by the Canadian company Carbon Engineering to capture CO₂ directly from air.⁹ In short, the process consists of two connected chemical loops, where CO₂ is captured in the first loop to subsequently react with Ca²⁺ (from the dissolution of Ca(OH)₂) forming CaCO₃. Calcination of CaCO₃ produces CO₂ and CaO, which is then hydrated to complete the cycle forming Ca(OH)₂. The cost range of the process was estimated to be between 49 and 232 \$ per tonne of CO₂ captured, which is far below previous estimates¹³ of 550 \$ per tonne of CO₂. A second company, the Swiss Climeworks promotes and supplies a similar technology.^{9, 13} As of 2021, 19 direct air capture plants are operating worldwide with a combined annual capacity of 0.01 Mt CO₂. A total of about 40 Mt of CO₂ is captured worldwide each year across all technologies.¹⁴ This is by far not enough and thus substantial and rapid capacity improvements are required to have a significant contribution to the goal of reaching a net zero carbon economy by 2050-2070.

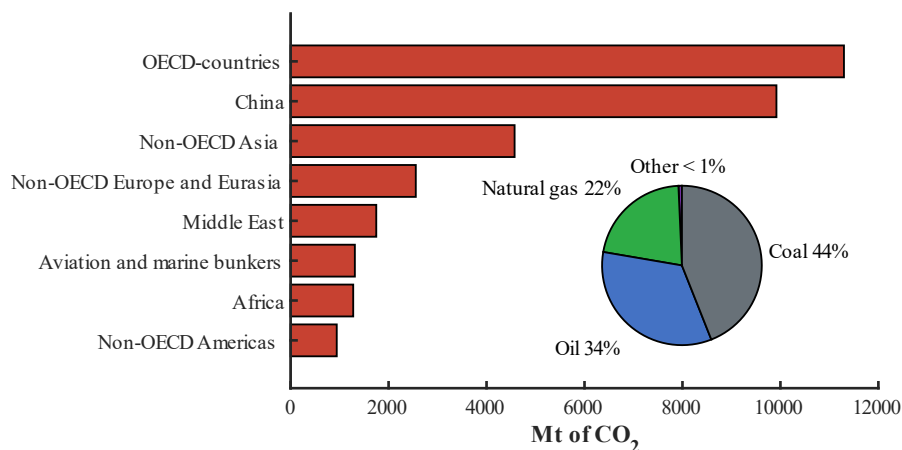


Figure 2.2. Share of the world's CO₂ emissions by fuel combustion only, per region and by fuel source, recorded in 2019.¹⁵

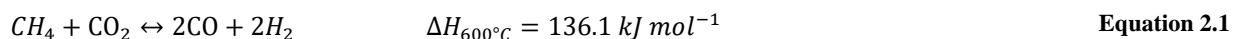
The carbon captured can be stored (CCS) or utilised (CCU). CCS involves the injection of liquid CO₂, achieved by compression of gaseous CO₂, into underground reservoirs such as deep saline formations and depleted oil and gas reservoirs. With CCS, the carbon cycle is not infinite, as carbon is sequestered by storing it deep in the ground. In addition, the likelihood of running out of suitable storage space is significant. Therefore, to increase the sustainability of the CO₂ capture process, and to balance the high operating and investment costs, the utilization of CO₂ and in particular the conversion into more valuable compounds is of interest. At present, a total of 230 Mt of CO₂ is utilised commercially each year. In comparison, the total amount of CO₂ emitted 2019 in China by fuel combustion alone is close to

10,000 Mt (see Figure 2.2). To date, the largest contributor to the CO₂ utilization market is the production of fertilizers, such as urea, at a capacity of 130 Mt of CO₂ per year.¹⁶ The CO₂ used for urea is sourced on-site from the production of ammonia. The enhanced oil recovery, which utilizes about 80 Mt of CO₂, is the largest CO₂ utilizing process sourcing their CO₂ off-site.

CO₂ can also be converted into more valuable products, by means of electrochemical, biological, mineralization, photosynthetic, photocatalytic and thermocatalytic processes.¹⁷ It must be noted that utilizing captured CO₂ does generally not reduce the eventual CO₂ concentration in the atmosphere but avoids the emission of new fossil-based carbon. The main concern of utilizing CO₂ in (thermo)catalytic reactions is the thermodynamic stability of the CO₂ molecule, which requires elevated temperatures to activate and is thus an energy consuming process. In addition, they usually require the addition of co-reactants to fully convert CO₂ and increase the economic viability of the process.¹⁸ Processes such as the (direct) CO₂ hydrogenation to methanol (or fuels) and CO₂ dry-reforming of hydrocarbons (usually methane) into synthesis gas have received a lot of interest in the past decades.¹⁸⁻²⁰ CO₂ hydrogenation to methanol is a matured process that has been commercialised at large scale using a Cu/ZnO/Al₂O₃ catalyst, however the CO₂ utilization capacity in the process is low.²¹ In Iceland, Carbon Recycling International (CRI) has developed the Emissions to Liquid (ETL) technology and were able to install the first commercial plant producing recycled carbon methanol (Vulcanol™) with a production capacity of 110,000 tonnes per year in 2021.²² In Germany, INERATEC has innovated various modular pilot plants, easily applicable to existing industries. Their primary focus is on the production of synthetic natural gas, synthetic fuels, chemicals and methanol, *via* the so-called Power-to-Liquid, Power-to-Gas and Gas-to-Liquid processes. The synthesis gas (a combination of CO and H₂, often at a ratio of 1:2) is produced either *via* the reverse water-gas-shift (RWGS) reaction or *via* the steam-assisted catalytic partial oxidation (CPOX) of methane. bse Methanol GmbH, in collaboration with BASF, developed the delocalized *Flex*Methanol units which produce methanol *via* the Power-to-Methanol process at a small scale. H₂, produced *via* electrolysis using excess current from renewable energy sources, and CO₂, obtained from off-stream gas, are used to produce methanol. In Canada, Carbon Engineering makes use of their innovative direct air capture (DAC) technology⁹ and turns the captured CO₂ into fuels, referred to as AIR TO FUELS, *via* (in)direct CO₂ hydrogenation.²³

CH₄ reforming in the presence of CO₂ (see Equation 2.1), commonly referred to as dry-reforming, was already reported on as early as 1888²⁴. The main interest in the reaction lies in its potential of producing synthesis gas, specifically at low H₂/CO ratios, which can be further converted to methanol or *via* the Fischer-Tropsch synthesis (FTS) to fuels. Currently, synthesis gas, and indeed hydrogen, is produced on world scale *via* steam reforming and/or partial oxidation of methane, and has a high CO₂

footprint.²⁵ The obtained synthesis gas is hydrogen rich and the (reverse) water-gas-shift reaction is a major side reaction affecting the final synthesis gas ratio. Most research on CH₄ dry-reforming focuses on a bifunctional catalyst including a noble metal and a support.^{26, 27} However, the use of noble metals at industrial scale is economically challenging and therefore the more abundant metals, nickel and cobalt, are more likely to be implemented on large scale. Linde, in collaboration with BASF, have launched commercial methane dry-reforming plants, operating with CO₂ as a feedstock and is based on these transition metals.²⁸



2.2 Light olefins, the world's chemical building block

Light olefins (alkenes) are known as the world's most important chemical building block. In fact, our everyday life is surrounded by products manufactured from alkenes as major feedstock. Ethylene in particular is used for the synthesis of polyethylene, ethylene oxide, ethylene dichloride or styrene. These compounds are then converted into items such as food packaging, textiles, PCV pipes and synthetic rubber, just to name a few. More than 200 Mt of ethylene is produced annually (in 2020), a value expected to increase to 300 Mt by 2025.²⁹ Commercially, ethylene is produced *via* steam cracking (SC), fluid catalytic cracking (FCC) or dehydrogenation (DH). Steam cracking is carried out through the mixing of steam and a hydrocarbon feedstock, usually fossil fuel based, in a tubular reactor at elevated temperatures ($\pm 850^\circ\text{C}$). The United States are the biggest ethylene producer with a total annual production of 28.4 Mt, followed by China with 13.9 Mt. Globally, crude oil is the main feedstock for steam cracking. The recent shale gas developments have made the use of ethane extracted from shale gas a lot more attractive. America has moved to produce a large amount of their ethylene from shale gas, China still uses predominantly crude oil.³⁰ With a shale gas feed, even shipping of ethane is within the profitability of the steam cracking process. However, converting a liquid-based steam cracker to an ethane-based steam cracker brings along a number of challenges, specifically in the downstream processes.^{31, 32}

Other pathways of producing ethylene are currently economically not viable as they are being compared to steam crackers and their production capacities. The Fischer-Tropsch synthesis (FTS), the CO hydrogenation over transition metal catalysts, is already a commercialized process producing linear alkanes, 1-alkenes and small amounts of oxygenates.^{33, 34} By tweaking the process conditions and catalyst compositions, larger amounts of olefins can be produced. However, the largest Fischer-Tropsch plant operations today, producing 140,000 barrels per day, required a total investment of 18 billion US dollars.

These high costs are mainly due to the expensive technology of the air separation unit required for the preparation of synthesis gas, which accounts for approximately 70 % of the total CAPEX cost.³⁴⁻³⁶ Synthesis gas can in turn also be used for the methanol synthesis. Subsequently, the methanol can be converted into a high purity short chain olefinic product *via* the so-called methanol to olefin (MTO) process. ExxonMobil first presented the MTO process in the late 1970s followed by patents from ExxonMobil and UOP Honeywell.³⁷⁻³⁹ The MTO processes are based on a zeolite (ExxonMobil) or a silico-aluminophosphate (UOP) catalyst. Disadvantages of the MTO process are mainly catalyst deactivation through coking and high CO₂ emissions *via* the water-gas shift (WGS) reaction.³¹ Direct hydrogenation of CO₂ to methanol is being studied academically^{40,41} but is not commercialized yet.

A more direct process forming light olefins is the oxidative coupling of methane (OCM). This technology was first pioneered by Keller and Bhasin⁴² and resulted in significant research activity both in industry and academia. OCM is typically the reaction between methane and oxygen forming ethane and water. Subsequently, the ethane reacts with the oxygen forming ethylene and water. Through over oxidation, CO₂ and CO are formed. The main disadvantages of this process are the highly exothermic reactions occurring and low ethylene yields. The current research towards industrializing the OCM technology focuses mainly on finding an industrially reliable and stable catalyst and reactor design.⁴³

Catalytic dehydrogenation of light alkanes is currently the second largest commercial technology producing light olefins. A major advantage of the process is that, in comparison to steam cracking, dehydrogenation is an on-purpose technique which could increase the yield of a specific olefin, rather than producing a wide range of products. In particular, the production of propylene *via* catalytic dehydrogenation has increased by up to 14 million tonnes annually.⁴⁴ Commercially there are two technologies available, the Catofin and the Oleflex process. The Catofin process, introduced by CB&I Lummus, was originally used to produce methyl tertiary-butyl ether (MTBE). MTBE used to be a fuel additive to increase the octane number of petrol, but after it was proven to pollute water resources, its market size declined. Subsequently, most Catofin-based plants were modified towards propane dehydrogenation. Where the Catofin process uses 8 parallel adiabatic fixed bed reactors, the Oleflex process, introduced by UOP Honeywell, uses fluidized bed reactors. The Catofin process employs a Cr₂O₃/Al₂O₃ catalyst at temperatures of approximately 575 °C and pressures between 0.2 and 0.5 bar. The Oleflex process utilizes a Pt-Sn-based catalyst at temperatures in the range of 525-705 °C and pressures between 1 and 3 bar. The main disadvantages of the catalytic dehydrogenation processes are the underlying highly endothermic reactions, low selectivity, coking and high noble metal loadings.^{31, 45}

From all processes discussed above, naphtha-based steam cracking has shown to be the most viable economically, but also environmentally, if comparing the total CO₂ emissions per tonne of high-value

chemicals (HVC), such as light olefins or aromatics (see Figure 2.3). Furthermore, a division is made between CO₂ emitted from energy generation to run the actual process and from the chemical reactions.

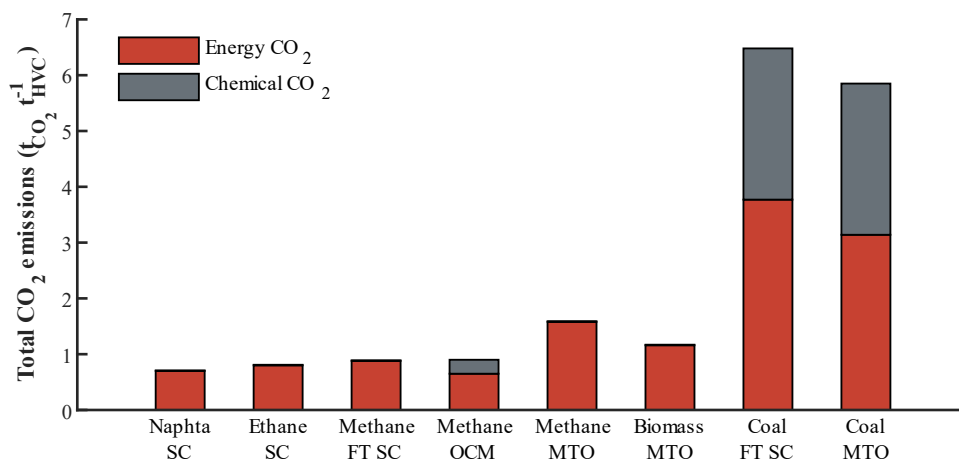


Figure 2.3. CO₂ emissions from different technologies producing light olefins (or aromatics) per tonne of high-value chemicals (HVC). Figure is adapted from Amghizar *et al.*³¹. Red bars indicate CO₂ emitted from energy generation; grey bars indicate CO₂ emitted from chemical reactions. Annotations indicate the carbon source (naphtha, ethane, methane, biomass or coal) and the process application (steam cracking (SC), Fischer-Tropsch (FT) synthesis, oxidative coupling of methane (OCM) and methanol to olefin (MTO)).

2.3 CO₂-assisted oxidative dehydrogenation of light alkanes

The oxidative dehydrogenation of light alkanes (C₂-C₄) by CO₂ (CO₂-ODH, see Equation 2.4) is seen as a promising alternative to the more common direct dehydrogenation (DH) route. The DH of alkanes (see Equation 2.2) is a highly endothermic reaction which requires temperatures starting from 600 °C to reach the conversion levels of interest. Besides being energy intensive, coking of the catalysts is a major challenge which requires frequent regeneration. Co-feeding an oxidant has proven to lower the reaction temperature significantly, thus lowering energy consumption and reducing the coking effect on the catalyst improving its lifetime. Oxidants such as oxygen⁴⁶⁻⁴⁹, nitrous oxide^{50, 51} and carbon dioxide⁵²⁻⁵⁷ have been researched. Oxygen co-feeding shifts the reaction from an endothermic reaction to a highly exothermic reaction and thus heat removal is required (see Equation 2.3). Besides that, over-oxidation of the alkane to CO_x lowers the selectivity towards olefins.⁵⁸ Nevertheless, similar or even better ethylene yields were reported compared to steam cracking, but limited knowledge is available regarding catalyst lifetime.⁵⁹ The use of N₂O has shown promising catalytic performances⁶⁰, however the most mentioned drawbacks of using N₂O as the oxidant are compound specific safety hazards.⁶¹ The focus of this study is on the co-feeding of CO₂, in particular to the dehydrogenation of ethane. CO₂ is often classified as a ‘soft oxidant’⁶¹⁻⁶⁶ and its introduction to the catalytic dehydrogenation of alkanes started to receive interest a

few decades ago. Fox *et al.*⁶⁷ reported early on that typical dehydrogenation catalysts, Cr₂O₃ or V₂O₅ supported on Al₂O₃, are the best for CO₂-ODH. In fact, the CO₂-ODH reaction mechanism was suggested to be a combination of DH and the RWGS (see Equation 2.5). The major side reaction that has been reported to occur is the dry-reforming of ethane with CO₂ (DR), producing synthesis gas (see Equation 2.6). Comparing the Gibbs free energy of reaction of CO₂-ODH, DH, DR and RWGS, as a function of temperature (see Figure 2.4) reveals that the dry-reforming reaction is the favoured reaction to occur, with a Gibbs free energy of below 0 kJ mol⁻¹ above 550 °C. Therefore, it is important to find a catalyst composition that is kinetically able to suppress the thermodynamically favoured dry-reforming reaction (via C-C bond scission) and support the CO₂-ODH reaction (C-H bond scission). Coking of the catalyst *via* the Boudouard reaction or ethane decomposition has been reported to be the major catalyst deactivation mechanism. Co-feeding of CO₂ could potentially suppress coking to an extent by producing carbon monoxide *via* the reverse Boudouard reaction (see Equation 2.7).⁶¹

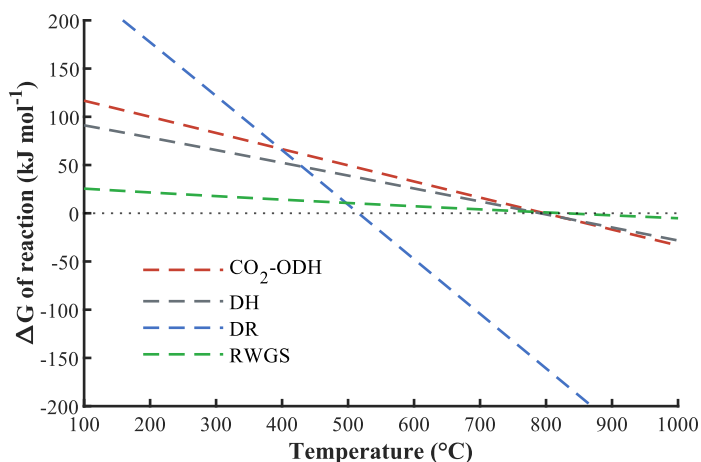
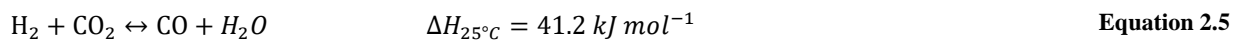
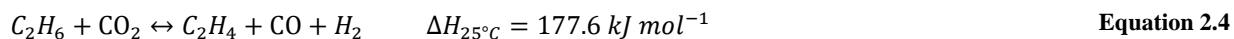
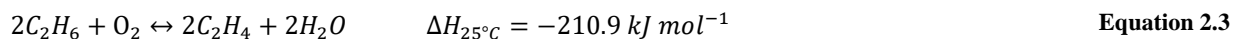
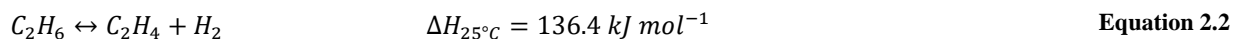
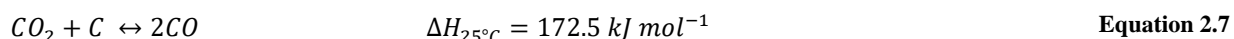
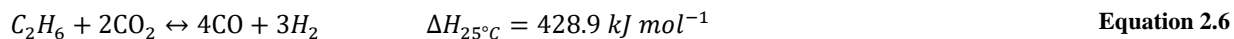


Figure 2.4. Gibbs free energy calculations as a function of temperature on the possible individual reactions to occur during CO₂-ODH of ethane.





The numerous reviews published recently, focusing fully or partially on the CO₂-ODH of light alkanes, shows the increased interest in the CO₂-ODH reaction.^{18, 61-63, 65, 68-72} The various authors commonly report on the use of (mixed) metal oxides (MO_x) as the most promising and studied catalyst systems for CO₂-ODH. In particular Cr₂O₃⁷³⁻⁸², V₂O₅^{59, 66, 83-86} or Ga₂O₃⁸⁷⁻⁸⁹ based systems have been extensively investigated. The activity of the metal oxide catalysts has predominantly been ascribed to either their redox properties performing a Mars van Krevelen type mechanism or their acid-base bifunctionality *via* a heterolytic dissociation mechanism. In addition to MO_x, other systems such as metallic, bimetallic, nitride and carbide systems were identified as possible catalysts.

2.3.1. Metal oxide catalysts

The most common materials used for CO₂-ODH of ethane are supported metal oxides. A reducible metal oxide can donate a lattice-oxygen, in a Mars-van-Krevelen type mechanism⁹⁰, abstracting a hydrogen from the alkane, forming a reduced valence state of the MO_x, accompanied by the production of water. The reduced MO_{x-1} subsequently undergoes a re-oxidation reaction *via* the activation of CO₂ to return to its original state, producing CO (see Figure 2.5).

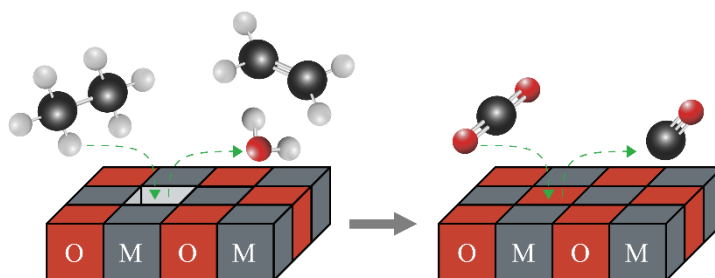


Figure 2.5. Graphical representation of a reducible metal oxide catalyst proceeding *via* a Mars-van-Krevelen type mechanism in the CO₂-ODH of ethane.

A second possible reaction mechanism involves a catalyst's acid-base bifunctionality, where it is often described that the acidic sites activate the substrate and the basic sites activate CO₂. Sato *et al.*⁹¹ proposed a mechanism based on an Al₂O₃ and a Na₂O/Al₂O₃ catalyst. Ethylbenzene is adsorbed on the acid sites of the Al₂O₃ catalyst. Subsequently, the basic sites of the catalyst abstract the α-hydrogen atom of the activated ethylbenzene, producing styrene and H₂ (see Figure 2.6). In case of the Na₂O/Al₂O₃

catalyst in the presence of CO₂, the basic site responsible for the activation of CO₂ is different from the basic sites responsible for the abstraction of the α-hydrogen atom. Activated CO₂ reacts with the abstracted hydrogen on the surface forming CO and water in addition to styrene (see Figure 2.7).

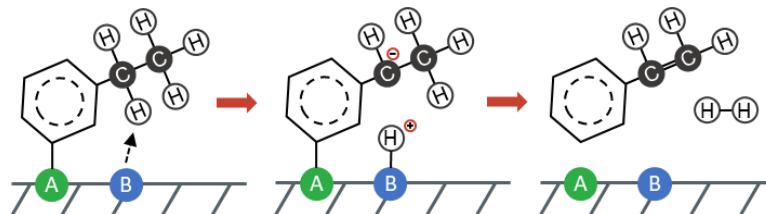


Figure 2.6. Graphical representation of the dehydrogenation of ethylbenzene to styrene and H₂ over an Al₂O₃ catalyst. Figure adapted from Sato *et al.*⁹¹.

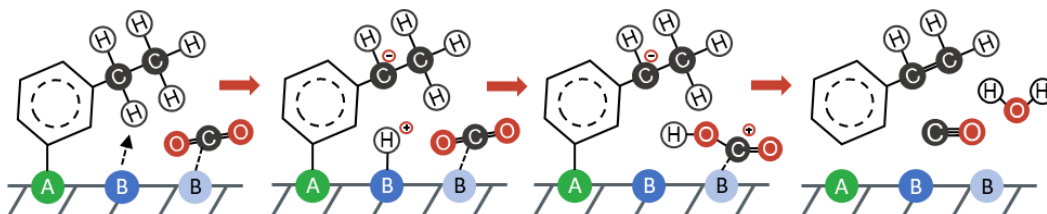


Figure 2.7. Graphical representation of the CO₂ assisted dehydrogenation of ethylbenzene to styrene, CO and water over a Na₂O/Al₂O₃ catalyst. Figure adapted from Sato *et al.*⁹¹.

The active metal oxides are often loaded onto a single or mixed metal oxide support material to increase the active surface area by anchoring the highly dispersed catalyst nanoparticles within the pores of the support. Additionally, some catalysts are designed to be bifunctional achieving a tandem reaction between the support and the loaded material. The support material can also modify the acidic and basic properties of the catalyst.

In a study by Nakagawa *et al.*⁹², a number of commercially available oxide catalysts were evaluated for their CO₂-ODH activity utilizing a feed gas composition comprising of a CO₂ to C₂H₆ at a ratio of 5:1 (see Figure 2.8). At the reaction temperature of 650 °C, some gas phase reaction was measured. This indicates that the oxides in Figure 2.8 beyond MgO did not show any catalytic activity. A slight improvement was observed from CeO₂ to ZrO₂, and a more significant catalytic activity was recorded for the samples from Ga₂O₃ to La₂O₃. Gallium oxide was found to be the most active and selective catalyst, under the chosen reaction conditions, with an ethylene yield of up to 18.6 %. It should be noted that catalytic data was only recorded for 30 minutes and no long-term activity was explored. In a follow up study, the support effect on Ga₂O₃-based catalysts was investigated by loading Ga on TiO₂, ZrO₂, ZnO, Al₂O₃ and SiO₂.⁹³ A higher activity was observed for the Ga-loaded samples on TiO₂, ZrO₂ and ZnO in

the presence of CO₂ in the feed (C₂H₆:CO₂ = 5:25 mL min⁻¹) than without (C₂H₆:Ar = 5:25 mL min⁻¹). On Al₂O₃ the activity dropped upon co-feeding CO₂ and on SiO₂ there was no significant effect. The performance of the Ga₂O₃/Al₂O₃ and Ga₂O₃/TiO₂ catalysts with CO₂ co-feeding was further investigated and the CO₂ co-feeding was replaced by steam (H₂O_(g)) co-feeding. At about 10 vol.-% of steam co-feeding, Ga₂O₃/TiO₂ achieves a similar ethylene yield and product spectrum as during CO₂ co-feeding. The ethylene yield for Ga₂O₃/Al₂O₃ decreases upon steam co-feeding. The difference observed can suggest that for Ga₂O₃/TiO₂, the steam produced in the presence of CO₂ enhances the dehydrogenation activity possibly by removing carbon deposits. On Al₂O₃, the produced steam during CO₂ co-feeding inhibits the dehydrogenation activity, possibly due to modified acidity on the surface of the catalyst.

Upon loading some of the investigated bulk metal oxides onto an oxidized diamond support material, the order of activity changed significantly from Ga₂O₃ > Cr₂O₃ > V₂O₅ > Mn₃O₄ > ZnO > CeO₂ > Fe₂O₃ > MoO₃ to Cr₂O₃ > V₂O₅ > MoO₃ > Ga₂O₃ > CeO₂ > Mn₃O₅ > Fe₂O₃ > MnO.⁹⁴ The activity of the metal oxides increased significantly upon dispersion onto the oxidized diamond support. Although the slightly increased surface area can play a role, the surface area of bulk and supported Ga₂O₃ and CeO₂ are similar, yet ethylene yield was increased significantly. Although the oxidized diamond alone did not yield any catalytic activity, the increased activity is suggested to be due to a weak interaction between the MO_x and the support as well as the supply of catalytically active sites for the dehydrogenation of C₂H₆ in the form of oxygen surface species.

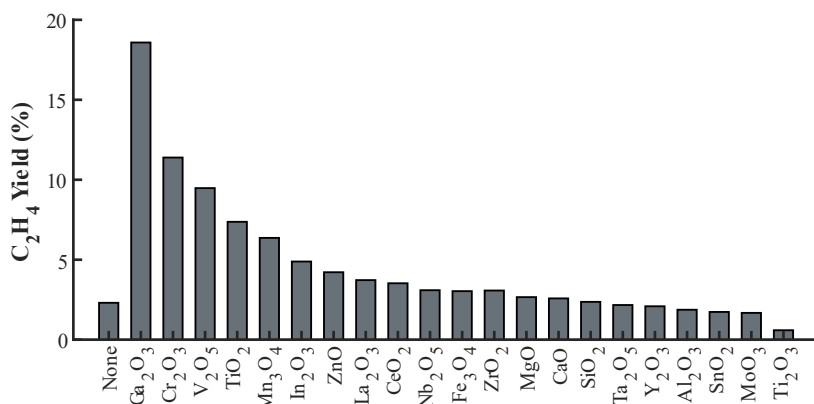


Figure 2.8. Metal oxides in the CO₂ oxidative dehydrogenation of C₂H₆. Process conditions: T = 650 °C, CO₂ to C₂H₆ ratio = 5:1, SV = 9 L h⁻¹·g_{cat}⁻¹. Figure adapted from Nakagawa *et al.*⁹².

In a study presented by Wang *et al.*⁹⁵ a Cr₂O₃/SiO₂ catalyst was exposed to ethane dehydrogenation conditions in the absence and presence of CO₂. It was found that the co-feeding of CO₂ increases ethane conversion (from 50 to 56 %, at 650 °C) and ethylene selectivity (from 90 to 93 %). On top of that, only for the catalyst tested in the absence of CO₂, carbon deposition was observed. Mimura *et al.*⁹⁶ also studied

Cr₂O₃ as potential catalyst for CO₂-ODH of ethane and loaded 5 wt.-% of Cr₂O₃ on zeolites with a SiO₂/Al₂O₃ ratio ranging between 4.8 (H-Y) and 1900 (H-ZSM-5). For comparison, V₂O₅ and Ga₂O₃ were also loaded (5 wt.-%) on H-ZSM-5 (SiO₂/Al₂O₃ = 1900). The most active catalysts are the H-ZSM-5 supported samples with a SiO₂/Al₂O₃ ratio of 190 and higher. The higher dehydrogenation activity was linked to a higher reducibility observed during H₂-TPR experiments. CO₂ co-feeding showed improvements to the dehydrogenation activity and the stability of the catalyst by removing coke from the catalyst surface.

Another study employing Cr₂O₃ as a catalyst used ZrO₂ as support material.⁹⁷ The catalytic performance of an unmodified Cr₂O₃/ZrO₂ catalyst and Fe, Ni, Mn and Co modified Cr₂O₃/ZrO₂ was evaluated (see Figure 2.9). At the conditions applied, the Ni promoted catalyst showed the highest ethane and CO₂ conversions. However, ethylene production was minimal in contrast to CO and methane, suggesting that the Ni promoted sample favours dry-reforming and cracking reactions. The Fe, Mn and Co promoted samples showed an increase in ethylene selectivity at similar conversion levels in comparison to the unpromoted sample. The differences observed between the four catalysts can be correlated to their respective acid and base characteristics, which were determined *via* NH₃ and CO₂ desorption, respectively. The Ni-promoted catalyst showed the largest amount of strong acid and base sites. Weak basic sites for the Fe, Mn and Co promoted catalysts together with the unpromoted catalyst were not observed. Therefore, it was concluded that strong acid and base pairs are responsible for the high activity towards the reforming and cracking reactions. The Co-promoted sample had the largest amount of weak acid sites which could be linked to an increase in ethane activation.⁹⁷

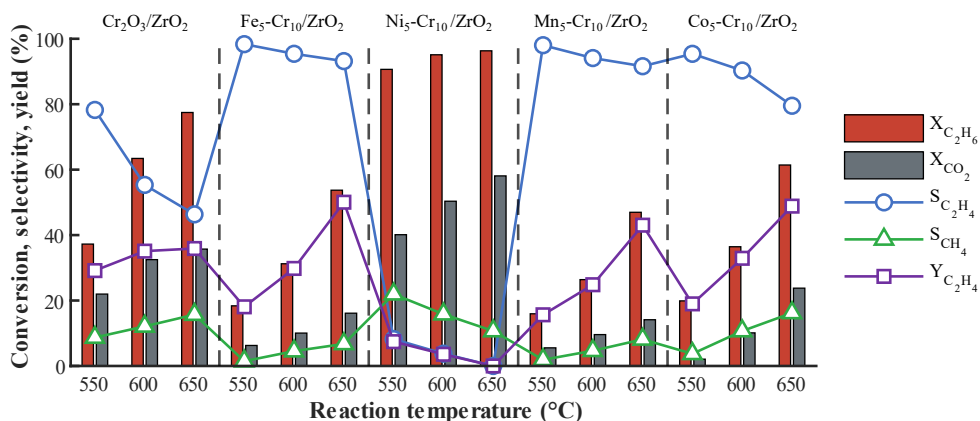


Figure 2.9. Catalytic performance of the unpromoted and promoted Cr₂O₃/ZrO₂ catalysts. Process conditions: CO₂ to C₂H₆ ratio = 3:1, SV = 4.5 L·h⁻¹·g⁻¹. Figure is reproduced with data obtained from Deng *et al.*⁹⁷.

Koirala *et al.*⁹⁸ studied the use of CoO_x on SiO₂ for the CO₂-ODH reaction, a well-known catalyst for processes such as the Fischer-Tropsch synthesis. At fairly low Co loadings, between 0.75 and 4.5 wt.-%,

decent ODH activity was observed with a selectivity to ethylene of over 80 % (700 °C, CO₂ to C₂H₆ ratio of 2.5 and GHSV of 6 L h⁻¹ g_{cat}⁻¹). The optimum Co loading was 0.75 wt.-% which showed an ethane conversion of 46 % and ethylene selectivity of 85 %. The higher activity observed for the lower Co loadings was linked to the highly dispersed Co²⁺ species identified by means of Ultraviolet-visible spectroscopy, XAS and XPS.

2.3.2. (Bi)metallic catalysts

In a study by Myint *et al.*⁹⁹ bimetallic catalysts were evaluated for their activity for CO₂-ODH of ethane. They were compared to their respective monometallic catalysts, all supported on commercial CeO₂. At a CO₂ to C₂H₆ feed ratio of 1:1, at 600 °C, the bimetallic catalysts show a significant improvement in catalyst stability in comparison to the monometallic catalysts. The highest activity was observed for CoPt/CeO₂ and NiMo/CeO₂, with the latter being of special interest as there are no precious metals involved. For all samples, high selectivity (between 68.7 and 99.5 %) towards CO were recorded, indicating high dry-reforming activity. The FeNi/CeO₂, Fe/CeO₂ and Mo/CeO₂ catalysts achieved an ethylene selectivity of up to 31 %.

Yan *et al.*¹⁰⁰ followed up on the above-described bimetallic system and studied NiFe catalysts supported on CeO₂, varying the Ni/Fe ratio. At 600 °C and a CO₂ to C₂H₆ feed ratio of 1 it was observed that the performance of the pure Ni catalyst (Ni₃/CeO₂) and pure Fe (Fe₃/CeO₂) catalyst show significant differences. While the former is more active in terms of C₂H₆ conversion (14 % vs 0.5 %), the latter is more selective to ethylene (0.9 % vs 38.3 %). A drastic change can be observed for the bimetallic catalysts. The Fe rich samples showed lower overall C₂H₆ conversions, but a significantly higher selectivity was recorded (> 66.7 %). At a Ni/Fe ratio of 1:3 and 3:1, the space velocity was adjusted to achieve similar C₂H₆ conversion levels. It is clear that the higher Ni content increases the CO selectivity which is supported by the significantly higher CO₂ conversion. The reaction is thus dominated by the dry-reforming of C₂H₆.

In a study performed in our own laboratories by Raseale *et al.*¹⁰¹, the effect of Fe to Ni ratio in a Fe_xNi_y alloy system, supported on overlayers of Cr and Zr oxides on γ -Al₂O₃ (CrO_x@Al₂O₃ and ZrO_x@Al₂O₃, respectively), was investigated under CO₂-ODH conditions with an equimolar feed of CO₂ and C₂H₆, 600 °C reaction temperature and atmospheric pressure. The two bare overlayer supports displayed quite different catalytic performance. No CO₂ and C₂H₆ conversion were recorded for the ZrO_x@Al₂O₃ overlayer, where CrO_x@Al₂O₃ had an initial C₂H₆ conversion of 5 % and CO₂ conversion of 2.5 %. A decrease in activity with TOS was observed, fully deactivating after 11 hours. The FeNi alloys had a significant impact on the Cr overlayer, but hardly improved the activity or selectivity of the Zr

overlayer. A higher ethylene selectivity is recorded with an increase in the Fe content of the alloy, however the activity decreased. The Fe_5Ni_1 on $\text{CrO}_x/\text{Al}_2\text{O}_3$ showed a CO_2 to C_2H_6 conversion ratio of 1 for the entire duration of the experiment, which suggests a pure CO_2 -ODH reaction. Overall, the Fe_xNi_y alloys increased the CO_2 activation, confirming the necessity of a tandem functionality between the oxide overlayers and the Fe_xNi_y nanoparticles.

2.3.3. Molybdenum carbide based catalysts

Molybdenum as a catalyst in the oxidative dehydrogenation reaction has been studied extensively. The Mo-based catalytic systems vary from molybdates^{46, 102-104} to (mixed) metal oxides^{48, 49, 105-108}, metallic⁹⁹ and carbides^{52-55, 109}. From all the different catalytic systems suitable for ODH, the system of interest for this study is limited to use of molybdenum carbide (Mo_xC_y), utilizing CO_2 as the oxidant. Molybdenum carbide has demonstrated to be a highly efficient catalyst for CO_2 activation^{110, 111} and alkane dehydrogenation^{69, 112}. Both mechanistic steps are key to achieve a successful CO_2 -ODH reaction. By activating CO_2 on the catalyst surface, oxygen surface species or a MoO_xC_y (sub)surface phase is produced. These oxygen sites then react with the alkane, *via* C-H bond scission, forming the olefin, while preventing the C-C bond cleavage (see Figure 2.10).⁵² An overview of past studies reporting on the utilization of Mo_xC_y -based catalysts for the CO_2 -ODH of ethane or propane is discussed in detail in the following section.

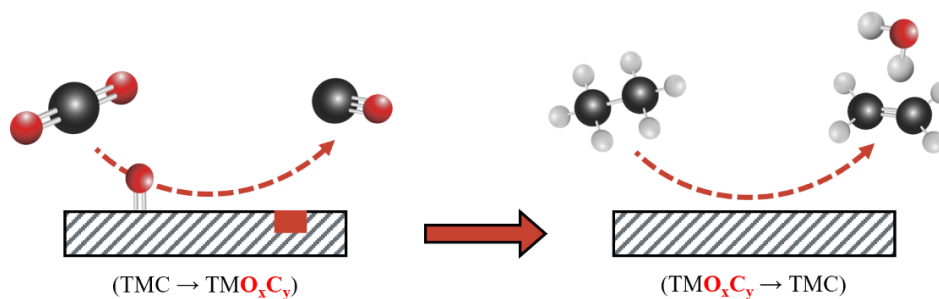


Figure 2.10. Graphical representation of the proposed ODH mechanism over transition metal carbide catalysts. A successful catalyst is required to support CO_2 activation to form oxygen surface species or MoO_xC_y . Subsequently, by means of the oxygen sites, ethane is activated by C-H bond scission, forming water and ethylene.

Solymosi and Németh^{53, 54} evaluated the catalytic performance of unsupported and supported Mo_xC_y on SiO_2 , of a hexagonal structure corresponding to $\beta\text{-Mo}_2\text{C}$, in ethane and propane CO_2 oxidative dehydrogenation. In both cases it was clear that the active phase of the Mo-based catalysts is the supported carbide phase. FTIR spectroscopic measurements of the interaction between the supported $\beta\text{-Mo}_2\text{C}$ catalyst and ethane, propane and CO_2 indicated ethane activation around 200 °C, propane around

300 °C and partial oxidation of the β -Mo₂C was observed at 500 °C, which progressed with increasing temperature. Mass spectrometry analysis of the exit gas showed the formation of CO at 550 °C. These observations are attributed to CO₂ dissociation on the catalytic surface. Simultaneously, XPS analysis confirmed the partial oxidation of the catalyst. However, in a CO₂ and propane atmosphere, no oxidation was observed suggesting the fast interaction of the propane with the oxidized Mo-species carburizing them back to β -Mo₂C.

In an attempt to extract more information regarding the reaction pathway applied during the ODH reaction of ethane in the presence of CO₂, Porosoff *et al.*⁵⁵ conducted a density functional theory study on the interaction of possible reaction intermediates on a Pt(111) and Mo₂C(001) surface, both shown to be active for the reverse water-gas-shift reaction. The DFT-study was based on earlier obtained data from the catalytic evaluation of a Pt supported on CeO₂ catalyst and a bulk β -Mo₂C catalyst, showing that the Pt/CeO₂ catalyst favours the dry-reforming reaction and β -Mo₂C favours the oxidative dehydrogenation reaction producing ethylene. It was observed that all reaction intermediates bind stronger to the Mo₂C(001) surface than to the Pt₍₁₁₁₎ surface. Furthermore, the difference in binding energy between Pt and Mo is more significant for the species containing an oxygen atom. As described earlier, the main difference between the two mechanisms of ODH and dry-reforming is which bond cleavage is favoured, i.e., the C-C scission (forming CH₄ or CO) or the C-H scission (forming ethylene). DFT results based on the enthalpy change for these two characteristic parts of the reaction mechanisms have shown that the Pt(111) and CeO₂(111) surfaces favour the C-C scission above the C-H scission, but both processes are exothermic (see Figure 2.11). On the Mo₂C(001) surface, the C-C scission is highly endothermic and the C-H scission exothermic, thus favouring the C-H scission. The DFT calculations certainly aid in the study towards the reaction mechanism occurring on Mo_xC_y-based catalysts, however, the consistent presence of a ‘clean’ Mo₂C(001) surface under reaction conditions is unlikely. A Mo₂C(001) surface with oxygen surface species might react very differently to the activation of C₂H₆ and/or CO₂ than MoO_xC_y. MoO_xC_y is often suggested to be the active phase for the dehydrogenation reaction, formed under reaction conditions on the (sub)surface of the catalyst particles.

Reaction experiments conducted on a bulk β -Mo₂C catalyst and supported β -Mo₂C on γ -Al₂O₃ and CeO₂ at 600 °C in a 1:1 mixture of CO₂:C₂H₆, showed a significant effect of the support. Alumina increased the activity in comparison to the pure carbide, while the CeO₂ supported sample showed lower activity. This could be explained by the acidic properties of γ -Al₂O₃ supporting ethane activation. For all catalysts, a significant deactivation was observed with time on stream. H₂ co-feeding (5 vol.-%) increased both C₂H₆ and CO₂ conversions, however CO selectivity increased simultaneously, ascribed to an increased reverse water-gas-shift activity. *In situ* XANES experiments confirmed the partial oxidation of

the catalyst upon the exposure to ethane and CO₂ at 600 °C and full oxidation upon the removal of ethane. It has been suggested that the formation of these oxygen species is required to increase the ethylene selectivity, however full oxidation is also responsible for the deactivation of the catalyst.

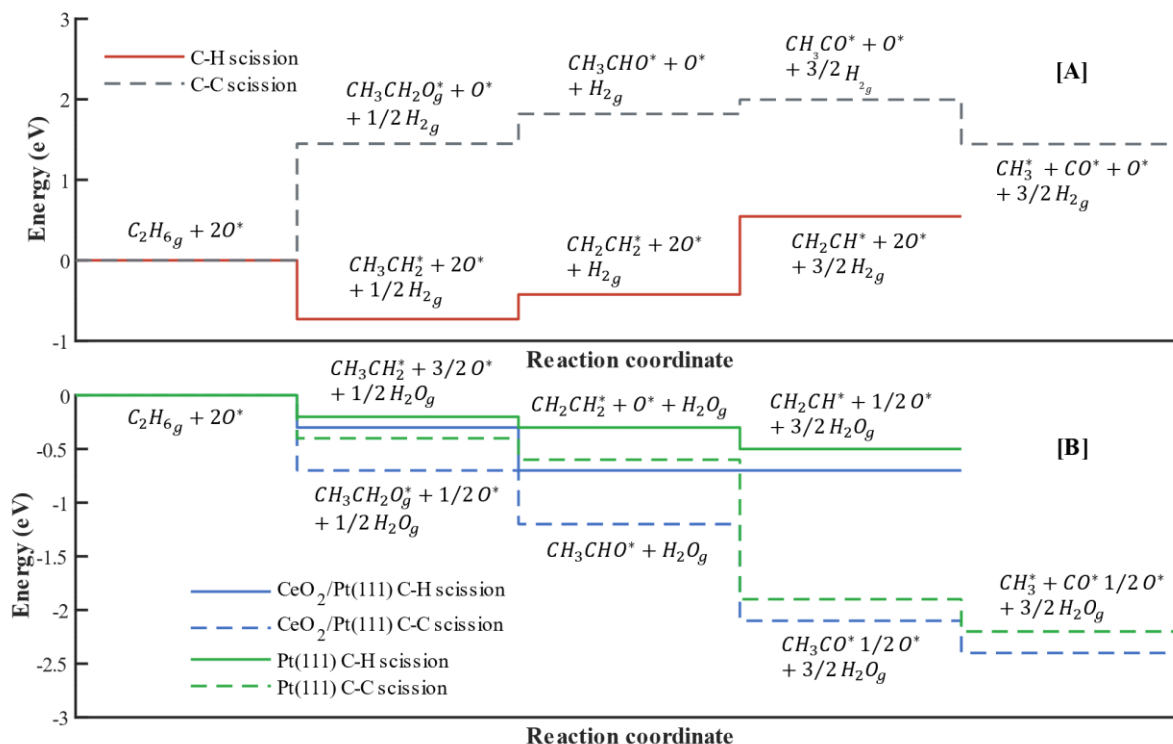


Figure 2.11. DFT-calculated energy profile of reforming and oxidative dehydrogenation of ethane over [A] Mo₂C(001) and [B] Pt(111) and CeO₂/Pt(111) surface. Figure reproduced from Porosoff *et al.*⁵⁵

Sullivan and Bhan¹⁰⁹ investigated the use of bulk β -Mo₂C in propane dehydrogenation in the absence and presence of H₂ and/or CO₂ at 550 °C. The direct dehydrogenation of propane and in the presence of CO₂ achieved a selectivity to propylene above 95 %. With H₂ co-fed, the propylene selectivity dropped significantly due to the formation of about 30 % CH₄, through C-C bond scission *via* hydrogenolysis. H₂/CO₂ co-feeding increased the CO formed *via* the reforming pathway by reaction of hydrocarbon fragments with oxidized surface sites (O*), produced from CO₂ dissociation. Kinetic modelling of the dehydrogenation reaction over oxidized site pairs (O*-O*), carbidic site pairs (*-*) and cooperative site pairs (O*-*) resulted in the highest dehydrogenation rates calculated for the O*-* site pairs. The highest propylene formation rate can thus be observed when the number of oxidized and carbidic sites are balanced.

In a study by Yao *et al.*⁵², the effect of different surface states on the catalytic performance of bulk β -Mo₂C in the CO₂-ODH of ethane was examined. In this study the surface oxidation state of Mo was

controlled by an in house developed pulse reactor experiment. To obtain the different surface states, three different pre-treatments were performed. A 50 % CO₂ in N₂ mixture was used to obtain an oxygen rich surface. A 50 % C₂H₆ in N₂ mixture to obtain a carbon rich surface and a pre-treatment in pure hydrogen to obtain a molybdenum rich surface. The C-rich surface sample showed significant deactivation, indicating carbon deposition blocking the active sites of the catalyst. The molybdenum rich surface started off with the highest activity, but together with the oxygen rich surface significant catalyst deactivation was observed with time on stream. To reach a similar starting conversion level to the molybdenum rich surface sample, the space velocity of the oxygen rich surface sample was lowered. The ethylene yield of the oxygen rich surface sample started at about 5 % decreasing with time on stream to 0.5 %. However, the molybdenum rich surface sample started at just below 2 % ethylene yield, which increased with time on stream to approximately 6 % followed by a decrease to 2.5 %.

They further investigated various loadings of Fe on the bulk β -Mo₂C catalysts to stabilize the oxygen surface species. At 0.5 wt.-% Fe, initial activity in terms of C₂H₆ conversion was slightly improved in comparison to the unpromoted sample. However, with time on stream (TOS), the sample deactivated at a faster rate. Increasing the Fe loading significantly decreased initial C₂H₆ conversion levels and a more rapid deactivation of the catalyst was observed. It was stated that 1 wt.-% Fe is optimal in terms of C₂H₄ yield. Detailed characterization, by means of XPS and *in situ* XRD, has indicated that the Fe-promoted samples show a higher affinity towards oxidation of the carbide phase to MoO₂.

A closer look at the pulse reactor experiments performed by Yao *et al.*⁵² reveals that the Mo-rich surface easily activates CO₂ forming surface oxygen species and CO, where the C-rich surface favours the reverse Boudouard reaction with the deposited carbon during the pre-treatment, which is indicated by a CO generated to surface C consumption ratio of 2. After sufficient removal of the surface carbon, the CO generation increased producing oxygen surface species. In the experiments exposing the catalyst to ethane, the Mo-rich surface shows significant amounts of carbon deposition and methane formation, where the O-rich shows ethylene formation in the first three pulses. As the surface oxygen species are removed with time on stream, the activity increases, and the ethylene yield decreases. This effect of oxygen surface species was further investigated by evaluating the catalytic performance of an oxygen modified Mo_xC_y catalyst, with the oxygen coverage determined by a CO₂ titration method. The main finding was that the conversion decreases with an increase in oxygen coverage, but the selectivity increases significantly resulting in a higher ethylene yield at high oxygen coverage. It was concluded that an ideal control of oxygen surface coverage is the key to the performance of β -Mo₂C in the CO₂-ODH reaction of light alkanes.

2.4 Molybdenum carbide catalyst

2.4.1. Synthesis methods of (supported) Mo_xC_y catalysts

Some pioneering work on the preparation of molybdenum (oxy)carbides was conducted under the leadership of the late M. Boudart. A series of molybdenum oxycarbides (MoO_xC_y) with varying composition and particle size were prepared by the decomposition of molybdenum carbonyls ($\text{Mo}(\text{CO})_6$), followed by vapor condensation in reactive gases (H_2 or CO) at low pressures (below 0.2 bar) and high temperatures (between 1100 and 1800 °C).¹¹³ The MoO_xC_y samples all exhibited the cubic fcc structure. A carbon deficient structure was obtained with varying compositions ($\text{MoO}_{0.5-2}\text{C}_{0.3-0.4}$) and X-ray crystallite sizes reported between 6 and 14 nm. Another sample was prepared by reducing MoO_3 in a H_2 atmosphere to metallic molybdenum and subsequently carburizing it in a 3:2 $\text{CH}_4:\text{H}_2$ mixture. An excess of CH_4 was established at 700 °C for 3 hours. Hexagonal $\beta\text{-Mo}_2\text{C}$ was synthesized, with a carbon content of 9.81 wt.-%, which is larger than the theoretical value for $\beta\text{-Mo}_2\text{C}$ (6.25 wt.-%), confirmed by the presence of graphitic carbon on its surface.

In 1985, Volpe and Boudart¹¹⁴, prepared bulk (fcc) $\alpha\text{-MoC}_{1-x}$ samples *via* a temperature-programmed reaction (TPRe) of $\gamma\text{-Mo}_2\text{N}$ in a CH_4 and H_2 atmosphere. The $\gamma\text{-Mo}_2\text{N}$ sample was previously synthesized by a TPRe of MoO_3 with NH_3 , with a specific surface area of 220 $\text{m}^2 \text{g}^{-1}$. The TPRe of $\gamma\text{-Mo}_2\text{N}$ in pure CH_4 produced H_2 , N_2 and NH_3 from 400 °C reaching a broad maximum at 530 °C which disappeared completely by 700 °C. After a H_2 treatment at 600 °C, the surface area of the $\alpha\text{-MoC}_{1-x}$ sample was 150 $\text{m}^2 \text{g}^{-1}$. Another TPRe was performed on $\gamma\text{-Mo}_2\text{N}$, with a feed of 1:4 $\text{CH}_4:\text{H}_2$ and a subsequent H_2 treatment. An increased surface area of 185 $\text{m}^2 \text{g}^{-1}$ was measured.

The above presented work led to a series of publications that eventually developed into the foundation for the research towards the formation of molybdenum carbide materials, either *via* the TPRe mechanism or carbonyl decomposition. Lee *et al.*¹¹⁵ focused on the synthesis of bulk hexagonal $\beta\text{-Mo}_2\text{C}$ reaching surface areas (S_g) as high as 100 $\text{m}^2 \text{g}^{-1}$. The preparation of $\beta\text{-Mo}_2\text{C}$ involved a TPRe of MoO_3 in a flowing mixture of 20 vol.-% CH_4 in H_2 . During the TPRe, a H_2O and CH_4 consumption profile was established (see Figure 2.12). Below 300 °C no activity was measured, and the sample was quickly heated to this temperature followed by a 1 °C min^{-1} heating rate up to 730 °C. Two distinct water formation peaks can be observed. After the first peak, the material was identified by means of XRD to be MoO_2 . Simultaneously with the second water formation peak a CH_4 consumption peak was observed, indicating the simultaneous reduction of MoO_2 and the incorporation of the C into the structure, forming $\beta\text{-Mo}_2\text{C}$ with a S_g of 60 $\text{m}^2 \text{g}^{-1}$. In the absence of CH_4 in the reaction mixture, two water formation peaks were observed as well, but the final product was identified as metallic Mo (Mo^0), with a S_g of 3 $\text{m}^2 \text{g}^{-1}$. When

exposing the same material to an isothermal treatment at 660 °C, a S_g of 5 m² g⁻¹ was recorded. Higher contents of CH₄ in the carburizing mixture showed to increase the surface area, up to about 100 m² g⁻¹ when using pure CH₄, however higher temperatures (> 750 °C) were required for complete reduction.

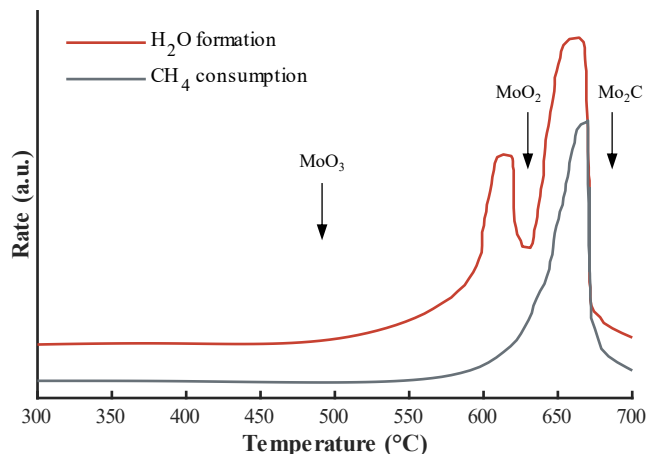


Figure 2.12: Temperature-programmed reaction of MoO₃ with 20 vol.-% CH₄ in H₂ reaction mixture while heating to 730 °C with 1 °C min⁻¹. Conditions: 0.5 g MoO₃, GHSV = 11 L h⁻¹ g_{cat}⁻¹. Figure is adapted from Lee *et al.*¹¹⁵.

The second article in the series focused on the preparation of cubic (metastable) α -MoC_{1-x}. In addition to the previously mentioned method of exposing Mo₂N to a TPre in 20 vol.-% CH₄ in H₂, Lee *et al.*¹¹⁶ synthesized cubic α -MoC_{1-x} powders *via* impregnation of MoO₃ with platinum and exposing it to the same TPre. The presence of platinum allowed for the same topotactic reaction (i.e., keeping the cubic structure intact) involving the simultaneous reduction and carburization of MoO₃. The presence of Pt decreased the temperature of the first reduction step from 530 to 130 °C, but the second reduction step was unaffected. A new methane consumption peak was observed, appearing simultaneously with the first reduction step. Exposure of the platinum promoted MoO₃ sample to the CH₄ and H₂ mixture at room temperature already resulted in the formation of H_xMoO₃ (molybdenum bronze). Temperature-programmed reduction (TPR) of the freshly prepared samples up to 1100 °C, revealed the presence of some oxygen and carbon impurities detected by the formation of CH₄ and CO. After the TPR, the metastable cubic phase transformed to the thermodynamically more stable hexagonal phase.

The third and last article of the series, published by Lee *et al.*¹¹⁷, describes the synthesis of γ -Al₂O₃ supported Mo_xC_y samples, prepared *via* an adapted method *via* the decomposition of Mo(CO)₆ described earlier. Metallic molybdenum clusters were prepared by sublimation of Mo(CO)₆ onto the alumina support at room temperature. By varying the exposure time of the support material to the saturated carrier gas, the Mo loading can be adjusted. Then, the saturator was bypassed and a H₂ flow was established at temperatures up to 700 °C and maintained for 1-3 hours, yielding Mo/Al₂O₃. The samples were

subsequently exposed to TPre using a 15-20 vol.-% CH₄ in H₂ mixture, forming Mo_xC_y at 650-700 °C. Although no crystal structure could be determined by means of XRD due to the low Mo loading and the overlapping reflexes of alumina, evidence on the formation of a carbide phase at around 660 °C, was obtained by X-ray adsorption spectroscopy (XAS) and the magnitude of the Fourier transform.

Most of the literature preparing molybdenum carbide materials for catalytic testing purposes, apply the above discussed TPre of a Mo-precursor in a reducing gas mixture containing a carbonaceous compound. The precursor is often ammonium heptamolybdate (AHM), a commercially available MoO₃, or an in house prepared Mo₂N. Although the most common reaction mixture contains 20 vol.-% CH₄ in H₂, many studies have reported the use of other compositions, varying the CH₄ concentration or using a different carbon source (CO or C_nH_{2n+2}, with n ≥ 2). The various reaction mixtures or TPre conditions can yield a variety of crystal structures, with the most common reported structures being (hcp) β-Mo₂C or (fcc) α-MoC_{1-x} (see Table 2.1).¹¹⁸ Less commonly reported crystal structures include the (hexagonal) η-MoC_x and (hexagonal) γ-MoC_x.¹¹⁹

The β-Mo₂C phase, stable at high temperatures, has an hcp crystal structure with an ABAB stacking sequence. The terminology used of this particular phase is inconsistent in literature and has also been referred to as α-Mo₂C¹²⁰, described as an orthorhombic (distorted) hcp structure stable at room temperature, or ε-Mo₂C, which has a hexagonal/trigonal hcp structure stable at intermediate temperatures. These phases are hard to be distinguished by lab-sourced XRD patterns. For catalytic studies, this phase is most commonly referred to as β-Mo₂C to prevent confusion to the cubic α-MoC_{1-x} phase. The α-MoC_{1-x} phase has a fcc crystal structure with an ABCABC stacking sequence. Another nomenclature (often in computational studies) used for this phase is δ-MoC. The cubic phase is often referred to as metastable, as it was shown to convert into the β-phase at higher temperatures. The third phase of interest is the η-MoC phase, which is of a hexagonal structure with an ABCACB stacking sequence. It is also reported to be a metastable phase. Lastly, γ-MoC has a hexagonal (simple) structure and appears in two different stacking sequences, AAAA or AABB (referred to as γ'-MoC). While γ-MoC is stable at room temperature, γ'-MoC is metastable at all temperatures and is suggested to be the intermediate phase between the β- and γ-phase.¹²¹

Table 2.1. Crystallographic information of common molybdenum carbide phases. Table is adapted from De Zanet and Kondrat¹¹⁸.

Phase	Type	Range of T (stability)	Structure	Lattice param. in Å (ICSD)	Space group (ICSD)	C atom position	Stacking sequence
β-Mo₂C^[a] HCP	α -Mo ₂ C	ζ -Fe ₂ N	Room Temperature 122-124	Orthorhombic (distorted) hcp	a = 4.724 b = 6.004 c = 5.199	Pbcn (60)	Octahedral ABAB
	ε -Mo ₂ C	ε -Fe ₂ N	Intermediate Temperature 122, 124	Hexagonal/Trigonal hcp	a = 5.190 b = 5.190 c = 4.724	P-31m (162)	Octahedral ABAB
	β -Mo ₂ C	Nb ₂ N/W ₂ C	High ^[b] Temperatures 121-124	Hexagonal (filled) hcp	a = 3.002 b = 3.002 c = 4.724	P63/mmc (194)	Octahedral ABAB
η -MoC	η -Mo ₃ C ₂	Metastable ¹²⁵⁻¹²⁷ Stable T > 1700 °C ¹²⁸	Hexagonal (complex) hcp	a = 3.010 b = 3.010 c = 14.610	P63/mmc (194)	Octahedral	ABCACB
α-MoC_{1-x}^[a] FCC	δ -MoC ^[c]	NaCl	Metastable ¹²⁶ Stable T > 1700 °C ¹²⁸	Cubic fcc	a = 4.270 b = 4.270 c = 4.270	Fm-3m (225)	Octahedral ABCABC
γ -MoC	(WC type)	Room Temperature 121, 126, 129	Hexagonal simple	a = 2.903 b = 2.903 c = 2.828	P-6m2 (187)	Trigonal prismatic	AAAA
γ' -MoC	TiAs/TiP	Always ^[d] Metastable 121, 125, 126	Hexagonal	a = 2.932 b = 2.932 c = 10.97	P63/mmc (194)	Trigonal prismatic/ Octahedral	AABB

By loading molybdenum carbide on a support material, the surface area of the catalyst can be increased significantly. A variety of techniques have been reported to prepare supported Mo_xC_y-based catalysts. Schlatter *et al.*¹³⁰ dissolved MoO₃ in heated NH₄OH and water, creating a slurry with Al₂O₃. The carbide structure was prepared by a 20 vol.-% CH₄ in H₂ treatment at 580 °C. Kim *et al.*¹³¹ followed the earlier described method of decomposing Mo(CO)₆ onto Al₂O₃ *via* a temperature-programmed treatment in H₂. Wang *et al.*¹³² utilized a single-step thermal carburization method of an aqueous mixture of ammonium heptamolybdate (AHM) and hexamethylenetetramine (HMT), impregnated on γ -Al₂O₃. By heating the sample in an Ar atmosphere, the decomposition of the precursor salts leads to the formation of γ -Mo₂N (from AHM) and then to the formation of β -Mo₂C at 700 °C (using HMT as the carbon source). This is a promising synthesis route for large scale quantities as it avoids the use of an explosive reaction mixture (such as CH₄/H₂). Gao *et al.*¹³³ also managed to avoid the use of a carbonaceous or reducing gas mixture and prepared β -Mo₂C nanoparticles supported on carbon nanotubes (CNT) from an organic-inorganic hybrid (Mo₃O₁₀(C₆H₈N)₂·2H₂O) precursor. The synthesis of these so-called

^[a] Names commonly found in the catalytical/experimental studies

^[b] Normally referred as the L'3 disordered phase

^[c] Also referred as α -MoC, δ is mainly found in the computational studies

^[d] Intermediate between β and γ during the carburization with CO (can be considered as an oxycarbide)

MoO_x/amine nanowires and the formation of β-Mo₂C nanoparticles is described in an earlier report by Gao *et al.*¹³⁴. The vast majority of literature reports on the use of the more common (incipient wetness or slurry) impregnation method of the Mo precursor salt.¹³⁵⁻¹⁵³ After impregnation the sample is either calcined prior to carburization to yield supported MoO₃, or directly exposed to a carburization treatment. Again, a large variety of carburization mixtures have been used and it has shown large effects on the crystal properties of the catalyst. The most obvious effect is the crystal structure obtained (fcc or hcp) or the amount of free carbon deposited on the surface of the catalyst.

2.4.2. Promoter addition and effect on Mo_xC_y catalysts

Addition of promoter material to Mo_xC_y-based catalysts can be achieved *via* various methods. The most common method is *via* impregnation of the promoter precursor. This can be done pre- or post-carburization of the carbide material. Promotion of the carbide with potassium completed prior to carburization has the possibility to partially form metallic Mo.^{149, 154} Hence potassium promotion on (bulk) β-Mo₂C is often completed after carburization (sample was passivated followed by impregnation with K₂CO₃). This treatment decreased the surface area significantly (from 38 to 8 m² g⁻¹).¹⁵⁵ A catalytic effect of potassium promotion on molybdenum carbide is the reduction of the rate of hydrogenation by increasing the electron density (K₂SO₄ or KCl) and/or block the active sites responsible for hydrogen adsorption (K₂CO₃, KOH, CH₃COOK).¹⁵⁶ Solymosi and Bugyi¹⁵⁷ studied the addition of potassium to a Mo₂C/Mo(100) surface and its effect on the adsorption behaviour of CO₂ and CO. The dissociation of CO₂ was enhanced due to negatively charged CO₂ species. However, higher potassium contents also increase the activity towards CO dissociation and the formation of carbonate-like surface species.

Quanli *et al.*¹⁵⁸ have shown that nickel promotion enhances the catalytic performance of Mo₂C/Al₂O₃ in the partial oxidation of methane (POM) to synthesis gas (CO and H₂ mixture). The catalysts were prepared *via* co-impregnation of the precursor salts (AHM and nickel nitrate) onto γ-Al₂O₃, followed by calcination (500 °C, 4 hours) and carburization (20 vol.-% CH₄ in H₂, 850 °C). The enhanced catalytic performance (in terms of activity and selectivity) of the Ni-promoted sample was attributed to various reasons. Ni showed to increase the degree of carburization, increase the specific surface area, prevent the formation of MoO₂ under reaction conditions and simultaneously produce the active phases (carbides and oxycarbides) for POM. The catalyst stability was also enhanced, due to its ability to prevent oxidation or sintering. The crystal structure observed after carburization in the presence of Ni was β-Mo₂C, which is in stark contrast to Jung *et al.*¹⁵⁹ who observed the formation of α-MoC_{1-x} *via* a MoO_xC_y intermediate. The latter authors also investigated the effect of Pt, Pd, Co, Cu and β-Mo₂C on the carburization process of bulk MoO₃ to Mo_xC_y. The carburization in the presence of Pt and Pd followed a similar route as the

Ni-promoted sample, resulting in the topotactic formation of α - MoC_{1-x} , with MoO_xC_y as the intermediate phase. Co, Cu and β - Mo_2C addition resulted in an initial reduction to MoO_2 followed by the carburization to β - Mo_2C .

Wyvrat *et al.*¹⁶⁰ prepared Pt-promoted Mo_2C by 1) impregnating the freshly carburized sample by means of a deaerated aqueous solution of chloroplatinic acid ($\text{H}_2\text{PtCl}_6 \cdot 6\text{H}_2\text{O}$) and 2) impregnated a carburized sample after exposure to a passivation treatment. When the Pt was not involved during the carburization process, the carbide samples contained a mixture of α - MoC_{1-x} and β - Mo_2C . The carburization treatment was performed in 15 vol.-% CH_4 in H_2 at 590 °C for 2 hours. The presence of α - MoC_{1-x} was not discussed by the authors, but the reduction/decomposition of AHM in H_2 atmosphere at 350 °C for 12 hours could possibly form molybdenum hydroxide (MoO_xH_y), which is reported to be one of the precursors for α - MoC_{1-x} . Passivation of the carbide prior to impregnation with platinum caused structural and catalytic differences to the sample impregnated without passivation treatment. The incorporation of the Pt particles onto the carbide surface is suggested to occur due to the redox reactions between Pt and Mo. This redox reaction is less efficient with an (oxidized) passivation layer and agglomeration of Pt particles was observed by means of SEM-EDS. The activity of the passivated samples was also heavily affected, despite a reactivation treatment of all samples prior to reaction in 15 vol.-% CH_4 in H_2 .

Besides the structural and kinetic effects of promotion, a change in physiochemical properties has also been observed upon the addition of various dopants. Vo *et al.*¹⁴² prepared α - MoC_{1-x} supported on γ - Al_2O_3 in the absence and presence of a promoter. The samples were synthesized *via* co-impregnation of AHM and the promoter precursor (K, Na, Co and Ce) onto the support material. Carburization was completed after calcination, in a 5:1 H_2 to C_3H_8 mixture at 700 °C. The number of strong acid sites decreased upon promotion ($\text{Co} \gg \text{Ce} > \text{Na} > \text{K}$) and the number of strong basic sites increased ($\text{K} > \text{Na} > \text{Ce} > \text{Co}$). These observed changes in catalytic properties can lead to significant alterations in reaction pathways as is shown by Cao *et al.*¹⁶¹ in the steam reforming of methanol over Pt, Cu or Ni promoted Mo_xC_y catalysts. The samples were prepared by mixing aqueous solutions of the two precursors, followed by calcination and carburization in 20 vol.-% CH_4 in H_2 . In this particular study, the interaction of the reactants and the carbide surface was investigated by means of temperature-programmed surface reactions. Cu- Mo_xC_y seems to promote the formation of formic acid (HCOOH) as the intermediate pathway at temperatures between 90 and 180 °C, but with increased temperatures, methyl-formate (HCOOCH_3) functions as the intermediate for β - Mo_2C , Ni- Mo_2C , Pt- Mo_xC_y and Cu- Mo_xC_y .

References

1. V. Masson-Delmotte, P. Zhai, A. Pirani, S. L. Connors, C. Péan, S. Berger, N. Caud, Y. Chen, L. Goldfarb, M. I. Gomis, M. Huang, K. Leitzell, E. Lonnoy, J. B. R. Matthews, T. K. Maycock, T. Waterfield, O. Yelekçi, R. Yu and B. Zhou, *Summary for Policymakers. In: Climate Change 2021: The Physical Science Basis. Contribution of Working Group I to the Sixth Assessment Report of the Intergovernmental Panel on Climate Change*, Report In Press., IPCC, Cambridge University Press, 2021.
2. H. Shaftel, R. Jackson, S. Callery and D. Bailey, The Causes of Climate Change, <https://climate.nasa.gov/>, (accessed October 28, 2019, 2019).
3. V. G. Azevedo, S. Sartori and L. M. S. Campos, CO₂ emissions: A quantitative analysis among the BRICS nations, *Renewable and Sustainable Energy Reviews*, 2018, **81**, 107-115.
4. C. J. Cleveland and C. Morris, in *Handbook of Energy*, 2014, DOI: 10.1016/b978-0-12-417013-1.00045-5, pp. 805-820.
5. J. Cook, N. Oreskes, P. T. Doran, W. R. L. Anderegg, B. Verheggen, E. W. Maibach, J. S. Carlton, S. Lewandowsky, A. G. Skuce, S. A. Green, D. Nuccitelli, P. Jacobs, M. Richardson, B. Winkler, R. Painting and K. Rice, Consensus on consensus: a synthesis of consensus estimates on human-caused global warming, *Environmental Research Letters*, 2016, **11**, 048002.
6. D. Archer, Checking the thermostat, *Nature Geoscience*, 2008, **1**, 289-290.
7. *Global Energy Review 2021*. <https://www.iea.org/reports/global-energy-review-2021>, IEA Publications, Paris, France, 2021.
8. IEA, *Direct Air Capture*. <https://www.iea.org/reports/direct-air-capture>, IEA Publications, Paris, 2021.
9. D. W. Keith, G. Holmes, D. St. Angelo and K. Heidel, A Process for Capturing CO₂ from the Atmosphere, *Joule*, 2018, **2**, 1573-1594.
10. X. Wu, Y. Yu, Z. Qin and Z. Zhang, The Advances of Post-combustion CO₂ Capture with Chemical Solvents: Review and Guidelines, *Energy Procedia*, 2014, **63**, 1339-1346.
11. M. Kanniche, R. Gros-Bonnivard, P. Jaud, J. Valle-Marcos, J.-M. Amann and C. Bouallou, Pre-combustion, post-combustion and oxy-combustion in thermal power plant for CO₂ capture, *Applied Thermal Engineering*, 2010, **30**, 53-62.
12. E. I. Koysoumpa, C. Bergins and E. Kakaras, The CO₂ economy: Review of CO₂ capture and reuse technologies, *The Journal of Supercritical Fluids*, 2018, **132**, 3-16.
13. R. Socolow, M. Desmond, R. Aines, J. Blackstock, O. Bolland, T. Kaarsberg, N. Lewis, M. Mazzotti, A. Pfeffer, K. Sawyer, J. Siirola, B. Smit and J. Wilcox, *Direct air capture of CO₂ with chemicals. A Technology Assessment for the APS Panel and Public Affairs*, American Physical Society, 2011.
14. *About CCUS*. <https://www.iea.org/reports/about-ccus>, IEA Publications, Paris, France, 2021.
15. *Key World Energy Statistics 2021*. <https://www.iea.org/reports/key-world-energy-statistics-2021>, IEA Publications, Paris, France, 2021.
16. *Putting CO₂ to Use*. <https://www.iea.org/reports/putting-co2-to-use>, IEA Publications, Paris, France, 2019.
17. Q. Zhu, Developments on CO₂-utilization technologies, *Clean Energy*, 2019, **3**, 85-100.
18. S. Kawi and Y. Kathiraser, CO₂ as an Oxidant for High-Temperature Reactions, *Frontiers in Energy Research*, 2015, **3**, 1-17.
19. Y. Chen, S. Choi and L. T. Thompson, Low temperature CO₂ hydrogenation to alcohols and hydrocarbons over Mo₂C supported metal catalysts, *Journal of Catalysis*, 2016, **343**, 147-156.
20. B. Zhao, B. Yan, Z. Jiang, S. Yao, Z. Liu, Q. Wu, R. Ran, S. D. Senanayake, D. Weng and J. G. Chen, High selectivity of CO₂ hydrogenation to CO by controlling the valence state of nickel using perovskite, *Chem Commun (Camb)*, 2018, **54**, 7354-7357.
21. G. C. Chinchon, P. J. Denny, J. R. Jennings, M. S. Spencer and K. C. Waugh, Review - Synthesis of Methanol, *Applied Catalysis*, 1988, **36**, 1-65.
22. C. R. International, CRI'S LARGEST CO₂-TO-METHANOL REACTOR INSTALLED IN ANYANG, <https://www.carbonrecycling.is/news-media/co2-to-methanol-reactor-installed-in-anyang>, (accessed 28 February, 2022).
23. C. Engineering, Carbon Engineering Demonstrates AIR TO FUELS, <http://carbonengineering.com/news-updates/ce-demonstrates-air-fuels/>, (accessed April 14, 2020).

24. J. Lang, Experimentelle Beiträge zur Kenntnis der Vorgänge bei der Wasser- und Heizgasbereitung, *Phys. Chem.*, 1888, **2**, 161-183.
25. C. M. Kalamaras and A. M. Efstathiou, Hydrogen Production Technologies: Current State and Future Developments, *Conference Papers in Energy*, 2013, **2013**, 1-9.
26. E. Alper and O. Yuksel Orhan, CO₂ utilization: Developments in conversion processes, *Petroleum*, 2017, **3**, 109-126.
27. K. Wittich, M. Krämer, N. Bottke and S. A. Schunk, Catalytic Dry Reforming of Methane: Insights from Model Systems, *ChemCatChem*, 2020, **12**, 2130-2147.
28. Linde, Innovative dry reforming process, <https://www.linde-engineering.com/en/innovations/innovate-dry-reforming/index.html>, (accessed April 14, 2020).
29. L. Fernández, Global production capacity of ethylene 2018-2025, <https://www.statista.com/statistics/1067372/global-ethylene-production-capacity/>, (accessed April 6, 2022).
30. L. Koottungal, *International survey of ethylene from steam crackers. Oil and Gas Journal*, 2015.
31. I. Amghizar, L. A. Vandewalle, K. M. Van Geem and G. B. Marin, New Trends in Olefin Production, *Engineering*, 2017, **3**, 171-178.
32. H. Zimmermann and R. Walzl, in *Ullmann's Encyclopedia of Industrial Chemistry*, 2009, DOI: 10.1002/14356007.a10_045.pub3.
33. H. Schulz, Short history and present trends of Fischer–Tropsch synthesis, *Applied Catalysis A: General*, 1999, **186**, 3-12.
34. M. E. Dry, The Fischer-Tropsch process 1950-2000, *Catalysis Today*, 2002, **71**, 227-241.
35. M. E. Dry, Practical and theoretical aspects of the catalytic Fischer-Tropsch process, *Applied Catalysis A: General*, 1990, **138**, 319-344.
36. D. Dillerop, H. van den Berg and A. G. J. van der Ham, Novel Syngas Production Techniques for GTL-FT Synthesis of Gasoline Using Reverse Flow Catalytic Membrane Reactors, *Industrial & Engineering Chemistry Research*, 2010, **49**, 12529-12537.
37. L. W. Miller, *United States Patent No. 6,166,282*, 2000, UOP LLC.
38. J. A. Montalbano, *United States Patent No. US 2011/0144404 A1*, 2011, UOP LLC.
39. M. J. G. Janssen and J. A. Zboray, *United States Patent No. 6,121,503*, 2000, Exxon Chemical Patents Inc.
40. F. Studt, I. Sharafutdinov, F. Abild-Pedersen, C. F. Elkjaer, J. S. Hummelshøj, S. Dahl, I. Chorkendorff and J. K. Nørskov, Discovery of a Ni-Ga catalyst for carbon dioxide reduction to methanol, *Nat Chem*, 2014, **6**, 320-324.
41. H. Bahruji, M. Bowker, G. Hutchings, N. Dimitratos, P. Wells, E. Gibson, W. Jones, C. Brookes, D. Morgan and G. Lalev, Pd/ZnO catalysts for direct CO₂ hydrogenation to methanol, *Journal of Catalysis*, 2016, **343**, 133-146.
42. G. E. Keller and M. M. Bhasin, Synthesis of Ethylene via Oxidative Coupling of Methane, *Journal of Catalysis*, 1982, **73**, 9-19.
43. A. Galadima and O. Muraza, Revisiting the oxidative coupling of methane to ethylene in the golden period of shale gas: A review, *Journal of Industrial and Engineering Chemistry*, 2016, **37**, 1-13.
44. C. Boswell, On-purpose technologies ready to fill propylene gap, <https://www.icis.com/resources/news/2012/04/16/9549968/on-purpose-technologies-ready-to-fill-propylene-gap/>, (accessed 16 October, 2018).
45. J. J. Sattler, J. Ruiz-Martinez, E. Santillan-Jimenez and B. M. Weckhuysen, Catalytic dehydrogenation of light alkanes on metals and metal oxides, *Chem Rev*, 2014, **114**, 10613-10653.
46. H. Boukhlof, A. Barama, R. Benrabaa, J. G. Caballero, A. Löfberg and E. Bordes-Richard, Catalytic activity in the oxidative dehydrogenation of ethane over Ni and/or Co molybdate catalysts: Synthesis and characterization, *Comptes Rendus Chimie*, 2017, **20**, 30-39.
47. P. Concepción, A. Galli and J. M. López Nieto, On The Influence Of The Acid-Base Character Of Catalysts On The Oxidative Dehydrogenation Of Alkanes, *Topics in Catalysis*, 1996, **3**, 451-460.
48. I. M. Gerzeliev, A. M. Gyl'maliev, A. Y. Popov and S. N. Khadzhev, Thermodynamic and quantum-chemical study of the oxidative dehydrogenation of ethane to ethylene, *Petroleum Chemistry*, 2015, **55**, 146-153.
49. L. Kong, J. Li, Z. Zhao, Q. Liu, Q. Sun, J. Liu and Y. Wei, Oxidative dehydrogenation of ethane to ethylene over Mo-incorporated mesoporous SBA-16 catalysts: The effect of MoO dispersion, *Applied Catalysis A: General*, 2016, **510**, 84-97.

50. E. Kondratenko, M. Cherian, M. Baerns, D. Su, R. Schlogl, X. Wang and I. Wachs, Oxidative dehydrogenation of propane over V/MCM-41 catalysts: comparison of O₂ and N₂O as oxidants, *Journal of Catalysis*, 2005, **234**, 131-142.
51. R. Bulánek, B. Wichterlová, K. Novoveská and V. Kreibich, Oxidation of propane with oxygen and/or nitrous oxide over Fe-ZSM-5 with low iron concentrations, *Applied Catalysis A: General*, 2004, **264**, 13-22.
52. S. Yao, B. Yan, Z. Jiang, Z. Liu, Q. Wu, J. H. Lee and J. G. Chen, Combining CO₂ Reduction with Ethane Oxidative Dehydrogenation by Oxygen-Modification of Molybdenum Carbide, *ACS Catalysis*, 2018, **8**, 5374-5381.
53. F. Solymosi and R. Németh, The oxidative dehydrogenation of ethane with CO₂ over Mo₂C/SiO₂ catalyst, *Catalysis Letters*, 1999, **62**, 197-200.
54. F. Solymosi, R. Németh and A. Oszkó, The oxidative dehydrogenation of propane with CO₂ over supported Mo₂C catalyst, *Studies in Surface Sciences and Catalysis*, 2001, **136**, 339-344.
55. M. D. Porosoff, M. N. Myint, S. Kattel, Z. Xie, E. Gomez, P. Liu and J. G. Chen, Identifying Different Types of Catalysts for CO₂ Reduction by Ethane through Dry Reforming and Oxidative Dehydrogenation, *Angew Chem Int Ed Engl*, 2015, **54**, 15501-15505.
56. E. Gomez, S. Kattel, B. Yan, S. Yao, P. Liu and J. G. Chen, Combining CO₂ reduction with propane oxidative dehydrogenation over bimetallic catalysts, *Nat Commun*, 2018, **9**, 1398.
57. M. A. Atanga, F. Rezaei, A. Jawad, M. Fitch and A. A. Rownaghi, Oxidative dehydrogenation of propane to propylene with carbon dioxide, *Applied Catalysis B: Environmental*, 2018, **220**, 429-445.
58. M. d. C. Rangel, A. P. d. M. Monteiro, M. Oportus, P. Reyes, M. d. S. Ramos and S. B. Lima, in *Greenhouse Gases - Capturing, Utilization and Reduction*, InTech, Liu, G., 2012, pp. 117-136.
59. F. Cavani, N. Ballarini and A. Cericola, Oxidative dehydrogenation of ethane and propane: How far from commercial implementation?, *Catalysis Today*, 2007, **127**, 113-131.
60. N. Shiju, M. Anilkumar, S. Mirajkar, C. Gopinath, B. Rao and C. Satyanarayana, Oxidative dehydrogenation of ethylbenzene over vanadia-alumina catalysts in the presence of nitrous oxide: structure-activity relationship, *Journal of Catalysis*, 2005, **230**, 484-492.
61. M. B. Ansari and S.-E. Park, Carbon dioxide utilization as a soft oxidant and promoter in catalysis, *Energy & Environmental Science*, 2012, **5**, 9419-9437.
62. X. Jiang, L. Sharma, V. Fung, S. J. Park, C. W. Jones, B. G. Sumpter, J. Baltrusaitis and Z. Wu, Oxidative Dehydrogenation of Propane to Propylene with Soft Oxidants via Heterogeneous Catalysis, *ACS Catalysis*, 2021, **11**, 2182-2234.
63. D. Mukherjee, S.-E. Park and B. M. Reddy, CO₂ as a soft oxidant for oxidative dehydrogenation reaction: An eco benign process for industry, *Journal of CO₂ Utilization*, 2016, **16**, 301-312.
64. E. Nowicka, C. Reece, S. M. Althahban, K. M. H. Mohammed, S. A. Kondrat, D. J. Morgan, Q. He, D. J. Willock, S. Golunski, C. J. Kiely and G. J. Hutchings, Elucidating the Role of CO₂ in the Soft Oxidative Dehydrogenation of Propane over Ceria-Based Catalysts, *ACS Catalysis*, 2018, **8**, 3454-3468.
65. S. T. Rahman, J.-R. Choi, J.-H. Lee and S.-J. Park, The Role of CO₂ as a Mild Oxidant in Oxidation and Dehydrogenation over Catalysts: A Review, *Catalysts*, 2020, **10**, 1075.
66. G. Raju, B. M. Reddy, B. Abhishek, Y.-H. Mo and S.-E. Park, Synthesis of C₄ olefins from n-butane over a novel VO_x/SnO₂-ZrO₂ catalyst using CO₂ as soft oxidant, *Applied Catalysis A: General*, 2012, **423-424**, 168-175.
67. D. B. Fox, E. H. Lee and M.-H. Rei, Carbon Dioxide as Hydrogen Acceptor in Dehydrogenation of Alkanes, *Industrial & Engineering Chemistry Product Research and Development*, 1972, **11**, 444-446.
68. G. Li, C. Liu, X. Cui, Y. Yang and F. Shi, Oxidative dehydrogenation of light alkanes with carbon dioxide, *Green Chemistry*, 2021, **23**, 689-707.
69. S. Wang and Z. H. Zhu, Catalytic Conversion of Alkanes to Olefins by Carbon Dioxide Oxidative Dehydrogenation A Review, *Energy & Fuels*, 2004, **18**, 1126-1139.
70. Y. Gao, L. Neal, D. Ding, W. Wu, C. Baroi, A. M. Gaffney and F. Li, Recent Advances in Intensified Ethylene Production—A Review, *ACS Catalysis*, 2019, **9**, 8592-8621.

71. E. Gomez, B. Yan, S. Kattel and J. G. Chen, Carbon dioxide reduction in tandem with light-alkane dehydrogenation, *Nature Reviews Chemistry*, 2019, **3**, 638-649.
72. Y. Gambo, S. Adamu, G. Tanimu, I. M. Abdullahi, R. A. Lucky, M. S. Ba-Shammakh and M. M. Hossain, CO₂-mediated oxidative dehydrogenation of light alkanes to olefins: Advances and perspectives in catalyst design and process improvement, *Applied Catalysis A: General*, 2021, **623**, 118273.
73. I. Takahara, W.-C. Chang, N. Mimura and M. Saito, Promoting effects of CO₂ on dehydrogenation of propane over a SiO₂-supported Cr₂O₃ catalyst, *Catalysis Today*, 1998, **45**, 55-59.
74. K. Takehira, Y. Ohishi, T. Shishido, T. Kawabata, K. Takaki, Q. Zhang and Y. Wang, Behavior of active sites on Cr-MCM-41 catalysts during the dehydrogenation of propane with CO₂, *Journal of Catalysis*, 2004, **224**, 404-416.
75. L. Liu, H. Li and Y. Zhang, Mesoporous silica-supported chromium catalyst: Characterization and excellent performance in dehydrogenation of propane to propylene with carbon dioxide, *Catalysis Communications*, 2007, **8**, 565-570.
76. M. A. Botavina, G. Martra, Y. A. Agafonov, N. A. Gaidai, N. V. Nekrasov, D. V. Trushin, S. Coluccia and A. L. Lapidus, Oxidative dehydrogenation of C₃-C₄ paraffins in the presence of CO₂ over CrOx/SiO₂ catalysts, *Applied Catalysis A: General*, 2008, **347**, 126-132.
77. L. Jin, J. Reutenauer, N. Opembe, M. Lai, D. J. Martenak, S. Han and S. L. Suib, Studies on Dehydrogenation of Ethane in the Presence of CO₂ over Octahedral Molecular Sieve (OMS-2) Catalysts, *ChemCatChem*, 2009, **1**, 441-444.
78. F. Zhang, R. Wu, Y. Yue, W. Yang, S. Gu, C. Miao, W. Hua and Z. Gao, Chromium oxide supported on ZSM-5 as a novel efficient catalyst for dehydrogenation of propane with CO₂, *Microporous and Mesoporous Materials*, 2011, **145**, 194-199.
79. J. Baek, H. J. Yun, D. Yun, Y. Choi and J. Yi, Preparation of Highly Dispersed Chromium Oxide Catalysts Supported on Mesoporous Silica for the Oxidative Dehydrogenation of Propane Using CO₂: Insight into the Nature of Catalytically Active Chromium Sites, *ACS Catalysis*, 2012, **2**, 1893-1903.
80. P. Michorczyk, K. Zeńczak, R. Niekurzak and J. Ogonowski, Dehydrogenation of propane with CO₂ – a new green process for propene and synthesis gas production, *npj*, 2012, **14**, 77-82.
81. T. Shishido, K. Shimamura, K. Teramura and T. Tanaka, Role of CO₂ in dehydrogenation of propane over Cr-based catalysts, *Catalysis Today*, 2012, **185**, 151-156.
82. T. A. Bugrova, V. V. Dutov, V. A. Svetlichnyi, V. Cortés Corberán and G. V. Mamontov, Oxidative dehydrogenation of ethane with CO₂ over CrOx catalysts supported on Al₂O₃, ZrO₂, CeO₂ and CexZr1-xO₂, *Catalysis Today*, 2019, **333**, 71-80.
83. K. Chen, A. T. Bell and E. Iglesia, The Relationship between the Electronic and Redox Properties of Dispersed Metal Oxides and Their Turnover Rates in Oxidative Dehydrogenation Reactions, *Journal of Catalysis*, 2002, **209**, 35-42.
84. G Rajua, B. M. Reddy and S.-E. Parkb, The Relationship between the Electronic and Redox Properties of Dispersed Metal Oxides and Their Turnover Rates in Oxidative Dehydrogenation Reactions, *Indian Journal of Chemistry*, 2012, **51A**, 1315-1324.
85. I. Ascoop, V. V. Galvita, K. Alexopoulos, M.-F. Reyniers, P. Van Der Voort, V. Bliznuk and G. B. Marin, The role of CO₂ in the dehydrogenation of propane over WO –VO /SiO₂, *Journal of Catalysis*, 2016, **335**, 1-10.
86. C. Wei, F. Xue, C. Miao, Y. Yue, W. Yang, W. Hua and Z. Gao, Dehydrogenation of Isobutane with Carbon Dioxide over SBA-15-Supported Vanadium Oxide Catalysts, *Catalysts*, 2016, **6**, 171.
87. P. Michorczyk, Dehydrogenation of propane to propene over gallium oxide in the presence of CO₂, *Applied Catalysis A: General*, 2003, **251**, 425-433.
88. Z. Shen, J. Liu, H. Xu, Y. Yue, W. Hua and W. Shen, Dehydrogenation of ethane to ethylene over a highly efficient Ga₂O₃/HZSM-5 catalyst in the presence of CO₂, *Applied Catalysis A: General*, 2009, **356**, 148-153.
89. R. Koirala, R. Buechel, F. Krumeich, S. E. Pratsinis and A. Baiker, Oxidative Dehydrogenation of Ethane with CO₂ over Flame-Made Ga-Loaded TiO₂, *ACS Catalysis*, 2014, **5**, 690-702.
90. C. Doornkamp and V. Ponec, The universal character of the Mars and Van Krevelen mechanism, *Journal of Molecular Catalysis A: Chemical*, 2000, **162**, 19-32.

91. S. Sato, M. Ohhara, T. Sodesawa and F. Nozaki, Combination of ethylbenzene dehydrogenation and carbon dioxide shift-reaction over a sodium oxide/alumina catalyst, *Applied Catalysis*, 1988, **37**, 207-215.
92. K. Nakagawa, M. Okamura, N. Ikenaga, T. Suzuki, K. Nakagawa, M. Okamura, T. Suzuki, T. Kobayashi and T. Kobayashi, Dehydrogenation of ethane over gallium oxide in the presence of carbon dioxide, *Chemical Communications*, 1998, **9**, 1025-1026.
93. K. Nakagawa, C. Kajita, Y. Ide, M. Okamura, S. Kato, H. Kasuya, N. o. Ikenaga, T. Kobayashi and T. Suzuki, Promoting effect of carbon dioxide on the dehydrogenation and aromatization of ethane over gallium-loaded catalysts, *Catalysis Letters*, 2000, **64**, 215-221.
94. K. Nakagawa, C. Kajita, N.-o. Ikenaga, T. Kobayashi, M. Nishitani-Gamo, T. Ando and T. Suzuki, Oxidized Diamond: A Novel Support for Catalytic Dehydrogenation, *Chemistry Letters*, 2000, **29**, 1100-1101.
95. S. Wang, K. Murata, T. Hayakawa, S. Hamakawa and K. Suzuki, Oxidative dehydrogenation of ethane by carbon dioxide over sulfate-modified Cr₂O₃/SiO₂ catalysts, *Catalysis Letters*, 1999, **63**, 59-64.
96. N. Mimura, I. Takahara, M. Inaba, M. Okamoto and K. Murata, High-performance Cr/H-ZSM-5 catalysts for oxidative dehydrogenation of ethane to ethylene with CO₂ as an oxidant, *Catalysis Communications*, 2002, **3**, 257-262.
97. S. Deng, H. Li, S. Li and Y. Zhang, Activity and characterization of modified Cr₂O₃/ZrO₂ nano-composite catalysts for oxidative dehydrogenation of ethane to ethylene with CO₂, *Journal of Molecular Catalysis A: Chemical*, 2007, **268**, 169-175.
98. R. Koirala, O. V. Safonova, S. E. Pratsinis and A. Baiker, Effect of cobalt loading on structure and catalytic behavior of CoO x /SiO₂ in CO₂-assisted dehydrogenation of ethane, *Applied Catalysis A: General*, 2018, **552**, 77-85.
99. M. Myint, B. Yan, J. Wan, S. Zhao and J. G. Chen, Reforming and oxidative dehydrogenation of ethane with CO₂ as a soft oxidant over bimetallic catalysts, *Journal of Catalysis*, 2016, **343**, 168-177.
100. B. Yan, S. Yao, S. Kattel, Q. Wu, Z. Xie, E. Gomez, P. Liu, D. Su and J. G. Chen, Active sites for tandem reactions of CO₂ reduction and ethane dehydrogenation, *Proc Natl Acad Sci U S A*, 2018, **115**, 8278-8283.
101. S. Raseale, W. Marquart, K. Jeske, G. Prieto, M. Claeys and N. Fischer, Supported Fe_xNi_y catalysts for the co-activation of CO₂ and small alkanes, *Faraday Discuss*, 2021, **229**, 208-231.
102. O. Lezla, E. Bordes, P. Courtine and G. Hecquet, Synergetic Effects in the Ni-Mo-O System, *Journal of Catalysis*, 1997, **170**, 346-356.
103. H. M. AbdelDayem and P. Ruiz, in *Spillover and Mobility of Species on Solid Surfaces*, 2001, DOI: 10.1016/s0167-2991(01)80050-1, pp. 363-370.
104. F. Dury, E. M. Gaigneaux and P. Ruiz, The active role of CO₂ at low temperature in oxidation processes: the case of the oxidative dehydrogenation of propane on NiMoO₄ catalysts, *Applied Catalysis A: General*, 2002, **242**, 187-203.
105. E. M. Thorsteinyon, T. P. Wilson, F. G. Young and H. Kasai, The Oxidative Dehydrogenation of Ethane over Catalysts containing Mixed Oxides of Molybdenum and Vanadium, *Journal of Catalysis*, 1977, **52**, 116-132.
106. K. Chen, S. Xie, A. T. Bell and E. Iglesia, Structure and Properties of Oxidative Dehydrogenation Catalysts Based on MoO₃/Al₂O₃, *Journal of Catalysis*, 2001, **198**, 232-242.
107. M. L. Balogun, S. Adamu, I. A. Bakare, M. S. Ba-Shammakh and M. M. Hossain, CO₂ Assisted Oxidative Dehydrogenation of Propane to Propylene over Fluidizable MoO₃/La₂O₃-γAl₂O₃ Catalysts, *Journal of CO₂ Utilization*, 2020, **42**, 101329.
108. R. Yao, J. E. Herrera, L. Chen and Y.-H. C. Chin, Generalized Mechanistic Framework for Ethane Dehydrogenation and Oxidative Dehydrogenation on Molybdenum Oxide Catalysts, *ACS Catalysis*, 2020, **10**, 6952-6968.
109. M. M. Sullivan and A. Bhan, Effects of oxygen coverage on rates and selectivity of propane-CO₂ reactions on molybdenum carbide, *Journal of Catalysis*, 2018, **357**, 195-205.
110. M. D. Porosoff, X. Yang, J. A. Boscoboinik and J. G. Chen, Molybdenum carbide as alternative catalysts to precious metals for highly selective reduction of CO₂ to CO, *Angew Chem Int Ed Engl*, 2014, **53**, 6705-6709.
111. X. Zhang, X. Zhu, L. Lin, S. Yao, M. Zhang, X. Liu, X. Wang, Y.-W. Li, C. Shi and D. Ma, Highly Dispersed Copper over β-Mo₂C as an Efficient and Stable Catalyst for the Reverse Water Gas Shift (RWGS) Reaction, *ACS Catalysis*, 2016, **7**, 912-918.

112. M. K. Neylon, S. Choi, H. Kwon, K. E. Curry and L. T. Thompson, Catalytic properties of early transition metal nitrides and carbides: n-butane hydrogenolysis, dehydrogenation and isomerization., *Appl. Catal. A: General*, 1999, **183**, 253-263.
113. L. Leclercq, K. Imura, S. Yoshida, T. Barbee and M. Boudart, Synthesis of New Catalytic Materials: Metal Carbides of the Group VI B Elements, *Studies in Surface Science and Catalysis*, 1979, **3**, 627-639.
114. L. Volpe and M. Boudart, Compounds of Molybdenum and Tungsten with High Specific Surface Area, *Journal of Solid State Chemistry*, 1985, **59**, 348-356.
115. J. S. Lee, S. T. Oyama and M. Boudart, Molybdenum Carbide Catalysts I. Synthesis of Unsupported Powders, *J. Catal.*, 1987, **106**, 125-133.
116. J. S. Lee, L. Volpe, F. H. Ribeiro and M. Boudart, Molybdenum Carbide Catalysts II. Topotactic Synthesis of Unsupported Powders, *J. Catal.*, 1988, **112**, 44-53.
117. J. S. Lee, S. T. Oyama and M. Boudart, Molybdenum Carbide Catalysts III. Turnover Rates for Hydrogenolysis of n-Butane, *J. Catal.*, 1990, **125**, 157-170.
118. A. De Zanet and S. A. Kondrat, A Review of Preparation Strategies for α -MoC_{1-x} Catalysts : Transition metal carbides attract growing attention, *Johnson Matthey Technology Review*, 2022, **66**, 285-315.
119. C. Wan, Y. N. Regmi and B. M. Leonard, Multiple phases of molybdenum carbide as electrocatalysts for the hydrogen evolution reaction, *Angew Chem Int Ed Engl*, 2014, **53**, 6407-6410.
120. A. N. Christensen, A Neutron Diffraction Investigation on a Crystal of α -Mo₂C, *Acta Chemica Scandinavica A*, 1977, **31**, 509-511.
121. K. Kuo and G. Hägg, A New Molybdenum Carbide, *Nature*, 1952, **170**, 245-246.
122. T. Epicier, J. Dubois, C. Esnouf, G. Fantozzi and P. Convert, Neutron powder diffraction studies of transition metal hemicarbides M₂C_{1-x}—II. In situ high temperature study on W₂C_{1-x} and Mo₂C_{1-x}, *Acta Metallurgica*, 1988, **36**, 1903-1921.
123. E. Parthe and V. Sadogopan, The structure of dimolybdenum carbide by neutron diffraction technique, *Acta Crystallographica*, 1963, **16**, 202-205.
124. K. Page, J. Li, R. Savinelli, H. N. Szumila, J. Zhang, J. K. Stalick, T. Proffen, S. L. Scott and R. Seshadri, Reciprocal-space and real-space neutron investigation of nanostructured Mo₂C and WC, *Solid State Sciences*, 2008, **10**, 1499-1510.
125. H. Nowotny, E. Parthé, R. Kieffer and F. Benesovsky, Das Dreistoffsystem: Molybdän—Silizium—Kohlenstoff, *Monatshefte für Chemie / Chemical Monthly*, 1954, **85**, 255-272.
126. E. V. Clougherty, K. H. Lothrop and J. A. Kafalas, A New Phase formed by High-Pressure Treatment : Face-centred Cubic Molybdenum Monocarbide, *Nature*, 1961, **191**, 1194.
127. E. Rudy, F. Benesovsky and K. Sedlatschek, Untersuchungen im System Niob-Molybdän-Kohlenstoff, *Monatshefte für Chemie und verwandte Teile anderer Wissenschaften*, 1961, **92**, 841-855.
128. H. W. Hugosson, O. Eriksson, L. Nordström, U. Jansson, L. Fast, A. Delin, J. M. Wills and B. Johansson, Theory of phase stabilities and bonding mechanisms in stoichiometric and substoichiometric molybdenum carbide, *Journal of Applied Physics*, 1999, **86**, 3758-3767.
129. J. Schuster, E. Rudy and H. Nowotny, Die "MoC"-Phase mit WC-Struktur, *Monatshefte für Chemie / Chemical Monthly*, 1976, **107**, 1167-1176.
130. J. C. Schlatter, S. T. Oyama, J. E. Metcalfe and J. M. Lambert, Jr., Catalytic Behavior of Selected Transition-Metal Carbides, Nitrides, and Borides in the Hydrodenitrogenation of Quinoline, *Industrial & Engineering Chemistry Research*, 1988, **27**, 1648-1653.
131. H. Kim, K. H. Lee and J. S. Lee, Carbon Monoxide Hydrogenation over Molybdenum Carbide Catalysts, *Research on Chemical Intermediates*, 2000, **26**, 427-443.
132. H. M. Wang, X. H. Wang, M. H. Zhang, X. Du, W. Li and K. Y. Tao, Synthesis of Bulk and Supported Molybdenum Carbide by a Single-Step Thermal Carburization Method, *Chemical Materials*, 2007, **19**, 1801-1807.
133. Q. Gao, C. Zhang, S. Wang, W. Shen, Y. Zhang, H. Xu and Y. Tang, Preparation of supported Mo(2)C-based catalysts from organic-inorganic hybrid precursor for hydrogen production from methanol decomposition, *Chem Commun (Camb)*, 2010, **46**, 6494-6496.

134. Q. Gao, C. Zhang, S. Xie, W. Hua, Y. Zhang, N. Ren, H. Xu and Y. Tang, Synthesis of Nanoporous Molybdenum Carbide Nanowires Based on Organic–Inorganic Hybrid Nanocomposites with Sub-Nanometer Periodic Structures, *Chemistry of Materials*, 2009, **21**, 5560-5562.
135. B. Dhandapani, S. Ramanathan, C. C. Yu, B. Fruhberger, J. G. Chen and S. T. Oyama, Synthesis, Characterization, and Reactivity Studies of Supported Mo₂C with Phosphorus Additive, *Journal of Catalysis*, 1998, **176**, 61-67.
136. F. Solymosi, R. Németh, L. Óvári and L. Egri, Reactions of Propane on Supported Mo₂C Catalysts, *Journal of Catalysis*, 2000, **195**, 316-325.
137. M. Tsuji, T. Miyao and S. Naito, Remarkable Support Effect of ZrO₂ upon the CO₂ Reforming of CH₄ over Supported Molybdenum Carbide Catalysts, *Catal. Lett.*, 2000, **69**, 195-198.
138. Weicheng Wu, Zili Wu, Changhai Liang, Xiaowei Chen, Pinliang Ying and C. Li, In Situ FT-IR Spectroscopic Studies of CO Adsorption on Fresh Mo₂C/Al₂O₃ Catalyst, *J. Phys. Chem. B*, 2003, **107**, 7088-7094.
139. J. M. Manoli, P. Da Costa, M. Brun, M. Vrinat, F. Maugé and C. Potvin, Hydrodesulfurization of 4,6-dimethyldibenzothiophene over promoted (Ni,P) alumina-supported molybdenum carbide catalysts: activity and characterization of active sites, *Journal of Catalysis*, 2004, **221**, 365-377.
140. D.-V. N. Vo and A. A. Adesina, Fischer–Tropsch synthesis over alumina-supported molybdenum carbide catalyst, *Applied Catalysis A: General*, 2011, **399**, 221-232.
141. D.-V. N. Vo and A. A. Adesina, Kinetics of the carbothermal synthesis of Mo carbide catalyst supported on various semiconductor oxides, *Fuel Processing Technology*, 2011, **92**, 1249-1260.
142. D.-V. N. Vo, T.-H. Nguyen, E. M. Kennedy, B. Z. Dlugogorski and A. A. Adesina, Fischer–Tropsch synthesis: Effect of promoter type on alumina-supported Mo carbide catalysts, *Catalysis Today*, 2011, **175**, 450-459.
143. S.-W. Chiang, C.-C. Chang, J.-L. Shie, C.-Y. Chang, D.-R. Ji and J.-Y. Tseng, Synthesis of alcohols and alkanes over potassium and vanadium promoted molybdenum carbides, *Journal of the Taiwan Institute of Chemical Engineers*, 2012, **43**, 918-925.
144. H. Al-Megren, T. Xiao, M. AlKinany, S. Aldree, Y. Huang, H. Chen, P. P. Edwards and V. Kuznetsov, High alcohol synthesis (HAS) from syngas over supported molybdenum carbide catalysts, *Applied Petrochemical Research*, 2013, **3**, 71-77.
145. H. Shou, L. Li, D. Ferrari, D. S. Sholl and R. J. Davis, Use of infrared spectroscopy and density functional theory to study the influence of rubidium on alumina-supported molybdenum carbide catalyst for higher alcohol synthesis from syngas, *Journal of Catalysis*, 2013, **299**, 150-161.
146. Q. Wu, J. M. Christensen, G. L. Chiarello, L. D. L. Duchstein, J. B. Wagner, B. Temel, J.-D. Grunwaldt and A. D. Jensen, Supported molybdenum carbide for higher alcohol synthesis from syngas, *Catalysis Today*, 2013, **215**, 162-168.
147. S. Boullouso-Eiras, R. Lødeng, H. Bergem, M. Stöcker, L. Hannevold and E. A. Blekkan, Catalytic hydrodeoxygenation (HDO) of phenol over supported molybdenum carbide, nitride, phosphide and oxide catalysts, *Catalysis Today*, 2014, **223**, 44-53.
148. T. Li, M. Virginie and A. Y. Khodakov, Effect of potassium promotion on the structure and performance of alumina supported carburized molybdenum catalysts for Fischer-Tropsch synthesis, *Applied Catalysis A: General*, 2017, **542**, 154-162.
149. M. D. Porosoff, J. W. Baldwin, X. Peng, G. Mpourmpakis and H. D. Willauer, Potassium-Promoted Molybdenum Carbide as a Highly Active and Selective Catalyst for CO₂ Conversion to CO, *ChemSusChem*, 2017, **10**, 2408-2415.
150. M. Abou Hamdan, S. Loidant, M. Jahjah, C. Pinel and N. Perret, TiO₂-supported molybdenum carbide: An active catalyst for the aqueous phase hydrogenation of succinic acid, *Applied Catalysis A: General*, 2019, **571**, 71-81.
151. C. G. Silva, F. B. Passos and V. T. da Silva, Influence of the support on the activity of a supported nickel-promoted molybdenum carbide catalyst for dry reforming of methane, *Journal of Catalysis*, 2019, **375**, 507-518.
152. M. Abou Hamdan, A. Nassereddine, R. Checa, M. Jahjah, C. Pinel, L. Piccolo and N. Perret, Supported Molybdenum Carbide and Nitride Catalysts for Carbon Dioxide Hydrogenation, *Front Chem*, 2020, **8**, 452.
153. M. Juneau, C. Pope, R. Liu and M. D. Porosoff, Support acidity as a descriptor for reverse water-gas shift over Mo₂C-based catalysts, *Applied Catalysis A: General*, 2021, **620**, 118034.

154. S. F. Zaman, N. Pasupulety, A. A. Al-Zahrani, M. A. Daous, S. S. Al-Shahrani, H. Driss, L. A. Petrov and K. J. Smith, Carbon monoxide hydrogenation on potassium promoted Mo₂N catalysts, *Applied Catalysis A: General*, 2017, **532**, 133-145.
155. K. Y. Park, W. K. Seo and J. S. Lee, Selective synthesis of light olefins from syngas over potassium-promoted molybdenum carbide catalysts, *Catalysis Letters*, 1991, **11**, 349-356.
156. J. S. Lee, S. Kim and Y. G. Kim, Electronic and geometric effects of alkali promoters in CO hydrogenation over K/Mo₂C catalysts, *Topics in Catalysis*, 1995, **2**, 127-140.
157. F. Solymosi and L. Bugyi, Effects of potassium on the chemisorption of CO₂ and CO on the Mo₂C/Mo(100) surface, *Catalysis Letters*, 2000, **66**, 227-230.
158. Z. Quanli, Z. Bing, Y. Jian, W. Jiaxin, Z. Jun, J. Shengfu and W. Hanqing, The promotion of nickel to Mo₂C/Al₂O₃ catalyst for the partial oxidation of methane to syngas, *New Journal of Chemistry*, 2003, **27**, 1633.
159. K. T. Jung, W. B. Kim, C. H. Rhee and J. S. Lee, Effects of Transition Metal Addition on the Solid-State Transformation of Molybdenum Trioxide to Molybdenum Carbides, *Chem. Mater.*, 2004, **16**, 307-314.
160. B. M. Wyratt, J. R. Gaudet and L. T. Thompson, Effects of passivation on synthesis, structure and composition of molybdenum carbide supported platinum water-gas shift catalysts, *Journal of Catalysis*, 2015, **330**, 280-287.
161. J. Cao, Y. Ma, G. Guan, X. Hao, X. Ma, Z. Wang, K. Kusakabe and A. Abudula, Reaction intermediate species during the steam reforming of methanol over metal modified molybdenum carbide catalysts, *Applied Catalysis B: Environmental*, 2016, **189**, 12-18.

3 Scope of the thesis

Mo_xC_y-based catalysts have not been studied extensively for the CO₂ assisted oxidative dehydrogenation (CO₂-ODH) of ethane.¹⁻⁵ The limited number of published articles that have been using (bulk) Mo_xC_y as a catalyst for this reaction have found promising catalytic results, mostly in terms of the selectivity to the desired product ethylene. However, severe catalyst deactivation is a major limitation and should be overcome to stimulate future catalyst development to create an economically feasible catalyst system for the CO₂-ODH. Deactivation of a Mo_xC_y catalyst in the CO₂-ODH reaction is caused by bulk oxidation of the carbide catalyst to its oxidic phases, in the presence of CO₂, or (in combination) due to carbon deposition covering the active sites on the surface of the catalyst.

The aim of this project is to identify the reaction mechanism that is prevalent on Mo₂C-based catalysts and to have a better understanding of the deactivation mechanism resulting in significant activity loss with time on stream. In particular, based on the newly developed understanding of both the reaction and the deactivation mechanism, it was attempted to avoid the severe catalyst deactivation, thus leading to an improved catalytic lifetime. Furthermore, based on literature reports it can be suggested that the CO₂ is activated on to the carbide forming oxygen surface species or a MoO_xC_y phase, followed by the activation of ethane on these oxygen sites.⁴ The role of the support is to be investigated given that bulk Mo₂C shows little activity. In addition, an extensive thermodynamic analysis of the CO₂-ODH system, including possible side and secondary reactions as well as the stability of the Mo₂C phase towards oxidation was conducted.

The synthesis (and the structure of this thesis) of the catalysts evaluated for their CO₂-ODH activity can be separated into three main parts. Firstly, the synthesis of supported Mo_xC_y nanoparticles was completed using different synthesis techniques, which include the common slurry impregnation technique of ammonium heptamolybdate onto the support material and the synthesis of MoO₃ nanoparticles, *via* a hybrid nanocrystal technique⁶⁻⁸ or a sol-gel method.⁹ The Mo_xC_y nanoparticles were then prepared *via* carburization treatment of the precursor materials, synthesized *via* each of the three techniques discussed. The carburization process was intensively studied using several *in situ* characterization techniques such as X-ray diffraction (XRD), Raman, X-ray adsorption spectroscopy (XAS) and thermogravimetric analysis (TGA). A variety of offline techniques were employed to confirm an acceptable discrepancy in terms of Mo loading, particle size and homogeneous distribution over the support material.

Secondly, the slurry impregnation technique was further employed to prepare Mo_xC_y nanoparticles supported on various metal oxide support materials (SiO₂, Al₂O₃, ZrO₂, Ga₂O₃, TiO₂ and CeO₂), bearing

different acid/base and redox properties. Due to the large difference in the surface area of each support, the emphasis of these samples was put on an equal molybdenum loading (20 wt.-%), well defined carbide composition (via Rietveld refinement) and confirmation of any carbon deposition (by means of Raman spectroscopy) upon the synthesis of the catalyst. The acid and base characteristics of the catalysts were determined *via* NH₃ and CO₂ temperature programmed desorption (TPD). The effect of the metal oxide support material on the affinity of the catalyst to activate CO₂ (as function of temperature) and the activity in the CO₂-ODH reaction were evaluated. In addition, several CO₂-ODH testing experiments were conducted in an attempt to improve the catalytic stability by co-feeding of H₂.

Thirdly, the performance of a Mo_xC_y catalyst supported on SiO₂ in the CO₂-ODH reaction mechanism was explored with the addition of a promoter (iron, platinum, nickel and potassium). The choice of the promoters was based on literature. The addition of iron has shown to increase CO₂-ODH performance by means of stabilizing the oxygen surface species⁵ and to weaken basic sites.¹⁰ Platinum has shown to form the (cubic) α -MoC_{1-x} phase¹¹ and can enhance C-H bond scission and suppress C-C bond cleavage.¹² Nickel and potassium have shown to cause a shift in the acidity of the catalysts^{13, 14}, a property known to influence the CO₂-ODH performance, specifically regarding reaction mechanism. The promotion effect on the carburization mechanism and the structural and chemical properties of the catalyst was extensively studied by means of several offline and *in situ* techniques. *In situ* XRD was employed to study the phase transformation from the precursor material to the final carbide composition. Electron microscopy techniques were used to confirm the close proximity and homogeneous distribution of the Mo and promoter metals on the SiO₂ support material. By means of CO₂-TPD, NH₃-TPD and temperature programmed CO₂ activation experiments, the acid/base properties as well as the affinity towards CO₂ activation as a function of temperature were investigated and linked to the presence of the promoter..

The catalytic performance and stability of all synthesized catalysts, carburized *in situ*, were studied in an in-house developed laboratory scale fixed bed reactor system. The catalysts were exposed to a variety of conditions, which include a range of reaction temperatures (550-750 °C) and co-feeding experiments of H₂ (at 0, 5, 10 or 17 vol.-%) or H₂O (at 4-5 vol.-%). The space velocity remained stable for the majority of the experiments (15 L h⁻¹ g_{cat}⁻¹) and the pressure was atmospheric. A special emphasis was put on the catalyst stability, by studying all catalyst for a period of 24 hours, and the determination of the reaction and deactivation mechanism. A deeper understanding of the reaction mechanism was obtained by closely monitoring the product species and the various product ratios that are coherently related to the number of possible side reactions. In addition, selected catalysts were evaluated under reverse water-gas-shift (RWGS) conditions. As the RWGS reaction is suggested to be a part of the reaction mechanism, highly active catalysts for the RWGS reaction¹⁵⁻¹⁷ are likely to support the RWGS in combination with DH, to

yield the overall CO₂-ODH reaction, as the reaction conditions are very similar. The catalysts were evaluated within a range of temperatures (400 to 600 °C) and varying the H₂ to CO₂ feed ratios (1, 2.5, 3.5 and 7.0) at atmospheric pressure.

References

1. F. Solymosi and R. Németh, The oxidative dehydrogenation of ethane with CO₂ over Mo₂C/SiO₂ catalyst, *Catalysis Letters*, 1999, **62**, 197-200.
2. F. Solymosi, R. Németh and A. Oszkó, The oxidative dehydrogenation of propane with CO₂ over supported Mo₂C catalyst, *Studies in Surface Sciences and Catalysis*, 2001, **136**, 339-344.
3. M. D. Porosoff, M. N. Myint, S. Kattel, Z. Xie, E. Gomez, P. Liu and J. G. Chen, Identifying Different Types of Catalysts for CO₂ Reduction by Ethane through Dry Reforming and Oxidative Dehydrogenation, *Angew Chem Int Ed Engl*, 2015, **54**, 15501-15505.
4. M. M. Sullivan and A. Bhan, Effects of oxygen coverage on rates and selectivity of propane-CO₂ reactions on molybdenum carbide, *Journal of Catalysis*, 2018, **357**, 195-205.
5. S. Yao, B. Yan, Z. Jiang, Z. Liu, Q. Wu, J. H. Lee and J. G. Chen, Combining CO₂ Reduction with Ethane Oxidative Dehydrogenation by Oxygen-Modification of Molybdenum Carbide, *ACS Catalysis*, 2018, **8**, 5374-5381.
6. W. Han, P. Yuan, Y. Fan, H. Liu and X. Bao, Synthesis, self-assembly and disassembly of mono-dispersed Mo-based inorganic-organic hybrid nanocrystals, *Journal of Materials Chemistry*, 2012, **22**, 12121-12127.
7. W. Han, P. Yuan, Y. Fan, G. Shi, H. Liu, D. Bai and X. Bao, Preparation of supported hydrodesulfurization catalysts with enhanced performance using Mo-based inorganic-organic hybrid nanocrystals as a superior precursor, *Journal of Materials Chemistry*, 2012, **22**, 25340-25353.
8. P. Yuan, Y. Guo, X. Li, Y. Yue, H. Zhu, T. Wang, Z. Bai and X. Bao, Dependence of Morphology, Dispersion and Hydrodesulfurization Performance of Active Phases in NiMo/SBA-15 on Loading Method, *ChemCatChem*, 2018, **10**, 3717-3725.
9. A. P. Amrute, S. Sahoo, A. Bordoloi, Y. K. Hwang, J.-S. Hwang and S. B. Halligudi, MoO₃/SiO₂: An efficient and selective catalyst for the synthesis 1,3-dioxolane and 1,3-dioxane, *Catalysis Communications*, 2009, **10**, 1404-1409.
10. S. Deng, H. Li, S. Li and Y. Zhang, Activity and characterization of modified Cr₂O₃/ZrO₂ nano-composite catalysts for oxidative dehydrogenation of ethane to ethylene with CO₂, *Journal of Molecular Catalysis A: Chemical*, 2007, **268**, 169-175.
11. J. S. Lee, L. Volpe, F. H. Ribeiro and M. Boudart, Molybdenum Carbide Catalysts II. Topotactic Synthesis of Unsupported Powders, *J. Catal.*, 1988, **112**, 44-53.
12. J. J. Sattler, J. Ruiz-Martinez, E. Santillan-Jimenez and B. M. Weckhuysen, Catalytic dehydrogenation of light alkanes on metals and metal oxides, *Chem Rev.*, 2014, **114**, 10613-10653.
13. F. Solymosi and L. Bugyi, Effects of potassium on the chemisorption of CO₂ and CO on the Mo₂C/Mo(100) surface, *Catalysis Letters*, 2000, **66**, 227-230.
14. P. Michorczyk, Dehydrogenation of propane to propene over gallium oxide in the presence of CO₂, *Applied Catalysis A: General*, 2003, **251**, 425-433.
15. M. Juneau, C. Pope, R. Liu and M. D. Porosoff, Support acidity as a descriptor for reverse water-gas shift over Mo₂C-based catalysts, *Applied Catalysis A: General*, 2021, **620**, 118034.
16. M. Juneau, M. Vonglis, J. Hartvigsen, L. Frost, D. Bayerl, M. Dixit, G. Mpourmpakis, J. R. Morse, J. W. Baldwin, H. D. Willauer and M. D. Porosoff, Assessing the viability of K-Mo₂C for reverse water-gas shift scale-up: molecular to laboratory to pilot scale, *Energy & Environmental Science*, 2020, **13**, 2524-2539.
17. X. Zhang, X. Zhu, L. Lin, S. Yao, M. Zhang, X. Liu, X. Wang, Y.-W. Li, C. Shi and D. Ma, Highly Dispersed Copper over β-Mo₂C as an Efficient and Stable Catalyst for the Reverse Water Gas Shift (RWGS) Reaction, *ACS Catalysis*, 2016, **7**, 912-918.

4 Experimental Methodology

4.1 Synthesis of supported molybdenum carbide nanoparticles

4.1.1. Slurry (wet) impregnation method

A slurry (often referred to as wet) impregnation method was utilised to support ammonium heptamolybdate tetrahydrate (AHM, $(\text{NH}_4)_6\text{Mo}_7\text{O}_{24}\cdot 4\text{H}_2\text{O}$, purchased from SAARCHEM PTY LTD (81.5 % MoO_3) or Merck (>99.3 %), South Africa) on a selection of support materials. Due to a large variation in sample batch size and support material utilised, a generalised method is described in short. In a typical synthesis yielding a 20 wt.-% Mo loading, 10 mL of a 0.038 M aqueous solution of AHM was added dropwise per gram of support material. The suspension was stirred for 30 minutes and dried in an oven at 120 °C overnight. Large batch sizes (up to 100 mL of solution) were first dried by means of a rotary evaporator using a 500 mL round-bottom Büchi flask at 60 °C, 72 mbar and 155 rpm, until a thick slurry was obtained prior to drying in the oven at 120 °C overnight.

The promoted samples were prepared *via* a slurry co-impregnation method, similar to the unpromoted samples. Per gram of support material, a 3 mL aqueous solution of the promoter precursor (iron(III) nitrate nonahydrate (>98 %), potassium nitrate (>99 %), nickel(II) nitrate hexahydrate (>98.5 %) or tetraamineplatinum(II) nitrate (99.995 %), all purchased from Sigma-Aldrich, South Africa) was mixed with 10 mL of a 0.038 M aqueous solution of AHM *via* dropwise addition while stirring continuously for 30 minutes followed by drying in the oven at 120 °C overnight.

Selected samples supported on SiO_2 were exposed to a calcination treatment at 400 °C for 5 hours in a tubular furnace with a heating rate of 5 °C min^{-1} , in an air flow of 3 L h^{-1} $\text{g}_{\text{cat}}^{-1}$. The samples were calcined either in absence, before or after addition of the promoter.

4.1.2. Sol-Gel method

A second method, the sol-gel method, was applied to obtain MoO_3 nanoparticles supported on SiO_2 . The method was adopted from Umbarkar *et al.*¹ and Amrute *et al.*² who employed MoO_3 supported on SiO_2 for the vapor phase nitration of benzene and the liquid phase condensation of anisole with paraformaldehyde, respectively. In a typical synthesis yielding a 20 wt.-% Mo loading, 100 mL of a 0.025 M AHM was dissolved in 100 mL of hot distilled water. The AHM solution was added dropwise to a solution of 37.16 mL tetraethyl orthosilicate (TEOS, Sigma Aldrich, 99.99 %) and 20 mL of 2-propanol (anhydrous, Sigma-Aldrich, 99.5 %), followed by a 3 hour aging step under continuous stirring. The obtained greenish precipitate was further aged inside the flask for 2 days at room temperature (RT),

resulting in a gel of the same colour. The gel was dried in an oven at 120 °C overnight, followed by calcination in a Nabertherm calcination oven at 500 °C for 10 hours in a stagnant air atmosphere.

4.1.3. Hybrid nanocrystal method

A third method, the hybrid nanocrystal (HNC) synthesis technique, was applied to obtain MoO₃ nanoparticles supported on SiO₂ or SBA-15. The method was first reported and developed³ by the group of Xiaojun Bao who prepared MoO₃ nanoparticles supported on Al₂O₃^{4, 5} and SBA-15^{6, 7}. For a typical synthesis, yielding a 20 wt.-% Mo loading, a 2.4 M hydrochloric acid (HCl, Kimix, 33 %) aqueous solution was added dropwise to 180 mL of 0.067 M aqueous sodium molybdate solution (Na₂MoO₄·2H₂O, Sigma-Aldrich, ≥99.5 %) while monitoring the pH. At a pH of 4.5, 40 mL of a 0.16 M cetyl trimethyl ammonium bromide (CTAB) aqueous solution (CTAB-to-Mo molar ratio of 0.53:1) was added dropwise under vigorous stirring (>1000 rpm). After the complete addition of CTAB, the pH was again adjusted to 4.5 by means of HCl addition. The mixture was stirred for another 2 hours. After completion, the white suspension was transferred to an autoclave and exposed to a hydrothermal deposition treatment of the crystals onto previously prepared SBA-15 (synthesised *via* a method reported by Nair⁸). The autoclave was heated to 100 °C while stirring (650 rpm) and held at that temperature for 12 hours. The mixture was washed with DI water, filtered using a Büchner funnel, and dried in an oven overnight at 60 °C. Once dry, the sample was calcined in a tubular furnace at 400 °C (heating rate 5 °C min⁻¹) for 5 hours in an air flow of 3 L h⁻¹ g_{cat}⁻¹.

4.1.4. Carburization method

In general, the prepared samples discussed in sections 4.1.1, 4.1.2 and 4.1.3, were carburized by means of a temperature-programmed reaction treatment in a 20 vol.-% CH₄ in H₂ atmosphere, a method first reported by Volpe and Boudart⁹, to prepare supported Mo_xC_y nanoparticles. The carburization conditions varied to the specifications of the experiment are all reported in their respective experimental methodology and in Table K.1. All samples were loaded into a ¼ in. quartz fixed-bed reactor (details about reactor unit can be found in section 4.3.1). Unless stated otherwise, the temperature was ramped at a rate of 1 °C min⁻¹, to a final temperature of 600 °C, holding it for 5 hours at the maximum temperature. The reaction gas mixture was fed to the reactor at a space velocity of 15 L h⁻¹ g_{cat}⁻¹ at atmospheric pressure. Some samples were carburized using a diluted reaction mixture, to the requirements of the respective reactor unit or product analysis technique, specified in their respective experimental methodology. After completion of the carburization, the catalyst was either passivated at RT (for *ex situ* characterization purposes) in a flow of 1 vol.-% O₂ in N₂ for 1 hour at a space velocity of 15 L h⁻¹ g_{cat}⁻¹ or directly exposed to testing conditions.

4.2 Characterization of supported molybdenum carbide nanoparticles

4.2.1. Powder X-Ray diffraction (XRD)

X-ray diffraction (XRD) was performed of the freshly synthesized samples and after catalytic testing to analyse the crystal phases and structures present. A D8 Advance diffractometer (Bruker, Germany) was equipped with a position sensitive detector (LYNXEYE) in Bragg Brentano geometry and a Co anode powered at 35 kV and 40 mA. The diffraction patterns were compared to reference data files (see Table 4.1) reported in the International Centre for Diffraction Data (ICDD) databases PDF-4+ 2021. All diffraction patterns were acquired in the 2θ range of 20° to 120° ($1/d = 0.19 \text{ 1/\AA}$ to 0.97 1/\AA), with a step size of 0.043° and 0.75 seconds per step. Quantitative analysis of the obtained diffraction spectra was conducted by way of Rietveld refinement¹⁰ using the TOPAS 5 software package (Bruker AXS).

Table 4.1. Overview of reference patterns used in this work obtained from the PDF-4+ (2019/20) in the ICDD database.

Phase	Name	Crystal System / space group	PDF-4+ identity
Mo ⁰	Molybdenum	Cubic / Im-3m (229)	00-042-1120
MoO ₂	Molybdenum(IV) oxide (tugarinovite)	Monoclinic / P21/c (14)	04-003-1961
<i>hP</i> -MoO ₃	Molybdenum(VI) oxide	Hexagonal / P63/m (176)	00-065-0141
<i>oP</i> -MoO ₃	Molybdenum(VI) oxide (molybdite)	Orthorhombic / Pbnm (62)	00-005-0508
β -Mo ₂ C	Molybdenum carbide	Hexagonal / P63/mmc (194)	00-035-0787
α -MoC _{1-x}	Molybdenum carbide	Cubic / Fm-3m (225)	04-004-2516
η -MoC _{0.59}	Molybdenum carbide	Hexagonal / P63/mmc (194)	04-013-5833
MoO _x C _y	Molybdenum Oxide Carbide	Cubic / Fm-3m (225)	00-017-0104
H _x MoO ₃	Hydrogen molybdenum oxide	Monoclinic / C2/m (12)	04-011-9826
(NH ₄) ₈ Mo ₁₀ O ₃₄	Ammonium Molybdenum Oxide	Triclinic (anorthic) / P-1 (2)	00-037-0381
(NH ₄) ₂ Mo ₄ O ₁₃	Ammonium Molybdenum Oxide	Triclinic (anorthic) / P-1 (2)	04-011-4665
γ -Al ₂ O ₃	Aluminum oxide	Cubic / Fd-3m (227)	04-005-4662
ZrO ₂	Zirconium oxide (baddeleyite)	Monoclinic / P21/c (14)	00-024-1165
Zr(MoO ₄) ₂	Zirconium molybdenum oxide	Hexagonal / P-31c (163)	00-038-1466
Ga ₂ O ₃	Gallium oxide	Monoclinic / C2/m (12)	04-007-1397
TiO ₂	Titanium oxide (rutile)	Tetragonal / P42/mnm (136)	00-021-1276
CeO ₂	Cerium oxide	Cubic / Fm-3m (225)	00-001-0800
Ce ₂ (MoO ₄) ₃	Cerium molybdenum oxide	Tetragonal / I41/a (88)	00-057-0952

4.2.2. Raman spectroscopy

Any form of carbon deposition on the freshly carburized or spent catalysts was analysed by means of Raman spectroscopy. The Raman spectra were collected using a Witec Confocal Raman Microscope Alpha300 and collected in the range of 3500 to 100 cm^{-1} using a 532 nm green laser under ambient conditions. The specific particles analysed were targeted using a CCD camera connected to a Zeiss EC Epiplan-Neufluar 100x/0.9 objective. The spectra were taken using a laser power of 2.5 mW, an integration time of 1.2 seconds and 20 accumulations. The software package WITecProject (WITec, Germany) was used for the data analysis. Alternatively, a Renishaw inVia Raman Microscope equipped with a green laser (532 nm) was used. The data analysis was then performed using the WiRE 3.4 HF5925 build 2377 software. The measurements were acquired with a laser power ranging between 20 and 60 mW. Table 4.2 represents the Raman bands of the bulk metal oxide support materials.

Table 4.2. Raman bands observed in literature of their respective metal oxide materials.

Phase	Raman bands (cm^{-1})													
oP-MoO ₃	114	127	158	196	218	245	283	292	335	364	379	665	817	995
m-ZrO ₂	117-180 pair	222	330	376	473	633								
Ga ₂ O ₃	201	350	417	527	631	653	767							
r-TiO ₂	134	231	438	604										
CeO ₂	250	464	550	595	830	860	950	1170						

4.2.3. Transmission electron microscopy (TEM)

TEM micrographs of selected samples were taken using a Tecnai F20 transmission electron microscope equipped with a field emission gun and operated at 200kV (Gatan). TEM imaging was done with a US4000 4kX4k CCD camera (Gatan). A small volume of the materials was dispersed in 100 % ethanol. A droplet of the suspension was transferred onto a holey carbon-coated copper grid and air dried.

4.2.4. Scanning electron microscopy (SEM)

SEM-EDS analysis was conducted on selected samples to examine the distribution of Mo over the samples on a high-resolution field emission Nova NanoSEM 230 (FEI) equipped with high resolution in-lens secondary, low voltage backscatter, STEM as well as Oxford X-Max silicon drift EDS detectors. Similar to the TEM grid preparation, a small volume of the materials was suspended in 100 % ethanol (or

water for the samples prepared *via* the HNC method) and subsequently transferred onto a carbon coated copper grid by means of 1 or 2 droplets and dried in air.

4.2.5. X-ray absorption spectroscopy (XAS)

Ex situ XAS transmission experiments were performed on selected samples at the Diamond Light Source facility at the B18 general purpose XAS beamline as part of the Block Allocation Group of the UK Catalysis Hub in December 2018. The samples were analysed at the Mo K-edge including three reference materials prepared in our laboratories, MoO₂, MoO₃ and β-Mo₂C (see Figure 4.1). Each scan was repeated 3 times to increase statistical relevance. The samples were all pressed into pellets with cellulose prior to the analysis. Data processing was performed using Athena from the Demeter software package.¹¹ The linear combination fitting tool was applied for all samples with the three reference materials, for phase quantification.

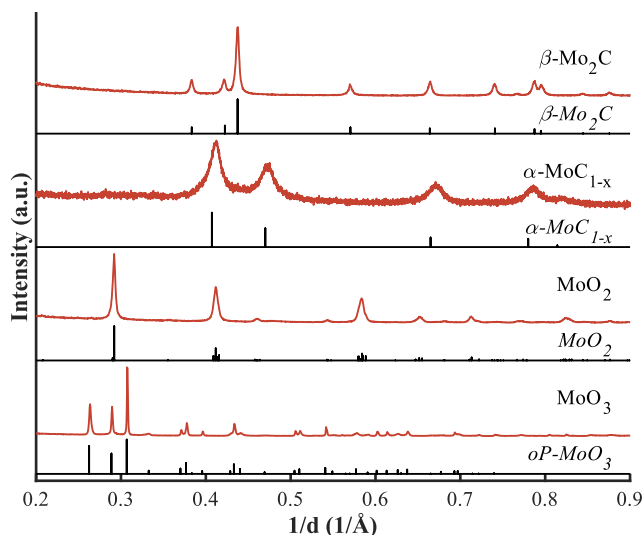


Figure 4.1. XRD patterns of the XAS reference materials.

4.2.6. Inductively Coupled Plasma-Optical Emission Spectroscopy (ICP-OES)

ICP-OES elemental analysis was performed on all samples using a Varian ES 730 ICP-Optical Emission Spectrophotometer. The samples were digested using a Mars 6 Microwave Digester. HNO₃, H₂SO₄, Aqua Regia, HCl and/or HF were used for digestion and H₃BO₃ for neutralization. The digested samples were transferred accurately to a volumetric flask and diluted to 50 mL using 2 wt.-% HNO₃. For the analysis, the sample was filtered using a 0.2 μm filter. 1 mL of the sample was pipetted into a 100 mL volumetric flask and made up with 2 wt.-% HNO₃ (i.e., 100 dilution factor).

4.2.7. Surface area and pore volume measurements

The surface area (S_g) and pore volume of selected materials was analysed by means of N_2 physisorption analysis using a Micromeritics TriStar II 3020. 50 mg of each sample was degassed at 150-200 °C overnight. By way of the Barrett, Joyner and Halenda (BJH) model the pore size distribution, pore volume and average pore diameters were derived from the desorption branch of the isotherm.

4.2.8. CO_2 temperature-programmed desorption (CO_2 -TPD)

The number and strength of the basic sites of selected samples were analysed by means of CO_2 -TPD experiments and were performed in a ¼ inch quartz tube fixed bed reactor (see section 4.3.1). Directly after completion of the carburization process (100 mg of catalyst was loaded prior to carburization), the samples were quenched to 300 °C and de-gassed in Ar for 30 minutes at 45 L h⁻¹ g_{cat}⁻¹. The samples were then cooled to 50 °C and exposed to a mixture of 50 vol.-% CO_2 in Ar. The mixture was fed to the samples at a space velocity of 12 L h⁻¹ g_{cat}⁻¹ for 30 minutes. Then, the samples were flushed in Ar at 45 L h⁻¹ g_{cat}⁻¹ for 1-2 hours at 50 °C. CO_2 -TPD measurements were performed between 50 and 800 °C at a heating rate of 10 °C min⁻¹ in Ar at a space velocity of 12 L h⁻¹ g_{cat}⁻¹. The effluent gas analysis was achieved by means of a mass spectrometer (MS, HPR-20 R&D, Hiden Analytical, see section 4.3.4 for more details on the product analysis).

4.2.9. NH_3 temperature-programmed desorption (NH_3 -TPD)

The number and strength of acid sites of selected samples was analysed by means of NH_3 -TPD experiments performed on a Micromeritics AutoChem II 2920 chemisorption analyser. 100 mg of each sample was carburized *in situ* prior to the NH_3 -TPD experiment. A mixture of 20 vol.-% CH_4 in H_2 (15 L h⁻¹ g_{cat}⁻¹) was fed to the samples while heating to 600 °C at 1 °C min⁻¹, holding for 5 hours. Following the carburization treatment, the samples were quenched to 300 °C in He atmosphere and degassed for 30 minutes at 30 L h⁻¹ g_{cat}⁻¹. It was subsequently cooled to 50 °C and exposed to a 1 vol.-% NH_3 in He mixture for 1 hour at 30 L h⁻¹ g_{cat}⁻¹. The samples were then flushed in He for 1 hour at 30 L h⁻¹ g_{cat}⁻¹. The NH_3 -TPD measurements were performed between 50 and 800 °C at a heating rate of 10 °C min⁻¹ in He at 18 L h⁻¹ g_{cat}⁻¹. The effluent gas analysis was achieved by means of an incorporated thermo-conductivity detector in the AutoChem analyser.

4.2.10. Temperature-programmed reaction of CO_2 (TP- CO_2)

Selected samples were exposed to a TP- CO_2 experiment to study their affinity towards CO_2 activation as a function of temperature. All experiments were performed directly after the carburization of the samples

in the ¼ inch quartz fixed bed reactor. Catalyst loading prior to carburization was 50 or 100 mg. The carburization process was completed by flowing 20 vol.-% CH₄ in H₂ over the samples at a space velocity of 15 or 30 L h⁻¹ g_{cat}⁻¹ while ramping the temperature by 1 °C min⁻¹ to 600 °C, with a holding time of 5 hours. After carburization, the samples were quenched to room temperature while flushing the reactor with Ar. At room temperature 1 vol.-% of CO₂ was added at a total space velocity of 60 L h⁻¹ g_{cat}⁻¹. The reactor temperature was increased to 700 °C at a heating rate of 1 or 5 °C min⁻¹. At 700 °C, the reaction temperature was held stable for 10 minutes before cooling back to RT. The effluent gas analysis was performed by means of mass spectrometry or online gas chromatography (GC, see section 4.3.4).

4.2.11. Thermogravimetric analysis (TGA)

The carburization process was followed by means of TGA analysis on selected samples. The experiments were performed in a Discovery SDT 650 instrument (TA instruments, USA). 5 to 30 mg of solid sample was loaded into an alumina pan in parallel with an empty reference pan. Carburization of the samples was completed by using a diluted mixture of 20 vol.-% CH₄ in H₂ by an inert gas (Ar/N₂) achieving an absolute H₂ content of 4 vol.-%, as per instrument requirements. A total flowrate of 100 mL min⁻¹ was set. The temperature was ramped up from 50 °C to 600 °C at a 1 °C min⁻¹ ramp rate.

4.2.12. *In situ* powder X-ray diffraction

Online XRD analysis was conducted to follow the phase transformation during the (calcination and) carburization of the SiO₂ and SBA-15 supported samples, in the presence and absence of a promoter material. The reaction was realised using a XRK900 Anton Paar reaction cell attached to a laboratory XRD (Bruker D8 Advance) equipped with a Mo source, powered at 50 kV and 35 mA, and a position sensitive detector (Bruker AXS Vantec). Every 5 minutes a scan was collected in the 2θ range of 10° to 28° (1/d = 0.25 to 0.65 1/Å) at a step size of 0.017° and time per step of 0.2 sec. To the specifications of the XRK reaction cell, during carburization, the 20 vol.-% CH₄ in H₂ feed gas was diluted in N₂, to achieve an absolute H₂ content of 10 vol.-%, at a space velocity of 40 L h⁻¹ g_{cat}⁻¹. In general, 150 mg of the powder samples was loaded in the flow through holder and subsequently exposed to calcination or carburizing conditions.

4.2.13. *In situ* Raman spectroscopy

The carburization process of the SiO₂ supported sample, synthesised *via* the slurry impregnation method, was followed by means of *in situ* Raman spectroscopy. 29 mg of powder sample were loaded on a P_{atm} Linkam cell using a 785 nm laser source (ITQ, Valencia). The cell was slightly modified to allow sample

temperatures up to 600 °C. A total flow of 30 mL min⁻¹ of the gas mixture (10 vol.-% CH₄, 40 vol.-% H₂, balance He) was established through the cell. Then the temperature was increased from RT to 600 °C in 50 °C steps. A heating rate of 3 °C min⁻¹ was set between the temperature levels. Raman spectra were recorded *in situ* at each temperature level. The sample was maintained at 600 °C for 5 hours before cooling down to RT while flowing the carburization mixture. At RT, the Raman spectra of the freshly carburized sample was collected. The cell was flushed with He at RT and then passivated in a 1 vol.-% O₂ in N₂ atmosphere (15 mL min⁻¹) for 2 hours. Spectra were recorded after the passivation treatment. Next, the carburization gas mixture was re-established, and the temperature was heated to 600 °C at a ramp rate of 3 °C min⁻¹. The sample was maintained at 600 °C for 1 hour before cooling down to RT. At RT, another spectrum was collected. The sample was flushed with He and another passivation treatment was established for 1 hour, as described above. The cell was opened up and the sample was exposed to air atmosphere overnight. Then the cell was closed and flushed with He before collecting another spectrum at RT. The cell was opened again, and a final spectrum was collected while the sample was exposed to air atmosphere. The heating experiment from RT to 600 °C in 50 °C steps was repeated, but in an air atmosphere.

4.2.14. *In situ* X-ray absorption spectroscopy

The carburization and TP-CO₂ experiments were also followed by means of *in situ* XAS analysis. The experiments were performed at the CAT-ACT beamline¹² of the KIT synchrotron in Karlsruhe, Germany. The XAS data (Mo-K edge) were recorded in transmission mode using ionization chambers. The energy of the Si(311) double crystal monochromator was calibrated by setting the first maximum of the first derivative of the XAS spectrum measured on Mo foil to the tabulated value of 20.000 keV. Data analysis was performed using Athena from the Demeter software package.¹¹ All samples were pressed into pellets, crushed and sieved to 100-200 µm. *In situ* experiments were performed in quartz capillaries of 1.5 mm diameter (20 µm wall thickness) as reactor. The reactor was placed inside a newly build oven made out of copper¹³ and covered with the X-ray transparent Kapton windows. The heating was realised using the resistance wires around ceramic rods, which were in turn placed above and below the capillary; the temperature was monitored by the thermocouple inside the oven calibrated to the temperature inside the capillary prior to the experiment (accuracy better than ±10 °C at 700 °C). The samples were first exposed to a carburization treatment in 20 vol.-% CH₄ in H₂. Temperature was increased to 380 °C with a linear ramp rate of 10 °C min⁻¹, followed by a further ramp to 650 °C with 2 °C min⁻¹. The temperature was held at 650 °C for 2.5 hours before cooling down to room temperature. Subsequently, the gas mixture was changed to 1 % CO₂ in He. The temperature was increased to 330 °C with 10 °C min⁻¹ followed by a

ramp to 740 °C at 5 °C min⁻¹. The temperature was held at 740 °C for 1 hour before the samples were cooled down to room temperature. The total gas flowrate of each experiment was 50 mL min⁻¹ controlled by the mass flow controllers (Bronkhorst, Germany). The EXAFS data up to $k = 16 \text{ \AA}^{-1}$ were recorded at room temperature before the carburization, after the carburization and after the temperature-programmed reaction with CO₂ (TP-CO₂). During the temperature-programmed reactions, rapid XANES spectra were measured (2 minutes per spectrum, from 19 900 to 20 400 eV) to monitor the changes in the chemical state of Mo during the carburization and TPR in CO₂. The reference materials (commercial MoO₂ and in-house prepared MoO₃, β -Mo₂C and α -MoC_{1-x}, see section 4.2.5) were diluted with cellulose to about 20 vol.-% of Mo and pressed in pellets for the transmission measurements.

4.3 Catalytic performance evaluation in CO₂-ODH and RWGS

4.3.1. Test unit and reactor set-up

All catalysts were carburized and tested in the test unit set-up shown in Figure 4.2, unless stated otherwise. All gases were fed into the reactor by means of mass flow controllers (Brooks Instruments) which were calibrated before use for each individual gas. Selected gases then combined prior to reaching 3-way valve 4 (3WV-4). The 3-way valve regulates the feed gas between the reactors and the bypass. When fed to the reactors, the reaction mixture was split by means of two equal length ($\pm 1\text{-}2 \text{ m}$) fused silica columns (Sigma Aldrich, 0.1 mm ID) due to an equal pressure drop over the two columns. The feed gas was then sent separately into two $\frac{1}{4}$ inch quartz tubes (Hilgenberg GmbH, Germany, $L = 150 \pm 0.5 \text{ mm}$, $OD = 6.36 \pm 0.3 \text{ mm}$, $ID = 4 \text{ mm}$, $S = 1.175 \pm 0.2 \text{ mm}$) at atmospheric pressure to allow for parallel analysis of two catalysts under the same reaction conditions. The two quartz tubes were heated by means of an insulated stainless-steel heating block, equipped with 4 heating cartridges (Thermon South Africa Pty Ltd, $L = 100 \text{ mm}$, 40 mm cold end, $D = 8 \text{ mm}$, 200 W, 230 V) and a centrally located thermocouple (see Figure H.1). The catalysts were tightly packed between two plugs of quartz wool in the middle of the quartz tube with silicon carbide (average particle size $\sim 1 \text{ mm}$) loaded on each side of the catalyst bed as a gas pre-heating zone (inlet) and to prevent the catalyst to move out of the isothermal zone (outlet). The silicon carbide was held in place with quartz wool on both the inlet and the outlet side of the reactor tube (see Figure H.2 for a schematic representation of a loaded reactor and the isothermal zone). The two reactor outlet gas streams were led through heated (80 °C) lines to two separate condensation traps, both at room temperature, to remove water from the product mixture. Subsequently, each line was sent through a 3-way solenoid valve (Bürkert), programmed to alternate the two reactor effluent gases between product analysis and venting. This allows for product analysis of one reactor at a time, with a consistent time interval. The product gas was either vented or analysed by online gas chromatography or mass

spectrometry (see section 4.3.4 on more information on the product analysis). The set-up was also equipped with a bypass line to allow the flow to stabilize before the reaction takes place. The bypass stream was sent through four needle valves to mimic the pressure drop observed through the fused silica columns. After the needle valves, the bypass, at atmospheric pressure, was sent to the online GC, MS or vented, as required.

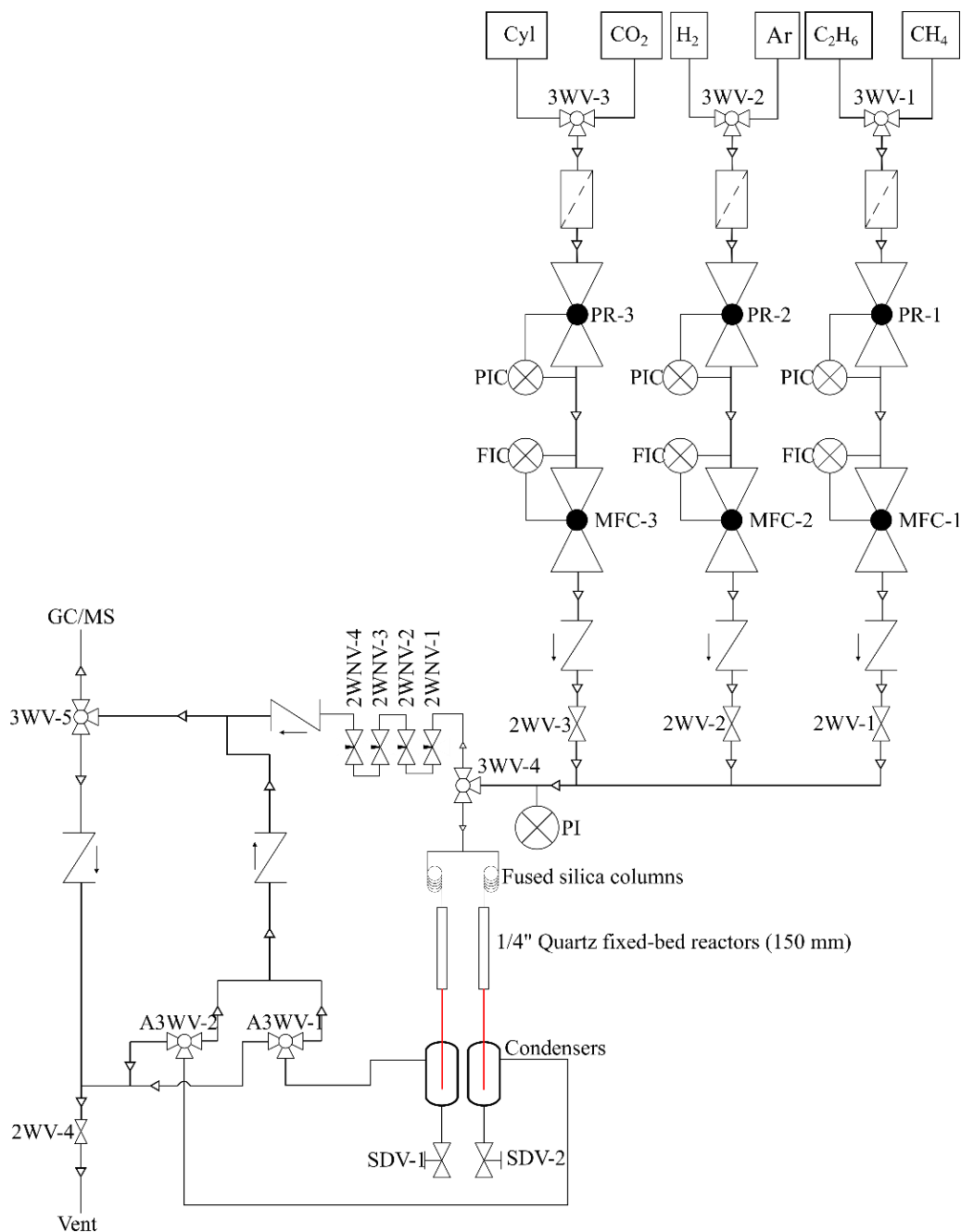


Figure 4.2. Process flow diagram of the rig set-up used for carburization and testing of the catalysts. Red lines are heated lines.

4.3.2. Experimental procedure for CO₂-ODH experiments

The evaluation of the catalysts' performance under CO₂-ODH conditions were conducted in the ¼ inch quartz fixed bed reactors. Upon completion of the carburization process, the reactor was flushed and cooled to 300 °C in an inert atmosphere by flowing Ar at 15 L h⁻¹ g_{cat}⁻¹. Subsequently, the reactor was isolated, and the feed gas was switched (at valve 3WV-4) to bypass the reactor to allow the reaction mixture to stabilize for 3-5 hours. Upon reaching a stable bypass flow, the reactor was heated (still in an inert atmosphere) to reaction temperature. The reaction was then started by switching the reactive gas flow back to the reactor. The product stream was analysed by means of online gas chromatography (see section 4.3.4). Upon termination of the reaction, the temperature of the reactor was cooled down to room temperature while flushing the reactor with an inert gas. At room temperature, the samples were passivated by means of a 1 vol.-% O₂ in N₂ flow, for 1 hour at a space velocity of 15 L h⁻¹ g_{cat}⁻¹. The catalysts were then exposed to spent catalyst characterization, which includes XRD and Raman spectroscopy.

A large variety of experiments were performed within a range of carburization and reaction conditions. All experiments are grouped based on the conditions used and the purpose of the study. A detailed overview of the different sets of experiments is given below.

Chapter 5: Effect of carburization and reaction conditions

In Chapter 5 the samples were prepared by means of the wet impregnation technique with a Mo target loading of 20 wt.-%. The samples were carburized at 700 °C and exposed to the following CO₂-ODH conditions: T = 550, 600, 650, 700 or 750 °C, P = 1 atm, SV = 9.4 L h⁻¹ g_{cat}⁻¹ and a CO₂:C₂H₆:Ar = 1:1:2 feed (see Table 4.3).

Table 4.3. Overview of CO₂-ODH experiments discussed in Chapter 5.

Sample	Carb. T. (°C)	ODH T. (°C)	CO ₂ : C ₂ H ₆ feed ratio	SV (L h ⁻¹ g _{cat} ⁻¹)	Gas supply	Comment
Mo _x C _y /SiO ₂	700	550, 600, 650, 700, 750	1:1	9.4	Mixture	-
Mo _x C _y /SiO ₂ -O ₂	700	550, 600, 650, 700, 750	1:1	9.4	Mixture	Exposure of freshly carburized sample to 1 vol.-% O ₂ for 30 minutes at room temperature
Mo _x C _y /SiO ₂ (ODH-550)	700	550	1:1	9.4	Mixture	-
Mo _x C _y /SiO ₂ (ODH-650)	700	650	1:1	9.4	Mixture	-
Mo _x C _y /SiO ₂ (ODH-750)	700	750	1:1	9.4	Mixture	-

Chapter 6: Effect of synthesis technique

In Chapter 6 the samples were prepared *via* three different synthesis techniques, each with a Mo loading of 20 wt.-%. The three synthesis techniques include the wet impregnation (WI, see section 4.1.1), the sol-gel method (SG, see section 4.1.2) and the hybrid nano-crystal route (HNC, see section 4.1.3). All samples were carburized at 600 °C and exposed to the following CO₂-ODH conditions: T = 600 °C, P = 1 atm, SV = 15 L h⁻¹ g_{cat}⁻¹ and a CO₂:C₂H₆:Ar = 1:1:2 feed (see Table 4.4).

Table 4.4. Overview of CO₂-ODH experiments discussed in Chapter 6.

Sample	Carb. T. (°C)	ODH T. (°C)	CO ₂ : C ₂ H ₆ feed ratio	SV (L h ⁻¹ g _{cat} ⁻¹)	Gas supply	Comment
Mo _x C _y /SiO ₂ -WI	600	600	1:1	15	Mixture	-
Mo _x C _y /SBA-15-HNC	600	600	1:1	15	Mixture	-
Mo _x C _y /SiO ₂ -HNC	600	600	1:1	15	Mixture	-
Mo _x C _y /SiO ₂ -SG	600	600	1:1	15	Mixture	-

Chapter 7: Effect of support material

In Chapter 7 the effect of different support materials on the performance of Mo_xC_y-based catalysts was evaluated. All samples were prepared *via* the wet-impregnation method (see section 4.1.1) with a Mo-loading of 20 wt.-%. All samples were carburized at 600 °C and exposed to a variety of reaction conditions, including the co-feeding of H₂ (see Table 4.5). The following CO₂-ODH conditions were employed: T = 600 °C, P = 1 atm, SV = 15 L h⁻¹ g_{cat}⁻¹ and a CO₂:C₂H₆:Ar = 1:1:2 feed. In the presence of H₂ co-feeding, a mixture of H₂ and N₂ was added to the already existing feed gas, increasing the SV to 18.2 L h⁻¹ g_{cat}⁻¹. The final H₂ concentrations fed to the reactor was set to 0, 5 and 17 vol.-%, in individual experiments.

Table 4.5. Overview of CO₂-ODH experiments discussed in Chapter 7.

Sample	Carb. T. (°C)	ODH T. (°C)	CO ₂ : C ₂ H ₆ feed ratio	SV (L h ⁻¹ g _{cat} ⁻¹)	Gas supply	Comment
SiO ₂	600	600	1:1	15	Mixture	-
ZrO ₂	600	600	1:1	15	Mixture	-
Ga ₂ O ₃	600	600	1:1	15	Mixture	-
TiO ₂	600	600	1:1	15	Mixture	-
Mo _x C _y /SiO ₂	600	600	1:1	15	Mixture	Same as Mo _x C _y /SiO ₂ -WI in Chapter 6

Mo _x C _y /Al ₂ O ₃	600	600	1:1	15	Mixture	-
Mo _x C _y /ZrO ₂	600	600	1:1	15	Mixture	-
Mo _x C _y /Ga ₂ O ₃	600	600	1:1	15	Mixture	-
Mo _x C _y /TiO ₂	600	600	1:1	15	Mixture	-
Mo _x C _y /CeO ₂	600	600	1:1	15	Mixture	-
Mo _x C _y /Al ₂ O ₃ (5:1)	600	600	5:1	15	Mixture	-
Mo _x C _y /ZrO ₂ (5:1)	600	600	5:1	15	Mixture	-
Mo _x C _y /Ga ₂ O ₃ (5:1)	600	600	5:1	15	Mixture	-
Mo _x C _y /SiO ₂ (0 % H ₂)	600	600	1:1	18.2	Mixture	0 vol.-% H ₂ co-feeding
Mo _x C _y /SiO ₂ (5 % H ₂)	600	600	1:1	18.2	Mixture	5 vol.-% H ₂ co-feeding
Mo _x C _y /SiO ₂ (10 % H ₂)	600	600	1:1	18.2	Mixture	10 vol.-% H ₂ co-feeding
Mo _x C _y /SiO ₂ (17 % H ₂)	600	600	1:1	18.2	Mixture	17 vol.-% H ₂ co-feeding
Mo _x C _y /ZrO ₂ (0 % H ₂)	600	600	1:1	18.2	Mixture	0 vol.-% H ₂ co-feeding
Mo _x C _y /ZrO ₂ (5 % H ₂)	600	600	1:1	18.2	Mixture	5 vol.-% H ₂ co-feeding
Mo _x C _y /ZrO ₂ (17 % H ₂)	600	600	1:1	18.2	Mixture	17 vol.-% H ₂ co-feeding
Mo _x C _y /Ga ₂ O ₃ (5 % H ₂)	600	600	1:1	18.2	Mixture	5 vol.-% H ₂ co-feeding
Mo _x C _y /Ga ₂ O ₃ (10 % H ₂)	600	600	1:1	18.2	Mixture	10 vol.-% H ₂ co-feeding

Chapter 8: Effect of promoter

In Chapter 8 the effect of the nature of the promoter and promotion sequence on the CO₂-ODH performance was investigated. Unless otherwise stated, the promoter was added to the sample *via* co-impregnation (Co-Imp), prior to carburization. In addition, an Fe-promoted sample was prepared *via* sequential-impregnation (Seq-Imp) or impregnation after calcination (Calc-Imp) (see section 4.1.1). A Pt-promoted sample was prepared *via* co-impregnation followed by a calcination treatment prior to carburization (Co-Imp-Calc). All samples were exposed to the following CO₂-ODH conditions: T = 600 °C, P = 1 atm, SV = 15 L h⁻¹ g_{cat}⁻¹ and a CO₂:C₂H₆:Ar = 1:1:2 feed. In addition, an Fe-promoted sample was also exposed to H₂ co-feeding (5 vol.-%, same procedure as in Chapter 7), a Pt-promoted and Ni-promoted sample to an increased CO₂ content in the feed (CO₂:C₂H₆:Ar = 5:1:6), and an unpromoted sample to H₂O co-feeding (see Table 4.6).

Table 4.6. Overview of CO₂-ODH experiments discussed in Chapter 8.

Sample	Carb. T. (°C)	ODH T. (°C)	CO ₂ : C ₂ H ₆ feed ratio	SV (L h ⁻¹ g _{cat} ⁻¹)	Gas supply	Comment
Mo _x C _y /SiO ₂ (IND)*	600	600	1:1	15	Individual	-
Mo _x C _y /SiO ₂ (IND)**	600	600	1:1	15	Individual	-
Mo _x C _y /SiO ₂ (MIX)*	600	600	1:1	15	Mixture	-
Mo _x C _y /SiO ₂ (MIX)**	600	600	1:1	15	Mixture	Same as Mo _x C _y /SiO ₂ -WI in Chapter 6
Fe-Mo _x C _y /SiO ₂	600	600	1:1	15	Mixture	Activity data normalized to Mo _x C _y /SiO ₂ (MIX)*
Pt-Mo _x C _y /SiO ₂	600	600	1:1	15	Individual	Activity data normalized to Mo _x C _y /SiO ₂ (IND)*
Ni-Mo _x C _y /SiO ₂	600	600	1:1	15	Mixture	Activity data normalized to Mo _x C _y /SiO ₂ (MIX)*
K-Mo _x C _y /SiO ₂	600	600	1:1	15	Mixture	Activity data normalized to Mo _x C _y /SiO ₂ (MIX)*
Fe-Mo _x C _y /SiO ₂ (Seq-Imp)	600	600	1:1	15	Mixture	Activity data normalized to Mo _x C _y /SiO ₂ (MIX)*
Fe-Mo _x C _y /SiO ₂ (Calc-Imp)	600	600	1:1	15	Individual	Activity data normalized to Mo _x C _y /SiO ₂ (IND)*
Mo _x C _y /SiO ₂ (Calc)	600	600	1:1	15	Individual	-
Pt-Mo _x C _y /SiO ₂ (Co-Imp-Calc)	600	600	1:1	15	Individual	-
Mo _x C _y /SiO ₂ (H ₂ O)	600	600	1:1	15	Individual	4-5 vol.-% H ₂ O co-feeding
Fe-Mo _x C _y /SiO ₂ (5 % H ₂)	600	600	1:1	18.2	Mixture	5 vol.-% H ₂ co-feeding
Pt-Mo _x C _y /SiO ₂ (5:1)	600	600	5:1	15	Mixture	-
Ni-Mo _x C _y /SiO ₂ (5:1)	600	600	5:1	15	Mixture	-

4.3.3. Experimental procedure for RWGS experiments

The initial procedure of the RWGS experimental procedure shows resemblance to the CO₂-ODH experimental procedure. After carburization of the catalysts, the reactor was cooled down to 300 °C while flushing the reactor with an inert gas (Ar/N₂). Stabilizing the reaction mixture was done bypassing the reactor. The reactor was heated to the required reaction temperature and then the gas flow was switched back to the reactor to start the reaction. Upon completion of the reaction, the reactor was cooled down to RT in a flow of inert gas. At RT, the samples were passivated by means of a 1 vol.-% O₂ in N₂ flow, for 1 hour at a space velocity of 15 L h⁻¹ g_{cat}⁻¹. The catalysts were then exposed to spent catalyst characterization, which includes XRD and Raman spectroscopy. The feed gas composition for the RWGS reaction was adjusted per experimental requirements. The H₂ to CO₂ feed gas ratio varied between 1:1 to 1:7 diluted in Ar (50:50 vol.-%). The product stream was analysed by means of online gas chromatography (see 4.3.4).

Chapter 6: Effect of synthesis technique

In Chapter 6, the effect of synthesis technique on the RWGS activity was evaluated. The three synthesis techniques include the wet impregnation (WI, see section 4.1.1), the sol-gel method (SG, see section 4.1.2) and the hybrid nano-crystal route (HNC, see section 4.1.3). All samples were carburized at 600 °C and exposed to the following RWGS conditions: T = 400, 500 or 600 °C, P = 1 atm, SV = 60 or 120 L h⁻¹ g_{cat}⁻¹ and a H₂:CO₂ = 1:1, 3.5:1 or 7:1 feed ratio (see Table 4.7). The space velocity is calculated based on reactive gases only; H₂ and CO₂.

Table 4.7. Overview of RWGS experiments discussed in Chapter 6.

Sample	Carb. T. (°C)	RWGS T. (°C)	H ₂ : CO ₂ feed ratio	SV (L h ⁻¹ g _{cat} ⁻¹)
Mo _x C _y /SiO ₂ -WI	600	400, 500 ,600	1:1	60
Mo _x C _y /SBA-15-WI	600	400, 500 ,600	1:1	60
Mo _x C _y /SBA-15-HNC	600	400	1:1	60
Mo _x C _y /SiO ₂ -WI	600	400	1:1, 3.5:1, 7:1	120
Mo _x C _y /SiO ₂ -SG	600	400	1:1, 3.5:1, 7:1	120

Chapter 8: Effect of promoter material

In Chapter 8, the effect of promoter material on the RWGS activity was evaluated. The samples were prepared *via* co-impregnation (see section 4.1.1). All samples were carburized at 600 °C and exposed to

the following RWGS conditions: $T = 600\text{ }^{\circ}\text{C}$, $P = 1\text{ atm}$, $SV = 60\text{ or }120\text{ L h}^{-1}\text{ g}_{\text{cat}}^{-1}$ and a $\text{H}_2:\text{CO}_2 = 2.5:1$ feed ratio (see Table 4.8). The space velocity is calculated based on reactive gases only; H_2 and CO_2 .

Table 4.8. Overview of RWGS experiments discussed in Chapter 8.

Sample	Carb. T. ($^{\circ}\text{C}$)	RWGS T. ($^{\circ}\text{C}$)	$\text{H}_2 : \text{CO}_2$ feed ratio	SV ($\text{L h}^{-1}\text{ g}_{\text{cat}}^{-1}$)
$\text{Mo}_x\text{C}_y/\text{SiO}_2$	600	600	2.5:1	60
$\text{Fe-Mo}_x\text{C}_y/\text{SiO}_2$	600	600	2.5:1	60
$\text{Pt-Mo}_x\text{C}_y/\text{SiO}_2$	600	600	2.5:1	60
$\text{Ni-Mo}_x\text{C}_y/\text{SiO}_2$	600	600	2.5:1	60
$\text{K-Mo}_x\text{C}_y/\text{SiO}_2$	600	600	2.5:1	60
$\text{Mo}_x\text{C}_y/\text{SiO}_2$	600	600	2.5:1	120
$\text{Fe-Mo}_x\text{C}_y/\text{SiO}_2$	600	600	2.5:1	120
$\text{Pt-Mo}_x\text{C}_y/\text{SiO}_2$	600	600	2.5:1	120
$\text{Ni-Mo}_x\text{C}_y/\text{SiO}_2$	600	600	2.5:1	120

4.3.4. Product analysis

Product analysis was performed either by means of an online GC equipped with three columns and thermal conductivity detectors (GC-TCD) or a bench-top triple filter quadrupole MS. The TP- CO_2 experiments were analysed by GC-TCD or MS. The GC-TCD was used when comparing the different synthesis techniques. For increased sensitivity, the TP- CO_2 experiments performed on the various promoted samples were analysed by MS. The carburization and CO_2 -TPD experiments were analysed by MS. The reaction data for both CO_2 -ODH as well as RWGS experiments were all analysed by means of GC-TCD.

GC-TCD

For the GC analysis, an Agilent 490 micro gas chromatograph equipped with three different dedicated thermal conductivity detectors was used for the analysis of Ar, N_2 , CO, CO_2 , H_2 , CH_4 , C_2H_4 and C_2H_6 (see Table I.1). The GC-TCD separates the various gases by their respective thermal conductivity in relation to the carrier gas (H_2 or Ar). In general, an inert gas was used as internal standard (Ar or N_2) as it does not react with the catalyst or the reaction mixture and can thus be used for quantitative analysis purposes. While it varies between experiments, the concentration of the reference gas is known and remains stable during the entire reaction. The reactants and products can thus be calculated based on their specific response factor (see Appendix A), respective to the inert gas used, and the known concentration of the

reference gas. GC calibration is performed to obtain the response factors of each gas, by analysing gas mixtures with known concentrations of each gas (see Table I.2). The concentration of each compound in the product gas can then be calculated using the known concentration of the inert gas and the response factors obtained. The Varian Galaxie Chromatography Data System 1.9.3.2 software package was used for data analysis purposes.

Mass spectrometry

A Hiden HPR-20 R&D mass spectrometer (Hiden Analytical, United Kingdom) equipped with a Quartz Inert Capillary and two detectors; the Faraday Cup and Secondary Electron Multiplier (SEM), was utilized for the continuous analysis of product gases obtained during the carburization procedure, TP-CO₂ and CO₂-TPD experiments. Massoft Professional control software was used for data analysis purposes. More details of the configuration of the mass spectrometer can be found in Table J.1

In general, the mass spectrometer ionizes the various compounds in the gas mixture to positive ions by electron-impact, creating a fragmentation pattern for each molecule (see Table J.2). In case of overlapping ion fragments (for example mass 28 for CO₂ and CO), the intensity of each fragment should be calibrated per compound to differentiate the contribution of each overlapping compound to the specified mass (see Appendix A for more details). For quantitative purposes, the various compounds are calibrated to an inert gas, in this study Ar, and their respective relative sensitivity factors (RSF) are calculated. The concentration of each compound can then be calculated using the known concentration of the inert gas and their respective RSF values (see Table J.2). The calibrations for the RSF of each compound, needs to be performed at concentrations similar to the expected concentration range of the product spectrum. In case of an unsuccessful calibration due to technical limitations, the theoretical RSF values were used. Each experiment was accompanied by an external source of Ar, with a continuous flow to the sample capillary to minimize the background contribution of air (N₂ and O₂) in between (and for selected samples during) experiments.

The background corrected CO₂ data obtained during CO₂-TPD were deconvoluted by means of several equal full width at half maximum (FWHM) Gaussian curves. It should be noted that during the curve-fitting process, the number of Gaussian curves was minimized while simultaneously attaining a good degree of similarity and consistency between the different samples in terms of peak temperatures and FWHM.

Conversion, selectivity, and yield

The activity of the catalysts for CO₂-ODH is usually expressed as the amount of reactant (C₂H₆ or CO₂) converted in relation to its respective amount fed into the reactor. This can also be described as the C₂H₆ ($X_{C_2H_6}$) or CO₂ (X_{CO_2}) conversion (see Equation 4.1).

$$X_r(\%) = \frac{(\dot{n}_{r,in} - \dot{n}_{r,out})}{\dot{n}_{r,out}} \cdot 100 \% \quad \text{Equation 4.1}$$

Where, X_r is the conversion, $\dot{n}_{r,in}$ the molar flow rate into the reactor and $\dot{n}_{r,out}$ the molar flow rate out of the reactor, of reactant r , i.e., C₂H₆ or CO₂.

The effectivity of the catalysts is usually reported by means of the product selectivity; the amount of product formed in relation to the reactant converted. However, due to the presence of carbon in both reactants and the large number of possible side reactions, the selectivity of the carbonaceous products is represented as C-%, calculated based on the number of carbons in all carbonaceous products (see Equation 4.2). It should be noted that the carbon detected on the surface of the spent catalysts through carbon depositions is of insufficient amount to influence the carbon balance.

$$S_p(C\%) = \frac{\dot{n}_p \cdot nC_p}{\sum_{i=1}^n (\dot{n}_{p,i} \cdot nC_{p,i})} \cdot 100 \% \quad \text{Equation 4.2}$$

Where, S_p is the carbon corrected selectivity, \dot{n}_p the molar flow rate, nC_p the number of carbons of product p and n the number of measured carbonaceous products (i.e., C₂H₄, CO and CH₄). The CO₂-ODH reaction produces one mole C₂H₄ and one mole CO and thus a maximum selectivity towards ethylene ($S_{C_2H_4}$) of 67 C-% can be achieved if the CO₂-ODH reaction would be the only reaction occurring. In the presence of an increased DR activity, the ethylene selectivity would decrease and the CO selectivity (S_{CO}) increase. An increased methanation activity would decrease both CO and C₂H₄ selectivity. If the direct dehydrogenation of C₂H₆ is taking place, the C₂H₄ selectivity increases.

Ethylene yield ($Y_{C_2H_4}$) is another measure of catalyst efficiency and can be described as the amount of ethylene formed ($\dot{n}_{C_2H_4}$) in relation to the amount of ethane fed into the reactor (see Equation 4.3).

$$Y_{C_2H_4}(\%) = \frac{\dot{n}_{C_2H_4}}{\dot{n}_{C_2H_6,in}} \cdot 100 \% \quad \text{Equation 4.3}$$

The multiple possible reactions happening simultaneously or subsequently during CO₂-ODH can be challenging to distinguish based on the conversion, selectivity, and yield data only. The C₂H₆ to CO₂ conversion ratio ($X_{C_2H_6}/X_{CO_2}$), and the H₂ to CO ($\dot{n}_{H_2}/\dot{n}_{CO}$), C₂H₄ to CO ($\dot{n}_{C_2H_4}/\dot{n}_{CO}$) and C₂H₄ to H₂ ($\dot{n}_{C_2H_4}/\dot{n}_{H_2}$) product ratios can assist in identifying possible reaction pathways occurring on the catalyst (see Table 4.9). At an equimolar CO₂ to C₂H₆ feed gas composition (1:1) and a dominant CO₂-ODH reaction pathway, $X_{C_2H_6}/X_{CO_2}$ equals 1. A dominant DR reaction pathway yields an $X_{C_2H_6}/X_{CO_2}$ of 0.5. An increase or a decrease in $X_{C_2H_6}/X_{CO_2}$ occurs when the activity towards DH or RWGS, respectively, increases. It must be noted that the RWGS reaction can only occur as a secondary reaction, with H₂ produced from DR or DH. The $X_{C_2H_6}/X_{CO_2}$ ratio at a CO₂ to C₂H₆ feed of 5:1 increases fivefold for both CO₂-ODH and DR. As the CO₂-ODH reaction does not produce any H₂, $\dot{n}_{H_2}/\dot{n}_{CO}$ decreases with an increase in CO₂-ODH activity. DR produces 4 moles of CO and 3 moles of H₂ which equals to a $\dot{n}_{H_2}/\dot{n}_{CO}$ of 0.75. The RWGS reaction will only decrease $\dot{n}_{H_2}/\dot{n}_{CO}$, when H₂ is sourced from DR. The direct dehydrogenation increases $\dot{n}_{H_2}/\dot{n}_{CO}$. With a dominant CO₂-ODH reaction pathway $\dot{n}_{C_2H_4}/\dot{n}_{CO}$ is 1 but decreases significantly when DR is dominant due to the conversion of C₂H₆ to CO. The DH will again have an increasing effect and the RWGS decreases $\dot{n}_{C_2H_4}/\dot{n}_{CO}$. The last product ratio, $\dot{n}_{C_2H_4}/\dot{n}_{H_2}$, is particularly focused on the DH reaction, at a ratio of 1. A decrease is observed when DR is prominent and a slight increase for both ODH as well as RWGS.

Table 4.9. The effect of reaction pathway on the conversion ratio (at a 1:1 and 5:1 CO₂ to C₂H₆ feed), the product ratios, and the C₂H₄ and CO selectivity.

Reaction	$X_{C_2H_6}/X_{CO_2}$		$\frac{\dot{n}_{H_2}}{\dot{n}_{CO}}$	$\frac{\dot{n}_{C_2H_4}}{\dot{n}_{CO}}$	$\frac{\dot{n}_{C_2H_4}}{\dot{n}_{H_2}}$	$S_{C_2H_4}$	S_{CO}
	1:1	5:1					
$C_2H_6 + CO_2 \leftrightarrow CO + C_2H_4 + H_2O$	1	5	~0	∞	∞	67 %	33 %
$C_2H_6 + 2CO_2 \leftrightarrow 4CO + 3H_2$	0.5	2.5	0.75	~0	~0	0 %	100 %
$C_2H_6 \leftrightarrow C_2H_4 + H_2$	∞	∞	∞	∞	1	100 %	0 %
$CO_2 + H_2 \leftrightarrow CO + H_2O$	~0	~0	~0	~0	∞	0 %	100 % ↑

References

1. S. B. Umbarkar, A. V. Biradar, S. M. Mathew, S. B. Shelke, K. M. Malshe, P. T. Patil, S. P. Dagde, S. P. Niphadkar and M. K. Dongare, Vapor phase nitration of benzene using mesoporous MoO₃/SiO₂ solid acid catalyst, *Green Chemistry*, 2006, **8**, 488.
2. A. P. Amrute, A. Bordoloi, N. Lucas, K. Palraj and S. B. Halligudi, Sol–Gel Synthesis of MoO₃/SiO₂ Composite for Catalytic Application in Condensation of Anisole with Paraformaldehyde, *Catalysis Letters*, 2008, **126**, 286-292.
3. W. Han, P. Yuan, Y. Fan, H. Liu and X. Bao, Synthesis, self-assembly and disassembly of mono-dispersed Mo-based inorganic–organic hybrid nanocrystals, *Journal of Materials Chemistry*, 2012, **22**, 12121-12127.
4. W. Han, P. Yuan, Y. Fan, G. Shi, H. Liu, D. Bai and X. Bao, Preparation of supported hydrodesulfurization catalysts with enhanced performance using Mo-based inorganic–organic hybrid nanocrystals as a superior precursor, *Journal of Materials Chemistry*, 2012, **22**, 25340-25353.
5. P. Yuan, C. Cui, W. Han and X. Bao, The preparation of Mo/γ-Al₂O₃ catalysts with controllable size and morphology via adjusting the metal-support interaction and their hydrodesulfurization performance, *Applied Catalysis A: General*, 2016, **524**, 115-125.
6. P. Yuan, Y. Guo, X. Li, Y. Yue, H. Zhu, T. Wang, Z. Bai and X. Bao, Dependence of Morphology, Dispersion and Hydrodesulfurization Performance of Active Phases in NiMo/SBA-15 on Loading Method, *ChemCatChem*, 2018, **10**, 3717-3725.
7. P. Yuan, J. Liu, Y. Li, Y. Fan, G. Shi, H. Liu and X. Bao, Effect of pore diameter and structure of mesoporous sieve supported catalysts on hydrodesulfurization performance, *Chemical Engineering Science*, 2014, **111**, 381-389.
8. M. M. Nair, PhD, Laval University, 2014.
9. L. Volpe and M. Boudart, Compounds of Molybdenum and Tungsten with High Specific Surface Area, *Journal of Solid State Chemistry*, 1985, **59**, 348-356.
10. H. M. Rietveld, A Profile Refinement Method for Nuclear and Magnetic Structures, *J. Appl. Cryst.*, 1969, **2**, 65-71.
11. B. Ravel and M. Newville, ATHENA, ARTEMIS, HEPHAESTUS: data analysis for X-ray absorption spectroscopy using IFEFFIT, *J Synchrotron Radiat*, 2005, **12**, 537-541.
12. A. Zimina, K. Dardenne, M. A. Denecke, D. E. Doronkin, E. Huttel, H. Lichtenberg, S. Mangold, T. Pruessmann, J. Rothe, T. Spangenberg, R. Steininger, T. Vitova, H. Geckeis and J. D. Grunwaldt, CAT-ACT-A new highly versatile x-ray spectroscopy beamline for catalysis and radionuclide science at the KIT synchrotron light facility ANKA, *Rev Sci Instrum*, 2017, **88**, 113113.
13. D. Eggart, A. Zimina, G. Cavusoglu, M. Casapu, D. E. Doronkin, K. A. Lomachenko and J. D. Grunwaldt, Versatile and high temperature spectroscopic cell for operando fluorescence and transmission x-ray absorption spectroscopic studies of heterogeneous catalysts, *Rev Sci Instrum*, 2021, **92**, 023106.

5 *In situ* carburization and CO₂-ODH performance of SiO₂ supported Mo_xC_y nanoparticles

In this chapter an in-depth analysis of the thermodynamics of the CO₂-ODH reaction as well as possible side reactions is discussed. The equilibrium composition of the entire system as a function of temperature, in the presence and absence of carbon and/or methane formation, and the thermodynamic phase transition between MoO₂ and Mo₂C, under CO₂-ODH reaction conditions is investigated. Experimentally, the (surface sensitive) phase evolution during the carburization process is studied by means of in situ XRD, TGA, XAS and in situ Raman spectroscopy. Furthermore, the effect of various possible reaction conditions on the CO₂-ODH catalytic performance is evaluated.

A section of the results reported in section 5.2 are part of a research article published as: W. Marquart, S. Raseale, G. Prieto, A. Zimina, B. B. Sarma, J.-D. Grunwaldt, M. Claeys, N. Fischer, ACS Catalysis 2021, 11, 1624-1639.

5.1 Thermodynamic analysis of the CO₂-ODH reaction

In section 2.3, the thermodynamic challenge of the CO₂-ODH reaction has been briefly described by means of the Gibbs free energy of the various possible side reactions. It is clear that the dry-reforming of ethane to synthesis gas is thermodynamically favoured and a catalyst system that kinetically activates the C-H bond and prevents C-C bond scission is required for a successful CO₂-ODH process. In this chapter we perform a thermodynamic analysis of the entire system, including all possible side and secondary reactions (see Table 5.1), product species and study the effect of reaction conditions. Previous studies have performed similar thermodynamic analyses, but the focus was either on the dehydrogenation of propane¹⁻⁴, n-butane^{5, 6} or they did not consider the coking effect or CO₂/CO methanation as a side reaction^{7, 8}. From our own laboratories⁹, the effect of coking and of the methanation reaction was incorporated. In this study, we would like to extend this work and consider different Mo phases (MoO₃, MoO₂ and Mo₂C) and observe the thermodynamic stability of these under reaction conditions.

The equilibrium conversion of each possible reaction can be calculated using the following format, considering the reversible reaction, $aA + bB \leftrightarrow cC + dD$, and the conversion of compound A defined by Equation 5.1.

$$X_A = \frac{F_{A,inlet} - F_{A,outlet}}{F_{A,inlet}}$$

Equation 5.1

Where F_x is the molar flow rate of compound x . The molar fraction (y_x) and partial pressure (P_x) of each compound can be calculated with Equation 5.2 and Equation 5.3, respectively.

$$y_x = \frac{F_x}{F_{tot}} \quad \text{Equation 5.2}$$

$$P_x = y_x \cdot P_{tot} \quad \text{Equation 5.3}$$

The ‘modelled’ equilibrium constant (K_p) for each reaction can then be defined by Equation 5.4.

$$K_p = \frac{[C]^c \cdot [D]^d}{[A]^a \cdot [B]^b} = \frac{\left[P_{tot} \cdot \left(\frac{F_C + X_{eq}}{F_A + F_B + F_C + F_D} \right) \right]^c \left[P_{tot} \cdot \left(\frac{F_D + X_{eq}}{F_A + F_B + F_C + F_D} \right) \right]^d}{\left[P_{tot} \cdot \left(\frac{F_A - X_{eq}}{F_A + F_B + F_C + F_D} \right) \right]^a \left[P_{tot} \cdot \left(\frac{F_B - X_{eq}}{F_A + F_B + F_C + F_D} \right) \right]^b} \quad \text{Equation 5.4}$$

$$= \frac{\left[P_{tot} \cdot (F_C + X_{eq}) \right]^c \left[P_{tot} \cdot (F_D + X_{eq}) \right]^d}{\left[P_{tot} \cdot (F_A - X_{eq}) \right]^a \left[P_{tot} \cdot (F_B - X_{eq}) \right]^b}$$

Simultaneously, the ‘calculated’ equilibrium constant can also be determined by Equation 5.5.

$$K_p = e^{\frac{-\Delta G_T^{rxn}}{RT}} \quad \text{Equation 5.5}$$

Where R is the ideal gas constant, T the reaction temperature and ΔG_T^{rxn} the Gibbs free energy of reaction at reaction temperature, which is calculated using Equation 5.6.

$$\Delta G_T^{rxn} = T \left(\frac{\Delta G_{298K}^{rxn}}{T_0} - \left[\left(-\nabla a^{rxn} T_0 - \frac{1}{2} \nabla b^{rxn} T_0^2 + \frac{\nabla c^{rxn}}{T_0} - \frac{1}{3} \nabla d^{rxn} T_0^3 + \Delta H_{298K}^{rxn} \right) \cdot \left(\frac{1}{T_0} - \frac{1}{T} \right) + \nabla a^{rxn} (\ln T - \ln T_0) + \frac{1}{2} \nabla b^{rxn} (T - T_0) + \frac{1}{2} \nabla c^{rxn} \left(\frac{1}{T^2} - \frac{1}{T_0^2} \right) + \frac{1}{6} \nabla d^{rxn} (T^2 - T_0^2) \right] \right) \quad \text{Equation 5.6}$$

Where ∇a^{rxn} , ∇b^{rxn} , ∇c^{rxn} and ∇d^{rxn} are the specific heat capacity coefficients of the reaction, calculated using the data obtained from Knacke *et al.*¹⁰ and Barin¹¹, for each reactant or product species. Finally, the equilibrium conversion can be ‘modelled’ by solving the ‘modelled’ K_p to the ‘calculated’ K_p .

Table 5.1. Overview of possible side reactions considered in the CO₂-ODH. Sorted in order from endothermic to exothermic at 25 °C and 1 bar pressure: Non-selective reaction (NSR), carbon formation (CF), dry-reforming of ethane (DR), CO₂-oxidative dehydrogenation of ethane (ODH), direct dehydrogenation of ethane (DH), ethane decomposition (EAD), methane decomposition (MD), reverse water-gas-shift (RWGS), ethylene decomposition (EED), ethane hydrogenolysis (EH), CO reduction (COR), methanation of CO₂ (MCO₂), Boudouard reaction (BR) and methanation of CO (MCO).

Reaction		$\Delta H_{25^\circ\text{C}}^f$ (kJ mol ⁻¹)	$\Delta G_{25^\circ\text{C}}^f$ (kJ mol ⁻¹)
NSR	$C_2H_6 + 5CO_2 \leftrightarrow 7CO + 3H_2O$	552.4	358.0
CF	$2C_2H_6 + 4CO_2 \leftrightarrow 5CO + 3C + 3H_2O + 3H_2$	463.9	269.9
DR	$C_2H_6 + 2CO_2 \leftrightarrow 4CO + 3H_2$	428.9	272.1
ODH	$CO_2 + C_2H_6 \leftrightarrow CO + C_2H_4 + H_2O$	177.6	129.0
DH	$C_2H_6 \leftrightarrow C_2H_4 + H_2$	136.4	100.4
EAD	$C_2H_6 \leftrightarrow 2C + 3H_2$	84.0	32.0
MD	$CH_4 \leftrightarrow C + 2H_2$	74.6	50.5
RWGS	$H_2 + CO_2 \leftrightarrow CO + H_2O$	41.2	28.6
EED	$C_2H_4 \leftrightarrow 2C + 2H_2$	-52.4	-68.4
EH	$C_2H_6 + H_2 \leftrightarrow 2CH_4$	-65.2	-69.0
COR	$CO + H_2 \leftrightarrow C + H_2O$	-131.3	-91.4
MCO ₂	$CO_2 + 4H_2 \leftrightarrow CH_4 + 2H_2O$	-164.7	-113.3
BR	$2CO \leftrightarrow CO_2 + C$	-172.5	-120.0
MCO	$CO + 3H_2 \leftrightarrow CH_4 + H_2O$	-205.9	-141.9

From the study of the thermodynamic equilibrium conversions as function of temperature of each of the discussed reactions within the temperature range of interest for the CO₂-ODH (500-700 °C), it is clear that the primary ethylene formation routes (ODH or DH) are thermodynamically the least favoured reactions (see Figure 5.1). All primary reactions that include the cleavage of ethane's C-C bond (NSR, CF, DR and EAD) are far more favourable assuming stoichiometric feed conditions. Secondary reactions can include RWGS, BR, EED, MCO₂, MCO, COR and EH.

Methane decomposition is a possible tertiary reaction. Carbon deposits can be produced *via* BR, CF, EAD, EED, MD or COR. However, with CO₂ in the feed, the Boudouard reaction can potentially be reversed, removing previously deposited carbon species.

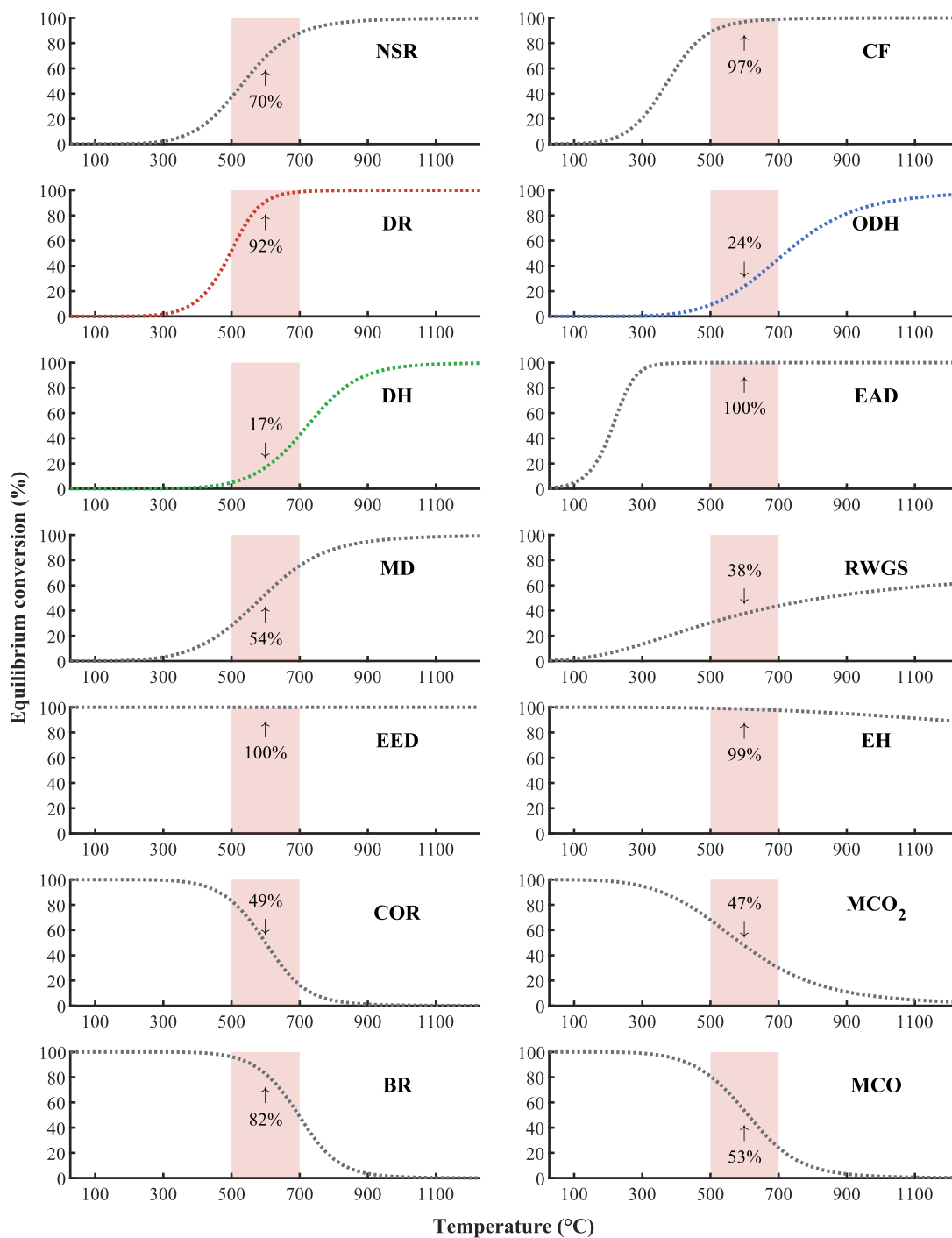


Figure 5.1. Thermodynamic equilibrium conversions as a function of temperature at 1 bar pressure of the non-selective reaction (NSR), carbon formation (CF), dry-reforming of ethane (DR), CO₂-oxidative dehydrogenation of ethane (ODH), direct dehydrogenation of ethane (DH), ethane decomposition (EAD), methane decomposition (MD), reverse water-gas-shift (RWGS), ethylene decomposition (EED), ethane hydrogenolysis (EH), CO reduction (COR), methanation of CO₂ (MCO₂), Boudouard reaction (BR) and methanation of CO (MCO). Red shaded area indicates temperature range of interest for CO₂-ODH. Compound specific thermodynamic data from Knacke *et al.*¹⁰.

Increasing the reaction pressure of the CO₂-ODH does not support the forward reaction. However, through increasing the CO₂ content in the feed gas or co-feeding an inert gas (dilution), the conversion level can be increased (see Figure 5.2). For the ODH reaction, at 600 °C and 1 bar pressure, the equilibrium conversion increases from 24 % at a CO₂ to C₂H₆ feed ratio of 1 and 0 % dilution, to 29 % by simply increasing the dilution to 50 %. Opposing the effect of pressure, dilution of the reaction feed increases the volume of the system, changing the partial pressures of both the reactants and products. The decrease in the relative volume ratio between reactants and products will shift the reaction towards the side with more gaseous compounds. Increasing the CO₂ content in the feed will increase the equilibrium conversion of ODH from 29 %, at feed ratio of 1 and dilution of 50 %, to 56 % at feed ratio of 4 and dilution of 50 %. It should be noted that an increase in CO₂ content or dilution also increases the equilibrium conversion for dry-reforming.

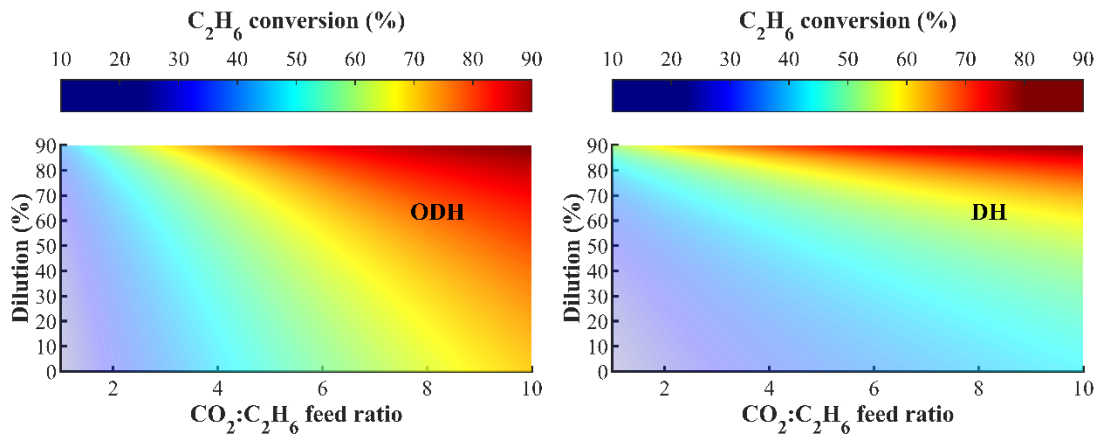


Figure 5.2. Thermodynamic equilibrium conversion for ODH and DH as a function of CO₂ to C₂H₆ feed ratio and dilution at 600 °C and 1 bar pressure. Compound specific thermodynamic data from Knacke *et al.*¹⁰.

Thermodynamic equilibrium product compositions can be calculated by minimizing the Gibbs free energy of the entire system (see Equation 5.7), which can be accomplished by varying the molar concentration of the various compounds and their corresponding chemical potentials (see Equation 5.8).

$$\Delta G_{T,P}^{system} = \sum n_i \mu_i \quad \text{Equation 5.7}$$

$$\mu_i^{T,P} = \Delta G_{25^\circ C}^f + RT \ln \frac{\frac{n_i}{\sum n} P}{100 kPa} \quad \text{Equation 5.8}$$

Where n_i is the molar concentration and μ_i the chemical potential of compound i . The Gibbs free energy of the entire system can be calculated using Equation 5.9, where a , b , c and d are the specific heat capacity coefficients of each individual compound.

$$\Delta G_T^f = T \left(\frac{\Delta G_{298K}^f}{T_0} - \left[\left(-aT_0 - \frac{1}{2}bT_0^2 + \frac{c}{T_0} - \frac{1}{3}dT_0^3 + H_{298K}^f \right) \left(\frac{1}{T_0} - \frac{1}{T} \right) + a(\ln T - \ln T_0) + \frac{1}{2}b(T - T_0) + \frac{1}{2}c \left(\frac{1}{T^2} - \frac{1}{T_0^2} \right) + \frac{1}{6}d(T^2 - T_0^2) \right] \right) \quad \text{Equation 5.9}$$

Based on the various possible reactions discussed and demonstrated in Figure 5.1, the individual compounds considered for the product equilibrium are $C_2H_{6(g)}$, $C_2H_{4(g)}$, $CO_{2(g)}$, $CO_{(g)}$, $H_2O_{(g)}$, $H_{2(g)}$, $CH_{4(g)}$ and $C_{(s)}$ (see Figure 5.3-A). This allows for all possible reactions to proceed to equilibrium, as a function of temperature, at 1 bar pressure with an equimolar CO_2 to C_2H_6 feed ratio. Within the temperature range of interest (500 °C – 700 °C), solid carbon (C) is the main carbon-containing product. C_2H_6 is fully converted and no C_2H_4 formation is observed. This reiterates the thermodynamic challenge faced by CO_2 -ODH or DH compared to DR, decomposition or methanation reactions. It must be noted that even though a thermodynamic equilibrium is calculated, it does not predict a reaction mechanism or provides a pathway analysis.

When all coke forming pathways are neglected (see Figure 5.3-B), a remarkable disappearance of H_2O over the full temperature range is observed. This suggests that the majority of the H_2O produced in Figure 5.3-A, is *via* CO reduction, as no secondary reaction with H_2O as the reactant can explain its disappearance. This could also suggest that the CH_4 formed is not *via* any methanation reaction, but rather *via* (exothermic) ethane hydrogenolysis (EH). With the H_2 (and CO) being sourced (formed) *via* the dry-reforming reaction, becoming more dominant from 500 °C. At 900 °C, DH partially replaces EH, shown by an increase in C_2H_4 and H_2 content.

When all CH_4 formation pathways are neglected, but the coke forming reactions included (see Figure 5.3-C), H_2O is formed in parallel with carbon and H_2 in a ratio of $C:H_2O:H_2 = 1.5:1:0.5$ at low temperatures. This supports the earlier suggestion that H_2O is mainly produced *via* COR. Between 500 °C and 700 °C, the CO_2 concentration shows a slight increase, with a simultaneous decrease in carbon and H_2O , suggesting a lower COR activity. The decrease in C and H_2O paralleled with an increase in H_2 , and eventually CO, concentration, showing the more dominant contribution of dry-reforming. H_2 is also produced *via* C_2H_6 decomposition, similar to the scenario described in Figure 5.3-A.

Lastly, in Figure 5.3-D, the thermodynamic equilibrium in the absence of CH_4 and C is calculated, which is a common approach in literature for this reaction system.^{2-5, 7} In essence, by neglecting any

carbon and CH₄ forming reactions, the equilibrium is calculated for the ODH, DH and dry-reforming reactions only. In that case, C₂H₆ and CO₂ only start to react from 300 °C, which is dominated by dry-reforming and at about 600 °C the dehydrogenation proceeds simultaneously.

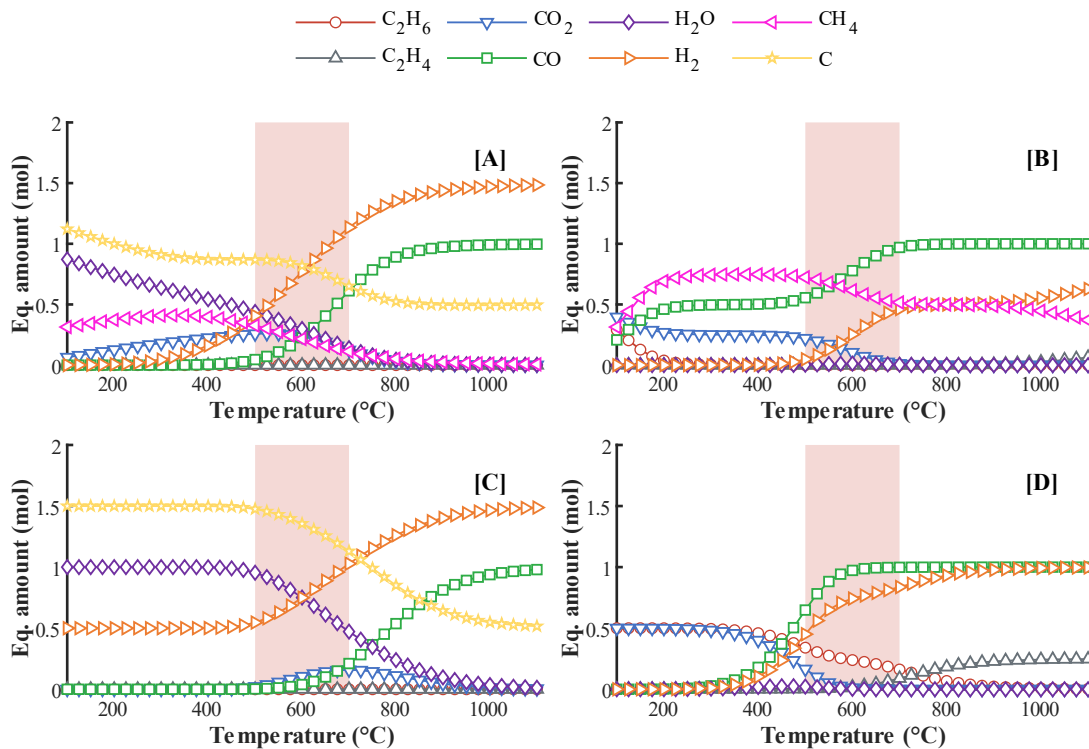


Figure 5.3. Product equilibrium of the CO₂-ODH system as a function of temperature. [A] All compounds considered, [B] carbon formation neglected, [C] methane formation neglected and [D] carbon and methane formation neglected. Red shaded area indicates temperature range of interest for CO₂-ODH. Compound specific thermodynamic data from Knacke *et al.*¹⁰.

Mo⁰, MoO₂, MoO₃ and Mo₂C are included into the calculation at a starting composition containing a CO₂:C₂H₆:Mo₂C molar ratio of 1:1:0.35. This ratio is in line with the reaction conditions discussed in section 4.3.2 and is equal to 20 mg Mo₂C in 12.5 mL of 1:1 CO₂ and C₂H₆. The addition of the various Mo phases results in a significant change in the product composition observed, specifically at lower temperatures (see Figure 5.4). A transition between MoO₂ and Mo₂C occurs around 500 °C in the presence of CH₄ which is slightly decreased when CH₄ formation pathways are neglected. Under the proposed reaction conditions (600 °C) the thermodynamically favoured Mo-phase is Mo₂C. No indication of MoO₃ or metallic Mo formation over the entire temperature range is observed. In the absence of C₂H₆ in the feed (see Figure A.1), the MoO₂-Mo₂C transition occurs at 600 °C. In contrast to a CO₂-ODH feed, MoO₂ does not disappear completely and increases again with an increased reaction temperature. Previously observed formation of MoO₂ under CO₂-ODH conditions is thus predominantly driven by kinetics rather than thermodynamic limitations.

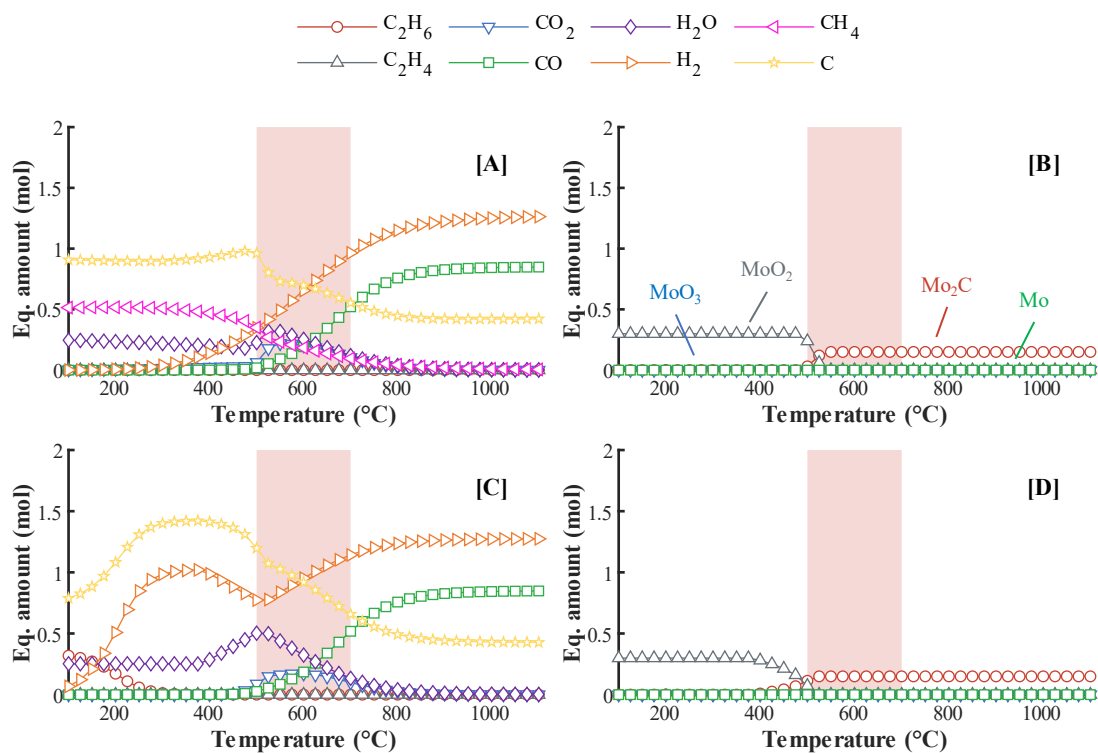


Figure 5.4. Product equilibrium of the system as a function of temperature including Mo-phases. [A] and [B] all compounds considered, [C] and [D] methane formation neglected. Red shaded area indicates temperature range of interest for CO₂-ODH. Compound specific thermodynamic data from Knacke *et al.*¹⁰.

5.2 *In situ* characterization of the carburization process

The carburization technique has shown to be highly sensitive to carbon deposition¹², which affects the active surface area by blocking catalytic sites and in consequence decrease performance. It is thus important to find the optimum carburization temperature; a balance between a high purity Mo_xC_y and excessive carbon deposition. In addition to surface carbon, surface oxygen species can be detrimental to the catalytic activity when they react with the carbon resulting in the formation of MoO_x.

A sample was prepared targeting a 20 wt.-% Mo loading on a nonporous SiO₂ support *via* a slurry impregnation (see section 4.1.1) of ammonium heptamolybdate (AHM/SiO₂). The SiO₂ support material was selected to confidently confirm the presence of the carbide phase, by way of XRD analysis. Because of the amorphous nature of SiO₂, overlap of diffraction reflexes is prevented, as would be the case on a crystalline metal oxide supports such as Al₂O₃.

During the carburization process of AHM/SiO₂, *in situ* XRD (see Figure 5.5-A, B, D) evidences the decomposition of ammonium decamolybdate ((NH₄)₈Mo₁₀O₃₄) to ammonium tetramolybdate

$(\text{NH}_4)_2\text{Mo}_4\text{O}_{13}$, which is first detected at 181 °C. The average crystallite size increases slightly during the transition from around 5 nm to 10 nm. The molybdate precursor is fully decomposed by 227 °C, where a molybdenum trioxide mixture of hexagonal (*hP*- MoO_3) and orthorhombic (*oP*- MoO_3) is formed with a crystallite size of around 9 and 6 nm, respectively. The orthorhombic phase becomes the dominant phase at 347 °C with a slight increase in crystallite size to around 9 nm. The reduction of MoO_3 to MoO_2 proceeds slowly, reflected by a long phase overlap, with the first MoO_2 diffractions appearing at 363 °C to eventually become a pure MoO_2 phase at 466 °C with a crystallite size of around 12 nm. The molybdenum carbide, in form of β - Mo_2C and η - Mo_2C , is initially observed after holding at 600 °C for 25 minutes and is the dominant phase after 95 minutes at 600 °C. The final carbide phase consists of a mixture of β - Mo_2C (44 wt.-%) and η - Mo_2C (56 wt.-%) with crystallite sizes of around 4 and 3.8 nm, respectively.

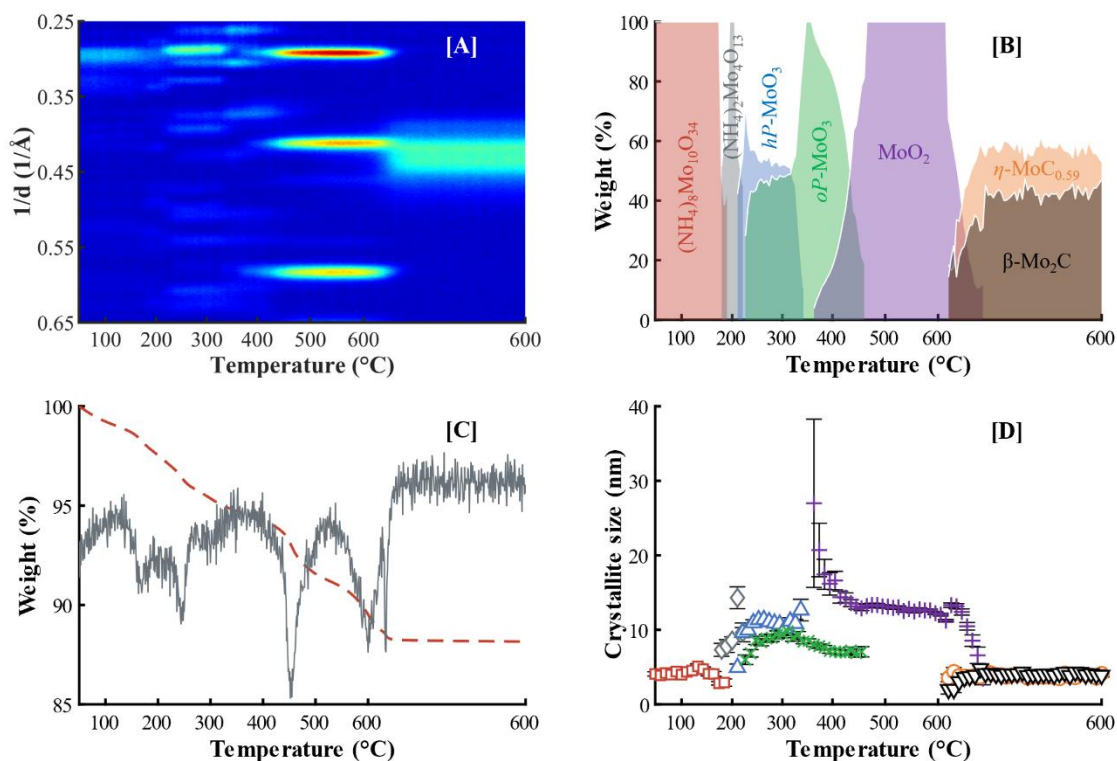


Figure 5.5. Carburization process of $\text{Mo}_x\text{C}_y/\text{SiO}_2$ as function of temperature, with [A] top view of *in situ* XRD patterns, [B] corresponding Rietveld refinement analysis with phase composition and [D] particle size and [C] TGA analysis with TG curve (red dashed line) and differential thermal analysis (DTA) signal (grey solid line). Conditions: $T_{\text{final}} = 600$ °C, $P = 1$ atm, heating rate = 1 °C min^{-1} , holding time = 5 hours.

The TG and DTA curves (see Figure 5.5-C) are in line with the XRD results, showing four significant weight changes and one small and broader signal, while increasing temperature. Together with the XRD analysis it can be confirmed that the two losses at approximately 169 °C and 247 °C represent the

decomposition of the molybdate to MoO_3 . The small broad signal indicates the transition from hexagonal to orthorhombic MoO_3 . At 450 °C, a major weight loss is associated to the reduction towards MoO_2 . Finally, at 600 °C the carburization of MoO_2 to Mo_2C takes place, which is completed after an hour time on stream. Similar observations are made during the carburization of bulk AHM (see Figure C.1) and in the study by Wienold *et al.*¹³ reporting on the decomposition of AHM in a diluted H_2 atmosphere at elevated temperatures.

The carburization of $\text{Mo}_x\text{C}_y/\text{SiO}_2$ was also studied by *in situ* Raman spectroscopy (see Figure 5.6-A). The molybdate precursor is fully decomposed below 200 °C in both air and carburization atmosphere. However, the decomposition pathway seems to be influenced from the early stages by the different atmospheres, as is indicated by the Raman band at 963 cm^{-1} . Interestingly, at temperatures above 200 °C, under carburization conditions, no clear Raman spectra for MoO_3 or MoO_2 are observed. A small broad band is observed at 250 and 300 °C around 721 cm^{-1} which can be linked to MoO_2 species, but it disappears at 350 °C.¹² Since Raman is not a bulk technique relying on long range order, these observations may suggest that the surface of the Mo particles carburize at much lower temperatures than for the bulk of the crystallites, as is observed by XRD. On the contrary, calcination of the precursor in air (see Figure 5.6-B) under otherwise identical experimental settings led to the detection of prominent MoO_3 Raman bands at 665 cm^{-1} ($\nu(\text{OMo}_3)$), 817 cm^{-1} ($\nu(\text{OMo}_2)$) and 994 cm^{-1} ($\nu(\text{Mo}=\text{O})$) in the entire temperature range of 150-600 °C. In a previous study from our laboratory, bulk carburized samples show MoO_3 Raman spectra after passivation, even though invisible to laboratory XRD analysis.¹⁴ The observed MoO_3 was proposed to be in form of an amorphous passivation layer formed before removal from the reactor. However, our latest *in situ* Raman spectroscopy results (see Figure 5.7) show that after the carburization of the catalyst, followed by passivation at room temperature, no MoO_3 is formed. This can be explained by a report of Ovari *et al.*¹⁵, who observed that at room temperature O_2 dissociates on the carbide surface but it does not oxidize. The passivated sample was then exposed to a reactivation treatment in an attempt to remove/re-carburize the oxygen/oxide surface layer (heated up to 600 °C at 3 °C min^{-1} in 10 vol.-% CH_4 , 40 vol.-% H_2 , balance He, and held at 600 °C for 1 hour) and again spectra were collected at RT and no Raman bands were observed. No signal associated to carbon deposits was detected either. Subsequently, the reactivated sample was passivated as described above, exposed to an air atmosphere overnight at RT and again spectra were collected, first in an inert atmosphere followed by an air atmosphere. In the inert atmosphere, neither MoO_3 nor MoO_2 were observed. The measurement in air atmosphere clearly showed oxidation, confirming that a local energy input due to laser irradiation in the presence of oxygen is necessary for the oxygen to react with the surface carbon resulting in the oxidation of the carbide to MoO_3 (bands at 817 and 991 cm^{-1}).

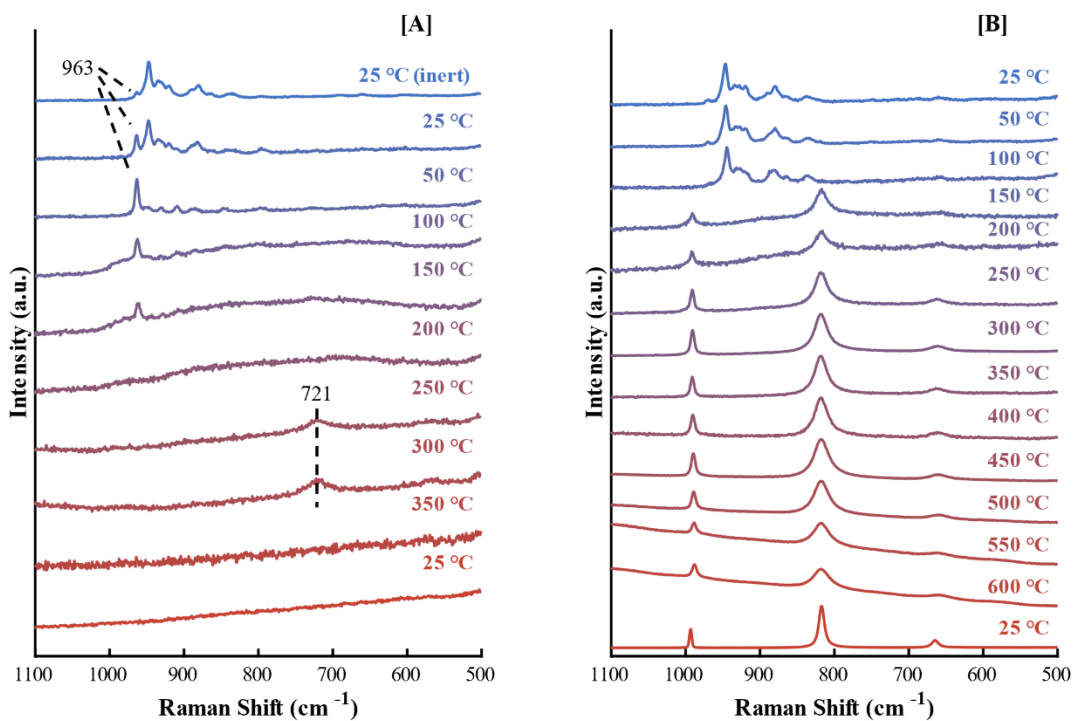


Figure 5.6. *In situ* Raman spectra collected for [A] the carburization and [B] the calcination of $\text{Mo}_x\text{C}_y/\text{SiO}_2$. Conditions: $T = 600\text{ }^\circ\text{C}$, $P = 1\text{ atm}$, heating rate = $3\text{ }^\circ\text{C min}^{-1}$. For the carburization a 10 vol.-% CH_4 , 40 vol.-% H_2 , balance He mixture was used at $60\text{ L h}^{-1}\text{ g}_{\text{cat}}^{-1}$.

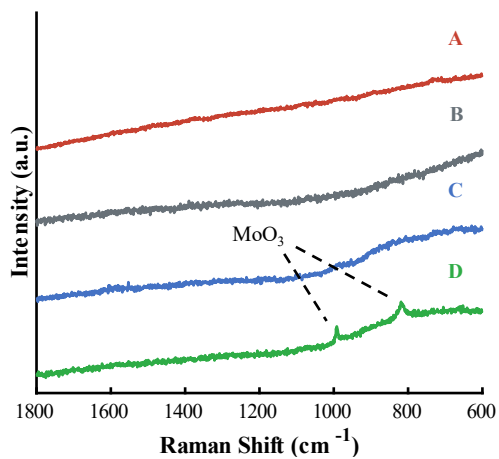


Figure 5.7. *In situ* Raman spectra collected at room temperature for $\text{Mo}_x\text{C}_y/\text{SiO}_2$ with [A] after passivation treatment, [B] after reactivation treatment of passivated sample, and [C, D] after exposure of the passivated-reactivated-passivated sample to air at room temperature overnight, recorded in [C] helium and [D] air atmosphere.

Ex situ XAS analysis was performed on bulk β -Mo₂C samples, carburized at different temperatures. In addition, the samples were exposed to air with and without a prior passivation treatment to study phase stability under atmospheric conditions. To quantify the changes in the XANES region indicated by the red arrows (see Figure 5.8-A), the derivative of each spectrum was fitted by means of a linear combination of MoO₃, MoO₂ and β -Mo₂C (see Table 5.2 and Figure G.1). Note that by means of XRD analysis (see Figure 5.8-B), the bulk carbides did not show any traces of η -MoC_{0.59} or MoO_xC_y (see Table 5.2), although this does not necessarily exclude them to be present on the surface. At a carburization temperature of 600 °C, the efficiency of a passivation treatment is evidenced by the significant difference in MoO₂ content (26.7 ± 0.7 wt.-% with passivation and 32.1 ± 0.8 wt.-% without passivation) suggesting a re-oxidation. XRD analysis of the non-passivated sample carburized at 600 °C indicates the presence of 5 wt.-% MoO₂ in the form of large crystallites (105.3 ± 9.8 nm).

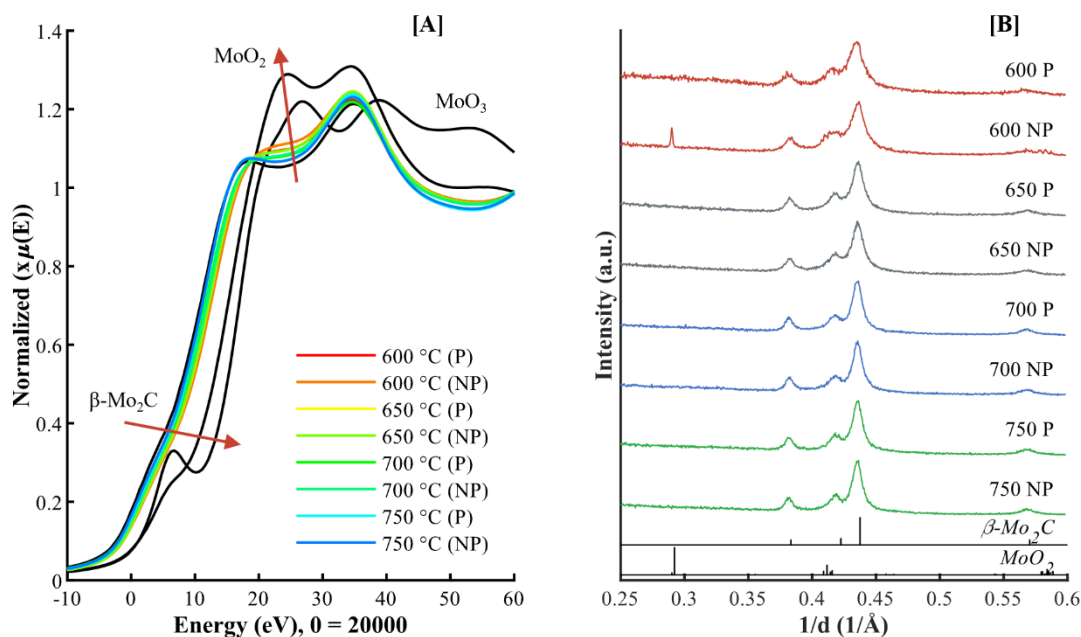


Figure 5.8. [A] Mo K-edge XANES region, shifted to 20,000 eV and [B] XRD patterns of bulk β -Mo₂C samples carburized at different temperatures, exposed to air with (P) and without (NP) passivation treatment. The XAS references, MoO₃, MoO₂ and β -Mo₂C, used for linear combination fitting are indicated in black.

The large crystallites are potentially originating from sintering due to the strong exothermic re-oxidation reaction, leading to localized temperature spikes, when suddenly exposed to a high concentration of oxygen (see Figure 5.9-A), such as in air. It appears that O₂ dissociation on the carbide surface without causing an oxidation of the Mo phase only proceeds when the oxidant is introduced at low concentrations at room temperature¹⁵ or lower, hence the passivation treatment of 1 vol.-% O₂,

preventing bulk oxidation (see Figure 5.9-B). With increasing temperature of carburization, the content of MoO₂ in the samples decreases, independent of a previous treatment, and the crystallite size of the carbide phase increases. While the latter is probably the effect of enhanced sintering during carburization, the former can be associated to the previously reported increase in carbon deposits creating a protective layer around a carbide core (see Figure 5.9-C). The MoO₂ content is believed to be a residue from the synthesis rather than stem from the re-oxidation by air, possibly in form of a core, too small/thin for XRD to detect, surrounded by a thick carbide shell.

Table 5.2. Phase composition *via* XANES linear combination fitting and XRD Rietveld analysis, including crystallite sizes, on bulk β -Mo₂C carburized at different temperatures and exposed to air with (P) and without (NP) passivation treatment.

Sample	XANES		XRD			
	MoO ₂	β -Mo ₂ C	MoO ₂		β -Mo ₂ C	
	wt.-% (error)	wt.-% (error)	wt.-% (error)	nm (error)	wt.-% (error)	nm (error)
600 °C (P)	26.7 (0.7)	73.3 (1.0)	-	-	100.0	7.5 (0.1)
600 °C (NP)	32.1 (0.8)	67.9 (1.0)	5.7 (0.2)	105.3 (9.8)	94.3 (0.2)	7.3 (0.1)
650 °C (P)	24.7 (0.8)	75.3 (1.1)	-	-	100.0	9.0 (0.1)
650 °C (NP)	24.3 (0.8)	75.7 (1.1)	-	-	100.0	8.7 (0.1)
700 °C (P)	16.9 (0.5)	83.1 (0.8)	-	-	100.0	13.8 (0.6)
700 °C (NP)	18.7 (0.6)	81.3 (0.9)	-	-	100.0	14.3 (0.7)
750 °C (P)	5.8 (0.7)	94.2 (1.0)	-	-	100.0	13.1 (0.6)
750 °C (NP)	5.9 (0.6)	94.1 (0.9)	-	-	100.0	14.9 (0.8)

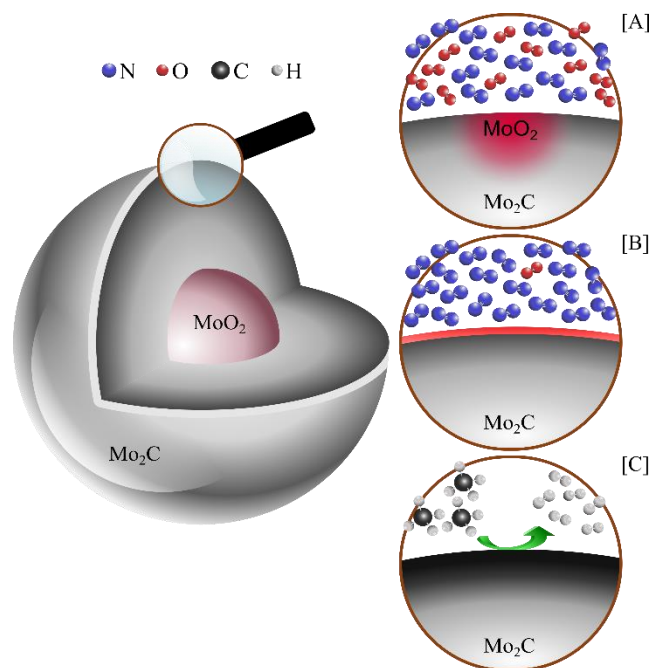


Figure 5.9. Schematic representation of bulk Mo_2C particles with a residual oxide core and different possible surface states and their effect on reactivity: **[A]** Bare carbide surface is partially re-oxidized, causing (and subsequently accelerated by) localized temperature spikes when exposed to high concentrations of oxygen such as in air. **[B]** O_2 is dissociated on a bare carbide surface at low partial pressures of the oxidant, forming a passivating layer around the carbide particle. **[C]** Thick layer of carbon deposits around the carbide particle at higher carburization temperatures, protecting the carbide surface from reoxidation in air (compare case **[A]**).

5.3 CO_2 -ODH catalytic performance

The CO_2 -ODH catalytic performance of $\text{Mo}_x\text{C}_y/\text{SiO}_2$ is evaluated within a range of reaction temperatures. In addition, the effect of an O_2 surface treatment on the catalytic performance is investigated. All experiments discussed in this section are conducted using an equimolar feed gas composition of CO_2 and C_2H_6 , diluted by 50 vol.-% Ar at a SV of $9.4 \text{ L h}^{-1} \text{ g}_{\text{cat}}^{-1}$. The samples were carburized at $700 \text{ }^\circ\text{C}$. XRD analysis of the freshly prepared samples suggest that after carburizing at $600 \text{ }^\circ\text{C}$, the sample contains 21.4 wt.-% $\beta\text{-Mo}_2\text{C}$ and 78.6 wt.-% $\eta\text{-MoC}_{0.59}$. The sample carburized at $700 \text{ }^\circ\text{C}$ shows a slight decrease in $\beta\text{-Mo}_2\text{C}$ content (14.4 wt.-%) however this is a negligible difference considering the Mo loading, the error of analysis and the similarity in the obtained patterns (see Figure 5.10).

To determine the optimum reaction temperature for CO_2 -ODH over Mo-based catalysts, a sample containing 20 wt.-% loading of Mo on SiO_2 support, carburized at $700 \text{ }^\circ\text{C}$, was evaluated for its performance within a range of reaction temperatures (see Figure 5.11). Each temperature was kept under isothermal conditions for 12 hours, starting from $550 \text{ }^\circ\text{C}$ increasing to $750 \text{ }^\circ\text{C}$, with a $50 \text{ }^\circ\text{C}$ step interval. After 12 hours at $750 \text{ }^\circ\text{C}$, the temperature was returned to $650 \text{ }^\circ\text{C}$ for 6 hours before termination of the

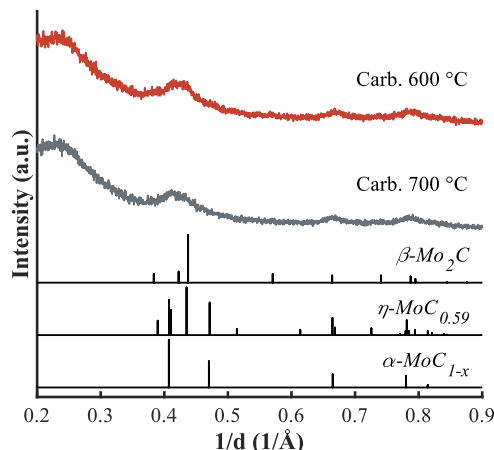


Figure 5.10. XRD patterns of freshly carburized samples at 600 °C and 700 °C.

reaction. Within each 12 hour holding step, catalyst deactivation is observed, which becomes more severe with an increase in temperature. At 550 °C, the ethane conversion ($X_{C_2H_6}$) is $\sim 1\%$, which drops to $\sim 0.6\%$ after 12 hours (-34.4 % decrease). Upon the increase to 600 °C, the conversion is enhanced to 2.4 % with a subsequent drop to 1.4 % after 12 hours (-41.7 % decrease). A further step increase in ethane conversion is observed upon reaching 650 °C, 700 °C as well as 750 °C, recording ethane conversions of 4.7 %, 7.2 % and 16.3 %, respectively. After 12 hours time on stream (TOS), the $X_{C_2H_6}$ decreased by -44.7 %, -44.4 % and -10 %, to 2.6 %, 4.0 % and 14.8 %, respectively. Upon returning to 650 °C, the catalyst shows to have suffered significant deactivation, only achieving an ethane conversion of $\sim 0.2\%$, equal to a -96 % decrease when compared to the initial conversion recorded at 650 °C (4.7 %).

In terms of CO_2 conversion, a similar trend is observed (see Figure 5.12), showing an increase in conversion with increased reaction temperatures and deactivation in each isothermal period. The C_2H_6 to CO_2 conversion ratio ($X_{C_2H_6}/X_{CO_2}$) starts just below 1 at 550 °C, and increases to 1.4 at 750 °C, which can suggest a more dominant dehydrogenation pathway with the increase in reaction temperature (see Figure 5.12). Besides achieving and maintaining a decent conversion, the selectivity towards C_2H_4 ($S_{C_2H_4}$) is another key factor to examine the performance of the catalyst for CO_2 -ODH. If the CO_2 -ODH mechanism is dominant, the maximum possible ethylene selectivity calculated based on carbonaceous products (C_2H_4 , CO and CH_4), is 67 C-% (indicated by the black line). Mo_xC_y/SiO_2 achieves an initial $S_{C_2H_4}$ of 60 C-%. Within the 12 hour isothermal period, the selectivity increased to 67 C-%. Upon the temperature ramp to 600, 650 and 700 °C, the selectivity drops back to 60 C-% but then quickly recovers to 67 C-%. Only at 750 °C and upon the return to 650 °C, the ethylene production decreased without recovery. The CO selectivity varies between 40 and 33 C-% and only a negligible amount of CH_4

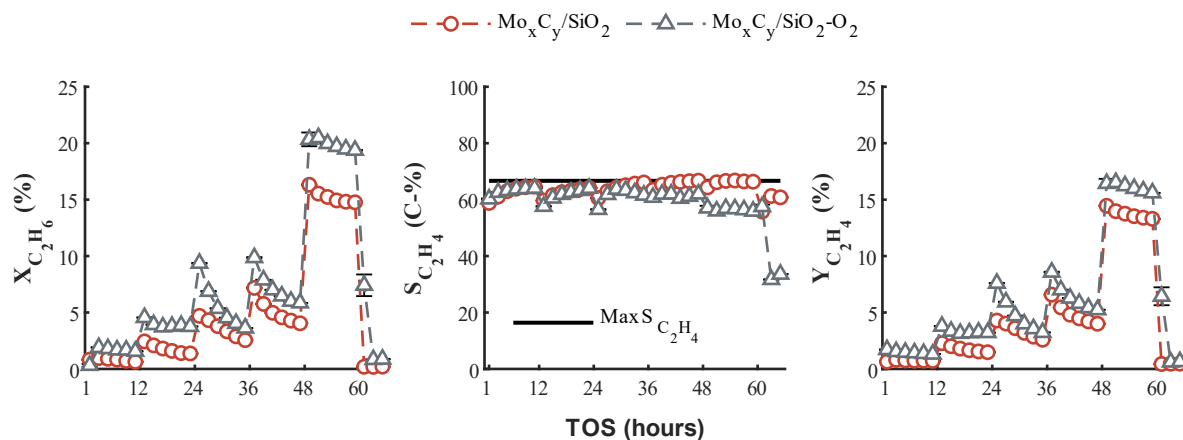


Figure 5.11. C₂H₆ conversion, C₂H₄ selectivity and C₂H₄ yield, of Mo_xC_y/SiO₂ and Mo_xC_y/SiO₂-O₂. Conditions: T = 550 °C (0-12 hours TOS), 600 °C (12-24 hours TOS), 650 °C (24-36 hours TOS), 700 °C (36-48 hours TOS), 750 °C (48-60 hours TOS) and 650 °C (60-66 hours TOS). P = 1 atm, SV = 9.4 L h⁻¹ g_{cat}⁻¹, C₂H₆:CO₂:Ar = 1:1:2. Theoretical maximum C₂H₄ selectivity for CO₂-ODH indicated by solid black line.

is detected. An ethylene selectivity close to the theoretical maximum for CO₂-ODH, suggests that all ethane converts into ethylene, which is confirmed by an ethylene yield ($Y_{C_2H_4}$) equal to $X_{C_2H_6}$. Although the selectivity data already clarifies that CO₂-ODH is the most prominent reaction, the product ratios of C₂H₄, CO and H₂ can possibly identify which side reactions occur simultaneously (see section 4.3.4). The $\dot{n}_{C_2H_4}/\dot{n}_{CO}$ ratio is close to 1, slightly dropping at each temperature interval, before recovering back to 1 (see Figure 5.12). An equal amount of C₂H₄ and CO produced is in line with the CO₂-ODH reaction. The slight drop suggests a temporarily higher CO formation, which is either formed by DR or RWGS. For RWGS to occur, H₂ needs to be produced either from DR or DH, with the latter causing the $\dot{n}_{C_2H_4}/\dot{n}_{CO}$ ratio to be 1. Thus, a drop in $\dot{n}_{C_2H_4}/\dot{n}_{CO}$ is likely due to DR, unless any other side reactions occur, such as reverse Boudouard (see Figure 5.1). The $\dot{n}_{H_2}/\dot{n}_{CO}$ ratio is more specifically related to DR, which should be 0.75 (3/4), if only DR occurs. Nevertheless, CO₂-ODH produces CO and DH produces H₂. A dominant CO₂-ODH reaction, with some minor DH, would cause values below 1 as well, further decreasing with the higher CO₂-ODH activity. The RWGS reaction causes a decrease in the $\dot{n}_{H_2}/\dot{n}_{CO}$ ratio, no matter whether the H₂ is sourced from DR or DH. The $\dot{n}_{H_2}/\dot{n}_{CO}$ is relatively stable within the 12 hour time period, suggesting the increased CO formation is equal to the increased H₂ formation, which can suggest DR. Although, the ratio is initially well below 0.75, caused by the dominant CO₂-ODH pathway. Upon increase in reaction temperature, $\dot{n}_{H_2}/\dot{n}_{CO}$ increases as well, which suggests an increased DH activity. The latter is also observed with the $\dot{n}_{C_2H_4}/\dot{n}_{H_2}$. When only DH would occur, $\dot{n}_{C_2H_4}/\dot{n}_{H_2}$ is equal to 1 and there is no CO formation whatsoever from CO₂-ODH, DR or RWGS. An increase in the $\dot{n}_{C_2H_4}/\dot{n}_{H_2}$ ratio

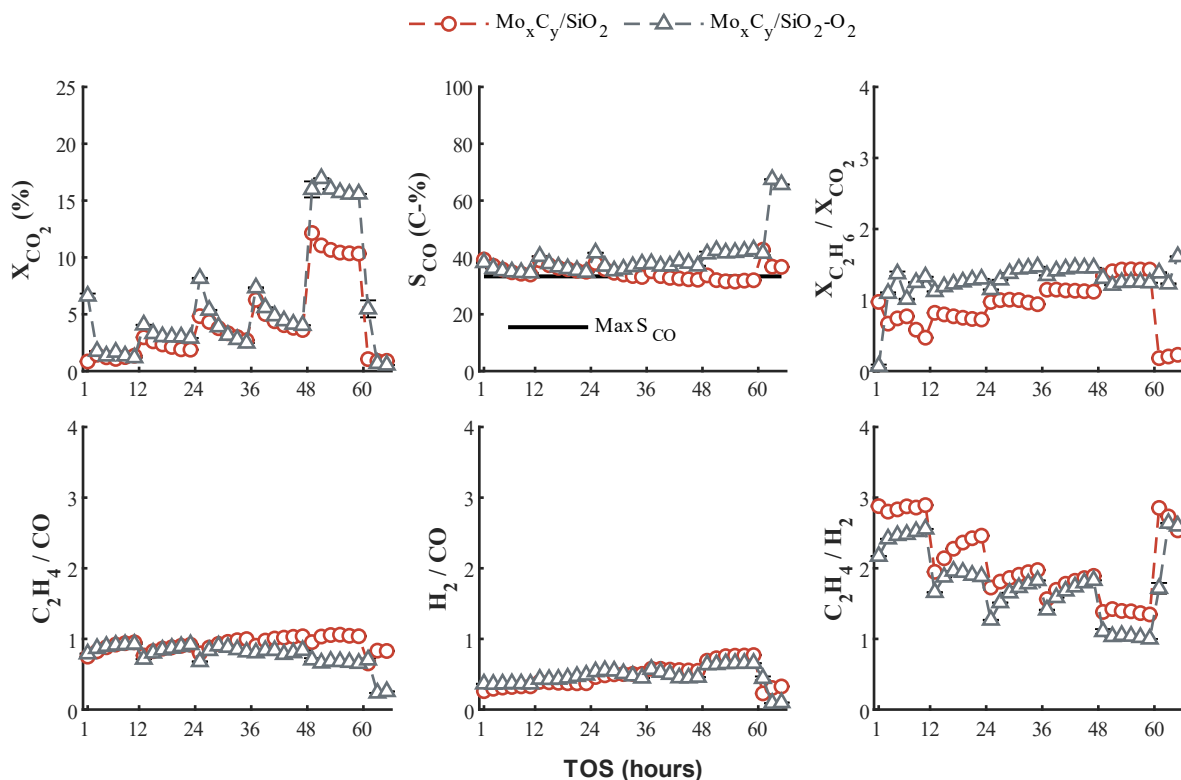


Figure 5.12. CO₂ conversion, CO selectivity, C₂H₆ to CO₂ conversion ratio, C₂H₄ to CO product ratio, H₂ to CO product ratio and C₂H₄ to H₂ product ratio, of Mo_xC_y/SiO₂ and Mo_xC_y/SiO₂-O₂. Conditions: T = 550 °C (0-12 hours TOS), 600 °C (12-24 hours TOS), 650 °C (24-36 hours TOS), 700 °C (36-48 hours TOS), 750 °C (48-60 hours TOS) and 650 °C (60-66 hours TOS). P = 1 atm, SV = 9.4 L h⁻¹ g_{cat}⁻¹, C₂H₆:CO₂:Ar = 1:1:2. Theoretical maximum CO selectivity for CO₂-ODH indicated by solid black line.

suggest an increased C₂H₄ formation (CO₂-ODH), or a decreased H₂ formation (consumed by RWGS). DR would cause a sharp drop in the ratio, as it consumes C₂H₆ and converts it into H₂. The $\dot{n}_{C_2H_4}/\dot{n}_{H_2}$ ratio starts off relatively high, and again showing a sharp drop upon increasing the temperature, slightly increasing within the 12 hours period. This suggest that upon the increase in reaction temperature, a short term increase in the occurrence of the DR pathway is observed. With further ramping temperature, the ratio remains lower, suggesting a more prominent DH activity.

The same sample was carburized, but upon completion of the carburization treatment, the sample was exposed to a 1 vol.-% O₂ in N₂ mixture at room temperature for 30 minutes. On completion, the reactor was flushed with Ar and then re-heated to the reaction temperature to subsequently be exposed to the same CO₂-ODH conditions (Mo_xC_y/SiO₂-O₂, see Figure 5.11 and Figure 5.12). Overall, a similar trend can be observed between Mo_xC_y/SiO₂ and Mo_xC_y/SiO₂-O₂, but the oxygen pre-treated sample shows slightly increased conversions, more prominently observed for X_{C₂H₆}, with a similar S_{C₂H₄}, thus

increasing $Y_{C_2H_4}$. An interesting observation is the significant improvement in catalyst stability at 600 °C, barely observing any deactivation for Mo_xC_y/SiO_2-O_2 . This effect is reversed at 650 °C, showing a much sharper decrease in conversion with TOS. The oxygen modification could possibly create more available oxygen surface species, increasing the C_2H_6 activation rate.^{16, 17}

The cause of catalyst deactivation can be determined as a combination of molybdenum oxidation and carbon deposition. Oxidation to MoO_2 is observed for both samples (see Figure 5.13) and determined via Rietveld refinement¹⁸ to represent about 15 wt.-% of the various Mo phases available (see Table K.2). SiO_2 has an amorphous structure and cannot be quantified by means of XRD. In addition, the presence of $\alpha-MoC_{1-x}$ is of interest, but its occurrence will be discussed in more detail later in this section.

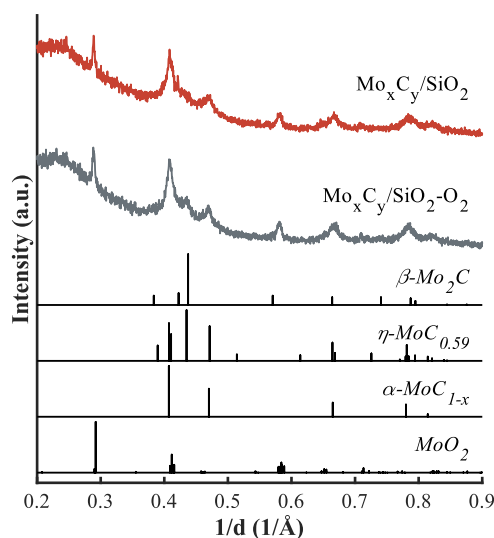


Figure 5.13. XRD patterns of the spent catalysts Mo_xC_y/SiO_2 and Mo_xC_y/SiO_2-O_2 , after exposure to CO_2 -ODH conditions over a range of reaction temperatures.

Raman spectroscopy confirmed the presence of amorphous or disordered carbon, shown by the two broad peaks obtained around 1350 and 1580 cm^{-1} , designated as D- and G-band, respectively (see Figure 5.14).¹⁹ Although Raman analysis does not quantify the amount of carbon deposited on the surface, the intensity ratio between the D- and G-band (I_D/I_G) as well as the full width at half maximum (FWHM) of the G-band is often used to identify the type of carbon deposited on the surface. Graphitic carbon will show a narrow G-band with a low I_D/I_G . Both samples almost have an identical intensity ratio and G-band width. The values are in close proximity to the values reported for glassy carbon.²⁰

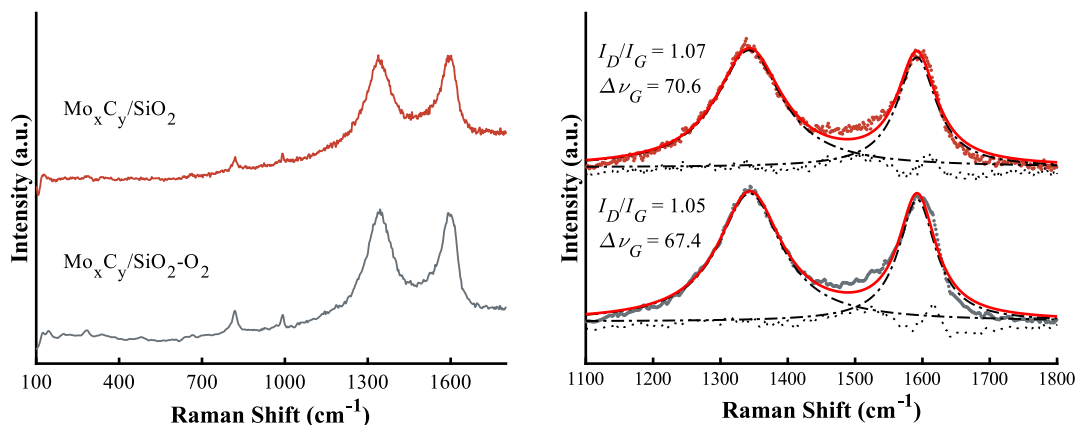


Figure 5.14. Raman spectra of the spent catalysts, $\text{Mo}_x\text{C}_y/\text{SiO}_2$ and $\text{Mo}_x\text{C}_y/\text{SiO}_2\text{-O}_2$, after exposure to $\text{CO}_2\text{-ODH}$ conditions over a range of reaction temperatures.

$\text{Mo}_x\text{C}_y/\text{SiO}_2$ was again exposed to three different reaction temperatures, 550 °C, 650 °C and 750 °C, but now in three individual experiments, each for 24 hours TOS (see Figure 5.15 and Figure B.1). The individual experiments allow for a more accurate study of the initial activity observed at each temperature range, without prior surface/bulk modifications. At 550 °C, the initial ethane conversion at 1 hour TOS is 3.7 %. At 650 °C and 750 °C, the initial conversion is significantly higher, recording 12.1 % and 21.0 %, respectively. The catalyst deactivates within the first 9-12 hours TOS after which it stabilizes. The jump in conversion at 750 °C observed, in both experiments, can be explained by the appearance of thermally activated C_2H_6 ²¹ and CO_2 reacting with solid C from the Mo_xC_y structure.²² The $S_{\text{C}_2\text{H}_4}$ for all reaction temperatures is close to 67 C-%, suggesting that the dominant reaction pathway is $\text{CO}_2\text{-ODH}$. At 750 °C, a lower $\dot{n}_{\text{C}_2\text{H}_4}/\dot{n}_{\text{H}_2}$ ratio is observed. Together with a conversion ratio above one, and a $\dot{n}_{\text{C}_2\text{H}_4}/\dot{n}_{\text{CO}}$ ratio close to 1, an increased H_2 formation from DR or DH is unlikely, however increased $\text{C}_2\text{H}_6/\text{C}_2\text{H}_4$ cracking (to solid C and H_2) is likely to occur at those temperatures.

The highest degree of oxidation (to MoO_2) is observed at a reaction temperature of 550 °C, determined *via* XRD analysis of the spent sample (see Figure 5.16 and Table K.2). The spent samples are further analysed by means of XANES (see Table 5.3). The slight discrepancies in the phase composition between the XRD and XANES data can be explained by the use of bulk references for the purpose of linear combination fitting of the supported samples. This is mainly observed in the quality of fit (Figure G.2). Nevertheless, the same trend is observed, showing a decrease in MoO_2 content with an increase in reaction temperature. This suggests, as discussed during the earlier presented thermodynamic analysis (see section 5.1), that (re-)carburization of the oxide phase can occur at higher reaction temperatures. This can also explain the presence of $\alpha\text{-MoC}_{1-x}$ in the spent samples after ODH at 650 °C and 750 °C, but not

observed for ODH at 550 °C. C₂H₆ has previously been reported as an alternative carbon source for the carburization process¹², forming α -MoC_{1-x}.²³, possibly *via* an oxycarbide intermediate (MoO_xC_y).²⁴ The MoO_xC_y phase has previously been suggested to be the active phase in CO₂-ODH for C-H bond cleavage.²⁵ Other studies have reported the formation of molybdenum oxyhydride (MoO_xH_y), which cannot be excluded, but the likeliness of its formation post reaction is minimal as supported by a study from Bouchy *et al.*²⁶ where the oxyhydride was formed upon reduction of MoO₃ in pure hydrogen at 350 °C for 24 h. This resulted in only a fraction of the sample to form MoO_xH_y, balanced by MoO₂. In the CO₂-ODH reaction, a carbon source is present at all times (C₂H₆, C₂H₄, CH₄ or C*), thus the formation of MoO_xC_y is more likely.

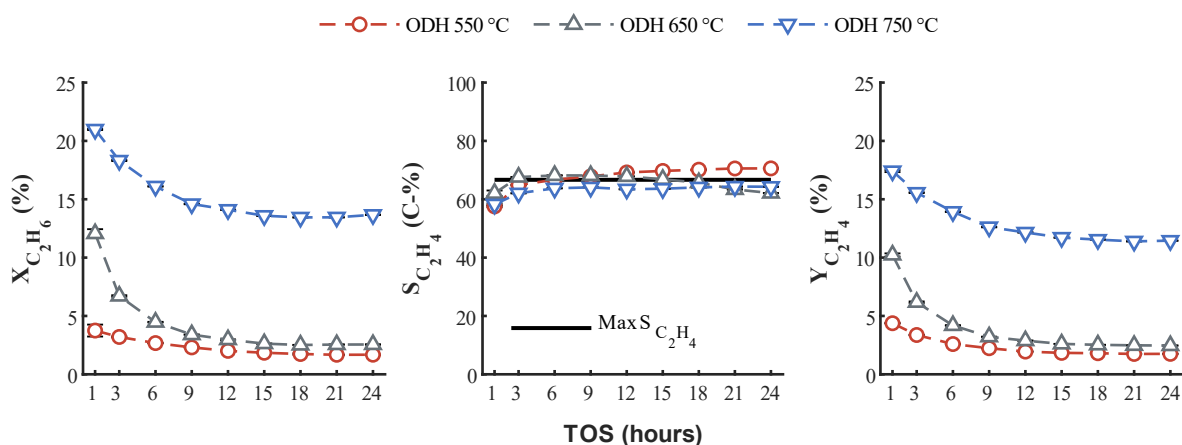


Figure 5.15. C₂H₆ conversion, C₂H₄ selectivity and C₂H₄ yield, of Mo_xC_y/SiO₂. Conditions: T = 550 °C, 650 °C or 700 °C, P = 1 atm, SV = 9.4 L h⁻¹ g_{cat}⁻¹, C₂H₆:CO₂:Ar = 1:1:2. Theoretical maximum C₂H₄ selectivity for CO₂-ODH indicated by solid black line.

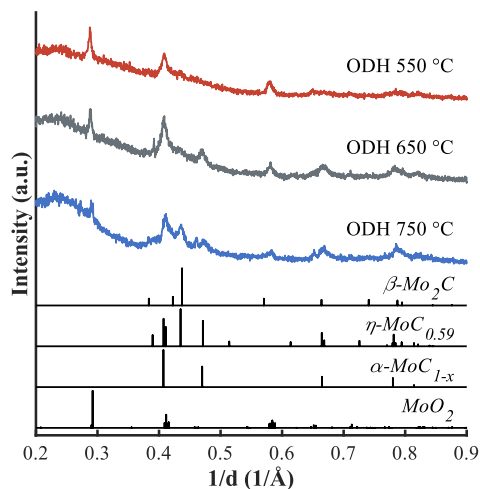


Figure 5.16. XRD patterns of the spent catalysts after exposure to CO₂-ODH conditions at 550 °C, 650 °C and 750 °C.

Table 5.3. Phase composition obtained *via* XANES linear combination fitting of a freshly carburized $\text{Mo}_x\text{C}_y/\text{SiO}_2$ at 700 °C, and exposed to CO_2 -ODH conditions at 550 °C, 650 °C and 750 °C.

Sample	$\beta\text{-Mo}_2\text{C}$ wt.-% (error)	MoO_2 wt.-% (error)	MoO_3 wt.-% (error)
Fresh	46.8 (1.3)	-	53.2 (2.6)
ODH 550 °C	62.9 (0.8)	13.8 (1.5)	23.3 (1.7)
ODH 650 °C	74.3 (1.1)	5.2 (2.1)	20.5 (2.4)
ODH 750 °C	82.1 (1.1)	-	17.9 (2.3)

Raman analysis confirms the presence of carbon on all three samples. The increase in temperature seems to slightly increase the I_D/I_G and decrease the G-band width. Although this does not mean a drastic change in the type of carbon present, it does suggest an increased disorder of the carbon species upon higher reactor temperatures.²⁵

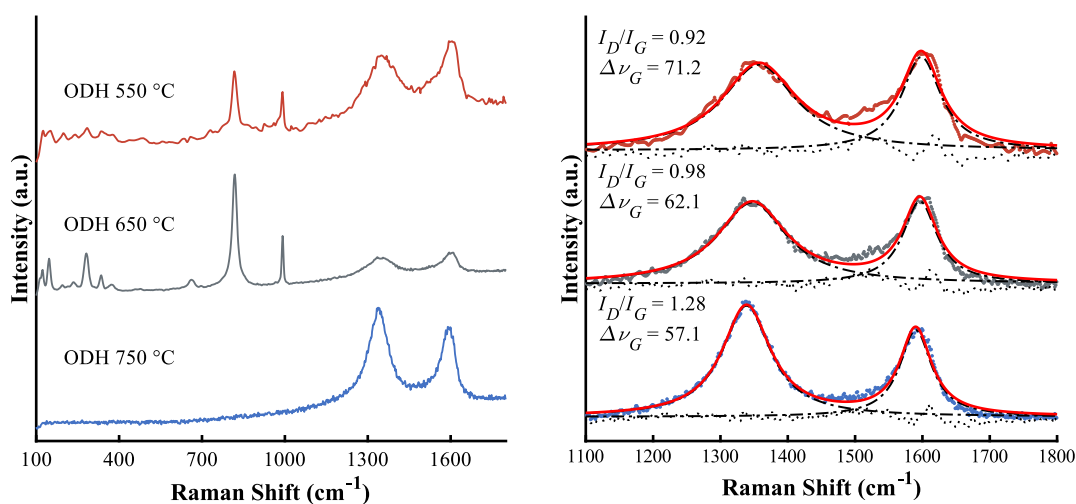


Figure 5.17. Raman spectra of the spent $\text{Mo}_x\text{C}_y/\text{SiO}_2$ after exposure to CO_2 -ODH conditions at 550, 650 and 750 °C.

5.4 Concluding remarks

The thermodynamic analysis of the endothermic CO_2 -ODH system concludes that under the proposed reaction conditions (600 °C), side reactions such as the dry-reforming of ethane as well as the direct dehydrogenation reaction are thermodynamically favoured over the ODH reaction. At lower temperatures, the methane or carbon formation routes are significantly more feasible and at higher temperature the syngas formation routes are dominant. The CO_2 -ODH equilibrium conversion can be pushed *via* dilution of the feed mixture or with an increased CO_2 content in the feed mixture. Gibbs free

energy minimization of the entire system concluded that both C_2H_4 and C_2H_6 are not stable in the evaluated temperature range. Only upon omitting CH_4 and solid carbon in the system, a slight increase in C_2H_4 concentration can be observed above 600 °C, formed *via* the direct dehydrogenation pathway. Oxidation of Mo_2C to MoO_x is thermodynamically not favoured at 600 °C, thus catalyst deactivation through oxidation is predominantly driven by kinetics. In the absence of C_2H_6 in the feed, Mo_2C and MoO_x are predicted to co-exist at 600 °C.

In situ XRD analysis confirmed that the carburization of AHM/SiO₂ to Mo_xC_y/SiO_2 proceeds *via* the decomposition of the AHM to *hP*- MoO_3 and eventually *oP*- MoO_3 , followed by the reduction to MoO_2 and finally carburization to a mixture of β - Mo_2C and η - $MoC_{0.59}$. *In situ* Raman analysis suggests that the carburization process of the surface of the nanoparticles occurs at temperatures as low as 350 °C. Additionally, the freshly carburized surface dissociates O_2 on the surface when exposed to low concentrations (1 vol.-%) and at room temperature. An increase in O_2 concentration or exposure to higher temperatures can cause a violent re-oxidation to MoO_2 .

The CO_2 -ODH performance of Mo_xC_y/SiO_2 was evaluated within a range of reaction temperatures. An increase in the reaction temperature shows an increase in the conversion of C_2H_6 and CO_2 , however a more rapid catalyst deactivation with time on stream is observed. At higher reaction temperatures, the oxidation of the carbide to MoO_2 is limited, most likely due to the re-carburization of MoO_xC_y or MoO_x by C_2H_6 as thermodynamically predicted. An oxygen treatment at room temperature prior to the reaction has caused the catalyst to have a higher initial activity, likely due to the available oxygen surface species. However, the oxygen surface species also caused a more severe catalyst deactivation, possible due to higher amount of carbon deposits either from ethylene decomposition or the re-carburization reaction. At 750 °C, the conversion showed a sharp increase in both C_2H_6 and CO_2 conversion, suggesting an increased thermal activation of both reactants. The CO_2 -ODH reaction is the most dominant reaction pathway occurring at all reaction temperatures tested. The initial higher activity is in parallel to a slightly increased DR presence, but the C_2H_4 selectivity remains above 60 C-%.

References

1. F. T. Zangeneh, A. Taeb, K. Gholivand and S. Sahebdehfar, Thermodynamic Equilibrium Analysis of Propane Dehydrogenation with Carbon Dioxide and Side Reactions, *Chemical Engineering Communications*, 2015, **203**, 557-565.
2. E. Gomez, S. Kattel, B. Yan, S. Yao, P. Liu and J. G. Chen, Combining CO₂ reduction with propane oxidative dehydrogenation over bimetallic catalysts, *Nat Commun*, 2018, **9**, 1398.
3. A. S. Sandupatla, K. Ray, P. Thaosan, C. Sivananda and G. Deo, Oxidative dehydrogenation of propane over alumina supported vanadia catalyst – Effect of carbon dioxide and secondary surface metal oxide additive, *Catalysis Today*, 2020, **354**, 176-182.
4. X. Jiang, L. Sharma, V. Fung, S. J. Park, C. W. Jones, B. G. Sumpter, J. Baltrusaitis and Z. Wu, Oxidative Dehydrogenation of Propane to Propylene with Soft Oxidants via Heterogeneous Catalysis, *ACS Catalysis*, 2021, **11**, 2182-2234.
5. X. Li, B. Yan, S. Yao, S. Kattel, J. G. Chen and T. Wang, Oxidative dehydrogenation and dry reforming of n-butane with CO₂ over NiFe bimetallic catalysts, *Applied Catalysis B: Environmental*, 2018, **231**, 213-223.
6. E. Gomez, B. Yan, S. Kattel and J. G. Chen, Carbon dioxide reduction in tandem with light-alkane dehydrogenation, *Nature Reviews Chemistry*, 2019, **3**, 638-649.
7. M. Myint, B. Yan, J. Wan, S. Zhao and J. G. Chen, Reforming and oxidative dehydrogenation of ethane with CO₂ as a soft oxidant over bimetallic catalysts, *Journal of Catalysis*, 2016, **343**, 168-177.
8. T. A. Bugrova, V. V. Dutov, V. A. Svetlichnyi, V. Cortés Corberán and G. V. Mamontov, Oxidative dehydrogenation of ethane with CO₂ over CrOx catalysts supported on Al₂O₃, ZrO₂, CeO₂ and CexZr1-xO₂, *Catalysis Today*, 2019, **333**, 71-80.
9. S. Raseale, W. Marquart, K. Jeske, G. Prieto, M. Claeys and N. Fischer, Supported Fe_xNi_y catalysts for the co-activation of CO₂ and small alkanes, *Faraday Discuss*, 2021, **229**, 208-231.
10. O. Knacke, O. Kubaschewski and K. Hesselmann, *Thermochemical properties of inorganic substances*, Springer-Verlag, Berlin, 2nd edn., 1991.
11. I. Barin, *Thermochemical Data of Pure Substances*, VCH Publishers, Inc., Weinheim, 3rd edn., 1995.
12. T. Mo, J. Xu, Y. Yang and Y. Li, Effect of carburization protocols on molybdenum carbide synthesis and study on its performance in CO hydrogenation, *Catalysis Today*, 2016, **261**, 101-115.
13. J. Wienold, Rolf E. Jentoft and T. Ressler, Structural Investigation of the Thermal Decomposition of Ammonium Heptamolybdate by in situ XAFS and XRD, *European Journal of Inorganic Chemistry*, 2003, DOI: 10.1002/ejic.200390138, 1058-1071.
14. W. Marquart, D. J. Morgan, G. J. Hutchings, M. Claeys and N. Fischer, Oxygenate formation over K/β-Mo₂C catalysts in the Fischer–Tropsch synthesis, *Catalysis Science & Technology*, 2018, **8**, 3806-3817.
15. L. Ovari, J. Kiss, A. P. Farkas and F. Solymosi, Surface and subsurface oxidation of Mo₂C/Mo(100): low-energy ion-scattering, auger electron, angle-resolved X-ray photoelectron, and mass spectroscopy studies, *J Phys Chem B*, 2005, **109**, 4638-4645.
16. M. M. Sullivan and A. Bhan, Effects of oxygen coverage on rates and selectivity of propane-CO₂ reactions on molybdenum carbide, *Journal of Catalysis*, 2018, **357**, 195-205.
17. S. Yao, B. Yan, Z. Jiang, Z. Liu, Q. Wu, J. H. Lee and J. G. Chen, Combining CO₂ Reduction with Ethane Oxidative Dehydrogenation by Oxygen-Modification of Molybdenum Carbide, *ACS Catalysis*, 2018, **8**, 5374-5381.
18. H. M. Rietveld, A Profile Refinement Method for Nuclear and Magnetic Structures, *J. Appl. Cryst.*, 1969, **2**, 65-71.
19. K. Dasgupta and D. Sathiyamoorthy, Disordered carbon—its preparation, structure, and characterisation, *Materials Science and Technology*, 2013, **19**, 995-1002.
20. D. S. Knight and W. B. White, Characterization of diamond films by Raman spectroscopy, *Journal of Materials Research*, 2011, **4**, 385-393.
21. S. A. Theofanidis, C. Loizidis, E. Heracleous and A. A. Lemonidou, CO₂-oxidative ethane dehydrogenation over highly efficient carbon-resistant Fe-catalysts, *Journal of Catalysis*, 2020, **388**, 52-65.

22. F. Solymosi, A. Oszkó, T. Bánsági and P. Tolmásov, Adsorption and Reaction of CO₂ on Mo₂C Catalyst, *The Journal of Physical Chemistry B*, 2002, **106**, 9613-9618.
23. A. De Zanet and S. A. Kondrat, A Review of Preparation Strategies for α -MoC_{1-x} Catalysts : Transition metal carbides attract growing attention, *Johnson Matthey Technology Review*, 2022, **66**, 285-315.
24. J. J. Sattler, J. Ruiz-Martinez, E. Santillan-Jimenez and B. M. Weckhuysen, Catalytic dehydrogenation of light alkanes on metals and metal oxides, *Chem Rev*, 2014, **114**, 10613-10653.
25. Y. Gambo, S. Adamu, G. Tanimu, I. M. Abdullahi, R. A. Lucky, M. S. Ba-Shammakh and M. M. Hossain, CO₂-mediated oxidative dehydrogenation of light alkanes to olefins: Advances and perspectives in catalyst design and process improvement, *Applied Catalysis A: General*, 2021, **623**, 118273.
26. C. Bouchy, S. B. D.-A. Hamid and E. G. Derouane, A new route to the metastable FCC molybdenum carbide α -MoC_{1-x}, *Chem. Commun.*, 2000, 125-126.

6 Supported Mo_xC_y via different synthesis techniques

In this chapter the thermodynamic analysis discussed in Chapter 5 was extended by exploring the reverse water-gas-shift reaction and its major side reaction, the methanation of CO_2 , focusing on the equilibrium conversion and the entire system. Experimentally, the synthesis and characterization of SiO_2 or SBA-15 supported Mo_xC_y nanoparticles, by means of three different synthesis techniques (wet impregnation, hybrid nano-crystals and sol-gel) is investigated. The effect of synthesis technique on the carburization process, the final carbide composition as well as their catalytic performance in CO_2 activation in the absence and presence of C_2H_6 or H_2 is discussed.

A section of the results reported in this chapter are part of research articles published as: W. Marquart, S. Raseale, G. Prieto, A. Zimina, B. B. Sarma, J.-D. Grunwaldt, M. Claeys, N. Fischer, *ACS Catalysis* 2021, 11, 1624-1639, and: W. Marquart, M. Claeys, N. Fischer, *Faraday Discussions* 2021, 230, 68-86.

6.1 Thermodynamic analysis of the RWGS reaction

In section 5.1, a comprehensive thermodynamic analysis of the CO_2 -ODH system is discussed. In this chapter, the thermodynamic analysis is extended by focusing on the reverse water-gas-shift reaction. The reverse water-gas-shift reaction is often suggested to be part of the CO_2 -ODH mechanism, where CO_2 reacts with H_2 produced from the direct dehydrogenation of ethane. CO_2 methanation (MCO_2) is a prominent side reaction and is thus included in the thermodynamic evaluation.

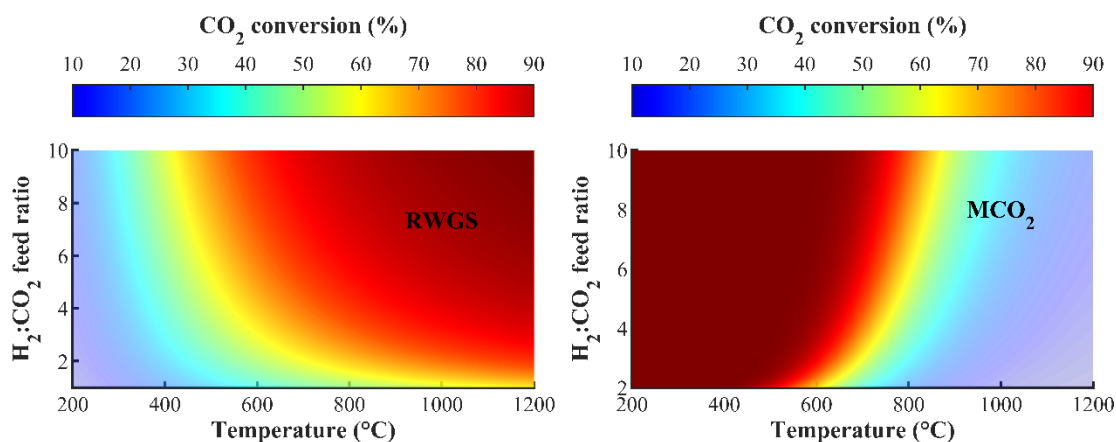


Figure 6.1. Effect of feed ratio (H_2 to CO_2) and temperature on the equilibrium conversion of the reverse water-gas-shift (RWGS) reaction and the methanation of CO_2 (MCO_2), at 1 bar pressure. Thermodynamic parameters are from Knacke *et al.*¹.

In order to understand which process conditions are required to achieve the maximum possible CO₂ conversion in the RWGS and CO₂ methanation, the thermodynamic equilibrium conversion is computed as a function of temperature and feed ratio. It is confirmed that higher temperatures and H₂ to CO₂ ratios yield higher CO₂ conversion in the RWGS (see Figure 6.1). However, a higher H₂ to CO₂ ratio also favours the CH₄ formation due to the increase in equilibrium conversion for the methanation reaction. The methanation of CO₂ is an exothermic reaction, thus an increase in temperatures decreases the equilibrium conversion.

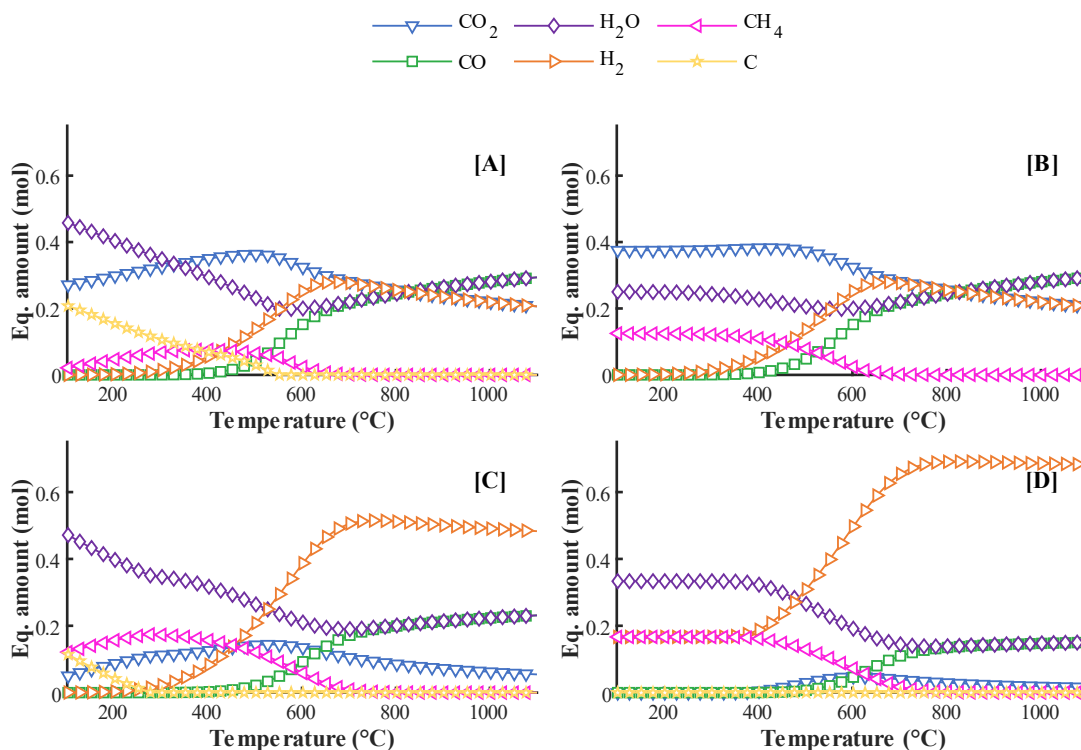


Figure 6.2. Product equilibrium of the RWGS system as a function of temperature at a H₂ to CO₂ feed ratio of 1 [A, B], 2.5 [C], or 5.0 [D], with [A, C, D] all compounds considered, and [B] carbon formation neglected. Compound specific thermodynamic data from Knacke *et al.*¹.

When minimalizing the Gibbs free energy of the RWGS system as a function of temperature, the following compounds are considered calculating the product equilibrium: CO_{2(g)}, CO_(g), H_{2O(g)}, H_{2(g)}, CH_{4(g)} and C_(s). At a stoichiometric feed ratio (H₂:CO₂) of 1 and 1 bar pressure (see Figure 6.2-A), the thermodynamic analysis suggests that at lower temperatures (below 400 °C) the reduction of CO₂ to H₂O and solid carbon (assumed as graphite) is the most favourable reaction. Simultaneously, at 400 °C the methanation reaction is predicted to reach its maximum. CO starts to form as the CH₄, C and H₂O concentrations drop, surpassing CH₄ concentrations at 530 °C. Above 750 °C a H₂O to CO product ratio of 1 is observed, the desired product ratio for stoichiometric RWGS. When all coke forming pathways are

neglected, the methanation contribution increases significantly, being the dominant carbon containing product below 450 °C (see Figure 6.2-B). Increasing the H₂ to CO₂ ratio to 2.5 (see Figure 6.2-C) or 5 (see Figure 6.2-D) suppresses carbon formation at lower temperatures, increasing the formation to methane and water.

6.2 Catalyst characterizatop: effect of synthesis techniques

6.2.1. Hybrid nano-crystal technique

The hybrid nano-crystal (HNC) technique was used to prepare Mo_xC_y nanoparticles supported on SiO₂ or SBA-15. In short, the synthesis technique allows for the formation of mono-dispersed Mo-based inorganic-organic HNCs made of Mo₈O₂₆⁴⁻ as the inorganic core and long-chain quaternary ammonium cations as the organic shell.^{2,3} Upon dispersion in ethanol, followed by drying for TEM analysis purposes, a lamellar mesostructure is obtained (see Figure 6.3-A, B). The HNCs were supported on SiO₂ or SBA-15 *via* dispersion in deionized water and a hydrothermal deposition treatment in an autoclave. The dispersed supported HNCs were dried and subsequently calcined at 400 °C for 5 hours (see section 4.1.3). Although a lot smaller in size, TEM micrographs of the supported MoO₃ on SBA-15 reveal the presence of similar lamellar mesostructures as observed before calcination (see Figure 6.3-C, D). XRD analysis confirms the formation of *oP*-MoO₃ with an average crystallite size of 55.3±1.4 nm (see Figure D.1).

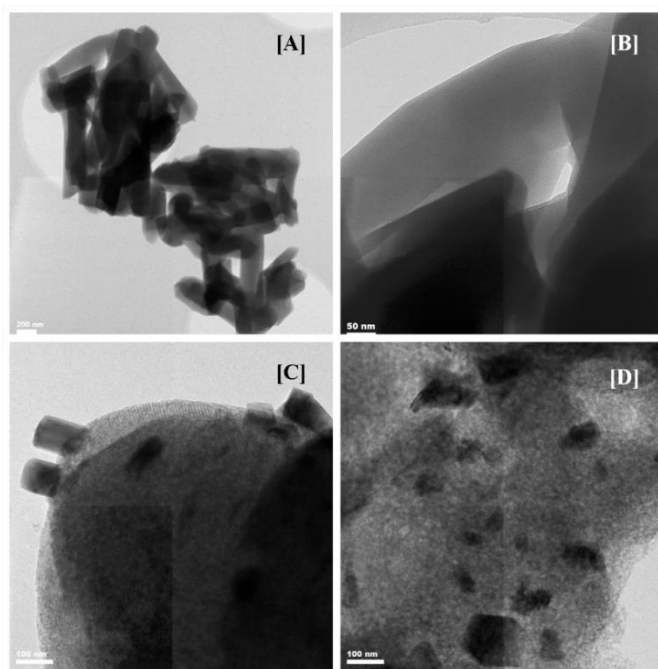


Figure 6.3. TEM micrographs of [A, B] freshly prepared hybrid nano-crystals and [C, D] MoO₃ supported on SBA-15 prepared *via* HNC synthesis route.

The carburization of $\text{Mo}_x\text{C}_y/\text{SBA-15-HNC}$ at $600\text{ }^\circ\text{C}$ was monitored by means of *in situ* XRD and TGA analysis. According to the XRD patterns and the corresponding Rietveld refinement analysis results (see Figure 6.4-A, B, D), the reduction of *oP*- MoO_3 to MoO_2 is first observed at $400\text{ }^\circ\text{C}$, becoming the dominant phase at $491\text{ }^\circ\text{C}$. Simultaneously, the average crystallite size is slightly reduced. First signs of $\eta\text{-MoC}_{0.59}$ can be observed by a broad reflex at $580\text{ }^\circ\text{C}$, followed by $\beta\text{-Mo}_2\text{C}$ at $600\text{ }^\circ\text{C}$. After 5 minutes at $600\text{ }^\circ\text{C}$ the MoO_2 reflections disappear completely. TGA analysis (see Figure 6.4-C) shows four significant weight losses, with the first as a small broad event at $250\text{ }^\circ\text{C}$. This observation is in contrast with the first detection of oxide reduction at $400\text{ }^\circ\text{C}$ by XRD, but it can be rationalized by an incomplete calcination process from AHM to *oP*- MoO_3 prior to TGA analysis, which is also shown by the continuous loss of mass from the beginning of the experiment (around 5 wt.-% in total). This is followed by a large and prolonged drop in mass which is associated to the reduction of *oP*- MoO_3 to MoO_2 starting at $407\text{ }^\circ\text{C}$ with a maximum at $467\text{ }^\circ\text{C}$. At around $567\text{ }^\circ\text{C}$, the mass loss observed is linked to the formation of the carbide. The carburization process lasts for at least 2.5 hours, after which no further change in weight is observed.

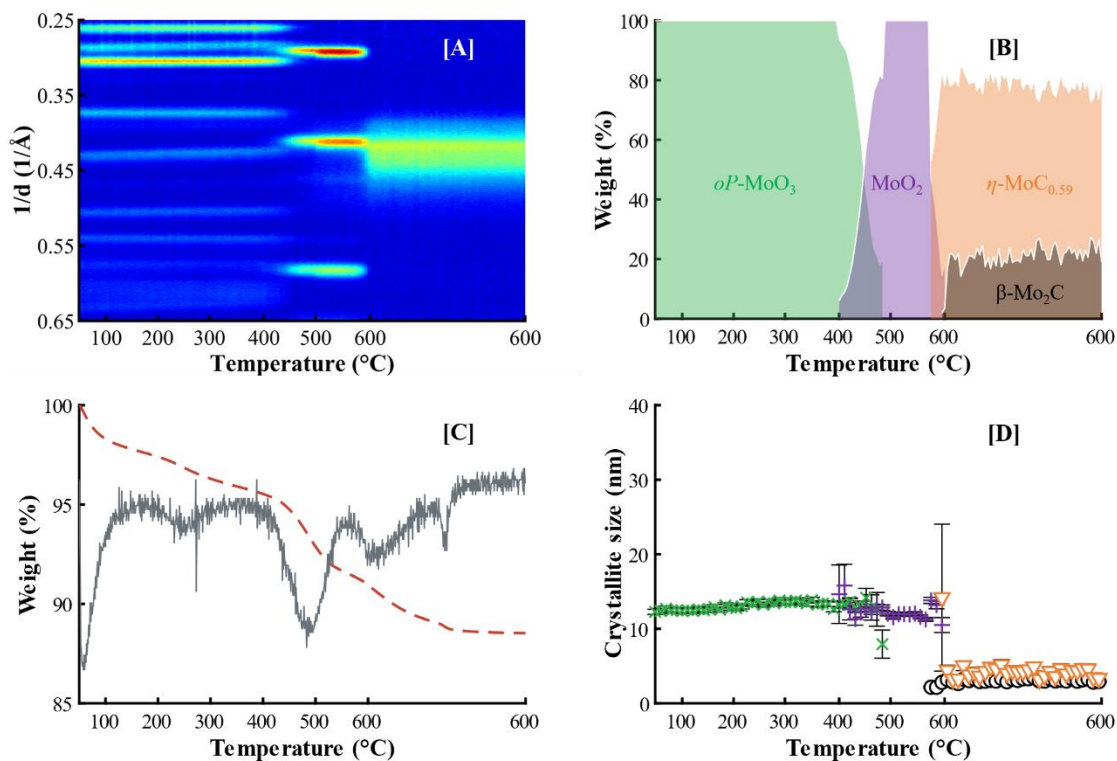


Figure 6.4. Carburization process of $\text{Mo}_x\text{C}_y/\text{SBA-15-HNC}$ as function of temperature, with [A] top view of *in situ* XRD patterns, [B] corresponding Rietveld refinement analysis with phase composition and [D] particle size and [C] TGA analysis with TG curve (red dashed line) and differential thermal analysis (DTA) signal (grey solid line). Conditions: $T_{\text{final}} = 600\text{ }^\circ\text{C}$, $P = 1\text{ atm}$, heating rate = $1\text{ }^\circ\text{C min}^{-1}$, holding time = 5 hours.

TGA results captured during the carburization of bulk MoO_3 (see Figure C.2) show no weight loss until 450 °C. Upon the formation of the carbide in the bulk sample, the measured weight loss is briefly higher than expected for a full conversion to the carbide. This could be explained by a partial reduction of MoO_2 to MoO_{2-x} prior to the incorporation of carbon in the structure. In the supported sample this behaviour could not be resolved possibly due to the lower Mo concentration in the sample. However, the carbide formation for the supported sample appears to be more facile at 600 °C, whereas the bulk sample only fully carburized at 650 °C.

6.2.2. Sol-Gel technique

The third technique used to prepare Mo_xC_y nanoparticles was the Sol-Gel method, adapted from the reports by Umbarkar *et al.*⁴ and Amrute *et al.*⁵. Upon calcination of the greenish precipitate at 500 °C for 10 hours (see section 4.1.2 for more details on the synthesis method), *oP*- MoO_3 supported on SiO_2 was achieved as confirmed by means of XRD analysis (see Figure D.1). Similar to $\text{MoO}_3/\text{SBA-15-HNC}$, the average crystallite size of *oP*- MoO_3 is refined to 48.3 ± 1.5 nm. The presence of large, agglomerated particles of MoO_3 on the SiO_2 support is observed in the TEM micrographs (see Figure 6.5).

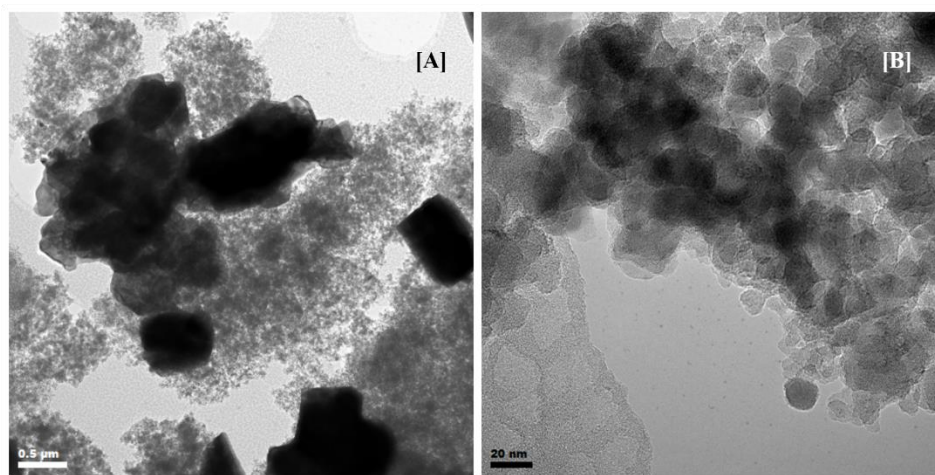


Figure 6.5. TEM micrographs of MoO_3 supported on SiO_2 prepared *via* the sol-gel method.

The carburization process to obtain $\text{Mo}_x\text{C}_y/\text{SiO}_2\text{-SG}$ was also followed by means of *in situ* XRD and a similar behaviour to $\text{Mo}_x\text{C}_y/\text{SBA-15-HNC}$ can be observed (see Figure 6.6). *oP*- MoO_3 starts reducing at 400 °C as can be seen by the appearance of the three major reflexes for MoO_2 , at 0.3, 0.42 and 0.58 $1/\text{Å}$. MoO_3 is then fully reduced by 498 °C, with MoO_2 becoming the only visible phase present. First reflexes showing the formation of Mo_xC_y ($\eta\text{-MoC}_{0.59}$ and/or $\beta\text{-Mo}_2\text{C}$), between 0.4 and 0.45 $1/\text{Å}$, are observed at 600 °C.

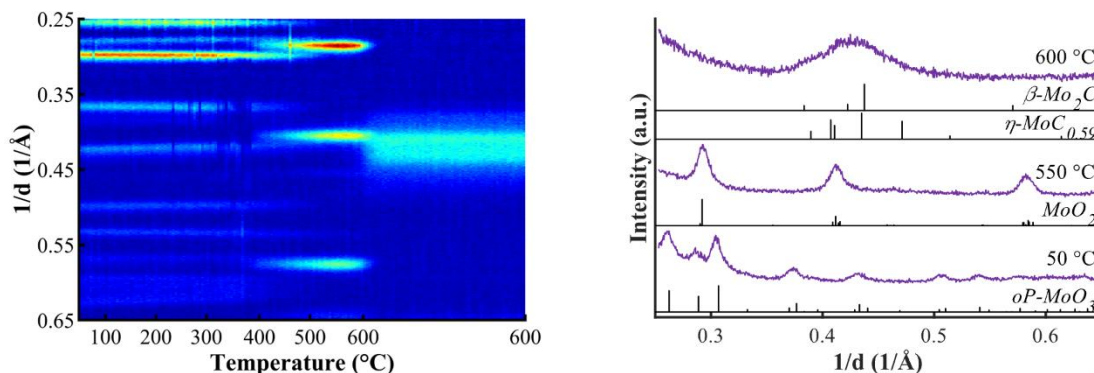


Figure 6.6. Carburization process of $\text{Mo}_x\text{C}_y/\text{SiO}_2\text{-SG}$ as function of temperature, with [A] top view of *in situ* XRD patterns [B] XRD patterns obtained at 50 °C, 550 °C and 600 °C.

6.2.3. Characterization of activated catalysts: effect of synthesis techniques

Based on the results obtained by studying the carburization process of $\text{Mo}_x\text{C}_y/\text{SiO}_2\text{-WI}$, in section 5.2, and the results discussed in section 6.2.1, for $\text{Mo}_x\text{C}_y/\text{SBA-15-HNC}$, and 6.2.2, for $\text{Mo}_x\text{C}_y/\text{SiO}_2\text{-SG}$, all samples evaluated for their catalytic performance in both RWGS as well as $\text{CO}_2\text{-ODH}$, were carburized at 600 °C for 5 hours with a ramp rate of 1 °C min^{-1} to maintain consistency. In addition to the above-mentioned samples, $\text{Mo}_x\text{C}_y/\text{SiO}_2\text{-HNC}$ as well as $\text{Mo}_x\text{C}_y/\text{SBA-15-WI}$ are prepared *via* the HNC and WI method, respectively. Although XRD analysis confirmed the presence of a carbide phase in all samples, the different synthesis techniques yielded variations in the compositions of the carbides, determined *via* Rietveld refinement (see Table 6.1 and Figure 6.7).

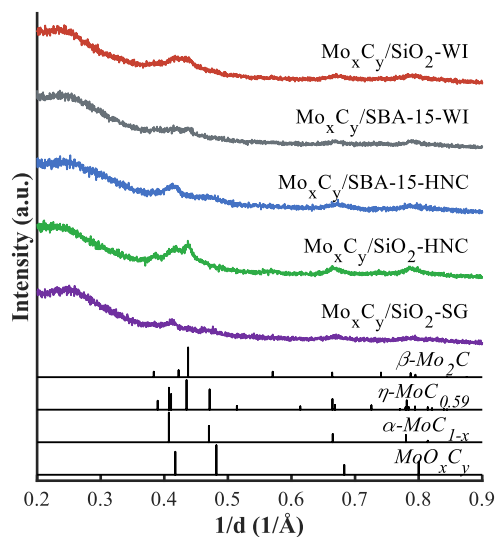


Figure 6.7. XRD patterns of the freshly carburized samples at 600 °C.

Table 6.1. Phase composition and crystallite sizes determined *via* XRD Rietveld analysis of the freshly carburized catalysts.

Sample	β -Mo ₂ C		η -MoC _{0.59}		α -MoC _{1-x} / MoO _x C _y	
	wt.-% (error)	nm (error)	wt.-% (error)	nm (error)	wt.-% (error)	nm (error)
Mo _x C _y /SiO ₂ -WI	21.4 (2.7)	4.9 (0.8)	78.6 (2.7)	3.3 (0.2)	-	-
Mo _x C _y /SBA-15-WI	19.4 (2.9)	9.2 (2.0)	80.6 (2.9)	4.6 (0.4)	-	-
Mo _x C _y /SBA-15-HNC	-	-	45.5 (4.6)	3.4 (0.5)	54.5 (4.6)	4.0 (0.4)
Mo _x C _y /SiO ₂ -HNC	37.5 (1.9)	6.3 (0.4)	62.5 (1.9)	3.4 (0.2)	-	-
Mo _x C _y /SiO ₂ -SG	-	-	55.8 (4.3)	4.4 (0.5)	44.2 (4.3)	5.7 (0.8)

The refinements of Mo_xC_y/SBA-15-HNC and Mo_xC_y/SiO₂-SG suggest the presence of a different phase than β -Mo₂C, as was observed by *in situ* XRD (see Figure D.3). The reflections at 0.41 and 0.48 1/Å can either be related to a cubic MoO_xC_y phase or α -MoC_{1-x}.^{6,7} The latter phase was observed in the CO₂-ODH spent samples in section 5.3 due to re-carburization of the oxidized sample in the ethane atmosphere at higher reaction temperatures (650 and 750 °C). Freshly prepared α -MoC_{1-x} is usually synthesized by carburization of Mo₂N⁸ or when promoted with platinum⁹, we therefore suggest that the observed phase in these freshly prepared samples is more likely MoO_xC_y, indicating the presence of an intermediate phase between the reduction and carburization step.¹⁰ β -Mo₂C is observed when the same samples are carburized at higher temperatures (see Figure D.4). However, higher temperatures also increase carbon deposition, which in turn blocks the catalytically active sites. Thus, these carbide composition discrepancies between *in situ* XRD and reactor carburization could be associated to variations in the heating system and gas flow patterns resulting from the differences between the dedicated fixed bed reactor and the XRK900 reactor chamber and reaffirm the sensitivity of the physical properties of Mo_xC_y on the carburization process and fluid dynamics, specifically at smaller particle sizes. In this work, molybdenum oxycarbide is described as cubic structure (space group: Fm-3m) with a stoichiometry of MoOC, as the MoO_xC_y phase (PDF 00-017-0104) is insufficiently described in literature and no pure phase was available prohibiting the use of alternative Rietveld refinement strategies such as PONKCS.¹¹ Besides β -Mo₂C or MoO_xC_y, all samples co-exist with a second carbide phase, (hexagonal) η -MoC_{0.59}, with an increased C/Mo ratio. The average crystallite size of the η -carbide for all samples is smaller than for β -Mo₂C or MoO_xC_y (see Table 6.1), suggesting a size dependent effect with the smaller particles to be more sensitive to form the over-carburized η -phase.¹² Carbon deposition during the carburization reaction is one of the major challenges while producing transition metal carbides, due to the decomposition of the carbonaceous source, in this case CH₄.

By means of TEM analysis it was confirmed that the carbide particles are evenly distributed over the SiO₂ support and no large variations in terms of particle size are observed. Due to the low contrast between the small carbide particles and the support, a reliable particle size distribution could not be extracted (see Figure 6.8) but the sizes measured are in line with the data obtained from *ex situ* XRD. No sign of excessive carbon formation is observed.

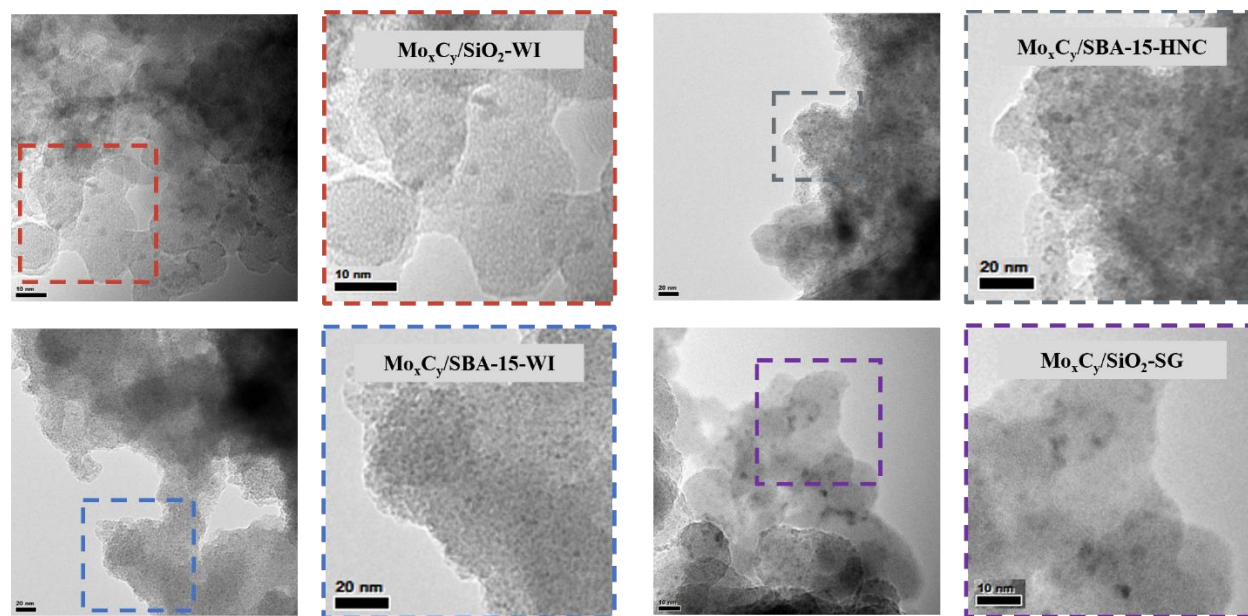


Figure 6.8. TEM micrographs of the freshly carburized samples at 600 °C. No micrographs available for Mo_xC_y/SiO₂-HNC.

SEM-EDS mapping confirms a homogenous distribution of the molybdenum over the support material for all samples, with minimum agglomeration of particles observed (see Figure 6.9).

Raman spectroscopy was employed to further probe the presence of carbonaceous deposits analysing multiple areas of each sample (see Figure 6.10). Mo_xC_y/SiO₂-WI is the only sample which showed some degree of carbon deposits identified by the D-band at 1350 cm⁻¹ and the G-band at 1580 cm⁻¹. These deposits are however not found throughout the sample.

BET analysis on all samples shows slight variations between the samples (see Table K.1). A drop in surface area is observed for Mo_xC_y/SiO₂-WI, compared to the surface area of AEROSIL® 200. Impregnation of an AHM solution onto non-porous SiO₂ does not seem to affect the support structure and the drop in surface area can thus be explained by carbon deposition during the carburization treatment. The samples supported on SBA-15 show a significant drop in surface area compared to the support material, SBA-15, alone. Prior to carburization, the average crystallite size of MoO₃/SBA-15-HNC is about 55 nm. The MoO₃ particles are thus located outside the pore structure, blocking pores, resulting in

the observed increase in average pore width (from 4.1 to 8.5 nm) and decrease in pore volume (from 0.68 to 0.47 cm³ g⁻¹) and BET surface area (from 825 to 209 m² g⁻¹). Carburization of the oxide particles to molybdenum carbide does not change the pore width significantly and the further decrease in BET surface area (147 m² g⁻¹) can be rationalized by the average crystallite size of Mo_xC_y/SBA-15-HNC (3.7 nm), which is close to the average pore diameter of the freshly prepared SBA-15 (4.1 nm), and thus likely causing further pore blockage. For Mo_xC_y/SBA-15-WI, the pore width did not increase much, however a drop in pore volume is the main cause for the loss of surface area. This can either be caused by the filling of the pores by the carbide particles or due to pore breakup of the support occurring during the robust carburization treatment. The surface area of the SiO₂ structure for Mo_xC_y/SiO₂-SG was not determined, however, it was previously confirmed that upon a 20 wt.-% Mo loading, the BET surface area drops from 450 to 86 m²/g.⁵

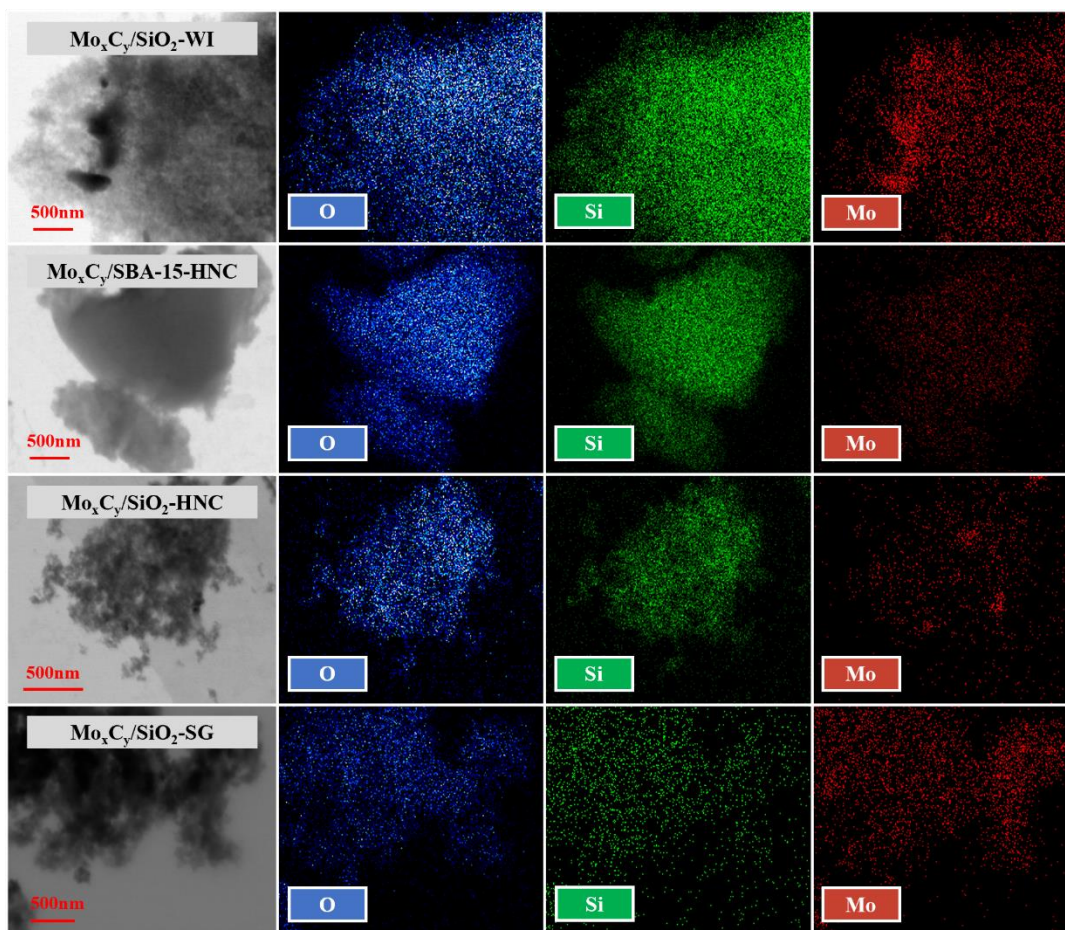


Figure 6.9. SEM-EDS micrographs and elemental mapping of the freshly carburized samples at 600 °C. No micrographs available for Mo_xC_y/SBA-15-WI.

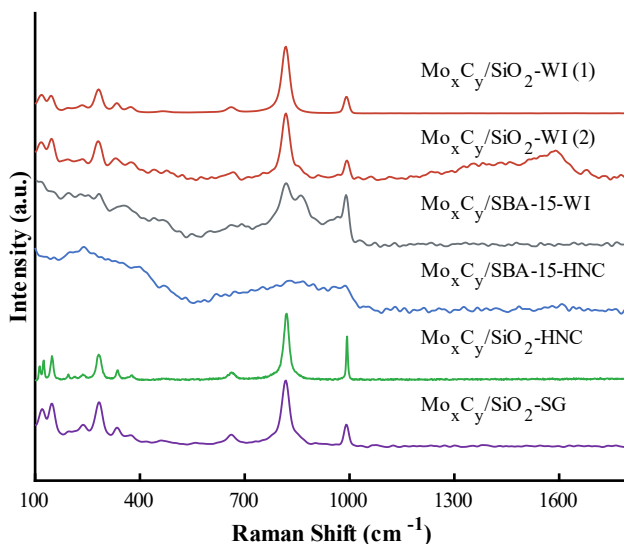


Figure 6.10. Raman spectra of freshly carburized samples at 600 °C.

6.3 CO₂ activation: effect of synthesis technique

The activation of thermodynamically stable CO₂ is the key step in the CO₂-ODH reaction. The formation of CO as function of temperature was used as probing reaction in the present study, both using a fixed-bed reactor set-up and *in situ* XAS. In the reactor studies, CO formation is first observed in the temperature range between 230 °C and 330 °C independent of the synthesis route (see Figure 6.11-A). At higher temperatures, between 530 °C and 580 °C, the CO formation rate increases significantly, reaching a maximum concentration of CO in the reactor outlet gas between 610 °C and 650 °C. Normalization of the CO yield to the Mo content (see Table K.8) shows that Mo_xC_y/SiO₂-WI shows the highest yield of CO at 645 °C. Mo_xC_y/SiO₂-SG, Mo_xC_y/SiO₂-HNC and Mo_xC_y/SBA-15-WI reach the peak formation rate at significantly lower temperatures (620 °C vs. 645 °C) suggesting a higher intrinsic activity or rather a higher affinity for re-oxidation. No correlation can be observed between the average mass specific Mo surface area of all five freshly carburized samples (Table K.8) and the observed CO yield. During the reaction, all five supported samples show oxidation to MoO₂ (see Figure 6.12) with an increased average crystallite size of 17.1 to 29.5 nm (see Table K.3), leading to a significant decrease in the average mass specific Mo surface area. Mo_xC_y/SBA-15-WI contains some leftover η-MoC_{0.59}, which is likely due to higher Mo content in the sample and the larger crystallite sizes observed in the freshly carburized sample (see Table 6.1).

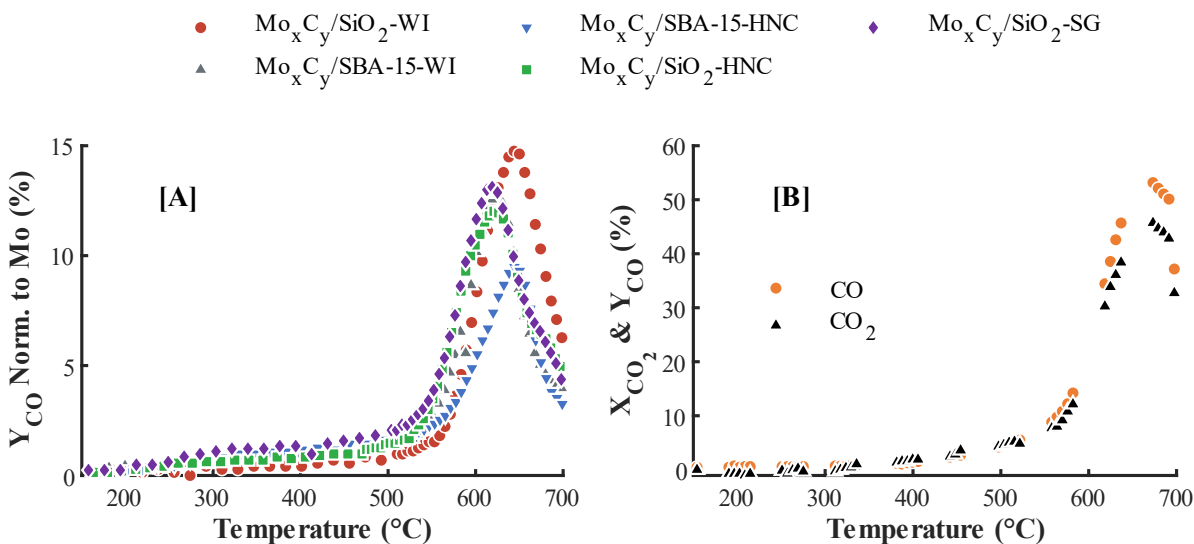


Figure 6.11. Temperature programmed CO₂ activation, with [A] CO yield normalized to mass of Mo content in the catalyst and [B] TP-CO₂ activation over bulk β -Mo₂C. Conditions: heating rate from RT to 700 °C at 1 °C min⁻¹ in 1 vol.-% CO₂/N₂ with a SV of 60 L h⁻¹ g_{cat}⁻¹ at a pressure of 1 atm.

Two main pathways can lead to the formation of CO. Option 1: CO₂ dissociates on the catalyst surface to CO and surface oxygen species, leading to the possible formation of Molybdenum oxycarbide (MoO_xC_y) on the surface and eventually bulk oxide. Option 2: *via* the reverse Boudouard reaction, removing carbon either from earlier deposited surface carbon or from the carbide. To understand which pathway is preferred, a similar CO₂ activation experiment is performed on bulk β -Mo₂C as higher quantities of CO are formed thus limiting uncertainties in data acquisition (see Figure 6.11-B). Surface activation of CO₂ will lead to an equal amount of CO formed compared to CO₂ reacted while the removal of carbon *via* the reverse Boudouard reaction yields two moles of CO per mole of CO₂ reacted. Since there were no other products observed, it is possible to assign all CO₂ reacted to CO formed. At temperatures below 530 °C, the molar rate of CO formed, and CO₂ reacted is equal, which suggests the CO₂ surface activation pathway to be dominant. At higher temperatures, the molar rate of CO formed is larger than CO₂ reacted, but the ratio is lower than 2. This could suggest that initially, due to CO₂ dissociation on the surface, oxygen species on the carbide surface are formed potentially leading to an oxycarbide like structure and subsequently, at temperatures above 530 °C, the surface oxygen species react with the carbon species from the carbide structure, liberating CO and forming MoO₂ (see Figure 6.12). The observed drop in CO formation at around 680 °C and the remaining carbide in the bulk sample, suggest that CO₂ dissociation is happening on the top surface layer(s) only and once these layers are oxidized, the catalyst becomes inactive for CO₂ activation. The incomplete oxidation of the bulk sample is likely due to the larger crystallite size resulting in a dense oxide layer protecting an inner carbide core.

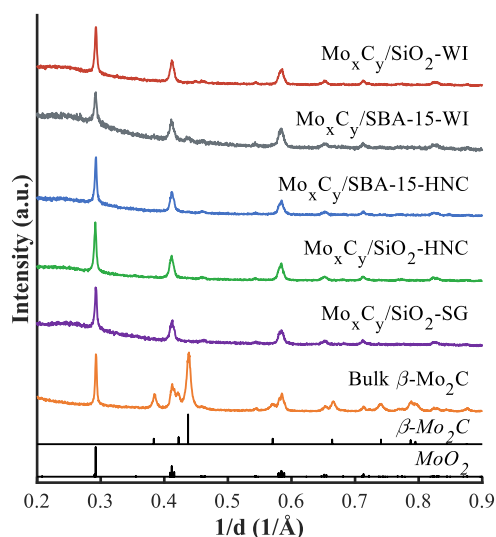


Figure 6.12. XRD patterns of the spent TP-CO₂ activation catalysts.

In situ XAS experiments were performed on three out of the five supported samples: Mo_xC_y/SiO₂-WI (see Figure 6.13), Mo_xC_y/SBA-15-HNC (see Figure 6.15) and Mo_xC_y/SiO₂-SG (see Figure 6.16). Each sample was exposed to an *in situ* carburization treatment followed by a temperature programmed reaction in 1 % CO₂/He. It must be highlighted that the carburization and CO₂ temperature programmed activation conditions vary from the earlier described synthesis and reactor studies. Under carburization conditions, the temperature was ramped to 380 °C (10 °C min⁻¹), followed by a further ramp to 650 °C (2 °C min⁻¹) holding at 650 °C of 2.5 hours. During exposure to CO₂, the temperature was ramped to 330 °C (10 °C min⁻¹) followed by a ramp to 740 °C (5 °C min⁻¹) holding at 740 °C for 1 hour. XAS measurements were taken at room temperature before (referred to as RT-1) and after the two different treatments, and XANES measurements were recorded throughout the temperature ramping. The *in situ* XANES spectra of Mo_xC_y/SiO₂-WI are presented by a top view plot (see Figure 6.13-A, B) accompanied by the linear combination fitting results of the different Mo-phases (see Figure 6.13-C, D). Unlike the *in situ* XRD results (see Figure 5.5), but similar to the *in situ* Raman observations (see Figure 5.6), no clear MoO₃ spectra is observed during the decomposition of the molybdate precursor in the presence of the carburization gas mixture (see Figure 6.14). This can be explained by the differences in temperature ramp rate between XRD (1 °C min⁻¹), Raman (3 °C min⁻¹) and XAS (10 °C min⁻¹) and sample presentation. Note that small differences in signal intensity in the spectra, between RT-1 and MoO₂ can be observed (indicated by the arrow in Figure 6.13-A). Due to the unavailability of further reference materials, RT-1 was used as reference for the molybdate in the XANES LCF.

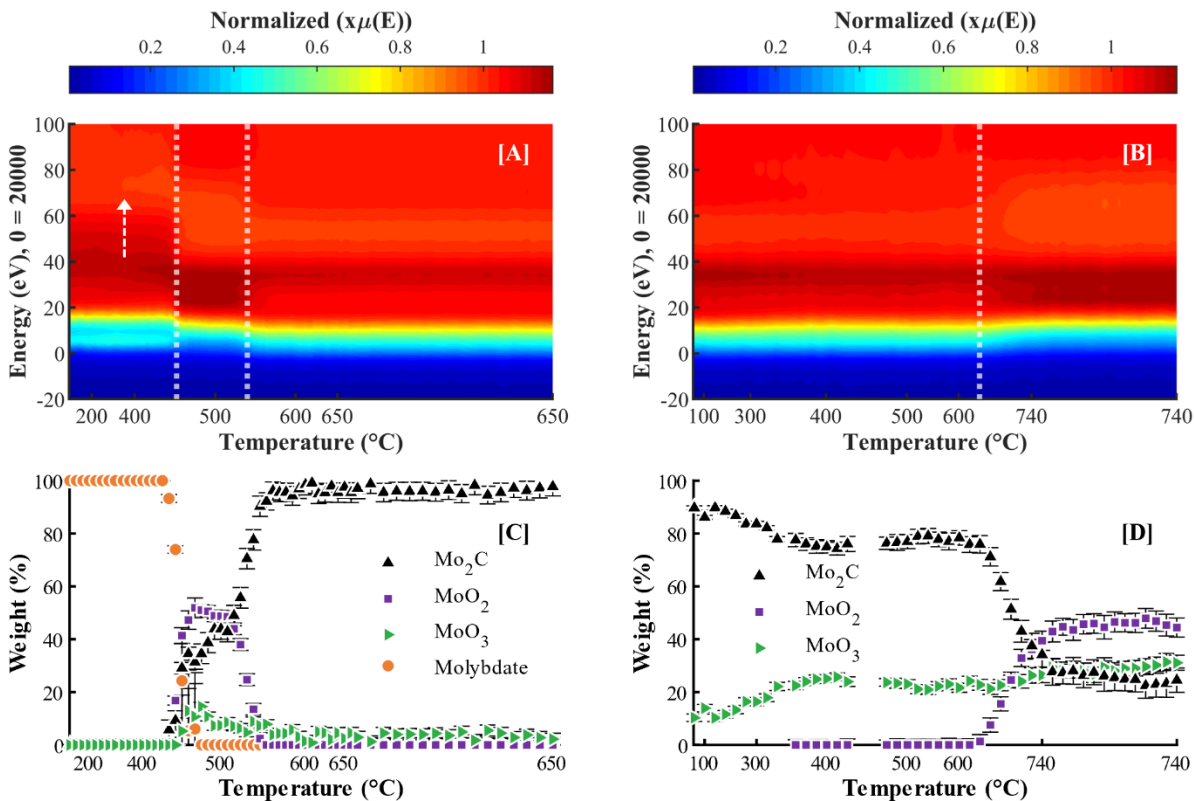


Figure 6.13. *In situ* XANES spectra on Mo_xC_y/SiO₂-WI with [A] carburization treatment and [B] TP-CO₂ activation and their corresponding LCF results in [C] and [D], respectively. For detailed experimental conditions, see section 4.2.14.

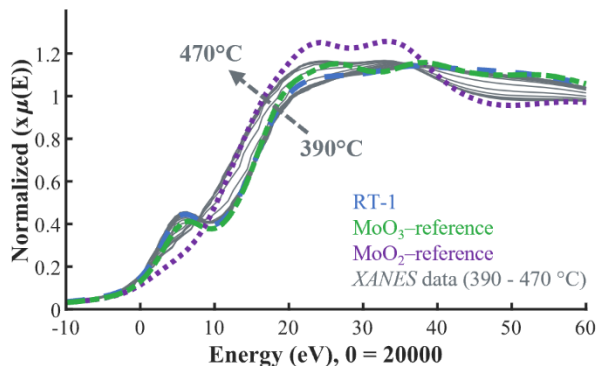


Figure 6.14. Normalized *in situ* XANES spectra of the Mo K edge, of Mo_xC_y/SiO₂-WI during carburization from 390 to 470 °C.

At 450 °C a phase change from the molybdate to MoO₂ is observed (see Figure 6.13-A, C). Linear combination fitting results suggest that the carburization of the formed oxide phase starts almost simultaneously, indicating a much lower carburization onset temperature than observed by XRD, but supporting the earlier described *in situ* Raman observations. The maximum MoO₂ content in the sample was observed to be about 50 wt.-%. At 520 °C the carbide phase becomes the dominant phase, reaching a

95 wt.-% carbide content at 550 °C. No significant change in the Mo-phase composition is observed during the 2.5-hour isothermal conditions at 650 °C.

The *in situ* XANES carburization of $\text{Mo}_x\text{C}_y/\text{SBA-15-HNC}$ displays two significant phase changes from MoO_3 to MoO_2 to Mo_2C (see Figure 6.15-A, C). The reduction of MoO_3 to MoO_2 starts at 460 °C. The formation of the carbide again appears to start simultaneously. The maximum MoO_2 content reached is 42 wt.-% at 500 °C, with the carbide becoming the dominant phase at 510 °C. The final carbide content of 88 wt.-% is observed after about 30 minutes holding at 650 °C, with the remainder being mainly MoO_3 .

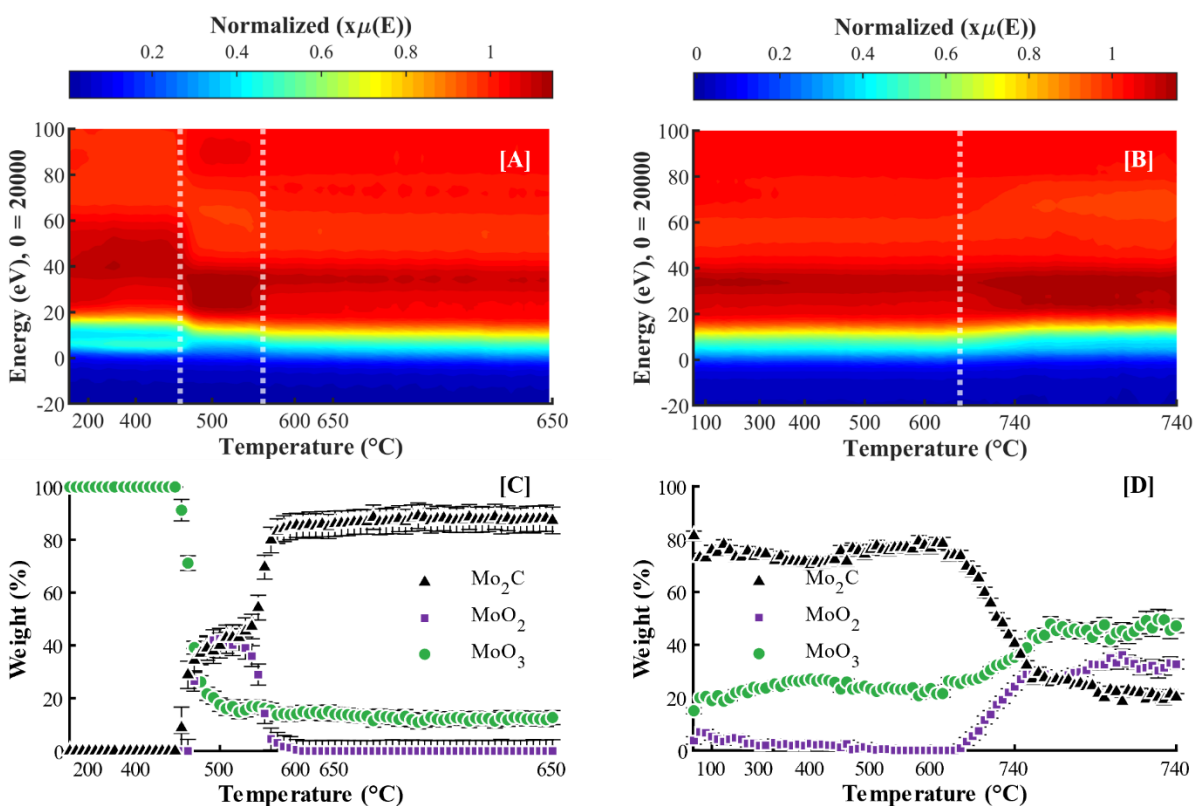


Figure 6.15. *In situ* XANES spectra on $\text{Mo}_x\text{C}_y/\text{SBA-15-HNC}$ with [A] carburization treatment and [B] TP- CO_2 activation and their corresponding LCF results in [C] and [D], respectively. For detailed experimental conditions, see section 4.2.14.

$\text{Mo}_x\text{C}_y/\text{SiO}_2\text{-SG}$, also starting from the MoO_3 phase, shows a similar behaviour during carburization (see Figure 6.16-A, C) with the reduction of MoO_3 starting at 410 °C and simultaneously forming the carbide phase. The maximum MoO_2 content was observed at 470 °C (51 wt.-%) with the carbide phase becoming dominant at 500 °C. The final carbide composition is estimated at 94 wt.-%, mainly balanced by MoO_3 . The observed differences in onset temperatures between the three samples ($\text{SG} < \text{WI} < \text{HNC}$)

are clearly evidencing a dependency of synthesis route and/or type of support material, during the early stages of the carburization process.

The compositions obtained from LCF of the XANES spectra collected at room temperature, after the carburization treatment, are in line with the above observations (see Table 6.2 and Figure G.3). The slight discrepancy between the fitting results of the RT spectra and *in situ* spectra can be rationalized by the noise induced at high temperatures but are within the usual LCF error (± 10 wt.-%). These compositions cannot be directly compared to the samples prepared inside the reactor, due to different carburization protocols with the higher ramp rate to be most likely the main cause for the leftover oxidic species.

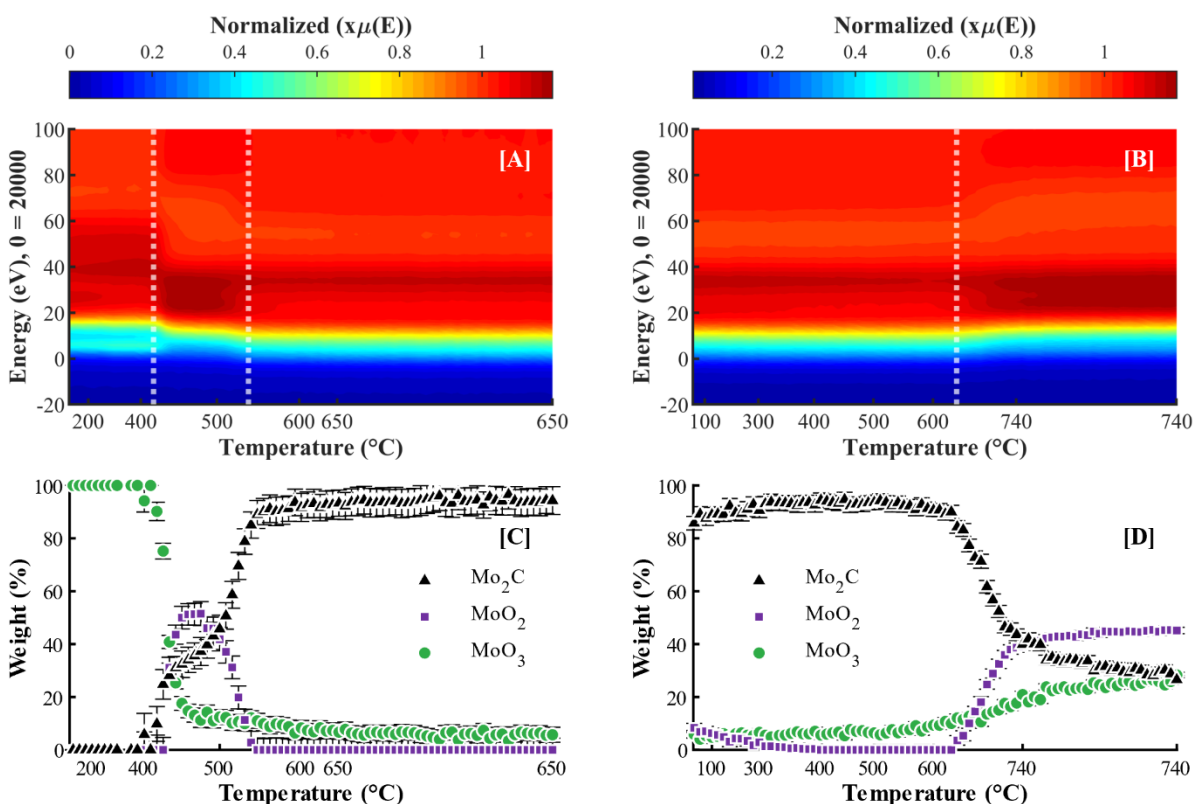


Figure 6.16. *In situ* XANES spectra on Mo_xC_y/SiO₂-SG with [A] carburization treatment and [B] TP-CO₂ activation and their corresponding LCF results in [C] and [D], respectively. For detailed experimental conditions, see section 4.2.14.

EXAFS analysis was performed to further investigate the different Mo oxide/carbide allotropes present in the samples as the normalized XANES spectra do not show clear differences between β -Mo₂C and α -MoC_{1-x} (no reference materials available for η -MoC_{0.59} and MoO_xC_y). In *k*-space, small but clearly visible features can be identified, distinguishing the two carbide phases (indicated by arrows in Figure 6.17-A). These observations confirm that no alpha-carbide phase is present. In *R*-space, the first and second shell, Mo-C and Mo-Mo, are indistinguishable between the alpha and beta carbide phase and each

sample can be fitted with a crystal structure corresponding to the beta-carbide phase. The only difference observed is between 4.5 and 6.0 Å (see Figure 6.17-B). All fits and corresponding fit parameters can be found in Figure G.4 and Table K.7). During the temperature programmed reaction with CO₂ over the freshly carburized samples, one significant step change in the XANES spectra is observed for all samples (see Figure 6.13-B for Mo_xC_y/SiO₂-WI, Figure 6.15-B for Mo_xC_y/SBA-15-HNC and Figure 6.16-B for Mo_xC_y/SiO₂-SG). LCFs of the *in situ* XANES spectra show that the oxidation onset temperature of Mo_xC_y to MoO₂ (and MoO₃) is between 630 and 650 °C. These results confirm the observations made during the reactor studies, despite the difference in temperature ramp rate. This strengthens the previously proposed CO₂ activation mechanism. Contrary to the XRD analysis after the reactor studies, the LCF results of the XAS spectra after CO₂ activation (see Table 6.2) indicate that the carbide does not only oxidize to MoO₂, but also to MoO₃. It is thus suggested that the crystallinity of MoO₃ is insufficient to be observed by XRD, e.g., that amorphous MoO₃ is formed, or it is located at the surface of the particles. A study presented by Solymosi *et al.*¹³ confirms the possible (surface) oxidation of Mo₂C to MoO₃ in the presence of CO₂ by means of XPS analysis. MoO₃ is reported as the dominant species at reaction temperatures of 800 °C.

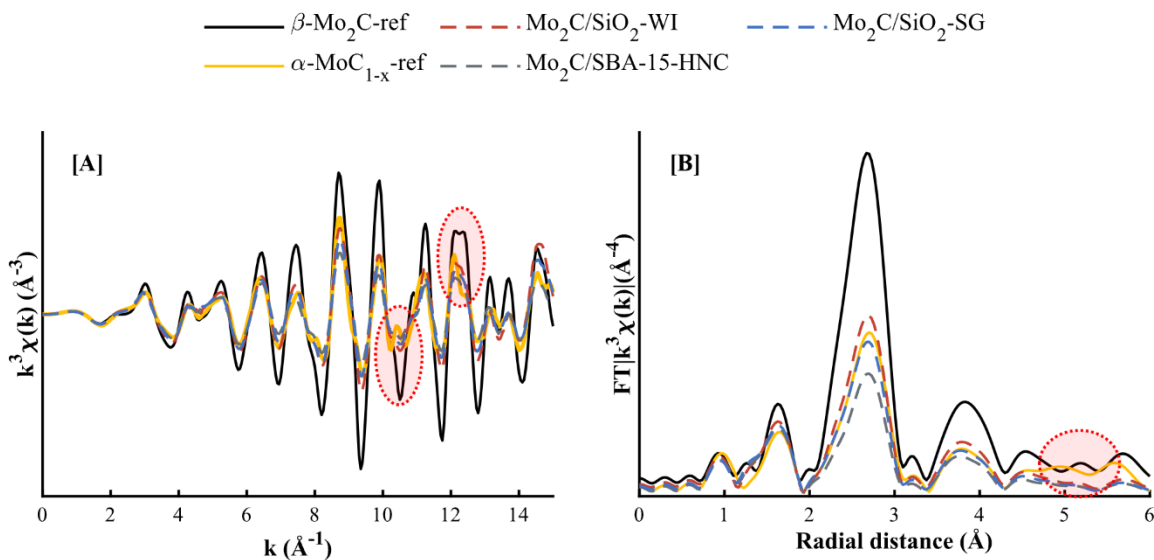


Figure 6.17. k^3 -weighted Mo K edge EXAFS spectra of Mo_xC_y/SiO₂-WI, Mo_xC_y/SBA-15-HNC, Mo_xC_y/SiO₂-WI, β -Mo₂C-reference and α -MoC_{1-x}-reference in [A] k-space and [B] R-space.

Table 6.2. Overview of phase quantification of the XANES spectra *via* linear combination fitting, measured at room temperature after carburization and after TP-CO₂ activation.

Sample	MoO ₃	MoO ₂	β-Mo ₂ C
	wt.-% (error)	wt.-% (error)	wt.-% (error)
Mo _x C _y /SiO ₂ -WI			
Fresh	5.9 (0.8)	0.0 (0.9)	94.1 (1.1)
TP-CO ₂	34.9 (1.0)	49.1 (1.2)	16.0 (1.5)
Mo _x C _y /SBA-15-HNC			
Fresh	12.7 (0.7)	1.6 (0.9)	85.7 (1.1)
TP-CO ₂	35.5 (0.8)	43.2 (0.9)	21.3 (1.2)
Mo _x C _y /SiO ₂ -SG			
Fresh	7.9 (0.7)	2.0 (0.9)	90.1 (1.1)
TP-CO ₂	36.6 (0.7)	45.4 (0.8)	18.0 (1.1)

6.4 RWGS performance: effect of synthesis technique

The samples, Mo_xC_y/SiO₂-WI, Mo_xC_y/SBA-15-WI, Mo_xC_y/SBA-15-HNC and MoO_xC_y/SiO₂-SG, were tested for their RWGS activity in a range of reaction conditions with varying CO₂ : H₂ ratios. At every temperature and H₂ to CO₂ feed ratio, the thermodynamic equilibrium conversion (X_{eq}) of the RWGS reaction was calculated for comparison to make sure that the observed conversion is not limited by thermodynamics. At a temperature of 400 °C, a H₂ to CO₂ ratio of 1 ($X_{eq} = 22.1\%$) and a space velocity of 60 L h⁻¹ g⁻¹_{cat} (of which 50 vol.-% is argon), the catalysts Mo_xC_y/SiO₂-WI* and Mo_xC_y/SBA-15-HNC show very similar conversions, close to X_{eq} , with $X_{CO_2} = 17\%$ and $X_{H_2} = 19\%$ for Mo_xC_y/SiO₂-WI* (see Figure 6.18-A, C). Mo_xC_y/SBA-15-WI is less active with a CO₂ and H₂ conversion of 11% and 12%, respectively. Freshly carburized, the molybdenum phases of both catalysts prepared *via* wetness impregnation consist of approximately 80 wt.-% η-MoC_{0.59} and 20 wt.-% β-Mo₂C (see Table 6.1). While the SBA-15 supported sample displays a slightly larger crystallite size for both carbide phases, this is somewhat overcompensated by the higher Mo content (see Table K.1 and Table K.8). During the exposure to RWGS conditions at different temperatures (see Figure 6.18-A), the carbide phase of Mo_xC_y/SBA-15-WI transitions fully into a pure η-MoC_{0.59} without crystallite growth, while the composition of Mo_xC_y/SiO₂-WI* remains largely unchanged with some crystallite growth (see Table K.6 and Table K.8). No oxidation to MoO₂ was observed (see Figure 6.19). At what stage of the reaction the

transition occurs is unfortunately currently unknown. The higher activity of the SiO₂ supported catalyst can be associated to the retention of the beta carbide phase which has previously been identified as more active in a study by Wan *et al.*¹⁴. Mo_xC_y/SBA-15-HNC, only tested at 400 °C for 24 hours, also transforms to a pure η-MoC_{0.59}, starting from a 30 wt.-% oxycarbide content (see Table 6.1 and Table K.6). The catalyst's activity is on par with Mo_xC_y/SiO₂-WI* and outperforms Mo_xC_y/SBA-15-WI by 100 °C (see Figure 6.18-A at 12 to 24 hours TOS) while displaying very comparable phase compositions and crystallite sizes (analysis of the spent catalysts, see Table K.6). The overall carbide surface area appears not to be responsible for the observed difference in performance, which is mirrored in the formation rate of CO in the CO₂ activation experiments between 330 and 580 °C (see Figure 6.11-B). A previous study by Kurlov *et al.* suggests that molybdenum oxycarbide is the active phase for the RWGS reaction.¹⁵ The different synthesis routes chosen can affect other parameters such as the location of the carbide crystals on the support.

All catalysts show over 98 % CO selectivity and less than 1 % CH₄ selectivity (see Figure 6.11-E, F). This clearly indicates that the thermodynamically more favoured CO₂ and CO methanation reactions (see Figure 5.1), are kinetically suppressed by the catalyst. The observed low concentrations of CH₄ formed can, in combination with experimental uncertainties, account for the observed temperature and sample independent 2-3 % over stoichiometric hydrogen conversion.

Increasing the H₂ to CO ratio at a reaction temperature of 400 °C is thermodynamically a more favourable condition for CO₂ methanation. However, when activating CO₂ together with green hydrogen to produce synthesis gas and subsequent fuels and chemicals, it is of interest to operate the RWGS at a higher than stoichiometric H₂ to CO₂ ratios to achieve higher CO₂ conversions and yield the desired synthesis gas composition at the reactor outlet.¹⁶ Both Mo_xC_y/SiO₂-WI (in this experiment referred to as Mo_xC_y/SiO₂-WI**), the best performing catalyst at varying reaction temperatures, and Mo_xC_y/SiO₂-SG, the catalyst with the apparent most facile CO₂ activation, were studied at feed ratios of 1, 3.5 and 7 and an increased space velocity of 120 L h⁻¹ g⁻¹_{cat} in a single experiment with intermittent flushing to set the new feed composition (see Figure 6.11-B, D, F). At all conditions, both catalysts achieve similar activity and selectivity. With a feed ratio of 1, X_{CO₂} is around 10 %, with minimum deactivation over 24 hours TOS and X_{H₂} of 12 to 14 %. Increasing the feed ratio to 3.5 (X_{eq} = 39.0 %) the CO₂ conversion increases to about 20 % for both catalysts, with again minimum deactivation observed after 24 hours TOS. A hydrogen conversion of 6-7 % corresponds to a 1:1 conversion ratio in moles. A feed ratio of 7 (X_{eq} = 50.7 %) further increases conversion levels without changing the stability of the catalyst. At the highest feed ratio, a methane selectivity of approximately 1.2 % is recorded, which decreases steadily with time on stream to below 1 %. While in the freshly carburized samples Mo_xC_y/SiO₂-WI and Mo_xC_y/SiO₂-SG

show clear differences, namely 20-24 wt.-% of the carbide phase in form of β - Mo_2C or oxycarbide for $\text{Mo}_x\text{C}_y/\text{SiO}_2\text{-WI}$ and $\text{Mo}_x\text{C}_y/\text{SiO}_2\text{-SG}$ respectively, the composition of the spent catalysts is nearly identical. Compared to the RWGS experiment at different temperatures, the β - Mo_2C component is hardly retained resulting in a predominantly η - $\text{MoC}_{0.59}$ active phase with very similar crystallite sizes.

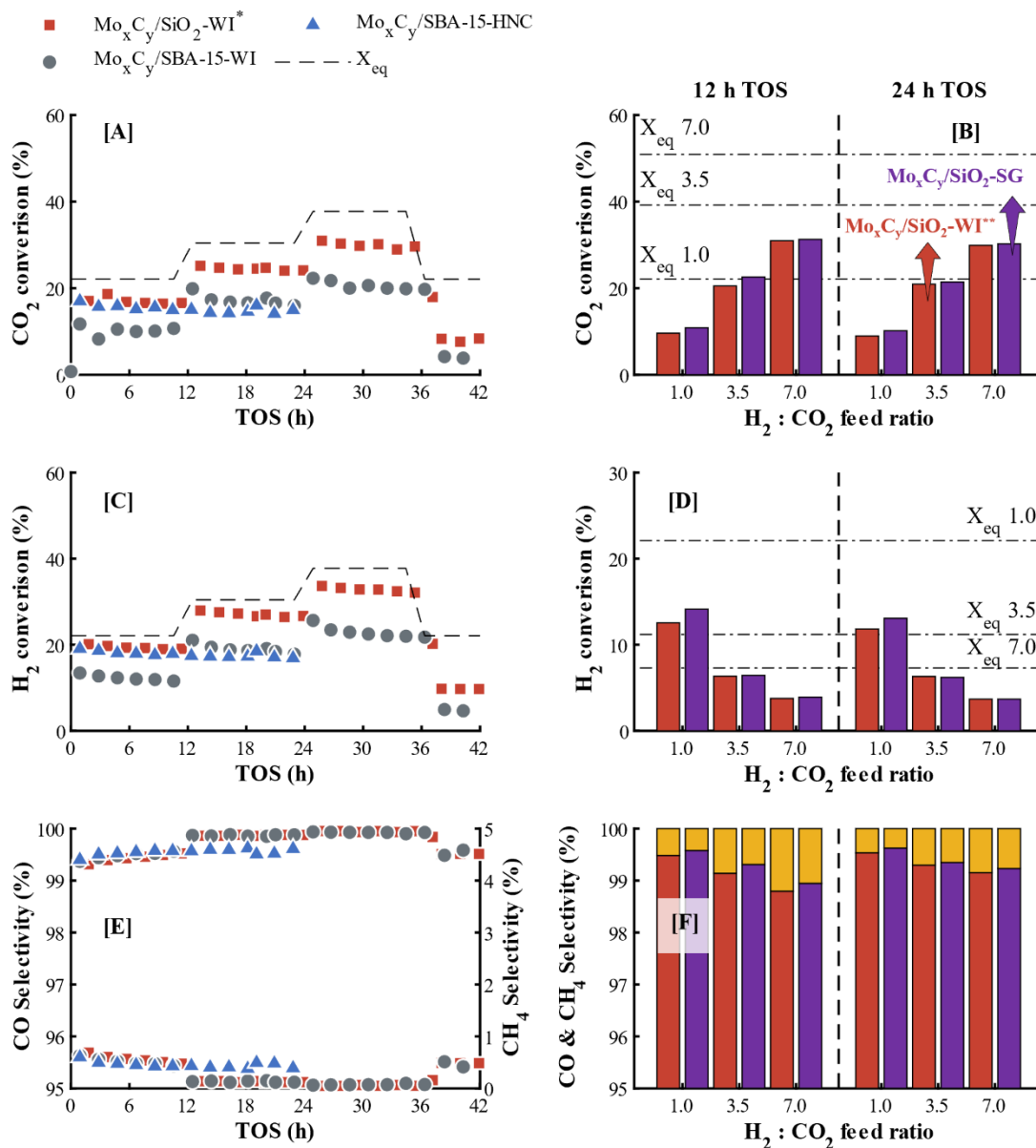


Figure 6.18. [A, B] CO_2 conversion, [C, D] H_2 conversion and [E, F] CO and CH_4 selectivity, of [A, C, E] $\text{Mo}_x\text{C}_y/\text{SiO}_2\text{-WI}^*$ and $\text{Mo}_x\text{C}_y/\text{SBA-15-WI}$ and $\text{Mo}_x\text{C}_y/\text{SBA-15-HNC}$, with $T = 400\text{ }^\circ\text{C}$ (0-12 hours TOS), $T = 500\text{ }^\circ\text{C}$ (12-24 hours TOS), $T = 600\text{ }^\circ\text{C}$ (24-36 hours TOS) and $400\text{ }^\circ\text{C}$ (36-42 hours TOS). For $\text{Mo}_x\text{C}_y/\text{SBA-15-HNC}$, $T = 400\text{ }^\circ\text{C}$ (0-24 hours TOS). H_2/CO_2 ratio = 1, $\text{SV} (\text{CO}_2 + \text{H}_2) = 60\text{ L h}^{-1}\text{ g}_{\text{cat}}^{-1}$. [B, D, F] $\text{Mo}_x\text{C}_y/\text{SiO}_2\text{-WI}^*$ and $\text{Mo}_x\text{C}_y/\text{SiO}_2\text{-SG}$: $T = 400\text{ }^\circ\text{C}$, H_2/CO_2 ratio of 1.0, 3.5 or 7.0. $\text{SV} = 120\text{ L h}^{-1}\text{ g}_{\text{cat}}^{-1}$. Thermodynamic equilibrium conversions for CO_2 and H_2 are displayed by X_{eq} .

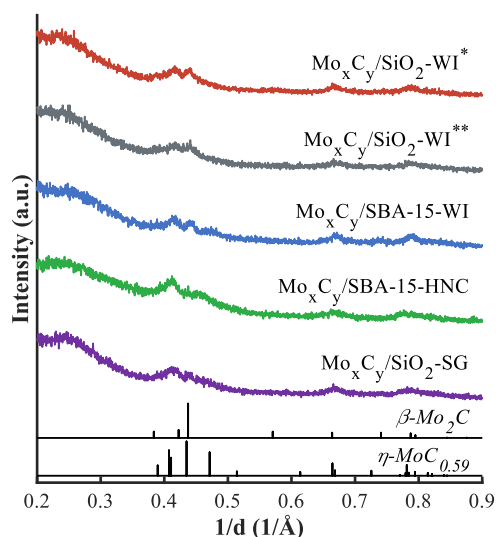


Figure 6.19. XRD patterns of the spent catalysts after exposure to various RWGS conditions.

For a closer comparison of the catalytic performance, the accumulated CO formed per feed ratio is calculated as function of time on stream (see Figure 6.20). It is apparent that at a feed ratio of $H_2:CO_2$ of 1, the catalyst prepared *via* the sol gel technique shows slight advantages compared to Mo_xC_y/SiO_2-WI^{**} , but at a feed ratio of 3.5 this trend is reversed. No difference in performance is observed at the highest hydrogen concentration ($H_2:CO_2$ of 7). As discussed earlier, Mo_xC_y/SiO_2-SG also shows the highest propensity to activate pure CO_2 which could be an indication of an enhanced redox activity. Such an enhancement is expected to be most prominent in the RWGS at low H_2 partial pressures.

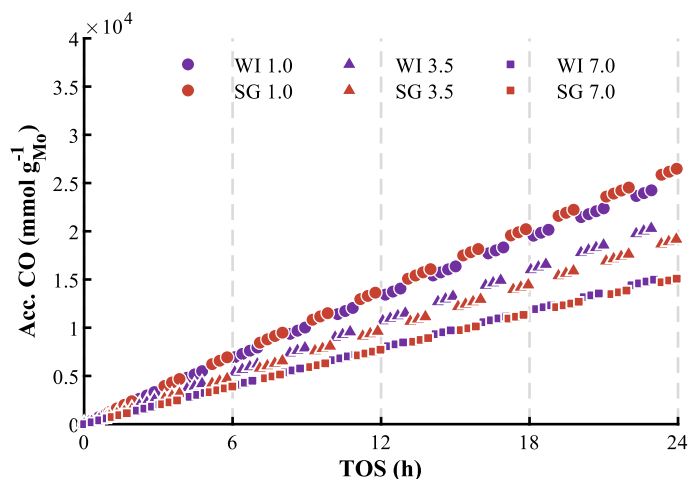


Figure 6.20. Accumulative formation of CO as a function of time under RWGS conditions normalized to the Mo content in the catalysts. Mo_xC_y/SiO_2-WI^{**} (red) and Mo_xC_y/SiO_2-SG (purple): $T = 400\text{ }^\circ\text{C}$ for 24 hours at H_2/CO_2 ratio of 1.0, 3.5 or 7.0. $SV = 120\text{ L h}^{-1}\text{ g}_{cat}^{-1}$.

6.5 CO₂-ODH performance: effect of synthesis technique

The CO₂-ODH catalytic performance of Mo_xC_y/SiO₂-WI is thoroughly investigated in section 5.3 within a range of reaction conditions. In this section, the activity of supported Mo_xC_y nanoparticles, synthesized and supported *via* three different techniques (WI, HNC and SG) are evaluated for their CO₂-ODH performance. All catalysts were tested under CO₂-ODH conditions for 24 hours with a reaction temperature of 600 °C at atmospheric pressure with a space velocity of 15 L h⁻¹·g_{cat}⁻¹ and an equimolar feed of CO₂ and C₂H₆ diluted in 50 vol.-% argon (see Figure 6.21 and Figure B.2). Ethane conversion is under these conditions thermodynamically limited at 28.6 % for CO₂-ODH, 98.5 % for dry-reforming (DR) and 29.7 % for direct dehydrogenation (DH).¹⁷

The performance of the catalysts prepared *via* different synthesis techniques, mainly differs during the first 12 hours TOS. After 1 hour TOS, Mo_xC_y/SiO₂-WI, Mo_xC_y/SBA-15-HNC and Mo_xC_y/SiO₂-HNC show similar ethane conversions, between 5 and 5.8 %. Mo_xC_y/SiO₂-SG achieves a much lower $X_{C_2H_6}$ of 2.1 % (see Figure 6.21). With time on stream, catalyst deactivation is observed for all three catalysts, although each sample shows a slight recovery in $X_{C_2H_6}$ between 3 and 12 hours TOS. This is believed to occur due to the formation of a ‘metastable’ MoO_xC_y phase under reaction conditions. After 12 hours TOS the difference in conversion levels between the four catalysts has become less, achieving $X_{C_2H_6}$ of approximately 1.6-2.9 %. In terms of CO₂ conversion, X_{CO_2} (see Figure B.2), a similar trend is observed for all four catalysts, however the conversion is slightly lower and decreases faster with time on stream, reaching close to 0 % after 12-18 hours TOS. A CO₂-ODH performing catalyst should achieve a stoichiometric conversion ratio ($X_{C_2H_6}/X_{CO_2}$) of 1. A ratio lower than 1 can indicate, but is not limited to, an increased dry-reforming (DR) activity and above 1 an increased direct dehydrogenation (DH) activity. After 1 hour TOS, Mo_xC_y/SiO₂-WI, Mo_xC_y/SBA-15-HNC and Mo_xC_y/SiO₂-HNC achieve conversion ratios between 1.13 and 1.29, respectively, but Mo_xC_y/SiO₂-SG records a ratio of 1.9, This suggests that Mo_xC_y/SiO₂-SG converts almost double the amount of ethane compared to CO₂ (see Figure B.2). All three catalysts show a sharp increase in $X_{C_2H_6}/X_{CO_2}$ with TOS indicating a significantly increased DH activity with limited CO₂ activation. A CO₂-ODH selective catalyst can reach a maximum C₂H₄ selectivity of 67 C-% and a CO selectivity of 33 C-% (as indicated in section 4.3.4), calculated based on the total carbonaceous products (C₂H₄, CH₄ and CO). Overall, all four catalysts show an increase in C₂H₄ selectivity (from approximately 60 to 80 C-%) with decreasing C₂H₆ conversion. The slight differences in selectivity observed between the three catalysts correlate with the earlier discussed conversion ratios. Mo_xC_y/SiO₂-SG reported the highest conversion ratios, suggesting a favoured DH mechanism, which aligns with the higher ethylene selectivity. Mo_xC_y/SiO₂-WI achieves the lowest conversion ratios, with the

lowest ethylene selectivity. Only a trace amount of CH₄ is observed for all four catalysts, correlating to a maximum selectivity of 2.5 C-%. No other hydrocarbon products are detected. The remaining product selectivity is balanced by CO (decreasing from 40 to 20 C-%). The high C₂H₄ selectivity and low CO selectivity suggest that all three catalysts mainly perform the CO₂-ODH reaction mechanism, with an enhanced DH activity further increasing with TOS. The DR of ethane and the methanation reaction are successfully suppressed. In terms of C₂H₄ yield, Mo_xC_y/SiO₂-WI and Mo_xC_y/SBA-15-HNC achieved initially the highest yield with 4.7-4.9 % after 1 hour TOS. Thereafter, Mo_xC_y/SiO₂-WI is swiftly outperformed by Mo_xC_y/SiO₂-HNC (see Figure 6.21), but Mo_xC_y/SBA-15-HNC remains the most efficient ethylene producing catalyst, up until 21 hours TOS. After 21 hours TOS, the ethylene yield of all four catalysts decreased to about 0.9-1.2 %.

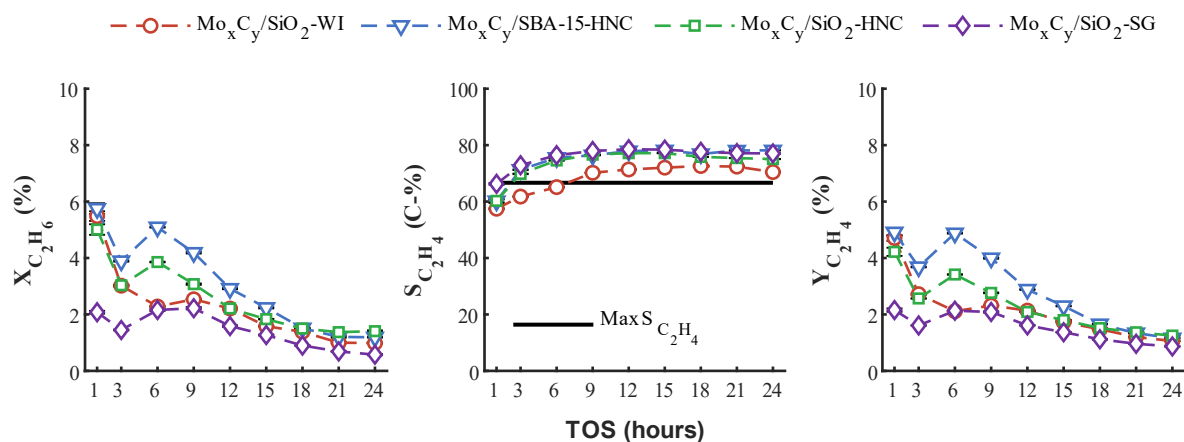


Figure 6.21. C₂H₆ conversion, C₂H₄ selectivity and C₂H₄ yield, of Mo_xC_y/SiO₂-WI, Mo_xC_y/SBA-15-HNC, Mo_xC_y/SiO₂-HNC and Mo_xC_y/SiO₂-SG evaluated under the following CO₂-ODH conditions: T = 600 °C, P = 1 atm, SV = 15 L h⁻¹ g_{cat}⁻¹, CO₂:C₂H₆:Ar = 1:1:2. Theoretical maximum C₂H₄ selectivity for CO₂-ODH indicated by solid black line.

The activity and selectivity trend observed between the catalysts can potentially be linked to the different carbide phases present. Mo_xC_y/SiO₂-WI and Mo_xC_y/SiO₂-HNC contain β-Mo₂C after carburization, previously shown to effectively activate CO₂.¹⁸ Mo_xC_y/SiO₂-SG and Mo_xC_y/SBA-15-HNC contain MoO_xC_y, previously suggested to play a prominent role in the activation of ethane¹⁹, without any (visible by XRD) presence of β-Mo₂C. The initial high activity of Mo_xC_y/SiO₂-WI and Mo_xC_y/SiO₂-HNC, can thus be explained by the higher activity towards CO₂ bond scission over the β-Mo₂C allotrope, producing oxygen surface species which possibly react faster with ethane, than Mo_xC_y/SiO₂-SG, which contains MoO_xC_y and possibly requires the removal of an oxygen from the oxycarbide lattice *via* a Mars van Krevelen type mechanism. The higher activity observed for Mo_xC_y/SBA-15-HNC does not agree with this but can be explained by the higher mass specific Mo surface area (see Table K.8) as well as a slightly higher MoO_xC_y content, supplying more active oxygen sites. This assumes that the CO₂ activation

efficiency of the η -carbide phase is significantly weaker playing a minor role in the activity of the sample. Similar observations were made during the RWGS experiments (see section 6.4) where the β -carbide and MoO_xC_y were suggested to be more active than the η -carbide phase.²⁰ Due to the large amount of oxygen surface species produced during CO_2 -ODH, the β - Mo_2C (and parts of η - $\text{MoC}_{0.59}$) in $\text{Mo}_x\text{C}_y/\text{SiO}_2$ -WI and $\text{Mo}_x\text{C}_y/\text{SiO}_2$ -HNC (quickly) oxidize to MoO_2 , whereas $\text{Mo}_x\text{C}_y/\text{SiO}_2$ -SG only loses about 10 wt.-% of its original 44.2 wt.-% MoO_xC_y to MoO_2 (see Figure 6.22 for the respective XRD patterns and Table K.2 for the quantifications from Rietveld refinement).

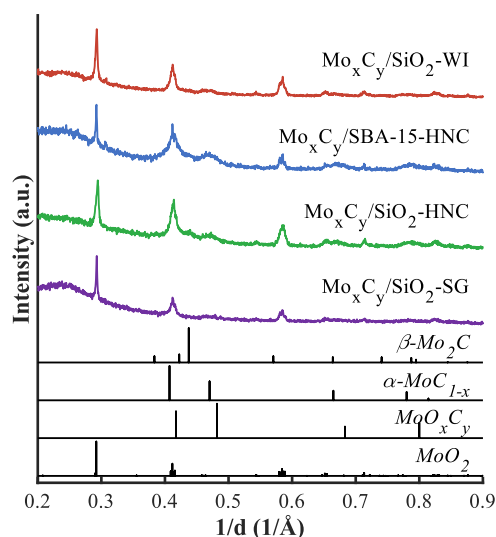


Figure 6.22. XRD patterns of the spent CO_2 -ODH catalysts.

The formation of MoO_3 under reaction conditions is not favoured thermodynamically (see Figure 5.4 in section 5.1), yet small reflexes in the XRD pattern of $\text{Mo}_x\text{C}_y/\text{SiO}_2$ -WI are observed, with the (0 2 1) plane at 0.3 1/Å being the most intense, which can only be assigned to MoO_3 . An optical inspection of $\text{Mo}_x\text{C}_y/\text{SiO}_2$ -WI post CO_2 -ODH reaction in the quartz reactor confirms the presence of MoO_3 (see Figure 6.23). A small section at the inlet side of the catalyst bed turned from black (Mo_xC_y) to light blue, the colour of MoO_3 . The SiO_2 supported Mo_xC_y catalysts, prepared *via* three different synthesis techniques, show minimal differences on the CO_2 -ODH performance with all three catalysts show promising selectivity towards ethylene, however significant catalyst deactivation with TOS could not be avoided. The main deactivation pathway of the catalysts is determined to be the oxidation of the active carbide phase to the inactive MoO_2 phase. The CO_2 is activated at a faster rate than C_2H_6 , leading to a large amount of unreacted oxygen surface species on the catalyst surface to react with the carbide instead and oxidizing the catalyst. To increase catalysts stability, the rate of removal of the oxygen surface species, by means of ethane activation to prevent re-oxidation must be enhanced.

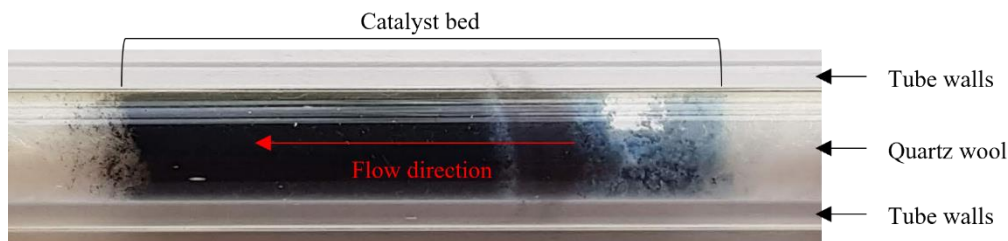


Figure 6.23. Optical inspection of $\text{Mo}_x\text{C}_y/\text{SiO}_2\text{-WI}$ post $\text{CO}_2\text{-ODH}$ reaction in the quartz reactor.

Raman analysis of the spent samples only revealed low intensity D- and G-bands for $\text{Mo}_x\text{C}_y/\text{SiO}_2\text{-WI}$, $\text{Mo}_x\text{C}_y/\text{SiO}_2\text{-HNC}$ and $\text{Mo}_x\text{C}_y/\text{SiO}_2\text{-SG}$ (see Figure 6.24). Unfortunately, no Raman spectra was obtained for $\text{Mo}_x\text{C}_y/\text{SBA-15-HNC}$. The limited intensity for the D- and G-band does not necessarily mean there is only limited carbon deposition occurring under the applied reaction conditions. Previous spent samples evaluated at a $\text{CO}_2\text{-ODH}$ reaction temperature of $550\text{ }^\circ\text{C}$ and $650\text{ }^\circ\text{C}$ (see Figure 5.17 in section 5.3) revealed higher D- and G-band intensities.

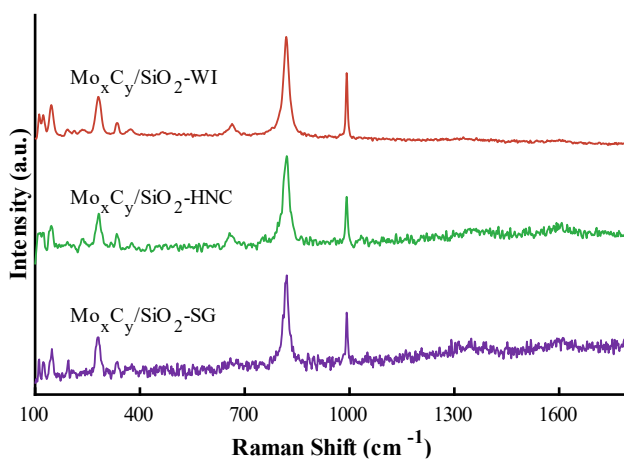


Figure 6.24. Raman spectra of the spent $\text{CO}_2\text{-ODH}$ catalysts. No data available for $\text{Mo}_x\text{C}_y/\text{SBA-15-HNC}$.

6.6 Concluding remarks

Preparation of Mo_xC_y nanoparticles, supported on a SiO_2 or SBA-15 support, yielded a variation in Mo_xC_y crystal phase composition, yet all achieved well dispersed nanoparticles within a similar crystallite size range. The presence of a MoO_xC_y phase in $\text{Mo}_x\text{C}_y/\text{SBA-15-HNC}$ and $\text{Mo}_x\text{C}_y/\text{SiO}_2\text{-SG}$, but not in the other samples, confirms the sensitivity and complexity of the carburization process, specifically at such small particle size.

Under RWGS conditions, all catalysts tested show high CO₂ conversion (up to 30 %) with an outstanding CO selectivity of above 99 %, even at high H₂ to CO₂ ratios of up to 7:1. This clearly shows the kinetic suppression of the thermodynamically favoured CO and CO₂ methanation. H₂ readily removes formed oxygen surface species forming H₂O, preventing the oxidation of the catalyst. Comparing the wetness impregnation catalysts, with comparable carbide phase composition and estimated carbide surface area after the carburization, the SiO₂ supported sample outperforms the SBA-15-supported sample at all tested temperatures. During the reaction, the β -carbide contribution converts completely into η -MoC_{0.59} over the SBA-15 sample, with no such phase change observed on the SiO₂ supported catalyst. When the MoO₃ hybrid nanocrystals are deposited on SBA-15, they perform on par with Mo_xC_y/SiO₂-WI, although the initial mixture of MoO_xC_y and η -MoC_{0.59} converts into 100 % η -MoC_{0.59} after only 24 hours TOS at the lowest reaction temperature. Mo_xC_y/SiO₂-WI and Mo_xC_y/SiO₂-SG showed very similar behaviour, despite that Mo_xC_y/SiO₂-SG is shown to oxidize at much lower temperatures in a diluted CO₂ stream, suggesting different redox behaviour. Only at the stoichiometric feed ratio, Mo_xC_y/SiO₂-SG seems to be slightly more active. Maybe, the effect of a material-specific higher redox activity is suppressed at higher hydrogen partial pressures. While Mo_xC_y/SiO₂-WI, Mo_xC_y/SiO₂-SG, and Mo_xC_y/SiO₂-HNC show a very similar catalytic performance, the slightly improved activity for the SG and HNC samples could suggest that MoO_xC_y can activate CO₂ in the same mechanism as β -Mo₂C on the C atoms, while also providing a Mars van Krevelen-type mechanism *via* the O atoms. The previously proposed formate route (formation of COOH intermediates species) can neither be confirmed nor ruled out with the presented data and will require further in situ investigations.

CO₂-ODH performance of the catalysts showed the largest variations in the first 12 hours TOS. Thereafter, the catalysts deactivate to similar conversion levels. All catalysts show to predominantly perform the CO₂-ODH pathway, with an increased occurrence of the DH pathway with time on stream. The activity of the catalyst can potentially be linked to their respective carbide compositions, suggesting a higher activity for the β -Mo₂C and MoO_xC_y phases over η -MoC_{0.59}. The lower activity for η -MoC_{0.59} is likely due to the higher C/Mo ratio in the sample. Catalyst deactivation was observed through both oxidation of the carbide phase to MoO_x and carbon deposition. Mo_xC_y/SBA-15-HNC seems to be the most efficient ethylene producing catalyst, likely due to the higher mass specific Mo surface area and the highest MoO_xC_y content (and lowest η -MoC_{0.59} content).

References

1. O. Knacke, O. Kubaschewski and K. Hesselmann, *Thermochemical properties of inorganic substances*, Springer-Verlag, Berlin, 2nd edn., 1991.
2. W. Han, P. Yuan, Y. Fan, H. Liu and X. Bao, Synthesis, self-assembly and disassembly of mono-dispersed Mo-based inorganic–organic hybrid nanocrystals, *Journal of Materials Chemistry*, 2012, **22**, 12121-12127.
3. W. Han, P. Yuan, Y. Fan, G. Shi, H. Liu, D. Bai and X. Bao, Preparation of supported hydrodesulfurization catalysts with enhanced performance using Mo-based inorganic–organic hybrid nanocrystals as a superior precursor, *Journal of Materials Chemistry*, 2012, **22**, 25340-25353.
4. S. B. Umbarkar, A. V. Biradar, S. M. Mathew, S. B. Shelke, K. M. Malshe, P. T. Patil, S. P. Dagde, S. P. Niphadkar and M. K. Dongare, Vapor phase nitration of benzene using mesoporous MoO₃/SiO₂ solid acid catalyst, *Green Chemistry*, 2006, **8**, 488.
5. A. P. Amrute, A. Bordoloi, N. Lucas, K. Palraj and S. B. Halligudi, Sol–Gel Synthesis of MoO₃/SiO₂ Composite for Catalytic Application in Condensation of Anisole with Paraformaldehyde, *Catalysis Letters*, 2008, **126**, 286-292.
6. A. Hanif, X. T., A. P. E. York, J. Sloan and M. L. H. Green, Study on the Structure and Formation Mechanism of MoC, *Chemical Materials*, 2002, **14**, 1009-1015.
7. P. Liang, H. Gao, Z. Yao, R. Jia, Y. Shi, Y. Sun, Q. Fan and H. Wang, Simple synthesis of ultrasmall β -Mo₂C and α -MoC_{1-x} nanoparticles and new insights into their catalytic mechanisms for dry reforming of methane, *Catalysis Science & Technology*, 2017, **7**, 3312-3324.
8. M. Tsuji, T. Miyao and S. Naito, Remarkable Support Effect of ZrO₂ upon the CO₂ Reforming of CH₄ over Supported Molybdenum Carbide Catalysts, *Catal. Lett.*, 2000, **69**, 195-198.
9. Y. Ma, G. Guan, C. Shi, A. Zhu, X. Hao, Z. Wang, K. Kusakabe and A. Abudula, Low-temperature steam reforming of methanol to produce hydrogen over various metal-doped molybdenum carbide catalysts, *International Journal of Hydrogen Energy*, 2014, **39**, 258-266.
10. P. Delporte, F. d. r. Meunier, C. Pham-Huu, P. Vennegues, M. J. Ledoux and J. Guille, Physical characterization of molybdenum oxycarbide catalyst; TEM, XRD and XPS, *Catalysis Today*, 1995, **23**, 251-267.
11. N. V. Y. Scarlett and I. C. Madsen, Quantification of phases with partial or no known crystal structures, *Powder Diffraction*, 2012, **21**, 278-284.
12. A. Shrestha, X. Gao, J. C. Hicks and C. Paolucci, Nanoparticle Size Effects on Phase Stability for Molybdenum and Tungsten Carbides, *Chemistry of Materials*, 2021, **33**, 4606-4620.
13. F. Solymosi, A. Oszkó, T. Bánsági and P. Tolmascov, Adsorption and Reaction of CO₂ on Mo₂C Catalyst, *The Journal of Physical Chemistry B*, 2002, **106**, 9613-9618.
14. C. Wan, Y. N. Regmi and B. M. Leonard, Multiple phases of molybdenum carbide as electrocatalysts for the hydrogen evolution reaction, *Angew Chem Int Ed Engl*, 2014, **53**, 6407-6410.
15. A. Kurlov, X. Huang, E. B. Deeva, P. M. Abdala, A. Fedorov and C. R. Muller, Molybdenum carbide and oxycarbide from carbon-supported MoO₃ nanosheets: phase evolution and DRM catalytic activity assessed by TEM and in situ XANES/XRD methods, *Nanoscale*, 2020, **12**, 13086-13094.
16. H. Kirsch, U. Sommer, P. Pfeifer and R. Dittmeyer, Power-to-fuel conversion based on reverse water-gas-shift, Fischer-Tropsch Synthesis and Hydrocracking: Mathematical modeling and simulation in Matlab/Simulink, *Chemical Engineering Science*, 2020, **227**, 115930.
17. S. Raseale, W. Marquart, K. Jeske, G. Prieto, M. Claeys and N. Fischer, Supported Fe_xNi_y catalysts for the co-activation of CO₂ and small alkanes, *Faraday Discuss*, 2021, **229**, 208-231.
18. S. Posada-Perez, F. Vines, P. J. Ramirez, A. B. Vidal, J. A. Rodriguez and F. Illas, The bending machine: CO₂ activation and hydrogenation on delta-MoC(001) and beta-Mo₂C(001) surfaces, *Phys Chem Chem Phys*, 2014, **16**, 14912-14921.

19. F. Solymosi and R. Németh, The oxidative dehydrogenation of ethane with CO₂ over Mo₂C/SiO₂ catalyst, *Catalysis Letters*, 1999, **62**, 197-200.
20. W. Marquart, S. Raseale, G. Prieto, A. Zimina, B. B. Sarma, J.-D. Grunwaldt, M. Claeys and N. Fischer, CO₂ Reduction over Mo₂C-Based Catalysts, *ACS Catalysis*, 2021, **11**, 1624-1639.

7 Mo_xC_y supported on various metal oxides

In this chapter the CO_2 -ODH related thermodynamic analysis is extended to determine the effect of co-feeding H_2 , H_2O or simply an inert gas on the equilibrium composition of the entire system and its effect on the oxidation state of the various possible Mo phases. Experimentally, the study continues with the use of Mo_xC_y -based catalysts, but here the carbide nanoparticles are supported on a range of metal oxide materials, with a range of redox and acid/base properties. These catalysts are characterized to confirm the presence of Mo_xC_y on the support as well as for their acid/base characteristics. Additionally, their affinity towards CO_2 activation via a temperature programmed reaction is evaluated. All catalysts are tested in the CO_2 -ODH reaction with a range of conditions, such as an increase in CO_2 content in the feed mixture as well as H_2 co-feeding. H_2O co-feeding, included in the thermodynamic analysis, will be experimentally discussed in Chapter 8.

*A section of the results reported in this chapter are part of a research article published as: W. Marquart, M. Claeys, N. Fischer, *Faraday Discussions* 2021, 230, 68-86.*

7.1 Thermodynamic analysis of the CO_2 -ODH reaction: effect of H_2 or H_2O co-feeding

In section 5.1 a comprehensive thermodynamic analysis of CO_2 -ODH of ethane was performed including all the possible side reactions, product species and different reaction conditions, e.g., temperature and feed gas composition as well as the different Mo compounds (MoO_3 , MoO_2 and Mo_2C). In this section the CO_2 -ODH thermodynamic analysis is extended by investigating the effect of H_2 , H_2O and/or co-feeding of inert. The feed composition was set at a CO_2 : C_2H_6 ratio of 1:1, while varying the H_2 , H_2O and/or inert concentration in the feed gas stream to up to 50 vol.-%. Upon H_2 co-feeding, the partial pressures of CO_2 and C_2H_6 are kept constant by simultaneously co-feeding an inert, (see experimental section 4.3.2). As described in the experimental section 4.3.2, the co-feeding of H_2O was achieved by saturating the feed gas mixture by bubbling the reactant mixture through a temperature-controlled water-bath. This allows for a consistent flow rate, however partial pressures of CO_2 and C_2H_6 decrease upon the increase in H_2O content. The same approach is applied during the thermodynamic analysis of co-feeding H_2O . The decreasing partial pressure of CO_2 and C_2H_6 does allow for the Mo concentration to be kept constant, relative to the total system.

Previous observations (see section 5.1) reveal that the concentration of the desired ODH product (C_2H_4) as well as of the reactant C_2H_6 under the chosen process conditions is zero at thermodynamic

equilibrium. This suggests that a good ODH catalyst should kinetically suppress all possible side reactions resulting in the conversion of C_2H_4 .¹ Co-feeding of hydrogen is not expected to bring any change to this result, but is specifically studied for its effect on the oxidation state of the molybdenum phase. Without considering Mo-species in the thermodynamic calculations, the formation of solid carbon (graphite) decreases in favour of CH_4 with an increase in H_2 concentration in the feed (see Figure A.2). The latter can be a direct result of the increased methanation reaction (from CO or CO_2), predicted at lower temperatures (below 530 °C), or simply the hydrogenation of solid carbon. The effect of hydrogen co-feeding at higher temperatures (above 530 °C) is less significant, even up to a H_2 concentration of 50 vol.-%. Adding Mo_2C to the feed composition, at a $CO_2:C_2H_6:Mo_2C$ molar ratio of 1:1:0.35 (molar composition close to the reactor studies described later in this study), results in a significant change in behaviour of most product species (see Figure 7.1-A). At 0 vol.-% of H_2 co-feeding and temperatures below 480 °C, the concentrations of CO_2 and H_2O are predicted to be significantly lower compared to the case in the absence of a Mo phase (see Figure A.2), while the concentration of CH_4 is higher. Mo is calculated to be present only in the form of MoO_2 . At 480 °C and above, a gradual transformation from MoO_2 to Mo_2C as a function of temperature, is predicted, suggesting a (re-)carburization reaction (see Figure 7.1-B). This reaction happens simultaneously with an initial increase in H_2O (a major product in the carburization reaction) and CO_2 concentration, followed by a gradual decrease of the latter two compounds. The co-feeding of hydrogen predicts a slight reduction of the carburization/oxidation onset temperature (from 470 °C at 0 % H_2 to 430 °C at 50 % H_2) stabilizing the active phase. Over the entire range of conditions, oxidation to MoO_3 or reduction to Mo^0 is not predicted.

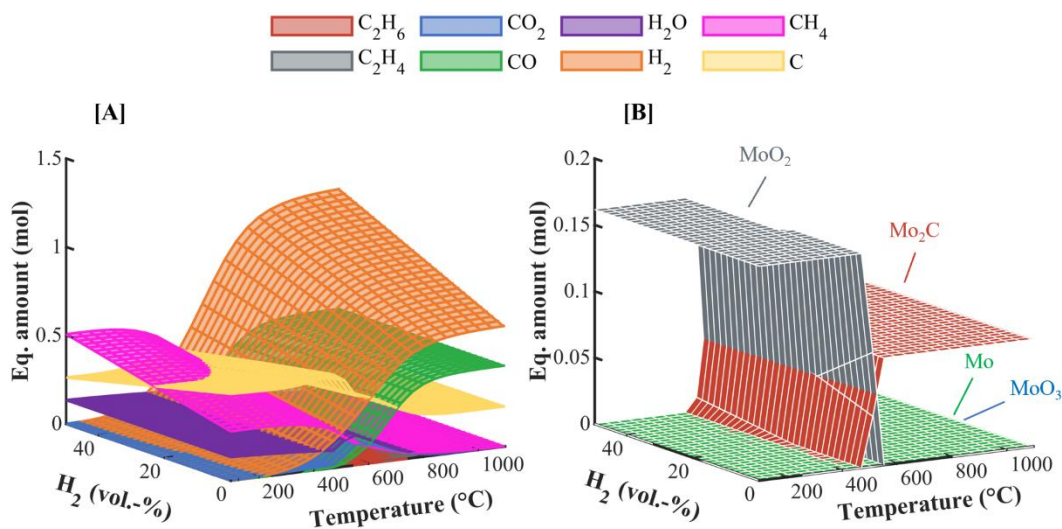


Figure 7.1. Product equilibrium of the CO_2 -ODH system as a function of temperature and H_2 co-feeding at a stoichiometric feed of CO_2 to C_2H_6 (1:1) and 1 bar pressure, with all compounds considered [A] including the four different Mo phases [B].

H₂O co-feeding with the CO₂-ODH reactant feed would ideally assist in the removal of carbon deposits. This can free up active surface sites and thus prolong catalyst lifetime. The thermodynamic analysis of H₂O co-feeding was performed to study the effect of H₂O on the product species, but in particular and similar to co-feeding H₂, the oxidation state of the Mo species in the presence of H₂O. An increase in H₂O content decreases the concentration of solid carbon (see Figure 7.2-A, as well as Figure A.3 without consideration of the Mo phases). In contrast to co-feeding H₂, the suppression of coke formation does not come simultaneously with the enhanced formation of CH₄. In fact, no significant changes can be observed amongst the product species, suggesting this to be rather an effect of dilution, due to the decreasing partial pressures of CO₂ and C₂H₆ upon co-feeding H₂O. Similar effects are observed when simply co-feeding an inert, which dilutes the reaction mixture (see Figure A.4). Interestingly, the inert co-feeding results in a drop in the MoO₂ content, starting from about 25 vol.-%, with a simultaneous increase in Mo₂C content. Nevertheless, the co-feeding of H₂, H₂O or inert, does not seem to thermodynamically affect the Mo composition at the proposed CO₂-ODH reaction temperature, i.e., 600 °C. Only in absence of C₂H₆ in the feed stream, the oxidation/carburization threshold moves to higher temperatures (see section 5.1 and Figure A.1).

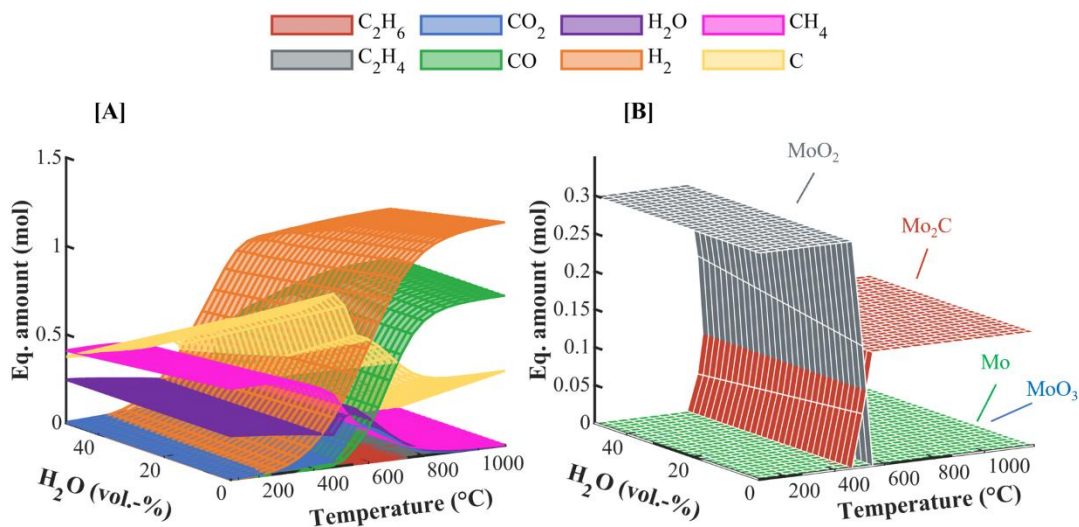


Figure 7.2. Product equilibrium of the CO₂-ODH system as a function of temperature and H₂O co-feeding at a stoichiometric feed of CO₂ to C₂H₆ (1:1) and 1 bar pressure, with all compounds considered [A] including the four different Mo phases [B].

7.2 Catalyst characterization: effect of MO_x support

In Chapter 6 we have shown that the preparation of supported Mo_xC_y catalysts *via* different synthesis techniques can lead to large differences in textural properties and carbide phase composition, also influenced by the sensitivity of the carburization treatment, especially at nanoparticle level. In this chapter, due to the large variety of samples and support materials, we focused on the following key aspects in terms of the synthesis of the different materials: all samples are prepared *via* the wet impregnation technique, with a total loading of ± 20 wt.-% Mo on the support material. The same carburization conditions are maintained for all samples with a confirmed formation of a carbide phase (β -carbide, η -carbide and/or oxycarbide) with similar crystallite sizes and homogeneously distributed over the metal oxide support material. Raman spectroscopy was used to confirm the absence of carbon deposits on the freshly carburized samples. Temperature-programmed CO_2 -activation (TP- CO_2) experiments, as well as temperature-programmed desorptions of CO_2 (CO_2 -TPD) and NH_3 (NH_3 -TPD) were performed to examine the effect of the support on the affinity towards CO_2 -activation and the acid and base properties of the catalysts.

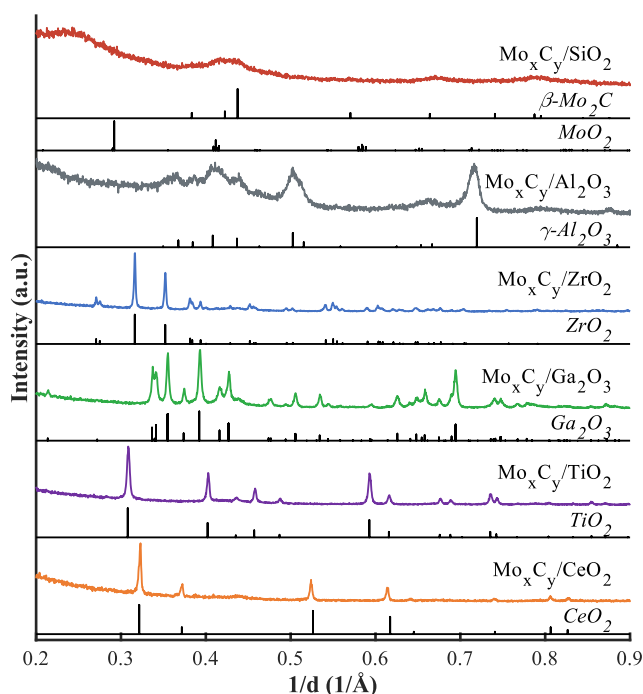


Figure 7.3. XRD patterns of the freshly carburized Mo_xC_y catalysts supported on SiO_2 , Al_2O_3 , ZrO_2 , Ga_2O_3 , TiO_2 or CeO_2 .

A molybdenum loading on all samples of about 20 wt.-% was confirmed by ICP-OES analysis (see Table K.1). All samples were carburized at 600 °C for 5 hours with a ramp rate of 1 °C min⁻¹. The formation of the carbide phase, crystal phase composition and average crystallite size is analysed by XRD (see Figure 7.3) in combination with Rietveld refinement (see Table 7.1). For Mo_xC_y/Al₂O₃ the alumina reflexes mask all evidence of molybdenum phases making quantification unfeasible. Mo_xC_y/SiO₂ contains an amorphous material represented by a broad feature in the experimental pattern at lower angles. The previously determined Mo allotrope composition (see Table 6.1) for Mo_xC_y/SiO₂ is therefore quantified as a proportion of the total Mo loading on the sample and does not represent the absolute amount in the sample. For comparison with the samples supported on crystalline metal oxides, the normalized Mo phase composition (normalized to the total Mo content in the sample obtained *via* ICP-OES) for Mo_xC_y/SiO₂ is also shown in Table 7.1. Variations in the carbide composition can be found in the samples prepared *via* wet impregnation on the different metal oxide support materials. Note that the carbide phase forms broad reflexes, most obvious in the range of 0.38-0.50 1/Å. This confirms that the carbide particles consist out of small crystallites and that the large contrast in crystallite size between the bulk metal oxide supports and the carbide nanoparticles can impact on the accuracy of the calculated phase composition (and thus vary from ICP-OES obtained Mo-loadings) and average crystallite size. β-Mo₂C was detected in all samples with η-MoC_{0.59} also present in the samples supported on ZrO₂ and Ga₂O₃. ZrO₂ was observed to be in the monoclinic phase and TiO₂ in the rutile structure. The crystallite sizes determined by Rietveld refinement, suggests that all carbide species are below 10 nm, which is line with previous observations of Mo_xC_y supported on SiO₂ discussed in Table 6.1.

Table 7.1. Phase composition and crystallite sizes determined *via* XRD Rietveld analysis of the freshly carburized Mo_xC_y catalysts supported on SiO₂, Al₂O₃, ZrO₂, Ga₂O₃, TiO₂ or CeO₂.

Sample	Metal oxide support		β-Mo ₂ C		η-MoC _{0.59}	
	wt.-% (error)	nm (error)	wt.-% (error)	nm (error)	wt.-% (error)	nm (error)
Mo _x C _y /SiO ₂	-	-	21.4 (2.7) (N. 4.1)	4.9 (0.8)	78.6 (2.7) (N. 15.1)	3.3 (0.2)
Mo _x C _y /Al ₂ O ₃	-	-	-	-	-	-
Mo _x C _y /ZrO ₂	82.0 (5.8)	56.0 (1.0)	8.7 (2.9)	3.8 (0.5)	9.26 (3.1)	2.5 (0.4)
Mo _x C _y /Ga ₂ O ₃	85.2 (0.6)	30.3 (0.3)	4.6 (0.3)	9.1 (0.8)	10.3 (0.5)	3.6 (0.3)
Mo _x C _y /TiO ₂	85.1 (0.8)	37.6 (0.5)	14.9 (0.8)	1.8 (0.1)	-	-
Mo _x C _y /CeO ₂	70.7 (2.0)	27.1 (0.3)	29.3 (2.0)	5.6 (0.7)	-	-

The carburizing conditions applied prevent carbon deposition which is confirmed by means of Raman spectroscopy (see Figure 7.4). No signs of the typical D- and G-band (at 1350 and 1580 cm^{-1} , respectively) are observed. The bands at 995 cm^{-1} , 817 cm^{-1} , 665 cm^{-1} and in the lower region between 100-380 cm^{-1} , which are visible in almost all samples, indicate the presence of MoO_3 .² Note that the re-oxidation of the carbide into MoO_3 has been confirmed to occur *via* the local energy input due to laser irradiation in air. The intensities of the oxide bands are therefore influenced by the exposure time of the laser on the sample.³ In addition, the alignment of the laser and the positioning of the sample can impact the intensity greatly, thus no direct correlation between intensity and quantity can be made across samples. The other bands visible in the different spectra represent their corresponding metal oxide support materials (see Table 4.2 for band identification).

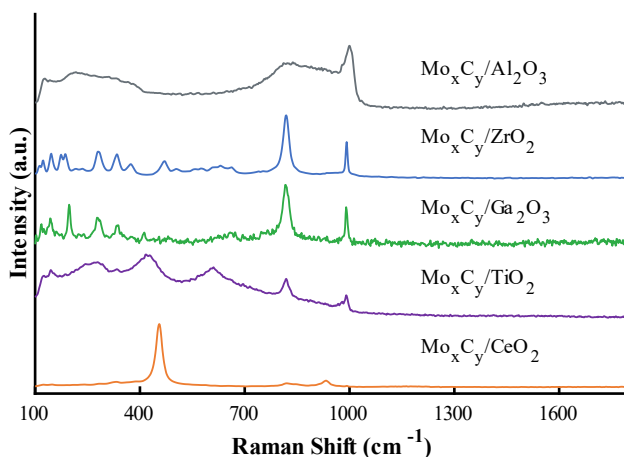


Figure 7.4. Raman spectra of the freshly carburized Mo_xC_y catalysts supported on SiO_2 , Al_2O_3 , ZrO_2 , Ga_2O_3 , TiO_2 or CeO_2 .

SEM-EDS mapping confirms a homogeneous distribution of the Mo particles over the support material for all samples, with minimal agglomeration observed (see Figure 7.5). N_2 physisorption analysis determined the BET surface area, pore volume and pore width of each sample (see Table K.1). It is no surprise that the SiO_2 and $\gamma\text{-Al}_2\text{O}_3$ supported samples show significantly larger surface areas than the non-porous reducible metal oxides (ZrO_2 , TiO_2 , CeO_2 and Ga_2O_3).

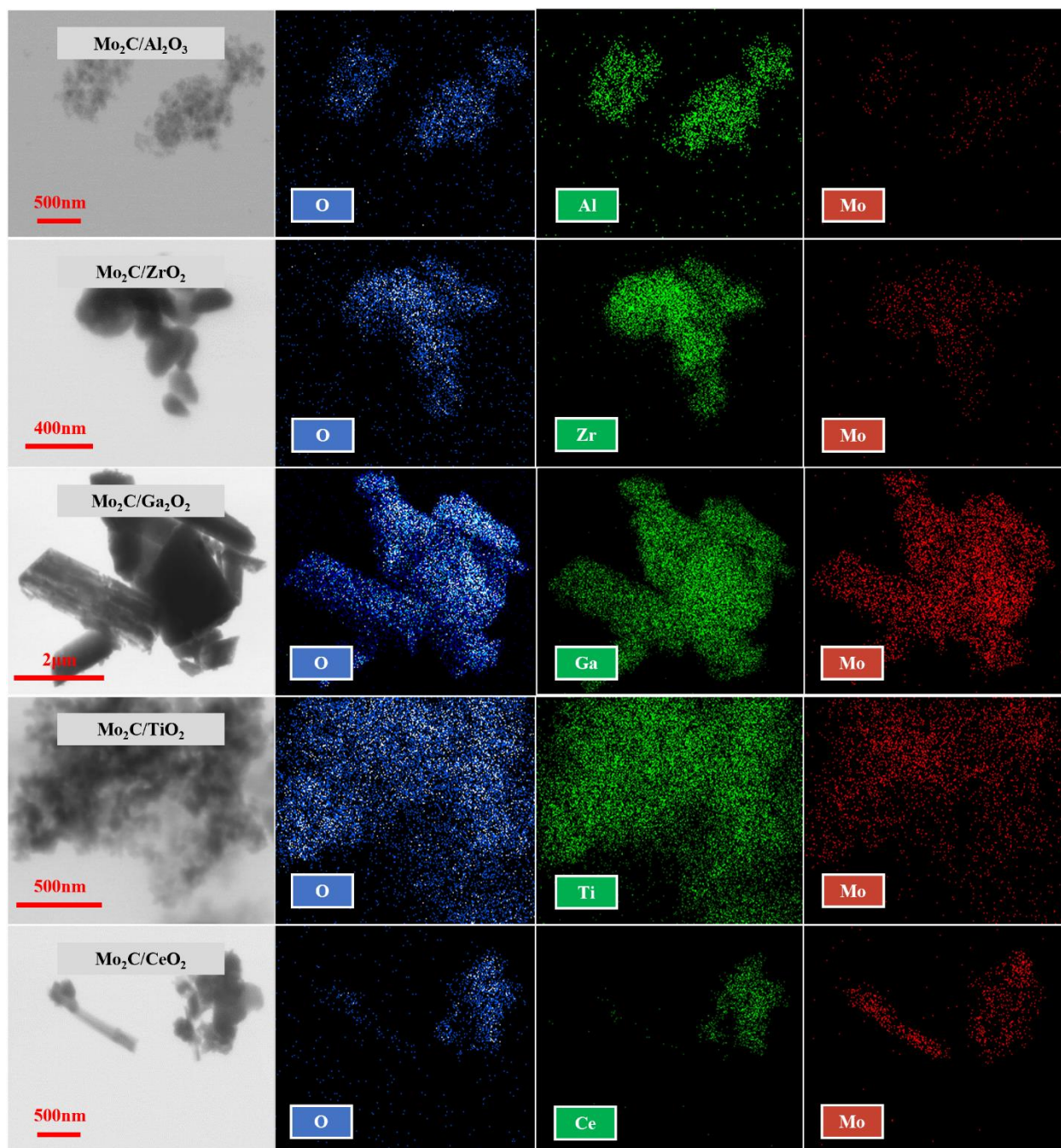


Figure 7.5. SEM-EDS micrographs and elemental mapping of the freshly carburized Mo_xC_y supported on SiO₂, Al₂O₃, ZrO₂, Ga₂O₃, TiO₂ or CeO₂.

7.3 Acid-base properties: effect of MO_x support

Acid and base pairs on the surface of the catalysts are believed to be the major contributors to the CO_2 -ODH reaction mechanism.⁴⁻⁶ Ethane is activated on acid sites, but the strength of the acidic site determines whether C-H or C-C bond cleavage occurs, with the latter enhancing the undesired dry-reforming and cracking reactions. Basic sites can assist in the activation of CO_2 , but very strong basic sites can lead to secondary CO dissociation. NH_3 and CO_2 temperature programmed desorption (TPD) experiments are common techniques used to study acid and base sites, respectively. Stronger acid/base sites require higher temperatures for the probe molecule to desorb from the catalytic surface. Each sample was exposed to both TPD programs to determine the amount and strength of acid/base sites on MO_x supported Mo_xC_y catalysts.

During each CO_2 -TPD experiment, CO_2 is first desorbed followed by CO desorption with increasing temperature. The observed desorption of CO can be attributed to thermal decomposition of surface oxygen complexes, commonly found in carbon-containing materials.^{7, 8} The desorbed CO_2 and CO were detected by mass spectrometry. The background corrected CO_2 desorption spectra were deconvoluted by means of several equal full width at half maximum (FWHM) Gaussian curves (see Figure 7.6). It should be noted that during the curve-fitting process, the number of Gaussian curves were minimized while simultaneously attaining a good degree of similarity and consistency between the different samples in terms of peak temperatures and FWHM (see Table K.9 for more details on the fits). The various CO_2 desorption peaks can be assigned to functional groups such as carboxylic acid sites between 130-300 °C and lactone sites between 350-600 °C.⁹ Trapezoidal numerical integration of the individual Gaussian curves (see Figure 7.7) reveals a significant change in the amount of CO_2 desorbed between the five different supports. In the absence of a CO_2 adsorption step (referred to as $\text{Mo}_x\text{C}_y/\text{SiO}$ (no CO_2) in Figure 7.6), CO_2 and CO gas desorption was still detected, confirming the presence of (sub-)surface oxygen complexes reacting with pre-adsorbed carbon deposits (broad CO_2 signal at 360 °C) or lattice carbon (CO signal starting from 400 °C). The latter leads to the decomposition of molybdenum carbide to metallic Mo, clearly observed by means of the (0 1 1) reflex of metallic Mo at 0.45 $1/\text{\AA}$ in the XRD patterns of the spent samples (see Figure 7.8). Another experiment in the absence of CO_2 adsorption was halted at 600 °C and subsequent XRD analysis confirmed that neither bulk decomposition nor changes to the carbide composition occurred despite the measured CO formation (see Figure D.2). Due to the large difference observed in the surface area between the bulk metal oxides (see Table K.1) the CO_2 desorbed signal is normalized to the surface area of each sample. The CO signal is normalized to the Mo content in each sample, determined by ICP-OES (see Table K.1), as it is expected that most of the desorbed CO originates from the decomposition of the carbide material.

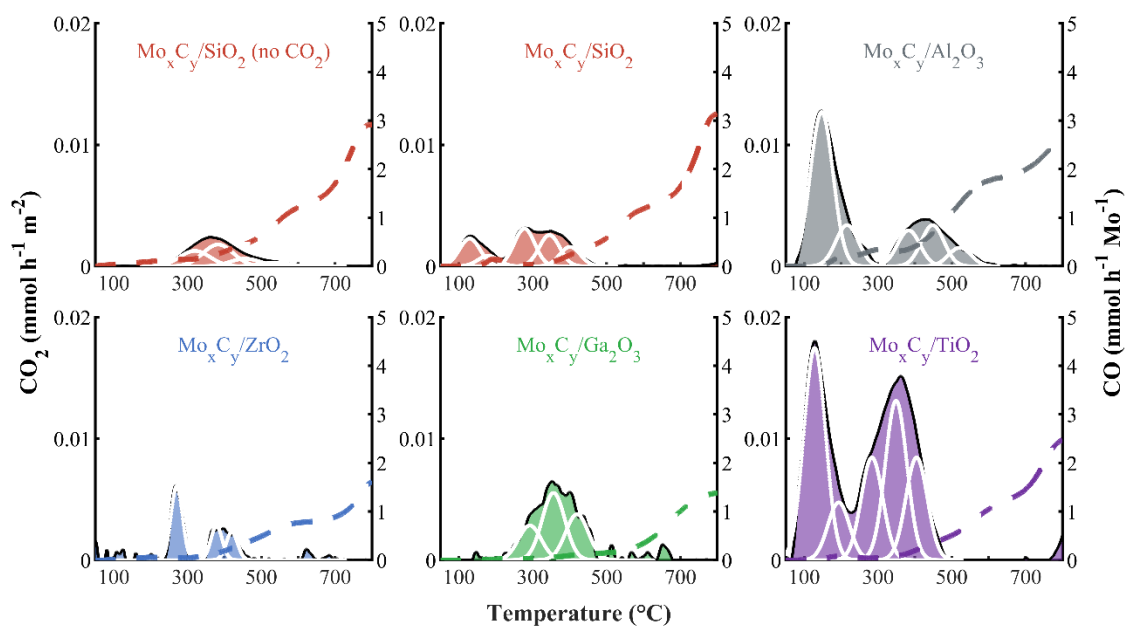


Figure 7.6. CO₂ temperature programmed desorption profiles of Mo_xC_y catalysts supported on SiO₂, Al₂O₃, ZrO₂, Ga₂O₃ or TiO₂, with one experiment supported on SiO₂, recorded omitting a CO₂ adsorption step. Temperature heated up to 800 °C at 10 °C min⁻¹, in an Ar atmosphere. Area plots: CO₂, with deconvoluted peaks in white, dashed lines: CO.

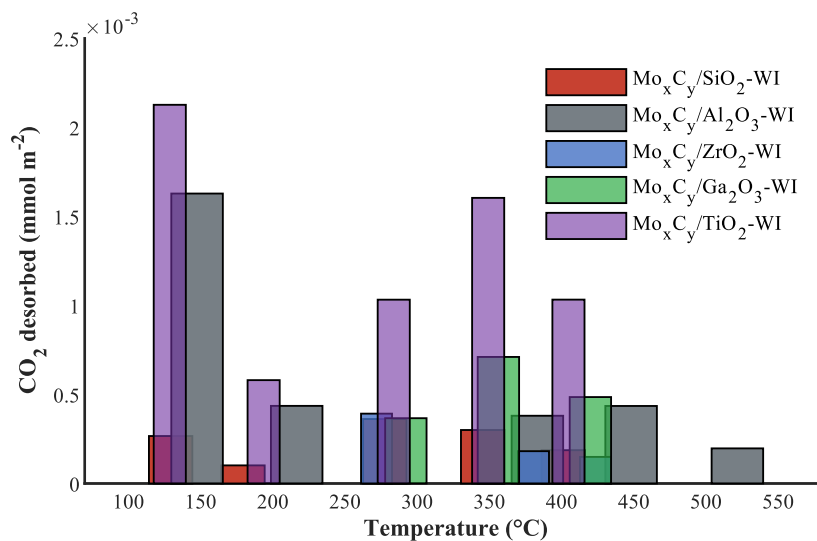


Figure 7.7. Overview of CO₂ desorbed (normalized to mmol per m² surface area) as a function of temperature recorded during CO₂ desorption of Mo_xC_y catalysts supported on SiO₂, Al₂O₃, ZrO₂, Ga₂O₃ or TiO₂.

Assuming that the CO₂ desorption between 300-500 °C is mainly caused by surface carbon removal, the desorption profile below 300 °C is of most interest with regards to the acid base properties. When

normalized to BET surface area, $\text{Mo}_x\text{C}_y/\text{TiO}_2$ shows the largest amount of weak basic sites, as is shown by CO_2 desorption observed around 130 °C. It is closely followed by $\text{Mo}_x\text{C}_y/\text{Al}_2\text{O}_3$, although its desorption temperature is slightly increased (150 °C). No weak basic sites can be observed for $\text{Mo}_x\text{C}_y/\text{ZrO}_2$ and $\text{Mo}_x\text{C}_y/\text{Ga}_2\text{O}_3$, and a minor signal is observed for $\text{Mo}_x\text{C}_y/\text{SiO}_2$ at 130 °C. Some stronger basic sites result in CO_2 desorption around 190 °C for $\text{Mo}_x\text{C}_y/\text{ZrO}_2$, 215 °C for $\text{Mo}_x\text{C}_y/\text{Al}_2\text{O}_3$, and 180 for $\text{Mo}_x\text{C}_y/\text{SiO}_2$. For $\text{Mo}_x\text{C}_y/\text{ZrO}_2$ and $\text{Mo}_x\text{C}_y/\text{Ga}_2\text{O}_3$, CO_2 desorption is only observed at 270 and 290 °C respectively. As indicated, the signals between 300 °C and 500 °C are disregarded, due to an overlap with signal originating from carbon removal. However, the much larger signal observed for $\text{Mo}_x\text{C}_y/\text{TiO}_2$ between 300 °C and 500 °C can suggest a combination of stronger basic sites and the removal of free carbon deposits.

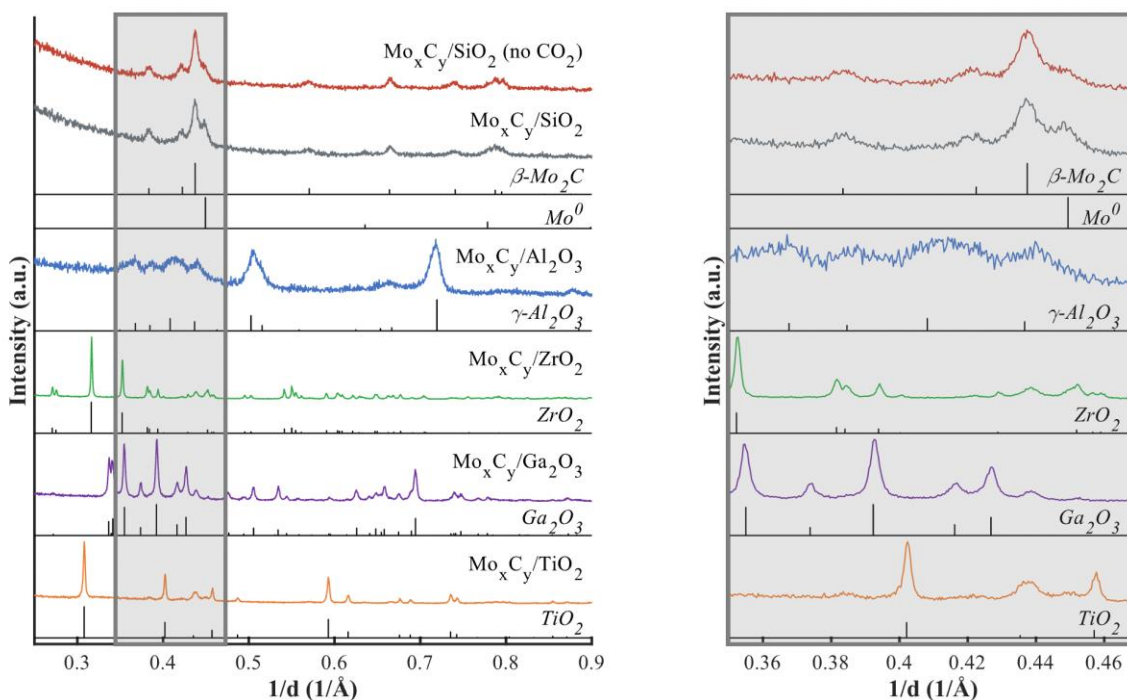


Figure 7.8. XRD patterns of the spent CO_2 -TPD Mo_xC_y catalysts supported on SiO_2 , Al_2O_3 , ZrO_2 , Ga_2O_3 or TiO_2 .

An increase in CO desorption with temperature was observed for all samples. XRD patterns of the spent samples confirm the decomposition to Mo^0 (see Figure 7.8) by Rietveld refinement (see Table K.4). The reflexes related to $\beta\text{-Mo}_2\text{C}$ are more intense and signs of $\eta\text{-MoC}_{0.59}$ are observed, suggesting that $\beta\text{-Mo}_2\text{C}$ is the more thermodynamically stable phase undergoing sintering, evidenced by the increase in crystallite size from a maximum of 9.1 nm in the freshly carburized samples (see Table 7.1) to up to 17.5 nm in the spent samples.

Four desorption events can be observed in the TCD signal of $\text{Mo}_x\text{C}_y/\text{SiO}_2$ (see Figure 7.9). Without an NH_3 pre-adsorption step ($\text{Mo}_x\text{C}_y/\text{SiO}_2$ (no NH_3)), the TCD signal shows overlapping features from about 400 °C onwards. The peak at 470 °C can be assigned to the removal of pre-adsorbed carbon *via* reaction with (sub-)surface oxygen complexes. This is a higher desorption temperature than discussed earlier and can be explained due to the difference in reactor set-up (fixed-bed reactor set-up for CO_2 -TPD vs AutoChem chemisorption analyser for NH_3 -TPD) and the corresponding variations in the temperature of the catalyst bed and heating rate.⁷ The rising signal starting above 600 °C is in line with the previously identified reaction of (sub-)surface oxygen species with carbon from the carbide structure forming Mo^0 .⁸ Based on previous literature reports on NH_3 -TPD, the signal at 100 °C is attributed to weak acid sites and the signal at 340 °C can be attributed to Brønsted acid sites.¹⁰ Although the strength of the acid sites observed for $\text{Mo}_x\text{C}_y/\text{Al}_2\text{O}_3$ are fairly similar to $\text{Mo}_x\text{C}_y/\text{SiO}_2$, we could compare the number of sites present in the sample when comparing the intensities to the respective peak at 470 °C. For $\text{Mo}_x\text{C}_y/\text{SiO}_2$, the signal at 100 °C and 340 °C is lower than the signal at 470 °C, which is reversed for $\text{Mo}_x\text{C}_y/\text{Al}_2\text{O}_3$. This could suggest a higher number of weak and Brønsted acid sites for $\text{Mo}_x\text{C}_y/\text{Al}_2\text{O}_3$. $\text{Mo}_x\text{C}_y/\text{ZrO}_2$ shows significantly lower desorption at 100 °C and ± 300 °C, followed by a signal at 500 °C. However, a much more intense event is observed around 750 °C, which can suggest the presence of strong Lewis acid

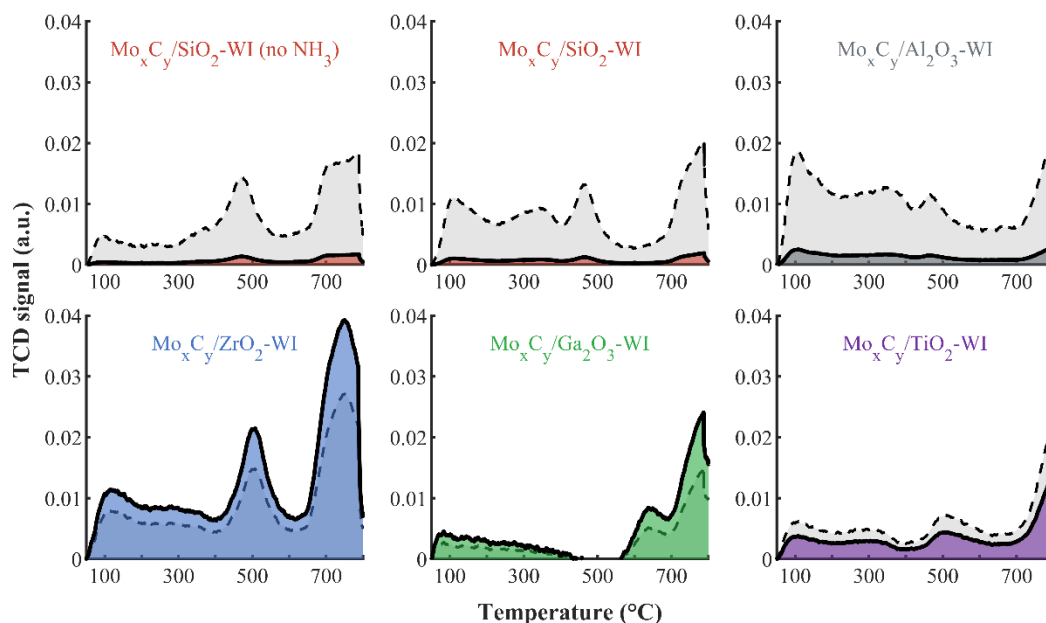


Figure 7.9. NH_3 temperature programmed desorption profiles normalized to surface area of Mo_xC_y catalysts supported on SiO_2 , Al_2O_3 , ZrO_2 , Ga_2O_3 or TiO_2 , with one experiment, supported on SiO_2 , recorded omitting a NH_3 adsorption step. The grey background signals (--) show the original data, prior to normalization. Temperature heated up to 800 °C at 10 °C min^{-1} , in a He atmosphere.

sites¹¹, despite the (co-)desorption of CO at that temperature range. This is supported by the lack of such an intense signal in CO₂-TPD of Mo_xC_y/ZrO₂ at a comparable temperature range. Mo_xC_y/Ga₂O₃ does not show any evidence of weak acid sites, however a signal at 640 °C is observed suggesting the presence of strong acid sites. For Mo_xC_y/TiO₂, besides the signals observed at 100 °C and 310 °C, a shoulder can be observed on the high temperature side of the peak at 500 °C, which might again suggest the presence of strong acid sites. This is supported by a study from Ferretto and Glisenti¹², who reported that TiO₂ in the rutile phase contains weak basic sites and strong acid sites.

XRD patterns of the spent samples after NH₃-TPD show a large difference to the samples after CO₂-TPD in terms of the metallic Mo content (see Figure 7.10 and Table K.5). This supports the earlier observation that the difference in experimental set-up can have a significant impact on both the carburization process (completed *in situ* prior to the TPD experiment) and the TPD experiment. Despite this, a consistent trend can be observed between the samples in both experiments, showing the dominance of β-Mo₂C as the carbide phase with a significantly increased crystallite size (up to 29.3 nm).

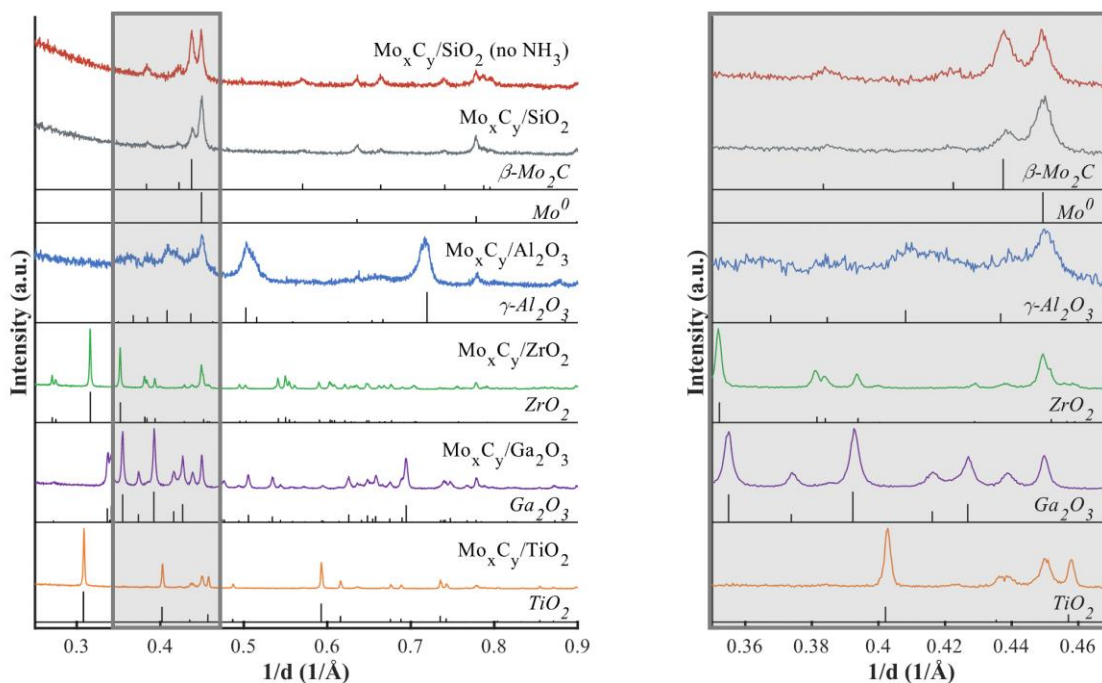


Figure 7.10. XRD patterns of spent NH₃-TPD Mo_xC_y catalysts supported on SiO₂, Al₂O₃, ZrO₂, Ga₂O₃ or TiO₂.

7.4 CO₂ activation: effect of MO_x support

In Chapter 6 we have described the CO₂ activation affinity of Mo_xC_y nanoparticles, supported on SiO₂, synthesized *via* three different methods. The activation of CO₂ was observed to proceed *via* CO₂ dissociation at temperatures below 530 °C. *In situ* XAS analysis confirmed the oxidation of the carbide to MoO₂ to start around 600 °C (when using a heating rate of 5 °C min⁻¹). The oxidation occurs due to the reaction of CO₂ with carbon from the molybdenum carbide crystal structure and can be described by Equation 5.1.



In this section we evaluate the effect the various metal oxide support materials have on the activation of CO₂ over Mo_xC_y nanoparticles, considering their acid/base properties as well as the carbide composition. In particular we look at the lower temperature region (≤ 600 °C), as that region would indicate whether the CO₂ dissociation mechanism (an important step for the CO₂-ODH as well as the RWGS reaction) is affected. Above 600 °C the resistance towards re-oxidation to MoO₂ can be observed, in both on-set temperature as well as total CO formed.

In terms of CO yield between 400 °C and 600 °C, the following order in activity is observed: Mo_xC_y/Al₂O₃ > Mo_xC_y/TiO₂ > Mo_xC_y/ZrO₂ = Mo_xC_y/SiO₂ >> Mo_xC_y/Ga₂O₃ (see Figure 7.11). Although Mo_xC_y/TiO₂, Mo_xC_y/ZrO₂ and Mo_xC_y/SiO₂ show a very similar formation rate below 560 °C, the CO formation rate for Mo_xC_y/TiO₂ slightly increases between 560 °C and 600 °C. Upon reaching the final temperature (700 °C), the order has changed significantly: Mo_xC_y/ZrO₂ > Mo_xC_y/TiO₂ > Mo_xC_y/SiO₂ >> Mo_xC_y/Al₂O₃ > Mo_xC_y/Ga₂O₃. The same order, considering the re-oxidation to MoO₂, is observed in the XRD patterns of the spent sample as well as the results of Rietveld refinement (see Figure 7.12 and Table K.3). Mo_xC_y/Ga₂O₃ did not show any bulk re-oxidation to MoO₂, and only a small reflex is visible for Mo_xC_y/Al₂O₃. A slightly higher oxidation is observed for Mo_xC_y/ZrO₂ compared to Mo_xC_y/TiO₂. It should be noted that the degree of oxidation for Mo_xC_y/SiO₂ is now significantly lower than previously discussed in section 6.3 (Figure 6.12). This can be rationalized by the higher heating rate (5 °C min⁻¹ vs 1 °C min⁻¹) in this experiment, despite the same final temperature (700 °C). A higher CO yield is also observed at a higher heating rate, suggesting that the re-oxidation is not instant, but gradually increases with temperature and time on stream. Thus, more CO₂ activating sites are available at higher temperatures, using a higher heating rate.

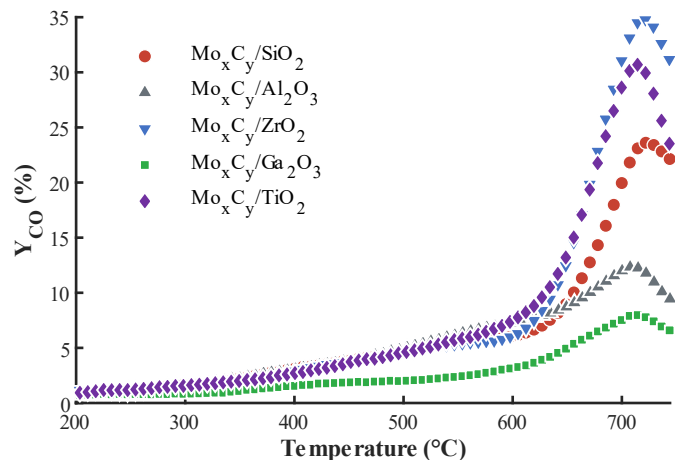


Figure 7.11. CO yield observed as a function of temperature, normalized to the mass fraction of Mo in the Mo_xC_y catalysts supported on SiO_2 , Al_2O_3 , ZrO_2 , Ga_2O_3 or TiO_2 . Temperature increased to 700 °C at 5 °C min^{-1} , holding for 10 minutes at maximum temperature at atmospheric pressure in 1 vol.-% CO_2 in Ar at a space velocity of 60 $\text{L h}^{-1} \text{g}_{\text{cat}}^{-1}$.

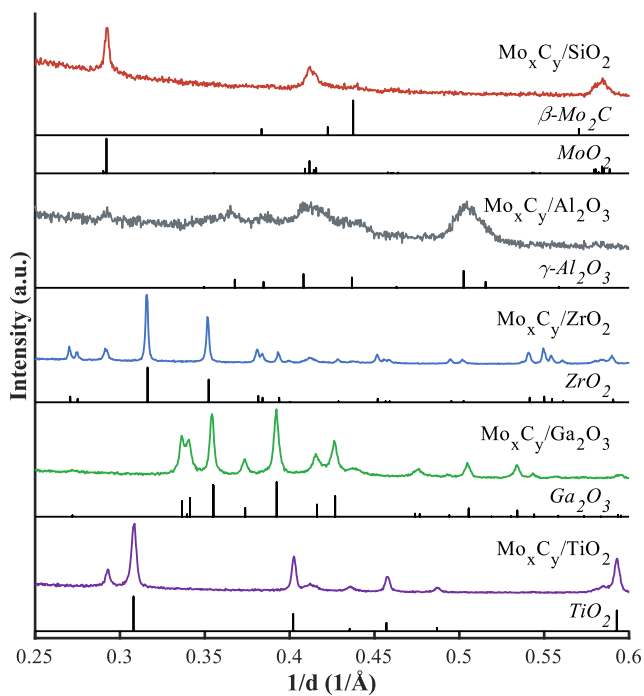


Figure 7.12. XRD patterns of the spent TP- CO_2 activation Mo_xC_y catalysts supported on SiO_2 , Al_2O_3 , ZrO_2 , Ga_2O_3 or TiO_2 .

7.5 CO₂-ODH performance: effect of MO_x support

7.5.1. Effect of support

All synthesized catalysts were tested under the same CO₂-ODH conditions for 24 hours at a reaction temperature of 600 °C, atmospheric pressure, space velocity of 15 L h⁻¹ g_{cat}⁻¹ and an equimolar feed of CO₂ and C₂H₆ diluted in 50 vol.-% argon. Ethane conversion is under these conditions thermodynamically limited at 28.6 % for CO₂-ODH, 98.5 % for dry-reforming (DR) and 29.7 % for direct dehydrogenation (DH).¹

The CO₂-ODH catalytic performance of Mo_xC_y supported on SiO₂ *via* the wet-impregnation method is discussed in section 6.5 and is again presented in this chapter for purposes of comparison. In an attempt to increase catalytic stability, Mo_xC_y is supported on a variety of metal oxides to target a tandem reaction between the Mo_xC_y nanoparticles and the metal oxide support. It is shown that CO₂ is readily activated on the carbide nanoparticles on an inert support (SiO₂). By applying metal oxide supports within in a range of redox and acid/base properties, the activation of C₂H₆ might be enhanced, removing oxygen surface species at a faster rate and thus prevent the oxidation of the carbide under reaction conditions. In essence, the metal oxide can assist in the activation of the C-H bond of the ethane. Subsequently, the adsorbed H atoms react with the oxygen surface species on the carbide nanoparticles, forming H₂O. A variety of metal oxide catalysts, previously shown to be active for CO₂-ODH,⁶ as well as stable under the carburization conditions required to form Mo_xC_y, were selected. Firstly, four of the six supports were evaluated without Mo loading under the same reaction conditions after being exposed to the carburization treatment. All four samples show minimum C₂H₆ and CO₂ conversion with a maximum of 1.4 % (see Figure B.3). In terms of product selectivity, Ga₂O₃ produces mainly C₂H₄ (84-93 C-%) balanced by CO, ZrO₂ reaches an ethylene selectivity of about 62-66 C-%, mainly balanced by CO, close to the maximum CO₂-ODH C₂H₄ selectivity. SiO₂ produces similar amounts of C₂H₄, but a more prominent CH₄ formation was observed. TiO₂ achieves a CO and C₂H₄ selectivity of about 50 C-%. No phase changes in the metal oxides were observed under reaction conditions (see Figure D.5). On all samples but SiO₂ the deposition of carbon species is observed (see Figure E.1). The lack of carbon deposition on SiO₂ could explain the earlier observed over oxidation of Mo_xC_y on SiO₂ to MoO₃, discussed in section 6.5. Only low intensity D- and G-bands were observed for all three Mo_xC_y/SiO₂ catalysts, prepared *via* the three different synthesis routes (see Figure 6.24). The limited activation of C₂H₆ on the support and lower formation of carbon deposits, could prevent the blockage of CO₂ activating sites, continuing to produce oxygen surface species.

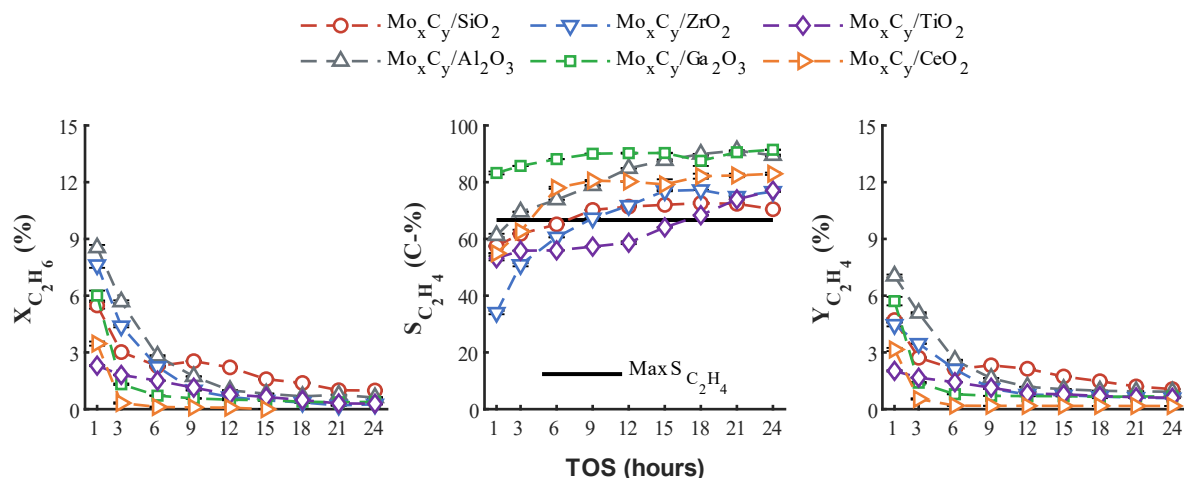


Figure 7.13. C_2H_6 conversion, C_2H_4 selectivity and C_2H_4 yield, of Mo_xC_y catalysts supported on SiO_2 , Al_2O_3 , ZrO_2 , Ga_2O_3 , TiO_2 and CeO_2 . CO_2 -ODH conditions: $T = 600\text{ }^\circ\text{C}$, $P = 1\text{ atm}$, $SV = 15\text{ L h}^{-1}\text{ g}_{cat}^{-1}$, $CO_2:C_2H_6:Ar = 1:1:2$. Theoretical maximum C_2H_4 selectivity for CO_2 -ODH indicated by solid black line.

The supported Mo_xC_y catalysts on the different metal oxides, show large differences in catalytic behaviour under CO_2 -ODH conditions (see Figure 7.13). A DFT-study by Helali *et al.*¹³ ranked numerous metal oxides by their reducibility by means of the respective energy required to produce oxygen vacancies. The metal oxides utilized in this study for CO_2 -ODH are ranked with decreasing reducibility: $CeO_2 > TiO_2$ -rutile $> Ga_2O_3 > SiO_2 > ZrO_2 > Al_2O_3$. While SiO_2 was classified as ‘irreducible’ and ZrO_2 as ‘intermediate’, the removal of an O atom is easier for Si due to the energy gain following the formation of a Si-Si bond. Mo_xC_y supported on the irreducible metal oxide Al_2O_3 , achieved the highest C_2H_6 conversion (8.3 %) and CO_2 conversion (5.7 %) after 1 hour TOS. Significant catalyst deactivation was observed in the first 9 hours TOS with a simultaneous increase in C_2H_4 selectivity (from 62 C-% to 89 C-%). No correlation could be made between carbide composition before and after reaction (see Figure 7.14), but significant carbon deposition is observed (see Figure 7.15). These observations suggest that supporting Mo_xC_y on Al_2O_3 , shows a dominant DH pathway with an initial DR activity causing $S_{C_2H_4}$ to drop below 67 C-%. With time on stream, the DH pathway becomes more dominant. Interestingly, Mo_xC_y/ZrO_2 achieves a higher CO_2 conversion (11.2 %) than C_2H_6 conversion (7.6 %) after 1 hour TOS. After 6 hours TOS, X_{CO_2} dropped to 1.6 % and $X_{C_2H_6}$ to 2.2 %. This drastic change in catalytic behaviour can also be observed in the product selectivity. At 1 hour TOS, Mo_xC_y/ZrO_2 recorded the lowest C_2H_4 selectivity (34 C-%) and the highest CO selectivity (63 C-%) of all tested catalysts. With the decrease in activity, a simultaneous increase in C_2H_4 selectivity (up to 77 C-%) indicates that Mo_xC_y/ZrO_2 transforms from a DR catalyst to a DH catalyst. The spent sample contained, besides a majority of MoO_2 , a low concentration of $Zr(MoO_4)_2$ (see Figure 7.14). Again, significant carbon deposits were observed as well.

It is suggested that the initial sharp drop in activity is related to the (partial) oxidation of the catalyst, but the prolonged deactivation is rather a combination of oxidation and carbon deposition. $\text{Mo}_x\text{C}_y/\text{Ga}_2\text{O}_3$ achieved a similar ethane conversion after 1 hour TOS (6 %) to $\text{Mo}_x\text{C}_y/\text{SiO}_2$, but a much lower CO_2 conversion (2.3 %). An initial C_2H_4 selectivity above 83 C-% suggests a high DH activity from the start of the reaction, which is similarly observed on pure Ga_2O_3 . The catalyst deactivated within 3 hours from a $X_{\text{C}_2\text{H}_6}$ of 6 % to 1.3 %. While oxidation of the carbide was confirmed (5.3 wt.-% MoO_2), the remaining carbide phases, and especially the beta-carbide, can be an indication that the catalyst was overwhelmed with carbon deposition (as observed by Raman) blocking the active Mo sites for CO_2 activation. $\text{Mo}_x\text{C}_y/\text{CeO}_2$ and $\text{Mo}_x\text{C}_y/\text{TiO}_2$, classified as most reducible, show significantly lower ethane conversions (3.3 % and 2.4 %, respectively). TiO_2 shows the lowest initial activity, but this is paired with a lower rate of deactivation with TOS. MoO_2 is the only molybdenum phase detected in the spent catalyst supported on TiO_2 . In $\text{Mo}_x\text{C}_y/\text{CeO}_2$, $\text{Ce}_2(\text{MoO}_4)_3$ was detected in addition to CeO_2 after reaction. Since this catalyst deactivated rapidly and completely with TOS, the formation of the molybdate phase can be assumed to be the main deactivation pathway.

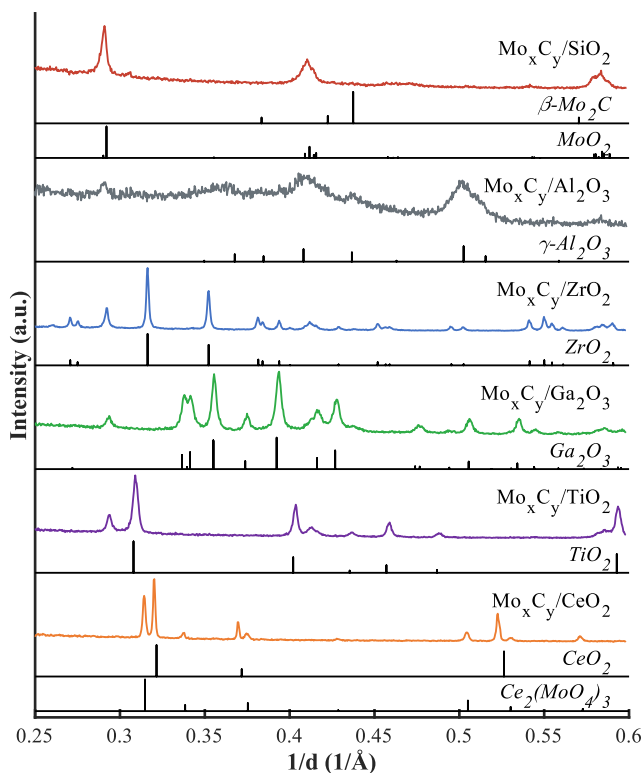


Figure 7.14. XRD patterns of the spent CO_2 -ODH Mo_xC_y catalysts supported on SiO_2 , Al_2O_3 , ZrO_2 , Ga_2O_3 , TiO_2 or CeO_2 .

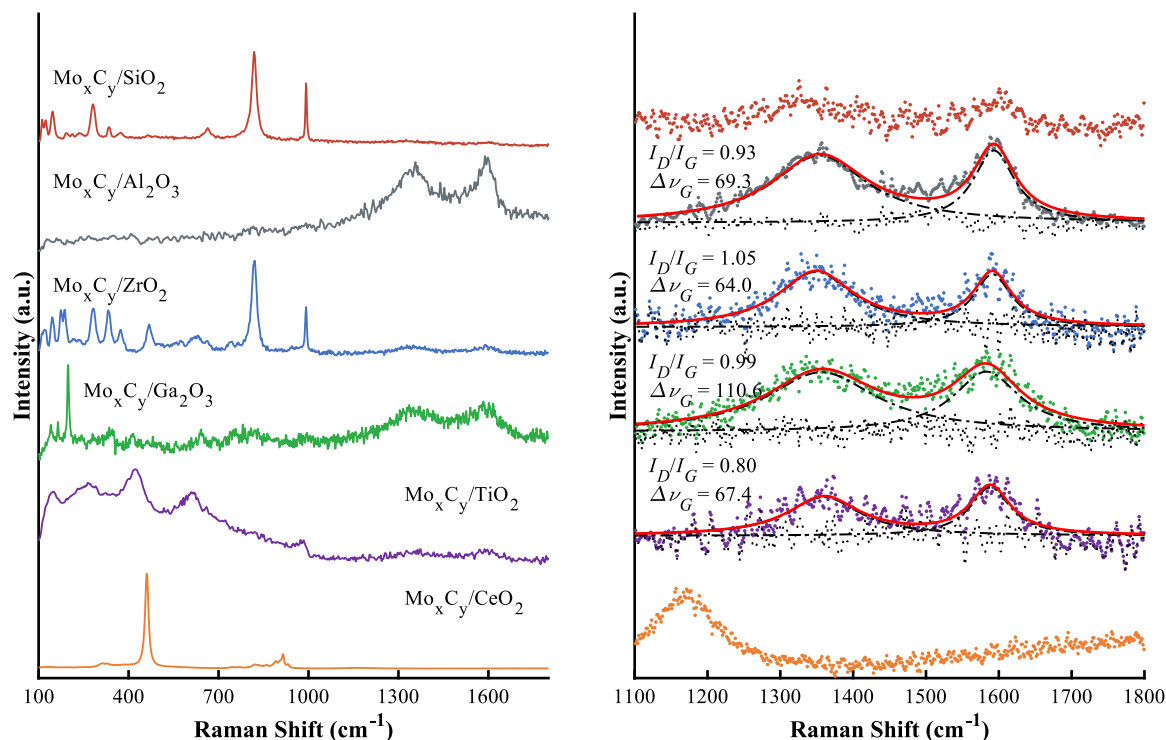


Figure 7.15. Raman spectra of the spent CO₂-ODH Mo_xC_y catalysts supported on SiO₂, Al₂O₃, ZrO₂, Ga₂O₃, TiO₂ or CeO₂.

7.5.2. Effect of feed composition

Nakagawa *et al.*⁶ reported the highest ethylene yields for Ga₂O₃ as a CO₂-ODH catalyst compared to all other metal oxides tested. It must be noted that the catalytic stability was not reported as data was only collected for 30 minutes. These results were achieved utilizing a CO₂ to C₂H₆ feed ratio of 5. The over-stoichiometric amount of CO₂ possibly enhances catalytic stability by the removal of carbon deposits *via* a reversed Boudouard reaction while at a 1:1 feed ratio, the carbon removal is insufficient.

A feed mixture containing a CO₂ to C₂H₆ feed ratio of 5 to 1 was evaluated for Mo_xC_y/Al₂O₃, Mo_xC_y/ZrO₂ and Mo_xC_y/Ga₂O₃ (see Figure 7.16). The initial $X_{C_2H_6}$ for Mo_xC_y/Al₂O₃ increased from 8.3 % to 13.0 % and for Mo_xC_y/Ga₂O₃ from 6.0 % to 9.6 %. However, the absolute amount of C₂H₆ converted is lower in a 5:1 feed ratio (see Figure 7.17). Mo_xC_y/Al₂O₃ and Mo_xC_y/Ga₂O₃ convert almost double the amount of C₂H₆ after 1 hour TOS in a 1:1 feed ratio. Mo_xC_y/ZrO₂ converts more than four times as much C₂H₆ after 1 hour TOS in a 1:1 feed ratio. After 6 hours TOS, Mo_xC_y/Al₂O₃ in the 1:1 feed ratio lost about 67 % of its initial activity but with a 5:1 ratio, it lost only 33 % (see Figure 7.17). From 6 hours TOS onwards, Mo_xC_y/Al₂O₃ in a 5:1 feed ratio outperforms the same catalyst in an equimolar feed. Although the initial amount of ethane converted by Mo_xC_y/ZrO₂ is significantly lower with a 5:1 feed than in a 1:1

feed ratio, the same catalyst outperforms the 1:1 feed ratio after 12 hours TOS. This is confirmed by the loss of $X_{C_2H_6}$ over time. After 24 hours TOS, Mo_xC_y/ZrO_2 has lost 97 % of its initial activity in a 1:1 feed ratio compared to 70 % in a 5:1 feed ratio. Exposure of Mo_xC_y/Ga_2O_3 to a 5:1 feed ratio only shows a slight advantage between 3 and 6 hours TOS. After 9 hours TOS, a 5:1 feed ratio caused a slightly more severe catalyst deactivation, having lost complete activity after 21 hours TOS (see Figure 7.17).

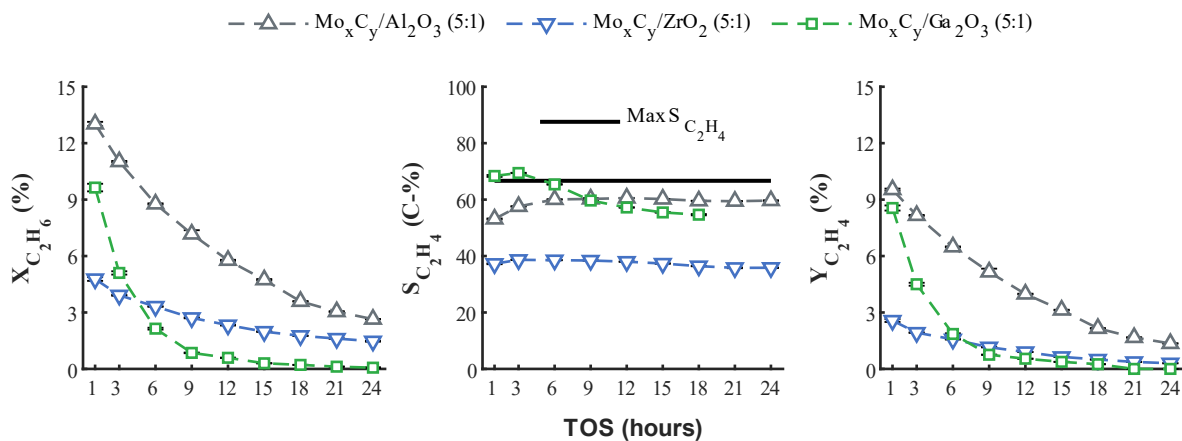


Figure 7.16. C_2H_6 conversion, C_2H_4 selectivity and C_2H_4 yield, of Mo_xC_y catalysts supported on Al_2O_3 , ZrO_2 and Ga_2O_3 . CO_2 -ODH conditions: $T = 600\text{ }^\circ\text{C}$, $P = 1\text{ atm}$, $SV = 15\text{ L h}^{-1}\text{ g}_{cat}^{-1}$, $CO_2:C_2H_6:Ar = 5:1:6$. Theoretical maximum C_2H_4 selectivity for CO_2 -ODH indicated by solid black line.

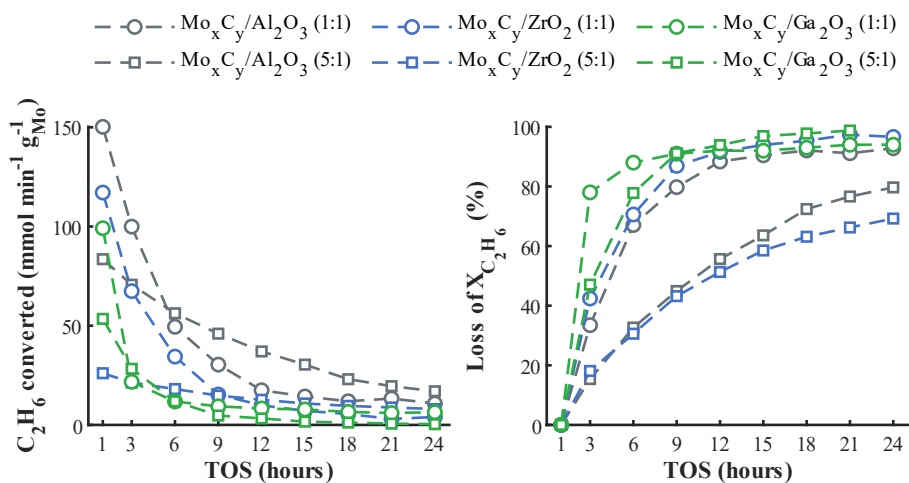


Figure 7.17. Absolute amount of ethane converted and loss of ethane conversion with time on stream of Mo_xC_y catalysts supported on Al_2O_3 , ZrO_2 and Ga_2O_3 evaluated in a 1:1 and 5:1 CO_2 to C_2H_6 feed ratio.

Mo_xC_y/Al_2O_3 achieves an initial $S_{C_2H_4}$ of 53 C-%, which increases with TOS close to the ODH theoretical maximum of 67 C-%. It can be suggested that the increased CO_2 content in the feed causes a slightly more dominant DR pathway and a simultaneous removal of surface carbon, freeing up active sites

responsible for CO₂ activation. This prevents the move to a DH dominant reaction pathway, as was observed with a 1:1 feed ratio. For Mo_xC_y/ZrO₂, using a 1:1 feed gas composition, $S_{C_2H_4}$ increased with TOS, but in a 5:1 feed ratio $S_{C_2H_4}$ is stabilized around 40 C-%, despite the decrease in conversion observed. This suggests a more dominant DR pathway, when exposed to a feed ratio of 5:1, which seems to be beneficial for its catalytic stability.

The XRD patterns of the spent samples (see Figure 7.18) and its corresponding Rietveld refinement (see Table K.2), indicate that both Mo_xC_y/Al₂O₃ and Mo_xC_y/ZrO₂ show the presence of MoO₂, but no (bulk) oxidation of the carbide is observed for Mo_xC_y/Ga₂O₃. It is therefore suggested that at a 1:1 feed ratio, carbon deposition blocks the tandem redox reaction between Mo₂C and Ga₂O₃. In a full catalytic cycle Mo₂C should activate CO₂, forming oxygen surface species, which in turn re-oxidize the Ga₂O_{3-x} site reduced due to C₂H₆ activation. However, severe carbon deposits prevent the O transfer to the metal oxide surface, to re-oxidize Ga₂O_{3-x}. The oxygen then reacts with the carbide instead, forming MoO_x. With an increased CO₂ content in the feed, CO₂ assists in the removal of the carbon, by means of the reverse Boudouard reaction, increasing the number of available active sites to activate CO₂ as well as C₂H₆. While bulk oxidation of the carbide has been prevented, catalyst deactivation is still occurring. It would be of great interest to study, with more surface sensitive techniques under process conditions, such as *in situ* XPS, *in situ* XAS or *in situ* Raman, whether not just the bulk particle but specifically the surface of the carbide particles remains carbidic.

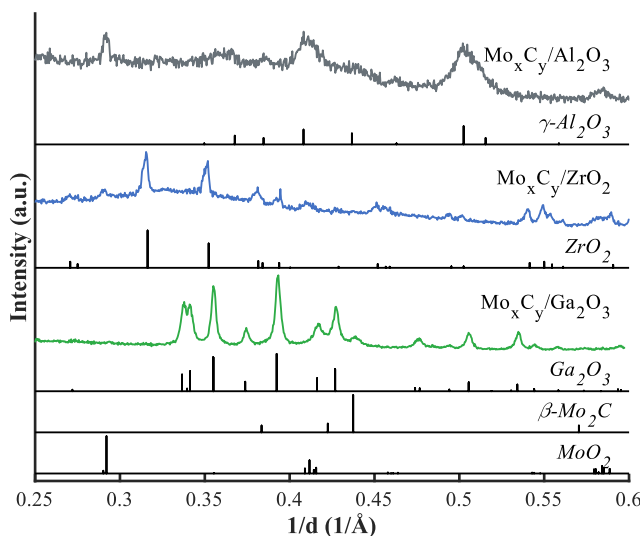


Figure 7.18. XRD patterns of the spent CO₂-ODH (5:1) Mo_xC_y catalysts supported on Al₂O₃, ZrO₂ or Ga₂O₃.

As the oxidation of the active carbide phase to the inactive oxide phase is, for most of the above presented catalysts, described to be one of the main catalyst deactivation mechanisms, H₂ was added to the feed stream as a stabilizing agent, enhancing the removal of oxygen species on the carbide surface. In addition, at a reaction temperature of 600 °C, H₂ has been reported to aid in the removal of carbon deposits from the surface, which can further improve catalyst stability.^{2, 14} Mo_xC_y/SiO₂, Mo_xC_y/ZrO₂ and Mo_xC_y/Ga₂O₃ were studied in the H₂ modified CO₂-ODH reaction (H₂/CO₂-ODH). H₂ was added to the feed stream in four concentrations: 0, 5, 10 and 17 vol.-%. N₂ was added to keep the partial pressure of CO₂ and C₂H₆ constant throughout the experiments. Therefore, at 0 vol.-% H₂, the difference in reaction conditions, to the previously discussed CO₂-ODH experiments, is a higher space velocity and a more diluted feed stream, from 50 to 58 vol.-%, which results in a thermodynamic CO₂-ODH equilibrium ethane conversion of 30.2 %.

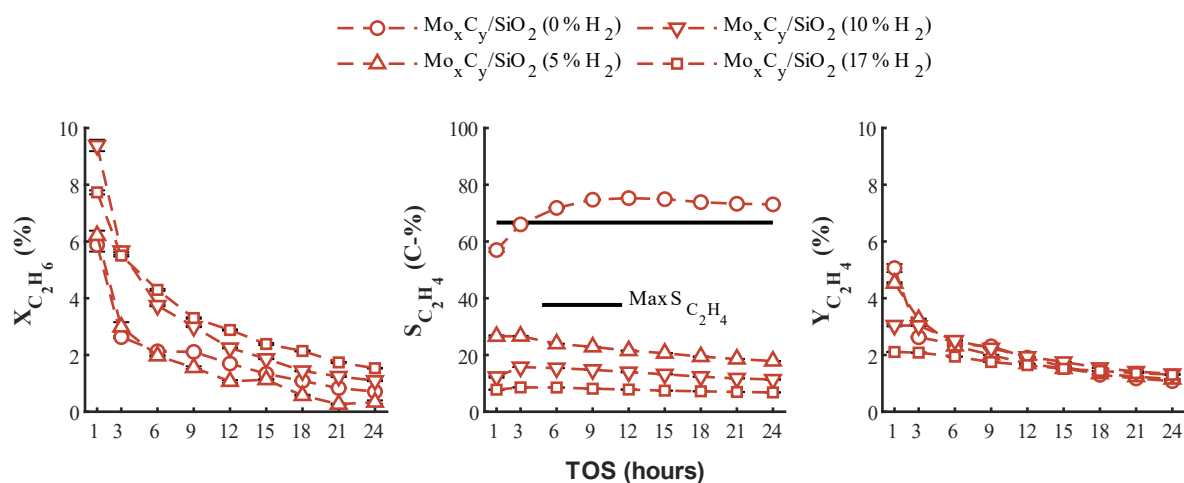


Figure 7.19. C₂H₆ conversion, C₂H₄ selectivity and C₂H₄ yield, of Mo_xC_y catalysts supported on SiO₂. H₂/CO₂-ODH conditions: T = 600 °C, P = 1 atm, SV = 18.2 L h⁻¹ g_{cat}⁻¹, CO₂:C₂H₆:Ar = 1:1:2, with H₂ co-feeding at 0, 5, 10 and 17 vol.-%. Theoretical maximum C₂H₄ selectivity for CO₂-ODH indicated by solid black line.

At 0 vol.-% H₂, the performance of Mo_xC_y/SiO₂ is very similar to previously discussed CO₂-ODH experiments (see Figure 7.19 and Figure B.6). In the presence of 5 vol.-% H₂, the conversion of C₂H₆ and its stability with time on stream for Mo_xC_y/SiO₂ shows no significant improvement. CO₂ conversion increased to about 20 %, which decreases with TOS to about 10 % (see Figure B.6). At 10 and 17 vol.-% H₂ co-feeding, the initial C₂H₆ conversion at 1 hour TOS increased to 9.4 and 7.7 % and the CO₂ conversion increased to 32 and 42 %, respectively. While S_{C₂H₄} shows a significant drop upon H₂ co-feeding, Y_{C₂H₄} only shows a slight decrease in the first 3 hours TOS. These observations suggest that the RWGS reaction occurs simultaneously with the CO₂-ODH reaction, and that the ODH mechanism

remains intact. In the first 3 hours TOS, the lower ethylene production can suggest that initially, on a fresh carbide surface, DR occurs simultaneously.

$\text{Mo}_x\text{C}_y/\text{ZrO}_2$ shows a lower initial activity at 0 vol.-% H_2 co-feeding than previously observed but reaches a comparable activity and selectivity (see Figure 7.20 and Figure B.7). The lower initial activity can possibly be explained by the increased content of $\text{Zr}(\text{MoO}_4)_2$ found in the spent catalyst (see Figure 7.21 and Table K.2). Upon the introduction of 5 vol.-% H_2 to the feed, a small improvement in C_2H_6 conversion (from 4.4 to 5.3 % at 1 hour TOS) and an increased stability is observed. At 0 vol.-% H_2 , after 6 hours TOS, 76 % of the initial C_2H_6 conversion was lost, but at 5 vol.-% H_2 a loss of 45 % is recorded. A similar CO_2 conversion to the one of $\text{Mo}_x\text{C}_y/\text{SiO}_2$ is observed, starting at about 20 % after 1 hour TOS, dropping to about 10 % at the end of the experiment. The increased RWGS activity significantly impacts the calculated carbon-based selectivity. However, in the absence of H_2 co-feeding, ethylene selectivity and C_2H_6 conversion show an inverse relationship. In the presence of H_2 , this trend becomes a direct relationship. The latter can be explained by the spent catalyst composition. A significantly lower amount of MoO_2 is detected in the spent samples and an increased $\beta\text{-Mo}_2\text{C}$ content is observed (see Figure 7.21 and Table K.2). The initial drop in activity can be related to the oxidation of the catalyst, however, with TOS, H_2 in combination with C_2H_6 re-carburizes the sample to $\beta\text{-Mo}_2\text{C}$, suggested to be the most active carbide phase for CO_2 activation. At 17 vol.-% H_2 co-feeding, $X_{\text{C}_2\text{H}_6}$ increased to 7.4 % for $\text{Mo}_x\text{C}_y/\text{ZrO}_2$, paralleled by an improved stability. After 6 hours TOS $\text{Mo}_x\text{C}_y/\text{ZrO}_2$ lost 35 % of the initial conversion, showing to be more stable than $\text{Mo}_x\text{C}_y/\text{SiO}_2$. After 24 hours TOS a loss in C_2H_6 conversion of 53 % was recorded.

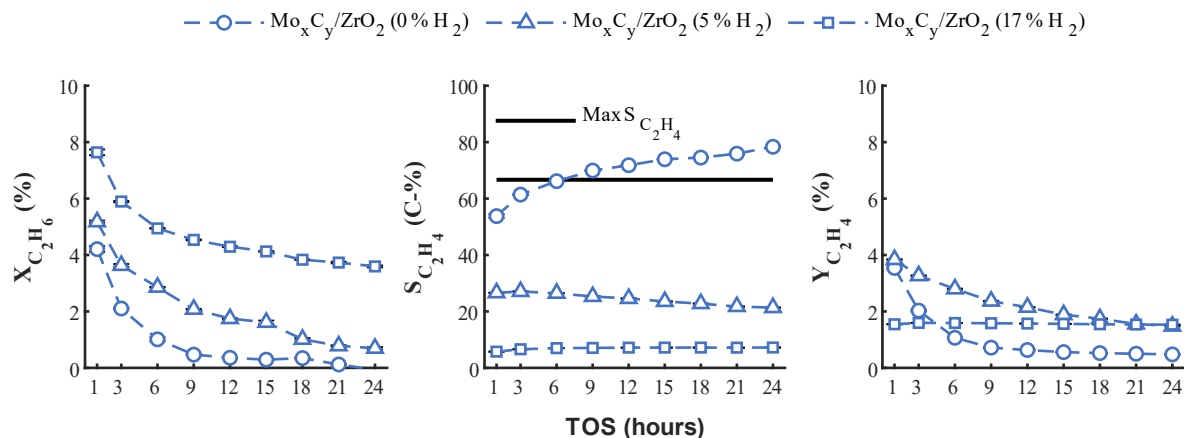


Figure 7.20. C_2H_6 conversion, C_2H_4 selectivity and C_2H_4 yield, of Mo_xC_y catalysts supported on ZrO_2 evaluated under the following $\text{H}_2/\text{CO}_2\text{-ODH}$ conditions: $T = 600^\circ\text{C}$, $P = 1\text{ atm}$, $\text{SV} = 18.2\text{ L h}^{-1}\text{ g}_{\text{cat}}^{-1}$, $\text{CO}_2:\text{C}_2\text{H}_6:\text{Ar} = 1:1:2$, with and without co-feeding of H_2 at 0, 5 and 17 vol.-%. Theoretical maximum C_2H_4 selectivity for $\text{CO}_2\text{-ODH}$ indicated by solid black line.

The methanation reaction is thermodynamically favoured over CO₂-ODH (see Figure 5.1) but even with H₂ co-feeding up to 17 vol.-%, CH₄ formation is limited, with a maximum of 2.8 C-%, indicating the successful suppression of the CO₂/CO methanation reaction over the carbide catalysts. As mentioned earlier, the carbon-based selectivity is overshadowed by the CO formation from RWGS and thus C₂H₄ yields are preferred to compare the ODH (and/or DH) performances. For Mo_xC_y/SiO₂ we already observed that the Y_{C₂H₄} at 0 vol.-% H₂ is nearly equal to that of 5, 10 or 17 vol.-%. This supports the observation that for Mo_xC_y/SiO₂, although less oxidation of the catalyst is observed in the spent sample, H₂ in the feed does not have a serious impact on the CO₂-ODH performance of the catalyst. For Mo_xC_y/ZrO₂, the Y_{C₂H₄} at 1 hour TOS with 0 and 5 vol.-% H₂ co-feeding, are nearly equal at 3.6-3.8 %. The increased stability of the catalyst mentioned earlier, can also be seen in the ethylene yield. At 0 vol.-% the yield drops to 0.6 % after 12 hours TOS. In the presence of 5 vol.-% H₂ the yield drops from 3.8 % to 2.1 %. When co-feeding 17 vol.-% H₂ the initial yield is significantly lower (1.6 %) but remains stable over the entire 24 hours TOS. The much higher X_{C₂H₆} yet lower Y_{C₂H₄} observed, suggests a more prominent dry-reforming pathway over Mo_xC_y/ZrO₂, in the presence of 17 vol.-% H₂. Nevertheless, a stable ethylene yield is achieved by a balanced CO₂-ODH and RWGS reaction pathway and the decrease in activity is mainly due to the decrease in activity to certain side reactions, such as dry-reforming or methanation.

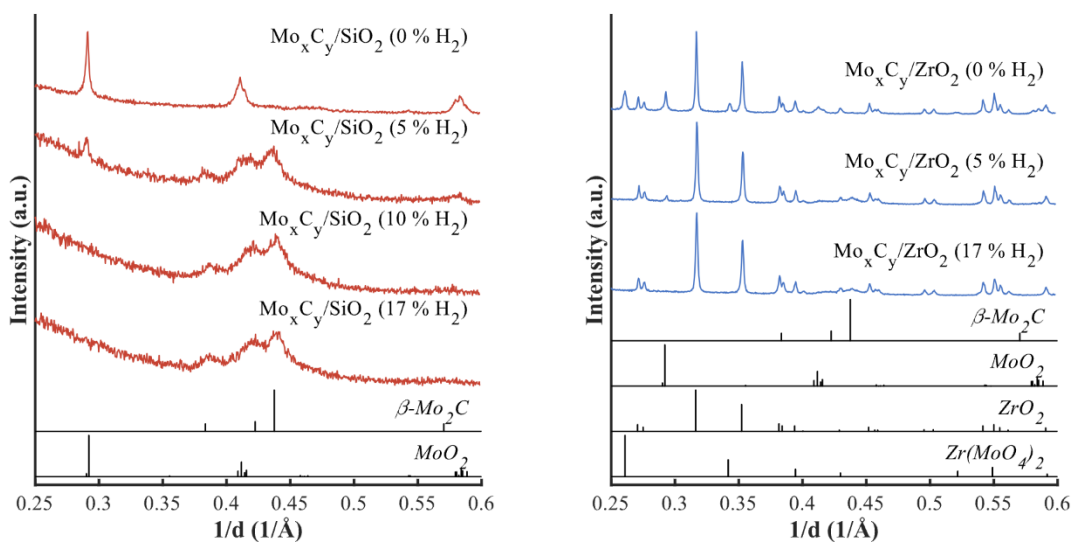


Figure 7.21. XRD patterns of the spent H₂/CO₂-ODH Mo_xC_y catalysts supported on SiO₂ or ZrO₂.

Carbon deposits are still observed (see Figure 7.22) which can now be due to a combination of the CO₂-ODH (e.g., C₂H₄ decomposition) and the re-carburization reaction. Interestingly, at 17 vol.-% H₂

co-feeding for $\text{Mo}_x\text{C}_y/\text{ZrO}_2$, no carbon deposition is observed. This supports the increased stability of the catalyst. At 0 vol.-% H_2 co-feeding, the D- and G-band ratio (I_D/I_G) is lower than in the presence of H_2 co-feeding, suggesting that H_2 co-feeding causes the carbon deposits to be less graphitic (ordered).

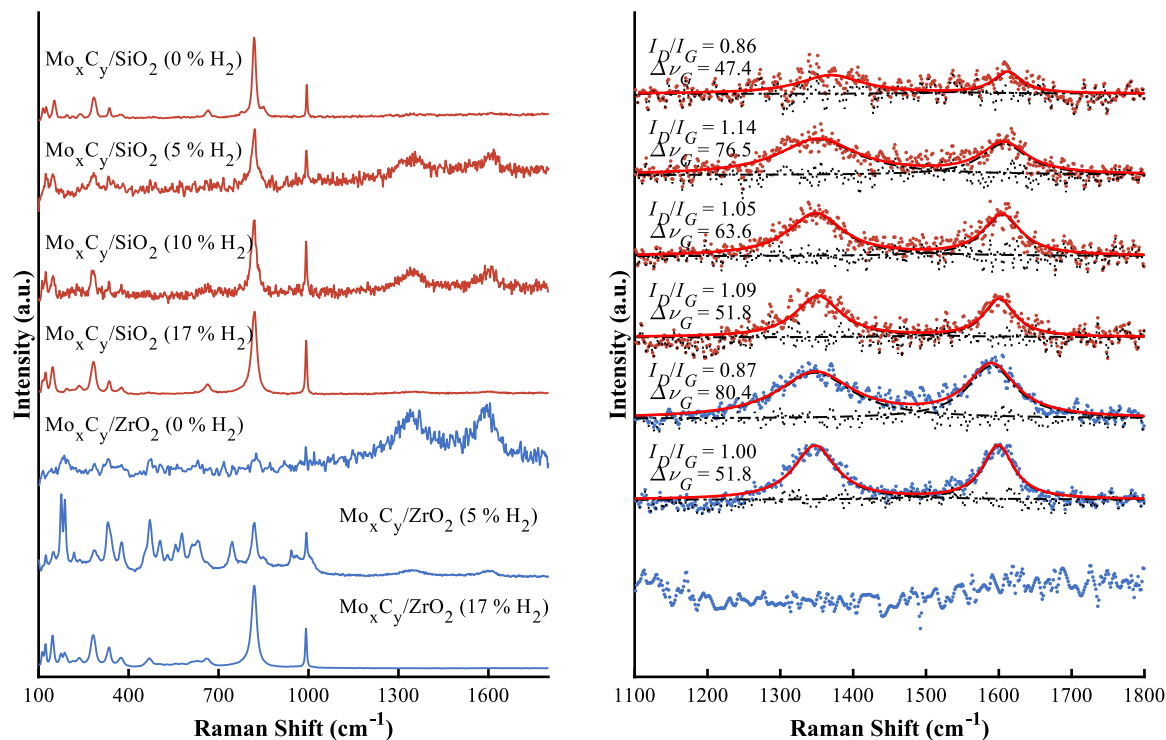


Figure 7.22. Raman spectra of the spent H_2/CO_2 -ODH Mo_xC_y catalysts supported on SiO_2 or ZrO_2 .

On $\text{Mo}_x\text{C}_y/\text{Ga}_2\text{O}_3$, H_2 co-feeding did not increase the initial $X_{\text{C}_2\text{H}_6}$, however, it did have a significant effect on the stability of the catalyst (see Figure 7.23 and Figure B.8). In addition, an increased stability in the $Y_{\text{C}_2\text{H}_4}$ is achieved. The enhanced performance for $\text{Mo}_x\text{C}_y/\text{Ga}_2\text{O}_3$ upon H_2 co-feeding is in particular interesting as thus far, even at a 5:1 feed ratio, the spent catalyst revealed minimal bulk oxidation. With H_2 co-feeding, no bulk oxidation of the carbide is observed (see Figure 7.24). It can thus be suggested that catalyst deactivation is mainly caused by carbon deposition. The co-fed H_2 can aid in the removal of surface carbon, or it can limit surface oxidation, which can result in the slightly slower deactivation, although no evidence was found. Thus, while for $\text{Mo}_x\text{C}_y/\text{SiO}_2$ and $\text{Mo}_x\text{C}_y/\text{ZrO}_2$ the increased C_2H_6 conversion is paired with a more prominent DR pathway, on $\text{Mo}_x\text{C}_y/\text{Ga}_2\text{O}_3$ the activity is enhanced by freeing up surface active sites through the removal of the over-stoichiometric amount of oxygen surface species, or *via* the removal of surface carbon. It would be of interest to further increase the H_2 content in the feed, to see if catalyst deactivation can be fully prevented. Alternatively, H_2O co-feeding could be an option for carbon removal.

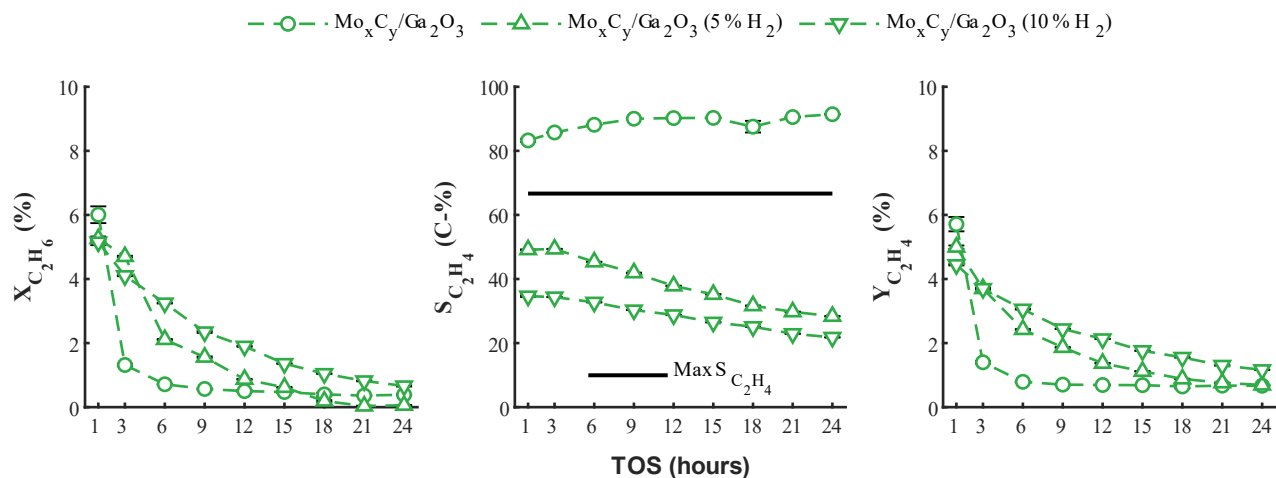


Figure 7.23. C_2H_6 conversion, C_2H_4 selectivity and C_2H_4 yield, of Mo_xC_y catalysts supported on Ga_2O_3 . H_2/CO_2 -ODH conditions: $T = 600\text{ }^\circ\text{C}$, $P = 1\text{ atm}$, $\text{SV} = 18.2\text{ L h}^{-1}\text{ g}_{\text{cat}}^{-1}$, $\text{CO}_2:\text{C}_2\text{H}_6:\text{Ar} = 1:1:2$, with co-feeding of H_2 at 5 or 10 vol.-%. Theoretical maximum C_2H_4 selectivity for CO_2 -ODH indicated by solid black line.

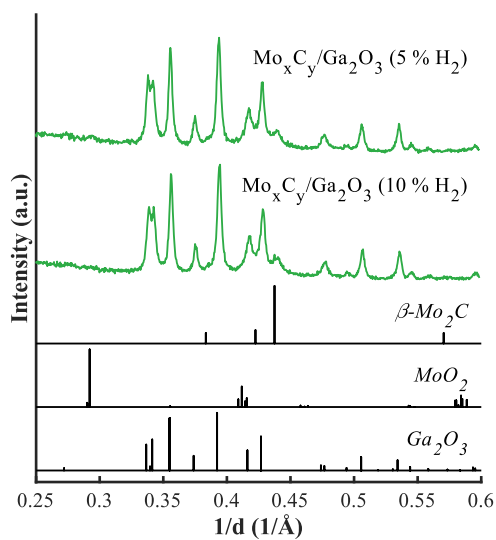


Figure 7.24. XRD patterns of the spent H_2/CO_2 -ODH Mo_xC_y catalysts supported on Ga_2O_3 .

7.6 Concluding remarks

Thermodynamic calculations have shown that co-feeding H_2 , H_2O or an inert, does not affect the thermodynamic stability of Mo_2C towards oxidation. At the proposed reaction temperature of $600\text{ }^\circ\text{C}$, Mo_2C is the most stable phase.

The addition of various metal oxide support materials to the Mo_xC_y catalyst system has shown to largely influence the acid and base properties, which then has a significant effect on the affinity to activate CO_2 as well as C_2H_6 . TP- CO_2 experiments revealed that dissociation was heavily restricted when supported on Ga_2O_3 but is enhanced on Al_2O_3 . This effect can also be observed under CO_2 -ODH reaction conditions. C_2H_6 is suggested to be activated on oxygen surface species or Mo_xC_y phase, produced from CO_2 activation. The addition of a Ga_2O_3 as support material, previously shown to be active for C_2H_6 activation, did not increase the overall activity compared to Mo_xC_y on the inert support SiO_2 , which can be due to the lack of produced oxygen surface species. Al_2O_3 on the other hand shows to increase CO_2 dissociation, which lead to an increased initial activity. Catalyst deactivation could not be prevented, which is caused due to both carbon deposition as well as oxidation of the carbide to MoO_2 . On SiO_2 , the carbide system remains the most stable with a 1:1 CO_2 to C_2H_6 feed ratio.

An increased CO_2 content seemed to be advantageous in terms of catalyst stability for both $\text{Mo}_x\text{C}_y/\text{Al}_2\text{O}_3$ and $\text{Mo}_x\text{C}_y/\text{ZrO}_2$, but not for $\text{Mo}_x\text{C}_y/\text{Ga}_2\text{O}_3$ (despite no oxidation observed). Especially $\text{Mo}_x\text{C}_y/\text{Al}_2\text{O}_3$ benefited from the higher CO_2 content. This suggests that the most active catalyst for CO_2 activation, managed to remove carbon deposits under reaction conditions, prolonging catalyst lifetime.

Co-feeding of H_2 had unique effects on the different catalyst systems. On $\text{Mo}_x\text{C}_y/\text{SiO}_2$, no significant effect was observed, besides the increased CO selectivity, produced *via* a RWGS reaction performing simultaneously to the CO_2 -ODH pathway. C_2H_6 conversions and C_2H_4 yield was not much affected. Oxidation of the catalysts was however prevented, but carbon deposition still occurred and caused the catalyst to deactivate rapidly. On $\text{Mo}_x\text{C}_y/\text{ZrO}_2$, H_2 co-feeding caused a significant increase in the C_2H_6 conversion, and it increased the stability of the catalyst, which further improved at higher H_2 concentrations. Again, CO selectivity increased due to an enhanced RWGS activity as well as an enhanced DR activity. However, the ethylene formation route also increased and stabilized upon 17 vol.-% H_2 co-feeding. This is believed to be due to achieving a stable reaction pathway balancing CO_2 -ODH and RWGS. The observed decrease in activity is mainly caused by the loss in activity towards side reactions such as CO_2 methanation or dry-reforming. Lastly, H_2 co-feeding on $\text{Mo}_x\text{C}_y/\text{Ga}_2\text{O}_3$ caused a surprising change in catalytic performance. In the absence of any H_2 co-feeding, or at a 5:1 CO_2 : C_2H_6 feed ratio, bulk oxidation on $\text{Mo}_x\text{C}_y/\text{Ga}_2\text{O}_3$ was limited. Thus, H_2 co-feeding to prevent catalyst oxidation was not expected to increase the activity of the catalyst. In 5 and 10 vol.-% H_2 co-feeding, $\text{Mo}_x\text{C}_y/\text{Ga}_2\text{O}_3$ did not show an increase in the initial C_2H_6 conversion, but a more stable performance was observed, without losing its ability to ethylene formation. This is particularly interesting and should be further investigated.

References

1. S. Raseale, W. Marquart, K. Jeske, G. Prieto, M. Claeys and N. Fischer, Supported Fe_xNi_y catalysts for the co-activation of CO₂ and small alkanes, *Faraday Discuss*, 2021, **229**, 208-231.
2. T. Mo, J. Xu, Y. Yang and Y. Li, Effect of carburization protocols on molybdenum carbide synthesis and study on its performance in CO hydrogenation, *Catalysis Today*, 2016, **261**, 101-115.
3. W. Marquart, S. Raseale, G. Prieto, A. Zimina, B. B. Sarma, J.-D. Grunwaldt, M. Claeys and N. Fischer, CO₂ Reduction over Mo₂C-Based Catalysts, *ACS Catalysis*, 2021, **11**, 1624-1639.
4. S. Deng, H. Li, S. Li and Y. Zhang, Activity and characterization of modified Cr₂O₃/ZrO₂ nano-composite catalysts for oxidative dehydrogenation of ethane to ethylene with CO₂, *Journal of Molecular Catalysis A: Chemical*, 2007, **268**, 169-175.
5. S. Sato, M. Ohhara, T. Sodesawa and F. Nozaki, Combination of ethylbenzene dehydrogenation and carbon dioxide shift-reaction over a sodium oxide/alumina catalyst, *Applied Catalysis*, 1988, **37**, 207-215.
6. K. Nakagawa, M. Okamura, N. Ikenaga, T. Suzuki, K. Nakagawa, M. Okamura, T. Suzuki, T. Kobayashi and T. Kobayashi, Dehydrogenation of ethane over gallium oxide in the presence of carbon dioxide, *Chemical Communications*, 1998, **9**, 1025-1026.
7. T. Ishii and T. Kyotani, in *Materials Science and Engineering of Carbon*, 2016, DOI: 10.1016/b978-0-12-805256-3.00014-3, pp. 287-305.
8. S. K. Bej, C. A. Bennett and L. T. Thompson, Acid and base characteristics of molybdenum carbide catalysts, *Applied Catalysis A: General*, 2003, **250**, 197-208.
9. H. Nishihara, Q.-H. Yang, P.-X. Hou, M. Unno, S. Yamauchi, R. Saito, J. I. Paredes, A. Martínez-Alonso, J. M. D. Tascón, Y. Sato, M. Terauchi and T. Kyotani, A possible bucky bowl-like structure of zeolite templated carbon, *Carbon*, 2009, **47**, 1220-1230.
10. Y. Shu, D. Ma, L. Xu, Y. Xu and X. Bao, Methane Dehydro-Aromatization Over Mo/Mcm-22 Catalysts: A Highly Selective Catalyst For The Formation Of Benzene, *Catal. Lett.*, 2000, **70**, 67-73.
11. K. Pokrovski, K. T. Jung and A. T. Bell, Investigation of CO and CO₂ Adsorption on Tetragonal and Monoclinic Zirconia, *Langmuir*, 2001, **17**, 4297-4303.
12. L. Ferretto and A. Glisenti, Surface Acidity and Basicity of a Rutile Powder, *Chemistry of Materials*, 2003, **15**, 1181-1188.
13. Z. Helali, A. Jedidi, O. A. Syzgantseva, M. Calatayud and C. Minot, Scaling reducibility of metal oxides, *Theoretical Chemistry Accounts*, 2017, **136**, 100.
14. W. Marquart, D. J. Morgan, G. J. Hutchings, M. Claeys and N. Fischer, Oxygenate formation over K/β-Mo₂C catalysts in the Fischer-Tropsch synthesis, *Catalysis Science & Technology*, 2018, **8**, 3806-3817.

8 Promoter addition to SiO₂ supported Mo_xC_y

In this chapter the study of Mo_xC_y-based catalysts is extended to explore the addition of a promoter (iron, potassium, nickel or platinum) to the Mo_xC_y nanoparticles. An extensive study is conducted to observe the promotional effect on the structural and chemical properties, CO₂ activation as well as its catalytic performance in the RWGS and CO₂-ODH of ethane. In addition, the effect of the promotion sequence as well as calcination prior to carburization, on the catalytic activity is studied. The catalysts are tested with a range of CO₂-ODH conditions, with selected catalysts exposed to increased CO₂ content in the feed mixture, as well as H₂ or H₂O co-feeding.

A section of the results reported in this chapter are part of a research article published as: W. Marquart, S. Raseale, M. Claeys, N. Fischer, ChemCatChem 2022, e202200267.

8.1 Catalyst characterization: effect of promotion

The effect of promotion sequence was evaluated for Fe and Pt promotion. For the Fe promoted samples (Fe-Mo_xC_y/SiO₂), the promoter was added in three different sequences. The sample was either prepared *via* co-impregnation (Co-Imp) of an aqueous solution containing both ammonium heptamolybdate as well as iron nitrate, or *via* a sequential impregnation (Seq-Imp) of both precursor salts, i.e., the sample was impregnated with AHM_(aq), dried and subsequently impregnated with Fe(NO₃)_{3(aq)}. The third approach includes a calcination step after the impregnation with AHM_(aq), to obtain MoO₃/SiO₂, followed by the impregnation with Fe(NO₃)_{3(aq)} (Calc-Imp). Pt promotion was established by the Co-Imp method and in addition a sample was calcined after co-impregnation of both precursors, prior to carburization, to obtain Pt-MoO₃/SiO₂, referred to as Co-Imp-Calc. Both potassium and nickel promoted catalysts are prepared *via* the co-impregnation route.

For comparison, an additional unpromoted sample was also exposed to a calcination step, to obtain MoO₃/SiO₂, prior to carburization. Like in the case of the direct carburization of AHM, *in situ* XRD experiments of the calcination to MoO₃ revealed the appearance of a mixture of *hP*-MoO₃ and *oP*-MoO₃ around 230 °C, followed by a dominant *oP*-MoO₃ phase at 340 °C (see Figure 8.1). In contrast to the treatment in a 20 vol.-% CH₄/H₂ mixture, no clear sign for the formation of (NH₄)₂Mo₄O₁₃ is observed, suggesting a harsher and more rapid decomposition in the air atmosphere.

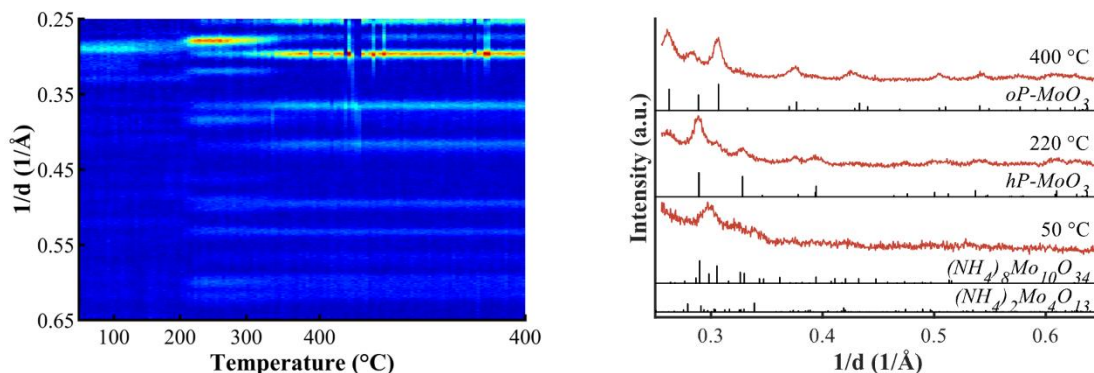


Figure 8.1 [left] Top view of *in situ* XRD patterns following the calcination process of MoO₃/SiO₂ as a function of temperature and [right] the individual patterns at 50, 220 and 400 °C (right). Conditions: T_{final} = 400 °C, P = 1 atm, heating rate = 1 °C min⁻¹, holding time = 5 hours.

The carburization process of AHM (without promotion) is discussed in section 5.2. In a typical carburization, AHM decomposes at 227 °C to a mixture of *hP*-MoO₃ and *oP*-MoO₃. At 347 °C, *oP*-MoO₃ becomes the dominant phase. Reduction to MoO₂ proceeds gradually between 363 °C and 466 °C. Finally, a mixture of η-MoC_{0.59} and β-Mo₂C is formed at 600 °C.

The carburization process in the fixed-bed reactor set-up was monitored by means of mass spectrometry (MS) monitoring the formation of H₂O, CO and CO₂. Carburization of AHM to Mo_xC_y shows a small H₂O formation peak at 290 °C, followed by a large signal with two distinctive peaks at 353 °C and 397 °C and finally a smaller H₂O formation event at 559 °C (see Figure 8.2-A). These observations are very much in line with the observed phase changes in the *in situ* XRD results, despite the significant difference in the reactor design and resulting hydrodynamics (Anton Paar XRK900 cell vs ¼ inch reactor tube). The first H₂O signal can be related to the slow decomposition of the molybdate into the trioxide mixture. The large signals at 353 °C and 397 °C are in line with the phase transformation and reduction from the MoO₃ mixture to MoO₂. The signal observed at 559 °C is due to the reduction of MoO₂ and the subsequent carburization to Mo_xC_y. Upon the formation of the carbide structure at 600 °C, CO and negligible amounts of CO₂ can be detected as well, suggesting that dissociated methane also acts as a reducing agent. The carburization of the calcined sample, MoO₃/SiO₂ (see Figure 8.2-B), shows two distinctive H₂O signals at 400 °C and 570 °C, with a broad signal around 275 °C. These signals are very much in line with the reduction of *oP*-MoO₃ to MoO₂ (at 400 °C) and the reduction of MoO₂ and subsequent carburization to Mo_xC_y.

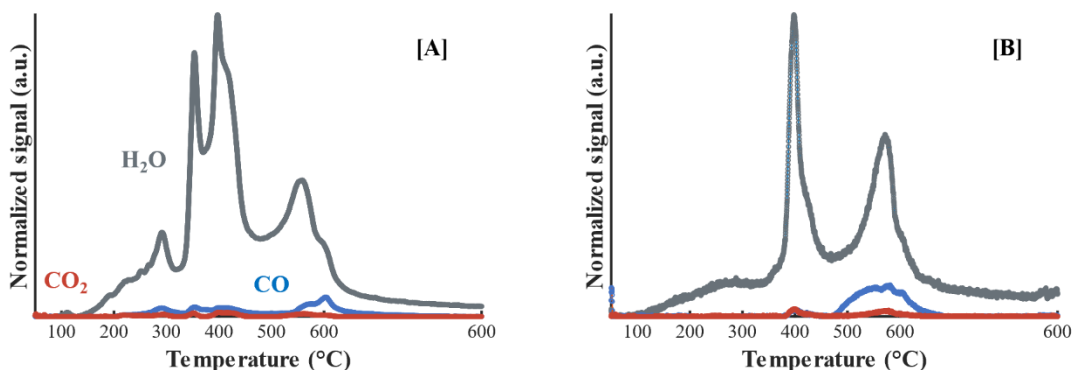


Figure 8.2: Carburization of [A] AHM/SiO₂ and [B] MoO₃/SiO₂ to Mo_xC_y, monitored by mass spectrometry *via* the formation of H₂O, CO and CO₂. Conditions: T_{final} = 600 °C, P = 1 atm, heating rate = 1 °C min⁻¹, holding time = 5 hours.

The carburization of MoO₃/SiO₂ to Mo_xC_y/SiO₂ yields a similar carbide allotrope composition compared to the direct carburization route of AHM/SiO₂ to Mo_xC_y (see Figure 8.3 and Table 8.1). The increase in the crystallite size for β-Mo₂C (9.8 vs 4.9 nm) could be explained by the large crystallites obtained after calcination of AHM/SiO₂ to MoO₃/SiO₂ at 400 °C (see Table 8.1).

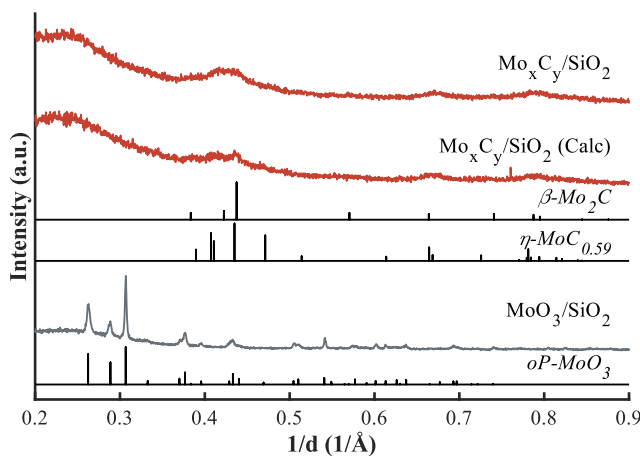


Figure 8.3. XRD patterns of Mo_xC_y/SiO₂ after direct carburization of AHM/SiO₂ and after calcination at 400 °C to MoO₃/SiO₂.

8.1.1. Fe promotion

Some initial changes in the carburization process are observed upon the addition of iron nitrate *via* co-impregnation (see Figure 8.4-A). The decomposition of the precursor molybdate to *hP*-MoO₃ occurs at 165 °C and is followed by the reduction to MoO₂ at 402 °C, without showing any evidence of a phase transformation from *hP*-MoO₃ to *oP*-MoO₃. The carburization onset temperature is slightly reduced in comparison to the unpromoted sample, observed at 516 °C. The reflexes identified as MoO₂ disappear completely at 600 °C. Although no Rietveld refinement was performed, the presence of the various

phases is confirmed by their most intense reflexes (see Figure 8.4-B). MS analysis of the carburization process of the Fe promoted sample in the fixed bed reactor shows a H₂O formation event at 230 °C (decomposition of molybdate), a large signal at 394 °C (reduction of *hP*-MoO₃) and a small event at 555 °C (reduction of MoO₂) (see Figure 8.4-C). Limited CO and CO₂ formation was measured.

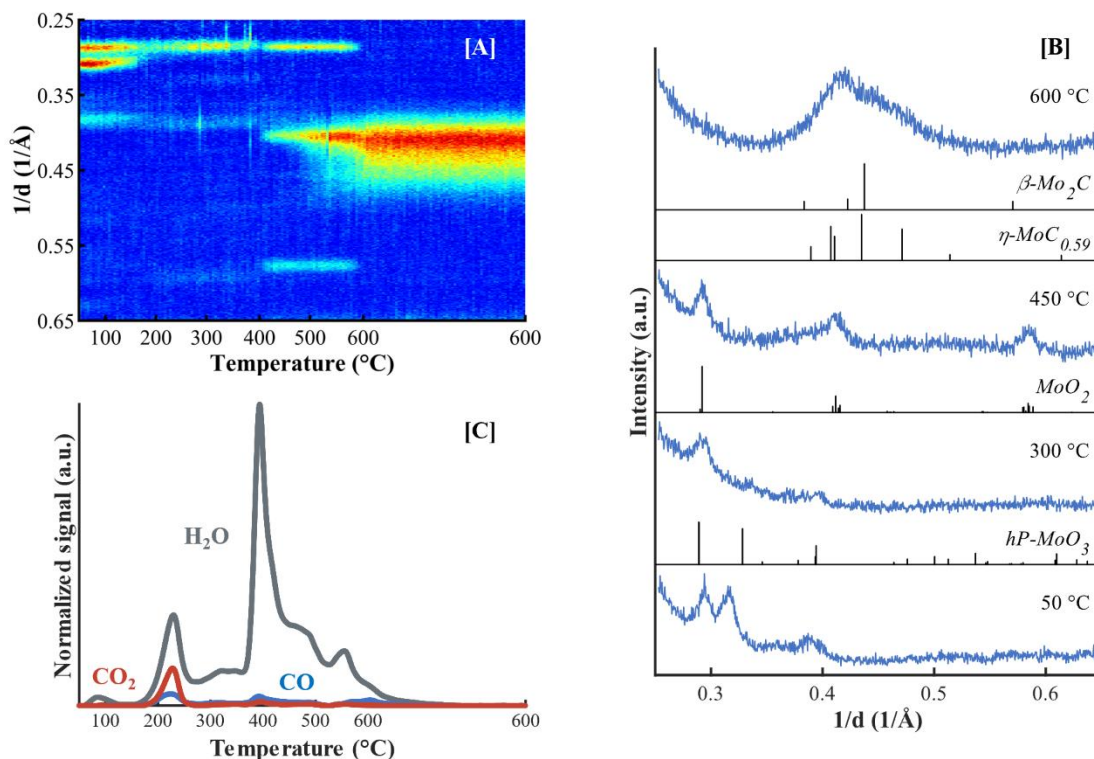


Figure 8.4. Carburization process of Fe-Mo_xC_y/SiO₂ (Co-Imp) as function of temperature, with [A] top view of *in situ* XRD patterns [B] individual patterns obtained at 50, 300, 450 and 600 °C and [C] mass spectrometry signal monitoring the formation of H₂O, CO and CO₂. Conditions: T_{final} = 600 °C, P = 1 atm, heating rate = 1 °C min⁻¹, holding time = 5 hours.

Fe was also impregnated after calcination to MoO₃/SiO₂. As calcination of AHM at 400 °C leads to the formation of *oP*-MoO₃, it is of particular interest to observe any changes in the remaining carburization process (from MoO₃ to Mo_xC_y) upon promotion with Fe. *In situ* carburization does not reveal any significant changes to the carburization process upon promoting MoO₃ with Fe when compared to MoO₃/SiO₂ (see Figure 8.5). The reduction of *oP*-MoO₃ to MoO₂ starts at 420 °C and is completed by 450 °C. The carburization starts at 600 °C.

The freshly carburized samples in the fixed bed reactor show slight intensity variations in their carbide allotrope reflexes (see Figure 8.6) which can also be observed in their composition determined *via* Rietveld refinement (see Table 8.1). All three samples contain a mixture of $\beta\text{-Mo}_2\text{C}$ and $\eta\text{-MoC}_{0.59}$. The crystallite sizes for each allotrope are similar over the three samples, with 7-8 nm for $\beta\text{-Mo}_2\text{C}$ and 4-5 nm

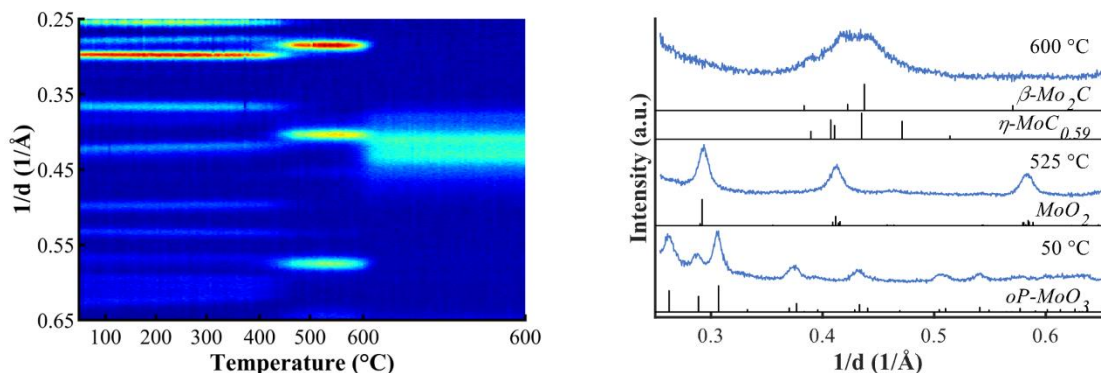


Figure 8.5. Carburization process of Fe-Mo_xC_y/SiO₂ (Calc-Imp) as function of temperature followed by *in situ* XRD (left) and the individual patterns at 50, 525 and 600 °C (right). Conditions: T_{final} = 600 °C, P = 1 atm, heating rate = 1 °C min⁻¹, holding time = 5 hours.

for *η*-MoC_{0.59}. The Calc-Imp sequence yielded the highest content of *β*-Mo₂C (61.3 wt.-%) followed by Seq-Imp with 44.9 wt.-% and Co-Imp with 14.1 wt.-%. The overall lower crystallite size obtained from the Co-Imp sequence can be hypothesized to be due to a closer interaction between the Fe and Mo precursors upon impregnation. The sequential impregnation might create larger distances between the Fe and Mo sites, causing differences in the occurring carburizing reactions. In addition, the two-step drying process at 120 °C might cause early stage sintering of the molybdate precursor. The promotion after calcination can be a combination of increased starting crystallite size, due to calcination, as is observed for the unpromoted sample, and the larger separation between the Fe and Mo sites, similar to sequential impregnation.

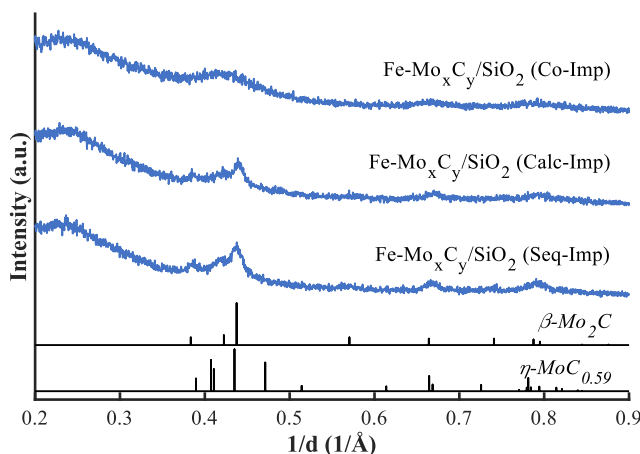


Figure 8.6. XRD patterns of the freshly carburized Mo_xC_y on SiO₂ promoted with Fe *via* co-impregnation (Co-Imp), after calcination (Calc-Imp) or sequential impregnation (Seq-Imp).

8.1.2. Pt promotion

Co-impregnating platinum nitrate has a drastic effect on the carburization process (see Figure 8.7-A). The molybdate decomposes to $hP\text{-MoO}_3$, at 206 °C. The $hP\text{-MoO}_3$ disappears at a significantly lower temperature of 268 °C compared to >400 °C for the un- or Fe- promoted sample. This has previously been attributed due to the enhanced H_2 dissociation and the simultaneous formation of molybdenum bronze (H_xMoO_3) or oxyhydride (MoO_xH_y).¹ No evidence of this phase was found in the obtained XRD patterns, however from 268 °C to 400 °C, no XRD pattern is observed, which suggests the presence of some form of an amorphous phase (see Figure 8.7-B). Instead of forming MoO_2 , the low temperature activation of CH_4 by Pt, leads to the formation of (cubic) MoO_xC_y from about 400 °C.² Full carburization to a mixture of cubic $\alpha\text{-MoC}_{1-x}$ and $\eta\text{-MoC}_{0.59}$ begins at 600 °C. The formation of cubic $\alpha\text{-MoC}_{1-x}$ in the presence of Pt is well known.³ Mass spectrometry analysis of the product gases confirms that the reduction of $hP\text{-MoO}_3$ occurs at significantly lower temperatures, at 294 °C for the Pt-promoted sample compared to 394 °C for the Fe-promoted sample (see Figure 8.7-C). Thereafter, minor events can be observed which can be assigned to the formation of MoO_xC_y and later cubic $\alpha\text{-MoC}_{1-x}$. Again, small amounts of CO and CO_2 were detected as well.

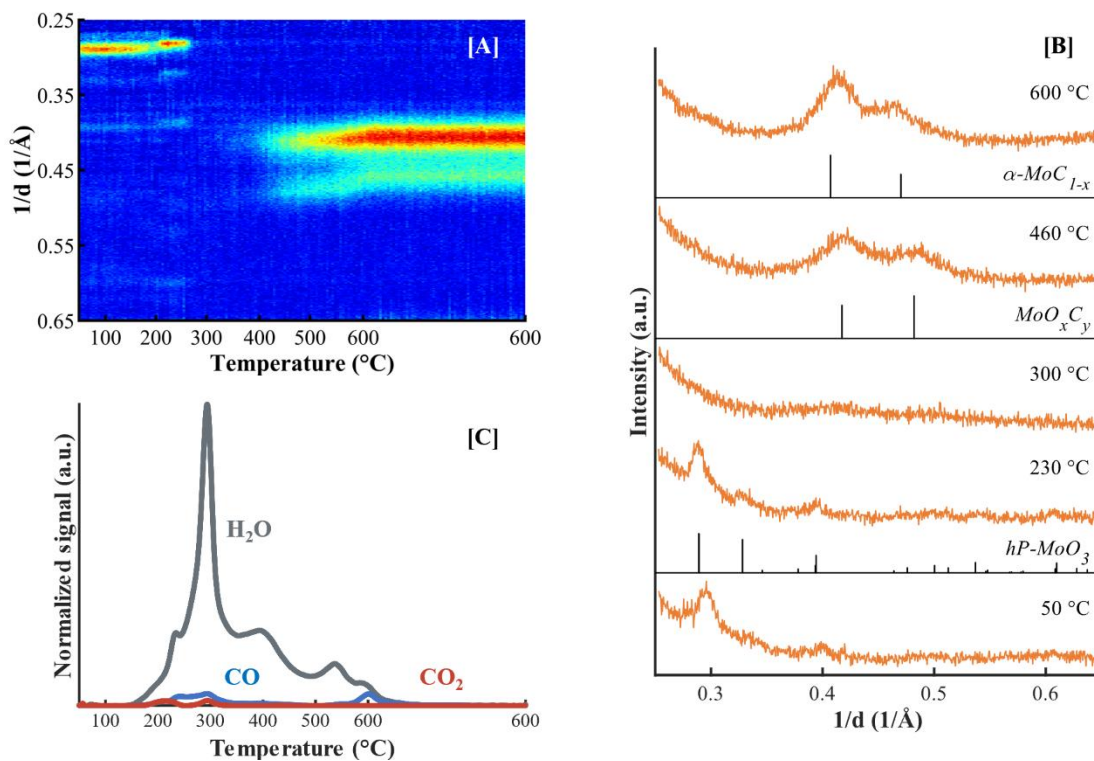


Figure 8.7. Carburization process of $\text{Pt-Mo}_x\text{C}_y/\text{SiO}_2$ (Co-Imp) as function of temperature, with [A] top view of *in situ* XRD patterns [B] individual patterns at 50, 230, 300, 460 and 600 °C and [C] mass spectrometry signal monitoring the formation of H_2O , CO and CO_2 . Conditions: $T_{\text{final}} = 600$ °C, $P = 1$ atm, heating rate = 1 °C min^{-1} , holding time = 5 hours.

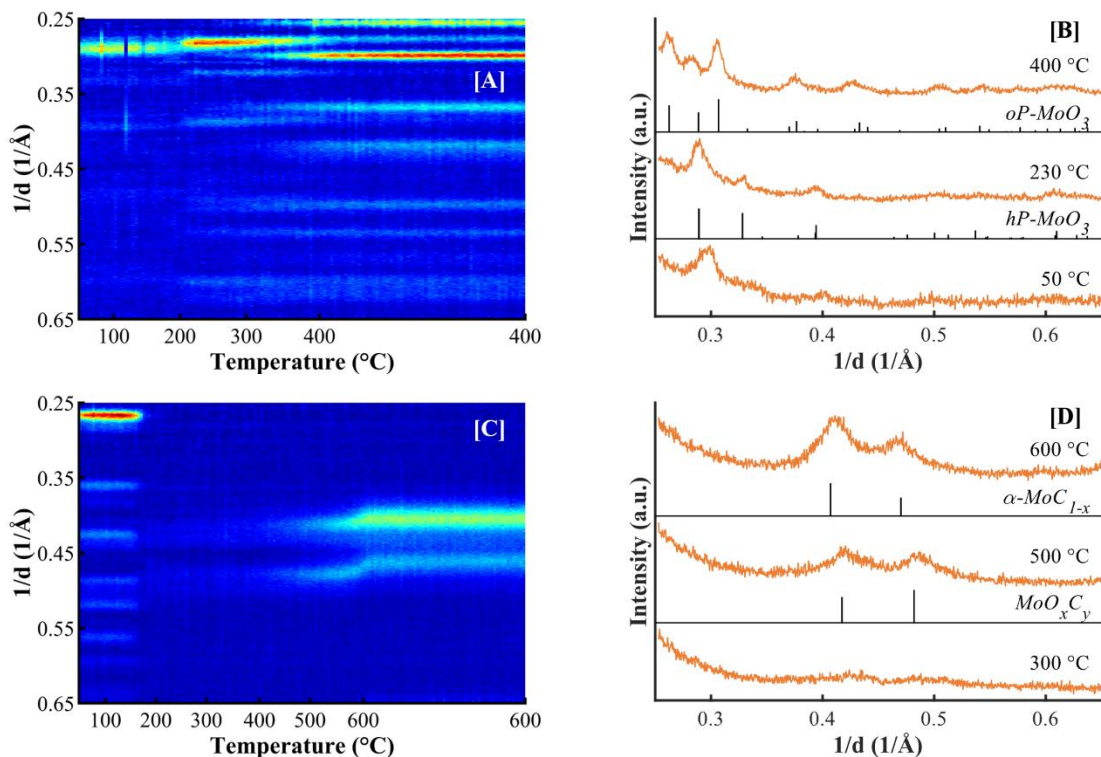


Figure 8.8. [A, B] Calcination process of Pt-MoO₃/SiO₂ and [C, D] carburization process of Pt-Mo_xC_y/SiO₂ (Co-Imp-Calc) as function of temperature, with [A, C] top view of *in situ* XRD patterns, [B, D] individual patterns at selected temperatures. Conditions: T_{final} = 600 °C, P = 1 atm, heating rate = 1 °C min⁻¹, holding time = 5 hours.

The calcination process of the co-impregnated Pt promoted sample to Pt-MoO₃/SiO₂ (see Figure 8.8-A) yields a very similar decomposition pathway to the unpromoted sample (see Figure 8.1). Prior to yielding the orthorhombic structure of MoO₃, the hexagonal structure is observed at 200 °C, which changes to a dominant orthorhombic structure at 400 °C. This is in stark contrast to the decomposition in the carburization gas mixture, which yields solely the hexagonal phase (see Figure 8.7). The same carburization procedure was performed for the calcined sample and monitored by *in situ* XRD (see Figure 8.8-C). The XRD pattern observed at room temperature was not identified as *oP*-MoO₃ or *hP*-MoO₃ but can be identified as H_xMoO₃. It was previously observed that Pt promoted MoO₃, in a flow of CH₄/H₂ mixture turned black, even at room temperature. H₂ dissociates on the Pt surface which is then followed by an H-atom spill over to the oxide surface and further diffuses into the MoO₃ lattice.³ To confirm the transformation of *oP*-MoO₃ to H_xMoO₃ at room temperature, a new sample was loaded and gases were switched between air and 20 vol.-% CH₄ in H₂ mixture (see Figure 8.9-A). In air atmosphere (a), the structure can be clearly identified as *oP*-MoO₃, the same as observed in the freshly calcined sample (see Figure 8.9-B). Upon exposure to the CH₄/H₂ mixture (b), within a matter of minutes, the intensities of the three reflexes observed between 0.25 and 0.3 1/Å decrease and a reflex at about 0.27 1/Å appears.

A slight shift to the left for the reflexes at higher angles is also observed. After removal of the CH₄/H₂ mixture, and re-exposure to air overnight, the structure returns to *oP*-MoO₃ (c), confirming that H_xMoO₃ is a metastable phase. Upon a longer exposure to the CH₄/H₂ mixture (d), a clear change in pattern is observed, which equals the starting pattern in Figure 8.8-C.

The carbides for both freshly carburized samples contain α -MoC_{1-x}, between 33 and 37 wt.-% at a crystallite size of 4.4 and 4.8 nm (see Figure 8.9-B and Table 8.1). The balance is made out of η -MoC_{0.59} (between 54 and 59 wt.-%) and a small amount of β -Mo₂C (between 4.2 and 12 wt.-%). The higher β -Mo₂C is observed for the un-calcined sample, Pt-Mo_xC_y/SiO₂ (Co-Imp). The calcined sample, Pt-Mo_xC_y/SiO₂ (Co-Imp-Calc), has a slightly larger crystallite size for β -Mo₂C (12.4 nm vs 7.4 nm). Although the effect of calcination on the crystal structure and crystallite size is not as significant as was observed in the un-promoted and Fe-promoted samples, the slightly increased crystallite size can again be explained by the large crystallite size observed for *oP*-MoO₃ after calcination at 400 °C (33.6 nm). The slightly increased β -Mo₂C content in the un-calcined sample can be rationalized by the decomposition to the hexagonal *hP*-MoO₃ phase in the carburizing gas mixture.

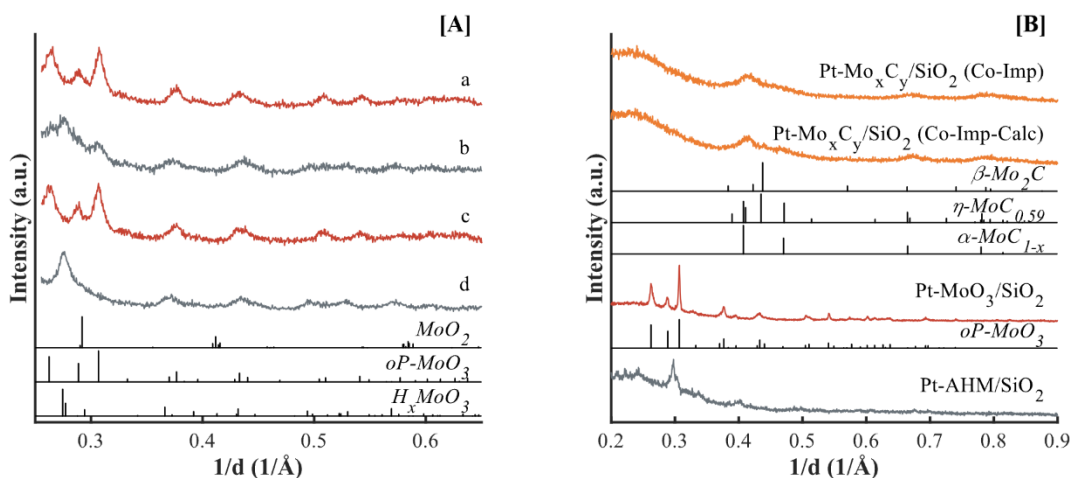


Figure 8.9. [A] XRD patterns of Pt-MoO₃/SiO₂ in (a) air atmosphere, (b) upon short term exposure to 20 vol.-% CH₄/H₂, followed by (c) overnight exposure to air and finally (d) long term exposure to 20 vol.-% CH₄/H₂. [B] XRD patterns of the freshly carburized Pt-Mo_xC_y/SiO₂ prepared *via* Co-Imp and Co-Imp-Calc, including patterns of the precursors Pt-MoO₃/SiO₂ and Pt-AHM/SiO₂.

8.1.3. Ni promotion

Co-impregnating nickel nitrate also has a severe effect on the carburization process, when compared to the unpromoted sample, and shows similar behaviour to Pt-Mo_xC_y/SiO₂ (Co-Imp). The molybdate decomposes to *hP*-MoO₃ at 170 °C which then disappears at 330 °C (see Figure 8.10-A). Between 330 °C and 400 °C, no clear XRD reflexes are observed (see Figure 8.10-B). While the observed phenomenon

likely occurs *via* a similar mechanism as described for the Pt-promoted sample, the decomposition of the molybdate seems to occur faster but the reduction of *hP*-MoO₃ is delayed from 268 °C to 330 °C. The clear formation of MoO_xC_y is observed at a similar temperature, from about 400 °C.² Full carburization to a mixture of cubic α -MoC_{1-x} and η -MoC_{0.59} begins at 578 °C. The formation of cubic α -MoC_{1-x} in the presence of Ni is not reported consistently in literature.^{4,5}

The analysis of the product gases upon carburization in the fixed bed reactor again correlates very well with the *in situ* XRD results (see Figure 8.10-C). A large H₂O signal at 300 °C indicating the reduction of *hP*-MoO₃ is followed by minor events, which can be assigned to the formation of MoO_xC_y and later the cubic α -MoC_{1-x} (and η -MoC_{0.59}). XRD and Rietveld analysis of the freshly carburized sample suggests a mixture of the three carbide phases, containing 12 wt.-% α -MoC_{1-x}, 22 wt.-% β -Mo₂C and 66 wt.-% η -MoC_{0.59} (see Figure 8.10-D and Table 8.1). The higher β -Mo₂C content over α -MoC_{1-x} content is in line with the inconsistent results obtained in literature regarding the crystal structure of the carbide upon carburization in the presence of a Ni promoter.

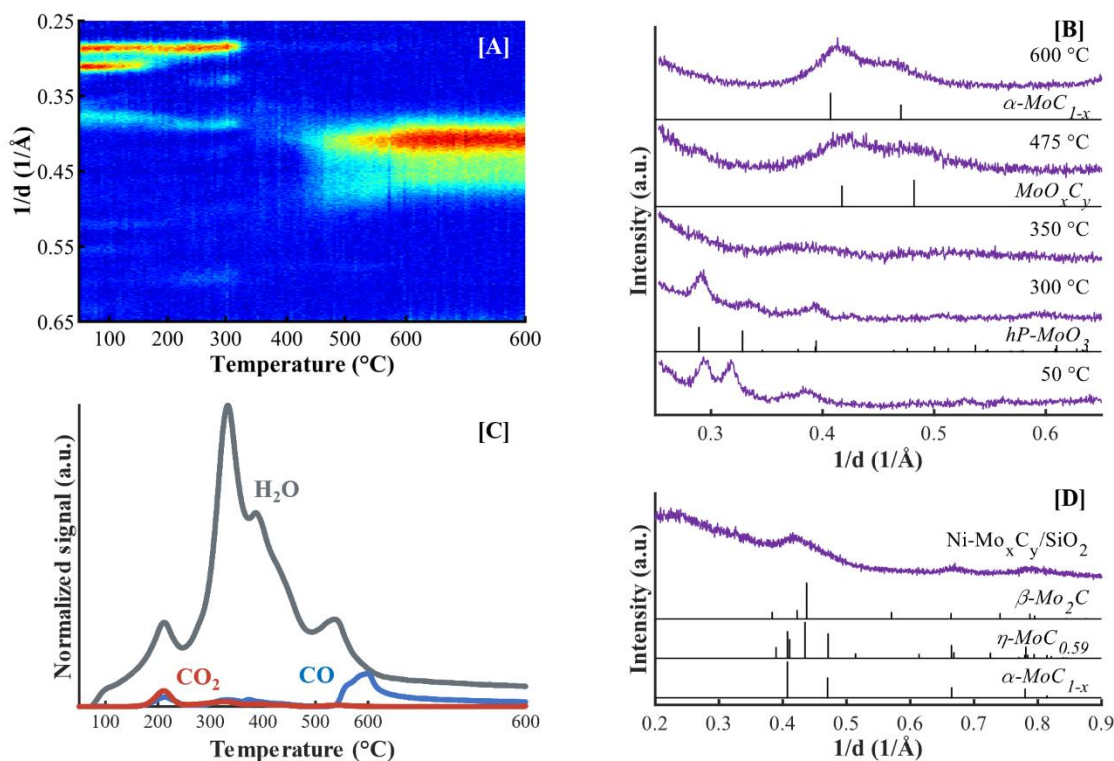


Figure 8.10. Carburization process of Ni-Mo_xC_y/SiO₂ as function of temperature, with [A] top view of *in situ* XRD patterns, [B] individual patterns at 50, 300, 550 and 600 °C, [C] mass spectrometry signal monitoring the formation of H₂O, CO and CO₂ and [D] XRD pattern of the freshly carburized sample Ni-Mo_xC_y/SiO₂. Conditions: T_{final} = 600 °C, P = 1 atm, heating rate = 1 °C min⁻¹, holding time = 5 hours.

8.1.4. K promotion

Despite the addition of potassium nitrate, the carburization process is similar to the unpromoted sample (see Figure 8.11-A). The molybdate decomposes at 231 °C to *oP*-MoO₃ as the dominant phase. First signs of reduction to MoO₂ can be observed at 407 °C and the phase becomes dominant at 469 °C, followed by the carburization at 600 °C.

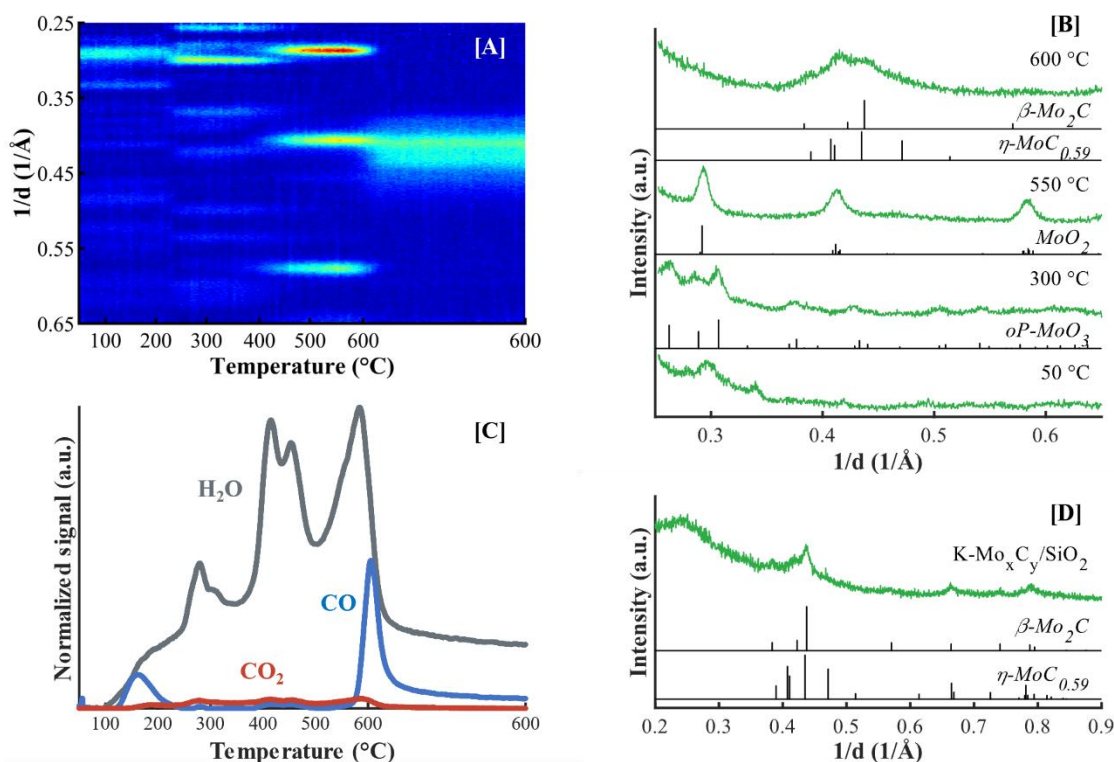


Figure 8.11. Carburization process of K-Mo_xC_y/SiO₂ as function of temperature, with [A] top view of *in situ* XRD patterns [B] individual patterns at 50, 300, 550 and 600 °C, [C] mass spectrometry signal monitoring the formation of H₂O, CO and CO₂ and [D] XRD pattern of the freshly carburized K-Mo_xC_y/SiO₂. Conditions: T_{final} = 600 °C, P = 1 atm, heating rate = 1 °C min⁻¹, holding time = 5 hours.

To the standard operation procedure of the mass spectrometer, either the reactant gas stream or the reactor effluent gas stream has to be diluted, maintaining a consistent CH₄ and H₂ absolute flowrate. The unpromoted, Fe, Pt and Ni-promoted samples were all analysed by diluting the effluent gas stream, staying consistent with the carburization procedure prior to catalytic testing. For K-Mo_xC_y/SiO₂ the reactant gas stream was diluted, hence a larger total flowrate was used during the carburization procedure, to maintain the absolute flowrates of CH₄ and H₂.

For comparison, the unpromoted sample was re-analysed with a diluted carburization mixture (see Figure 8.12). Again, the formation of water can be observed at three main events. A small event at 275 °C

(decomposition of the molybdate), a large signal at 385 °C (reduction from MoO₃ to MoO₂) and a large signal at 574 °C (combined reduction and carburization of MoO₂). The main difference observed between the experiment with a diluted reactant compared to the case of a diluted effluent stream, is the significantly larger CO signal observed at 600 °C. These differences can be rationalized by the changes in contact time or partial pressures of the carburization mixture. However, further investigations are required to confirm if these changes affect the physicochemical properties of the samples.

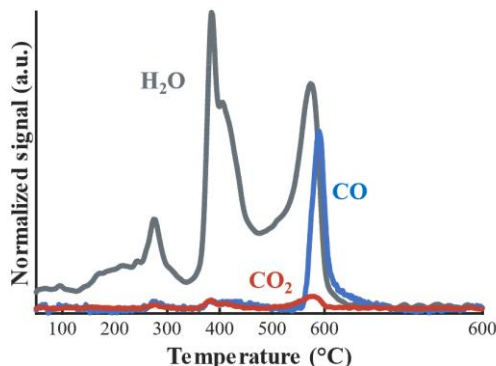


Figure 8.12. Carburization of Mo_xC_y/SiO₂ with a diluted carburization mixture, monitored by mass spectrometry *via* the formation of H₂O, CO and CO₂. Conditions: T_{final} = 600 °C, P = 1 atm, heating rate = 1 °C min⁻¹, holding time = 5 hours.

For K-Mo_xC_y/SiO₂, the H₂O signal is comparable to the unpromoted sample, with a slightly reduced ratio between the H₂O signals at 415 °C and 584 °C, which could indicate a higher degree of reduction of the MoO₂ in the presence of potassium. Although no sign of metallic Mo is observed in the freshly carburized K-Mo_xC_y/SiO₂ (see Figure 8.11-D and Table 8.1), a higher degree of reduction of MoO₂ is supported by literature reporting the formation of metallic Mo after carburization of potassium promoted MoO_x.⁶ The CO signal, which indicates the carburization process, is comparable to the unpromoted sample carburized with a diluted reaction mixture.

Table 8.1. Overview of phase quantification and crystallite sizes determined *via* Rietveld analysis of the synthesized catalysts.

Sample	β -Mo ₂ C		η -MoC _{0.59}		α -MoC _{1-x} / MoO _x C _y		<i>oP</i> -MoO ₃	
	wt.-% (error)	nm (error)	wt.-% (error)	nm (error)	wt.-% (error)	nm (error)	wt.-% (error)	nm (error)
MoO ₃ /SiO ₂	-	-	-	-	-	-	100	39 (1.2)
Mo _x C _y /SiO ₂ (Calc)	15.5 (2.0)	9.8 (1.7)	84.6 (2.0)	3.2 (0.2)	-	-	-	-
Fe-Mo _x C _y /SiO ₂ (Co-Imp)	14.1 (3.1)	7.2 (1.9)	85.9 (3.1)	4.1 (0.4)	-	-	-	-
Fe-Mo _x C _y /SiO ₂ (Calc-Imp)	61.3 (2.8)	7.0 (0.4)	38.7 (2.8)	4.9 (0.6)	-	-	-	-
Fe-Mo _x C _y /SiO ₂ (Seq-Imp)	44.9 (3.1)	7.6 (0.7)	55.1 (3.1)	3.8 (0.4)	-	-	-	-
Pt-Mo _x C _y /SiO ₂ (Co-Imp)	12.4 (2.3)	7.4 (1.7)	53.9 (4.1)	4.4 (0.4)	33.7 (4.1)	4.4 (0.5)	-	-
Pt-MoO ₃ /SiO ₂	-	-	-	-	-	-	100	33.6 (1.1)
Pt-Mo _x C _y /SiO ₂ (Co-Imp-Calc)	4.2 (1.9)	12.4 (6.7)	59.2 (4.2)	4.7 (0.4)	36.6 (4.1)	4.8 (0.5)	-	-
Ni-Mo _x C _y /SiO ₂ (Co-Imp)	21.6 (3.1)	4.5 (0.7)	66.4 (3.4)	4.1 (0.3)	11.9 (2.4)	6.1 (1.3)	-	-
K-Mo _x C _y /SiO ₂ (Co-Imp)	33.2 (1.9)	8.4 (0.6)	66.8 (1.9)	3.2 (0.2)	-	-	-	-

8.1.5. Characterization of activated catalysts: effect of promotion

Each sample, all prepared *via* co-impregnation, was prepared targeting a loading of 20 wt.-% Mo and 1 wt.-% promoter. ICP-OES and BET analysis of the freshly carburized samples are shown in Table K.1. The surface area of 20 wt.-% Mo₂C on SiO₂ (123 m²/g) shows a slight drop when calcined prior to carburization or upon the (co-)impregnation with the various metals. Sequential impregnation of Fe does not show a difference in BET surface area compared to the co-impregnated sample, but a clear difference is observed in the pore width and pore volume.

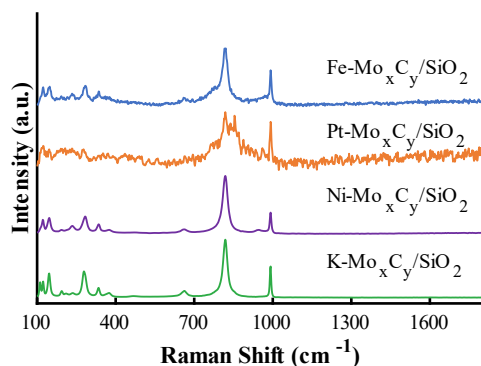


Figure 8.13. Raman spectra of the freshly carburized Fe-Mo_xC_y/SiO₂, Pt-Mo_xC_y/SiO₂, Ni-Mo_xC_y/SiO₂ and K-Mo_xC_y/SiO₂, prepared *via* co-impregnation.

The freshly carburized samples were analysed by means of Raman spectroscopy to identify any presence of carbon deposition occurring during carburization (see Figure 8.13). The presence of the D- and G-band (1350 and 1600 cm^{-1} , respectively), representing surface carbon, was not observed.

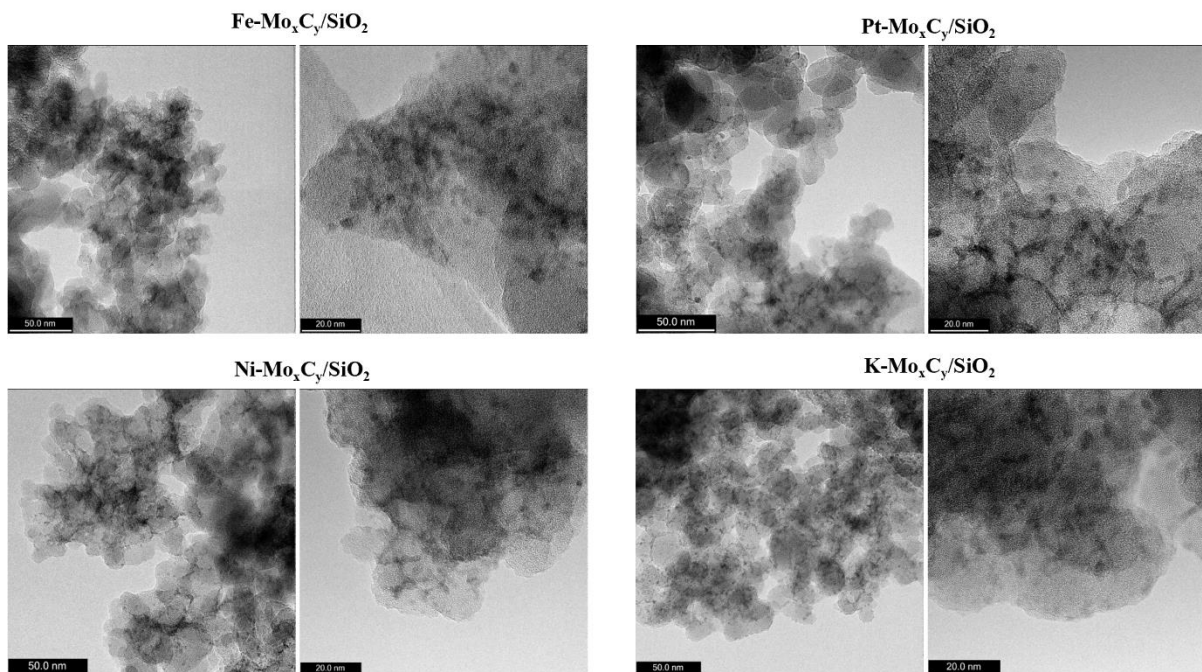


Figure 8.14. TEM micrographs of the freshly carburized Fe-Mo_xC_y/SiO₂, Pt-Mo_xC_y/SiO₂, Ni-Mo_xC_y/SiO₂ and K-Mo_xC_y/SiO₂, prepared *via* co-impregnation.

Transmission electron microscopy (TEM) analysis was employed to confirm the homogeneously distributed particles on the SiO₂ support material with minimal variations in terms of the particle size (see Figure 8.14). Although no reliable particle size distribution could be extracted due to the low contrast between the small carbide particles and the support, it can be estimated that all particles are well below 10 nm in diameter. In line with the earlier Raman analysis, no clear indication of carbon deposition is observed in the micrographs.

By means of scanning electron microscopy (SEM) the even distribution of Mo and the promoter metal on the SiO₂ support and more importantly the co-location of the Mo and promoter metal could be confirmed (see Figure 8.15). In the presence of K, some agglomeration of Mo_xC_y particles is detected which supports the larger crystallite sizes determined *via* Rietveld refinement.

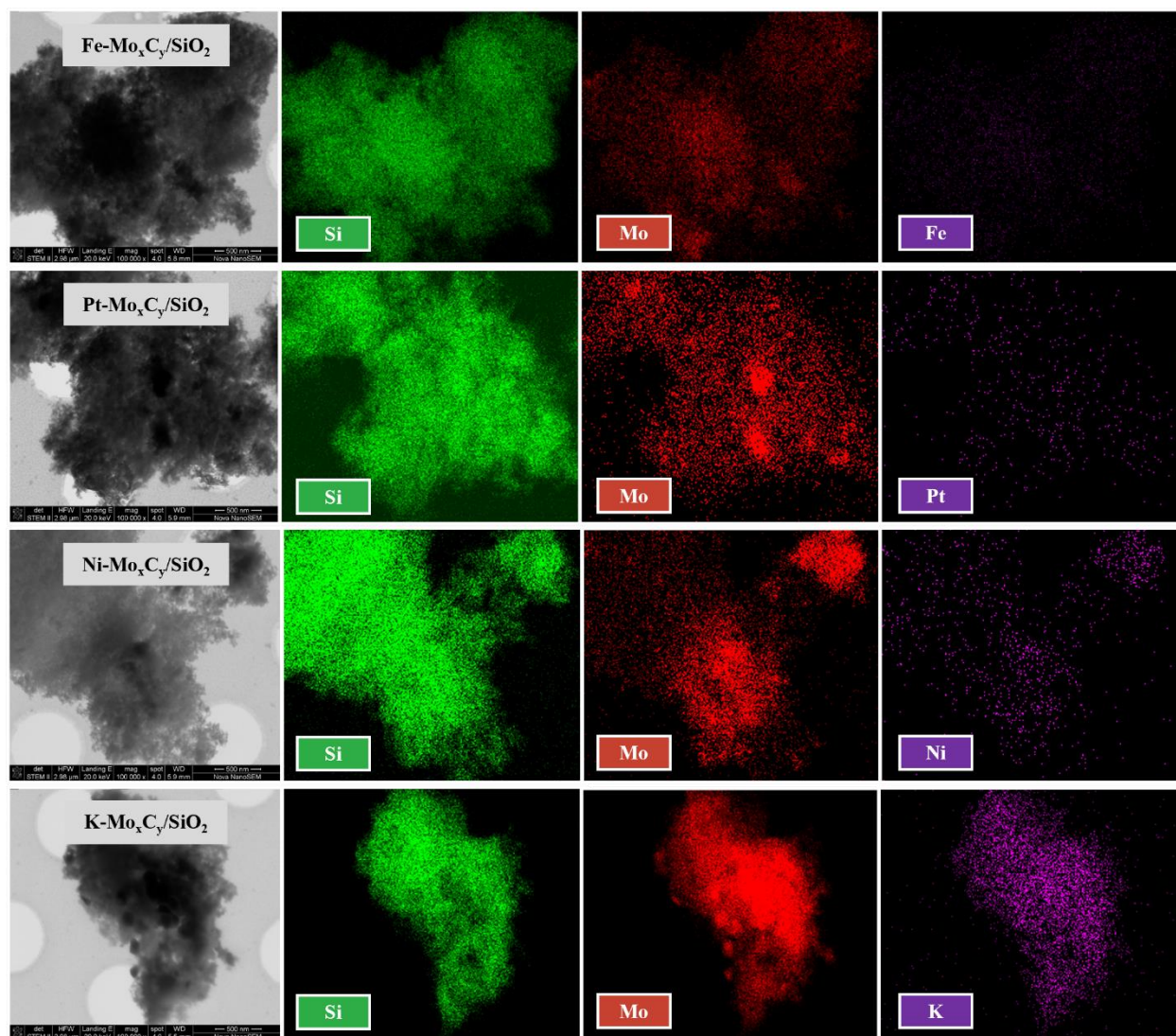


Figure 8.15. SEM-EDS micrographs and elemental mapping of the freshly carburized Fe-Mo_xC_y/SiO₂, Pt-Mo_xC_y/SiO₂, Ni-Mo_xC_y/SiO₂ and K-Mo_xC_y/SiO₂, prepared *via* co-impregnation.

8.2 Acid-base properties: effect of promotion

Each of the co-impregnated samples were analysed by means of NH₃ and CO₂-TPD to determine the amount and strength of acid/base sites on SiO₂ supported Mo_xC_y catalysts and whether these can be tuned by means of promotion. CO₂-TPD experiments revealed the presence of CO₂ and CO desorption peaks within a range of temperatures (see Figure 8.16). The unpromoted sample (previously discussed in section 7.3) is included in the plot. The CO₂ and CO desorbed are normalized to the amount of Mo in the sample as no large differences the surface area are observed. As previously discussed, the CO₂ desorption between 300 and 500 °C is likely due to removal of carbon deposits. This suggests that the desorption

profile below 300 °C is of most interest with regards to the number and strength of the basic sites. Trapezoidal numerical integration of the individual Gaussian curves (see Figure F-2) reveals the amount of CO₂ desorbed, grouped to the temperature corresponding to the peak of each fit. Between 100 and 150 °C, the desorption peak for Fe, Pt and Ni promoted samples is shifted to a slightly higher temperature, with the largest shift observed for Pt-Mo_xC_y/SiO₂ from 130 °C to 147 °C. In the same temperature range, potassium promotion shows double the number of basic sites rather than increasing their strength. Around 200 °C, no signal is observed for the Pt or Fe promoted sample. Ni and K show an increased number of sites at this increased strength. Just below 300 °C, a significant larger signal is observed for Ni, showing the presence of some a large number of strong basic sites.

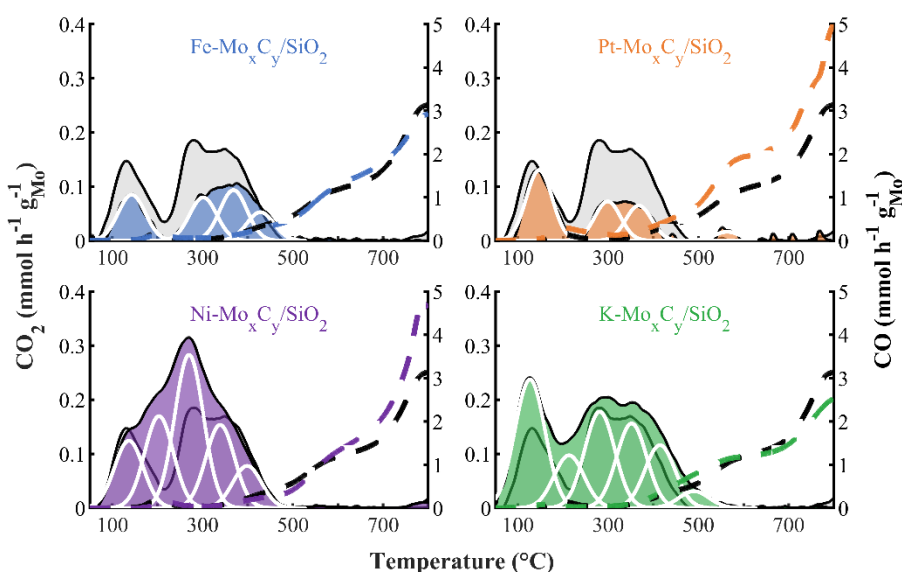


Figure 8.16. CO₂ temperature programmed desorption of Fe-Mo_xC_y/SiO₂, Pt-Mo_xC_y/SiO₂, Ni-Mo_xC_y/SiO₂ and K-Mo_xC_y/SiO₂. Temperature heated up to 800 °C at 10 °C min⁻¹ in an Ar atmosphere. Area plots: CO₂, with deconvoluted peaks in white, dashed lines: CO. The unpromoted sample is shown in the background of each plot by the grey area and black line plot.

The NH₃-TPD experiments reveal an inversed trend in terms of acid sites, compared to the basic sites determined by CO₂-TPD. The direct comparison between the unpromoted and the promoted samples suggests a slightly increased signal for Fe-Mo_xC_y/SiO₂, a similar signal for Pt-Mo_xC_y/SiO₂ and decreased signals for Ni-Mo_xC_y/SiO₂ and K-Mo_xC_y/SiO₂. The unpromoted, Ni and Pt promoted samples show the largest amount of Brønsted acid sites at 340 °C⁷, but almost no NH₃ desorption can be detected for K-Mo_xC_y/SiO₂, in line with literature suggesting that potassium promotion leads to a decrease in the number of acid sites.^{6, 8} Fe-Mo_xC_y/SiO₂ shows a significantly higher signal at 470-500 °C. This can be explained by an overlapping signal between stronger acid sites⁹ and (sub)surface oxygen complexes reacting with pre-adsorbed carbon, such a signal was not observed during CO₂-TPD. The Ni promoted

sample shows a detectable amount of strong Lewis acid sites at 640 °C, despite the increase in CO formation linked to the decomposition of the carbide structure.

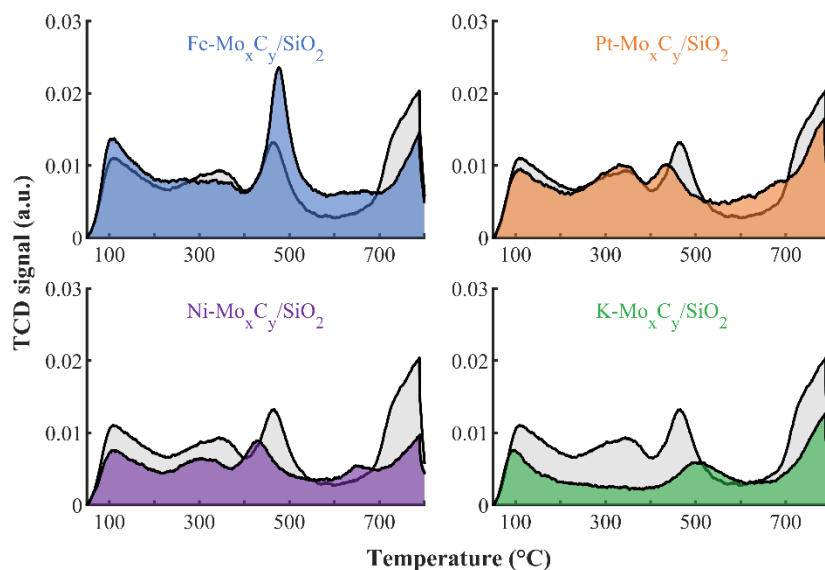


Figure 8.17. NH₃ temperature programmed desorption of Fe-Mo_xC_y/SiO₂, Pt-Mo_xC_y/SiO₂, Ni-Mo_xC_y/SiO₂ and K-Mo_xC_y/SiO₂. Temperature heated up to 800 °C at 10 °C min⁻¹, in an He atmosphere. The unpromoted sample is presented in the background of each plot by the grey area plot.

XRD analysis of the spent CO₂- and NH₃-TPD samples confirm the presence of metallic Mo, due to decomposition of the carbide at higher temperatures (see Figure 8.18, Table K.4 and Table K.5). A difference is observed between the two techniques in terms of metallic Mo content, with a higher content observed for the spent samples after NH₃-TPD. Interestingly, the Fe and Ni promoted samples show no bulk decomposition during CO₂-TPD and a lower degree of decomposition during NH₃-TPD, either in terms of the Mo⁰ content (Ni-Mo_xC_y/SiO₂) or Mo⁰ crystallite size (Fe-Mo_xC_y/SiO₂).

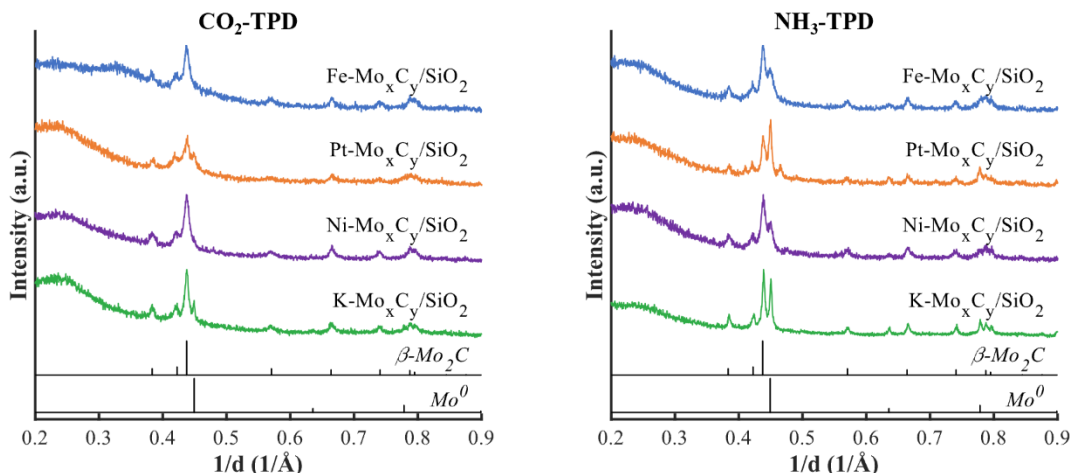


Figure 8.18. XRD patterns of the spent samples after CO₂- and NH₃-TPD experiments of Fe-Mo_xC_y/SiO₂, Pt-Mo_xC_y/SiO₂, Ni-Mo_xC_y/SiO₂ and K-Mo_xC_y/SiO₂.

8.3 CO₂ activation: effect of promotion

The effect of promotion on the affinity of the catalysts towards the activation of CO₂ as a function of temperature (TP-CO₂) was examined. Each sample was cooled to 50 °C after carburization and exposed to a 1 vol.-% CO₂ in Ar atmosphere. At a heating rate of 5 °C/min, the CO formed is detected by means of mass spectrometry (see Figure 8.19). CO is first observed for all samples at 300 °C. This indicates that CO₂ can be activated in the absence of a co-reactant (such as H₂ or hydrocarbons) at relatively low temperatures. While all samples observe a continuous rise in CO yield as the temperature increases, the K promoted sample shows the lowest CO formation up to about 630 °C. Between 500 °C and 600 °C, both Fe-Mo_xC_y/SiO₂ and Ni-Mo_xC_y/SiO₂ show a slightly higher CO yield than the unpromoted and Pt-Mo_xC_y/SiO₂. Thereafter, for all samples, the CO concentration in the reactor outlet gas rapidly increases, with the highest CO yield observed for the unpromoted, Pt-Mo_xC_y/SiO₂ and K-Mo_xC_y/SiO₂. As discussed in section 6.3 and 7.4, the CO formed between 300 °C and 600 °C can be assigned to the dissociation of CO₂ on the surface of the catalyst forming oxygen surface species followed by CO desorption (CO₂ ↔ O* + CO). The rapid increase of CO yield from 600 °C onwards, was previously assigned to the reaction with the carbon from the lattice and subsequently leads to bulk oxidation of the carbide (CO₂ + C* ↔ 2CO). The Fe and Ni promoted samples show a significantly lower CO yield peak at 700 °C. The X-ray diffractograms of the spent samples confirmed that both samples show no to minimal degree of oxidation in comparison to Mo_xC_y/SiO₂, K-Mo_xC_y/SiO₂ and Pt-Mo_xC_y/SiO₂ (see Figure 8.19 and Table K.3). While this supports the earlier statement regarding the CO observed between 300 °C and 600 °C as a result of CO₂ dissociation on the catalyst surface, this does not exclude surface oxidation,

undetectable by XRD, which in turn can decrease the affinity towards CO₂ activation at higher temperatures. In addition, Fe-Mo_xC_y/SiO₂ and Ni-Mo_xC_y/SiO₂ showed to be more resistant to decomposition of the carbide structure during the CO₂- and NH₃-TPD experiments. This suggests that the Fe and Ni promotion somehow improves the Mo-C bond strength and renders them less sensitive to the oxygen surface species produced during CO₂ dissociation. For Ni-Mo_xC_y/SiO₂ the higher number of strong basic sites present on the sample could cause strongly bonded oxygen surface species and prevent desorption thereof *via* the reaction with lattice carbon. K-Mo_xC_y/SiO₂ showed an increase in weaker basic sites, which does not seem to sufficiently lower the activation energy for CO₂ dissociation (see the lower CO yield below 600 °C), but once activated at higher temperatures, it reacts easily with the lattice carbon causing the oxidation of the carbide.

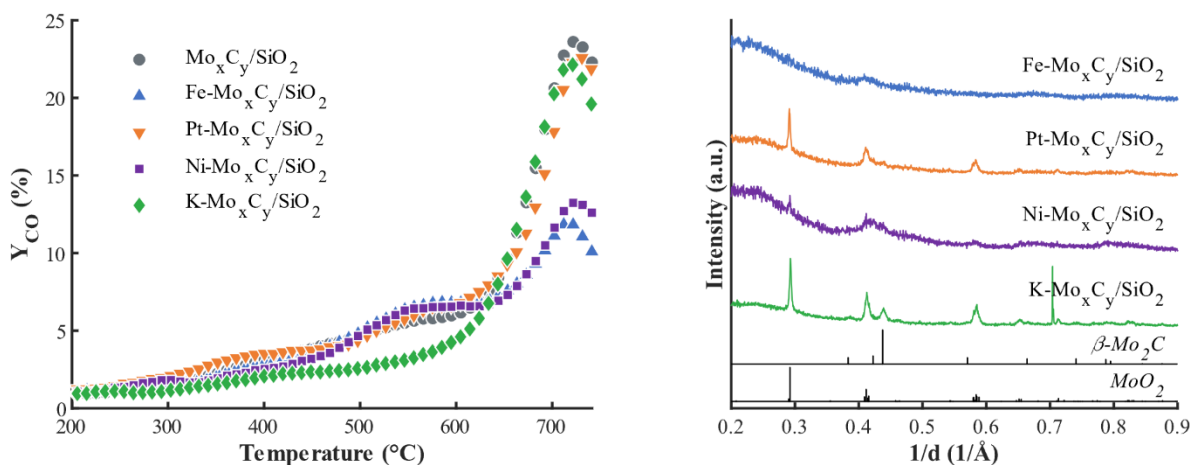


Figure 8.19. [left] CO yield observed as a function of temperature of Fe-Mo_xC_y/SiO₂, Pt-Mo_xC_y/SiO₂, Ni-Mo_xC_y/SiO₂ and K-Mo_xC_y/SiO₂, normalized to the mass fraction of Mo in the catalysts. Temperature increased to 700 °C at 5 °C min⁻¹, holding for 10 min at maximum temperature at atmospheric pressure in 1 vol.-% CO₂ in Ar at a space velocity of 60 L h⁻¹ g_{cat}⁻¹. [right] XRD patterns of the spent TP-CO₂ activation experiments.

8.4 RWGS performance: effect of promotion

In section 6.4 the RWGS performance of unpromoted Mo_xC_y catalysts was discussed and a high activity towards the RWGS reaction at reaction temperatures between 400 °C and 600 °C and at H₂ to CO₂ ratios between 1 and 7 was observed.¹⁰⁻¹⁴ More importantly, minimal catalyst deactivation and low methanation activity was paired with the high activity. It is therefore of interest to study if the different promoter materials have any impact on the RWGS reaction and whether this performance can be linked to their performances in the CO₂-ODH reaction (discussed in section 8.5). Each catalyst was evaluated in a H₂ to CO₂ feed ratio of 2.5 at 600 °C for 36 hours TOS. At first the samples were exposed to a space velocity of 60 L h⁻¹ g_{cat}⁻¹ excluding Ar (see Figure 8.20). At these conditions, almost all catalysts, except

K-Mo_xC_y/SiO₂, show an initial CO₂ conversion between 50-52 % (see Figure 8.20-A). Minimal catalyst deactivation was observed with TOS up until 35 hours. K-Mo_xC_y/SiO₂ showed slightly lower conversion levels initially, and significant catalyst deactivation was observed dropping to about 30 % CO₂ conversion after 35 hours TOS. CO selectivity for all catalysts is well above 99 % (see Figure 8.20-C), suggesting minimal to no methanation activity, even though it is thermodynamically feasible under these conditions (see section 6.1). No catalyst oxidation to MoO_x was observed for any of the catalysts (see Figure 8.20-D).

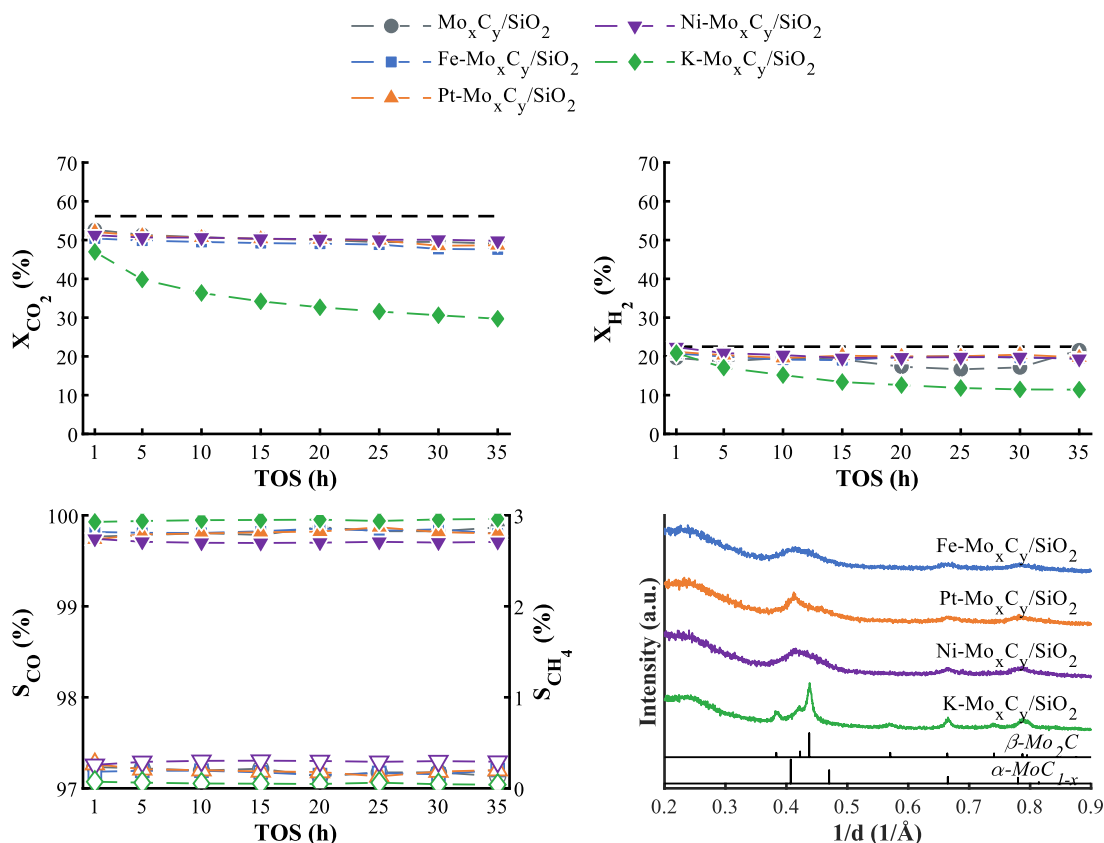


Figure 8.20. [A] CO₂ conversion, [B] H₂ conversion, [C] CO selectivity (solid markers) and CH₄ selectivity (open markers) of Mo_xC_y/SiO₂, Fe-Mo_xC_y/SiO₂, Pt-Mo_xC_y/SiO₂, Ni-Mo_xC_y/SiO₂ and K-Mo_xC_y/SiO₂ and [D] XRD patterns of the spent RWGS catalysts. Conditions: T = 600 °C for 36 h TOS at H₂/CO₂ ratio of 2.5. SV = 60 L h⁻¹ g_{cat}⁻¹.

The conversion of CO₂ for all catalysts (except K-Mo_xC_y/SiO₂) was close to the thermodynamic equilibrium conversion of 56 %. The space velocity was increased twofold to drop the conversion levels well below thermodynamic equilibrium to allow for a reliable comparison between the different catalysts, especially regarding possible catalyst deactivation. All catalysts but K-Mo_xC_y/SiO₂ were thus tested at a space velocity of 120 L h g_{cat}⁻¹, keeping the other reaction conditions constant (a H₂ to CO₂ feed ratio of 2.5, at 600 °C for 36 hours) (see Figure 8.21). Under these conditions, Ni-Mo_xC_y/SiO₂ yielded the highest

conversion of 43 % after 1 hour TOS with minimal catalyst deactivation observed up until 35 hours TOS (see Figure 8.21-A). While $\text{Mo}_x\text{C}_y/\text{SiO}_2$ showed a similar initial CO_2 conversion after 1 hour TOS, a slight drop in activity can be observed with TOS (to 38 % after 35 hours). For $\text{Fe-Mo}_x\text{C}_y/\text{SiO}_2$ and $\text{Pt-Mo}_x\text{C}_y/\text{SiO}_2$, 36 % of the CO_2 is converted after 1 hour TOS, with minimal deactivation up until 35 hours TOS. The selectivity towards CO was again well above 99 % for all catalysts (see Figure 8.21-C). Again, the spent catalysts did not show any sign of oxidation towards MoO_2 or MoO_3 (see Figure 8.21). Rietveld analysis of the spent samples presented in Figure 8.20 and Figure 8.21, shows some minor changes compared to the freshly carburized materials (see Table K.6). Overall, a slight increase in $\beta\text{-Mo}_2\text{C}$ content can be observed for almost all samples after the exposure to 36 hours of RWGS conditions. Additionally, a small increase of the crystallite sizes could account for the observed minor catalyst deactivation. This suggests that catalyst deactivation observed for $\text{K-Mo}_x\text{C}_y/\text{SiO}_2$ is not influenced by a change in crystal structure, but possibly due to the formation of carbonate-like surface compounds or due to the dissociation of re-adsorbed CO.¹⁵

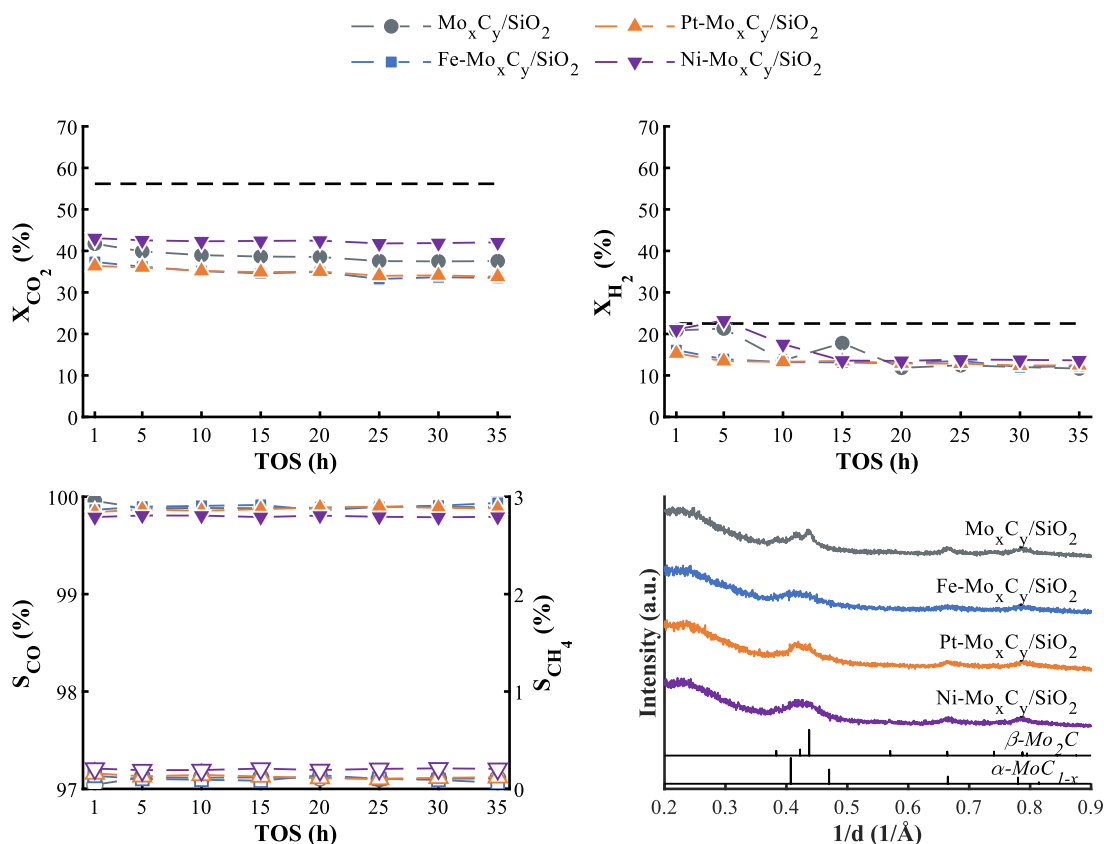


Figure 8.21. [A] CO_2 conversion, [B] H_2 conversion, [C] CO selectivity (solid markers) and CH_4 selectivity (open markers) of $\text{Mo}_x\text{C}_y/\text{SiO}_2$, $\text{Fe-Mo}_x\text{C}_y/\text{SiO}_2$, $\text{Pt-Mo}_x\text{C}_y/\text{SiO}_2$ and $\text{Ni-Mo}_x\text{C}_y/\text{SiO}_2$ and [D] XRD patterns of the spent RWGS catalysts. Conditions: $T = 600\text{ }^\circ\text{C}$ for 36 h TOS at H_2/CO_2 ratio of 2.5. $\text{SV} = 120\text{ L h}^{-1}\text{ g}_{\text{cat}}^{-1}$.

8.5 CO₂-ODH performance: effect of promotion

8.5.1. Use of different gas supply on Mo_xC_y/SiO₂

All catalysts discussed in this chapter were evaluated for their CO₂-ODH catalytic performance for 24 hours. An equimolar feed gas composition of CO₂ and C₂H₆, diluted by 50 vol.-% Ar was fed to the reactor at a space velocity of 15 L h g_{cat}⁻¹. The reaction temperature was set to 600 °C. The various samples were tested using different gas supplies, either combined from individual pure gas cylinders (IND) or using a single cylinder pre-mix (MIX) (see section 4.3.2). The unpromoted sample was exposed to both feed gas sources, which revealed slight differences in catalytic performance with changing gas supply, however, reproducible a data was generated within the same type of gas supply (see Figure 8.22). The samples belonging to the repeat of experiments are separated by means of a single (*) or double (**) asterisk. The data for Mo_xC_y/SiO₂ (MIX)** is previously discussed in section 6.5 (referred to as “Mo_xC_y/SiO₂-WI”) and section 7.5 (referred to as “Mo_xC_y/SiO₂”). The differences in catalytic performance between the two gas supplies can mainly be observed in the initial stages of the reaction (<12 hours TOS). After 1 hour TOS, the unpromoted sample sourcing the feed from individual cylinders, Mo_xC_y/SiO₂ (IND)* and Mo_xC_y/SiO₂ (IND)**, show an C₂H₆ conversion ($X_{C_2H_6}$) of about 9 % and a CO₂ conversion (X_{CO_2}) of 9.9 and 13.9 %, respectively, which is almost twice as high as when sourcing the feed from the pre-mix cylinder, Mo_xC_y/SiO₂ (MIX)* and Mo_xC_y/SiO₂ (MIX)** (see Figure B-9). The activity then shows a sharp decrease up to 6 hours TOS for all samples. Although less abruptly, both the C₂H₆ and CO₂ conversion continue to decrease for all catalysts, up until 24 hours TOS. In terms of product selectivity, all samples show a rapid increase in C₂H₄ selectivity (and simultaneously a decrease in CO selectivity) from about 50 C-% at 1 hour TOS to 65 C-% at 6 hours TOS, stabilizing at about 70 C-% after 24 hours.

The difference in performance between the two gas supplies is supported by the spent catalyst characterization. By means of XRD analysis, a significantly higher degree of oxidation is observed for the samples exposed to the single mixture cylinder (see Figure 8.23-A and Table K.2). The single cylinder mixture might have contained a larger impurity content, such as O₂, which causes the increased oxidation and thus more rapid deactivation. Interestingly, a small content of α-MoC_{1-x} is observed for both Mo_xC_y/SiO₂ (IND)* and Mo_xC_y/SiO₂ (IND)**, despite the absence of the cubic structure in the freshly carburized sample (see Table 8.1). The formation of α-MoC_{1-x} under reaction conditions, was previously observed in section 5.3 after exposure of Mo_xC_y/SiO₂ to a CO₂-ODH reaction temperature of 650 or 750 °C, and might be the result of a carburization mechanism similar to the one observed during the

carburization of Pt-Mo_xC_y/SiO₂ (see Figure 8.9-B) and Ni-Mo_xC_y/SiO₂ (Figure 8.10-D) with MoO_xC_y as an intermediate phase.^{16, 17}

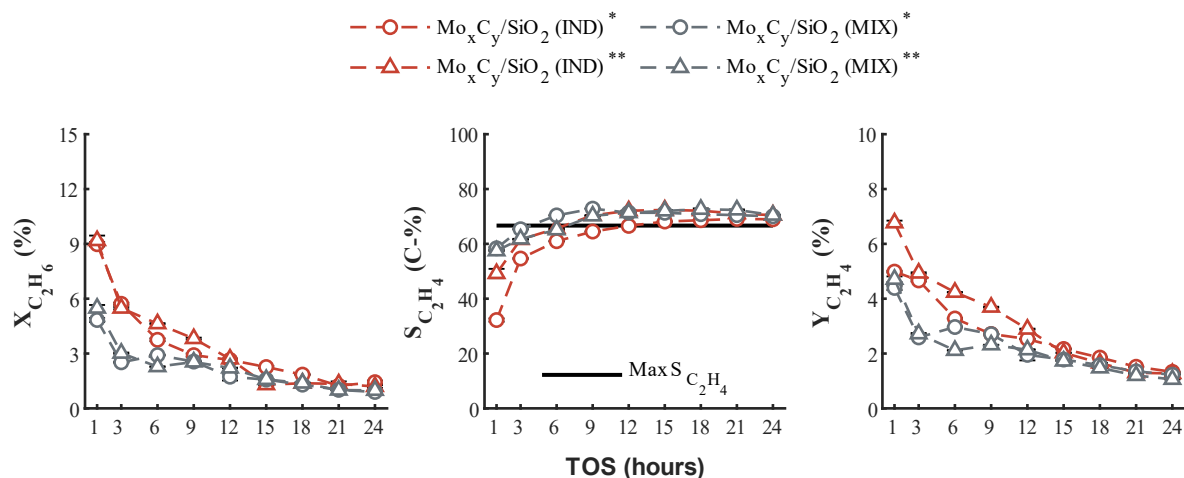


Figure 8.22. C₂H₆ conversion, C₂H₄ selectivity and C₂H₄ yield, of Mo_xC_y supported on SiO₂, with the feed gas sourced from individual gas cylinders (IND) or single cylinder pre-mix (MIX). CO₂-ODH conditions: T = 600 °C, P = 1 atm, SV = 15 L h⁻¹ g_{cat}⁻¹, CO₂:C₂H₆:Ar = 1:1:2. Theoretical maximum C₂H₄ selectivity for CO₂-ODH indicated by solid black line.

Mo_xC_y/SiO₂ (IND) was repeatedly tested under the same reaction conditions and the reaction was terminated at 1, 3 and 12 hours TOS and passivated prior to exposure to air. By means of XRD analysis of the recovered samples (see Figure 8.23-B), it can be confirmed that bulk catalyst oxidation towards MoO₂ already starts in the first 3 hours of the reaction. No MoO₂ could be detected after 1 hour TOS. Between 12 and 24 hours TOS, the degree of oxidation seems to have somewhat stabilized, but the formation of α-MoC_{1-x} is not yet detected at 12 h TOS (see Table K.2). It is therefore suggested that the sharp decrease in activity up to 12 hours TOS can mainly be assigned to an increase in the degree of oxidation. CO₂ activation creates oxygen surface species (O*). Too strongly bonded oxygen surface species can cause oxidation of the active sites (most likely the sites responsible for CO₂ activation, i.e., the basic sites). Due to the resulting decrease in CO₂ activation, the number of oxygen surface species creating active sites required for the activation of C₂H₆ decreases as well, thus a drop in overall activity is observed. In addition, carbon deposition, which can occur by the decomposition of C₂H₄, causes a further blockage of active sites, ultimately preventing a site regeneration *via* a Mars van Krevelen type mechanism. A study by Porosoff *et al.*¹⁸ reported, by means of DFT calculations (see section 2.3.3, Figure 2.11), that upon the activation of ethane by O*, the Mo_xC_y surface prefers to recombine atomic hydrogen (H*) to desorb as H₂ gas over the highly endothermic formation of OH (*via* O* + H* → OH*) or H₂O (*via* OH* + H* → H₂O). This leaves O* behind and causes catalyst oxidation.

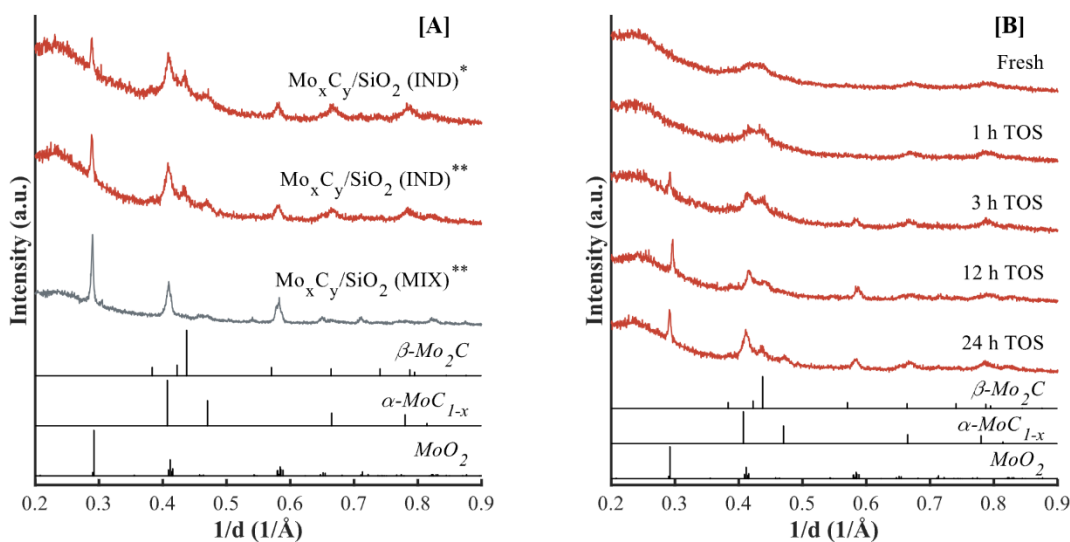


Figure 8.23. XRD patterns of spent CO₂-ODH experiments of Mo_xC_y supported on SiO₂ with [A] the spent samples exposed to different gas supplies (Mo_xC_y/SiO₂ (MIX)^{**} is presented in Figure 8.26) and [B] the repeatedly tested Mo_xC_y/SiO₂ (IND), terminated at 1, 3 and 12 h TOS. The fresh and the 24 h TOS (same as Mo_xC_y/SiO₂ (IND)^{**}) samples are presented again for comparison.

Despite the large activity differences observed in the initial 12 hours TOS, very similar behaviour in terms of the reaction pathway development over time can be observed. The type of reaction occurring (ODH, DR, DH and/or RWGS) can possibly be identified by analysing the conversion ratio ($X_{C_2H_6}/X_{CO_2}$), and product ratios ($\dot{n}_{C_2H_4}/\dot{n}_{CO}$, $\dot{n}_{H_2}/\dot{n}_{CO}$ and $\dot{n}_{C_2H_4}/\dot{n}_{H_2}$) of each sample, with significant shifts observed with time on stream (see Figure 8.24). See section 4.3.4 for a more detailed discussion regarding the ratios and their relation to the reaction pathways. At the start of the reaction, the conversion ratio is close to 1, which increases with TOS. The $\dot{n}_{C_2H_4}/\dot{n}_{CO}$ and $\dot{n}_{H_2}/\dot{n}_{CO}$ ratios also increase with TOS, suggesting a decreased CO formation and/or a shift in the reaction pathway from a low-level DR activity to ODH/DH. The conversion ratio shows a sharp increase, supporting a more dominant DH pathway. The relatively consistent $\dot{n}_{C_2H_4}/\dot{n}_{H_2}$ ratio shows only a minor increase, suggesting that the DH activity does not increase, but rather that the DR activity decreases. A more dominant DH pathway increases the ethylene selectivity above the theoretical CO₂-ODH maximum of 67 C-%. It should be noted that the performance of the catalysts has shown to be highly sensitive, and that conversion and product ratios are directly correlated to the quality of the data and the experiment performed (think of slight variations in feed composition between the two respective experiments). Hence, the slight differences observed between Mo_xC_y/SiO₂ (IND)^{*} and Mo_xC_y/SiO₂ (IND)^{**}, can seem to have a large impact on the absolute ratios. Nevertheless, general trends, in terms of reaction pathways can still be observed and should be more emphasized than the absolute numbers.

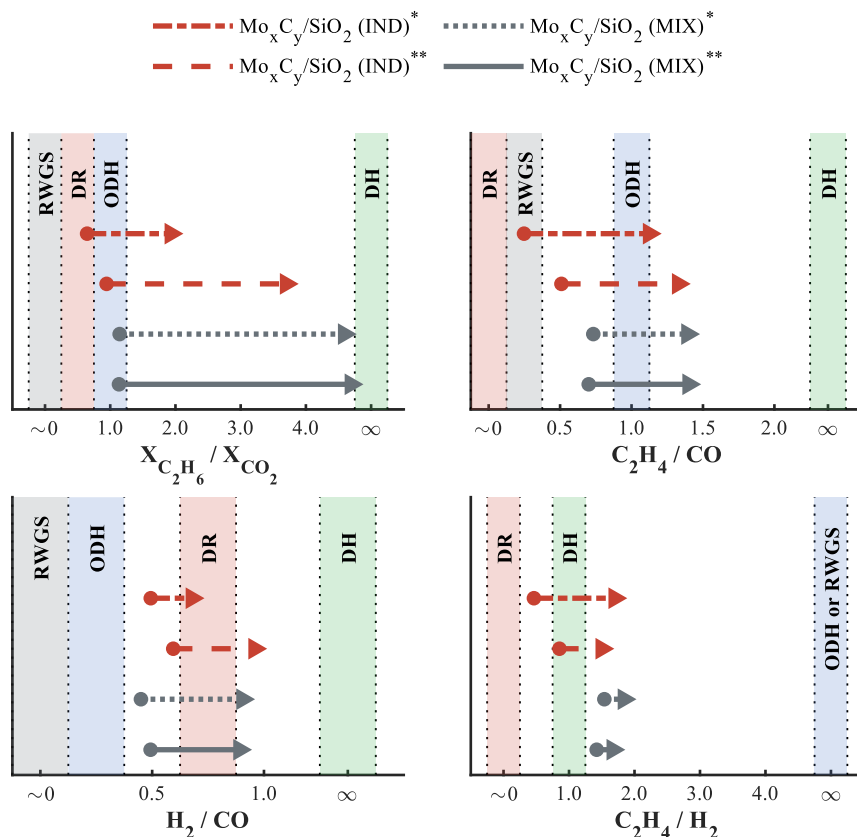


Figure 8.24. Schematic representation of C_2H_6 to CO_2 conversion ratio, C_2H_4 to CO product ratio, H_2 to CO product ratio and C_2H_4 to H_2 product ratio, of Mo_xC_y supported on SiO_2 , with the feed gas sourced from individual gas cylinders (IND) or single cylinder pre-mix (MIX). CO_2 -ODH conditions: $T = 600\text{ }^\circ\text{C}$, $P = 1\text{ atm}$, $SV = 15\text{ L h}^{-1}\text{ g}_{cat}^{-1}$, $CO_2:C_2H_6:Ar = 1:1:2$.

8.5.2. Effect of promotion

To be able to compare conversion levels between all promoted and unpromoted samples, the C_2H_6 and CO_2 conversions are normalized to the unpromoted catalyst using the same gas supply. Upon co-impregnating Fe, Pt, Ni or K, the initial conversion for both C_2H_6 and CO_2 is lower than for the unpromoted sample (see Figure 8.25 and Figure B-10). The potassium promoted sample shows hardly any activity after 1 hour TOS and is completely deactivated after 12 hours TOS. Pt- Mo_xC_y/SiO_2 shows a lower $X_{C_2H_6}$ and X_{CO_2} compared to Mo_xC_y/SiO_2 and a slightly faster deactivation can be observed, although remaining close to the conversion levels of the unpromoted sample. Ni- Mo_xC_y/SiO_2 shows a lower conversion than Mo_xC_y/SiO_2 up until 12 hours TOS. Thereafter, Ni- Mo_xC_y/SiO_2 outperforms the unpromoted sample. Only Fe- Mo_xC_y/SiO_2 shows a significant improvement in catalytic activity in comparison to Mo_xC_y/SiO_2 despite the lower conversions observed at 1 hour TOS. At 12 hours TOS the

C₂H₆ conversion is about 1.8 times higher than that of Mo_xC_y/SiO₂, which increases to more than two times at 24 hours TOS.

The C₂H₄ and CO selectivity seem to be minimally affected by the change in gas supply, thus these are not normalized. Some slight variations are observed upon promotion, but in essence all samples show an C₂H₄ selectivity close to the theoretical maximum (67 C-%). Fe-Mo_xC_y/SiO₂, Pt-Mo_xC_y/SiO₂ and Ni-Mo_xC_y/SiO₂ show an increased initial C₂H₄ selectivity after 1 hour TOS in comparison to the unpromoted sample, with Fe-Mo_xC_y/SiO₂ recording the highest at 70 C-%. A negligible amount of CH₄ is detected for all samples.

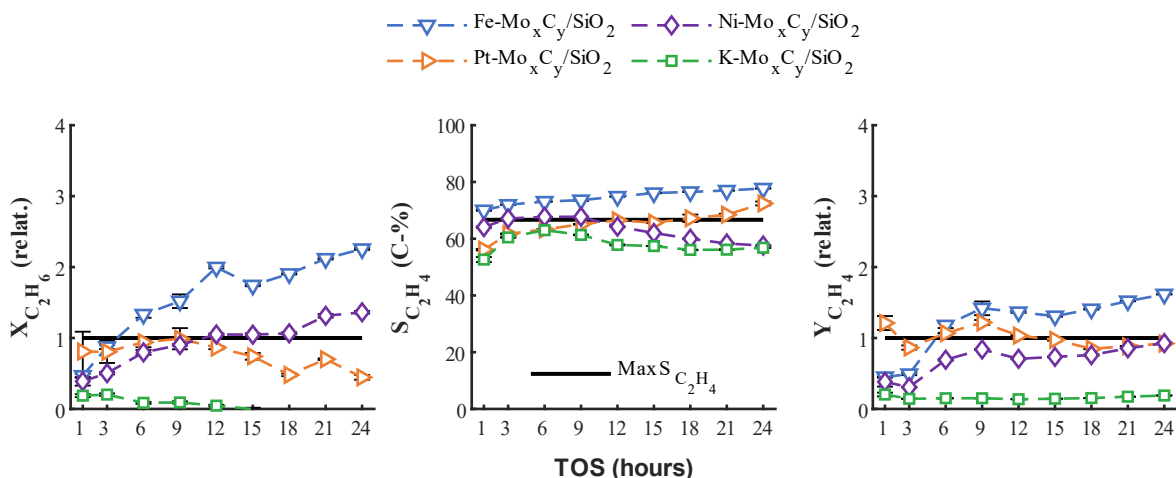


Figure 8.25. C₂H₆ conversion (relative to unpromoted sample), C₂H₄ selectivity and C₂H₄ yield (relative to unpromoted sample), of Mo_xC_y supported on SiO₂, promoted with iron, platinum, nickel or potassium. CO₂-ODH conditions: T = 600 °C, P = 1 atm, SV = 15 L h⁻¹ g_{cat}⁻¹, CO₂:C₂H₆:Ar = 1:1:2. Theoretical maximum C₂H₄ selectivity for CO₂-ODH indicated by solid black line.

The C₂H₄ yield of Pt-Mo_xC_y/SiO₂ is very similar to that of the unpromoted sample for the full 24 hours. Fe-Mo_xC_y/SiO₂, Ni-Mo_xC_y/SiO₂ and K-Mo_xC_y/SiO₂ show a lower ethylene yield than the unpromoted catalyst in the first 3 hours TOS, after 6 hours under reaction conditions Fe-Mo_xC_y/SiO₂ outperforms all other samples in terms of Y_{C₂H₄}.

In section 6.5 (Figure 6.23), we have described the difference in colour between the front and rear part of the spent catalyst bed. In this section, we separated the samples based on the colour difference, with an exception for Pt-Mo_xC_y/SiO₂. It should be noted that the split was not equal in terms of catalyst mass or volume and that the XRD based quantifications reported below are merely an analysis of the individual sections. It is observed that a high degree of catalyst oxidation occurs at the inlet side of the catalyst bed (see Figure 8.26 and Table K.2). K-Mo_xC_y/SiO₂^{front} fully oxidized to 100 wt.-% *oP*-MoO₃ while a mixture of MoO₂ and *oP*-MoO₃ was observed for Mo_xC_y/SiO₂^{front}, Fe-Mo_xC_y/SiO₂^{front} and Ni-

$\text{Mo}_x\text{C}_y/\text{SiO}_2^{\text{front}}$. In the rear portion of the catalyst bed, $\text{K-Mo}_x\text{C}_y/\text{SiO}_2^{\text{rear}}$ also oxidized, to a mix of 56 wt.-% MoO_2 and 44 wt.-% $oP\text{-MoO}_3$. No reflexes of any carbidic phase could be detected. The loss of acid sites and increased number of basic sites resulted in a high degree of oxidation during $\text{CO}_2\text{-ODH}$, likely beyond the pathways of RWGS or DR, but simply *via* CO_2 dissociation until all active sites are oxidized. $\text{Mo}_x\text{C}_y/\text{SiO}_2^{\text{rear}}$ contains some remaining $\eta\text{-MoC}_{0.59}$. Interestingly, similar to the observations made in $\text{Mo}_x\text{C}_y/\text{SiO}_2$ (IND)* and $\text{Mo}_x\text{C}_y/\text{SiO}_2$ (IND)** (see Figure 8.23-A), (cubic) $\alpha\text{-MoC}_{1-x}$ was also observed in $\text{Fe-Mo}_x\text{C}_y/\text{SiO}_2^{\text{rear}}$, despite the use of the single cylinder mixture gas and that there was no indication of a cubic phase in the freshly carburized sample. The slightly reduced number of basic sites detected on $\text{Fe-Mo}_x\text{C}_y/\text{SiO}_2$, in comparison to the unpromoted sample, and an increased number of acid sites, appears to prevent over-oxidation of the (oxy)carbide, forming $\alpha\text{-MoC}_{1-x}$, and thus results in a higher activity.

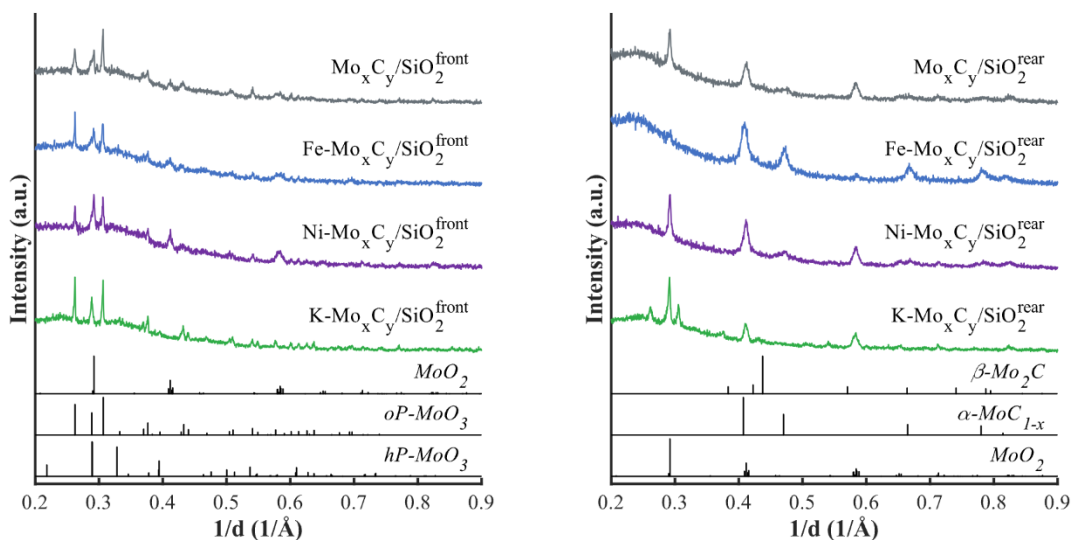


Figure 8.26. XRD patterns of the spent $\text{CO}_2\text{-ODH}$ catalysts of Mo_xC_y supported on SiO_2 , promoted with iron, platinum, nickel or potassium.

Raman analysis of all spent samples showed that carbon deposition mainly occurs at the rear side of the catalyst bed (see Figure 8.27), evidenced by the D- and G-band at 1350 cm^{-1} and 1580 cm^{-1} , respectively. The front side of the catalyst bed did not show any evidence for carbon deposits, which is in line with the observed XRD results. $\text{K-Mo}_x\text{C}_y/\text{SiO}_2$ does not show any indication of carbon deposition independent of location in the bed, confirming that the deactivation of the potassium promoted sample is mainly associated to the oxidation towards MoO_x .

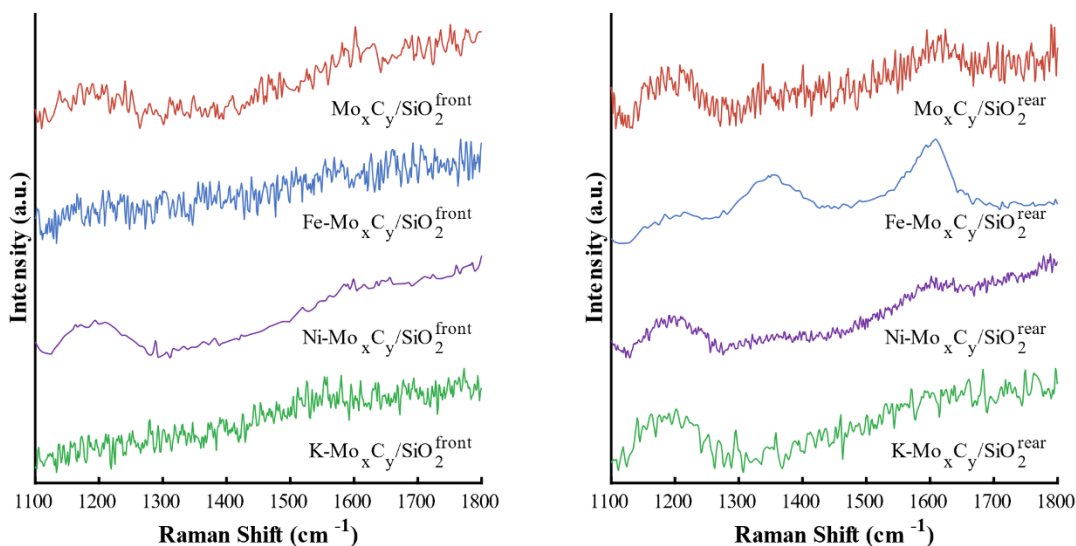


Figure 8.27. Raman spectra of the spent CO₂-ODH catalysts of Mo_xC_y supported on SiO₂, promoted with iron, platinum, nickel or potassium.

The lower degree of oxidation and thus higher stability for Fe-Mo_xC_y/SiO₂ is supported by the $X_{C_2H_6}/X_{CO_2}$ ratio and the product ratios ($\dot{n}_{H_2}/\dot{n}_{CO}$, $\dot{n}_{C_2H_4}/\dot{n}_{CO}$ and $\dot{n}_{C_2H_4}/\dot{n}_{H_2}$) all pointing towards an increased DH activity with time on stream (see Figure 8.28). During TP-CO₂ activation, it was observed that the CO formation rate for Fe-Mo_xC_y/SiO₂ is slightly higher between 500 °C and 600 °C and significantly lower at 700 °C (compared to the unpromoted sample). This means that Fe-Mo_xC_y/SiO₂ shows to be able to activate CO₂, forming somewhat of a protective surface layer of weakly bonded O*, preventing catalyst oxidation even at temperatures up to 700 °C. Ni-Mo_xC_y/SiO₂ showed the highest CO formation rate between 500 °C and 600 °C and also a lower CO formation rate at 700 °C, despite a significant increase in the number and strength of the basic sites. A minor decrease in the weak acid site concentration and the presence of strong acid sites results in a slightly enhanced dry-reforming activity, further increasing with time on stream. This is confirmed by the observed increase for $\dot{n}_{H_2}/\dot{n}_{CO}$ and decrease for $\dot{n}_{C_2H_4}/\dot{n}_{CO}$ product ratios (see Figure 8.28). The Ni promoted sample outperformed all other studied catalysts in the RWGS reaction, which can be explained by its high affinity towards CO₂ activation at 600 °C, with rapid oxygen surface species removal by H₂. K-Mo_xC_y/SiO₂ performed poorly compared to all other samples, in terms of both CO₂-ODH and RWGS activity. The significant deactivation observed in the RWGS cannot be explained by bulk oxidation as determined by means of XRD. Further investigations would be required to determine this deactivation mechanism, however the lower CO formation rate during TP-CO₂ activation between 500 °C and 600 °C is in line with these results.

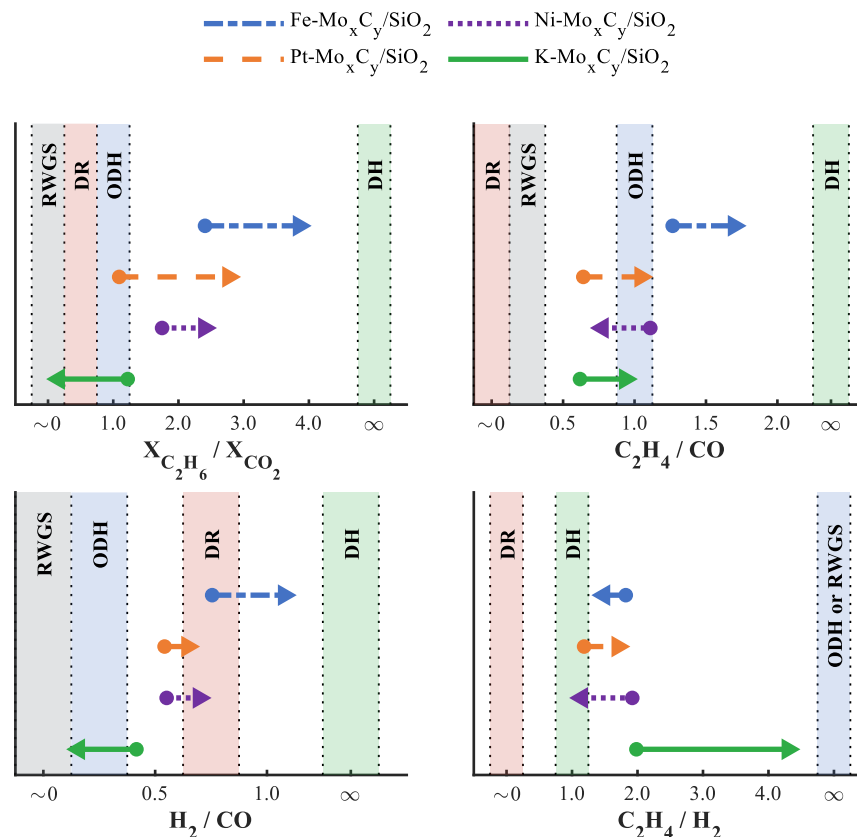


Figure 8.28. Schematic representation of C_2H_6 to CO_2 conversion ratio, C_2H_4 to CO product ratio, H_2 to CO product ratio and C_2H_4 to H_2 product ratio, of Mo_xC_y supported on SiO_2 , promoted with iron, platinum, nickel or potassium. CO_2 -ODH conditions: $T = 600\text{ }^\circ\text{C}$, $P = 1\text{ atm}$, $SV = 15\text{ L h}^{-1}\text{ g}_{\text{cat}}^{-1}$, $CO_2:C_2H_6:Ar = 1:1:2$.

The performance of the Pt promoted sample does not show large differences to the unpromoted sample, which is of particular interest because Pt promotion had the most significant effect on the carbide composition. The addition of Pt caused a slight increase in the number of Brønsted acid sites and a more severe decrease in the number of stronger basic sites. This supports the slightly higher direct dehydrogenation activity observed which is paired with a high degree of carbon deposition (see Figure 8.29). Most interesting is the absence of any catalyst oxidation (see Figure 8.33-B), with a final carbide structure of 43 wt.-% $\alpha\text{-}MoC_{1-x}$ balanced by $\eta\text{-}MoC_{0.59}$ (see Table K.2). This is supported by the decrease in strong basic sites, which prevents strongly bonded oxygen surface species.

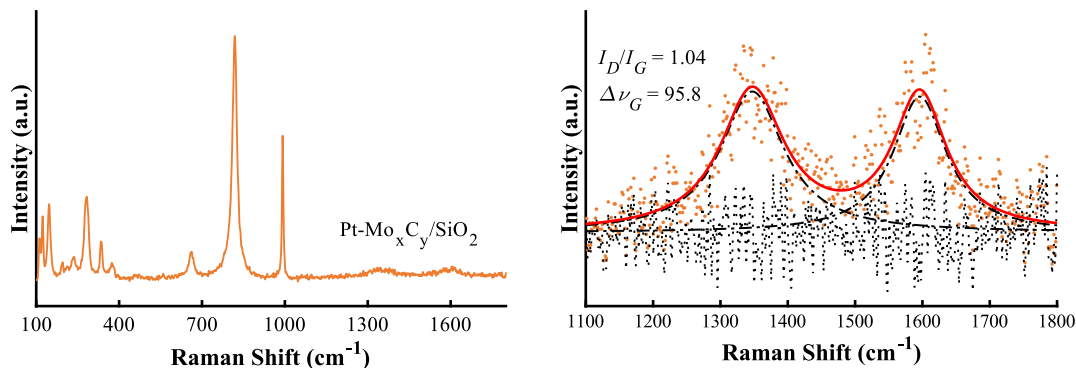


Figure 8.29. Raman spectrum of the spent Pt-Mo_xC_y/SiO₂.

The catalytic performance of the Fe promoted sample in the CO₂-ODH reaction is highly affected by the promotional sequence applied, mainly in terms of activity. The performance of the sample prepared *via* sequential impregnation (Fe-Mo_xC_y/SiO₂ (Seq-Imp)) is tested using the single mixture cylinder feed and the sample exposed to calcination prior to the promotion with Fe (Fe-Mo_xC_y/SiO₂ (Calc-Imp)) is tested using the individual gas cylinder feed. Thus, the C₂H₆ and CO₂ conversion as well as the C₂H₄ yield is normalized to the unpromoted catalyst using the same gas supply (see Figure 8.30 and Figure B-11). Fe-Mo_xC_y/SiO₂ (Seq-Imp) shows a significantly lower initial activity and deactivates quickly. Fe-Mo_xC_y/SiO₂ (Calc-Imp) shows initially a similar C₂H₆ conversion but is outperformed by Fe-Mo_xC_y/SiO₂ (Co-Imp) after 9 hours TOS. In terms of product selectivity, the calcined sample shows a slightly higher initial CO selectivity.

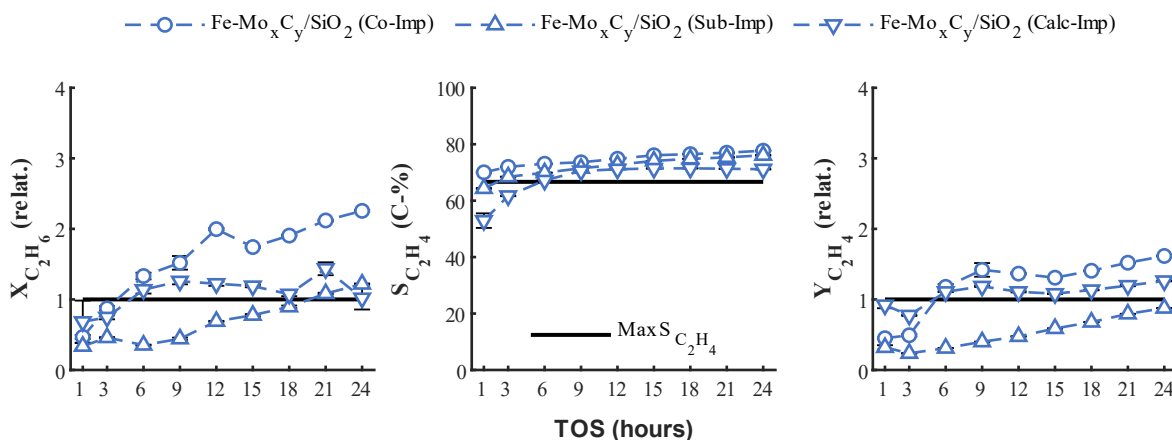


Figure 8.30 C₂H₆ conversion (relative to unpromoted sample), C₂H₄ selectivity and C₂H₄ yield (relative to unpromoted sample), of Fe-Mo_xC_y/SiO₂, promoted *via* co-impregnation, sequential impregnation or after calcination. CO₂-ODH conditions: T = 600 °C, P = 1 atm, SV = 15 L h⁻¹ g_{cat}⁻¹, CO₂:C₂H₆:Ar = 1:1:2. Theoretical maximum C₂H₄ selectivity for CO₂-ODH indicated by solid black line.

Before discussing the performance of the various Fe promoted samples in more detail, the effect of calcination is discussed. The unpromoted sample exposed to calcination prior to carburization ($\text{Mo}_x\text{C}_y/\text{SiO}_2$ (Calc)) also shows an increased initial CO_2 conversion and CO selectivity (see Figure B-12). This is in parallel to an increased C_2H_6 conversion, yet a decreased C_2H_4 yield (see Figure 8.31). This means, at 1 hour TOS, $\text{Mo}_x\text{C}_y/\text{SiO}_2$ (Calc) follows predominantly the dry-reforming pathway. From 3 hours TOS, the C_2H_6 and CO_2 conversion has dropped to the same level as the directly carburized sample. This behaviour is also observed in the product selectivity and ethylene yield.

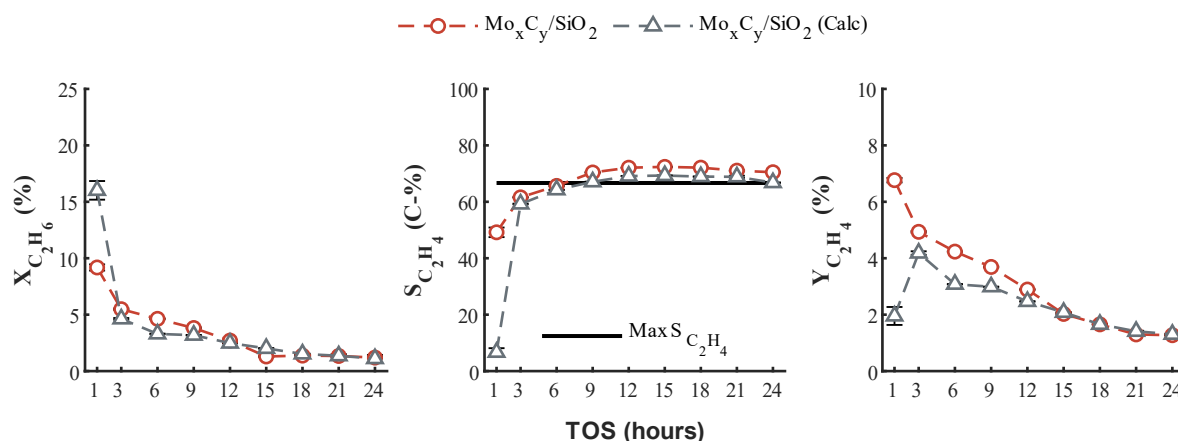


Figure 8.31. C_2H_6 conversion, C_2H_4 selectivity and C_2H_4 yield, of $\text{Mo}_x\text{C}_y/\text{SiO}_2$ carburized with and without prior calcination. CO_2 -ODH conditions: $T = 600$ °C, $P = 1$ atm, $\text{SV} = 15$ L h^{-1} $\text{g}_{\text{cat}}^{-1}$, $\text{CO}_2:\text{C}_2\text{H}_6:\text{Ar} = 1:1:2$. Theoretical maximum C_2H_4 selectivity for CO_2 -ODH indicated by solid black line.

The main difference between the freshly carburized $\text{Mo}_x\text{C}_y/\text{SiO}_2$ and $\text{Mo}_x\text{C}_y/\text{SiO}_2$ (Calc) is the larger crystallite size observed for $\beta\text{-Mo}_2\text{C}$ (see Table 8.1) and the drop in BET surface area (see Table K.1). In the spent sample, a higher degree of oxidation is observed for $\text{Mo}_x\text{C}_y/\text{SiO}_2$ (Calc), at the expense of the $\beta\text{-Mo}_2\text{C}$ content (see Figure 8.33 and Table K.2). It can be suggested that the formation of the metastable ODH active phase, MoO_xC_y , from larger $\beta\text{-Mo}_2\text{C}$ crystallites/particles is slower/less sensitive compared to smaller crystallites/particles. As $\beta\text{-Mo}_2\text{C}$ is suggested to be the most active CO_2 dissociating phase, the incubation time for $\beta\text{-Mo}_2\text{C}$ to change to MoO_xC_y is significantly delayed, allowing for more O^* to be produced. At the same time, the ethane is solely activated on the formed O^* , which might be the cause for the enhanced C-C bond scission over C-H bond scission, thus promoting the dry-reforming reaction. In agreement with the earlier argument by Porosoff *et al.*¹⁸, the H-atoms are recombined and desorbed as H_2 gas, leaving O^* behind, which then oxidize $\beta\text{-Mo}_2\text{C}$ to MoO_2 , and simultaneously create the required MoO_xC_y (surface) phase, enhancing the C_2H_4 formation as observed at 3 h TOS. The latter increases the carbon deposition on the catalyst surface causing the observed catalyst deactivation with time on stream.

The above hypothesis is supported by the catalytic performance of Pt-Mo_xC_y/SiO₂ (Co-Imp-Calc). Calcination prior to carburization for the Pt promoted sample did not enhance the C₂H₆ or CO₂ conversion, on the contrary, a slightly lower activity is observed when compared to Pt-Mo_xC_y/SiO₂ (Co-Imp) (see Figure 8.32). The calcination process did not affect the (cubic) α-MoC_{1-x} content or size in the freshly carburized sample (see Table 8.1). A lower β-Mo₂C content is observed with a slightly increased η-MoC_{0.59} content. In terms of product selectivity, the calcined sample shows very comparable performance to the directly carburized sample. Again, no (bulk) oxidation was observed upon termination of the reaction (see Figure 8.33), with a carbide composition containing 38.4 wt.-% α-MoC_{1-x}, balanced by η-MoC_{0.59} (see Table K.2).

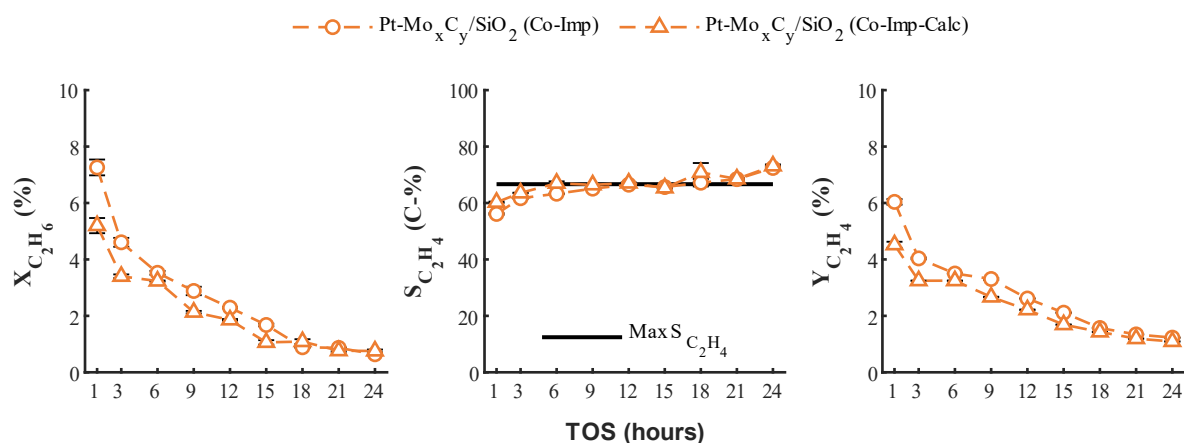


Figure 8.32. C₂H₆ conversion, C₂H₄ selectivity and C₂H₄ yield, of Pt-Mo_xC_y/SiO₂, promoted *via* co-impregnation and carburized with and without prior calcination. CO₂-ODH conditions: T = 600 °C, P = 1 atm, SV = 15 L h⁻¹ g_{cat}⁻¹, CO₂:C₂H₆:Ar = 1:1:2. Theoretical maximum C₂H₄ selectivity for CO₂-ODH indicated by solid black line.

Spent catalyst characterization of Fe-Mo_xC_y/SiO₂ (Seq-Imp) reveals the absence of α-MoC_{1-x}, which suggests that no MoO_xC_y is formed under reaction conditions (see Figure 8.33 and Table K.2). This can explain the rapid loss in activity with TOS. In addition, a high degree of oxidation is observed in the form of MoO₂ and *oP*-MoO₃. The calcined sample, Fe-Mo_xC_y/SiO₂ (Calc-Imp), shows a much smaller α-MoC_{1-x} content in the spent sample than Fe-Mo_xC_y/SiO₂ (Co-Imp) and a higher degree of oxidation. This suggests that under reaction conditions, the formation of the CO₂-ODH active MoO_xC_y is limited and that the higher β-Mo₂C content in the freshly carburized samples (compared to Fe-Mo_xC_y/SiO₂ (Co-Imp)) can possibly create more oxygen surface species, causing the catalyst to oxidize and deactivate. The suggested theory can also explain the low activity and rapid deactivation observed for K-Mo_xC_y/SiO₂, as the potassium promoted sample contained a high β-Mo₂C content at larger crystallite size. It is suggested that β-Mo₂C is responsible for a high CO₂ dissociation activity, but without the formation of MoO_xC_y, the oxygen surface species cause catalyst oxidation or are removed *via* C-C bond scission of C₂H₆, increasing

the dry-reforming activity. If MoO_xC_y is formed, the DH activity increases, however, C_2H_4 decomposition causes carbon deposition.

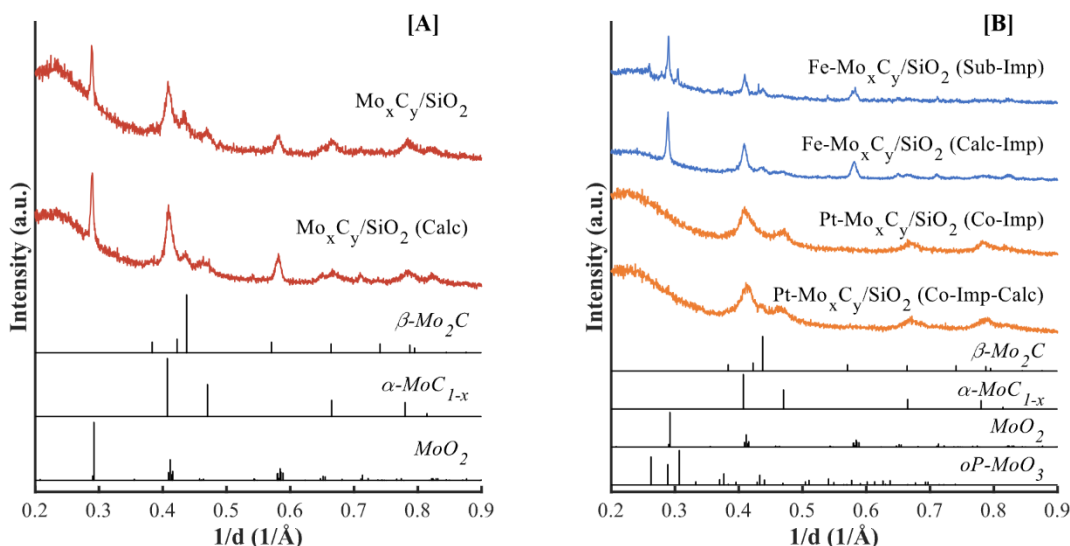


Figure 8.33. XRD patterns of the spent CO_2 -ODH of [A] $\text{Mo}_x\text{C}_y/\text{SiO}_2$ carburized with and without prior calcination and [B] - $\text{Mo}_x\text{C}_y/\text{SiO}_2$, promoted *via* co-impregnation, sequential impregnation or after calcination and $\text{Pt-Mo}_x\text{C}_y/\text{SiO}_2$, promoted *via* co-impregnation and carburized with and without prior calcination.

8.5.3. Effect of feed composition

In terms of catalyst oxidation, the performance data shown under RWGS conditions confirmed that H_2 removes surface oxide species from the dissociation of CO_2 at a significant faster rate compared to ethane acting as reducing agent, suppressing oxidation. The results discussing the co-feeding of H_2 (see section 7.5) have shown that for $\text{Mo}_x\text{C}_y/\text{SiO}_2$, although suppressing oxidation, no significant improvement in the CO_2 -ODH activity was observed, but that the RWGS activity was enhanced.¹⁹ In this study, in an attempt to improve catalytic stability, co-feeding of 5 vol.-% H_2 to the Fe promoted sample ($\text{Fe-Mo}_x\text{C}_y/\text{SiO}_2$ (5 % H_2)) did decrease the degree of oxidation (see Figure 8.37-A), however this was not advantageous to the conversion of C_2H_6 , nor the selectivity towards C_2H_4 (see Figure 8.34). While in the absence of H_2 co-feeding, the conversion of C_2H_6 slightly increased with TOS, this is not the case when co-feeding H_2 . The initial C_2H_6 conversion is the same (2.5 %), but then continues to decrease up until 24 hours TOS. As expected, the CO_2 conversion increased significantly showing an initial conversion of about 12 % decreasing slightly with TOS. Ethylene yield shows a similar decreasing trend, starting at 2.6 %. Based on these results, it is concluded that for $\text{Fe-Mo}_x\text{C}_y/\text{SiO}_2$ (5 % H_2), H_2 removes the oxygen surface species, suppressing the formation of the CO_2 -ODH active oxycarbide phase. This is supported by the absence of any reflexes of the MoO_xC_y or the cubic $\alpha\text{-MoC}_{1-x}$ phase in the XRD pattern of the spent (see Table K.2).

In addition, carbon deposition, as observed by means of Raman analysis (see Figure 8.37-B), blocks the active sites responsible for the removal of the oxygen surface species causing the oxidation of β - Mo_2C to MoO_2 .

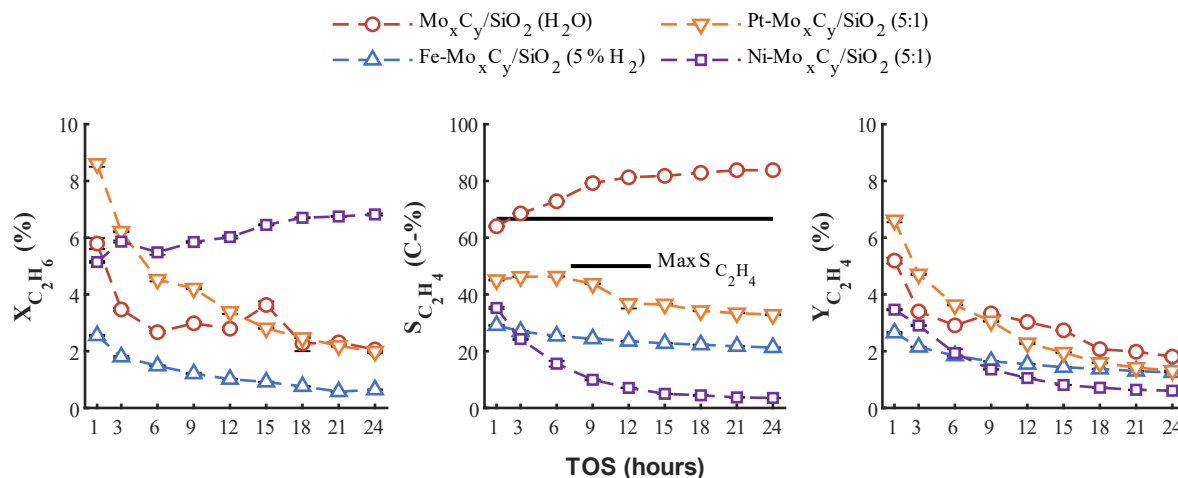


Figure 8.34. C_2H_6 conversion, C_2H_4 selectivity and C_2H_4 yield, of the following samples exposed to varying feed compositions: water co-feeding for $\text{Mo}_x\text{C}_y/\text{SiO}_2$, co-feeding of 5 vol.-% H_2 for $\text{Fe-Mo}_x\text{C}_y/\text{SiO}_2$, a 5:1 CO_2 to C_2H_6 feed ratio for $\text{Pt-Mo}_x\text{C}_y/\text{SiO}_2$ and $\text{Ni-Mo}_x\text{C}_y/\text{SiO}_2$. CO_2 -ODH conditions, see section 4.3.2 for more details. Theoretical maximum C_2H_4 selectivity for CO_2 -ODH indicated by solid black line.

The results discussed in section 7.5 with an increased CO_2 content in the feed showed that the rate of deactivation could be slowed down, as the higher CO_2 removes or prevents carbon deposition. On the other hand, the higher oxidative potential could also lead to enhanced carbide oxidation. A CO_2 to C_2H_6 feed ratio of 5 to 1 was fed over the Pt promoted ($\text{Pt-Mo}_x\text{C}_y/\text{SiO}_2$ (5:1)) and Ni promoted ($\text{Ni-Mo}_x\text{C}_y/\text{SiO}_2$ (5:1)) samples. $\text{Pt-Mo}_x\text{C}_y/\text{SiO}_2$ did not oxidize in a 1 to 1 feed ratio. The initial conversion for $\text{Pt-Mo}_x\text{C}_y/\text{SiO}_2$ (5:1) increased to 8.6 %, however catalyst deactivation was not prevented (see Figure 8.34). Ethane conversion drops to about 2 % after 24 hours TOS, although still higher than the ethane conversion for Pt promoted sample at a 1 to 1 feed ratio (about 1 %). The CO selectivity is 53 C-% after 1 hour TOS, increasing to 65 C-% after 24 hours TOS. Interestingly, although the absolute amounts of C_2H_4 formed are lower (see Figure B-14), the ethylene yield is very similar for $\text{Pt-Mo}_x\text{C}_y/\text{SiO}_2$ at both feed gas compositions. This could suggest that the increased C_2H_6 conversion is due to an enhanced DR activity, happening simultaneously with the ODH pathway, keeping the sites responsible for the formation of ethylene intact. The $\dot{n}_{\text{H}_2}/\dot{n}_{\text{CO}}$ ratio declines with TOS, due to a secondary RWGS reaction (see Figure 8.35). This causes the conversion ratio to first increase from approximately 3.0 to above 4.0, but then drops again due to the increased RWGS activity. The higher concentration of CO_2 in the feed does cause the oxidation of the carbide (see Figure 8.37-A and Table K.2). $\text{Ni-Mo}_x\text{C}_y/\text{SiO}_2$ (5:1) has a 2.7

time increase in the initial ethane conversion (5.1 %) in comparison to same catalyst at a CO₂ to C₂H₆ feed ratio of 1 to 1 (1.9 %). The ethane conversion further increased with TOS reaching about 7 % after 24 hours TOS. Simultaneously, the C₂H₄ selectivity decreases, and the CO selectivity increases to 95 C-% after 24 hours TOS. It is clear that DR (and to some extent RWGS) becomes the dominant reaction pathways for the Ni promoted sample with a 5:1 CO₂ to C₂H₆ feed. Full oxidation to MoO₂ is observed in the spent catalyst (see Figure 8.37-A and Table K.2). Despite the over-stoichiometric CO₂ content in the feed, carbon deposition could not be prevented for both Pt-Mo_xC_y/SiO₂ (5:1) and Ni-Mo_xC_y/SiO₂ (5:1) (see Figure 8.37-B).

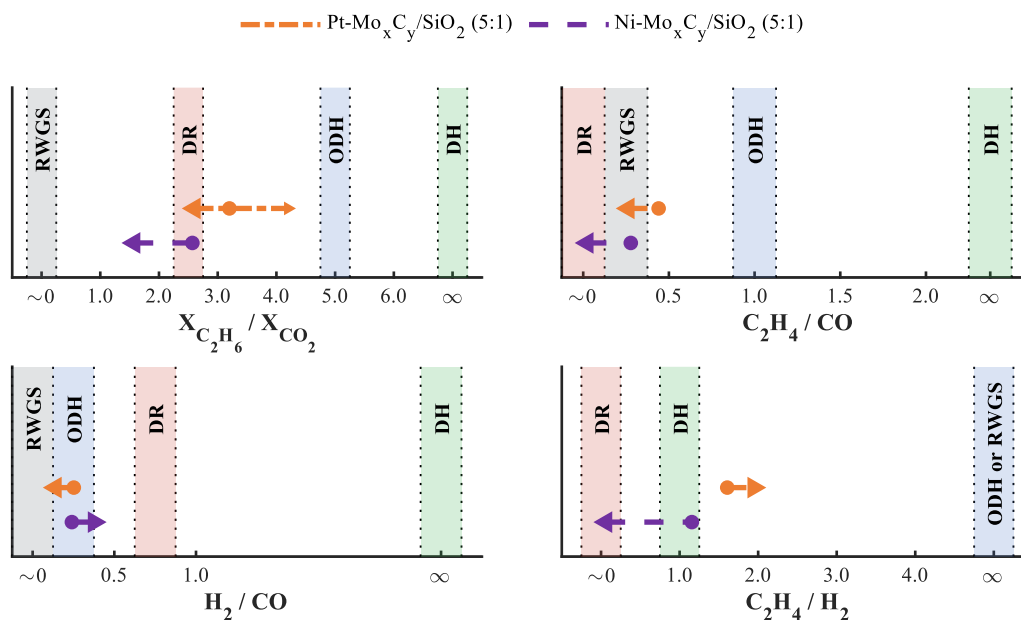


Figure 8.35. Schematic representation of C₂H₆ to CO₂ conversion ratio, C₂H₄ to CO product ratio, H₂ to CO product ratio and C₂H₄ to H₂ product ratio, of Pt-Mo_xC_y/SiO₂ and Ni Pt-Mo_xC_y/SiO₂. CO₂-ODH conditions: T = 600 °C, P = 1 atm, SV = 15 L h⁻¹ g_{cat}⁻¹, CO₂:C₂H₆:Ar = 5:1:6.

Another common measure to reduce or prevent carbon deposition during CO₂-ODH is the co-feeding of H₂O. Steam can react with surface carbon²⁰ producing CO and H₂. Mo_xC_y/SiO₂ was exposed to a CO₂ to C₂H₆ feed ratio of 1 to 1 with the feed gas (sourced from individual gas cylinders) saturated with water at 30 °C, which results in a H₂O content of about 4-5 vol.-%. The co-feeding of H₂O caused a slight decline in the initial activity with a C₂H₆ conversion of 5.7 % after 1 hour TOS and remained lower up until 12 hours TOS (see Figure 8.34). However, the conversion of C₂H₆ is more stable with an C₂H₆ conversion of 2.5 % after 24 hours TOS (compared to 1.1 % in the absence of H₂O co-feeding). C₂H₄ selectivity was increased and remained higher over the entire duration of the experiment. The conversion

ratio ($X_{C_2H_6}/X_{CO_2}$) and product ratios all suggest a shift in reaction mechanism towards DH with TOS (see Figure 8.36).

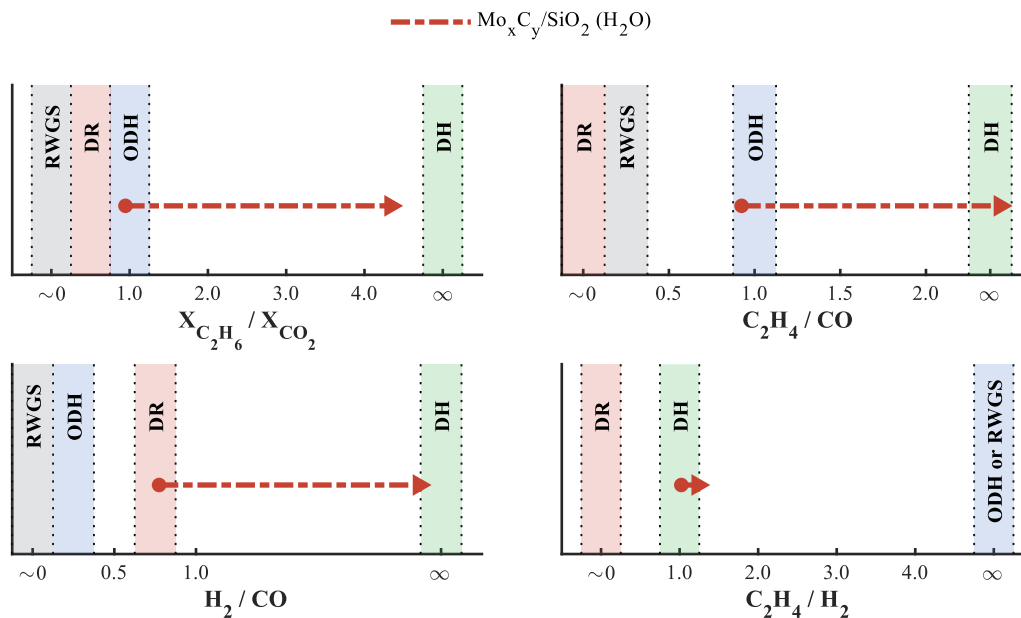


Figure 8.36. Schematic representation of C_2H_6 to CO_2 conversion ratio, C_2H_4 to CO product ratio, H_2 to CO product ratio and C_2H_4 to H_2 product ratio, of $Mo_xC_y/SiO_2 \cdot H_2O/CO_2$ -ODH conditions: $T = 600 \text{ }^\circ\text{C}$, $P = 1 \text{ atm}$, $SV = 15 \text{ L h}^{-1} \text{ g}_{cat}^{-1}$, $CO_2:C_2H_6:Ar = 1:1:2$, with H_2O co-feeding of about 4-5 vol.-%.

Spent catalyst characterization revealed an increased MoO_2 content (54 wt.-%) in comparison to Mo_xC_y/SiO_2 (IND) (see Figure 8.37-A and Table K.2), and Raman spectroscopy evidenced the presence of surface carbon (see Figure 8.37-B). The steam in the feed gas stream is therefore proposed to prevent or suppress carbon deposition on the acid sites responsible for C_2H_6 activation but does not improve the stability of the basic sites for CO_2 activation.

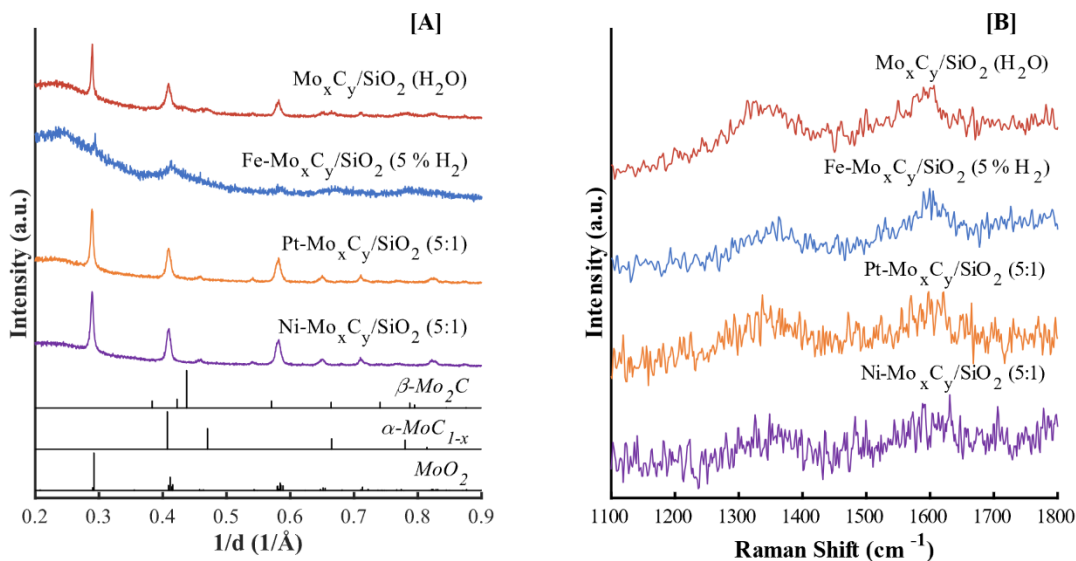


Figure 8.37. [A] XRD patterns and [B] Raman spectra of the spent CO₂-ODH catalysts exposed to varying feed compositions: water co-feeding for Mo_xC_y/SiO₂, co-feeding of 5 vol.-% H₂ for Fe-Mo_xC_y/SiO₂, a 5:1 CO₂ to C₂H₆ feed ratio for Pt-Mo_xC_y/SiO₂ and Ni-Mo_xC_y/SiO₂.

8.6 Concluding remarks

The carburization process and physiochemical properties of molybdenum carbide show significant changes upon the addition of iron, potassium, nickel or platinum. Although the crystal structures of Fe-Mo_xC_y/SiO₂ and K-Mo_xC_y/SiO₂ are similar to the unpromoted sample, in the presence of Fe a decreased β-Mo₂C content and a decrease in surface area is observed. Potassium promotion resulted in an increase in the β-Mo₂C content with an increased crystallite size, possibly due to the increased degree of reduction upon the formation of the carbide. Ni and Pt followed a different carburization pathway, by forming an intermediate phase of MoO_xC_y followed by α-MoC_{1-x}.

The acid and base characteristics of Mo_xC_y were also greatly influenced by the addition of a promoter. K addition decreased the number of acid sites and increased the number of basic sites, with the latter also observed when adding nickel. However, with nickel the appearance of strong acid sites was observed. These characteristics can be directly related to their respective CO₂-ODH performance. Potassium addition decreased the catalytic activity significantly due to the decreased number of acid sites, limiting ethane activation and suppressing the rapid removal of oxygen surface species resulting in severe catalyst oxidation. Even under RWGS conditions, severe catalyst deactivation was observed for K-Mo_xC_y/SiO₂. Lower potassium content could possibly be beneficial and should be further investigated. The addition of iron or nickel decreased the initial activity, but with TOS the promoted catalysts

outperform the unpromoted sample. Specifically, iron showed promising catalytic stability and an increased ethylene selectivity, which is likely due to enhanced stability of the oxygen surface species and/or the formation of MoO_xC_y . $\text{Ni-Mo}_x\text{C}_y/\text{SiO}_2$ achieved the highest activity for the RWGS reaction with minimal formation of CH_4 , even at a H_2 to CO_2 ratio of 2.5. This can be explained by the increased number of basic sites, which are mainly responsible for the enhanced CO_2 activation. Pt promotion resulted in a slight decrease in C_2H_6 conversion and a more severe drop in CO_2 conversion, indicating a higher degree of direct dehydrogenation. This is paired with a high degree of carbon deposition and an absence of catalyst oxidation. An increased CO_2 content did not enhance the stability much, with only a slight increase in C_2H_6 conversion. The ethylene yield was almost equal, despite a significant increase in CO selectivity. This confirms that the dry-reforming of C_2H_6 is the main contributor to the enhanced ethane conversion. The over-stoichiometric amount of CO_2 fed to the catalyst oxidizes the carbide. H_2 co-feeding limited carbon deposition, however, on $\text{Fe-Mo}_x\text{C}_y/\text{SiO}_2$, the catalyst stability was not enhanced. This is likely due to the faster removal of oxygen surface species created *via* CO_2 activation, limiting the formation of the most active phase for CO_2 -ODH, i.e., MoO_xC_y . Co-feeding of H_2O does enhance the catalyst stability without completely preventing carbon deposition. An increase in C_2H_4 selectivity was observed, suggesting that steam removes or prevents the formation of carbon deposits on the sites responsible for C_2H_6 activation.

References

1. A. De Zanet and S. A. Kondrat, A Review of Preparation Strategies for α -MoC_{1-x} Catalysts : Transition metal carbides attract growing attention, *Johnson Matthey Technology Review*, 2022, **66**, 285-315.
2. K. T. Jung, W. B. Kim, C. H. Rhee and J. S. Lee, Effects of Transition Metal Addition on the Solid-State Transformation of Molybdenum Trioxide to Molybdenum Carbides, *Chem. Mater.*, 2004, **16**, 307-314.
3. J. S. Lee, L. Volpe, F. H. Ribeiro and M. Boudart, Molybdenum Carbide Catalysts II. Topotactic Synthesis of Unsupported Powders, *J. Catal.*, 1988, **112**, 44-53.
4. Z. Hao, X. Li, Y. Tian, T. Ding, G. Yang, Q. Ma, N. Tsubaki and X. Li, Influence of Carbon Content in Ni-Doped Mo₂C Catalysts on CO Hydrogenation to Mixed Alcohol, *Catalysts*, 2021, **11**, 230.
5. Y. Ma, G. Guan, P. Phanthong, X. Hao, W. Huang, A. Tsutsumi, K. Kusakabe and A. Abudula, Catalytic Activity and Stability of Nickel-Modified Molybdenum Carbide Catalysts for Steam Reforming of Methanol, *The Journal of Physical Chemistry C*, 2014, **118**, 9485-9496.
6. M. D. Porosoff, J. W. Baldwin, X. Peng, G. Mpourmpakis and H. D. Willauer, Potassium-Promoted Molybdenum Carbide as a Highly Active and Selective Catalyst for CO₂ Conversion to CO, *ChemSusChem*, 2017, **10**, 2408-2415.
7. Y. Shu, D. Ma, L. Xu, Y. Xu and X. Bao, Methane Dehydro-Aromatization Over Mo/Mcm-22 Catalysts: A Highly Selective Catalyst For The Formation Of Benzene, *Catal. Lett.*, 2000, **70**, 67-73.
8. P. Michorczyk, Dehydrogenation of propane to propene over gallium oxide in the presence of CO₂, *Applied Catalysis A: General*, 2003, **251**, 425-433.
9. S. W. Paleg, PhD, University of Michigan, 2019.
10. W. Marquart, S. Raseale, G. Prieto, A. Zimina, B. B. Sarma, J.-D. Grunwaldt, M. Claeys and N. Fischer, CO₂ Reduction over Mo₂C-Based Catalysts, *ACS Catalysis*, 2021, **11**, 1624-1639.
11. M. D. Porosoff, X. Yang, J. A. Boscoboinik and J. G. Chen, Molybdenum carbide as alternative catalysts to precious metals for highly selective reduction of CO₂ to CO, *Angew Chem Int Ed Engl*, 2014, **53**, 6705-6709.
12. X. Zhang, X. Zhu, L. Lin, S. Yao, M. Zhang, X. Liu, X. Wang, Y.-W. Li, C. Shi and D. Ma, Highly Dispersed Copper over β -Mo₂C as an Efficient and Stable Catalyst for the Reverse Water Gas Shift (RWGS) Reaction, *ACS Catalysis*, 2016, **7**, 912-918.
13. J. Gao, Y. Wu, C. Jia, Z. Zhong, F. Gao, Y. Yang and B. Liu, Controllable synthesis of α -MoC_{1-x} and β -Mo₂C nanowires for highly selective CO₂ reduction to CO, *Catalysis Communications*, 2016, **84**, 147-150.
14. X. Liu, C. Kunkel, P. Ramírez de la Piscina, N. Homs, F. Viñes and F. Illas, Effective and Highly Selective CO Generation from CO₂ Using a Polycrystalline α -Mo₂C Catalyst, *ACS Catalysis*, 2017, **7**, 4323-4335.
15. F. Solymosi and L. Bugyi, Effects of potassium on the chemisorption of CO₂ and CO on the Mo₂C/Mo(100) surface, *Catalysis Letters*, 2000, **66**, 227-230.
16. R. Yao, J. E. Herrera, L. Chen and Y.-H. C. Chin, Generalized Mechanistic Framework for Ethane Dehydrogenation and Oxidative Dehydrogenation on Molybdenum Oxide Catalysts, *ACS Catalysis*, 2020, **10**, 6952-6968.
17. F. Solymosi, R. Németh and A. Oszkó, The oxidative dehydrogenation of propane with CO₂ over supported Mo₂C catalyst, *Studies in Surface Sciences and Catalysis*, 2001, **136**, 339-344.
18. M. D. Porosoff, M. N. Myint, S. Kattel, Z. Xie, E. Gomez, P. Liu and J. G. Chen, Identifying Different Types of Catalysts for CO₂ Reduction by Ethane through Dry Reforming and Oxidative Dehydrogenation, *Angew Chem Int Ed Engl*, 2015, **54**, 15501-15505.
19. W. Marquart, M. Claeys and N. Fischer, Conversion of CO₂ and small alkanes to platform chemicals over Mo₂C-based catalysts, *Faraday Discuss*, 2021, **230**, 68-86.
20. X. Longya, L. Liwu, W. Qingxia, Y. Li, W. Debao and L. Weichen, in *Natural Gas Conversion V, Proceedings of the 5th International Natural Gas Conversion Symposium*, 1998, DOI: 10.1016/s0167-2991(98)80498-9, pp. 605-610.

9 Conclusions and Summary

In this thesis, a comprehensive study is presented towards the application of Mo_xC_y -based catalysts for the CO_2 -assisted oxidative dehydrogenation of ethane. Mo_xC_y -based catalysts have shown to be promising candidates for this reaction as it can activate both CO_2 and C_2H_6 , with a high selectivity towards the desired product, ethylene.¹⁻⁴ The major pitfall for further development of these catalysts for potential upscaling, is the poor catalyst stability. The deactivation of the catalyst is mainly caused by carbon deposition and oxidation of the carbide phase to the lesser active oxide phases³. In addition, bulk carbide catalysts have shown poor performance in terms of catalyst activity and selectivity, when compared to supported Mo_xC_y nanoparticles. The poor stability of the catalyst goes beyond the here suggested Mo_xC_y system and is a general trend for all CO_2 -ODH catalyst.⁵⁻¹² Hence, most literature reports on short term experiments, focusing on the initial activity and product selectivity. This work reports on 24 hour experiments, in an attempt to create a deeper understanding of the deactivation mechanism and the various possible side reactions occurring on Mo_xC_y -based catalysts. This was completed by an extensive (*in situ*) characterization study of the carburization process and the freshly carburized samples for an accurate comparison to the spent catalysts. The freshly carburized samples were then exposed to a variety of reaction temperatures, co-feeding experiments and RWGS conditions, to identify the possible reaction pathways and increasing catalytic stability by preventing the oxidation and or carbon deposition to occur. The project was extended by varying the synthesis technique, dispersion on various metal oxide supports and *via* promoter addition.

The synthesis of the catalyst, specifically focusing on the carburization process, was extensively studied by means of *in situ* characterization techniques such as XRD, XAS and Raman spectroscopy, to monitor the phase evolution from the precursor (AHM or MoO_3) to Mo_xC_y . The freshly carburized catalysts revealed to contain one or a combination of any of the following carbide phases: β - Mo_2C , η - $\text{MoC}_{0.59}$, α - MoC_{1-x} or MoO_xC_y . Varying the synthesis technique, between common slurry (wet) impregnation (WI), a hybrid nanocrystal technique^{13, 14} (HNC) or a sol-gel method¹⁵ (SG), and two silica-based supports (SiO_2 and SBA-15), five samples were synthesized. When carburized at 600 °C in a 20 vol.-% CH_4 in H_2 mixture. $\text{Mo}_x\text{C}_y/\text{SiO}_2$ -SG and $\text{Mo}_x\text{C}_y/\text{SBA-15}$ -HNC both produced a mixture of η - $\text{MoC}_{0.59}$ and MoO_xC_y . The presence of MoO_xC_y instead of α - MoC_{1-x} is difficult to distinguish by means of the respective XRD patterns, but EXAFS analysis confirmed that the presence of α - MoC_{1-x} is unlikely. $\text{Mo}_x\text{C}_y/\text{SiO}_2$ -WI, $\text{Mo}_x\text{C}_y/\text{SBA-15}$ -WI and $\text{Mo}_x\text{C}_y/\text{SiO}_2$ -HNC all yielded a combination of β - Mo_2C and η - $\text{MoC}_{0.59}$. The presence of MoO_xC_y is suggested to occur due to the delayed carburization for both $\text{Mo}_x\text{C}_y/\text{SBA-15}$ -HNC and $\text{Mo}_x\text{C}_y/\text{SiO}_2$ -SG, possibly due to a stronger interaction between the Mo-

particles and the support originated from the synthesis technique. At higher carburization temperatures (650 °C), β -Mo₂C was observed.

Additionally, a range of metal oxide support materials were employed, i.e. Al₂O₃, ZrO₂, Ga₂O₃, TiO₂ and CeO₂. The samples were prepared *via* wet impregnation and all samples yielded a carbide composition containing η -MoC_{0.59} and/or β -Mo₂C. No evidence of MoO_xC_y or α -MoC_{1-x} was observed by XRD, bearing in mind the large contrast in crystallite size between the metal oxide support and the Mo_xC_y particles.

By addition of a promoter, i.e., Fe, Pt, Ni or K, *via* co-impregnation (Co-Imp) on a SiO₂ support, the carburization process as well as the final carbide composition was significantly altered, especially upon promotion with Pt and Ni. *In situ* XRD revealed that MoO_xC_y is a precursor phase of α -MoC_{1-x} during the carburization process upon promotion with Pt and Ni. Fe promotion caused the decomposition of the molybdate to *hP*-MoO₃ only, but no large differences in carbide composition to the unpromoted sample is observed when promoted *via* co-impregnation. A sequential promotion (Seq-Imp) or promotion after calcination (Calc-Imp), caused an increase in the β -Mo₂C content. Potassium promotion did not visibly alter the carburization process (by means of *in situ* XRD), but the freshly carburized sample contained slightly larger crystallite sizes, which could be caused due to a more intense reduction of MoO_x, as observed by online MS analysis of the effluent gas (possibly forming some metallic Mo).

The BET surface area of each catalysts seemed to be predominantly determined by the support material and is only slightly affected by the Mo_xC_y nanoparticles. All catalysts showed to produce below 10 nm sized Mo_xC_y nanoparticles, well distributed over the support material, as observed by TEM and SEM-EDS. Raman analysis revealed minimal to no carbon deposition to have occurred during carburization.

Besides the structural effects the different synthesis techniques, support materials and promoter had on the supported Mo_xC_y nanoparticles, effects on the chemical properties and the affinity to activate CO₂ were also observed. On all catalysts, in a diluted CO₂ atmosphere, at temperatures between 300 and 530 °C, CO₂ is activated *via* dissociation on the surface. At higher temperatures, for selected samples, the carbide oxidized to MoO₂. When compared to the baseline catalyst, Mo_xC_y/SiO₂-WI, the different support materials and the different promoter additions showed to have the largest influence on the CO₂ activation behaviour. On Ga₂O₃, both the CO yield *via* CO₂ dissociation at the lower temperature range (530 – 600 °C) and the CO peak yield is much lower than the SiO₂ supported sample. No oxidation to MoO₂ was observed. For ZrO₂ and TiO₂ supported sample, the CO peak yield increased, suggesting higher affinity towards oxidation.

Promotion with potassium significantly decreased the CO₂ activation *via* dissociation on the surface, but at higher temperatures a similar degree of oxidation was observed compared to the unpromoted sample. The slight increase in weaker basic sites did not seem to influence CO₂ dissociation below 600 °C. Fe and Ni promoted sample achieved a slight increase in CO₂ dissociation at lower temperatures and showed to be more resistant to oxidation at higher temperatures.

In terms of acid-base sites, Al₂O₃ and TiO₂ increased the number and strength of basic sites available. Ga₂O₃ and especially ZrO₂, increased the number of acid sites available. The Ni and K promoted samples increased the number of basic sites, and a decrease was observed for the Fe and Pt promoted samples. A reverse effect was observed for the number and strength of the acid sites, although Ni did show the presence of some strong acid sites.

Reverse water-gas-shift performance was evaluated for all silica supported samples and activities close to thermodynamic equilibrium (with respect to the applied reaction conditions) was observed for all catalysts, as well as a remarkable stability over the entire period tested, except for the K-promoted sample. Promotion of the carbide nanoparticles with potassium is very sensitive towards the promoter loading and it is suggested that the loading is too high. This potentially causes the formation of carbonate like surface compounds as well as over-reduction to metallic Mo. No oxidation or carbon deposition was observed on any of the samples exposed to the wide range of RWGS conditions.

All the characteristics discussed could be directly related to the CO₂-ODH performance of each catalyst, including potential reaction pathways and deactivation mechanisms. While the performance of the catalysts prepared *via* different synthesis techniques did not vary significantly, some effects regarding the carbide composition and CO₂ activation behaviour can be observed. All five catalysts showed to predominantly follow the CO₂-ODH reaction pathway, with a slightly more prominent DH pathway observed with time on stream. Although the largest differences are observed in the first 12 hours TOS, the Mo_xC_y/SBA-15-HNC showed to be the most efficient C₂H₄ producing catalyst, which is likely due to the higher mass specific Mo surface area and the highest MoO_xC_y content.

The different metal oxide supports showed a much larger effect on the catalytic performance. On all samples, the Mo_xC_y nanoparticles remained consistent and achieved a high selectivity to C₂H₄. The lowest C₂H₄ selectivity observed for Mo_xC_y/ZrO₂ initially but increases with TOS (as the conversion decreases). This suggests that while initially a predominant dry-reforming pathway is achieved, the deactivation of the catalyst causes a shift in the reaction pathway, likely due to the covering of the ZrO₂ support by carbon and the oxidation of the carbide creating active oxygen sites. H₂ co-feeding prevented the oxidation of the catalyst, which resulted in a more dominant DR pathway. The observed deactivation can

be explained by a loss in DR activity, since a stable ethylene yield was achieved upon co-feeding 17 vol.-% H₂. This suggests the occurrence of a balanced reaction pathway between the RWGS and CO₂-ODH reaction. Mo_xC_y/Al₂O₃ showed an initial higher activity with an C₂H₄ selectivity of over 60 C-%, with again a sharp decrease in activity accompanied by a more dominant DH pathway. When exposed to a 5:1 CO₂ to C₂H₆ feed mixture, the deactivation rate could be slowed down and simultaneously a more stable C₂H₄ selectivity was observed. This is likely due to the removal of surface carbon *via* reverse Boudouard, freeing up active sites for the co-activation of CO₂ and C₂H₆. Mo_xC_y/Ga₂O₃ might be the most interesting sample of all. While in a stoichiometric feed composition the activity drops drastically with TOS, which is suggested due to the dominant DH pathway causing carbon deposition *via* ethylene decomposition as limited oxidation is observed. At a 5:1 feed, no oxidation was observed, yet the deactivation rate was similar to the stoichiometric feed. Only upon co-feeding H₂, the stability of the catalyst was enhanced, which is of particular interest as oxidation did not show to be the main deactivation pathway. It is hypothesized that the H₂ co-feeding aided into the removal of carbon deposits as well as prevented surface oxidation, invisible by XRD.

Fe promotion has shown to potentially increase catalyst stability, suggested due to the stabilization of the oxygen surface species, creating a MoO_xC_y phase. However, at prolonged TOS, oxidation and carbon deposition could not be prevented which eventually caused severe catalyst deactivation. The rapid removal of these oxygen surface species was achieved by means of H₂ co-feeding. However, this prevented the formation of the more active MoO_xC_y phase as is observed in the spent catalyst by the absence of α-MoC_{1-x}. Pt promotion caused a more dominant DH pathway, which is supported by the absence of oxidation in a stoichiometric feed composition and significant amount of carbon deposition. An increased CO₂ content did not enhance the (O)DH activity, but showed an additional DR activity, while maintaining the DH activity as is observed by the enhanced C₂H₆ conversion while achieving a similar ethylene yield. The Ni promoted sample showed to shift to a more dominant DR pathway with TOS, which is further increased with an increase in the CO₂ content in the feed. Potassium promotion caused a severe drop in activity, which is in line with the lower affinity to CO₂ activation and the unstable RWGS performance. This can be mainly explained by the loss in acid sites, limiting C₂H₆ activation, causing severe oxidation of the carbide to MoO_x. While not observed by means of XRD or surface sensitive techniques, the formation of metallic Mo^{16, 17} or carbonate like surface compounds¹⁸ can also cause the poor performance.

References

1. F. Solymosi and R. Németh, The oxidative dehydrogenation of ethane with CO₂ over Mo₂C/SiO₂ catalyst, *Catalysis Letters*, 1999, **62**, 197-200.
2. F. Solymosi, R. Németh and A. Oszkó, The oxidative dehydrogenation of propane with CO₂ over supported Mo₂C catalyst, *Studies in Surface Sciences and Catalysis*, 2001, **136**, 339-344.
3. M. D. Porosoff, M. N. Myint, S. Kattel, Z. Xie, E. Gomez, P. Liu and J. G. Chen, Identifying Different Types of Catalysts for CO₂ Reduction by Ethane through Dry Reforming and Oxidative Dehydrogenation, *Angew Chem Int Ed Engl*, 2015, **54**, 15501-15505.
4. S. Yao, B. Yan, Z. Jiang, Z. Liu, Q. Wu, J. H. Lee and J. G. Chen, Combining CO₂ Reduction with Ethane Oxidative Dehydrogenation by Oxygen-Modification of Molybdenum Carbide, *ACS Catalysis*, 2018, **8**, 5374-5381.
5. S. Wang and Z. H. Zhu, Catalytic Conversion of Alkanes to Olefins by Carbon Dioxide Oxidative Dehydrogenation A Review, *Energy & Fuels*, 2004, **18**, 1126-1139.
6. M. B. Ansari and S.-E. Park, Carbon dioxide utilization as a soft oxidant and promoter in catalysis, *Energy & Environmental Science*, 2012, **5**, 9419-9437.
7. S. Kawi and Y. Kathiraser, CO₂ as an Oxidant for High-Temperature Reactions, *Frontiers in Energy Research*, 2015, **3**, 1-17.
8. D. Mukherjee, S.-E. Park and B. M. Reddy, CO₂ as a soft oxidant for oxidative dehydrogenation reaction: An eco benign process for industry, *Journal of CO₂ Utilization*, 2016, **16**, 301-312.
9. E. Gomez, B. Yan, S. Kattel and J. G. Chen, Carbon dioxide reduction in tandem with light-alkane dehydrogenation, *Nature Reviews Chemistry*, 2019, **3**, 638-649.
10. Y. Gambo, S. Adamu, G. Tanimu, I. M. Abdullahi, R. A. Lucky, M. S. Ba-Shammakh and M. M. Hossain, CO₂-mediated oxidative dehydrogenation of light alkanes to olefins: Advances and perspectives in catalyst design and process improvement, *Applied Catalysis A: General*, 2021, **623**, 118273.
11. X. Jiang, L. Sharma, V. Fung, S. J. Park, C. W. Jones, B. G. Sumpter, J. Baltrusaitis and Z. Wu, Oxidative Dehydrogenation of Propane to Propylene with Soft Oxidants via Heterogeneous Catalysis, *ACS Catalysis*, 2021, **11**, 2182-2234.
12. G. Li, C. Liu, X. Cui, Y. Yang and F. Shi, Oxidative dehydrogenation of light alkanes with carbon dioxide, *Green Chemistry*, 2021, **23**, 689-707.
13. W. Han, P. Yuan, Y. Fan, H. Liu and X. Bao, Synthesis, self-assembly and disassembly of mono-dispersed Mo-based inorganic-organic hybrid nanocrystals, *Journal of Materials Chemistry*, 2012, **22**, 12121-12127.
14. W. Han, P. Yuan, Y. Fan, G. Shi, H. Liu, D. Bai and X. Bao, Preparation of supported hydrodesulfurization catalysts with enhanced performance using Mo-based inorganic-organic hybrid nanocrystals as a superior precursor, *Journal of Materials Chemistry*, 2012, **22**, 25340-25353.
15. A. P. Amrute, S. Sahoo, A. Bordoloi, Y. K. Hwang, J.-S. Hwang and S. B. Halligudi, MoO₃/SiO₂: An efficient and selective catalyst for the synthesis 1,3-dioxolane and 1,3-dioxane, *Catalysis Communications*, 2009, **10**, 1404-1409.
16. M. D. Porosoff, J. W. Baldwin, X. Peng, G. Mpourmpakis and H. D. Willauer, Potassium-Promoted Molybdenum Carbide as a Highly Active and Selective Catalyst for CO₂ Conversion to CO, *ChemSusChem*, 2017, **10**, 2408-2415.
17. S. F. Zaman, N. Pasupulety, A. A. Al-Zahrani, M. A. Daous, S. S. Al-Shahrani, H. Driss, L. A. Petrov and K. J. Smith, Carbon monoxide hydrogenation on potassium promoted Mo₂N catalysts, *Applied Catalysis A: General*, 2017, **532**, 133-145.
18. F. Solymosi and L. Bugyi, Effects of potassium on the chemisorption of CO₂ and CO on the Mo₂C/Mo(100) surface, *Catalysis Letters*, 2000, **66**, 227-230.

10 Recommendations and Future Work

To further study the Mo_xC_y -based catalytic system and to improve the stability of the catalyst, mainly by preventing the oxidation of the carbide to MoO_x and carbon deposition, while maintaining high ethylene yields, the following experimental approaches are recommended:

- The synthesis techniques used in this study showed to yield a variation of carbide compositions, when applying consistent carburization conditions, which mainly caused differences in the CO_2 -ODH catalytic performance at the early stages of the reaction. To confirm the effect of the different carbide allotropes on the catalyst system, it is recommended to attempt to achieve a more reproducible synthesis technique that produces higher purities of each carbide phase. Ideally, the synthesized catalysts are characterized using more sophisticated techniques (such as synchrotron based techniques), which are not limited by the small crystallite sizes, to confidently distinguish between the different allotropes.
- The above recommendation can be extended by attempting to produce pure phases of MoO_xC_y , $\alpha\text{-MoC}_{1-x}$ and $\beta\text{-Mo}_2\text{C}$ via the synthesis route discussed using Pt promotion. The *in situ* XRD patterns collected during the carburization process of $\text{Pt-Mo}_x\text{C}_y/\text{SiO}_2$, confirmed the presence of MoO_xC_y at around 500 °C and $\alpha\text{-MoC}_{1-x}$ at 600 °C. $\beta\text{-Mo}_2\text{C}$ is thermodynamically the most stable phase, so an increase in carburization temperature should yield a purer $\beta\text{-Mo}_2\text{C}$ phase. Differences in active surface area might be observed due to the various levels of carbon deposition, but these could possibly be removed through a pre-treatment in steam or H_2 .
- The support effect observed in this study is most likely also influenced by the large differences in surface area (although conversions were observed within a similar range). Synthesizing metal oxide support materials with similar surface area, can possibly increase the initial activity of the Mo_xC_y -based catalysts.
- $\text{Mo}_x\text{C}_y/\text{Al}_2\text{O}_3$ evaluated using a 5:1 CO_2 to C_2H_6 feed composition, decreased the deactivation rate significantly and simultaneously produced higher absolute amounts of ethylene. An additional H_2 co-feed, can possibly prevent oxidation and further improve the CO_2 -ODH performance of the Al_2O_3 supported catalyst.

- The Ga_2O_3 supported sample showed minor oxidation in a 1:1 feed, no oxidation in a 5:1 feed, and an improved stability upon co-feeding H_2 . Synchrotron based EXAFS and XPS analysis could both be interesting techniques to observe the (surface) oxidation state of the carbide particles under reaction conditions in the various feed compositions. This can assist in the identification of the reaction mechanism, but more interestingly, the improved catalytic stability upon H_2 co-feeding.
- Lastly, and in essence a combination of the last three recommendations, it is believed that an improved surface area for $\text{Mo}_x\text{C}_y/\text{Ga}_2\text{O}_3$, and/or an increase in the H_2 content in the feed mixture, with the addition of Ni to increase the basic sites and thus increase CO_2 activation or the addition of K to decrease acid site strength and thus limit the DH pathway and preventing substantial amount of carbon deposition, could potentially create a model catalyst that is a highly efficient and stable C_2H_4 producing catalyst, and should be further explored.

Appendix

A Thermodynamic analysis of CO₂-ODH

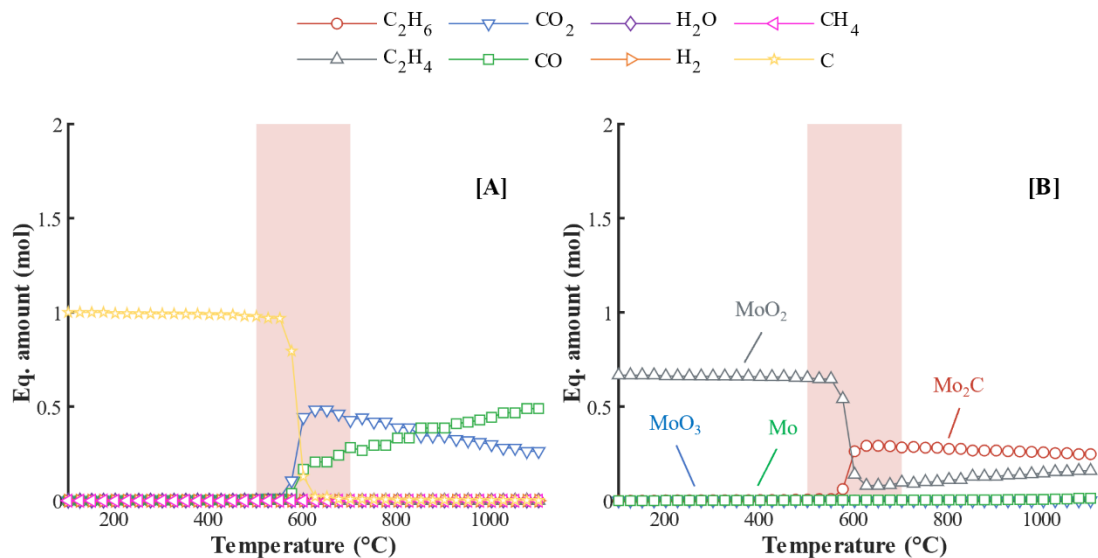


Figure A.1. Product equilibrium of the Mo system in the presence of CO₂, as a function of temperature, with all CO₂-ODH compounds considered [A] including the four different Mo phases [B]. Red shaded area indicates temperature range of interest for CO₂-ODH. Compound specific thermodynamic data from Knacke *et al.*¹.

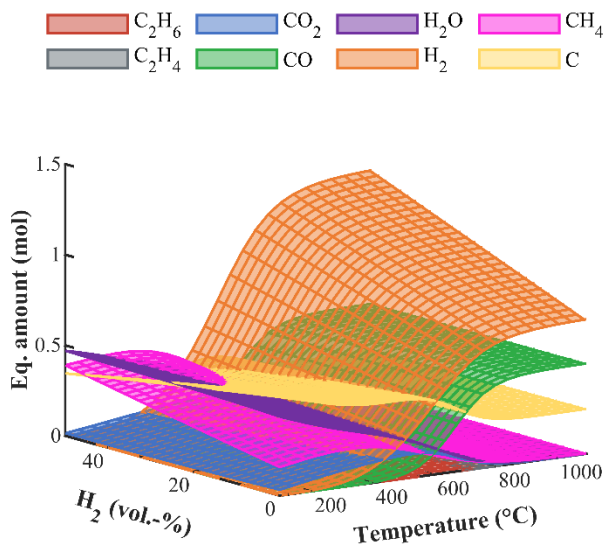


Figure A.2. Product equilibrium of the CO₂-ODH system as a function of temperature and H₂ co-feeding at a stoichiometric feed of CO₂ to C₂H₆ (1:1) and 1 bar pressure, with all compounds considered.

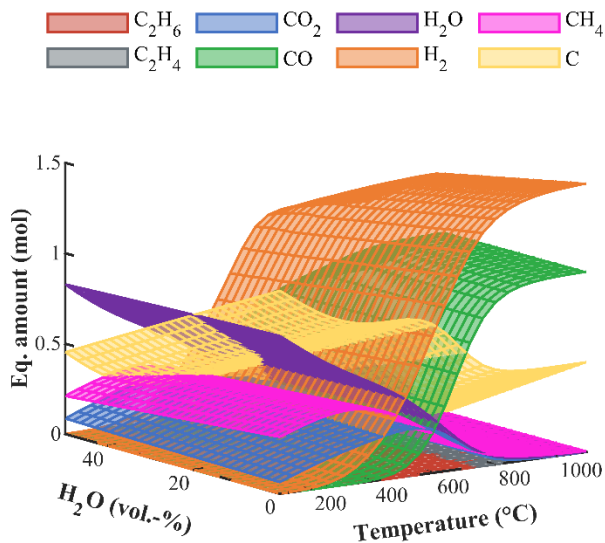


Figure A.3. Product equilibrium of the CO₂-ODH system as a function of temperature and H₂O co-feeding at a stoichiometric feed of CO₂ to C₂H₆ (1:1) and 1 bar pressure, with all compounds considered.

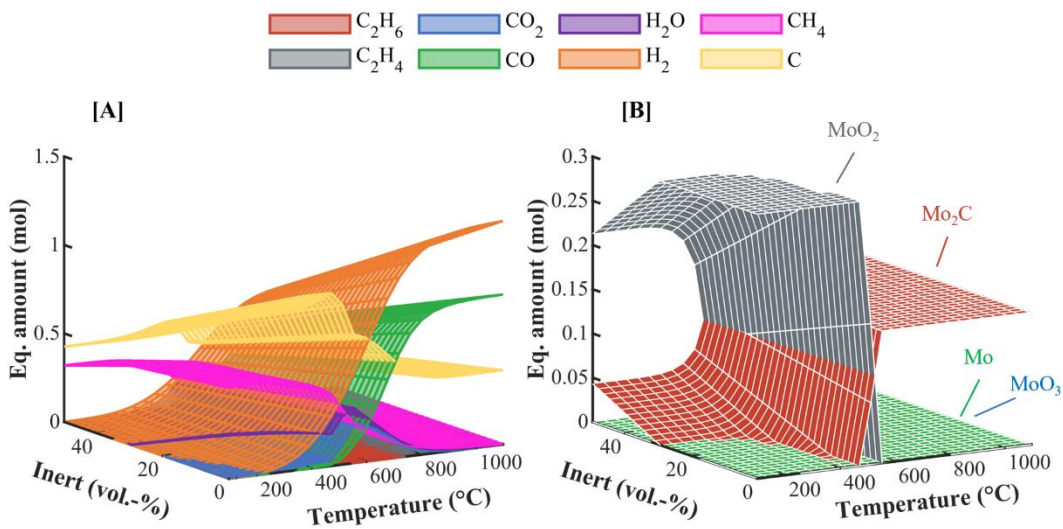


Figure A.4. Product equilibrium of the CO₂-ODH system as a function of temperature and inert co-feeding at a stoichiometric feed of CO₂ to C₂H₆ (1:1) and 1 bar pressure, with all compounds considered [A] including the four different Mo phases [B].

1. O. Knacke, O. Kubaschewski and K. Hesselmann, *Thermochemical properties of inorganic substances*, Springer-Verlag, Berlin, 2nd edn., 1991.

B CO₂-ODH testing results of selected samples

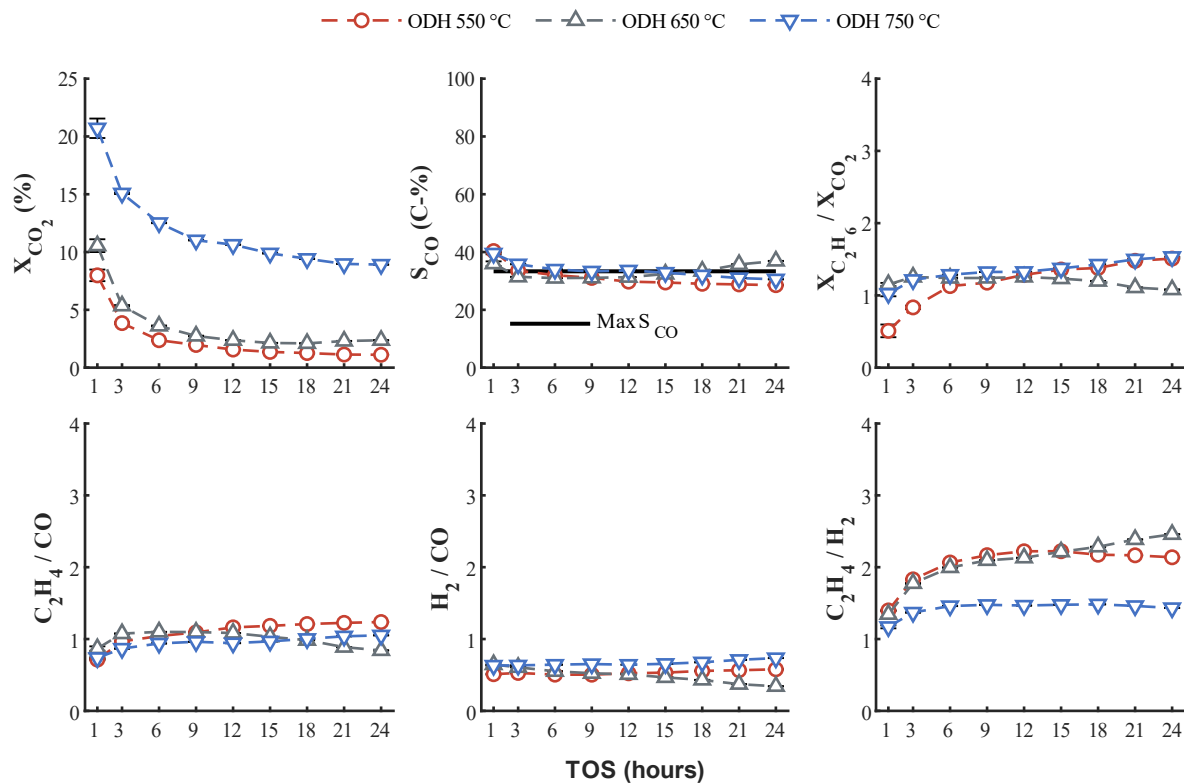


Figure B.1. CO₂ conversion, CO selectivity and C₂H₆ to CO₂ conversion ratio, C₂H₄ to CO product ratio, H₂ to CO product ratio and C₂H₄ to H₂ product ratio, of Mo_xC_y/SiO₂, evaluated within a range of reaction temperatures. Conditions: T = 550 °C, 650 °C or 700 °C, P = 1 atm, SV = 9.4 L h⁻¹ g_{cat}⁻¹, C₂H₆:CO₂:Ar = 1:1:2. Theoretical maximum CO selectivity for CO₂-ODH indicated by solid black line.

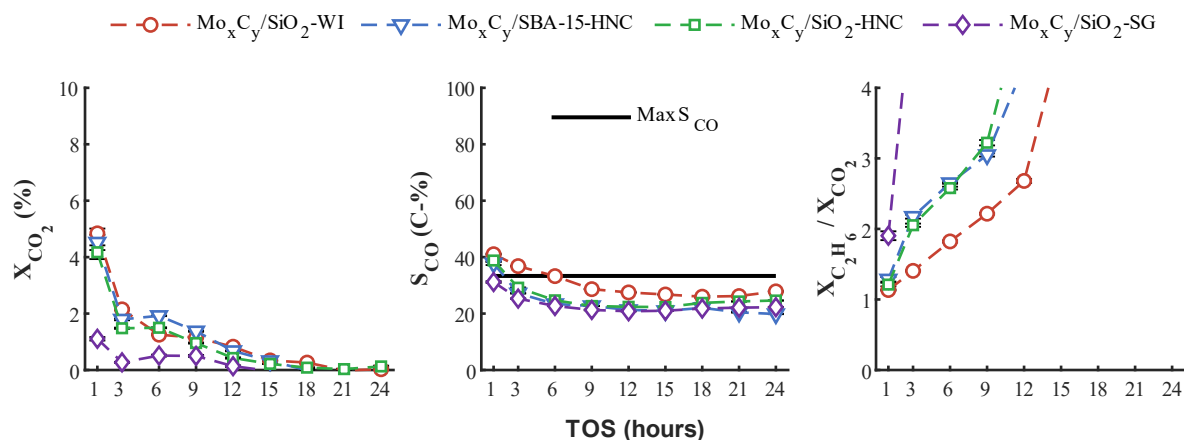


Figure B.2. CO₂ conversion, CO selectivity and C₂H₆ to CO₂ conversion ratio of Mo_xC_y/SiO₂-WI, Mo_xC_y/SBA-15-HNC, Mo_xC_y/SiO₂-HNC and Mo_xC_y/SiO₂-SG. Conditions: T = 600 °C, P = 1 atm, SV = 15 L h⁻¹ g_{cat}⁻¹, CO₂:C₂H₆:Ar = 1:1:2. Theoretical maximum CO selectivity for CO₂-ODH indicated by solid black line.

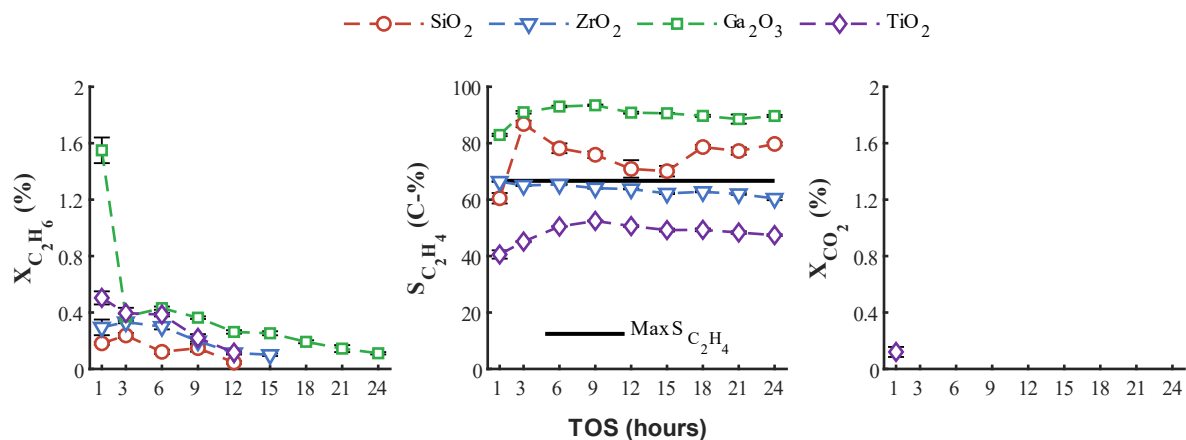


Figure B.3. C₂H₆ conversion, C₂H₄ selectivity and CO₂ conversion, of bulk metal oxide supports, SiO₂, ZrO₂, Ga₂O₃ and TiO₂. CO₂-ODH conditions: T = 600 °C, P = 1 atm, SV = 21.4 L h⁻¹ g_{cat}⁻¹, CO₂:C₂H₆:Ar = 1:1:2. Theoretical maximum C₂H₄ selectivity for CO₂-ODH indicated by solid black line.

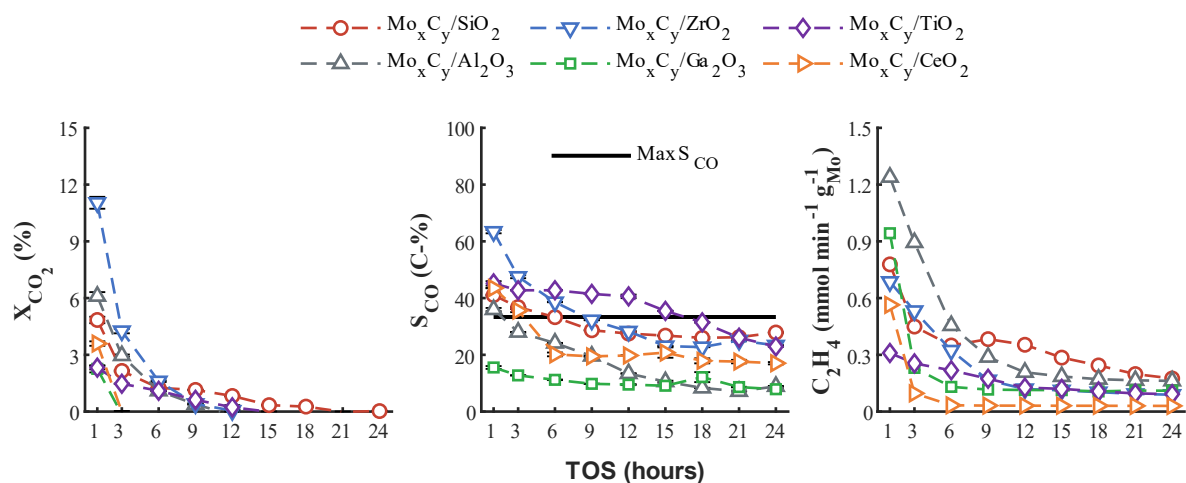


Figure B.4. CO₂ conversion, CO selectivity and C₂H₄ formation rate of Mo_xC_y supported on SiO₂, Al₂O₃, ZrO₂, Ga₂O₃, TiO₂ and CeO₂. CO₂-ODH conditions: T = 600 °C, P = 1 atm, SV = 15 L h⁻¹ g_{cat}⁻¹, CO₂:C₂H₆:Ar = 1:1:2. Theoretical maximum CO selectivity for CO₂-ODH indicated by solid black line.

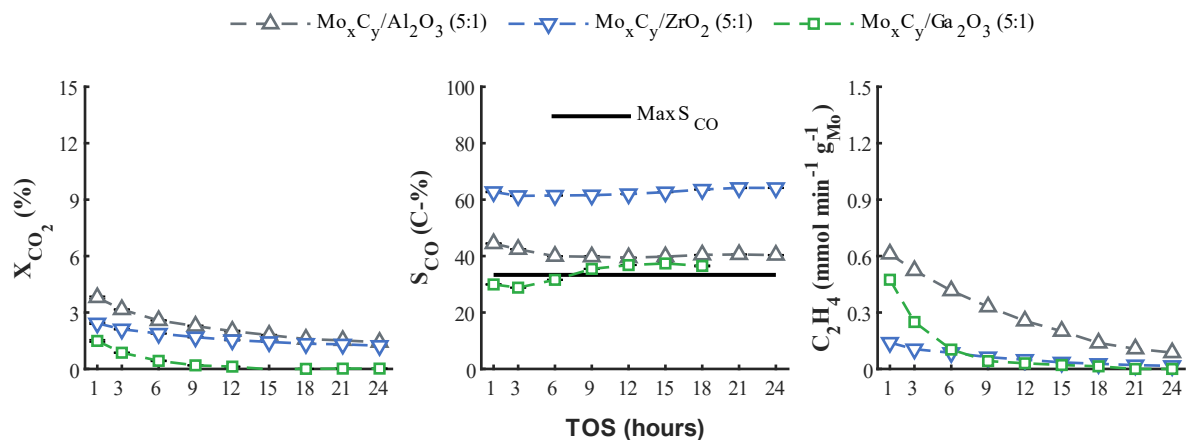


Figure B.5. CO₂ conversion, CO selectivity and C₂H₄ formation rate of Mo_xC_y supported on Al₂O₃, ZrO₂ and Ga₂O₃. CO₂-ODH conditions: T = 600 °C, P = 1 atm, SV = 15 L h⁻¹ g_{cat}⁻¹, CO₂:C₂H₆:Ar = 5:1:6. Theoretical maximum CO selectivity for CO₂-ODH indicated by solid black line.

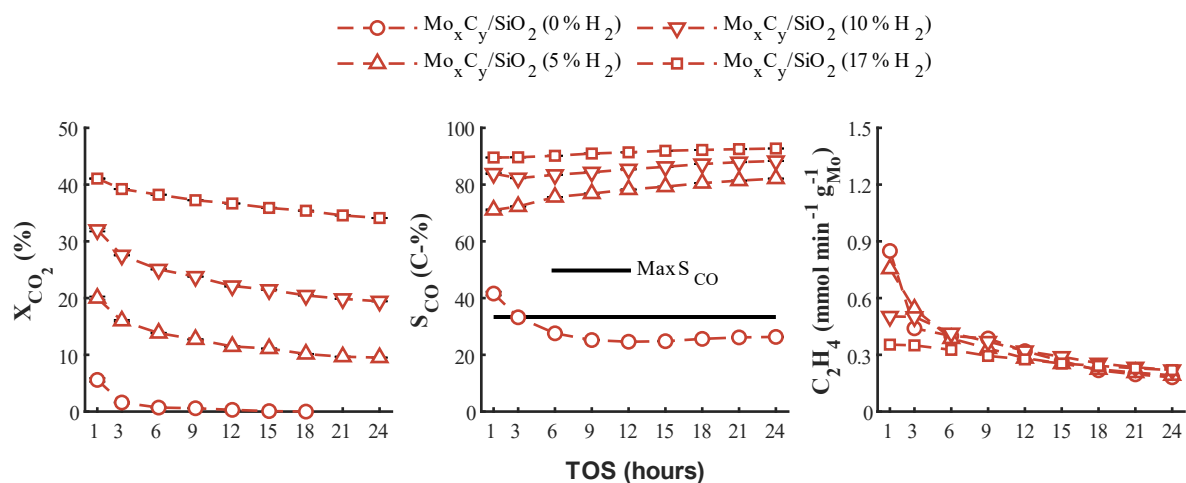


Figure B.6. CO₂ conversion, CO selectivity and C₂H₄ formation rate of Mo_xC_y supported on SiO₂. H₂/CO₂-ODH conditions: T = 600 °C, P = 1 atm, SV = 15 L h⁻¹ g_{cat}⁻¹, CO₂:C₂H₆:Ar = 1:1:2, with H₂ co-feeding at 0, 5, 10 and 17 vol.-%. Theoretical maximum CO selectivity for CO₂-ODH indicated by solid black line.

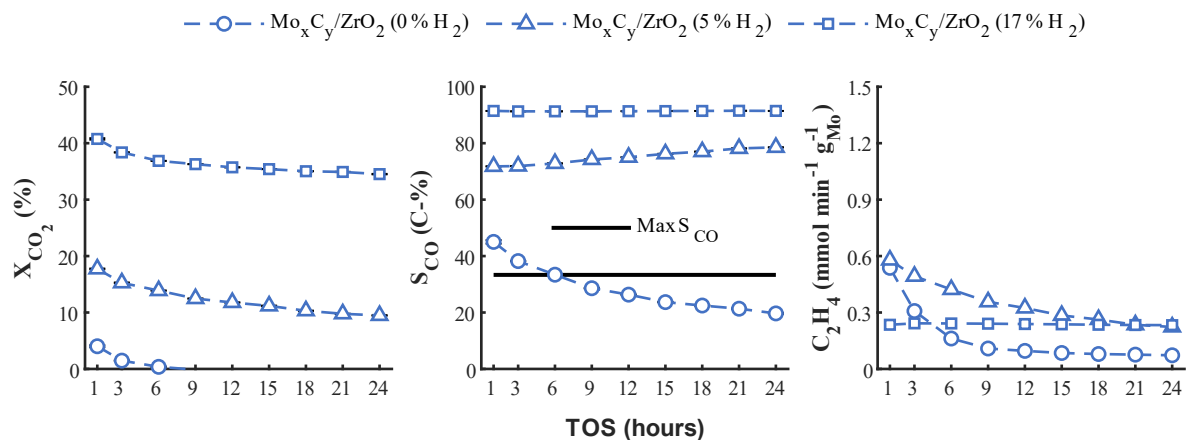


Figure B.7. CO₂ conversion, CO selectivity and C₂H₄ formation rate of Mo_xC_y supported on ZrO₂. H₂/CO₂-ODH conditions: T = 600 °C, P = 1 atm, SV = 15 L h⁻¹ g_{cat}⁻¹, CO₂:C₂H₆:Ar = 1:1:2, with H₂ co-feeding at 0, 5 and 17 vol.-%. Theoretical maximum CO selectivity for CO₂-ODH indicated by solid black line.

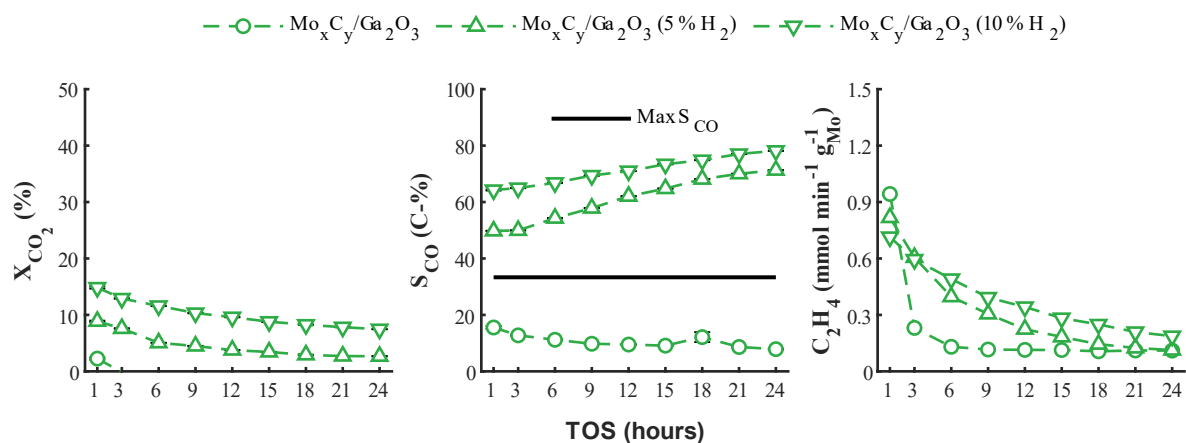


Figure B.8. CO₂ conversion, CO selectivity and C₂H₄ formation rate of Mo_xC_y supported on Ga₂O₃. H₂/CO₂-ODH conditions: T = 600 °C, P = 1 atm, SV = 15 L h⁻¹ g_{cat}⁻¹, CO₂:C₂H₆:Ar = 1:1:2, with H₂ co-feeding at 5 and 17 vol.-%. Theoretical maximum CO selectivity for CO₂-ODH indicated by solid black line.

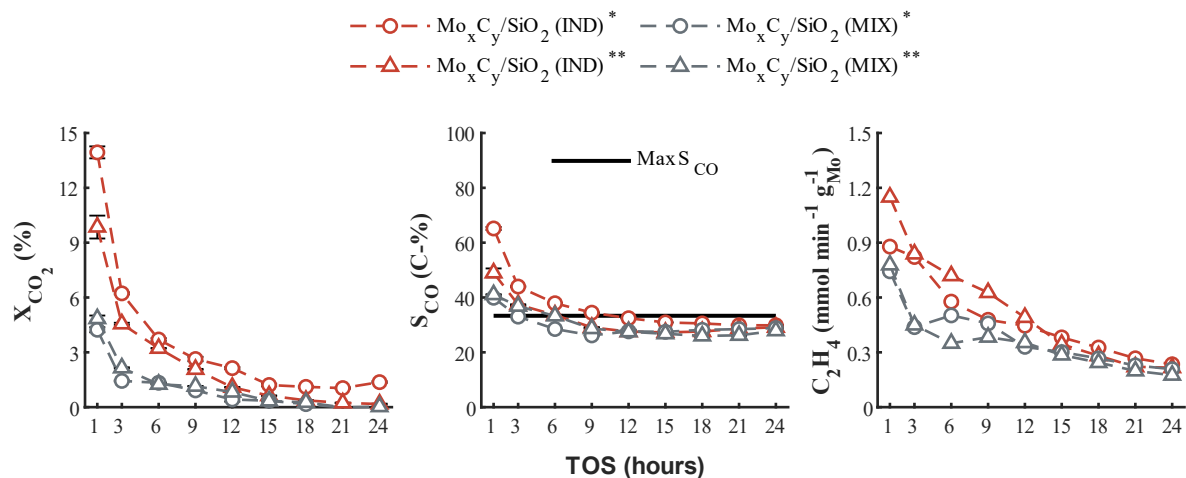


Figure B-9. CO₂ conversion, CO selectivity and C₂H₄ formation rate, of Mo_xC_y supported on SiO₂, with the feed gas sourced from individual gas cylinders (IND) or single cylinder pre-mix (MIX). CO₂-ODH conditions: T = 600 °C, P = 1 atm, SV = 15 L h⁻¹ g_{cat}⁻¹, CO₂:C₂H₆:Ar = 1:1:2. Theoretical maximum CO selectivity for CO₂-ODH indicated by solid black line.

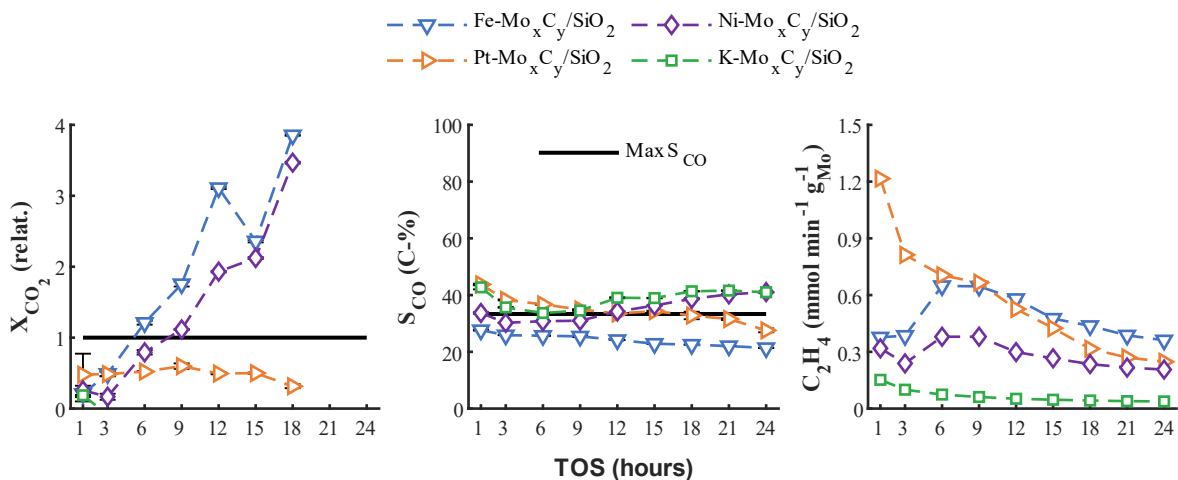


Figure B-10. CO₂ conversion (relative to unpromoted sample), CO selectivity and C₂H₄ formation rate, of Mo_xC_y supported on SiO₂, promoted with iron, platinum, nickel or potassium. CO₂-ODH conditions: T = 600 °C, P = 1 atm, SV = 15 L h⁻¹ g_{cat}⁻¹, CO₂:C₂H₆:Ar = 1:1:2. Theoretical maximum CO selectivity for CO₂-ODH indicated by solid black line.

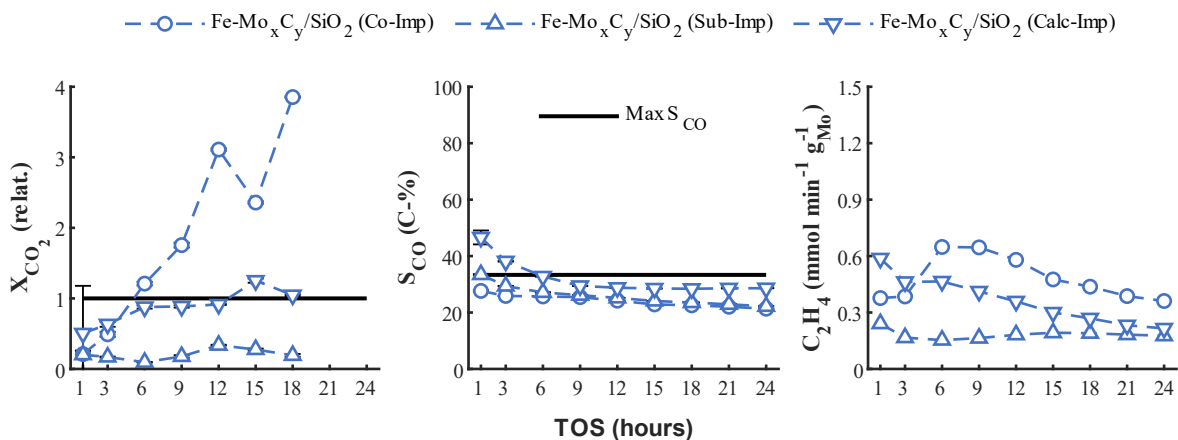


Figure B-11. CO₂ conversion (relative to unpromoted sample), CO selectivity and C₂H₄ formation rate, of Fe-Mo_xC_y/SiO₂, promoted *via* co-impregnation, sequential impregnation or after calcination. CO₂-ODH conditions: T = 600 °C, P = 1 atm, SV = 15 L h⁻¹ g_{cat}⁻¹, CO₂:C₂H₆:Ar = 1:1:2. Theoretical maximum CO selectivity for CO₂-ODH indicated by solid black line.

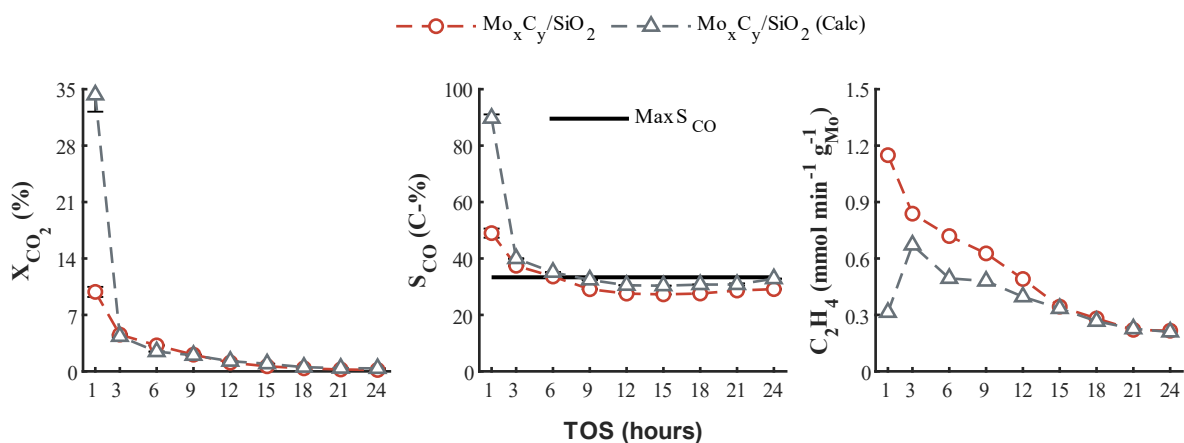


Figure B-12. CO₂ conversion, CO selectivity and C₂H₄ formation rate, of Mo_xC_y/SiO₂ carburized with and without prior calcination. CO₂-ODH conditions: T = 600 °C, P = 1 atm, SV = 15 L h⁻¹ g_{cat}⁻¹, CO₂:C₂H₆:Ar = 1:1:2. Theoretical maximum CO selectivity for CO₂-ODH indicated by solid black line.

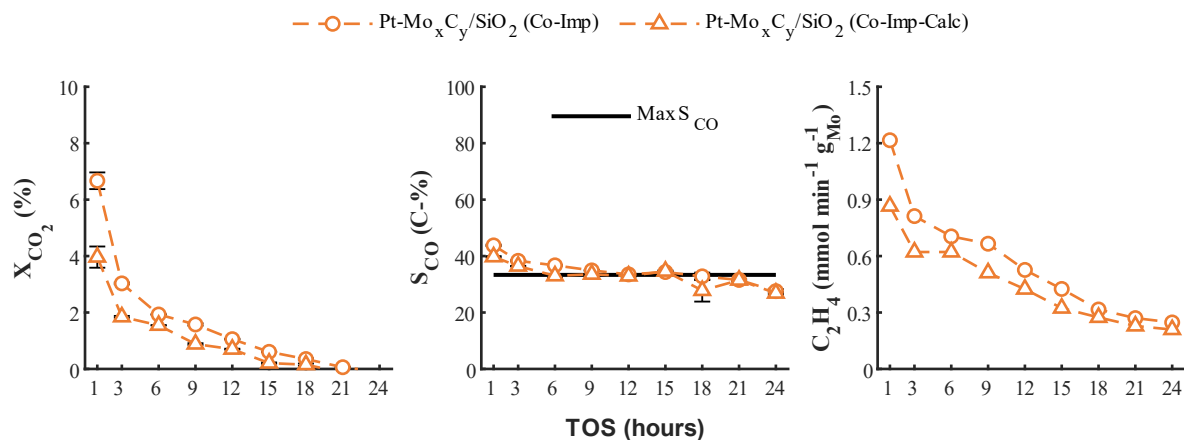


Figure B-13. CO₂ conversion, CO selectivity and C₂H₄ formation rate, of Pt-Mo_xC_y/SiO₂, promoted *via* co-impregnation and carburized with and without prior calcination. CO₂-ODH conditions: T = 600 °C, P = 1 atm, SV = 15 L h⁻¹ g_{cat}⁻¹, CO₂:C₂H₆:Ar = 1:1:2. Theoretical maximum CO selectivity for CO₂-ODH indicated by solid black line.

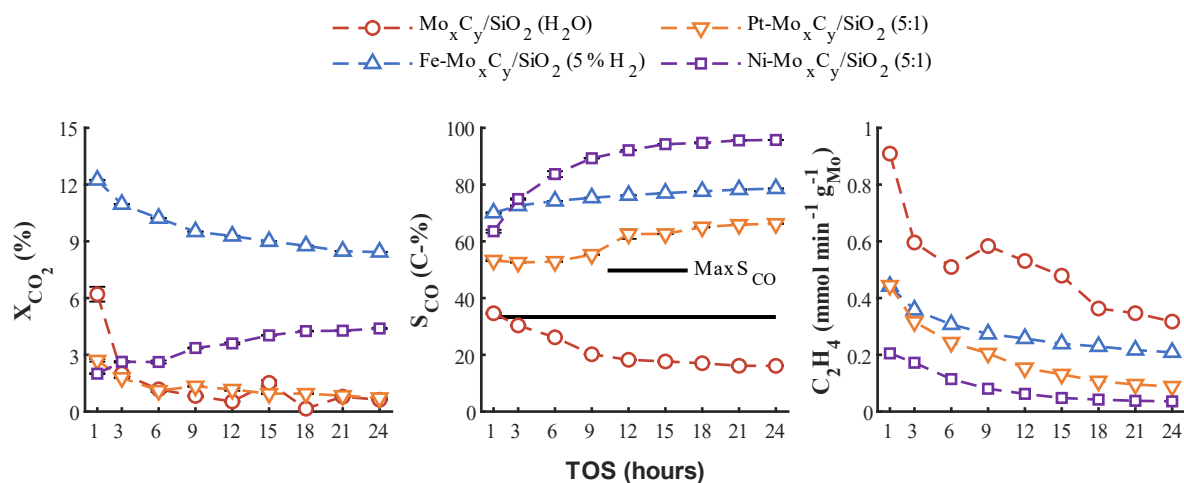


Figure B-14. CO₂ conversion, CO selectivity and C₂H₄ formation rate, of the following samples exposed to varying feed compositions: water co-feeding for Mo_xC_y/SiO₂, co-feeding of 5 vol.-% H₂ for Fe-Mo_xC_y/SiO₂, a 5:1 CO₂ to C₂H₆ feed ratio for Pt-Mo_xC_y/SiO₂ and Ni-Mo_xC_y/SiO₂. CO₂-ODH conditions, see section 4.3.2 for more details. Theoretical maximum CO selectivity for CO₂-ODH indicated by solid black line.

C TGA measurements of selected samples

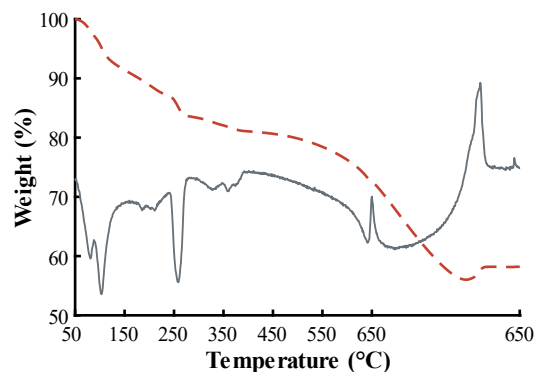


Figure C.1. TGA analysis of the carburization process of bulk ammonium heptamolybdate with TG curve (red dashed line) and differential thermal analysis (DTA) signal (grey solid line). Conditions: $T = 650\text{ °C}$, $P = 1\text{ atm}$, heating rate = 1 °C min^{-1} and holding time = 5 hours.

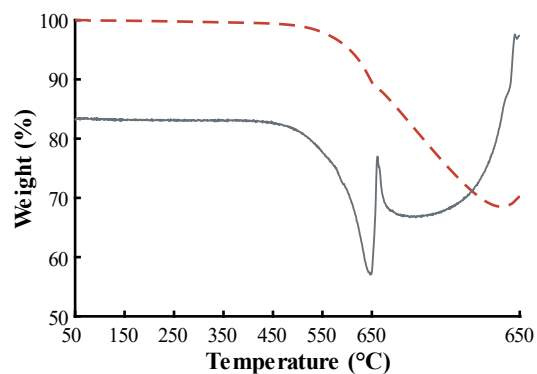


Figure C.2. TGA analysis of carburization process of bulk MoO₃ with TG curve (red dashed line) and differential thermal analysis (DTA) signal (grey solid line). Conditions: $T = 650\text{ °C}$, $P = 1\text{ atm}$, heating rate = 1 °C min^{-1} and holding time = 5 hours.

D XRD and Rietveld refined patterns of selected samples

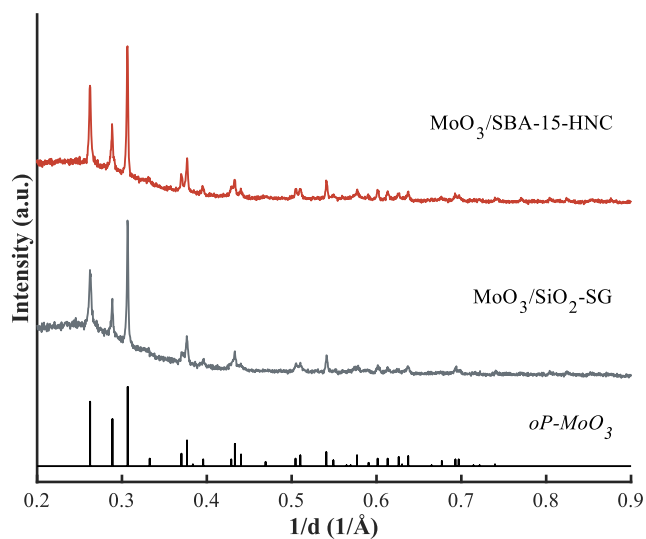


Figure D.1. XRD patterns of MoO₃/SBA-15-HNC, calcined at 400 °C, and MoO₃/SiO₂-SG, calcined at 500 °C.

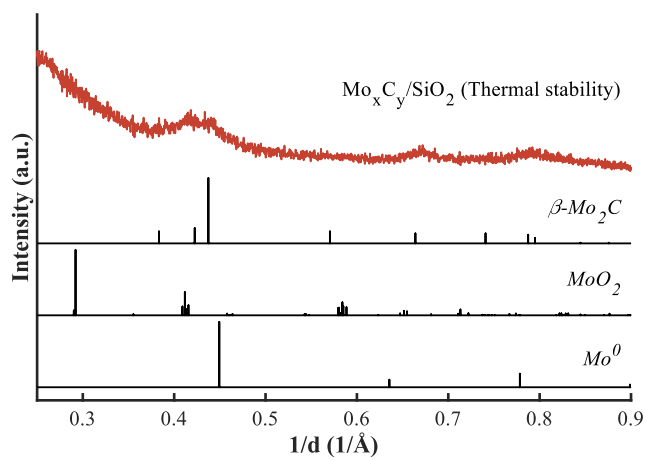


Figure D.2. XRD pattern of Mo_xC_y/SiO₂ after being exposed to a thermal treatment up until 600 °C, to confirm thermal stability of the catalyst prior to reaction.

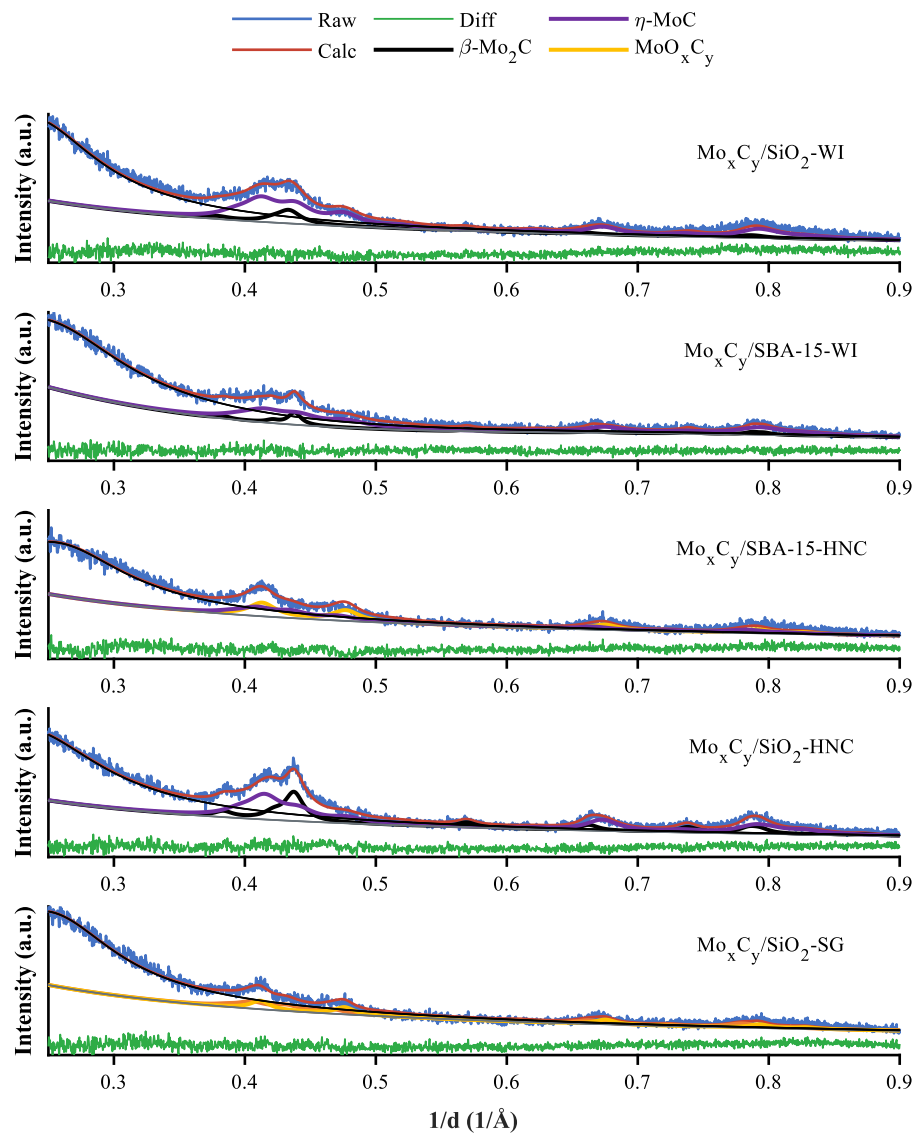


Figure D.3. Rietveld refined patterns displaying the raw, calculated, difference, crystal phases, background, and amorphous phase (representing SiO₂ or SBA-15) data of the freshly carburized samples at 600 °C.

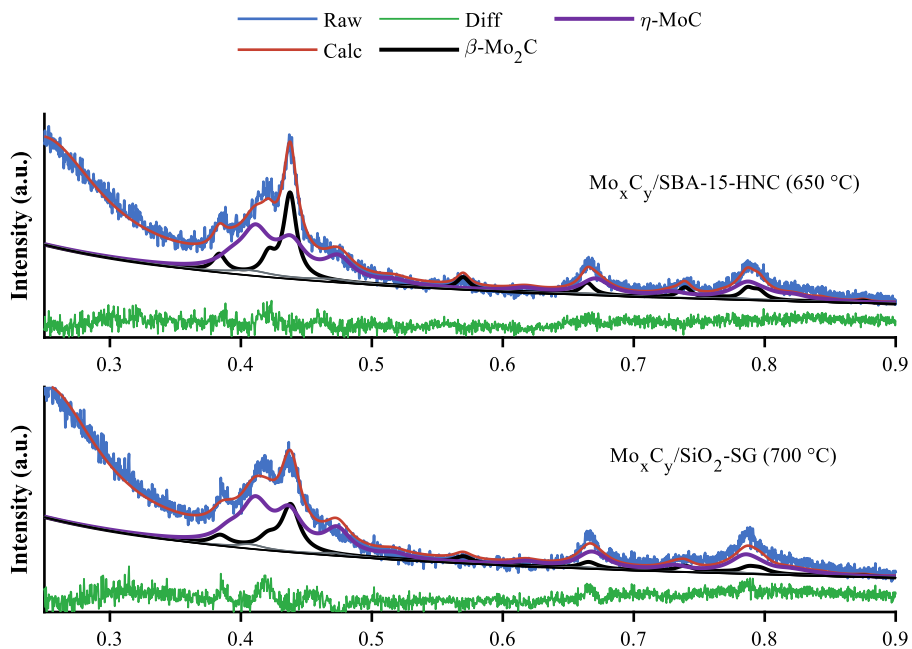


Figure D.4. Rietveld refined patterns displaying the raw, calculated, difference, crystal phases, background, and amorphous phase (representing SiO_2 or SBA-15) data of $\text{Mo}_x\text{C}_y/\text{SBA-15-HNC}$ carburized at 650 °C and $\text{Mo}_x\text{C}_y/\text{SiO}_2\text{-SG}$ carburized at 700 °C.

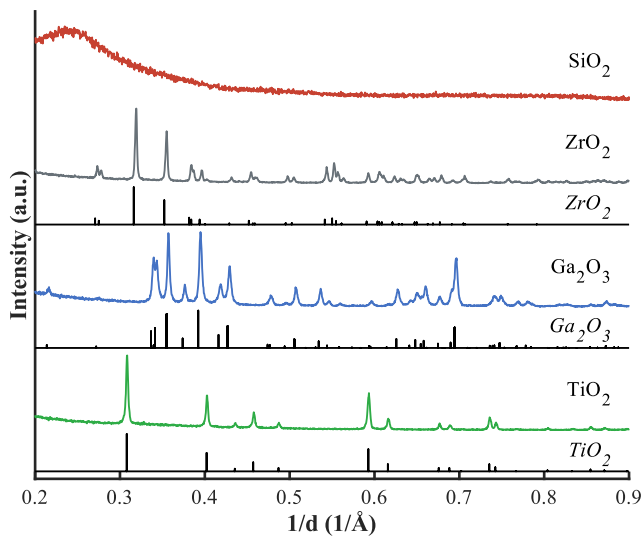


Figure D.5. XRD patterns of the spent $\text{CO}_2\text{-ODH}$ catalysts, of bulk metal oxide supports, SiO_2 , ZrO_2 , Ga_2O_3 and TiO_2 . Conditions: $T = 600$ °C, $P = 1$ atm, $\text{SV} = 21.4$ $\text{L h}^{-1} \text{g}_{\text{cat}}^{-1}$, $\text{CO}_2:\text{C}_2\text{H}_6:\text{Ar} = 1:1:2$.

E Raman spectra of selected samples

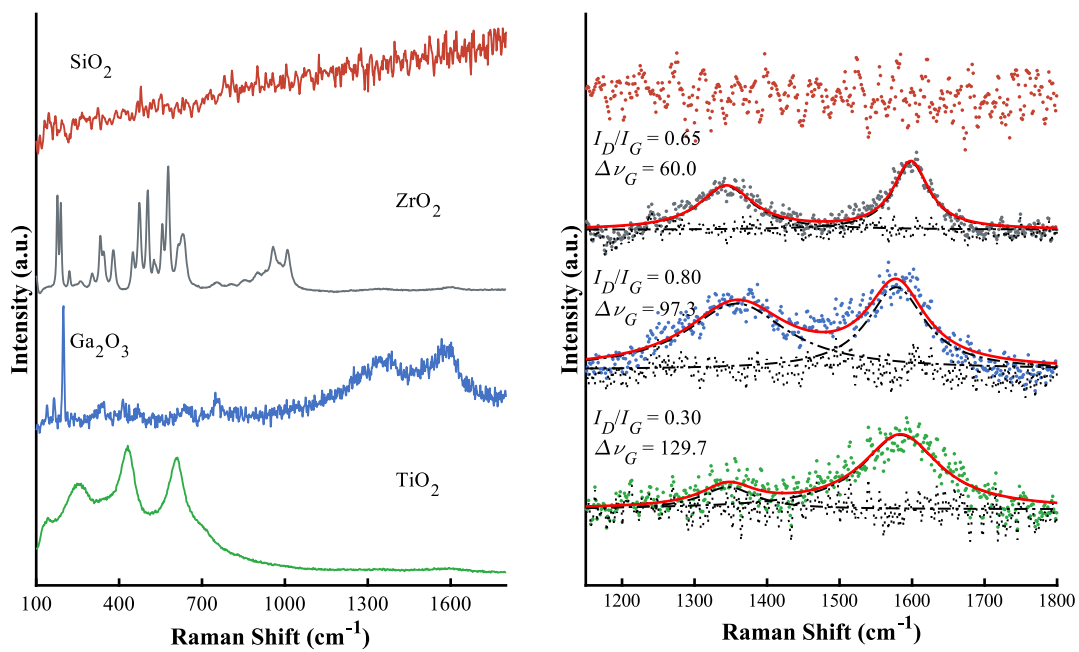


Figure E.1. Raman spectra of the spent CO₂-ODH catalysts, of bulk metal oxide supports, SiO₂, ZrO₂, Ga₂O₃ and TiO₂. Conditions: T = 600 °C, P = 1 atm, SV = 21.4 L h⁻¹ g_{cat}⁻¹, CO₂:C₂H₆:Ar = 1:1:2.

F CO₂-TPD results of selected samples

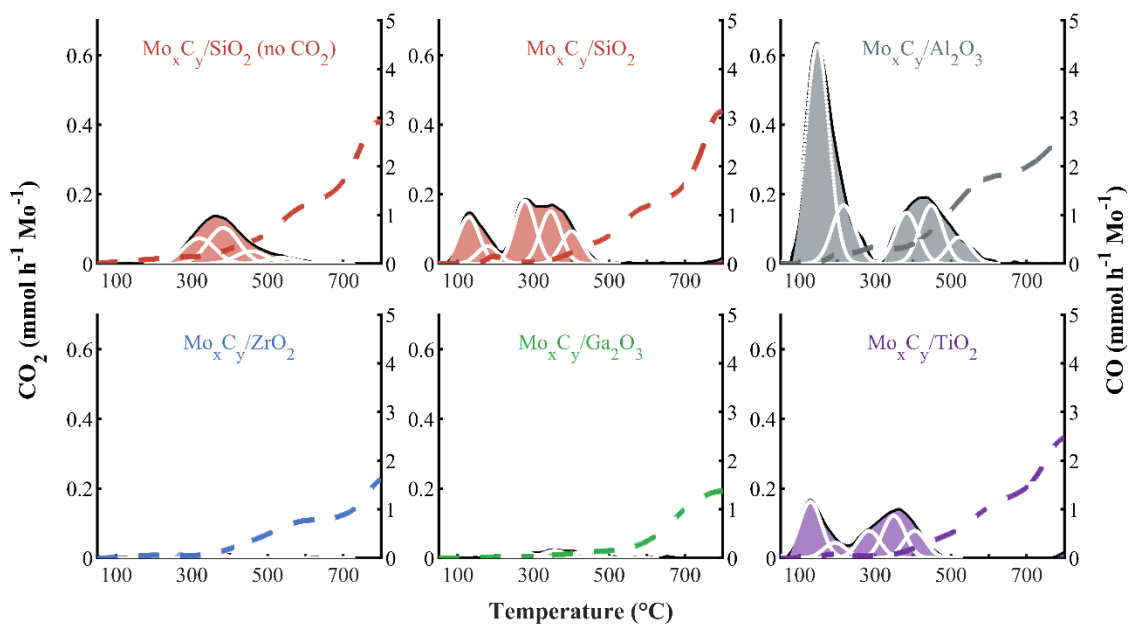


Figure F.1. CO₂ temperature programmed desorption profiles of Mo_xC_y supported on SiO₂, Al₂O₃, ZrO₂, Ga₂O₃ and TiO₂. CO₂ and CO signals normalized to Mo content in the sample.

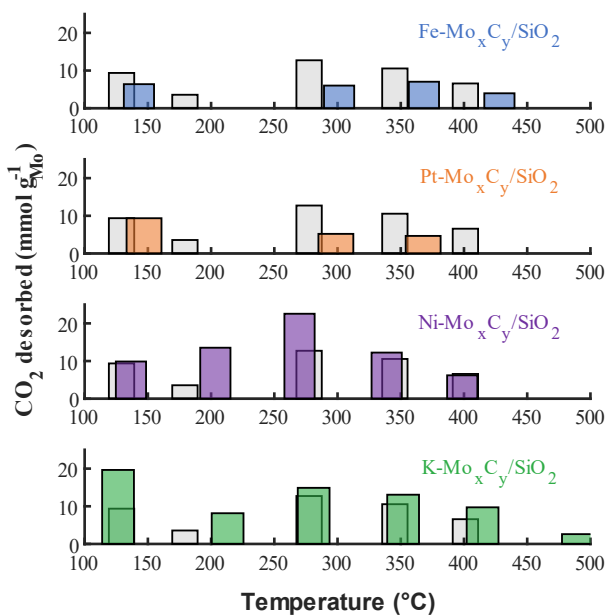


Figure F.2. Overview of CO₂ desorbed (normalized to mmol per gram of molybdenum) as a function of temperature recorded during CO₂ desorption of Fe-Mo_xC_y/SiO₂, Pt-Mo_xC_y/SiO₂, Ni-Mo_xC_y/SiO₂ and K-Mo_xC_y/SiO₂.

G XANES linear combination fits and EXAFS radial distribution fits

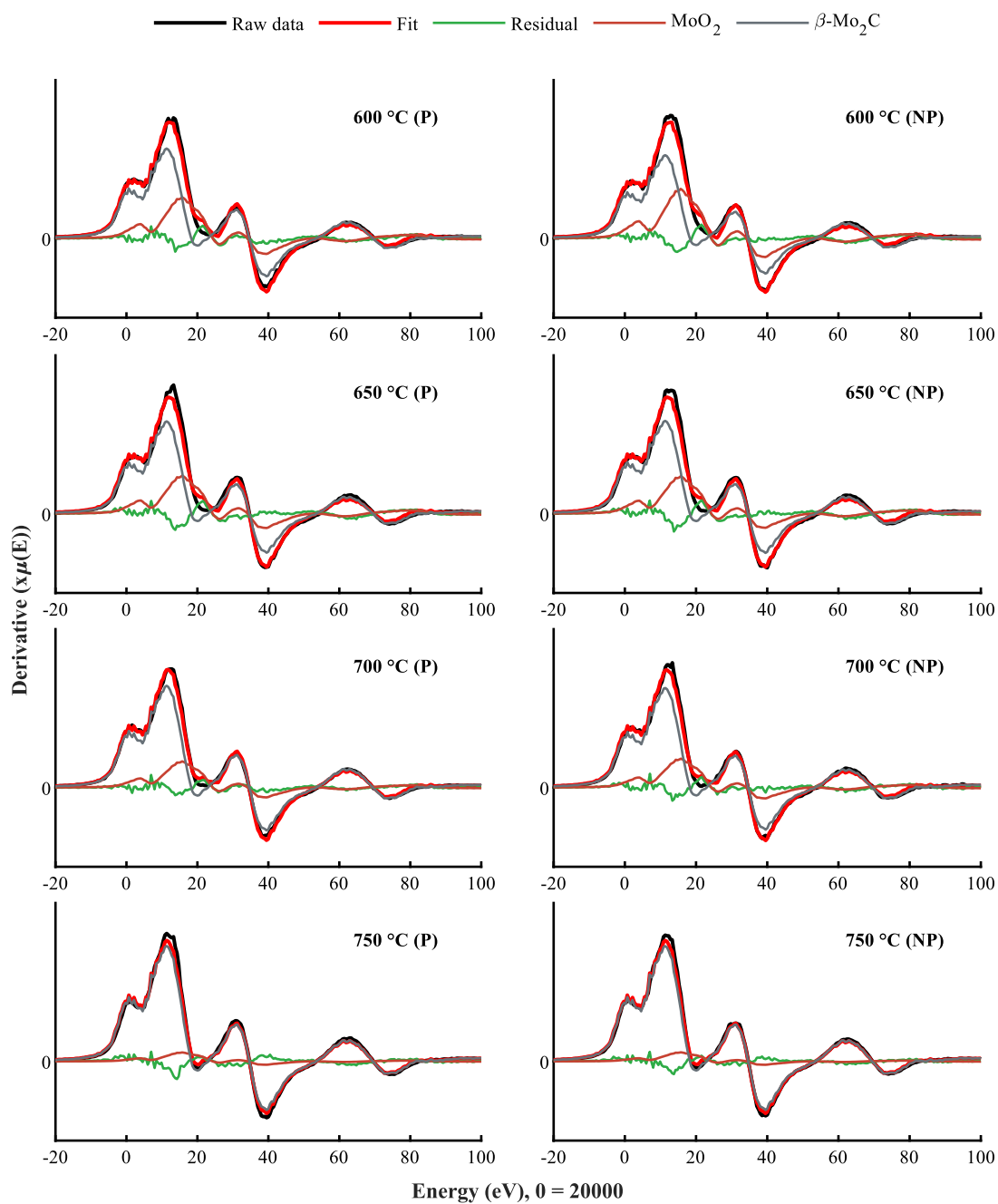


Figure G.1. Linear combination fits on the first derivative of the normalized absorption, corresponding to Table 5.2, of bulk Mo₂C samples carburized at different temperatures, with and without passivation.

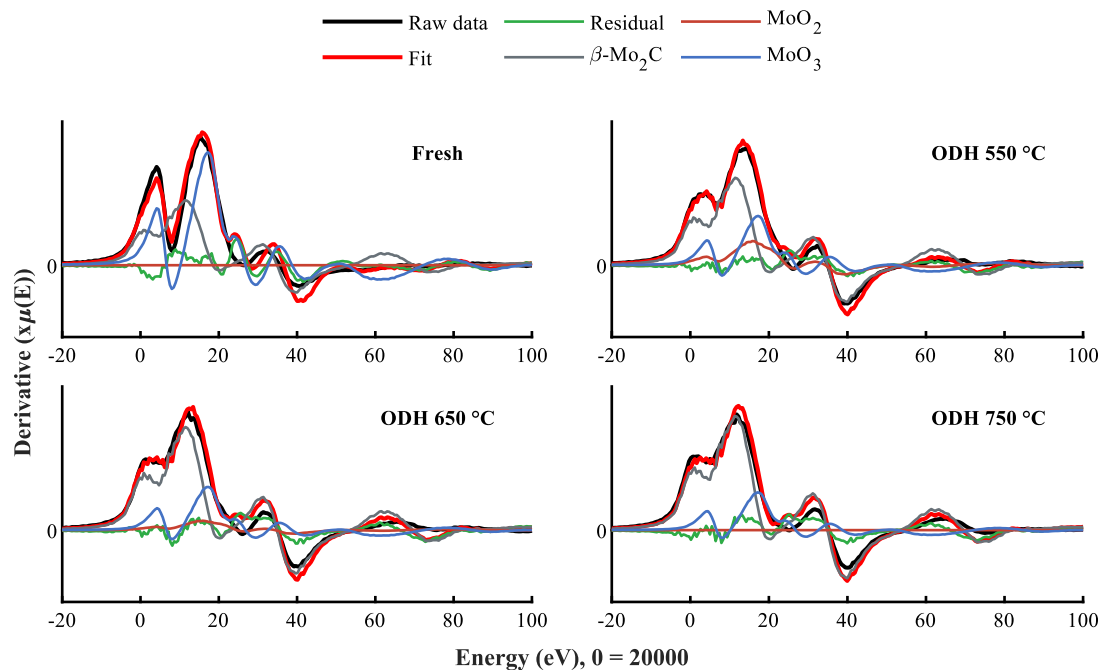


Figure G.2. Linear combination fits on the first derivative of the normalized absorption, corresponding to Table 5.3, of a freshly carburized $\text{Mo}_x\text{C}_y/\text{SiO}_2$ at 700 °C, and exposed to CO_2 -ODH conditions at 550 °C, 650 °C and 750 °C.

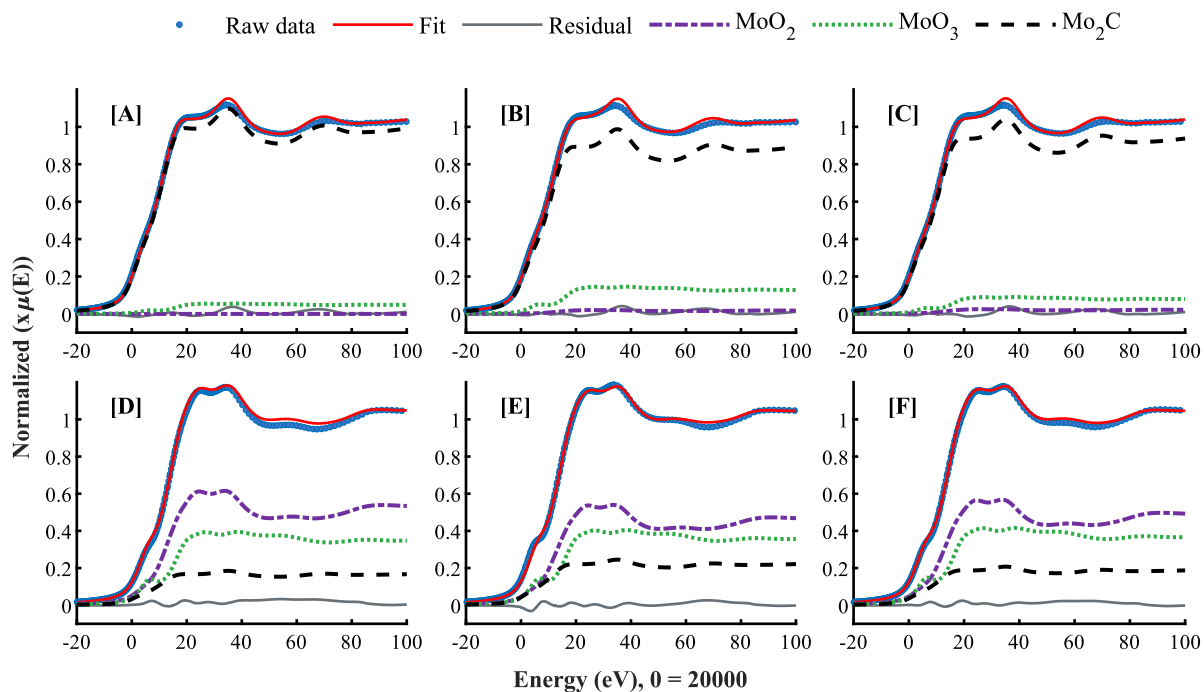


Figure G.3. LCF of Mo K XANES spectra (Mo K-edge at 20,000 eV shifted to 0 eV), corresponding to

Table 6.2, obtained at room temperature of [A & D] $\text{Mo}_x\text{C}_y/\text{SiO}_2\text{-WI}$, [B & E] $\text{Mo}_x\text{C}_y/\text{SBA-15-HNC}$ and [C & F] $\text{Mo}_x\text{C}_y/\text{SiO}_2\text{-SG}$ after [A-C] carburization and [D-F] TP- CO_2 activation.

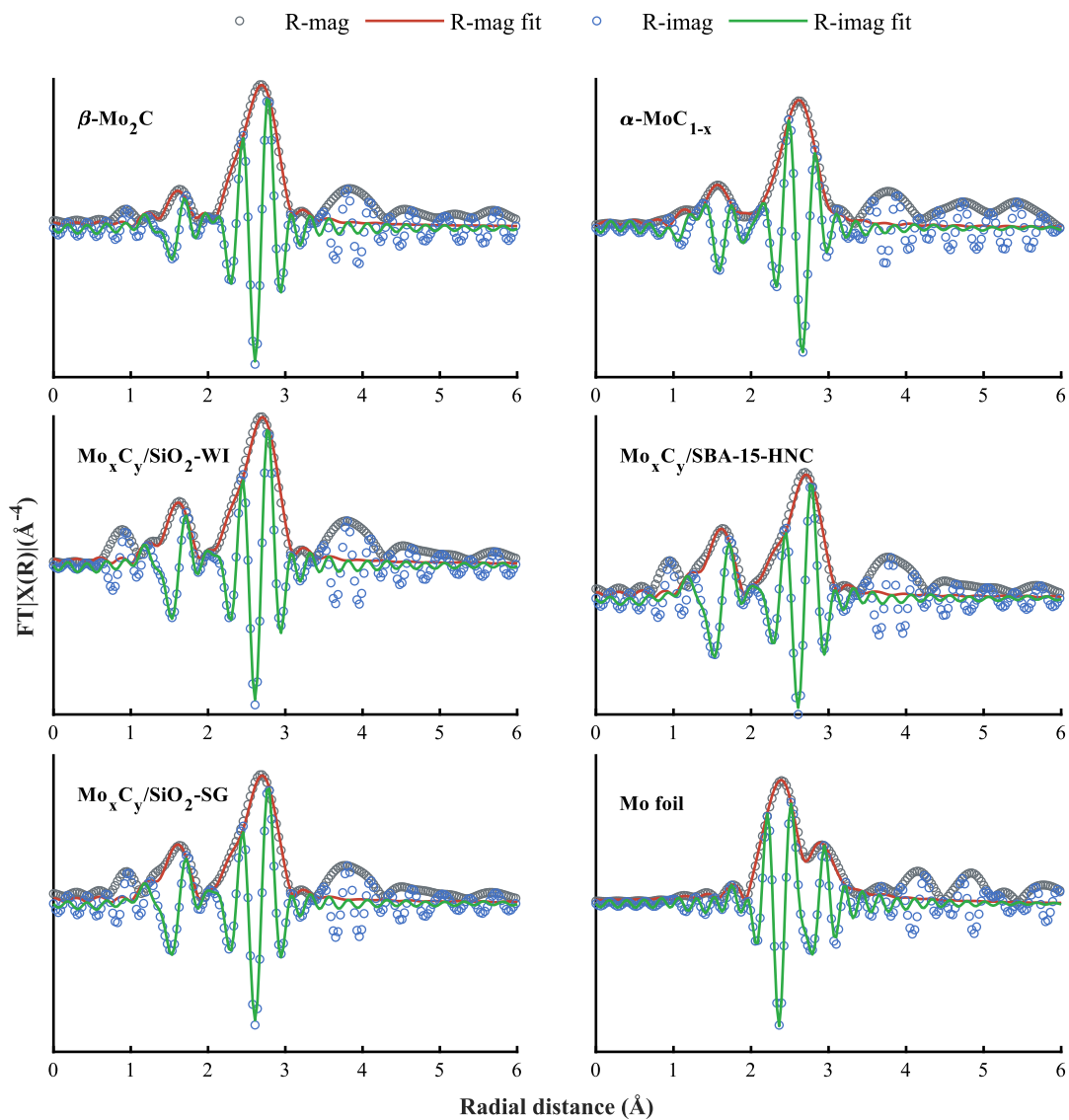


Figure G.4. Radial distribution fits to a $\beta\text{-Mo}_2\text{C}$ crystallographic data set with ICSD code 39461 (k^3 -weighted FT EXAFS data).

H Reactor heating block design and reactor packing

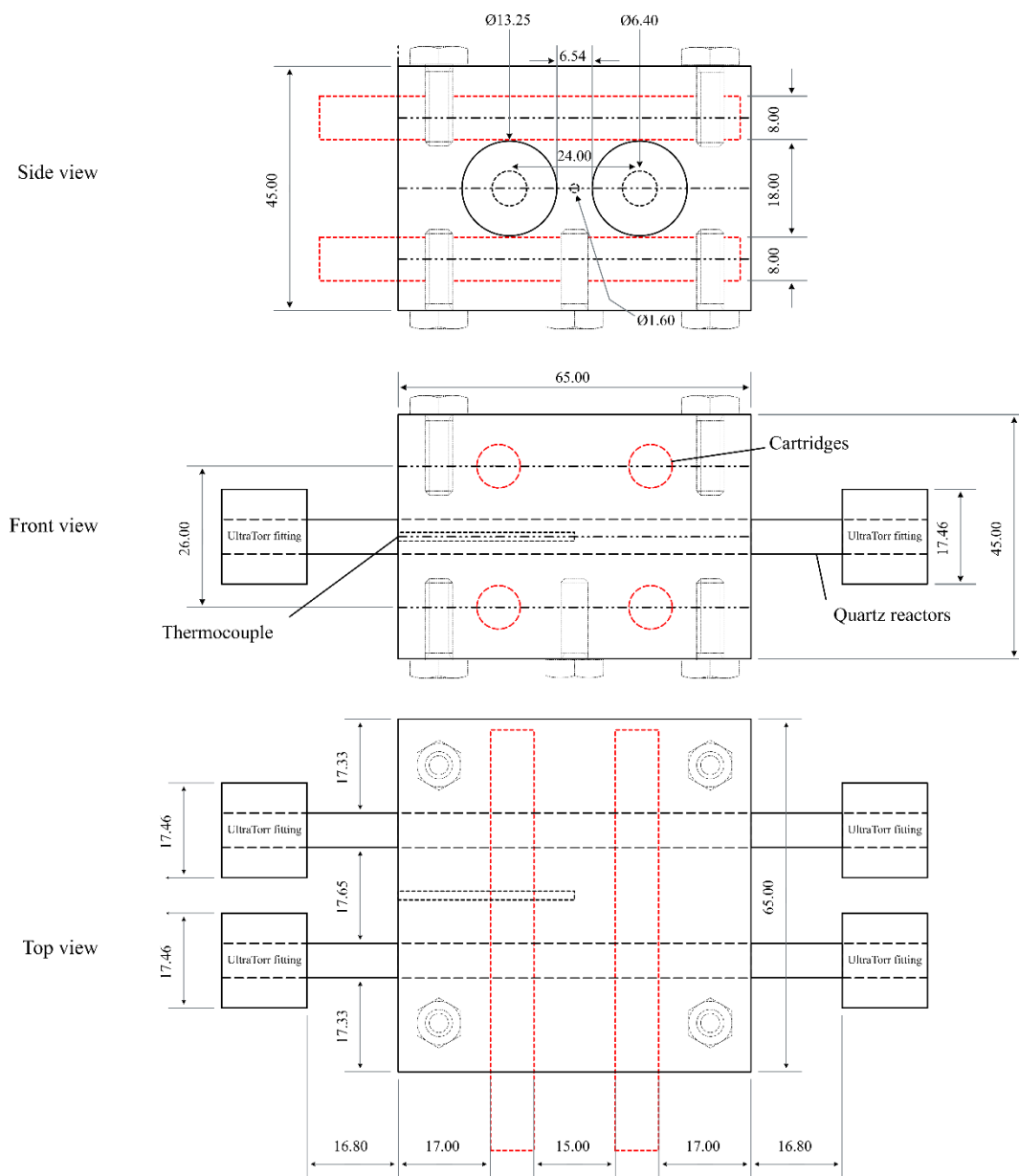


Figure H.1. Schematic overview of heating block equipped with heating cartridges.

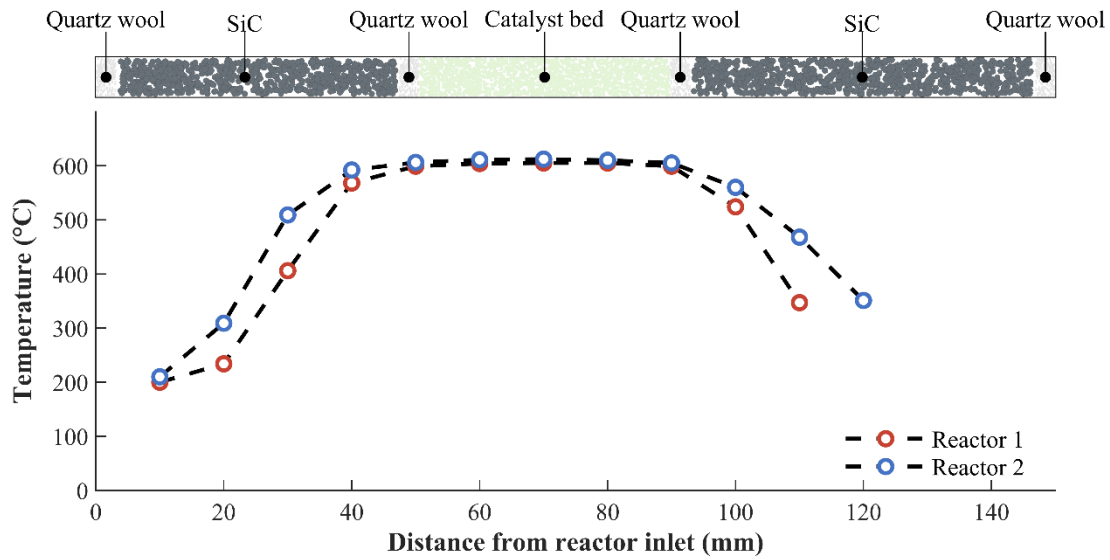


Figure H.2. Schematic overview of reactor packing and calibration of isothermal zone.

I GC-TCD configuration and calibration details

The calibration of the GC-TCD is completed by analysing a mixture of gases with a known concentration of the compounds of interest. For CO₂-ODH a calibration mixture containing 20 vol.-% CO₂, 20 vol.-% C₂H₆, 9.7 vol.-% C₂H₄, 4.8 vol.-% He and 45.5 vol.-% Ar (AFROX, South Africa) was used. In addition, a standard calibration mixture containing 10.2 vol.-% CO₂, 20 vol.-% CO, 14.3 vol.-% CH₄, 5.1 vol.-% N₂, 10.2 vol.-% Ar and 40.2 vol.-% H₂ was used for the remaining compounds encountered during the CO₂-ODH reaction. The relation of each compound to Ar can be expressed by Equation I.1.

$$f_{Ar} \cdot \frac{[Ar]}{A_{Ar}} = f_x \cdot \frac{[x]}{A_x} \quad \text{Equation I.1}$$

Where, f_x is the response factor of compound x , $[x]$ the concentration of compound x in the mixture, A_x the peak area of compound x obtained in the TCD-chromatogram. Thus, the response factor of each compound as a function of Ar can be calculated by Equation I.2.

$$f_x^{f(Ar)} = \frac{f_x}{f_{Ar}} = \frac{[Ar] \cdot A_x}{A_{Ar} \cdot [x]} \quad \text{Equation I.2}$$

Under reaction conditions the concentration of compound x can be calculated by restructuring Equation I.2 into Equation I.3.

$$[x] = \frac{[Ar] \cdot A_x}{A_{Ar} \cdot f_x^{f(Ar)}} \quad \text{Equation I.3}$$

Table I.1. GC-TCD configuration.

Agilent 490	Channel 1	Channel 2	Channel 3
Elutes in order of increasing retention time	H ₂ , CO	Ar, N ₂ , CH ₄ , CO	Mix ^[e] , CH ₄ , CO ₂ , C ₂ H ₄ , C ₂ H ₆
Column	Molsieve 5Å	Molsieve 5Å	PoraPlot Q
Column length	10	20	10
Carrier gas	Ar	H ₂	H ₂
Injection time	100 ms	100 ms	100 ms
Injector temperature	80 °C	80 °C	80 °C
Column oven temperature	80 °C	70 °C	60 °C
Column pressure	150 kPa	120 kPa	80 kPa
Stabilization time	5 s	5 s	5 s
Sampling time	35 s	35 s	35 s
Backflush	120 s	120 s	n/a

Table I.2. TCD calibration of CO₂-ODH mixture and standard gas mixture,

Compound	Concentration (vol.-%)	A_x^1	A_x^2	A_x^3	A_x^4	Average	$f_x^{f(Ar)}$
CO ₂ -ODH specialized mixture							
CO ₂	20.0	3917.3	3920.0	3919.5	3919.6	3919.1	1.65
C ₂ H ₆	20.0	3997.5	4000.5	4000.0	4000.8	3999.7	1.68
C ₂ H ₄	9.7	1897.2	1898.6	1898.4	1898.6	1898.2	1.64
Ar	45.5	5417.8	5419.4	5422.4	5419.9	5419.9	1.00
Standard gas mixture							
CO ₂	10.2	1997.3	1997.2	1996.4	1997.5	1997.1	1.63
CO	20.0	1872.5	1871.8	1872.6	1872.4	1872.3	0.78
CH ₄	14.3	1215.0	1214.8	1215.5	1215.5	1215.2	0.71
N ₂	5.1	636.7	636.7	636.5	636.7	636.7	1.03
H ₂	40.2	37228.7	37246.2	37180.5	37215.4	37217.7	7.69
Ar	10.2	1229.1	1228.6	1228.5	1228.6	1228.7	1.00

^[e] Mixture of Ar, N₂ and CO not retained in column

J MS configuration and calibration details

To calculate the RSF of CO₂ in relation to Ar, a mixture containing 1 vol.-% of CO₂ in Ar was analysed overnight and continuous readings of m/z 44 and 40 were taken. The RSF value was then calculated using Equation J.1.

$$RSF_{CO_2} = \frac{P_{CO_2}}{[CO_2]} \cdot \frac{[Ar]}{P_{Ar}} \quad \text{Equation J.1}$$

Where P_{CO_2} is the measured raw partial pressure of CO₂ (mbar), $[CO_2]$ is the concentration of CO₂ in the mixture (1 vol.-%), $[Ar]$ is the concentration of Ar in the mixture and P_{Ar} is the measured partial pressure of Ar (mbar).

The concentration of compound x in the effluent gas can then be calculated using Equation J.2.

$$[x] = \frac{[Ar] \cdot P_x}{RSF_x \cdot P_{Ar}} \quad \text{Equation J.2}$$

In general, the most intense m/z value is used for the analysis of various compounds. However, in some cases the cracking pattern between two compounds overlap (such as m/z 28 for CO₂ and CO). In those cases, the contribution of CO₂ to m/z 28 needs to be considered when utilizing m/z 28 to determine the concentration of CO. The contribution of CO₂ to m/z 28 can be calculated when analysing pure CO₂, using Equation J.3.

$$Ratio_{28/44} = \frac{P_{CO_2(m/z\ 28)}}{P_{CO_2(m/z\ 44)}} \cdot 1000 \quad \text{Equation J.3}$$

Where $P_{CO_2(m/z\ 28)}$ is the partial pressure of CO₂ at m/z 28, and $P_{CO_2(m/z\ 44)}$ is the partial pressure of CO₂ at m/z 44. The corrected contribution of CO in the effluent gas of the experiment to mass 28 can then be calculated by Equation J.4.

$$P_{CO(m/z\ 28)} = P_{total(m/z\ 28)} - \frac{P_{CO_2(m/z\ 44)}}{1000} \cdot Ratio_{28/44} \quad \text{Equation J.4}$$

Table J.1. MS configuration details.

Group	Name	Value	Units	Inherits
Detector	Curtail-clipping	0	(1=on, 0=off)	None
	Multiplier	1038	V	None
Filter	Focus	-90	V	None
	Delta-m	0	%	None
Quad	Resolution	0	%	None
	Cage	3	V	None
	Electron-energy	70	V	None
Source	Emission	500	μA	None
	Mass	5.5	amu	None
Other	Mode-change-delay	1000	ms	None

Table J.2. Compound specific cracking patterns and library RSF values.

Compound	m/z values and intensity									RSF values
CO ₂	m/z	44	16	28	12	22	45	46	29	0.88 ^[1]
	Intensity	1000	99	74	44	14	13	4	1	
CO	m/z	28	12	29	16	14	30			0.77
	Intensity	1000	21	12	6	6	2			
CH ₄	m/z	16	15	14	13	17	12	2		0.59
	Intensity	1000	819	85	34	16	11	3		
H ₂	m/z	2								0.66
	Intensity	1000								
H ₂ O	m/z	18	17	16	2	20	19			0.75
	Intensity	1000	230	11	7	3	1			
Ar	m/z	40	20	36	38					1.00
	Intensity	1000	176	3	1					

^[1] RSF value for CO₂ calculated by calibration.

K Supplementary tables

Table K.1. Sample nomenclature and physiochemical properties of all synthesized samples.

Sample	Synthesis technique	Calcination (°C)	Carburization (°C)	Support	Promoter	Mo (wt.-%)	Promoter (wt.-%)	S _{BET} (m ² g ⁻¹)	V _t (cm ³ g ⁻¹)	D (Å)
Mo _x C _y /SiO ₂	Wet-impregnation	n/a	700	SiO ₂	n/a		n/a	n/a	n/a	n/a
Mo _x C _y /SiO ₂ (Calc)	Wet-impregnation	400	600	SiO ₂	n/a	18.1	n/a	86	0.60	270
Mo _x C _y /SiO ₂ (-WI)	Wet-impregnation	n/a	600	SiO ₂	n/a		n/a	123	0.95	335
AEROSIL ® 200	n/a	n/a	n/a	n/a	n/a	n/a	n/a	200	n/a	n/a
MoO ₃ /SBA-15-HNC	Hybrid nano-crystal	400	n/a	SBA-15	n/a	n/a	n/a	209	0.47	85
Mo _x C _y /SBA-15-HNC	Hybrid nano-crystal	400	600	SBA-15	n/a	23.9	n/a	147	0.35	54
Mo _x C _y /SBA-15-WI	Wet-impregnation	n/a	600	SBA-15	n/a	29.7	n/a	171	0.35	71
SBA-15	n/a	n/a	n/a	n/a	n/a	n/a	n/a	825	0.68	41
Mo _x C _y /SiO ₂ -HNC	Hybrid nano-crystal	400	600	SiO ₂	n/a	15.1	n/a	119	0.79	272
Mo _x C _y /SiO ₂ -SG	Sol-Gel	500	600	SiO ₂	n/a	18.1	n/a	176	0.86	174
Mo _x C _y /Al ₂ O ₃	Wet-impregnation	n/a	600	Al ₂ O ₃	n/a	16.9	n/a	84	0.54	255
Mo _x C _y /ZrO ₂	Wet-impregnation	n/a	600	ZrO ₂	n/a	20.4	n/a	8	0.03	181
Mo _x C _y /Ga ₂ O ₃	Wet-impregnation	n/a	600	Ga ₂ O ₃	n/a	18.8	n/a	7	0.03	255
Mo _x C _y /TiO ₂	Wet-impregnation	n/a	600	TiO ₂	n/a	20.5	n/a	19	0.12	301
Mo _x C _y /CeO ₂	Wet-impregnation	n/a	600	CeO ₂	n/a	17.1	n/a	8	0.05	220
Fe-Mo _x C _y /SiO ₂ (Calc-Imp)	Wet-impregnation	400	600	SiO ₂	Fe	23.3	1.34	81	0.53	274
Fe-Mo _x C _y /SiO ₂ (Seq-Imp)	Wet sequential-impregnation	n/a	600	SiO ₂	Fe	20.1	1.87	110	0.45	172
Fe-Mo _x C _y /SiO ₂ (Co-Imp)	Wet co-impregnation	n/a	600	SiO ₂	Fe	20.5	0.99	108	0.81	323

Pt-Mo _x C _y /SiO ₂ (Co-Imp)	Wet co-impregnation	n/a	600	SiO ₂	Pt	16.0	0.86	104	0.63	248
Pt-Mo _x C _y /SiO ₂ (Co-Imp-Calc)	Wet co-impregnation	400	600	SiO ₂	Pt			n/a	n/a	n/a
Ni-Mo _x C _y /SiO ₂ (Co-Imp)	Wet co-impregnation	n/a	600	SiO ₂	Ni	18.5	0.83	76	0.65	352
K-Mo _x C _y /SiO ₂ (Co-Imp)	Wet co-impregnation	n/a	600	SiO ₂	K	20.9	0.85	113	0.94	333

Table K.2. Overview of phase quantification and crystallite size determined *via* XRD Rietveld analysis of the spent CO₂-ODH catalysts.

Sample	MoO ₂		<i>oP</i> -MoO ₃		β -Mo ₂ C		η -MoC _{0.59}		α -MoC _{1-x} / MoO _x C _y		Support	
	wt.-% (error)	nm (error)	wt.-% (error)	nm (error)	wt.-% (error)	nm (error)	wt.-% (error)	nm (error)	wt.-% (error)	nm (error)	wt.-% (error)	wt.-% (error)
Chapter 5												
Mo _x C _y /SiO ₂	14.5 (1.5)	27.0 (2.8)	-	-	14.0 (3.0)	5.4 (1.0)	24.9 (5.7)	3.5 (0.7)	46.6 (4.6)	5.1 (0.3)	-	-
Mo _x C _y /SiO ₂ -O ₂	17.4 (1.6)	22.0 (1.8)	-	-	20.3 (2.8)	5.9 (0.8)	25.8 (5.0)	4.2 (0.8)	36.4 (3.6)	6.2 (0.5)	-	-
ODH 550 °C	30.6 (1.1)	19.4 (1.3)	-	-	-	-	69.4 (1.1)	3.7 (0.2)	-	-	-	-
ODH 650 °C	18.3 (1.0)	20.1 (1.9)	-	-	-	-	64.2 (1.6)	4.5 (0.3)	17.5 (1.6)	10.5 (1.1)	-	-
ODH 750 °C	16.9 (2.0)	18.9 (3.0)	-	-	15.3 (2.9)	12.4 (2.2)	49.8 (4.7)	6.1 (0.7)	17.9 (3.9)	9.5 (1.8)	-	-
Chapter 6												
Mo _x C _y /SiO ₂ -WI	70.2 (1.2)	30.5 (0.9)	0.5 (1.1)	57.9 (25.6)	-	-	29.3 (0.9)	6.5 (0.4)	-	-	-	-
Mo _x C _y /SBA-15-HNC	20.0 (0.7)	46.8 (2.9)	-	-	-	-	60.9 (1.5)	4.1 (0.2)	19.1 (1.6)	6.7 (0.8)	-	-
Mo _x C _y /SiO ₂ -HNC	49.9 (0.7)	22.3 (0.8)	-	-	-	-	50.1 (0.7)	4.9 (0.2)	-	-	-	-
Mo _x C _y /SiO ₂ -SG	66.2 (2.1)	49.7 (3.0)	-	-	-	-	-	-	33.8 (2.1)	6.6 (0.8)	-	-
Chapter 7												
Mo _x C _y /SiO ₂	70.2 (1.2) (N. 13.5)	30.5 (0.9)	0.5 (1.1) (N. 0.1)	57.9 (25.6)	-	-	29.3 (0.9) (N. 5.6)	6.5 (0.4)	-	-	-	-
Mo _x C _y /Al ₂ O ₃	-	-	-	-	-	-	-	-	-	-	-	-

Sample	MoO ₂		<i>oP</i> -MoO ₃		β -Mo ₂ C		η -MoC _{0.59}		α -MoC _{1-x} / MoO _x C _y		Support	
	wt.-% (error)	nm (error)	wt.-% (error)	nm (error)	wt.-% (error)	nm (error)	wt.-% (error)	nm (error)	wt.-% (error)	nm (error)	wt.-% (error)	wt.-% (error)
Mo _x C _y /ZrO ₂ ^[g]	18.9 (0.2)	46.4 (1.4)	-	-	-	-	-	-	-	-	79.6 (0.3)	75.3 (1.0)
Mo _x C _y /Ga ₂ O ₃	5.3 (0.2)	28 (1.8)	-	-	2.0 (0.2)	15.9 (2.2)	7.2 (0.4)	3.6 (0.3)	-	-	85.5 (0.5)	29.6 (0.3)
Mo _x C _y /TiO ₂	10.8 (0.2)	31.9 (1.4)	-	-	-	-	-	-	-	-	89.2 (0.2)	39.2 (0.5)
Mo _x C _y /CeO ₂ ^[h]	-	-	-	-	-	-	-	-	-	-	47.2 (0.4)	113.1 (2.5)
Mo _x C _y /Al ₂ O ₃ (5:1)	-	-	-	-	-	-	-	-	-	-	-	-
Mo _x C _y /ZrO ₂ (5:1)	19.1 (1.1)	14.5 (1.4)	-	-	-	-	-	-	-	-	80.9 (1.1)	30.8 (1.1)
Mo _x C _y /Ga ₂ O ₃ (5:1)	-	-	-	-	3.3 (0.2)	16.2 (1.5)	10.1 (0.4)	4.1 (0.3)	-	-	86.6 (0.5)	29.4 (0.3)
Mo _x C _y /SiO ₂ (0 % H ₂)	70.2 (1.2) (N. 13.5)	30.5 (0.9)	-	-	-	-	37.7 (0.8) (N. 7.3)	5.7 (0.3)	-	-	-	-
Mo _x C _y /SiO ₂ (5 % H ₂)	-	-	-	-	40.8 (1.7) (N. 7.9)	6.2 (0.4)	52.3 (1.7) (N. 10.1)	3.6 (0.2)	-	-	-	-
Mo _x C _y /SiO ₂ (10 % H ₂)	18.9 (0.2)	46.4 (1.4)	-	-	50.2 (2.0) (N. 9.7)	5.3 (0.4)	49.8 (2.0) (N. 9.6)	6.4 (0.5)	-	-	-	-
Mo _x C _y /SiO ₂ (17 % H ₂)	5.3 (0.2)	28 (1.8)	-	-	53.9 (2.0) (N. 10.4)	4.6 (0.3)	46.1 (2.0) (N. 8.9)	6.1 (0.4)	-	-	-	-
Mo _x C _y /ZrO ₂ (0 % H ₂) ^[i]	10.8 (0.2)	31.9 (1.4)	-	-	-	-	-	-	-	-	76.1 (0.3)	74.3 (1.0)
Mo _x C _y /ZrO ₂ (5 % H ₂)	-	-	-	-	17.5 (0.4)	5.3 (0.2)	-	-	-	-	79.9 (0.4)	69.6 (0.9)

^[g] Bal. Zr(MoO₄)₂: 1.5 ± 0.2 wt.-% 59.8 ± 14.7 nm

^[h] Bal. Ce₂(MoO₄)₃: 52.8 ± 0.4 wt.-% 94.3 ± 3.7 nm

^[i] Bal. Zr(MoO₃)₂: 11.0 ± 0.2 wt.-% 48.9 ± 2.1 nm

Sample	MoO ₂		<i>oP</i> -MoO ₃		β -Mo ₂ C		η -MoC _{0.59}		α -MoC _{1-x} / MoO _x C _y		Support	
	wt.-% (error)	nm (error)	wt.-% (error)	nm (error)	wt.-% (error)	nm (error)	wt.-% (error)	nm (error)	wt.-% (error)	nm (error)	wt.-% (error)	wt.-% (error)
Mo _x C _y /ZrO ₂ (17 % H ₂)	-	-	-	-	20.2 (0.4)	4.3 (0.2)	-	-	-	-	79.8 (0.4)	66.9 (0.9)
Mo _x C _y /Ga ₂ O ₃ (5 % H ₂)	19.1 (1.1)	14.5 (1.4)	-	-	3.5 (0.3)	15.0 (1.7)	9.6 (0.5)	5.1 (0.4)	-	-	86.9 (0.5)	30.5 (0.4)
Mo _x C _y /Ga ₂ O ₃ (10 % H ₂)	-	-	-	-	4.0 (0.3)	14.5 (1.4)	10.3 (0.5)	4.7 (0.4)	-	-	85.7 (0.5)	30.2 (0.4)

Chapter 8

Mo _x C _y /SiO ₂ ^{front}	15.6 (1.1)	75.9 (13.1)	84.4 (1.1)	39.0 (2.5)	-	-	-	-	-	-	-	-
Mo _x C _y /SiO ₂ ^{rear}	63.0 (1.4)	22.8 (1.1)	-	-	-	-	37.0 (1.4)	8.1 (0.7)	-	-	-	-
Fe-Mo _x C _y /SiO ₂ ^{front}	35.8 (2.1)	31.4 (4.1)	64.2 (2.1)	67.6 (7.4)	-	-	-	-	-	-	-	-
Fe-Mo _x C _y /SiO ₂ ^{rear}	3.1 (0.8)	57.4 (29.5)	-	-	-	-	26.2 (2.7)	4.7 (0.9)	70.6 (2.7)	8.9 (0.3)	-	-
Ni-Mo _x C _y /SiO ₂ ^{front}	46.2 (1.8)	32.9 (2.7)	53.8 (1.8)	55.5 (5.8)	-	-	-	-	-	-	-	-
Ni-Mo _x C _y /SiO ₂ ^{rear}	48.2 (0.9)	25.7 (1.1)	-	-	-	-	-	-	51.8 (0.9)	5.4 (0.2)	-	-
K-Mo _x C _y /SiO ₂ ^{front}	-	-	100	65 (3.9)	-	-	-	-	-	-	-	-
K-Mo _x C _y /SiO ₂ ^{rear}	56.2 (1.6)	38.3 (1.8)	43.8 (1.6)	36.7 (3.4)	-	-	-	-	-	-	-	-
Mo _x C _y /SiO ₂ (IND) *	16.6 (1.3)	24.5 (2.2)	-	-	14.8 (2.2)	7.6 (1.1)	53.5 (3.2)	4.8 (0.3)	15.0 (2.8)	6.7 (1.0)	-	-
Mo _x C _y /SiO ₂ (IND) **	27.5 (2.8)	25.7 (1.7)	-	-	18.6 (3.1)	6.8 (1.1)	37.9 (5.4)	5.8 (1.0)	16.0 (4.5)	6.5 (1.7)	-	-
Mo _x C _y /SiO ₂ (MIX) **	70.2 (1.2)	30.5 (0.9)	0.5 (1.1)	57.9 (25.6)	-	-	29.3 (0.9)	6.5 (0.4)	-	-	-	-
Mo _x C _y /SiO ₂ (1 h TOS)	-	-	-	-	26.6 (2.6)	5.8 (0.8)	73.4 (2.6)	3.9 (0.2)	-	-	-	-
Mo _x C _y /SiO ₂ (3 h TOS)	13.4 (1.0)	30.3 (4.1)	-	-	27.2 (2.6)	5.4 (0.8)	59.4 (2.5)	4.5 (0.3)	-	-	-	-
Mo _x C _y /SiO ₂ (12 h TOS)	34.8 (2.0)	29.2 (2.0)	-	-	25.7 (2.8)	6.3 (1.1)	39.5 (2.7)	5.5 (0.8)	-	-	-	-

Sample	MoO ₂		<i>oP</i> -MoO ₃		β -Mo ₂ C		η -MoC _{0.59}		α -MoC _{1-x} / MoO _x C _y		Support	
	wt.-% (error)	nm (error)	wt.-% (error)	nm (error)	wt.-% (error)	nm (error)	wt.-% (error)	nm (error)	wt.-% (error)	nm (error)	wt.-% (error)	wt.-% (error)
Mo _x C _y /SiO ₂ (Calc)	37.6 (2.0)	23.4 (1.0)	-	-	7.2 (1.8)	8.2 (2.0)	39.0 (2.8)	5.5 (0.4)	16.2 (2.3)	7.1 (0.8)	-	-
Fe-Mo _x C _y /SiO ₂ (Seq-Imp)	55.8 (2.3)	38.8 (2.1)	22.5 (1.9)	74.4 (13.1)	8.8 (1.8)	13.9 (3.9)	12.9 (2.2)	11.0 (2.8)	-	-	-	-
Fe-Mo _x C _y /SiO ₂ (Calc-Imp)	57.8 (4.8)	25.7 (0.8)	-	-	13.0 (2.2)	9.0 (1.4)	10.9 (5.8)	6.7 (3.0)	18.3 (3.9)	6.3 (1.3)	-	-
Pt-Mo _x C _y /SiO ₂ (Co-Imp)	-	-	-	-	-	-	56.9 (2.5)	3.8 (0.3)	43.1 (2.5)	6.0 (0.4)	-	-
Pt-Mo _x C _y /SiO ₂ (Co-Imp-Calc)	-	-	-	-	-	-	61.6 (3.3)	3.5 (0.3)	38.4 (3.3)	4.9 (0.5)	-	-
Mo _x C _y /SiO ₂ (H ₂ O)	54.3 (0.8)	31.3 (1.1)	-	-	-	-	45.7 (0.8)	6.3 (0.3)	-	-	-	-
Fe-Mo _x C _y /SiO ₂ (5 % H ₂)	17.2 (1.9)	26.0 (6.1)	-	-	-	-	82.8 (1.9)	4.2 (0.4)	-	-	-	-
Pt-Mo _x C _y /SiO ₂ (5:1)	100	20.8 (0.4)	-	-	-	-	-	-	-	-	-	-
Ni-Mo _x C _y /SiO ₂ (5:1)	100	22.4 (0.4)	-	-	-	-	-	-	-	-	-	-

Table K.3. Overview of phase quantification and crystallite size determined *via* Rietveld refinement of the spent TP-CO₂ activation catalysts.

Sample	MoO ₂		β-Mo ₂ C		η-MoC _{0.59}		α-MoC _{1-x} / MoO _x C _y		Support	
	wt.-% (error)	nm (error)	wt.-% (error)	nm (error)	wt.-% (error)	nm (error)	wt.-% (error)	nm (error)	wt.-% (error)	nm (error)
Mo _x C _y /SiO ₂ -WI	100	29.1 (0.6)								
Mo _x C _y /SBA-15-WI	81.6 (1.4)	17.1 (0.6)			18.4 (1.4)	8.0 (1.1)				
Mo _x C _y /SBA-15-HNC	100	29.5 (0.6)								
Mo _x C _y /SiO ₂ -HNC	100	27.2 (0.5)								
Mo _x C _y /SiO ₂ -SG	100	29.1 (0.8)								
Bulk β-Mo ₂ C	34.1 (0.2)	36.8 (0.7)					65.9 (0.2)	14.2 (0.2)		
Mo _x C _y /SiO ₂	69.1 (2.9) (N. 13.3)	32.9 (1.5)	8.6 (1.9) (N. 1.7)	11.5 (3.4)	22.2 (2.8) (N. 4.3)	4.5 (1.0)	-	-	-	-
Mo _x C _y /Al ₂ O ₃	-	-	-	-	-	-	-	-	-	-
Mo _x C _y /ZrO ₂	12.1 (0.3)	39.2 (2.1)	5.0 (0.5)	6.1 (0.9)	-	-	-	-	82.6 (0.5)	76.0 (1.2)
Mo _x C _y /Ga ₂ O ₃	-	-	8.7 (0.3)	6.4 (0.3)	-	-	7.8 (0.5)	4.0 (0.3)	83.5 (0.5)	30.8 (0.3)
Mo _x C _y /TiO ₂	8.5 (0.2)	32.7 (1.7)	2.0 (0.3)	7.3 (1.4)	-	-	-	-	89.5 (0.3)	39.4 (0.6)
Fe-Mo _x C _y /SiO ₂	-	-	-	-	40.6 (15.0)	5.4 (2.3)	59.4 (15.0)	4.2 (1.2)	-	-
Pt-Mo _x C _y /SiO ₂	54.2 (2.9)	34.1 (1.6)	21.0 (2.4)	6.3 (1.0)	-	-	24.7 (3.4)	3.1 (0.6)	-	-
Ni-Mo _x C _y /SiO ₂	11.4 (1.0)	28.5 (5.2)	-	-	88.6 (1.0)	3.6 (0.2)	-	-	-	-
K-Mo _x C _y /SiO ₂	69.4 (0.7)	32.5 (1.0)	30.6 (0.7)	11.6 (0.6)	-	-	-	-	-	-

Table K.4. Overview of phase quantification and crystallite size determined *via* Rietveld refinement of the spent CO₂-TPD catalysts.

Sample	Metal oxide support		β -Mo ₂ C		η -MoC _{0.59}		Mo ⁰	
	wt.-% (error)	nm (error)	wt.-% (error)	nm (error)	wt.-% (error)	nm (error)	wt.-% (error)	nm (error)
Mo _x C _y /SiO ₂ (no CO ₂)	-	-	91.2 (0.8) (N. 17.5)	12.8 (0.3)			8.8 (0.8) (N. 1.7)	19.3 (2.6)
Mo _x C _y /SiO ₂			65.8 (2.1) (N. 12.7)	12.1 (0.4)	18.8 (2.4) (N. 3.6)	4.8 (0.9)	15.4 (0.9) (N. 3.0)	15.0 (1.1)
Mo _x C _y /Al ₂ O ₃	-	-	-	-			-	-
Mo _x C _y /ZrO ₂	84.2 (0.3)	75.5 (0.9)	11.6 (0.2)	17.1 (0.6)			4.2 (0.2)	23.4 (1.5)
Mo _x C _y /Ga ₂ O ₃	94.9 (0.2)	33.0 (0.4)	4.8 (0.2)	18.9 (1.1)			0.4 (0.1)	24.6 (3.4)
Mo _x C _y /TiO ₂	87.8 (0.3)	51 (0.8)	9.2 (0.3)	15.9 (0.7)			3.1 (0.2)	12.4 (1.2)
Fe-Mo _x C _y /SiO ₂			67.7 (3.6)	10.9 (0.4)	32.3 (3.6)	3.3 (0.6)	-	-
Pt-Mo _x C _y /SiO ₂			49.1 (2.0)	10.0 (1.5)	41.7 (2.2)	3.7 (0.4)	9.4 (0.9)	14.8 (1.9)
Ni-Mo _x C _y /SiO ₂			99.4 (0.4)	10.4 (0.2)	-	-	0.7 (0.4)	55.9 (67.8)
K-Mo _x C _y /SiO ₂			93.0 (0.6)	11.8 (0.3)	-	-	7.0 (0.6)	34.3 (5.4)

Table K.5. Overview of phase quantification and crystallite size determined *via* Rietveld refinement of the spent NH₃-TPD catalysts.

Sample	Metal oxide support		β -Mo ₂ C		Mo ⁰	
	wt.-% (error)	nm (error)	wt.-% (error)	nm (error)	wt.-% (error)	nm (error)
Mo _x C _y /SiO ₂ (no NH ₃)	-	-	66.3 (0.9) (N. 12.8)	17.1 (0.7)	33.7 (0.9) (N. 6.5)	22.8 (1.1)
Mo _x C _y /SiO ₂	-	-	38.3 (16.9) (N. 7.4)	16.9 (1.0)	61.7 (1.0) (N. 11.9)	20.5 (0.6)
Mo _x C _y /Al ₂ O ₃	-	-	-	-	-	-
Mo _x C _y /ZrO ₂	84.3 (0.3)	76.2 (1.3)	3.3 (0.2)	25.7 (3.2)	12.4 (0.2)	47.8 (1.8)
Mo _x C _y /Ga ₂ O ₃	88.0 (0.2)	33.1 (0.4)	5.9 (0.2)	25.1 (1.1)	6.0 (0.1)	39.1 (1.2)
Mo _x C _y /TiO ₂	88.5 (0.3)	80.8 (1.6)	3.9 (0.2)	29.3 (2.6)	7.6 (0.2)	29.3 (1.2)
Fe-Mo _x C _y /SiO ₂	-	-	65.3 (1.0)	14.2 (0.5)	34.7 (1.0)	9.2 (0.5)
Pt-Mo _x C _y /SiO ₂	-	-	52.1 (1.0)	16.0 (0.7)	37.9 (0.9)	21.5 (0.9)
Ni-Mo _x C _y /SiO ₂	-	-	78.5 (1.0)	13.3 (0.4)	21.5 (1.0)	14.6 (1.1)
K-Mo _x C _y /SiO ₂	-	-	69.5 (0.6)	19.7 (0.5)	30.5 (0.6)	25.9 (1.0)

Table K.6. Overview of phase quantification and crystallite size determined *via* Rietveld refinement of the spent RWGS catalysts.

Sample	β -Mo ₂ C		η -MoC _{0.59}		α -MoC _{1-x} / MoO _x C _y	
	wt.-% (error)	nm (error)	wt.-% (error)	nm (error)	wt.-% (error)	nm (error)
Chapter 6						
Mo _x C _y /SiO ₂ -WI*	23.6 (2.8)	6.5 (1.1)	76.4 (2.8)	4.1 (0.2)	-	-
Mo _x C _y /SiO ₂ -WI**	6.1 (2.1)	9.6 (4.1)	93.9 (2.1)	2.5 (0.2)	-	-
Mo _x C _y /SBA-15-WI	-	-	100	4.2 (0.2)	-	-
Mo _x C _y /SBA-15-HNC	-	-	100	3.5 (0.2)	-	-
Mo _x C _y /SiO ₂ -SG	-	-	100	3.5 (0.2)	-	-
Chapter 8 (SV = 60 L h⁻¹ g_{cat}⁻¹)						
Fe-Mo _x C _y /SiO ₂	18.2 (4.3)	4.2 (1.2)	81.8 (4.3)	3.9 (0.3)	-	-
Pt-Mo _x C _y /SiO ₂	18.4 (5.9)	3.6 (1.2)	47.7 (8.3)	3.5 (0.8)	33.9 (7.2)	4.4 (0.8)
Ni-Mo _x C _y /SiO ₂	23.5 (3.5)	3.6 (0.6)	76.5 (3.5)	3.6 (0.2)	-	-
K-Mo _x C _y /SiO ₂	62.5 (1.3)	9.6 (0.3)	37.5 (1.3)	4.8 (0.3)	-	-
Chapter 8 (SV = 120 L h⁻¹ g_{cat}⁻¹)						
Mo _x C _y /SiO ₂	48.2 (2.4)	6.7 (0.5)	51.8 (2.4)	4.6 (0.5)	-	-
Fe-Mo _x C _y /SiO ₂	19.9 (5.2)	5.2 (1.8)	80.1 (5.2)	3.9 (0.4)	-	-
Pt-Mo _x C _y /SiO ₂	20.1 (3.5)	4.9 (1.1)	79.9 (3.5)	4.1 (0.3)	-	-
Ni-Mo _x C _y /SiO ₂	35.3 (3.0)	4.4 (0.5)	64.7 (3.0)	4.1 (0.3)	-	-

Table K.7. Fit parameter corresponding to the radial distribution fits in Figure G.4. For Mo foil, crystal structure with ICSD code 76147 was used. S_o^2 is amplitude reduction factor, CN is coordination number, E_0 is energy shift, R is radial distance, DW is Debye-Waller factor and r is quality of fit.

Sample	S_o^2 (k)	CN Mo-C	CN Mo-Mo	E_0 (eV)	R (Å) Mo-C	R (Å) Mo-Mo	DW (Å ²) Mo-C	DW (Å ²) Mo-Mo	r-factor
Mo foil	0.95	-	-	4.7 ± 0.9	-	2.720 ± 0.005 3.147 ± 0.005	-	0.0037 ± 0.0006	0.009
β -Mo ₂ C reference	0.95 (set)	3.1 ± 0.7	4.7 ± 0.7	6.1 ± 0.8	2.077 ± 0.040	2.943 ± 0.013 3.016 ± 0.013	0.0039 ± 0.0040	0.0041 ± 0.0009	0.013
α -MoC _{1-x} reference	0.95 (set)	1.9 ± 0.8	2.7 ± 0.5	-5.8 ± 1.5	2.108 ± 0.009	2.945 ± 0.016 3.018 ± 0.016	0.0021 ± 0.0031	0.0053 ± 0.0011	0.038
Mo ₂ C/SiO ₂ -WI	0.95 (set)	2.9 ± 0.5	2.7 ± 0.5	6.8 ± 0.9	2.092 ± 0.025	2.946 ± 0.016 3.018 ± 0.016	0.0042 ± 0.0027	0.0047 ± 0.0011	0.017
Mo ₂ C/SBA-15-HNC	0.95 (set)	3.1 ± 0.7	2.0 ± 0.6	7.2 ± 1.6	2.099 ± 0.018	2.948 ± 0.018 3.019 ± 0.018	0.0054 ± 0.0034	0.0053 ± 0.0019	0.037
Mo ₂ C/SiO ₂ -SG	0.95 (set)	3.2 ± 0.8	2.6 ± 0.6	6.1 ± 1.5	2.093 ± 0.024	2.945 ± 0.016 3.017 ± 0.016	0.0053 ± 0.0036	0.0053 ± 0.0016	0.031

Table K.8. Surface area to volume ratio normalized to Mo content of fresh and spent samples.

Sample	Norm. Mo content	Average crystallite size (nm)	Mo-based SA/V ratio (S_g / volume / norm. Mo content)
Freshly carburized			
Mo _x C _y /SiO ₂ -WI	0.61	3.7	1.00
Mo _x C _y /SBA-15-WI	1.00	5.5	1.09
Mo _x C _y /SBA-15-HNC	0.80	3.7	1.30
Mo _x C _y /SiO ₂ -HNC	0.51	3.9	0.78
Mo _x C _y /SiO ₂ -SG	0.61	5.0	0.73

Spent TP-CO₂ (reactor)

Mo _x C _y /SiO ₂ -WI	0.61	29.1	0.13
Mo _x C _y /SBA-15-WI	1.00	21.3	0.28
Mo _x C _y /SBA-15-HNC	0.80	29.5	0.16
Mo _x C _y /SiO ₂ -HNC	0.51	26.9	0.11
Mo _x C _y /SiO ₂ -SG	0.61	29.1	0.13

Spent RWGS samples

Mo _x C _y /SiO ₂ -WI*	0.61	4.7	0.78
Mo _x C _y /SiO ₂ -WI**	0.61	2.9	1.05
Mo _x C _y /SBA-15-WI	1.00	4.2	1.43
Mo _x C _y /SBA-15-HNC	0.80	3.4	1.38
Mo _x C _y /SiO ₂ -HNC	n/a	n/a	n/a
Mo _x C _y /SiO ₂ -SG	0.61	3.0	1.04

Spent CO₂-ODH samples

Mo _x C _y /SiO ₂ -WI	0.61	23.6	0.25
Mo _x C _y /SBA-15-WI	n/a	n/a	n/a
Mo _x C _y /SBA-15-HNC	0.80	13.1	0.46
Mo _x C _y /SiO ₂ -HNC	0.51	13.6	0.44
Mo _x C _y /SiO ₂ -SG	0.61	35.1	0.17

Table K.9. Overview of peak positions, peak width (FWHM) and the goodness of fit (R^2), obtained through curve fitting CO₂ desorption spectra.

Sample	Desorption Temperatures (°C)							FWHM (°C)	R^2
Mo _x C _y /SiO ₂ (no CO ₂)	-	-	320	383	456	535	611	96	0.999
Mo _x C _y /SiO ₂	130	180	278	346	402	-	-	66	0.996
Mo _x C _y /Al ₂ O ₃	148	217	-	383	448	521	-	72	0.995
Mo _x C _y /ZrO ₂	-	-	271	379	420	-	-	36	0.939
Mo _x C _y /Ga ₂ O ₃	-	-	292	356	420	-	-	73	0.977
Mo _x C _y /TiO ₂	129	194	284	349	405	-	-	69	0.994

L Curriculum vitae

Personal details

Name	Wijnand Marquart
Date of birth	12-May-1994 <i>Houten, The Netherlands</i>
Nationality	Dutch

Education

07/2018 – 07/2022	PhD, Chemical Engineering <i>University of Cape Town, Department of Chemical Engineering, Catalysis Institute and DSI-NRF Centre of Excellence in Catalysis c*change, Cape Town, South Africa.</i> Thesis: Application of Molybdenum Carbide Catalysts in the CO ₂ -assisted Oxidative Dehydrogenation of Ethane. Supervisors: Assoc. Prof Nico Fischer and Prof. Michael Claeys
02/2016 – 02/2018	MSc, Chemical Engineering <i>University of Cape Town, Department of Chemical Engineering, Catalysis Institute and DSI-NRF Centre of Excellence in Catalysis c*change, Cape Town, South Africa.</i> Thesis: Effect of ammonia co-feeding on oxygenates over K-Mo ₂ C in the Fischer-Tropsch synthesis. <i>With distinction in dissertation.</i> Supervision: Assoc. Prof Nico Fischer and Prof. Michael Claeys
08/2011 – 08/2015	BSc, Chemical Engineering <i>University of Applied Sciences Utrecht (Hogeschool Utrecht), Institute for Life Sciences and Chemistry, Utrecht, The Netherlands</i>
09/2007 – 06/2011	Senior general secondary education (HAVO) <i>Dongemond College, Raamsdonksveer, The Netherlands.</i>

Internships

08/2013 – 01/2014	Intern at One-Eighty-Degrees <i>Cape Town, South Africa</i>
11/2014 – 07/2015	Intern at South Africa Institute for Advanced Materials Chemistry <i>University of the Western Cape, Cape Town, South Africa</i>

Awards and Scholarships

02/2022 – 07/2022	National Research Foundation Student Extension Support
05/2022	CATSA International Student Travel Grant, Catalysis Society of South Africa
06/2018 – 12/2021	DSI-NRF Centre of Excellence in Catalysis c*change bursary
2018, 2x 2020	EBE Research Student Award
09/2017	Faculty International Student Bursary

Journal Publications

2022	<p>M. Khasu, W. Marquart, A.J. Mayer, S. Dann, S.A. Kondrat, M. Claeys, N. Fischer</p> <p><i>“Empowering catalyst supports – unleashing the hidden potential of promoters”</i></p> <p>in preparation.</p> <p>W. Marquart, S. Raseale, M. Claeys, N. Fischer</p> <p><i>“Promoted Mo_xC_y-based catalysts for the CO₂ oxidative dehydrogenation of ethane”</i></p> <p>ChemCatChem, 2022, 14 (13), e202200267.</p>
2021	<p>S. Raseale, W. Marquart, K. Jeske, G. Prieto, M. Claeys, N. Fischer</p> <p><i>“Supported Fe_xNi_y catalysts for the co-activation of CO₂ and small alkanes”</i></p> <p>Faraday Discuss 2021, 229, 208-231.</p> <p>W. Marquart, S. Raseale, G. Prieto, A. Zimina, B.B. Sarma, J.D. Grunwaldt, M. Claeys, N. Fischer</p> <p><i>“CO₂ Reduction over Mo₂C-Based Catalysts”</i></p> <p>ACS Catalysis 2021, 11, 1624-1639.</p> <p>W. Marquart, M. Claeys, N. Fischer</p> <p><i>“Conversion of CO₂ and small alkanes to platform chemicals over Mo₂C-based catalysts”</i></p> <p>Faraday Discuss 2021, 230, 68-86</p>

2019	M. Wolf, S.J. Roberts, W. Marquart, E.J. Olivier, N.T.J. Luchters, E.K. Gibson, C.R.A. Catlow, J.H. Neethling, N. Fischer, M. Claeys <i>“Synthesis, characterisation and water-gas shift activity of nano-particulate mixed-metal (Al, Ti) cobalt oxides”</i> Dalton Trans 2019 , 48, 13858-13868.
2018	W. Marquart, D.J. Morgan, G.J. Hutchings, M. Claeys, N. Fischer <i>“Oxygenate formation over K/β-Mo₂C catalysts in the Fischer–Tropsch synthesis”</i> Catalysis Science & Technology 2018 , 8, 3806-3817.

Oral Presentations

05/2022	The 27 th North American Catalysis Society Meeting
USA	S. Raseale, <u>W. Marquart</u> , G. Prieto, M. Claeys, N. Fischer <i>“Oxidative Dehydrogenation of Ethane with CO₂ over Metal Oxide Overlayer Supported Fe_xNi_y Catalysts: Overlayer Support Effects”</i>
05/2022	The 27 th North American Catalysis Society Meeting
USA	M. Khasu, W. Marquart, A.J. Mayer, S. Dann, S.A. Kondrat, M. Claeys, <u>N. Fischer</u> <i>“Empowering Catalyst Supports – Unleashing the Potential of Promoters”</i>
11/2021	ECGP’15 International Symposium
Virtual	<u>W. Marquart</u> , M. Claeys, N. Fischer <i>“Conversion of CO₂ and C₂H₆ to platform chemicals over Mo₂C-based catalysts”</i>
11/2021	31 st International CATSA conference
Virtual	<u>W. Marquart</u> , M. Claeys, N. Fischer <i>“Oxidative dehydrogenation of C₂H₆ utilizing CO₂ over Mo₂C-based catalysts”</i>
04/2021	Carbon Dioxide Utilisation: Faraday Discussion
Virtual	<u>W. Marquart</u> , M. Claeys, N. Fischer <i>“Conversion of CO₂ and small alkanes to platform chemicals over Mo₂C-based catalysts”</i>

05/2020	Hypothesis XV (<i>Keynote lecture</i>)
Virtual	W. Marquart, S. Raseale, G. Prieto, M. Claeys, <u>N. Fischer</u> “CO ₂ reduction on Mo ₂ C”
05/2019	12 th Natural Gas Conversion Symposium
USA	W. Marquart, D.J. Morgan, G.J. Hutchings, M. Claeys, <u>N. Fischer</u> “Oxygenate formation over K/β-Mo ₂ C Catalysts – Role of Preparation and Promotion”
11/2017	28 th International CATSA conference
South Africa	<u>W. Marquart</u> , D.J. Morgan, G.J. Hutchings, M. Claeys, N. Fischer “K-Mo ₂ C as catalysts for high oxygenate selectivity in the FT synthesis”

Poster Presentations

07/2022	55. Jahrestreffen Deutscher Katalytiker
Germany	W. Marquart, M. Claeys, <u>N. Fischer</u>
05/2022	The 27 th North American Catalysis Society Meeting
USA	<u>W. Marquart</u> , M. Claeys, N. Fischer
03/2021	2021 #RSC Poster Twitter Conference
Twitter	<u>W. Marquart</u> , S. Raseale, G. Prieto, A. Zimina, B.B. Sarma, J.D. Grunwaldt, M. Claeys, N. Fischer
03/2020	2020 #RSC Poster Twitter Conference
Twitter	<u>W. Marquart</u> , M. Claeys, N. Fischer
11/2019	30 th International CATSA conference
South Africa	<u>W. Marquart</u> , M. Claeys, N. Fischer
03/2019	52. Jahrestreffen Deutscher Katalytiker
Germany	W. Marquart, D.J. Morgan, G.J. Hutchings, M. Claeys, <u>N. Fischer</u>
11/2018	29 th International CATSA conference
South Africa	<u>W. Marquart</u> , D.J. Morgan, G.J. Hutchings, M. Claeys, N. Fischer
03/2018	Syngas Convention 3
South Africa	<u>W. Marquart</u> , D.J. Morgan, G.J. Hutchings, M. Claeys, N. Fischer

<i>05/2018</i>	Engineering and Built Environment 5 th Research Expo
<i>South Africa</i>	<u>W. Marquart</u> , M. Claeys, N. Fischer
<i>05/2017</i>	Engineering and Built Environment 4 th Research Expo
<i>South Africa</i>	<u>W. Marquart</u> , M. Claeys, N. Fischer

Workshops

<i>03/2022</i>	Machine learning for process engineers
<i>South Africa</i>	
<i>11/2018</i>	ANSDAC workshop on synchrotron and neutron data analysis
<i>South Africa</i>	
<i>03/2018</i>	Syngas Convention, Autumn School
<i>South Africa</i>	